Yoshie Ishikawa · Takahiro Nakamura ·
Morihisa Saeki · Tadatake Sato · Teruki Sugiyama ·
Hiroyuki Wada · Tomoyuki Yatsuhashi *Editors*

# High-Energy Chemistry and Processing in Liquids

Springer

# High-Energy Chemistry and Processing in Liquids

Yoshie Ishikawa · Takahiro Nakamura ·
Morihisa Saeki · Tadatake Sato · Teruki Sugiyama ·
Hiroyuki Wada · Tomoyuki Yatsuhashi
Editors

# High-Energy Chemistry and Processing in Liquids

Springer

*Editors*
Yoshie Ishikawa
National Institute of Advanced Industrial Science and Technology (AIST)
Tsukuba, Japan

Morihisa Saeki
National Institutes for Quantum Science and Technology (QST)
Takasaki, Japan

Teruki Sugiyama
National Yang Ming Chiao Tung University
Hsinchu City, Taiwan

Tomoyuki Yatsuhashi
Osaka City University
Osaka, Japan

Takahiro Nakamura
Tohoku University
Sendai, Japan

Tadatake Sato
National Institute of Advanced Industrial Science and Technology (AIST)
Tsukuba, Japan

Hiroyuki Wada
Tokyo Institute of Technology
Yokohama, Japan

ISBN 978-981-16-7797-7 ISBN 978-981-16-7798-4 (eBook)
https://doi.org/10.1007/978-981-16-7798-4



This Springer imprint is published by the registered company Springer Nature Singapore Pte Ltd.
The registered company address is: 152 Beach Road, #21-01/04 Gateway East, Singapore 189721, Singapore

# Preface

The synthesis of nanomaterials and processing of nanostructures are of great significance to a wide range of fields, including chemistry, physics, biology, medicine, electronics, mechanics, and material science. Tracing the history of the methodological developments, we realize that the physical and/or chemical transformation of metals and nonmetals as well as molecules in ultimate reaction environments created by a focused laser beam, discharges, ion implantations, or microwaves has been increasingly recognized. Although the production of characteristic nano- and submicron-sized products and functional nanostructures under such extreme conditions has been extensively studied, it remains to be clarified how materials react with highly concentrated active species and/or under a very confined high-temperature and high-pressure condition. Therefore, in this book, the members of a New Area Research Group, "High-energy Chemistry in Liquid," of The Chemical Society of Japan decided to summarize the current status of high-energy chemistry and processing, particularly in the liquid phase, for a variety of materials, such as metals, semiconductors, insulators (glasses), carbons, and molecules. Descriptions of a wide range of topics are given from the perspective of a variety of research methodologies, fundamental physical and chemical processes, material preparations, and applications, to review how a high-energy source interacts with materials, and what the key factors are that determine the quality and quantity of nanoproducts and nanoprocessing. Many leading researchers in this field contributed to the project; we are confident that the resulting volume will be of much interest to a broad range of readers.

This book consists of three parts which explore the characteristic chemistry and processing of different target materials using various energy deposition processes. Part I describes the high-energy chemistry and processing particularly for metals. The application and fundamental of photothermal bubble generation triggered by laser pulses are overviewed. In addition, the preparation of metal and solid solution alloy nanoparticles by laser-induced nucleation and the production of core–shell or magnetic metal nanoparticles by plasma-assisted electrolysis are summarized. Application for the recovery of precious metals from spent nuclear fuel by laser-induced particle formation and strategies for controlling the nanoparticle surface by laser ablation in liquids are also described. Part II collects information on the

high-energy processing of nonmetals. The details of the production mechanisms for crystalline spherical submicrometer particles by laser melting in liquid followed by the strategy for mass production using continuous flow system and laser-induced backside wet etching of hard and brittle transparent materials are reviewed from the viewpoint of industrial applications, and the preparation of nanodiamonds with controllable luminescence properties, low-threshold and wavelength tunable random lasers, and colloidal luminescent silicon quantum dots as well as inorganic nanomaterials for optical applications like bioimaging is described. Part III focuses on the high-energy chemistry of nonmetals. Promotion of various chemical reactions by microwave irradiation and modification of morphology and electronic structures of carbon-based electrocatalysts by ion implantation are described, and unique laser processing and chemical processes such as polymorphism control of amino acid crystals by optical trapping-induced crystallization, defect engineering of photocatalysis for the enhancement of photocurrent or hydroxyl radical generation, and building up molecules to carbon nanoparticles in laser-induced plasma filaments are introduced.

Finally, we express our sincere gratitude to all the contributors, whose deep insights on this field should make this book an invaluable resource.

Tsukuba, Japan — Yoshie Ishikawa
Sendai, Japan — Takahiro Nakamura
Takasaki, Japan — Morihisa Saeki
Tsukuba, Japan — Tadatake Sato
Hsinchu City, Taiwan — Teruki Sugiyama
Yokohama, Japan — Hiroyuki Wada
Osaka, Japan — Tomoyuki Yatsuhashi

# Contents

# Part I
# High-Energy Chemistry and Processing of Metals

# Chapter 1
# Laser-Induced Bubble Generation on Excitation of Gold Nanoparticles


**Shuichi Hashimoto and Takayuki Uwada**

**Abstract** This chapter focuses on pulsed-laser-induced explosive boiling of the liquid medium adjacent to gold nanoparticles that are suspended in solution. Although the laser-induced cavitation via multiphoton absorption has been known for a long time, photothermal generation of steam bubbles on irradiating the nanoparticles is by far efficient because of surface plasmon excitation. Basic properties of pulsed-laser-induced photothermal bubbles such as threshold laser fluences, bubble lifetimes and nanoparticle temperatures have been investigated experimentally. Such experiments inspired much interest from theoretical and computational studies, which accelerated thorough understanding of the fundamental processes of the temperature-induced phase transition confined to the local area surrounding the nanoparticles. Furthermore, it has been demonstrated recently that photothermal bubbles have found unprecedented applications such as promoting microscale lasing, enormously enhancing the speed of photophoretic movement for nanoparticles and sensitizing photoporation through cell membranes. We will discuss the application point of view also in this task. Finally, we will refer to underlying challenges and future prospects of the transient vapor nanobubbles.

**Keywords** Gold nanoparticles · Pulsed-laser excitation · Localized surface plasmon resonance · Plasmonic nanobubbles · Photothermal effect

## 1.1 Introduction

Gold nanoparticles (Au NPs) that represent plasmonic nanoparticles are excellent light absorbers and light scatterers at the resonance wavelengths in the visible region.

S. Hashimoto (✉)
Advanced Engineering Courses, NIT Gunma College, 580 Toriba-machi, Maebashi 371-8530, Japan
e-mail: hashichem@gunma-ct.ac.jp

T. Uwada
Department of Chemistry, Josai University, 1 Chome-1 Keyakidai, Sakado, Saitama 350-0248, Japan
e-mail: uwada@josai.ac.jp



Y. Ishikawa et al. (eds.), *High-Energy Chemistry and Processing in Liquids*,
https://doi.org/10.1007/978-981-16-7798-4_1

This is because Au NPs greater than 2–3 nm support localized surface plasmon resonance (LSPR) that is described by a coherent oscillation of conduction-band electrons interacting with incoming light [1]. The excitation of LSPR affords an ultrafast series of events [2]. Photoexcitation of AuNPs and subsequent relaxation processes are given briefly in Fig. 1.1. Figure 1.1a represents LSPRs or simply plasmons, and this LSPR collects incident light far more efficiently than the physical cross section of the Au NP (Fig. 1.1a lower column). LSPRs have incredibly short lifetime and decay both radiatively and nonradiatively (Fig. 1.1b). The former plays a key role in the plasmonic enhancement of the electric field in the near-field regime, whereas the latter decay is responsible for generating hot electrons of very high kinetic energies (Fig. 1.1b lower column). The hot electrons decay through collisions with electrons and lattice (Fig. 1.1c): relaxation from a non-Fermi to Fermi electron distribution through electron–electron (e–e) scattering, cooling of hot-electron gas through electron–phonon (e–ph) scattering and heat dissipation from Au NPs to the environment (Fig. 1.1d) through phonon–phonon (ph–ph) scattering.

This chapter focuses on interaction of pulsed lasers with plasmonic nanoparticles suspended in solution, resulting in vapor nanobubble generation. As mentioned above, thermal conduction from photo-irradiated NPs raises the temperature of the surrounding medium (Fig. 1.1d). When the medium heating exceeded the threshold of liquid–gas phase transition, bubbles were generated through boiling of the local liquid next to the NPs, while liquid bath is at room temperature [3, 4]. In this context, such vapor nanobubbles are photothermally generated nanobubbles because light-to-heat conversion by Au NP is the fundamental origin. The photothermal nanobubbles

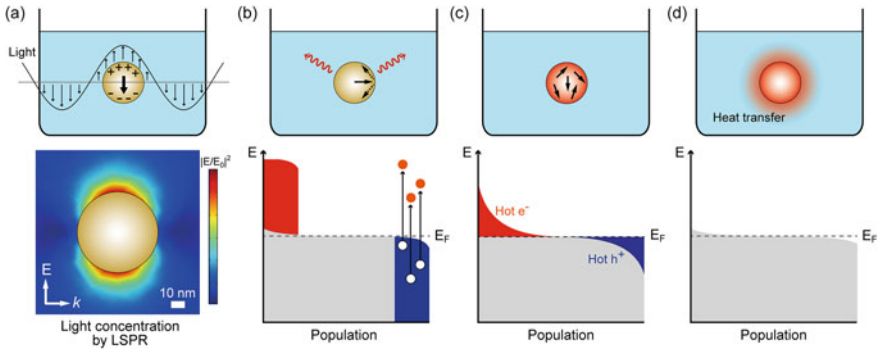


**Fig. 1.1** Sequential events that occur on photoexcitation of AuNPs. **a** upper: light absorption generates LSPR that is a coherent oscillation of conduction electrons. Lower: light condensation that is significantly greater than its physical cross section. **b** In the first 1–100 fs following Landau damping, the non-thermal distribution of electron–hole pairs decays either through re-emission of photons or through carrier multiplication caused by electron–electron interactions. **c** Hot carriers will redistribute their energy by electron–electron scattering processes on a timescale ranging from 100 fs to 1 ps. **d** Heat conduction to the surroundings on a timescale ranging from 100 ps to 10 ns. $E_F$ represents Fermi energy

are transient species and have a typical lifetime of a few nanoseconds when the duration of laser pulses used for generation is shorter than 10 ns. The bubble formation occurred in water from a superheated liquid state at approximately 550 K, not at the boiling temperature of 373 K [5]. This phenomenon may deserve commenting, and we will come back this point later. The bubble lifetimes were largely dependent on the maximum bubble sizes. Further, the threshold laser fluence, the onset of nanobubble production, depended on the NP diameter [6–8]. The detailed discussion of the bubble threshold may shed light on the fundamental process of heat transfer leading to bubble formation [9, 10]. Here, we highlight the photothermal micro/nanobubbles that dynamically grow and collapse on the surface of NPs subject to short pulsed-laser illumination. Note that the discussion of cavitation bubbles is not within the scope of our study because the cavitation bubbles have been observed on pulsed-laser illumination of liquids in the absence of NPs [11]. Cavitation is a phenomenon in which the static pressure of a liquid reduces to below the liquid's vapor pressure, leading to the formation of small vapor-filled cavities in the liquid.

This chapter will not include the description of bubble formation through continuous wave (CW) laser illumination of Au NPs because of a limited space. Due to long lifetimes up to several seconds, the CW laser-induced bubbles provided rich physics and chemistry [12]. Readers interested in further information are encouraged to refer to the literature [13]. At this moment, we should point out the merit of transient nanobubbles generated by short pulse excitation over the long-lived bubbles produced by CW illumination. By outputting a high peak power within a limited pulse duration, pulsed-laser excitation can provide the means to obtain high spaciotemporal control for bubbles. Since the heat transfer to the medium completes within nano- to microseconds, medium heating is insignificant without heat accumulation. As a result, bubble energy can effectively be applied for mechanical works and shock/acoustic waves. On the other hand, CW laser excitation results in significant heat accumulation that can be inadequate for biological systems.

## 1.2 Bubble Generation on Short Pulsed-Laser Excitation of Colloidal Au NPs

Historically speaking, photothermal microbubbles have been observed by diffraction-limited imaging on pulsed-laser irradiation of black microparticles suspended in solution [14]. Subsequently, the Plech group pursued picosecond time-resolved studies of nanobubble dynamics on femtosecond laser excitation of colloidal Au NPs, combined with monitoring by the picosecond puled X-ray scattering form a synchrotron radiation [3, 4]. The X-ray scattering was not very straightforward to visualize bubble dynamics such as diameter change with time. However, it was powerful to observe the lattice melting of Au NPs on laser illumination [15]. Thus, Au NPs were found to be heated possibly at least to a liquid state during the bubble formation. Lapotko, on the other hand, has focused on the single particle measurement of bubbles using a Au NP

immobilized on a substrate under the optical microscope [16]. Besides imaging, his group measured the time growth and decay of the light scattering signals associated with a bubble from a Au NP at a fixed wavelength on 0.5 ns pulsed-laser excitation. It was not until the picosecond time-resolved measurement by the Hashimoto group that optical extinction (absorption and scattering) spectra in the visible region were characterized for colloidal Au NPs during the bubble formation/collapse [8]. Bubble dynamics were characterized by the time-dependent spectral changes that provided the direct information of bubbles distinct from the particle heating and cooling. The three groups: Plech, Lapotko and Hashimoto have investigated experimentally the fundamental properties of plasmonic nanobubbles such as bubble nucleation temperature, threshold fluences and bubble lifetimes by taking advantage of their own methods. We will discuss below these fundamental issues regarding plasmonic nanobubbles.

Before getting into the details of nanobubble properties, we describe how we can follow the nanobubble dynamics using the optical spectroscopy. The transient extinction spectra of colloidal Au NPs exhibited the ultrafast bleaching of the characteristic LSPR band, followed by the recovery of the bleaching signals. A prototypical example is given in Fig. 1.2a in which 60-nm-diameter Au NPs were excited by a 15 ps laser at an excitation wavelength of 355 nm [8]. The transient bleaching signals were instantaneously observed with the laser pulse followed the remarkably fast recovery. The origin of such bleaching/recovery of the transient signals was ascribed to heating and cooling of the Au NPs [17]. This transient spectral change can be reproduced by LSPR spectra dependent on temperature, given in Fig. 1.2b, which is the spectral simulation based upon Mie theory [1]. With increase in temperature, LSPR undergoes the significant broadening that causes LSPR spectral bleaching in the transient spectra on laser illumination, the extent of which strongly depends on the particle temperature. It was found that the lattice temperature of ~1000 K was reached at high pump intensities. The time trace of the bleaching/recovery signals completed after a sufficient time has elapsed because of heat conduction to the surrounding medium. However, it has been demonstrated that the amplitude of the background signals increased as the pump laser intensity increased (Fig. 1.2c). The background signals are an optical signature of bubble formation. The experimental data showed a threshold laser intensity that produces the particle temperature of $550 \pm 50$ K [5].

The bubble signals are basically caused by Rayleigh light scattering that largely depends on the bubble diameter ($r^6$-dependence) [8]. A greater scattering signal is generated as the bubble diameter increases. From Fig. 1.2c, we note that the scattering from bubble is superimposed on the LSPR bleaching of Au NPs. The spectral simulation using a concentric core–shell structure of the bubble/Au NP is in Fig. 1.2d. The graph reveals that such simulated spectra well-reproduce the experimental ones and that more positive extinction signals occur for bubbles with greater diameters. Note, however, that negative extinction is predicted to occur for bubbles with small diameters in which the bubbles act to reduce the absorption of Au NP because of the reduced refractive index of the medium surrounding the Au NP, rather giving an enhanced light scattering that increases total extinction.

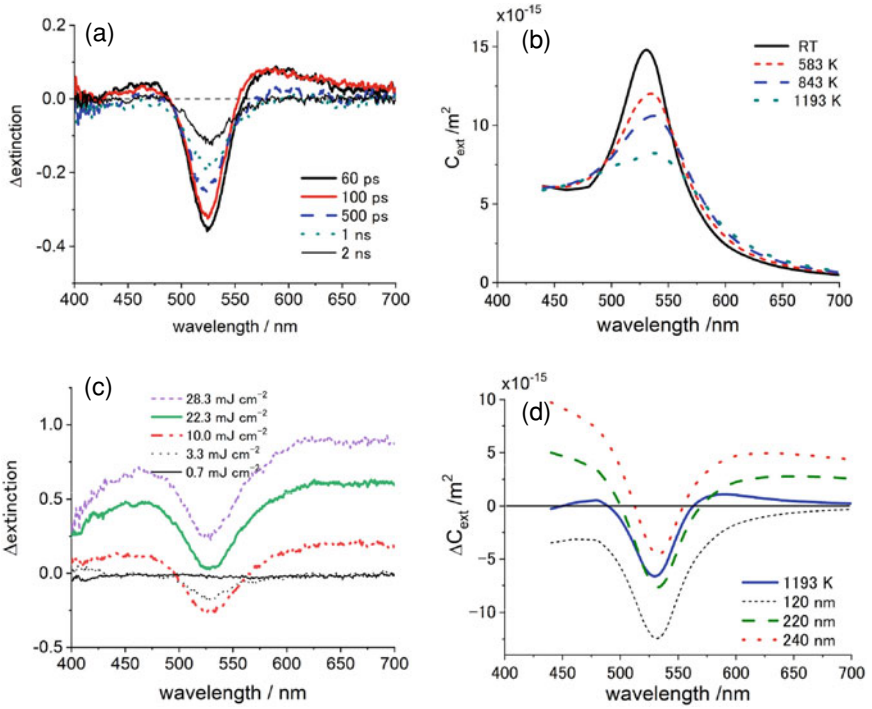


**Fig. 1.2** Pump-probe measurements of transient extinction (absorption and scattering) spectra of 60-nm-diameter aqueous colloidal Au NPs excited by a 15 ps laser at the excitation wavelength of 355 nm: **a** transient extinction spectra in the absence of bubbles at 60 MPa hydrostatic pressure; **b** simulated temperature-dependent extinction spectra of 60-nm-diameter aqueous Au NP, which interpret the observation in (**a**); **c** experimental bubble spectra at various excitation intensities at a time delay of 2 ns (at 0.1 MPa); **d** simulated bubble spectra of various diameters (concentric Au NP core-bubble shell structures are assumed). Adapted with permission from Katayama et al. [8] (Copyright 2014 American Chemical Society)

We have stated already the concentric core–shell bubble model that may form because of an effective heat transfer from the metal surface. Besides the core–shell structure that was captured by optical microscopy for microbubbles, two other types have been proposed [18, 19]. Figure 1.3 summarizes the bubble models (upper) and the scanning electron microscopy (SEM) images (lower) in which bubbles were trapped using tetraethoxysilane as a trapping agent. In the SEM experiment, the bubbles were generated by irradiating nanosecond pulsed lasers with a wavelength of 355 nm in aqueous colloidal Au NPs.

In the transient X-ray scattering and extinction spectral measurements quoted above [3, 6], such a core–shell model has been successfully employed for estimating bubble diameters from time-resolved spectroscopic measurements [6, 8]. The confetti (b) can be found in the earliest stage of bubble nucleation, and this structure has been observed by the transmission electron microscopy (TEM) coupled with femtosecond

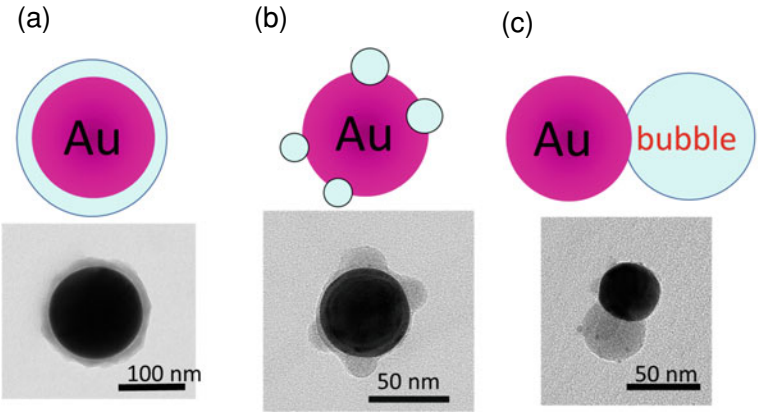


**Fig. 1.3** Bubble structure models; **a** core–shell, **b** confetti and **c** Janus. SEM images are unpublished results from Hashimoto laboratory

laser excitation [18]. The Janus structure (c) has been proposed initially without experimental proof [19]. The bubble trapping experiment suggested indirectly the existence of all three structures at the nanoscale.

Now, we discuss three important properties of bubbles, bubble generation temperature (~550 K), threshold laser fluence and bubble lifetimes. First, we interpret how the pulsed-laser-induced plasmonic bubbles have been rationalized to occur from superheated solvent next to the NPs using the phase diagrams of water [20]. Figure 1.4a upper column compares line shapes of P(V) at different temperatures for Van der Waals fluid. Notably, the boiling temperature $T_b$ and critical temperature $T_c$ are of relevance to the phase transitions. At temperatures above $T_c$, the isotherms are monotonic, implying that only one state can exist at a given pressure. At temperatures below $T_c$, phase coexistence of liquid (L) and gas (G) can occur. Liquid-to-gas transition occurs along the line L to G. A red line shows the coexistence curve, and the light blue area represents the region of coexistence. Further, the yellow zone separated by a spinodal curve (red dashed line) predicts unusual behavior. In the latter area of the diagram, we can see that pressure increase causes volume expansion $(\partial P/\partial V)_T > 0$, meaning that the system is not stable. Another important point is that during the volume change from L to G on the isotherm curves molecules experience an energy barrier because of the concave shape of Helmholtz free energy, F, as shown in the lower column. The energy barrier we can see for the curve at $T_b$ is the origin of superheating. Thus, fluid can remain liquid even if the boiling temperature is exceeded. However, the height of the energy barrier gradually decreases on going from $T_b$ to $T_c$. As a result, boiling is more likely to occur for superheated water at temperatures $T > T_b$.

Figure 1.4b represents a diagram that expresses pressure as a function of temperature for water. If a Au NP in water is heated by laser illumination from 293 K at a constant pressure of 1 atm, the water temperature next to the NP increases along the

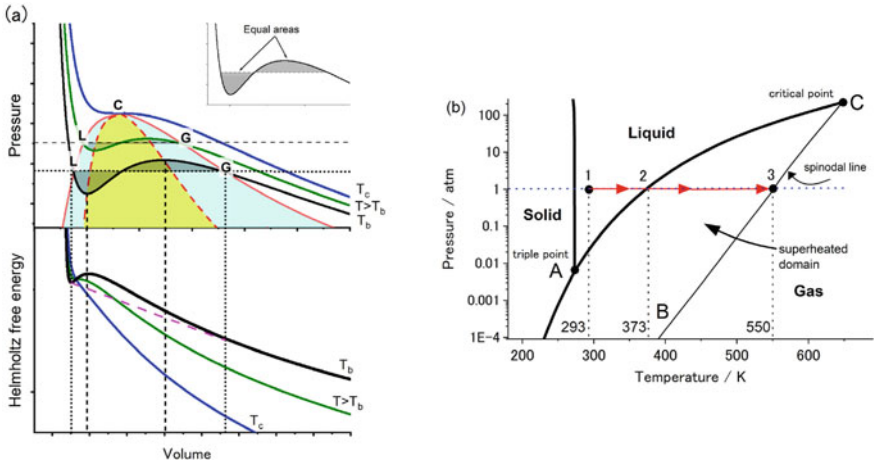


**Fig. 1.4** **a** Upper: Series of P-V diagrams of isotherms of increasing temperatures from boiling temperature ($T_b$) to critical point ($T_c$); Lower: corresponding Helmholtz free energy versus V curves. **b** Phase diagram that represents pressure as a function of temperature for water. All the possible states, gas, liquid and solid, are shown

horizontal line, reaching first a boiling temperature of 373 K. If the NP is suspended in clean water contained in a chamber with smooth surfaces, it is likely that superheating occurs until the spinodal temperature of 550 K is reached. The spinodal represents the intrinsic stability limit of the liquid $\left((\partial T/\partial S)_P = 0;\ (\partial P/\partial V)_T = 0\right)$. At the spinodal, the superheated liquid phase is no longer stable with respect to the random density fluctuations [21]. As a result, an explosive boiling occurs, generating a steam bubble. This is a situation that is predicted for isolated Au NPs.

Although the heating of isolated Au NPs results in bubble generation at a particle temperature T ~ 550 K, the CW laser heating of Au NP aggregates formed in water induced formation of micrometric bubbles at a temperature that coincides with the boiling point of water under atmospheric pressure [22]. This result was interpreted by the collective heating effect [13]. If many NPs closely located are heated, water molecules undergo heating from many NPs simultaneously. As a result, the heating of the solvent is no longer limited to a nanoscale local space around a Au NP, but a certain volume of water can be heated, resulting in a situation similar to bulk heating. Further, if the CW laser is used instead of the pulse, heat accumulation takes place with time. These are the explanations for the working principle of collective heating.

Second, we look into the threshold laser fluence versus Au NP radius/diameter for bubble formation.

Figure 1.5 gives both experimental and computational curves from different laboratories.

Siems et al. observed monotonous decrease with increasing diameter (filled red squares in Fig. 1.5a) [6], whereas Katayama et al. observed a bathtub shape with a minimum at 60-nm-diameter (Fig. 1.5b) [8]. The monotonous decrease has also

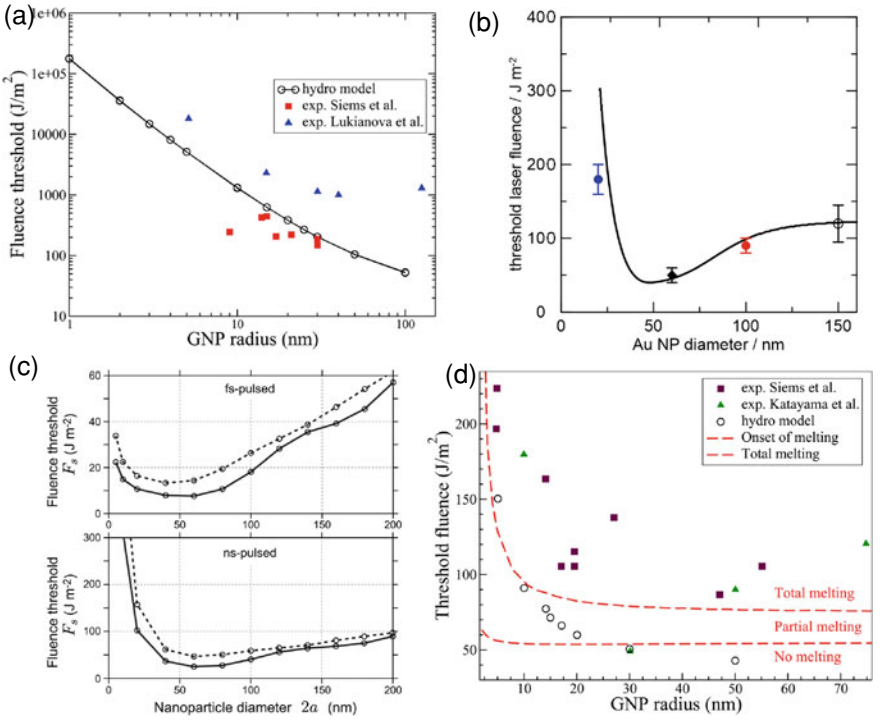


**Fig. 1.5** Bubble formation threshold as a function of Au NP radius/diameter. **a** Comparison between the simulation for nanosecond pulses (Lombard et al. [10]) and the experiments by Siems et al. [6] (red squares; nanosecond pulses at the wavelength of 355 nm) and Lukianova et al. [7] (blue triangles; 0.5 ns pulses at the wavelength of 532 nm). **b** Transient extinction spectroscopy measurement with 15 ps laser excitation at a wavelength [8]. **c** Computational results by Baffou et al. [9] both for fs- and ns-pulses at the wavelengths of 355 nm (dashed line) and 532 nm (solid line). **d** Comparison between the simulation by Lombard et al. [10] and the experiments by Siems et al. [6] (red squares) and Katayama et al. [8] (blue triangles). **a** and **d** Adapted with permission from Lombard et al. [10]. (Copyright 2017 American Chemical Society). **b** Adapted with permission from Katayama et al. [8] (Copyright 2014 American Chemical Society). **c** Adapted with permission from Metwally et al. [9]. (Copyright 2015 American Chemical Society)

been observed by Lukianova et al. by using a single particle light scattering measurement [7]. Note, however, that their threshold values (filled blue triangles in Fig. 1.5a) were much higher than the values obtained by Siems et al. The monotonous decrease observed is intuitively understandable because the particle cooling depends on the surface-to-volume ratio and cooling is faster for smaller diameters [23]. Indeed, with the rigorous computational method using a hydrodynamic model and thermal model, the Marebia group obtained a monotonous decrease curve [10]. Their hydrodynamic model used in-depth treatment of bubble generation in terms of density change of water. The previous thermal model calculated spaciotemporal distribution of temperatures in the medium surrounding a Au NP [24]. By contrast to the result of Merabia,

numerical calculations using the thermal model by Baffou shown in Fig. 1.5c have displayed that the dependence of the fluence threshold with respect to the nanoparticle diameter features a bathtub profile [18], with a minimum fluence threshold at around 60 nm in diameter, in good agreement with the experimental observation by the Hashimoto group given in Fig. 1.5b. The points of discussion by Baffou are as in the following.

(i) The threshold fluence increase for small NPs is due to fast energy release to the surroundings.
(ii) The threshold fluence increase for large NPs arises from the nonlinear absorption cross section with respect to the NP volume. For small diameters below 60 nm, the absorption cross section is proportional to the NP volume but saturates.
(iii) Under fs-pulsed illumination, and under the assumption of no interface thermal resistivity, the maximum temperature increase $\delta T_{NP}$ can simply be calculated using $\delta T_{NP} = \sigma_{abs} F / V c_m$ ($\sigma_{abs}$: absorption cross section of the NP, $F$: fluence of the pulse, $V$: NP volume and $c_m$: volumetric heat capacity of gold), without conducting numerical simulations, except for NP diameters smaller than 40 nm.
(iv) A NP interface thermal resistivity has no effect under ns-pulsed illumination, except for large NPs and large values of the interface thermal resistivity.
(v) A NP interface thermal resistivity has a strong effect in the fs-pulsed regime, irrespective of the nanoparticle diameter.

With respect the curve shape, computational curve by the Merabia group and that by the Baffou group is somewhat contradictory. Although the Merabia group was aware of the previous result by Baffou et al., the former did not comment on this point. The Merabia's group were much concerned about the difference of their computational result from the experimental threshold values. They argued that the threshold values by hydrodynamic calculation may have remarkable improvement if they consider the melting Au NPs during the bubble formation (Fig. 1.5d). With bubble generation, melting and evaporation of Au NPs have been postulated previously since the particle temperatures can go somewhat uncontrollably high inside the bubble [24].

At this point, we highlight the issue that the single particle study gave at least an order of magnitude greater threshold fluences of colloidal experiment (Fig. 1.5a). To account for their greater values, the Lapotko group ascribed to the Laplace pressure, the effect of surface tension, on the threshold of a bubble generation by optical heating. The Laplace pressure is given by $P_{Laplace} = 2\gamma / R_{bubble}$ ($\gamma$: surface tension, $R_{Bubble}$: bubble radius) and acts to collapse a bubble to a greater extent as the radius is smaller. However, the calculation by the Merabia group revealed that the effect of the Laplace pressure is minor [10]. From the experimental point of view, we can point out that measuring an accurate fluence is challenging because of uncertainties in measuring beam diameters and intensities under the microscope.

Finally, we describe bubble lifetimes on pulsed-laser excitation. Ensemble studies on 100 fs excitation of bubble dynamics using time-resolved X-ray measurements revealed that the lifetime of a bubble surrounding a 9-nm-diameter Au NP was

400 ps (max. bubble diameter: 20 nm) at 40 mJ $cm^{-2}$, and the lifetime of a bubble surrounding a 36-nm-diameter Au NP was 1.7 ns (max. bubble diameter: 75 nm) at 13.8 mJ $cm^{-2}$ that is a threshold fluence [3, 4]. The bubble dynamics were well modeled using the Rayleigh–Plesset equation [25]. The Hashimoto group observed the bubble lifetime of 10 ns for 60-nm-diameter colloidal Au NPs irradiated with 15 ps lasers at a wavelength of 355 nm and a fluence f 5.2 mJ $cm^{-2}$ (threshold fluence), using a transient extinction spectroscopy [8]. The maximum diameter observed was $260 \pm 40$ nm. In this case, the bubble decay time was much longer than the rise time, which is inconsistent with the Rayleigh–Plesset equation. The Lapotko group measured the bubble lifetime by observing the optical scattering response of a single Au NP that was excited by a 532 nm laser with a pulse width of 0.5 ns. They obtained bubble lifetimes of $18 \pm 3.5$ ns for a 30-nm-diameter Au NP and $9 \pm 1$ ns for single 90 and 250-nm-diameter Au NPs [7, 12]. They found that the lifetime of NP-generated bubbles increased with increasing incident fluence and that the vapor bubble lifetime was proportional to the maximum bubble diameter. Although the proportionality of bubble lifetime and maximum diameter is a rule of sum that well-describes the plasmonic nanobubbles, systematic studies are still lacking to describe precisely the pulse width-, fluence- and particle size-dependent lifetimes.

## 1.3 Recent Applications

The vapor nanobubbles photothermally generated using Au NPs have been demonstrated for potential applications in cancer therapy using bubble-induced shock waves [26], photoacoustic imaging using photoacoustic signals from bubbles [27] or solar energy conversion exploiting photothermal boiling of water [28]. These areas are still in progress to produce meaningful outcomes. Of particular interest is the solar bubble generation that has a potential application to sterilizing water in developing countries [29]. Recently, we have seen unprecedented applications of pulsed-laser-induced plasmonic bubbles in various fields. Here overview a few examples.

### *1.3.1 High-Speed Movement of Au NPs Encapsulated in a Nanoscale Bubble*

Light can move objects through optical forces, enabling optical delivery of microparticles and NPs [30]. The optical manipulation is applicable to optical sorting, i.e., separation of particles exploiting particle size and material properties such as a refractive index. Previously, it was not feasible to give control over the velocities of moving particles. The achieved moving speed was 10–100 $\mu m\ s^{-1}$ so far [31, 32]. Here, we show an example of bubble-induced high-speed motions realized by irradiating femtosecond laser pulses at a high repetition rate.

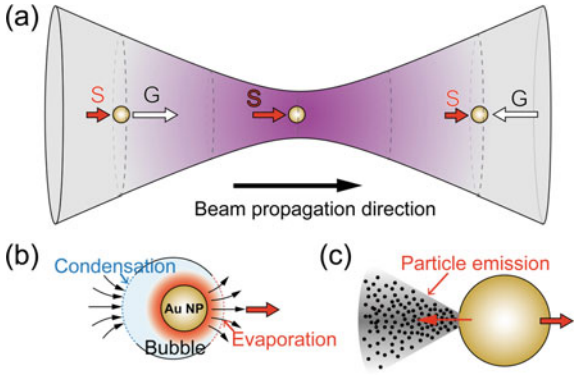


**Fig. 1.6** **a** Optical forces acting on Au NPs along the laser beam propagation direction. S represents the scattering force, while G represents the gradient force. The direction and the magnitude of the forces are dependent on the location relative to the laser focus. **b** Bubble-induced propulsion. **c** Acceleration due to heating-induced emission of small particles

In this case, directed motions of silica-core Au-shell NPs (100-nm-diameter silica-core 10-nm-thick Au shell) suspended in water were activated by irradiating a 800 nm (center wavelength) laser beam with a repetition rate of 80.7 MHz (the pulsed duration is 94 fs, and the time interval between pulses is 12.4 ns) [33]. The fs laser was focused by passing through a 20 × objective lens (numerical aperture: 0.4). The power of 690 mW exceeded the bubble formation threshold, and the bubble encapsulated the NPs. As a result, some NPs were found to move along the beam propagation direction (positive motion), and some in the opposite direction (negative motion). Au NPs moved with unprecedented speeds both for the positive (maximum speed: 336,000 $\mu m\ s^{-1}$) and for the negative (maximum speed: 245,000 $\mu m\ s^{-1}$) directions. The forward and backward movements were produced by not only optical pushing but also pulling forces from a single Gaussian beam. Optical forces that may act on the NP can depend on the location relative to the laser focus as illustrated in Fig. 1.6. The two major forces are gradient force (G) and scattering force (S). The gradient force, G heads to the laser focus where the magnitude of G is zero because it depends on the intensity gradient. On the contrary, S is always in the direction of beam propagation, and its magnitude is proportional to the laser intensity. It is reasonable to assume that the optical force at the initial position determines the particle movement.

The enormously high speeds observed were interpreted as the following: While the laser-excited NP encapsulated in a bubble moves forward, it keeps evaporating water, maintaining a vapor cushion in front of it, and extends the bubble boundary forward.

Although not described in the study above, we suspect a potential effect of laser-induced evaporation that can accelerate the Au NPs. Without a continuous boosting mechanism, it seems difficult to maintain such a high speed that was originally realized by initial optical forces. As already mentioned, Au NPs can melt and evaporate inside the bubble [24] because of high-intensity laser heating. It has been demonstrated that ~40 $\mu m$-sized spherical stainless particles were accelerated in air caused by an evaporative propulsion force in the direction of laser beam propagation when irradiated with a 1070 nm CW laser with an output of 1–2 MW $cm^{-2}$ [34]. In this case, an approximate speed of 12,500,000 $\mu m\ s^{-1}$ was achieved. Additionally, it

has been demonstrated that micrometer-sized platinum and other metal particles migrated inside melt borosilicate glass at a speed of 10,000 μm $s^{-1}$ in the counter direction of the laser beam when illuminated by 514 nm CW laser at a power of 1 MW $cm^{-2}$ [35]. These results suggest that evaporative propulsion can significantly accelerate the movement of particle under laser heating.

### *1.3.2 Micro- and Nano-Lasers Encapsulated in Bubble*

Plasmonic bubbles have been applied to optical enhancer for laser oscillation at small scales. In one approach, photoexcitation of a single plasmonic NP in solution enabled a whispering-gallery-mode (WGM) droplet resonator associated with small micro/nanobubbles, formed by laser-induced heating [36]. Droplets containing dye-generated lasing modes with wavelengths depend on the size of the droplet, refractive index of the medium and surrounding environment. It was demonstrated that colloidal suspension of 20-nm-diameter Au NPs gave cavity diameters of 4.8 μm with a free spectral range (FSR) of 12 nm when excited with a 130 fs pulse with a central wavelength of 400 nm and at a repetition rate of 1 kHz (Fig. 1.7a). The droplets containing Coumarin 500 and plasmonic NPs showed sharp emission peaks in the wavelength range of 475–515 nm. WGM resonators are usually fabricated from solid-state materials. Soft cavities created with liquids or gels permit direct sensing where an optical cavity is both the sensing unit and the sample under analysis. In addition, soft cavities enable strong interactions of a plasmonic NP with the WGMs because of its location inside the cavity mode.

Another example is a solid-type laser named spaser (**s**urface **p**lasmon **a**mplification by **s**timulated **e**mission of **r**adiation). The spaser consists of a plasmonic NP surrounded by a nanoshell of the gain medium (Fig. 1.7b, left). The spaser can generate a single mode emission that is a spectrally tunable bright light

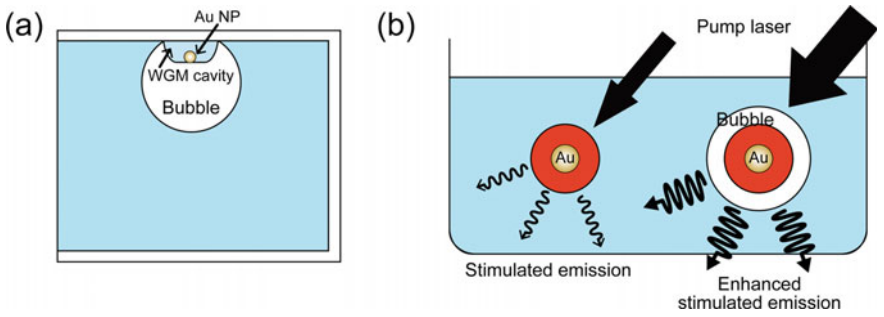


**Fig. 1.7** Schematic of bubble-enhanced surface plasmon lasers; **a** single plasmonic NP in solution realizing a whispering-gallery-mode (WGM) droplet resonator associated with small micro/nanobubbles, **b** left: so-called spaser consisting of a Au NP core and a silica-shell embedded with laser dye molecules; right: a spaser encapsulated in a photothermal nanobubble

without saturation. The properties originate from stimulated emission amplification effects. Specifically, the plasmonic nanolaser was constructed by a core–shell structure consisting of a Au NP surrounded by a silica-shell doped with a uranine (disodium fluorescein) dye [37]. In this example, the excitation was provided by an OPO laser at a wavelength of 488 nm with 5–7 ns pulses. Using a 22 nm spaser with a 10 ± 1.9-nm-diameter Au NP core and a 6 ± 2.2 nm-thick shell, the lasing threshold was observed at a laser energy fluence of 26 ± 6.3 mJ $cm^{-2}$. For a lager 60 nm spaser, the threshold was reduced to 1.9 ± 0.6 mJ $cm^{-2}$. Above the threshold, the light output—pump in dependence demonstrated a straight line with emission spectral narrowing from 30–40 nm to 8–10 nm. Further increase in pump fluence led to the formation of vapor nanobubbles around spasers due to laser heating of the spaser particle leading to evaporation of the liquid medium surrounding the particle (Fig. 1.7b right). The appearance of bubbles is accompanied by nonlinear enhancement of stimulated emission intensity and further width narrowing. The maximum ratio of the stimulated emission intensity to the spontaneous emission background was 740 ± 95. The narrowest emission peak observed was 0.8 ± 0.2 nm. Both parameter levels were significant improvements over the previous results.

The origin of enhancement of spasing due to nanobubble formation has been ascribed to strong refractive, scattering and thermal lens effects in highly localized heated areas, especially in the associated bubbles that can be responsible for the light concentrating and redirecting. The original (without a nanobubble) spaser is a nanoshell with a Au core covered with dielectric shell containing dye molecules to produce the gain, embedded in water (the uniform medium). When a nanobubble is formed, another nanoshell appears between the gain shell and the embedding medium that contains water vapor. According to the authors, the main effect of the formation of a vapor nanobubble around the spaser is that dielectric screening of the surface plasmon-induced charge is reduced. This leads to an increase in the surface plasmon frequency, $\omega_n$. In fact, the spaser frequency increases from the initial value of $\omega_n = 2.5$ eV in the absence of the nanobubble to $\omega_n = 2.6$ eV for a 30 nm radius nanobubble. If the gain medium working frequency, $\omega_n$, exceeds the plasmon frequency, then the nanobubble formation brings the spaser closer to a perfect resonant condition. Consequently, the stimulated radiation of the surface plasmons becomes more efficient, which has been shown by this article. Presumably, the nanobubbles can provide dynamic optical feedback from its "wall" boundary, as well as refraction effects that can also lead directional emission.

### *1.3.3 Plasmonic Nanobubble Can Disrupt Cell Membrane and Biofilm*

There is a great interest in delivering macromolecular agents into living cells for therapeutic purpose. Physical methods including electroporation using electric pulses and sonoporation using ultrasounds have been developed but they still suffer from

limited success in throughput and cell viability. Most importantly, translocation of the therapeutic macromolecules from the endosomes after endocytosis into the cytoplasm remains a major bottleneck. To overcome the difficulty, plasmonic nanobubble was used as a promising candidate for a physical approach to permeate the cell membrane [38].

First, Au NPs were adsorbed onto HeLa cells' surface from solution. Subsequently, positively charged Au NPs (70 nm) were used to facilitate interaction with the negatively charged cell membrane. Following the incubation of cells, Au NPs were adsorbed. A pulsed-laser irradiation was performed (pulse duration: 7 ns; wavelength: 561 nm from OPO laser). A low energy led to the heating of the cell membrane, while vapor nanobubbles were formed at high laser intensities above the threshold, 1.02 J $cm^{-2}$. The threshold observed is much higher than those observed previously in aqueous solution. Confocal microscopy images were acquired to test the viability of the cells labeled with calcein red-orange AM and the intracellular delivery of fluorescein isothiocyanate (FITC)-dextran (10 kDa). There was no noticeable decrease in cell viability up to 2.04 J $cm^{-2}$. Further increasing the laser fluence to 4.08 J $cm^{-2}$ reduced the number of positive cells, likely due to the onset of cytotoxic effect of vapor nanobubbles that can damage cells when they grow large. FITC-dextran loading was much more efficient when mediated by plasmonic nanobubbles than by direct heating of the plasma membrane. For instance, the loading efficiency of 10 kDa FITC-dextran increased 2.5 fold by heating at 0.38 J $cm^{-2}$ from the control, whereas it increased 12.5 fold of control by irradiation at nanobubble-forming 4.08 J $cm^{-2}$.

The conceptual scheme of photoporation on cell membrane to introduce polymers into cells is shown in Fig. 1.8. In this scheme, direct laser-induced photopo-

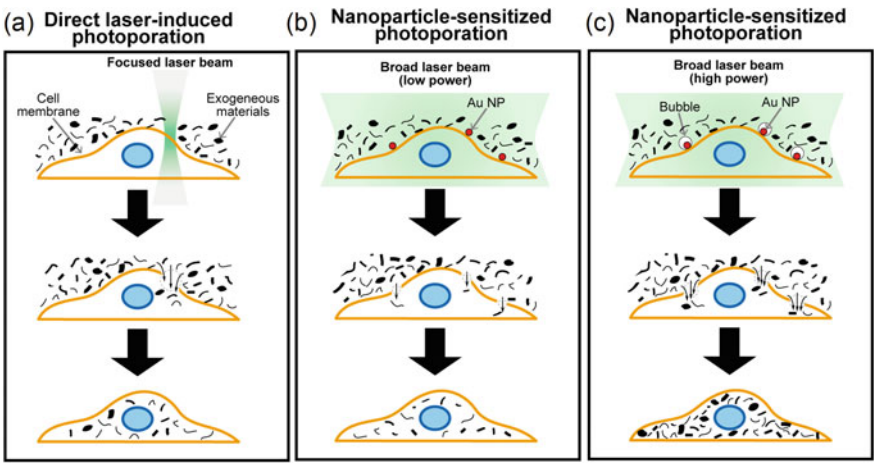


**Fig. 1.8** Schematic overview of laser-induced photoporation on cell membrane, followed by the introduction of polymers into cells. **a** Direct laser-induced photoporation, **b** Au NP-assisted photoporation due to heating of the cell membrane at relatively small laser intensities, and **c** Au NP-assisted photoporation assisted by heating-induced bubble formation around the Au NPs

ration without Au NPs (a), Au NP-assisted photoporation due to heating of the cell membrane (b) and Au NP-assisted photoporation assisted by laser-induced bubble formation around the Au NPs (c) is compared. The direct photoporation (a) can cause damages or kill the cells because of focused laser illumination, whereas the focused illumination can be avoided in the presence of Au NPs (b, c) because of efficient heat generation local to the membranes even with low intensities. There is little damage to the cells because of unfocused illumination. In (b), the resultant pores are small in sizes, and the number of pores is small because of weak intensities. By contrast, in (c), both the sizes of pore diameters and the numbers of pores will be increased compared with (b). As a result, more polymers can be incorporated into the cells. Still, the cell viability is maintained up to at a certain laser intensity.

The other application is to destroy biofilms exploiting plasmonic nanobubbles [39]. Biofilm forms when bacteria adhere to surfaces in moist environments by excreting a slimy, glue-like substance. Sites for biofilm formation include all kinds of surfaces. The biofilms serve to the decreased sensitivity of bacteria toward antibiotics. Thus, it is important to disturb biofilm integrity to improve antibiotics diffusion. The experimental result has shown that bacteria were loaded with cationic 70 nm Au NPs and that subsequent laser illumination of 7 ns pulses at 561 nm (fluence: 1.69 J $cm^{-2}$) resulted in plasmonic bubble formation inside the biofilms. Such nanobubble formation has led to substantial biofilm disruption, increasing antibiotic tobramycin efficacy up to 1–3 orders of magnitude. Enhancing antibiotic penetration through biofilm via laser-induced plasmonic nanobubble is a promising rout to solve the problem of biofilm-related infections.

## 1.4 Summary and Future Outlook

This chapter overviewed pulsed-laser-induced explosive bubble formation from solvent next to plasmonic Au NPs. The mechanism is regarded as purely photothermal boiling and not ascribable to cavitation, when the excitation wavelengths corresponding to the LSPR of Au NPs are employed. Although fundamental physics behind the transient plasmonic bubbles has been revealed in every detail using rigorous simulations [9, 10], still both experimental and computational efforts are needed to precisely characterize threshold fluences and state of materials inside the bubbles. For instance, experimental improvement such as single particle/single shot measurement is needed to avoid ensemble averaging effect. The dynamics governing particle melting/evaporation during bubble formation has not been fully characterized theoretically. We should point out that bubble generation using pulsed lasers has its own merit over CW laser-induced bubble generation. Since pulsed lasers have the advantage of outputting a high peak power within a limited pulse duration, they can provide means to obtain high spaciotemporal control for bubbles [40]. On the contrary, CW laser excitation results in severe medium heating for long period of time, which results in collective medium heating [13]. Such a heating can be

harmful to biological systems. As future prospects, the transient plasmonic nanobubbles can contribute to chemistry as photothermal nanoreactors for promising use. In the past, we saw the enhanced photothermal evaporation and size reduction of Au NPs inside the bubbles [24]. We expect that catalytic reactions of molecules concentrated on the outer surface of Au NPs can proceed triggered by bubble generation. Most importantly, the chemical reactions can be confined only at Au surfaces in a steam environment, while outer liquid space is kept at room temperature. Thus, we may see an impressive development of various nanochemisry in such an unconventional environment in the years to come.

## References


1. U. Kreibig, M. Vollmer, *Optical Properties of Metal Clusters* (Springer, Berlin, 1995). https://doi.org/10.1007/978-3-662-09109-8
2. M.L. Brongersma, N.J. Halas, P. Nordlander, Plasmon-induced hot carrier science and technology. Nat. Nanotech. **10**, 25−34 (2015). https://www.nature.com/articles/nnano.2014.311
3. V. Kotaidis, A. Plech, Cavitation dynamics on the nanoscale. Appl. Phys. Lett. **87**, 213102. (2005). https://doi.org/10.1063/1.2132086
4. V. Kotaidis, C. Dahmen, G. von Plessen, F. Springer, A. Plech, Excitation of nanoscale vapor bubbles at the surface of gold nanoparticles in water. J. Chem. Phys. **124**(2006). https://doi.org/10.1063/1.2187476
5. M. Hu, H. Petrova, G.V. Hartland, Investigation of the properties of gold nanoparticles in aqueous solution at extremely high lattice temperatures. Chem. Phys. Lett. **391**, 220–225 (2004). https://doi.org/10.1016/j.cplett.2004.05.016
6. A. Siems, S.A.L. Weber, J. Boneberg, A. Plech, Thermodynamics of nanosecond nanobubble formation at laser-excited metal nanoparticles. New J. Phys. **13**, 043018 (2011). https://doi.org/10.1088/1367-2630/13/4/043018
7. E. Lukianova-Hleb, L.Y. Hu, L. Latterini, L. Tarpani, S. Lee, R.A. Drezek, J.H. Hafner, D.O. Lapotko, Plasmonic nanobubbles as transient vapor nanobubbles generated around plasmonic nanoparticles. ACS Nano **4**, 2109 (2010). https://doi.org/10.1021/nn1000222
8. T. Katayama, K. Setoura, D. Werner, H. Miyasaka, S. Hashimoto, Picosecond-to-nanosecond dynamics of plasmonic nanobubbles from pump–probe spectral measurements of aqueous colloidal gold nanoparticles. Langmuir **30**, 9504−9513 (2014) https://pubs.acs.org/doi/abs/https://doi.org/10.1021/la500663x.
9. K. Metwally, S. Mensah, G. Baffou, Fluence threshold for photothermal bubble generation using plasmonic nanoparticles. J. Phys. Chem. C **119**, 28586−28596 (2015). https://doi.org/10.1021/acs.jpcc.5b09903
10. J. Lombard, T. Biben, S. Merabia, Threshold for vapor nanobubble generation around plasmonic nanoparticles. J. Phys. Chem. C **121**(28), 15402–15415 (2017). https://doi.org/10.1021/acs.jpcc.7b01854
11. A. Vogel, S. Busch, U. Parlitz, Shock wave emission and cavitation bubble generation by picosecond and nanosecond optical breakdown in water. J. Acoust. Soc. Am. **100**, 148−165 (1996). https://doi.org/10.1121/1.415878
12. G. Baffou, J. Polleux, H. Rigneault, S. Monneret, Super-heating and micro-bubble generation around plasmonic nanoparticles under cw illumination. J. Phys. Chem. C **118**, 4890–4898 (2014). https://doi.org/10.1021/jp411519k
13. G. Baffou, *Thermoplasmonics Heating Metal Nanoparticles Using Light* (Cambridge University Press, Cambridge, England, 2017). https://doi.org/10.1017/9781108289801

14. C.P. Lin, M.W. Kelly, Cavitation and acoustic emission around laser-heated microparticles. Appl. Phys. Lett. **72**, 2800−2802 (1998). https://doi.org/10.1063/1.121462
15. A. Plech, V. Kotaidis, S. Gresillon, C. Dahmen, G. von Plessen, Laser-induced heating and melting of gold nanoparticles studied by time-resolved x-ray scattering. Phys. Rev. **B70**, 195423 (2004). https://doi.org/10.1103/PhysRevB.70.195423
16. E.Y. Lukianova-Hleb, D.O. Lapotko, Influence of transient environmental photothermal effects on optical scattering by gold nanoparticles. Nano. Lett. **9**, 2160−2166 (2009). https://doi.org/10.1021/nl9007425
17. C. Burda, X. Chen, X.R. Narayanan, R.M.A. El-Sayed, Chemistry and properties of nanocrystals of different shapes. Chem. Rev. **105**, 1025–1102 (2005). https://doi.org/10.1021/cr030063a
18. X. Fu, B. Chen, J. Tang, A.H. Zewail, Photoinduced nanobubble-driven superfast diffusion of nanoparticles imaged by 4D electron microscopy. Sci. Adv. **3**, e1701160 (2017). https://advances.sciencemag.org/content/3/8/e1701160
19. E. Acosta, M.G. Gonz´alez, P.A. Sorichetti, G.D. Santiago, Laser-induced bubble generation on a gold nanoparticle: A nonsymmetrical description. Phys. Rev. E **92**, 062301 (2015). https://doi.org/10.1103/PhysRevE.92.062301
20. S. aus der Wiesche, C. Rembe, E.P. Hofer, Boiling of superheated liquids near the spinodal: I General theory. Heat Mass Transf. **35**, 25−31 (1999). https://doi.org/10.1007/s002310050294
21. A. Vogel, V. Venugopalan, Mechanisms of pulsed laser ablation of biological tissues. Chem. Rev. **103**, 577–644 (2003). https://doi.org/10.1021/cr010379n
22. Z. Liu, W.H. Hung, M. Aykol, D. Valley, S.B. Cronin, Optical manipulation of plasmonic nanoparticles, bubble formation and patterning of SERS aggregates. Nanotechnology **21**(2010). https://doi.org/10.1088/0957-4484/21/10/105304
23. M. Hu, G.V. Hartland, Heat dissipation for Au particles in aqueous solution: Relaxation time versus size. J. Phys. Chem. B **106**, 7029–7033 (2002). https://doi.org/10.1021/jp020581+
24. S. Hashimoto, D. Werner, T. Uwada, Studies on the interaction of pulsed lasers with plasmonic gold nanoparticles toward light manipulation, heat management, and nanofabrication. J. Photochem. Photobiol. C **13**, 28–54 (2012). https://doi.org/10.1016/j.jphotochemrev.2012.01.001
25. M.S. Plesset, M. Prosperetti, Bubble dynamics and cavitation. Ann. Rev. Fluid Mech. **9**, 145–185 (1977). https://doi.org/10.1146/annurev.fl.09.010177.001045
26. D. Lapotko, Plasmonic nanobubbles as tunable cellular probes for cancer theranostics. Cancers **3**, 802–840 (2011). https://doi.org/10.3390/cancers3010802
27. T. Yin, P. Wang, R. Zheng et al., Nanobubbles for enhanced ultrasound imaging of tumors. Int. J. Nanomed. **7**, 895–904 (2012). https://doi.org/10.2147/IJN.S28830
28. O. Neumann, A.S. Urban, J. Day et al., Solar vapor generation enabled by nanoparticles. ACS Nano **7**, 42–49 (2013). https://doi.org/10.1021/nn304948h
29. Li. Wang, Y. Feng, K. Wang et al., Solar water sterilization enabled by photothermal nanomaterials. Nano Energy **87** (2021) 106158. https://doi.org/10.1016/j.nanoen.2021.106158
30. P. Zemanker, G. Volpe, A. Jonas et al., Perspective on light-induced transport of particles: From optical forces to phoretic motion. Adv. Opt. Photon. **11**, 577–678 (2019). https://doi.org/10.1364/AOP.11.000577
31. A. Königer, W. Köhler, Optical Funneling and trapping of gold colloids in convergent laser beams. ACS Nano **6**, 4400–4409 (2012). https://doi.org/10.1021/nn301080a
32. V. Kajorndejnukul, W. Ding, S. Sukhov et al., Linear momentum increase and negative optical forces at dielectric interface. Nature Photon. **7**, 787–790 (2013). https://www.nature.com/articles/nphoton.2013.192
33. E. Lee, D. Huang, T. Luo, Ballistic supercavitating nanoparticles driven by single Gaussian beam optical pushing and pulling forces. Nat. Commun. **11**, 2404 (2020). https://www.nature.com/articles/s41467-020-16267-9
34. T. Mitra, A.K. Brown, D.M. Bernot et al., Laser acceleration of absorbing particles. Opt. Express **26**, 6639–6652 (2018). https://doi.org/10.1364/OE.26.006639

35. Metal particle manipulation by laser irradiation in borosilicate glass. Opt. Express **18**, 20313–20320 (2010). https://doi.org/10.1364/OE.18.020313
36. R. Sato, J. Henzie, S. Ishii, K. Takazawa, Y. Takeda, Plasmonic-induced self-assembly of WGM cavities via laser cavitation. Opt. Express **28**, 31923–31931 (2020). https://doi.org/10.1364/OE.401662
37. E. Galanzha, R. Weingold, D. Nedosekin et al., Spaser as a biological probe. Nat. Commun. **8**, 15528 (2017). https://doi.org/10.1038/ncomms15528
38. R. Xiong, K. Raemdonck, K. Peynshaert et al., Comparison of gold nanoparticle mediated photoporation: Vapor nanobubbles outperform direct heating for delivering macromolecules in live cells. ACS Nano **8**, 6288–6296 (2014). https://doi.org/10.1021/nn5017742
39. E. Teirlinck, R. Xiong, T. Brans et al., Laser-induced vapour nanobubbles improve drug diffusion and efficiency in bacterial biofilms. Nat. Commun. **9**, 4518 (2018). https://www.nature.com/articles/s41467-018-06884-w
40. C.J. Trout, J.A. Clapp, J.C. Griepenburg, Plasmonic carriers responsive to pulsed laser irradiation: a review of mechanisms, design, and applications. New J. Chem. (2021). https://doi.org/10.1039/D1NJ02062E

# Chapter 2
# Metal and Alloy Nanoparticles Formed by Laser-Induced Nucleation Method


**Takahiro Nakamura**

**Abstract** Tightly focused high-energy femtosecond pulsed laser can create an intense optical field near the focal point. When this intense optical field is formed in the aqueous solution, solvated electrons and radicals are generated by laser-induced photochemical decomposition of water molecules. Due to the strong reducing power of solvated electrons, metal ions in the solution are reduced to form nanoparticles (NPs). In addition, sequential pulsed-laser irradiation causes fragmentation of the formed NPs similar to a scheme of pulsed-laser ablation in liquid, in which the surface of the NPs is negatively charged, resulting in a stable colloidal suspension of NPs without the addition of dispersants. We named this laser-induced physico-chemical NP synthesis method as laser-induced nucleation method. By utilizing this technique, we have succeeded in fabricating not only various noble metal NPs but also solid-solution alloy NPs, which are difficult to fabricate by conventional thermal equilibrium methods due to their immiscible nature. The constituent elements in alloy NPs are the uniformly distributed, and the elemental composition reflects the mixing ratio of the ions in the solution. In this chapter, the reactions in the laser-induced NP formation and some examples for metal and solid-solution alloy NPs produced by the laser-induced nucleation method are introduced.

**Keywords** Femtosecond laser · Nanoparticles · Solid-solution alloy · Colloidal suspension

## 2.1 Introduction

Laser processing, which is the application of laser light to materials science, has expanded to not only heating and welding using laser light as a heat source, but also cutting, drilling, surface modification, and marking using ablation reactions, and particle and thin film formation using pulsed-laser ablation (PLA). In addition, it is applying to additive manufacturing, such as powder-bed fusion [1] and laser

T. Nakamura (✉)
Institute of Multidisciplinary Research for Advanced Materials, Tohoku University, Sendai, Miyagi 980-8577, Japan
e-mail: nakamu@tohoku.ac.jp



Y. Ishikawa et al. (eds.), *High-Energy Chemistry and Processing in Liquids*,
https://doi.org/10.1007/978-981-16-7798-4_2

cladding [2]. The laser processing using an unfocused beam needs that the laser wavelength corresponds to absorption band of the material. Meanwhile, a focused beam of high-energy pulsed laser allows to process materials that do not absorb the laser beam by nonlinear optical effects near the focal point. In this case, the laser light source can be selected according to physical properties of the target material and content of the process, because the laser wavelength is free from the absorption of the target material.

Most of laser processing is carried out under atmospheric conditions or in a vacuum, and at the same time, it has recently been reported for a laser processing that utilizes the unique reaction field of a solid material in liquid by irradiating it with laser light. For example, in the pulsed-laser ablation in liquid (PLAL), a pulsed laser beam is focused and irradiated on a solid material immersed or dispersed in a liquid that is transparent to the laser beam. In the PLAL, the energy of the laser beam is absorbed only by the solid material in the liquid, and the resulting ablation reaction produces fine particles "smaller" than the raw material. The formation of various metal nanoparticles (NPs) [3] and organic NPs [4] has been reported. In contrast, in the pulsed-laser melting in liquid (PLML) method [5–8], the aggregates of NPs dispersed in the liquid absorb the energy of the unfocused pulsed laser beam and melt and solidify to produce submicron spherical particles "larger" than the raw material. The submicron spherical particles obtained by this method are relatively uniform in size due to the fact that the average particle size is determined by the energy density of the irradiated laser in relation to the absorption cross section for the laser beam and the heat capacity of the particle [8]. In addition, they have a crystalline structure despite their spherical shape. As described above, the laser processing is widely used in both top-down and bottom-up methods. And in most cases, the laser processing is used to change the shape of the material with maintaining its crystalline structure and properties. Therefore, the laser fluence (energy density, J/cm$^2$) is controlled to a certain level in order to minimize the heat-affected zone (HAZ) as much as possible in laser cutting and drilling, to suppress the generation of large particles called debris or fragments in particle and thin film formation, or to prevent phase transformation of materials.

On the other hand, with the markedly progress of ultrashort pulse laser technology, current laser is capable of forming unexplored ultra-dense energy fields due to its high peak power characteristics. The irradiation of an ultrashort laser pulse with a very short duration to the target material generates ultra-dense energy field. It induces nonlinear and non-equilibrium reactions, which are different from thermal equilibrium reactions of heat, photolysis, and ionization in conventional laser processes.

We have studied the fabrication of metal and alloy NPs in the high energetic field produced by focused femtosecond laser pulses which is named as "laser-induced nucleation method". In this chapter, we introduce the reactions in laser-induced nucleation method and the fabrication of metal and solid-solution alloy NPs with controlled compositions.

## 2.2 Formation Mechanism of NPs by Laser-Induced Nucleation Method

For the formation of metal NPs, the chemical reduction in liquid is widely used. In the method, metal ions are reduced to zero-valent atoms by adding a reducing agent into a solution containing various metal ions (nucleation), and the subsequent ripening process (nuclear growth) is controlled by the reaction conditions such as pH and temperature to produce NPs with the desired size and shape. In addition, NPs are usually prepared by adding dispersants to the solution or by coexisting with supporting materials, because NPs are active due to the large specific surface area, and need to be stabilized by coating their surface with dispersants or by fixing them to supporting materials.

On the other hand, it has been reported that Au NPs are formed through photochemical reduction in the strong light field generated by focusing an ultrashort pulsed laser beam into an aqueous solution containing gold ions [9–18]. Formation of Au NPs in the laser-excited field in our study is introduced as an example [10]. Figure 12. shows laser irradiation of an aqueous solution of gold ion (a) just after starting and (b) after 15 min irradiation. An aqueous solution of tetrachloroauric (III) acid trihydrate ($HAuCl_4 \cdot 3H_2O$) with a concentration of $2.5 \times 10^{-4}$ mol $dm^{-3}$ was held in a synthetic fused silica cuvette. A femtosecond pulsed laser beam with a wavelength of 800 nm, a pulse width of 100 fs, and an average pulse energy of 5.5 mJ was tightly focused through an aspheric lens with a focal length of 8 mm and a numerical aperture of 0.5 for a fixed period of time at a specified repetition rate. Bright plasma was observed near the focal point by the laser irradiation, white light emission through the nonlinear optical effect was confirmed behind the focal point along the direction of laser incidence, and oxygen and hydrogen gas were generated near the focal point (Fig. 2.1a). These phenomena suggest the decomposition of water

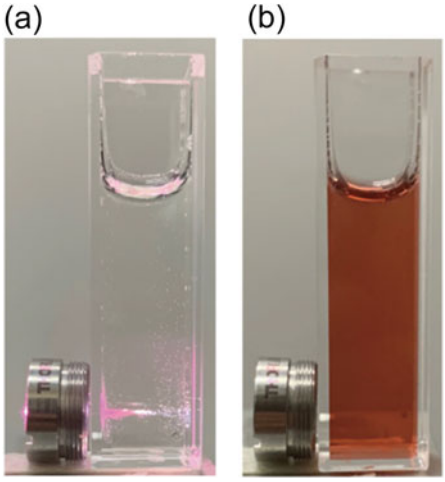


**Fig. 2.1** Laser irradiation of an aqueous gold chloride solution **a** just after starting and **b** after 15 min irradiation

molecules by a high-intensity field near the focal point. The aqueous solution, which was colorless and transparent before laser irradiation, turned red after a certain period of laser irradiation (Fig. 2.1b). The UV-visible absorption spectrum of the aqueous solution after laser irradiation showed an absorption peak around 520 nm, which was attributed to the localized surface plasmon resonance (SPR) of the Au NPs. The particles formed in the solution were observed by transmission electron microscopy, and it was confirmed that spherical Au NPs with an average diameter of less than 5 nm were formed.

The formation mechanism of the NPs is presumed to be based on the following reaction [19–24],

$$H_2O\,(nh\nu) \rightarrow e^- + H^+ + OH \tag{2.1}$$

$$e^- \rightarrow e^-_{aq} \tag{2.2}$$

$$H_2O\,(nh\nu) \rightarrow H^{\cdot} + OH^{\cdot} \tag{2.3}$$

$$2OH^{\cdot} \rightarrow H_2O_2 \tag{2.4}$$

$$H^{\cdot} + H_2O \rightarrow H_3O^+ + e^-_{aq} \tag{2.5}$$

$$M^+ + e^-_{aq} \rightarrow M^0 \tag{2.6}$$

$$M^0 \rightarrow M^0_2 \rightarrow \cdots \rightarrow M^0_n \tag{2.7}$$

Nonlinear optical effects such as multiphoton absorption and avalanche photoionization occur, and the energy of the laser light is absorbed by water molecules. In the process, water molecules are decomposed (2.1), and solvated electrons ($e^-_{aq}$), hydrogen radicals ($H^{\cdot}$), and hydroxyl radicals ($OH^{\cdot}$) are produced (2.2 and 2.3). The hydrogen radicals are consumed on the order of picoseconds (2.5) and are not considered to contribute to the reduction reaction [21]. On the other hand, the redox potential of solvated electrons is $-2.77\ V_{SHE}$, and their lifetime in pure water is several hundred nanoseconds [20]. Therefore, gold ions in aqueous solution are reduced by solvated electrons to zero-valent gold atoms (2.6), which grow to form Au NPs (7). At the same time, the hydroxyl radicals oxidize water to form hydrogen peroxide (2.4). Formation mechanism of Au NPs by the laser-induced method has been intensively studied by Tibbets group [14, 15]. According to their dedicated effort, size and size distribution of Au NPs could be tuned by manipulating the nucleation and growth rate by controlling solution pH and addition of hydroxyl radical scavengers.

The zeta potential of Au NPs prepared under specific conditions was −35 mV (the pH of the aqueous solution is about 3.0), and dispersion state of formed colloidal suspension was stable over several months without the addition of dispersants.

Figure 2.2 shows (a) real-time UV-visible absorption spectra of the colloidal suspension of Au NPs and (b) variation of peak absorbance as a function of irradiation period [25]. The absorption peak originated from SPR of Au NPs increased with irradiation period (Fig. 2.2a), and when the repetition rate of the laser pulse was 100 Hz, the absorption peak reached its maximum in about 14 min (Fig. 2.2b). This is thought to be due to the reduction of all the gold ions in the aqueous solution.

Figure 2.3 shows the UV-visible absorption spectra of the colloidal dispersions in which the laser irradiation was stopped after 9 min, while the gold chloride ions in the aqueous solution were being reduced, and the colloidal dispersions in which the laser irradiation was continued for 20 min after all the gold ions in the solution were reduced. In the colloidal suspension of Au NPs prepared with a short laser irradiation

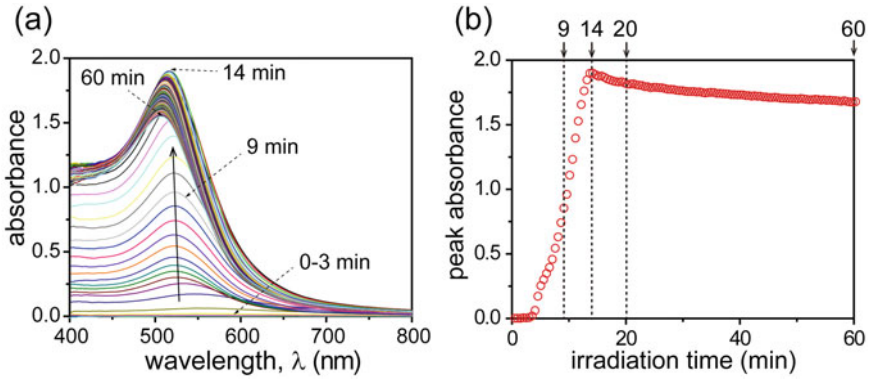


**Fig. 2.2** **a** Real-time UV-visible absorption spectra of the colloidal suspension of Au NPs and **b** variation of peak absorbance as a function of irradiation period. Reproduced from Ref. [25] under the terms of the CC-BY 4.0 license. Copyright: (2022) The Authors, published by Hosokawa Powder Technology Foundation

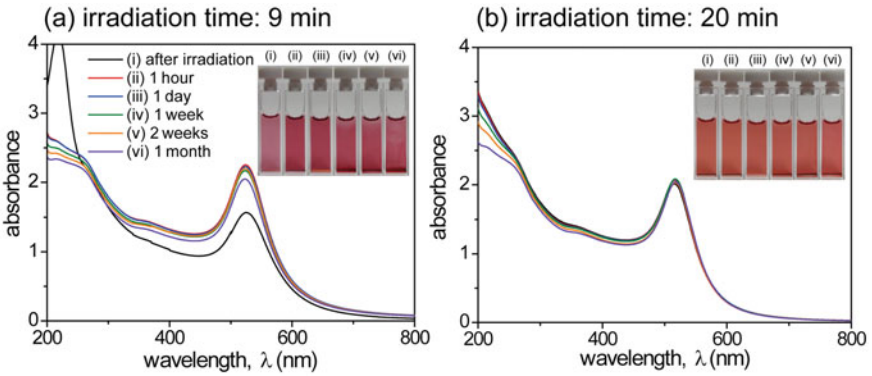


**Fig. 2.3** Time evolution of colloidal suspensions of Au NPs prepared by **a** 9 min and **b** 20 min laser irradiation

time (9 min) (Fig. 2.3a), the autocatalytic reaction of the Au NPs formed by the laser irradiation reduced the remaining gold ions in the aqueous solution, causing crystal growth of the formed Au NPs and subsequent aggregation and precipitation. Therefore, the dispersion state of the colloidal suspension was not sustained. On the other hand, in the colloidal Au NPs dispersion (20 min, Fig. 2.3b), which was continuously irradiated even after all the gold chloride ions had been reduced, there was no change in the color and absorption spectrum of the colloidal suspension after one month. This is thought to be due to the fragmentation of the formed NPs by sequential laser irradiation, in a scheme similar to pulsed-laser ablation in liquid (PLAL), and Au NPs are stabilized by bonding with oxygen [26]. According to the study on Au NPs formation by PLAL, the surface state of Au NPs depends on the pH of the solution and is reported to be Au-$O^-$ at pH > 5.8 and Au-OH at pH < 5.8. The pH of the colloidal suspension of Au NPs prepared by the method was approximately 3.0, so the surface structure of the Au NPs was assumed to be Au-OH. The Au NPs prepared in this way can be fixed simply by dropping a colloidal suspension onto a substrate, and it is easy to form composite materials in combination with various carriers while maintaining the excellent surface properties of the NPs. By using this technique, platinum (Pt) [27] and silver (Ag) NPs [28] can be also fabricated.

## 2.3 Formation of Solid-Solution Alloy Nanoparticles from Mixed Solutions by Laser-Induced Nucleation Method

In the laser-induced nucleation method, since the target of laser irradiation is an aqueous solution, it is easy to form alloy NPs by laser irradiation of aqueous solutions containing multiple metallic ions. As mentioned above, we have successfully prepared colloidal suspension of Au and Ag NPs by the method. The synthesis of these NPs involved aqueous solutions prepared by dissolving gold (III) chloride trihydrate ($HAuCl_4 \cdot 3H_2O$) or silver (I) nitrate ($AgNO_3$, both from Fujifilm Wako Pure Chemicals) in ultrapure water (18.2 MΩ, arium® pro UV, Sartorius). When these solutions were mixed, silver chloride (AgCl) insoluble in water was produced above a certain ionic concentration. Therefore, to prepare a mixed aqueous solution, we separately prepared each aqueous solution of metal ions with a concentration of $2.5 \times 10^{-4}$ mol $dm^{-3}$, added 0.1 vol% ammonia water to them, and then mixed them with desired molar concentration of metal ions in each prepared aqueous solution to suppress the formation of silver chloride. Figure 2.4 shows the colloidal suspension of NPs prepared by laser irradiation of mixed aqueous solutions of Au and Ag ions with different mixing ratios and corresponding UV-visible absorption spectra of the colloidal suspensions. The aqueous solutions before laser irradiation were colorless and transparent in all cases, but the colloidal suspensions after laser irradiation showed a systematic change from yellow to reddish purple depending on the mixing ratio of metallic ions (Fig. 2.4a). The absorption spectra of the colloidal suspensions

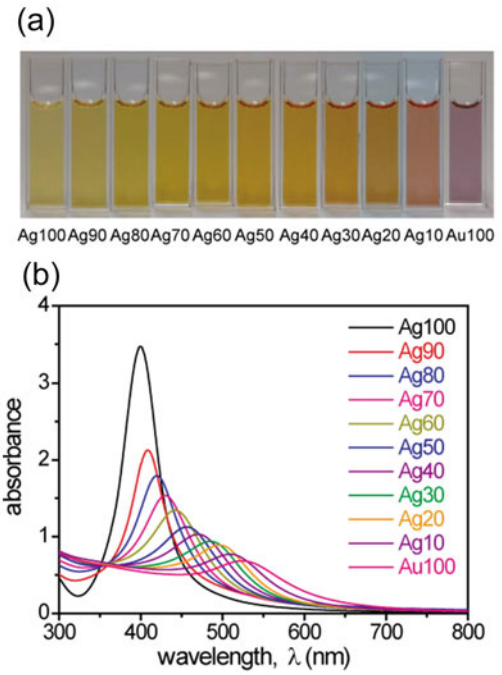


**Fig. 2.4** **a** Colloidal suspensions prepared by laser irradiation of mixed aqueous solutions of Au and Ag ions with different mixing ratios, **b** corresponding UV-visible absorption spectra

of Ag and Au NPs showed absorption peaks of SPR near 400 and 520 nm, respectively, while those shifted to the longer wavelength side as the molar ratio of gold ions in the mixture increased (Fig. 2.4b). The absorption peak positions in the spectra as a function of the molar ratio of Au in the aqueous solutions are shown in Fig. 2.5. The absorption peak position in the absorption spectrum showed a proportional relationship to the molar ratio of Au in the aqueous solution, suggesting the formation of composition-controlled Au-Ag alloy NPs by laser irradiation of mixture solutions.

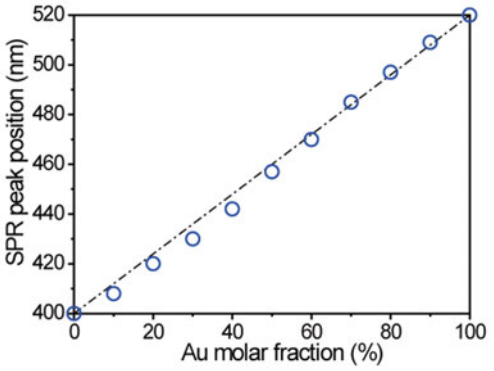


**Fig. 2.5** Relationship between SPR peak positions in the absorption spectra and the molar ratio of Au in the mixed aqueous solutions

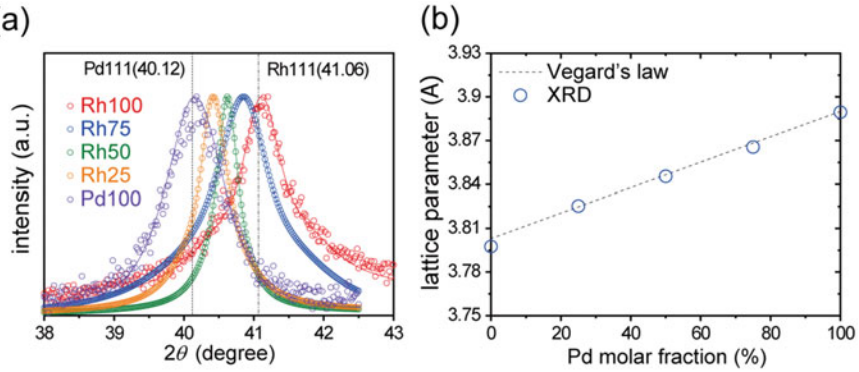


**Fig. 2.6** Relationship between **a** X-ray diffraction patterns of alloy NPs prepared by laser irradiation of mixed aqueous solutions of Rh and Pd ions and **b** lattice constants determined from X-ray peak positions and the molar ratio of Pd in the mixed aqueous solutions

Since Au and Ag have redox potentials of +0.93 $V_{SHE}$ and +0.7996 $V_{SHE}$, respectively, co-reduction with a relatively strong reducing agent is necessary to produce Au-Ag alloy NPs by chemical reduction. The formation of Au-Ag alloy NPs in the laser-induced nucleation method can be attributed to the high reducing power of the hydrated electrons described above.

While Au-Ag binary alloys are considered to be easy to form in terms of thermal energy because they form solid-solution alloy in bulk, the laser-induced nucleation method can also produce non-equilibrium alloy NPs which are difficult to fabricate by conventional methods [29–34]. As an example, we show the formation of rhodium (Rh)–palladium (Pd) binary alloy NPs. Rhodium (III) chloride trihydrate ($RhCl_3 \cdot 3H_2O$) and palladium (II) chloride ($PdCl_2$, both from Fujifilm Wako Pure Chemicals) were dissolved in extra pure water to prepare aqueous solutions with a concentration of $2.5 \times 10^{-4}$ mol $dm^{-3}$. The laser irradiation was performed on the mixed aqueous solutions. Figure 2.6 shows the results of X-ray diffraction measurements of the fabricated NPs and the relationship between the molar ratio of Pd in the solution and the interplanar spacings determined from the peak positions. The X-ray diffraction peak exhibited a single Gaussian pattern characteristic of the face-centered cubic structure, and the peak positions were systematically shifted according to the metal ion mixing ratio in the aqueous solution. The interplanar spacings of the NPs calculated from the positions of the X-ray diffraction peaks and the mixing ratio of metallic ion in the aqueous solution were proportional according to the Vegard's law, indicating the formation of Rh-Pd alloy NPs with a tunable composition. In addition, elemental mapping of the alloy NPs obtained by scanning transmission electron microscopy–energy dispersive X-ray analysis (STEM–EDS) (Fig. 2.7) showed that rhodium and palladium are uniformly distributed in the particles, confirming the formation of solid-solution alloy NPs. Because of the wide immiscibility gap in the Rh-Pd binary phase diagram, solid-solution alloy NPs are difficult to fabricate in thermal equilibrium. The laser-induced nucleation method allows the co-reduction

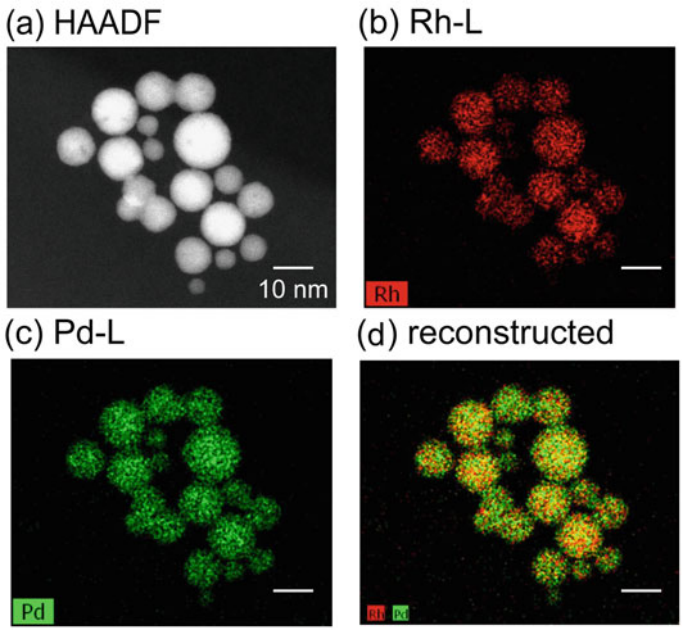


**Fig. 2.7** STEM-EDS mappings of alloy NPs prepared by laser irradiation of Rh and Pd mixed aqueous solutions. **a** HAADF-STEM image, two-dimensional mapping image of **b** Rh and **c** Pd, and **d** superimposed two-dimensional image of Rh and Pd

of multiple ions by radicals with strong reducing power. In addition, it also induces the non-equilibrium reactions, where the reduction occurs repeatedly in a very short time during the radical lifetime formed by each irradiated laser pulse. As the result of this, an alloy structure was formed before the atoms diffuse in thermal equilibrium condition. This is different from conventional chemical reduction or reduction by radicals caused by continuous high-energy irradiation such as electron beams or gamma rays.

## 2.4 Summary

In this chapter, we report on the fabrication of multigrid all-solid-solution alloy NPs by a laser-induced nucleation method using an intense reaction field created by ultrashort laser pulses and the reaction field as a novel physicochemical nanoparticle synthesis method. The works showed that this method enables us to control the composition of alloys with combinations that are normally difficult to fabricate in the full rate solid-solution state. We are currently working on the construction of a mass synthesis system and the preparation of surface-modified nanoparticle colloids,

which are stable in water and modified with desired modifiers, for a wide range of applications of the prepared NPs.

**Acknowledgements** The author thanks Mr. Yuichiro Hayasaka for his help with STEM-EDS analysis.

## References

1. B.P. Conner, G.P. Manogharan, A.N. Martof, L.M. Rodomsky, C.M. Rodomsky, D.C. Jordan, J.W. Limperos, Making sense of 3-D printing: Creating a map of additive manufacturing products and services. Addit. Manuf. **1–4**, 64–76 (2014). https://doi.org/10.1016/j.addma.2014.08.005
2. Y. Sato, M. Tsukamoto, T. Shobu, Y. Funada, Y. Yamashita, T. Hara, M. Sengoku, Y. Sakon, T. Ohkubo, M. Yoshida, N. Abe, In situ X-ray observations of pure-copper layer formation with blue direct diode lasers. Appl. Phys. Sci. **480**, 861–867 (2019). https://doi.org/10.1016/j.apsusc.2019.03.057
3. Z. Yan, D.B. Chrisey, Pulsed laser ablation in liquid for micro-/nanostructure generation. J. Photochem. Photobiol. C: Photochem. Rev. **13**, 204–223 (2012). https://doi.org/10.1016/j.jphotochemrev.2012.04.004
4. R. Yanagihara, T. Asahi, Y. Ishibashi, O. Odawara, H. Wada, Fabrication of naphthalocyanine nanoparticles by laser ablation in liquid and application to contrast agents for photoacoustic imaging. Jpn. J. Appl. Phys. **57**(2018). https://doi.org/10.7567/JJAP.57.035001
5. Y. Ishikawa, Q. Feng, N. Koshizaki, Growth fusion of submicron spherical boron carbide particles by repetitive pulsed laser irradiation in liquid media. Appl. Phys. A **99**, 797–803 (2010). https://doi.org/10.1007/s00339-010-5745-6
6. Y. Ishikawa, T. Sasaki, N. Koshizaki, Submicron-sized boron carbide particles encapsulated in turbostratic graphite prepared by laser fragmentation in liquid medium. J. Nanosci. Nanotechnol. **10**, 5467–5470 (2010). https://doi.org/10.1166/jnn.2010.1947
7. H.Q. Wang, A. Pyatenko, K. Kawaguchi, X. Li, Z. Swiatkowska-Warkocka, N. Koshizaki, Selective pulsed heating for the synthesis of semiconductor and metal submicrometer spheres. Angew. Chem. Int. Ed. **49**, 6361–6364 (2010). https://doi.org/10.1002/anie.201002963
8. A. Pyatenko, H. Wang, N. Koshizaki, Growth mechanism of monodisperse spherical particles under nanosecond pulsed laser irradiation. J. Phys. Chem. C **118**, 4495–4500 (2014). https://doi.org/10.1021/jp411958v
9. C. Zhao, S. Qu, J. Qiu, C. Zhu, Photoinduced formation of colloidal Au by a nearinfrared femtosecond laser. J. Mater. Res. **18**, 1710–1714 (2003). https://doi.org/10.1557/JMR.2003.0235
10. T. Nakamura, Y. Mochidzuki, S. Sato, Fabrication of gold nanoparticles in intense optical field by femtosecond laser irradiation of aqueous solution. J. Mater. Res. **23**, 968–974 (2008). https://doi.org/10.1557/jmr.2008.0115
11. B. Tangeysh, K.M. Tibbetts, J.H. Odhner, B.B. Wayland, R.J. Levis, Gold nanoparticle synthesis using spatially and temporally shaped femtosecond laser pulses: Post-irradiation auto-reduction of aqueous $[AuCl_4]^-$. J. Phys. Chem. C **117**, 18719–18727 (2013). https://doi.org/10.1021/jp4056494
12. J.H. Odhner, K.M. Tibbetts, B. Tangeysh, B.B. Wayland, R.J. Levis, Mechanism of improved Au nanoparticle size distributions using simultaneous spatial and temporal focusing for femtosecond laser irradiation of aqueous $KAuCl_4$. J. Phys. Chem. C **118**, 23986–23995 (2014). https://doi.org/10.1021/jp507873n
13. N. Nakashima, K. Yamanaka, M. Saeki, H. Ohba, S. Taniguchi, T. Yatsuhashi, Metal ion reductions by femtosecond laser pulses with micro-joule energy and their efficiencies. J. Photochem. Photobiol. A **319–320**, 70–77 (2016). https://doi.org/10.1016/J.JPHOTOCHEM.2015.12.021

14. K.M. Tibbetts, B. Tangeysh, J.H. Odhner, R.J. Levis, Elucidating strong field photochemical reduction mechanisms of aqueous $[AuCl_4]^-$: Kinetics of multiphoton photolysis and radical-mediated reduction. J. Phys. Chem. A **120**, 3562–3569 (2016). https://doi.org/10.1021/acs.jpca.6b03163
15. V.K. Meader, M.G. John, C.J. Rodrigues, K.M. Tibbetts, Roles of free electrons and $H_2O_2$ in the optical breakdown-induced photochemical reduction of aqueous $[AuCl_4]^-$. J. Phys. Chem. A **121**, 6742−6754 (2017). https://doi.org/10.1021/acs.jpca.7b05370
16. C.J. Rodrigues, J.A. Bobb, M.G. John, S.P. Fisenko, M.S. El-Shall, K.M. Tibbetts, Nucleation and growth of gold nanoparticles initiated by nanosecond and femtosecond laser irradiation of aqueous $[AuCl_4]^-$. Phys. Chem. Chem. Phys. **20**, 28465–28475 (2018). https://doi.org/10.1039/C8CP05774E
17. H. Belmouaddine, M. Shi, P.-L. Karsenti, R. Meesat, L. Sanche, D. Houde, Dense ionization and subsequent non-homogeneous radical-mediated chemistry of femtosecond laser-induced low density plasma in aqueous solutions: Synthesis of colloidal gold. Phys. Chem. Chem. Phys. **19**, 7897–7909 (2017). https://doi.org/10.1039/C6CP08080D
18. H. Belmouaddine, M. Shi, L. Sanche, D. Houde, Tuning the size of gold nanoparticles produced by multiple filamentation of femtosecond laser pulses in aqueous solutions. Phys. Chem. Chem. Phys. **20**, 23403–23413 (2018). https://doi.org/10.1039/C8CP02054J
19. K. Kurihara, J. Kizling, P. Stenius, J.H. Fendler, Laser and pulse radiolytically induced colloidal gold formation in water and in water-in-oil microemulsions. J. Am. Chem. Soc. **105**, 2574–2579 (1983). https://doi.org/10.1021/ja00347a011
20. D.N. Nikogosyan, A.A. Oraevsky, V.I. Rupasov, Two-photon ionization and dissociation of liquid water by powerful laser UV radiation. Chem. Phys. **77**, 131–143 (1983). https://doi.org/10.1016/0301-0104(83)85070-8
21. R.A. Crowell, D.M. Bartels, Multiphoton ionization of liquid water with 3.0−5.0 eV photons. J. Phys. Chem. **100**, 17940−17949 (1996). https://doi.org/10.1021/jp9610978
22. A. Reuther, A. Laubereau, D.N. Nikogosyan, Primary photochemical processes in water. J. Phys. Chem. **100**, 16794–16800 (1996). https://doi.org/10.1021/jp961462v
23. S.L. Chin, S. Lagace, Generation of $H_2$, $O_2$, and $H_2O_2$ from water by the use of intense femtosecond laser pulses and the possibility of laser sterilization. Appl. Opt. **35**, 907–911 (1996). https://doi.org/10.1364/AO.35.000907
24. S. Pommeret, F. Gobert, M. Mostafavi, I. Lampre, J.-C. Mialocq, Femtochemistry of the hydrated electron at decimolar concentration. J. Phys. Chem. A **105**, 11400–11406 (2001). https://doi.org/10.1021/jp0123381
25. T. Nakamura, Y. Yamazaki, S. Sato, Synthesis of noble metals and their alloy nanoparticles by laser-induced nucleation in a highly intense laser field (2020). https://doi.org/10.14356/kona.2022002
26. J.-P. Sylvestre, S. Poulin, A. Kabashin, E. Sacher, M. Meunier, J.H.T. Luong, Surface chemistry of gold nanoparticles produced by laser ablation in aqueous media. J. Phys. Chem. B **108**, 16864–16869 (2004). https://doi.org/10.1021/jp047134+
27. T. Nakamura, K. Takasaki, A. Ito, S. Sato, Fabrication of platinum particles by intense, femtosecond laser pulse irradiation of aqueous solution. Appl. Surf. Sci. **255**, 9630–9633 (2009). https://doi.org/10.1016/j.apsusc.2009.04.092
28. T. Nakamura, H. Magara, Y. Herbani, S. Sato, Fabrication of silver nanoparticles by highly intense laser irradiation of aqueous solution. Appl. Phys. A **104**, 1021 (2011). https://doi.org/10.1007/s00339-011-6499-5
29. Y. Herbani, T. Nakamura, S. Sato, Synthesis of platinum-based binary and ternary alloy nanoparticles in an intense laser field. J. Coll. Int. Sci. **375**, 78–87 (2012). https://doi.org/10.1016/j.jcis.2012.02.030
30. T. Nakamura, Y. Herbani, S. Sato, Fabrication of solid-solution gold–platinum nanoparticles with controllable compositions by high-intensity laser irradiation of solution. J. Nanopart. Res **14**, 785 (2012). https://doi.org/10.1007/s11051-012-0785-9

31. M.S.I. Sarker, T. Nakamura, Y. Herbani, S. Sato, Fabrication of Rh based solid-solution bimetallic alloy nanoparticles with fully-tunable composition through femtosecond laser irradiation in aqueous solution. Appl. Phys. A **110**, 145–152 (2013). https://doi.org/10.1007/s00339-012-7467-4
32. M.S.I. Sarker, T. Nakamura, S. Sato, Composition-controlled ternary Rh–Pd–Pt solid-solution alloy nanoparticles by laser irradiation of mixed solution of metallic ions. J. Mater. Res. **29**, 856–864 (2014). https://doi.org/10.1557/jmr.2014.62
33. M.S.I. Sarker, T. Nakamura, S. Sato, All-proportional solid-solution Rh–Pd–Pt alloy nanoparticles by femtosecond laser irradiation of aqueous solution with surfactant. J. Nanopart. Res. **17**, 259 (2015). https://doi.org/10.1007/s11051-015-3056-8
34. M.S.I. Sarker, T. Nakamura, S. Kameoka, Y. Hayasaka, S. Sato, Enhanced catalytic activity of inhomogeneous Rh-based solid-solution alloy nanoparticles. RSC Adv. **9**, 38882–38890 (2019). https://doi.org/10.1039/C9RA06167C

# Chapter 3
# Laser-Induced Particle Formation: Its Applications to Precious Metal Recovery from Spent Nuclear Fuel and Fundamental Studies

**Morihisa Saeki**

**Abstract** Separation of precious metals (PMs) from industrial waste is a crucial technique, because they are used in industrial materials and for decorations. Over the past decade, we have developed the technique of PM separation using laser-induced particle formation (LIPF), where $PM^{n+}$ ions in waste solutions are selectively converted into PM nanoparticles by nanosecond pulsed UV laser irradiation. Since LIPF separates PMs via the laser irradiation and is a contactless method, it offers PM recovery from toxic and radioactive waste solutions. Thus, we show that LIPF can be used for PM recovery from the solution of spent nuclear fuel (SNF), which contains more than 20 types of metals and radioactive actinides. Moreover, fundamental studies on the LIPF mechanism suggest that the multiphoton absorption of the intense pulsed light by the $PM^{n+}$ ion promotes the autocatalytic growth of PM nanoparticles. This phenomenon is a characteristic of high-energy processing. In this chapter, the basic principles, background, and applications of LIPF-based PM separation, as well as fundamental studies on LIPF process, are introduced.

**Keywords** Laser-induced particle formation · LIPF-based separation · Precious metals · Nanosecond pulsed laser · Autocatalytic growth · Multi-photon process

## 3.1 Introduction

Precious metals (PMs) are rare metals with a high economic value, such as gold (Au), silver (Ag), palladium (Pd), platinum (Pt), rhodium (Rh), iridium (Ir), ruthenium (Ru), and osmium (Os). They possess a high melting temperature, high corrosion resistance, and excellent mechanical properties. Thus, pure PMs and their alloys are used in many industrial materials, such as exhaust gas catalysts, electronic components, crucibles, and so on [1, 2]. In addition, Au, Ag, Pt, Pd, and their alloys are valuable for decoration. Despite the large demand for PMs, their world production

M. Saeki (✉)
Quantum Beam Science Research Directorate, National Institutes for Quantum Science and Technology (QST), 1233 Watanukimachi, Takasaki-shi, Gunma 370-1292, Japan
e-mail: saeki.morihisa@qst.go.jp



Y. Ishikawa et al. (eds.), *High-Energy Chemistry and Processing in Liquids*,
https://doi.org/10.1007/978-981-16-7798-4_3

is limited (25,000 tons of Ag, 3,200 tons of Au, 210 tons of Pd, and 170 tons of Pt in 2020) [3]. In addition, the supply and price of PMs can be easily influenced as their production is restricted to certain countries.

Therefore, recycling from industrial waste is essential for a stable PM supply. Wet separation methods have been developed for PM recovery, such as electrolytic reduction, ion exchange, solvent extraction, and precipitation [1, 2, 4]. The separation methods are generally selected depending on the $PM^{n+}$ ion concentration [1]. Although the existing separation techniques enable us to effectively separate PMs from industrial waste, the electrolytic reduction and the ion exchange have a technical difficulty in the recovery of PMs, which is strongly adsorbed on electrode metal plates and ion-exchange resins in the separation. Moreover, because the waste solution is harmful to the human body, the existing separation techniques pose health risks for the operators.

To separate PMs from toxic and radioactive waste solutions, we have developed PM separation based on laser-induced particle formation (LIPF) process over the past decade [5–12]. In LIPF-based PM separation, PM ions are separated from waste solutions in the form of PM nanoparticles, which are generated by UV laser irradiation (a detailed explanation is presented in Sect. 3.2). In particular, LIPF-based separation is advantageous in PM recovery from toxic and radioactive waste solutions, because it separates PMs through a contactless process without any separation substance (electrode plates and ion-exchange resins) and reduces health risks to the operators.

Prior to our studies on the applications and fundamentals of LIPF-based PM separation, LIPF had been mainly considered for the preparation of PM nanoparticles [13, 14] rather than PM recovery, whereas the LIPF mechanism had been overlooked. However, LIPF can be used for the separation of even a single PM from more than 20 types of metals [7]. Moreover, fundamental study on the LIPF process shows that the reaction rate is promoted by multiphoton absorption of the intense pulsed light by the $PM^{n+}$ ion [9], which is characteristic of high-energy processing. This chapter introduces the basic principles (Sect. 3.2), background (Sect. 3.3), and applications of LIPF-based PM separation (Sect. 3.4) and the fundamentals of the LIPF process in a Pd solution (Sect. 3.5).

## 3.2 Basic Principles of LIPF-Based PM Separation

Figure 3.1a illustrates the concept of LIPF-based PM separation from a solution of spent nuclear fuel (SNF), which is discharged from nuclear power plants, as an example of industrial wastewater. The application of LIPF-based PM separation from an SNF solution is described in Sect. 3.4.3. SNF contains PMs (Pd, Rh, and Ru) along with actinides (Ac), lanthanides (Ln), molybdenum (Mo), and zirconium (Zr) [15]. $PM^{n+}$ ions in the SNF solution are complexed with counterpart anions ($NO_3^-$, $Cl^-$, and so on) and $H_2O$. $PM^{n+}$ ion complexes possess charge transfer (CT) bands in the UV region, and their optical excitation results in electron transfer from the complex ligand to the $PM^{n+}$ ion.

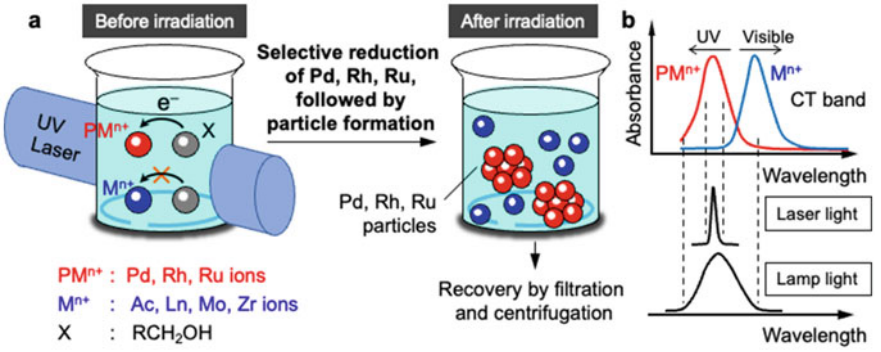


**Fig. 3.1** **a** Concept of LIPF-based PM separation. **b** Optical excitations of CT bands by the UV laser and the UV lamp. Adapted from Ref. [12] with permission from The Japan Society for Analytical Chemistry (Copyright 2018)

The LIPF process involves the reaction mechanism as follows [6, 12]: The irradiation of the UV laser to the SNF solution, where alcohol is added as a reduction aid, generates an electronically excited $PM^{n+}$ ion, $(PM^{n+})^*$:

$$PM^{n+} + h\nu \rightarrow \left(PM^{n+}\right)^* \tag{3.1}$$

The $(PM^{n+})^*$ ion reacts with the alcohol, reducing it to the $PM^0$ neutral by

$$\left(PM^{n+}\right)^* + \frac{n}{2}RCH_2OH \rightarrow PM^0 + \frac{n}{2}RCHO + nH^+ \tag{3.2}$$

while the alcohol is oxidized into aldehydes. The generated $PM^0$ neutrals form PM nanoparticles by spontaneous aggregation,

$$kPM^0 \rightarrow \left(PM^0\right)_k, \tag{3.3}$$

due to the lack of repulsion forces between the ions. When the $(PM^0)_k$ nanoparticles grow up to a given size, which is assumed to be below a few nanometers, they commence to behave as catalysts. The PM nanocatalysts promote the photoreduction of the $PM^{n+}$ ion by repeating the reaction:

$$\left(PM^0\right)_m + PM^{n+} + \frac{n}{2}RCH_2OH + h\nu \rightarrow \left(PM^0\right)_{m+1} + \frac{n}{2}RCHO + nH^+. \tag{3.4}$$

This reduction process (Eq. 3.4) is called autocatalytic growth, the kinetics of which has been analyzed based on the reaction models proposed by Finke et al. [16–18]. Autocatalytic growth plays a significant role in the formation of PM nanoparticles, as described in Sect. 3.5.2.

While the absorption of the UV photon by $PM^{n+}$ leads to the formation of PM nanoparticles, the irradiation of the UV laser to the coexisting $M^{k+}$ ions (M = Ac, Ln, Mo, Zr) hardly result in the formation of nanoparticles, because most $M^{k+}$ ions do not absorb UV photons due to the absence of the CT band in the UV region. Although some $M^{k+}$ ion complexes have CT bands in the UV region, they are not reduced to $M^0$ neutrals due to the large potential barrier in the reduction path. For these reasons, PMs are separated from coexisting metals in the form of nanoparticles and recovered by filtration and centrifugation. Notably, PM recovery from the SNF solution is used as an example, and the LIPF-based PM separation can be applied to other waste solutions, such as a plating solution.

LIPF-based PM separation is often performed by the irradiation of the UV laser to the waste solution, whereas the UV lamp is also available in LIPF-based PM separation [19]. Figure 3.1b presents the comparison of UV laser and lamp irradiations to a mixture of $PM^{n+}$ and $M^{k+}$ ions, where the CT bands of ion complexes energetically neighbor each other. UV laser irradiation is preferable to lamp irradiation in the selective photo excitation of the $PM^{n+}$ ion, because the UV laser generates a narrow-wavelength light. Here, the laser wavelength is adjusted to the CT band wavelength of the $PM^{n+}$ ion complex, in order to enhance the photoexcitation efficiency by the UV laser irradiation. Contrarily, the UV lamp emits a broad-wavelength light, the irradiation of which excites the CT bands of ion complexes in a wide-wavelength region. Thus, the irradiation of the UV lamp leads to the simultaneous excitation of the CT bands of $PM^{n+}$ and $M^{k+}$ ions. The simultaneous excitation of both ions may decrease LIPF-based PM separation efficiency. The UV laser is more appropriate as a UV light source than the UV lamp for LIPF-based PM separation.

## 3.3 Background of LIPF-Based PM Separation

LIPF is used for not only metal separation but also nanoparticle preparation. Several reviews have already summarized the applications of LIPF to PM nanoparticle formation [13, 14]. Here, we focus on LIPF-based PM separation.

The application of laser-induced reduction (Eqs. 3.1 and 3.2) to metal separation was first reported by Donohue in the 1970s. He applied laser-induced reduction to metal separation in a dilute $H_2SO_4$ solution containing $Fe^{3+}$ and $Co^{3+}$ ion complexes [20]. By irradiating a nitrogen laser (337 nm) or Ar ion lasers (351–515 nm) to the sample solution, the CT bands of $Fe^{3+}$ and $Co^{3+}$ ion complexes were excited. The photoexcited $Fe^{3+}$ and $Co^{3+}$ ions were easily reduced to $Fe^{2+}$ and $Co^{2+}$ ions due to the largely positive standard electrode potential (E°) values of $Fe^{3+} + e^- \rightarrow Fe^{2+}$ (0.77 eV) and $Co^{3+} + e^- \rightarrow Co^{2+}$ (1.9 eV) [21]. Meanwhile, UV laser irradiation failed to reduce $Fe^{2+}$ and $Co^{2+}$ ions to $Fe^0$ and $Co^0$ neutrals due to the large potential barrier in the reduction path, although the detailed mechanism has remained unclear. Therefore, the reduction of $Fe^{3+}$ and $Co^{3+}$ ions stops with the formation of $Fe^{2+}$ and $Co^{2+}$. This situation is different from the laser-induced reduction of $PM^{n+}$ ions, where $PM^{n+}$ ions are reduced into $PM^0$ neutrals. In this report, $Fe^{2+}$ and $Co^{2+}$ ions

were recovered by the precipitation reaction:

$$2\left[M^{III}\left(C_2O_4^{2-}\right)_3\right]^{3-} + h\nu \rightarrow 2\left[M^{II}(C_2O_4)\right] \downarrow + 3C_2O_4^{2-} + 2CO_2 \ (M = Fe \text{ and } Co)\,. \tag{3.5}$$

Here, oxalate ion ($C_2O_4^{2-}$) was added in the sample solution as a complex ligand. $Fe^{II}(C_2O_4)$ and $Co^{II}(C_2O_4)$ precipitates were recovered via centrifugation. Figure 3.2 presents the dependence of the separation factor β, which was the molar concentration ratio of Fe to Co in the precipitations, on the laser wavelength. The $\beta$ values of the lower curve were less than 1 in the entire wavelength range because the $Co^{3+}$ ion is more reduced than the $Fe^{3+}$ ion due to the larger E° of $Co^{3+} + e^- \rightarrow Co^{2+}$. The β value is maximized around 355 nm. It indicates that the separation efficiency can be optimized by adjusting the irradiation laser wavelength.

Donohue further applied laser-induced reduction to an $H_2O$/alcohol solution containing $Ln^{k+}$ ions and demonstrated the successful separation of Eu [22] and Ce [23] from other Ln species. Nakashima et al. also reported the laser-induced reduction of $Ln^{k+}$ ions, such as $Eu^{3+}$ [24–26], $Sm^{3+}$ [27, 28], and $Yb^{3+}$ [29]. One of their research aims was to apply laser-induced reduction to the separation of Ln and Ac metals from high-level wastes [24]. The most distinguished point of Nakashima's works was the demonstration of a resonant two-photon reduction in $Ln^{k+}$ ions using femtosecond-, picosecond-, and nanosecond-pulsed lasers. Figure 3.3 summarizes the photoreduction schemes of the CT band by one-photon and two-photon processes

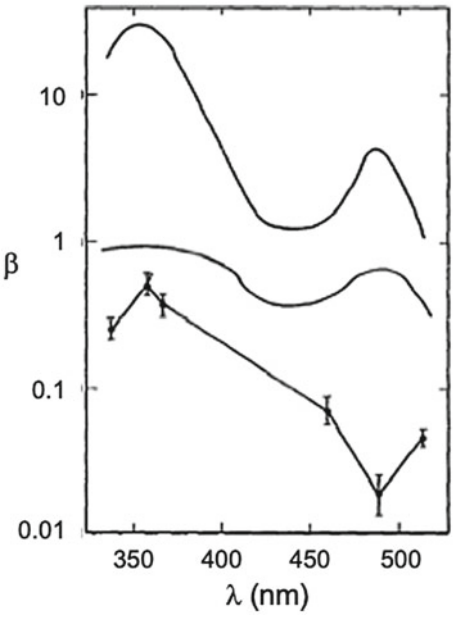


**Fig. 3.2** Dependence of the separation factor $\beta$ on the irradiation laser wavelength using laser-induced reduction (lower curve). The upper and center curves are the $\beta$ values estimated based on the absorption coefficient and quantum yields for the reduction (Eq. 3.5). Adapted from Ref. [20], Copyright 1977, with permission from Elsevier

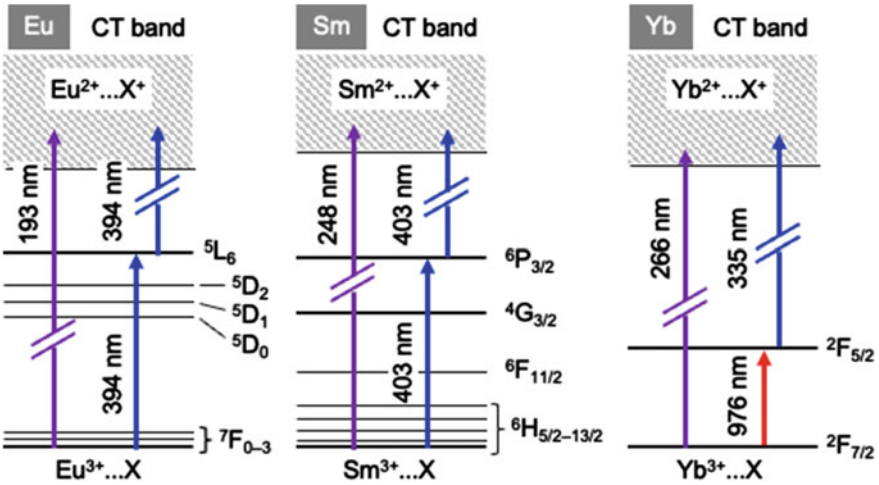


**Fig. 3.3** Photoreduction schemes of the CT band by one-photon and two-photon processes employed in Eu [22, 24–26], Sm [27, 28], and Yb [29] by Donohue and Nakashima

employed in Donohue and Nakashima's works. $Ln^{k+}$ ions have sharp absorption bands in the UV–Vis–IR regions, which are attributed to 4f–4f transitions. The excitation of the CT band by two-photon reduction via 4f–4f transitions reduces $Ln^{k+}$ ions with high selectivity because 4f–4f transition energies depend on the lanthanide ion type (394 nm in $Eu^{3+}$, 403 nm in $Sm^{3+}$, and 976 nm in $Yb^{3+}$). Based on the scheme in Fig. 3.3, Nakashima has successfully reduced $Eu^{3+}$, $Sm^{3+}$, and $Yb^{3+}$ ions to $Eu^{2+}$, $Sm^{2+}$, and $Yb^{2+}$ ions, respectively. Donohue's and Nakashima's works gave fundamental idea about the metal recovery using the laser-induced reduction, though strictly speaking they were not the LIPF process.

Donohue has demonstrated that laser irradiation reduces $Ln^{3+}$ ions into $Ln^{2+}$ ions, which are recovered as compounds involving $C_2O_4^{2-}$ and $SO_4^{2-}$ [22, 23]. Conversely, $Ln^{3+}$ ions are not recovered by laser irradiation in the $HNO_3$ and HCl solutions. Moreover, the LIPF studies of PMs have shown that UV laser irradiation to $PM^{n+}$ ions generates PM nanoparticles in the $HNO_3$ and HCl solutions containing the alcohol [13, 14]. These results motivated us to apply LIPF-based PM separation to a mixture of $PM^{n+}$ and $Ln^{k+}$ ions. The separation of $PM^{n+}$ from $Ln^{k+}$ was first demonstrated by Song et al. in 2001 [30]. In their work, a nanosecond-pulsed 355-nm laser was irradiated to an $H_2O$/EtOH solution involving $PdCl_2$ and $DyCl_3$ for 4 h. Figure 3.4 presents the change in the transmission spectra before and after laser irradiation. It shows that the transmittance of the $Pd^{2+}$ ion increases with the precipitation of Pd particles generated by LIPF, whereas the transmittance of the $Dy^{3+}$ ion remained the same during laser irradiation. This result indicated that the Pd metal was successfully separated from Dy via LIPF-based PM separation.

Before we introduced LIPF-based PM separation in 2012 [5], the LIPF research had been stagnant because of the lack of appropriate applications and insights into the

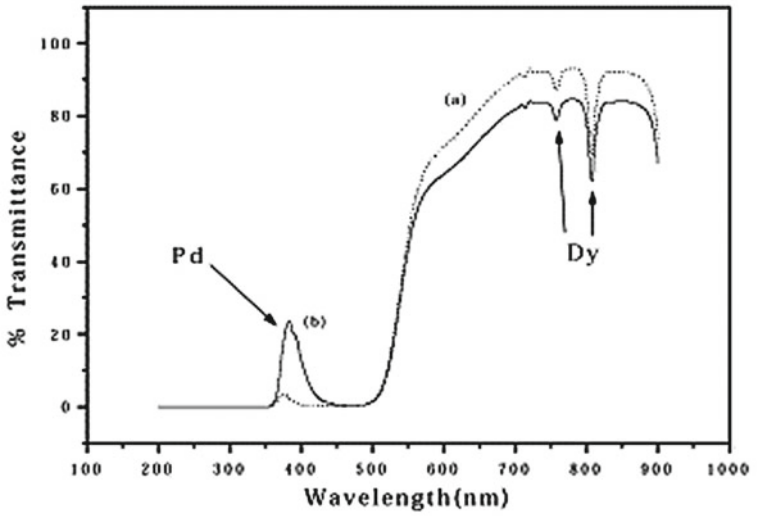


**Fig. 3.4** Transmission spectra of the $PdCl_2$ and $DyCl_3$ mixture in the $H_2O$/EtOH solution: **a** before laser irradiation and **b** after laser irradiation for 4 h. Reprinted from Ref. [30], Copyright 2001, with permission from Elsevier

LIPF mechanism. As suggested by Song [30], LIPF-based separation is an adequate technique for PM recovery from the SNF, which contains a few kilograms of Pd, Rh, and Ru in 1-ton SNF (Fig. 3.5). However, there was no report on the LIPF-based PM separation from a real SNF solution. We firstly investigated the recovery efficiency of Pd, Rh, and Ru in the LIPF-based PM separation from a mixture solution with Ln [5]. Then, the experimental parameters to maximize the recovery efficiency were investigated in the LIPF-based PM separation of Pd from a simulated solution containing 14 metals (Rb, Sr, Zr, Mo, Ru, Rh, Pd, Cs, Ba, La, Ce, Pr, Nd, and Sm) [8]. Finally, using the optimized parameters in the 14-metal solution, we verified the applicability of LIPF-based PM separation to Pd recovery from a real SNF solution [7,

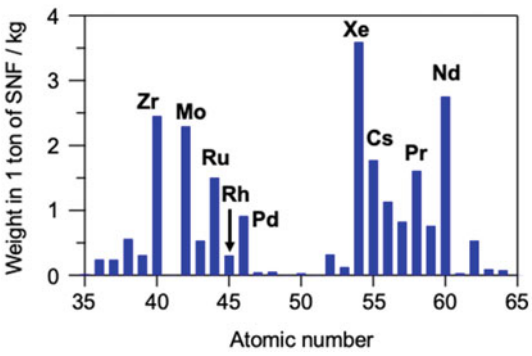


**Fig. 3.5** Weights of the fission products other than actinides in 1 ton of SNF. The graph was made based on Table data in Ref. [15]

10]. Moreover, in the development of LIPF-based PM separation, we found that size of the metal particle generated by LIPF depends on the laser irradiation conditions [6]. To reveal the relationship between the laser irradiation conditions and particle size, the LIPF mechanism was studied by in situ time-resolved X-ray absorption spectroscopy (XAS) [9]. The details of these studies are described in the following sections.

## 3.4 Application of LIPF-Based PM Separation to SNF Solution

### *3.4.1 LIPF-Based Separation of Pd, Rh, and Ru from a Mixture Solution with Nd*

Although Song et al. showed the LIPF-based separation of Pd from Ln based on the transmission increase in the $Pd^{2+}$ absorption band [30], they did not quantitatively analyze the recovery efficiency of the Pd metal. In addition, LIPF-based PM separation had not been applied to Rh and Ru metals. We investigated the LIPF-based separation of Pd, Rh, and Ru from Nd, which are abundantly included in SNF (Fig. 3.5) [5].

The sample solution was prepared by dissolving $PdCl_2$, $RhCl_3$, $RuCl_3$, and $NdCl_3$ solids in an $H_2O$/EtOH solution (v/v = 1/1). The fourth harmonic of an Nd:YAG laser (266 nm) was employed as the UV light source because the 266-nm photon is absorbed by the $Pd^{2+}$, $Rh^{3+}$, and $Ru^{3+}$ ions but not by the $Nd^{3+}$ ion (Fig. 3.6). The 266-nm pulsed laser (intensity, 20 mJ/pulse) was irradiated to the sample solution containing $Pd^{2+}$, $Rh^{3+}$, $Ru^{3+}$, and $Nd^{3+}$ (0.5 mM each) for 40 min. The PM particles were recovered using a 0.2 μm filter.

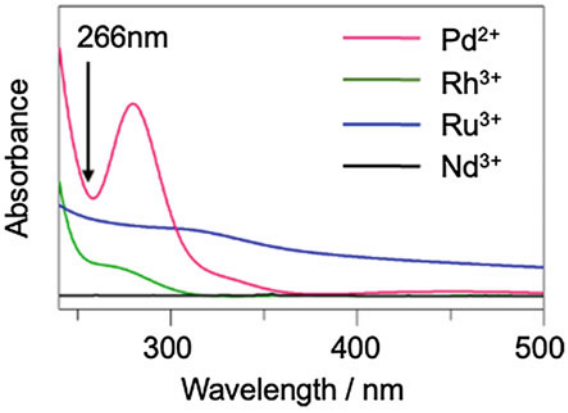


**Fig. 3.6** Examples of UV–Vis absorption spectra of the $H_2O$/EtOH solutions of $PdCl_2$, $RhCl_3$, $RuCl_3$, and $NdCl_3$. Note that spectral shapes are changed by the addition of the $Cl^-$ ion. In this condition, some $Ru^{3+}$ ions may exist as $RuCl_3$ particles with low solubility in the solution

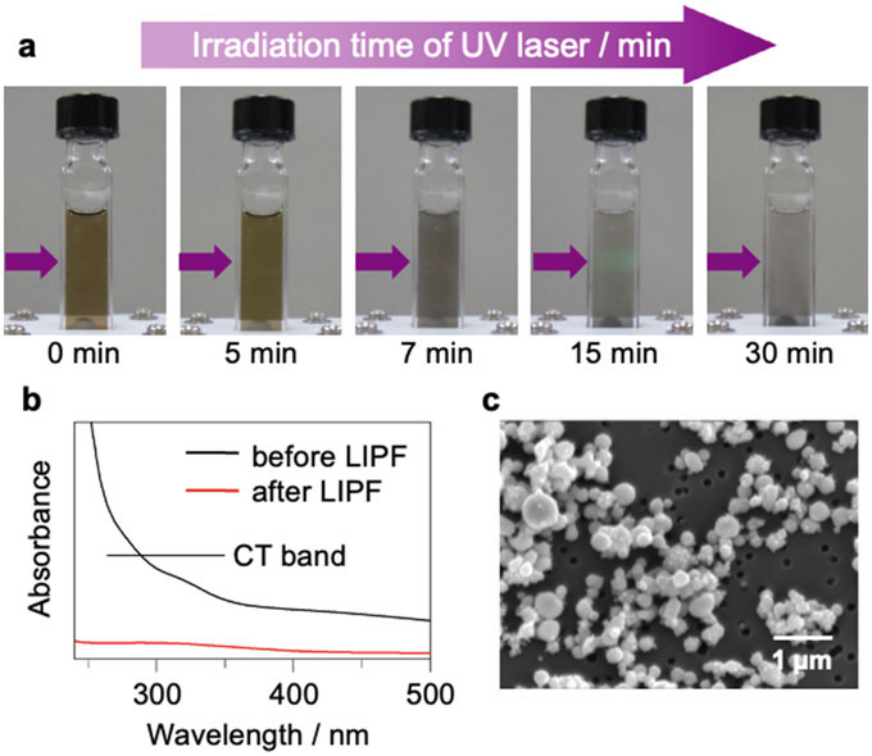


**Fig. 3.7** **a** Photographs of sample solutions during laser irradiation. **b** UV–Vis spectrum of the sample solution before and after LIPF. **c** TEM image of the recovered PM particles. Adapted from Ref. [5]

Figure 3.7a presents the photographs of sample solutions during laser irradiation. The color of the sample solution was light brown at 0 min, changed to gray at 7 min, and then became transparent at 30 min because of the precipitation of the generated PM particles. Figure 3.7b presents the UV–Vis spectrum of the sample solution before and after LIPF. It shows the disappearance of the CT band of the $Pd^{2+}$, $Rh^{3+}$, and $Ru^{3+}$ mixture after LIPF-based separation. Figure 3.7c shows a scanning electron microscope (SEM) image of the recovered PM particles, which were spherical with a size of 0.1–0.5 µm.

To determine the recovery efficiency, we measured the concentration of metal ions in the original and filtrate solutions, $[M]_{orig}$ and $[M]_{fil}$, via inductively coupled plasma atomic emission spectroscopy (ICP-AES). The recovery efficiencies of Pd, Rh, Ru, and Nd were determined using the following equation:

$$\text{Recovery } (\%) = \frac{[M]_{orig} - [M]_{fil}}{[M]_{orig}}. \tag{3.6}$$

The ICP-AES measurement determined that the recovery efficiency was 100% for Pd, 99% for Rh, 69% for Ru, and <1% for Nd. Here, we note the possibility that some Ru samples may have been recovered as the $RhCl_3$ compound, which had low solubility in the solution. Based on the recovery efficiencies, we concluded that the LIPF method separated the Rh and Ru metals as well as the Pd from the Ln metals [5].

### *3.4.2 Recovery of Pd from a Simulated SNF Solution Containing 14 Metals*

SNF contains artificial radioactive nuclides with long half-life periods, such as $^{90}Sr$, $^{99}Tc$, $^{107}Pd$, and $^{137}Cs$ [15, 31]. The abundance ratio of artificial radioactive nuclides in SNF is a fingerprint of the nuclear power plant because it depends on the burnup and operating time of the reactor. The $^{107}Pd$ nuclide, the half-life of which is 6.5 million years, is one of the artificial radioactive nuclides used to track the source of SNF [7, 10, 31]. The abundance ratio of $^{107}Pd$ against stable Pd isotopes ($^{104}Pd$, $^{105}Pd$, $^{106}Pd$, $^{108}Pd$, and $^{110}Pd$) is essential for the safety assessment of the environmental radioactivity of SNF.

When the artificial radioactive nuclides emit $\gamma$ rays, they can be easily identified and quantified by $\gamma$-ray spectrometry. However, the $^{107}Pd$ isotope is difficult to be quantified via $\gamma$-ray spectrometry as it scarcely emits $\gamma$ rays during $\beta$ decay [7, 31]. In this case, ICP mass spectrometry (ICP-MS) is appropriate for the quantitative analysis of $^{107}Pd$. The ICP-MS analysis of $^{107}Pd$ in SNF needs pretreatment, in which the Pd metal is separated from dozens of metals to avoid spectral interference in the mass spectrum. The pretreatment should be performed by a rapid and contactless operation, because the operator is exposed to radiation during the separation. To develop a safe operation for SNF pretreatment, we investigated the LIPF-based separation of Pd from the simulated SNF solution [8].

The recovery efficiency in LIPF-based PM separation depends on the EtOH concentration in the sample solution ($H_2O$/EtOH mixture), laser irradiation time, and laser irradiation intensity. The parameters should be adjusted for the effective separation of Pd from SNF. First, we optimized these parameters to maximize the recovery efficiency (Eq. 3.6) of Pd from a simulated SNF solution, which contained 14 nonradioactive metals (Rb, Sr, Zr, Mo, Ru, Rh, Pd, Cs, Ba, La, Ce, Pr, Nd, and Sm). The concentrations of the metal ions were determined based on the database of the real SNF [15]. LIPF was performed by irradiating the nanosecond-pulsed 355-nm laser to the $HNO_3$ solution of the 14 metals containing EtOH.

Figure 3.8a demonstrates the dependence of Pd recovery on the EtOH concentration in the region of 0–50 v/v% (EtOH/$H_2O$+EtOH). The Pd recovery, which was 0% in the absence of EtOH (0 v/v%), increased from 1 to 40 v/v% and decreased beyond 40 v/v%. The addition of EtOH not only aids in the reduction of the $Pd^{2+}$ ion but also stabilizes the $Pd^{2+}$ ion by solvation. The balance between the former

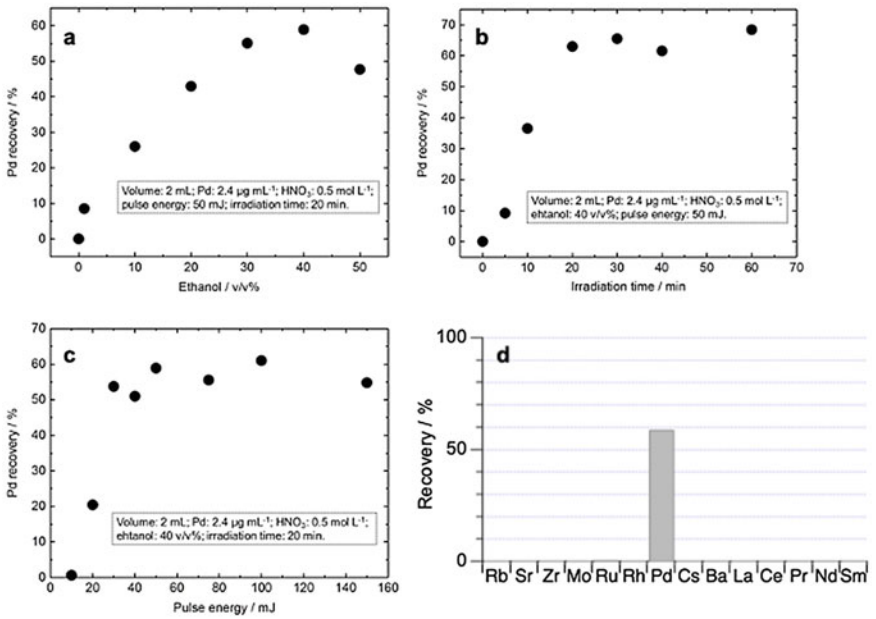


**Fig. 3.8** **a** Dependence of Pd recovery on ethanol concentration, **b** irradiation time, and **c** pulse energy. **d** Recovery of 14 elements by LIPF-based PM separation using optimized parameters. Reprinted and adapted from Ref. [8] with permission from The Japan Society for Analytical Chemistry (Copyright 2017)

and latter effects is assumed to determine the optimum EtOH concentration in LIPF-based PM separation. Figures 3.8b and c present the dependence of the recovery efficiency of Pd on the laser irradiation time and the laser pluse energy in 40 v/v% EtOH. The Pd recovery increased with the irradiation time and remained constant after 20 min of laser irradiation. The Pd recovery showed a positive correlation with the laser intensity in the region of 0–50 mJ/pulse and no dependence beyond a laser intensity of 50 mJ/pulse. We applied the optimum parameters (EtOH concentration, 40 v/v%; irradiation time, 20 min; and intensity, 100 mJ/pulse) to Pd separation and recovered ~60% of Pd while reducing the percentage of other 13 metals to below 1%, as presented in Fig. 3.8d.

### *3.4.3 Recovery of Pd from Real SNF Solution*

In the next step, LIPF-based separation was applied to Pd recovery from the real SNF solution using the parameters determined from the simulated solution [7]. The SNF solution was prepared by dissolving a single fuel pellet in the $HNO_3$ solution. The fuel pellet was irradiated in a Japanese pressurized water reactor with a burnup of

44.9 GWd/t and a cooling period of 10,257 days. Figure 3.9 presents the procedure of LIPF-based separation for the ICP-MS analysis of $^{107}$Pd. Sample solutions were prepared by adding natural Pd samples (comparison standard) to SNF solutions and adjusting the $HNO_3$ concentration to 0.5 M and the EtOH concentration to 40 v/v%. LIPF-based separation was performed by irradiating the nanosecond-pulsed 355-nm laser (intensity, 100 mJ/pulse) to the sample solutions for 20 min. The Pd particles generated by LIPF were recovered using a 0.1 μm filter.

Table 3.1 lists the recoveries for each component in Pd precipitates obtained from two sample solutions. In both sample solutions, LIPF-based separation successfully recovered Pd with an efficiency of ~90% while suppressing the contamination of Ac to an undetectable level and that of Ln to below 0.1%.

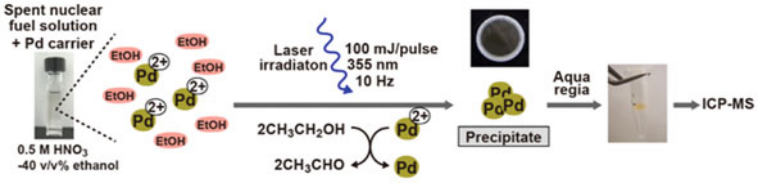


**Fig. 3.9** Procedure of LIPF-based PM separation for the ICP-MS analysis of $^{107}$Pd. Reprinted with permission from Ref. [7] (Copyright 2016 American Chemical Society)

**Table. 3.1** Recoveries (%) for each component in Pd precipitates obtained from two SNF solutions.

| Element | SP–1 | SP–2 | Element | SP–1 | SP–2 |
|---|---|---|---|---|---|
| PM | | | Others | | |
| Pd | 91.4 ± 0.5 | 88.0 ± 0.5 | Rb | 0.07 | 0.21 |
| Ru | 0.03 | 0.04 | Sr | 0.26 | 0.32 |
| Rh | 0.05 | 0.29 | Zr | 0.02 | 0.03 |
| Ln | | | Mo | <0.01 | 0.02 |
| La | 0.05 | 0.07 | Tc | 0.45 | 1.02 |
| Ce | 0.08 | 0.10 | Cs | 0.03 | 0.02 |
| Pr | 0.05 | 0.07 | Ba | 0.10 | 0.07 |
| Nd | 0.03 | 0.04 | | | |
| Sm | <0.01 | 0.01 | | | |
| Ac | | | | | |
| U | <0.01 | <0.01 | | | |
| Np | <0.01 | <0.01 | | | |
| Pu | <0.01 | <0.01 | | | |
| Am | <0.01 | <0.01 | | | |
| Cm | <0.01 | <0.01 | | | |

Reprinted with permission from Ref. [7] (Copyright 2016 American Chemical Society)

Finally, the ratio of the $^{107}$Pd isotope to the $^{238}$U isotope in the SNF solution was determined by the ICP-MS measurement of the acid solution involving the recovered Pd particles. The ICP-MS measurement elucidated that the SNF solution contains 239 ± 9 ng of $^{107}$Pd per 1 mg of $^{238}$U. This is the first report on the quantitative analysis of $^{107}$Pd in SNF [7].

## 3.5 Fundamentals of the LIPF Process in a Pd Solution

### *3.5.1 Dependence of LIPF Efficiency on Laser Pulse Conditions*

As described in Sect. 3.4.2, the laser irradiation time and laser intensity are important parameters in the LIPF process. Previous works on LIPF-based PM separation had used pulsed laser as a UV light source [5–8, 30]. In the pulsed laser, the pulse conditions (pulse repetition rate and pulse fluence) may be important parameters other than the irradiation time and intensity, although their contribution to the LIPF process was not investigated until recently. The pulsed laser stores the flashlamp energy in the optical cavity by activating a variable attenuator (Q-switch) and can change the pulse repetition rate by controlling the Q-switch. By using a Q-switched device, we compared the recovery efficiencies in LIPF-based PM separation at low and high repetition rates. The averaged irradiation fluences were made the same by increasing pulse fluences for the low repetition rate and decreasing pulse fluences for the high repetition rate (averaged fluence = pulse repetition rate × pulse fluence). We investigated the metal recovery efficiency and the recovered particle size in changing the pulse repetition rate and the pulse fluence under constant averaged fluence and discussed the influence of them on the LIPF process [6].

A 0.5-M $HNO_3$ solution of 5-mM $Pd^{II}Cl_2$ and 20-mM $Na_2Mo^{VI}O_4$ containing 1-v/v% EtOH was prepared and used as the sample solution. It is regarded as a simple simulated solution of SNF because the Pd and Mo metals are abundantly contained in SNF (Fig. 3.5). LIPF-based PM separation was performed by the irradiation of nanosecond-pulsed 355-nm lasers with a low repetition rate and high fluence (10 Hz and 64 mJ/cm$^2$) and with a high repetition rate and low fluence (30 kHz and 22 μJ/cm$^2$). The averaged irradiation fluence was set to 0.64 W/cm$^2$ in both laser irradiation scenarios. The generated Pd particles were recovered using a 0.2 μm filter.

Figure 3.10a presents the temporal changes in the Pd and Mo concentrations during the laser irradiations with the low (10 Hz) and high (30 kHz) repetition rates. Both irradiations showed that the recovery efficiencies of Pd increased immediately after the laser irradiation and became constant after 15 min, whereas the recovery efficiencies of Mo remained at 0% for 20 min. These results indicate that the Pd metal was successfully separated from Mo using the LIPF method. Further, the Pd recovery after the laser irradiation for 20 min was 84% for the 10 Hz repetition rate and 72% for the 30-kHz repetition rate. This result indicates that the recovery efficiency in

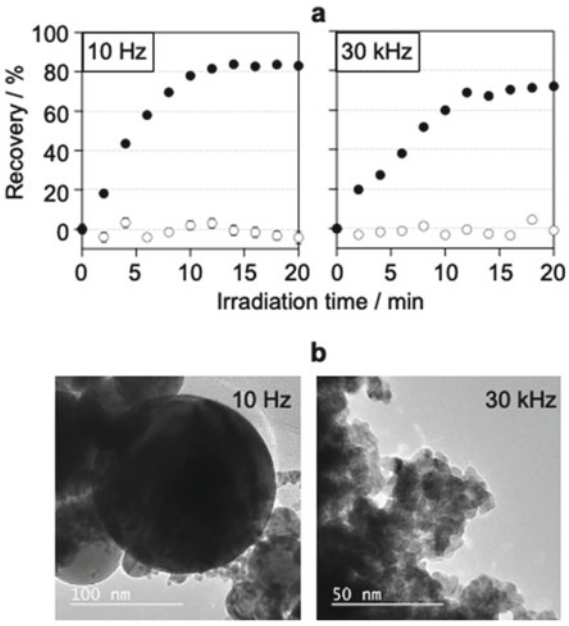


**Fig. 3.10** **a** Temporal changes in the Pd and Mo recovery efficiencies at 10 and 30 kHz repetition rates. **b** TEM images of Pd particles recovered after irradiation at 10 and 30 kHz repetition rates. Adapted from Ref. [6], Copyright 2014, with permission from Elsevier

LIPF is influenced by the pulse repetition rate and fluence in the presence of the same input energy.

To find the reason why the recovery efficiency changed depending on the pulse repetition rate and fluence, we observed the shape of the recovered Pd particles using a transmission electron microscope (TEM). As presented in Fig. 3.10b, the TEM images showed the formation of submicron particles (0.1–0.5 μm) in the LIPF using the 10-Hz laser and the formation of only nanoparticles (<10 nm) using the 30-kHz laser. The submicron particles were not observed in the TEM images in the 30 kHz laser. In the recovery, a 0.2 μm filter caught the submicron particles and the nanoparticle aggregates, while it missed the isolated nanoparticles. We concluded that the laser pulse conditions (pulse repetition rate and fluence) drastically change size of the particles generated by the LIPF, and that the formation of submicron Pd particle in the 10-Hz laser contributes to increase of the recovery efficiency [6].

### *3.5.2 LIPF Process in Pd Solution Using in Situ Time-Resolved XAS*

As described in Sect. 3.2, the LIPF process involves a series of elementary reactions (Eqs. 3.1–3.4), which was constructed by the analogy with the lamp-induced particle formation in the presence of a photoactivator (PA) [32, 33]. In the lamp-induced particle formation, the $PM^{n+}$ ion is reduced by a photoexcited photoactivator (PA)*

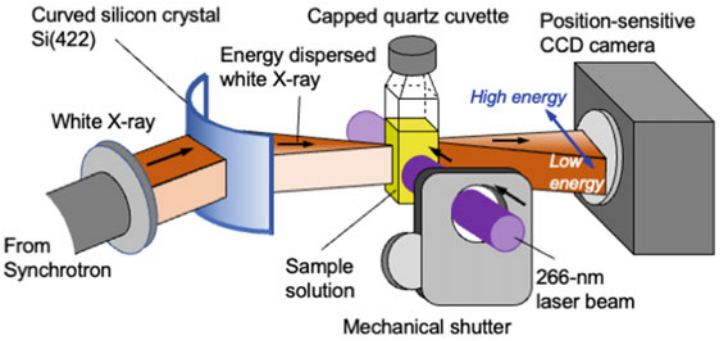


**Fig. 3.11** Experimental setup for the dispersive XAFS measurements of LIPF in the Pd solution

or a photoactivator radical PA• as follows:

$$\mathrm{PA} + h\nu \rightarrow (\mathrm{PA})^* \text{ or } \mathrm{PA}\cdot$$

$$\mathrm{PM}^{n+} + (\mathrm{PA})^* \text{ or } \mathrm{PA}\cdot \rightarrow \mathrm{PM}^0 + \text{PA products} . \tag{3.7}$$

However, the reaction model (Eqs. 3.1–3.4) for the LIPF process had not been discussed until we conducted a reaction study on the Pd solution. The reaction studies on lamp-induced particle formation suggest that the time-resolved X-ray absorption fine structure (XAFS) spectroscopy is a powerful tool for investigating the photoinduced reduction of $PM^{n+}$ followed by particle formation [32, 33]. The XAFS data give information on the oxidation state of Pd species in the reduction of $Pd^{2+}$ to $Pd^0$ and the geometries of $Pd^{2+}$ ion complexes and Pd particles. Thus, we investigated the LIPF process in the $H_2O$/EtOH solution of $Pd^{2+}$ using time-resolved XAFS spectroscopy [9].

Figure 3.11 presents the experimental setup for the time-resolved XAFS measurement in the dispersive mode. In the dispersive XAFS measurement, a white X-ray from the synchrotron enters the curved silicon crystal Si(422) to disperse X-ray energy. We focused the dispersed X-ray on the sample solution, which was placed on the beamline, and detected the transmitted X-ray using a position-sensitive CCD camera. The dispersive mode enables us to obtain one absorption spectrum via one X-ray irradiation. The XAFS spectra were measured around Pd K-edge (24.4 keV). In situ observation of LIPF was performed by synchronizing the opening of the laser shutter with the start of the dispersive XAFS measurement. The sample solution was prepared by mixing 30-mM $PdCl_2$ in 100-mM NaCl solution and 2-g/L poly(vinylpyrrolidone) in EtOH in the ratio of 1:1 (v/v). The pulse fluence of the nanosecond-pulsed UV laser (wavelength, 266 nm; repetition rate, 10 Hz) was adjusted in the region of 0–59.7 mJ/cm$^2$.

Figure 3.12 presents the typical spectra of time-resolved XAFS in the region of 24.30–24.85 keV at a laser fluence of 59.7 mJ/cm$^2$. The spectral shape in the

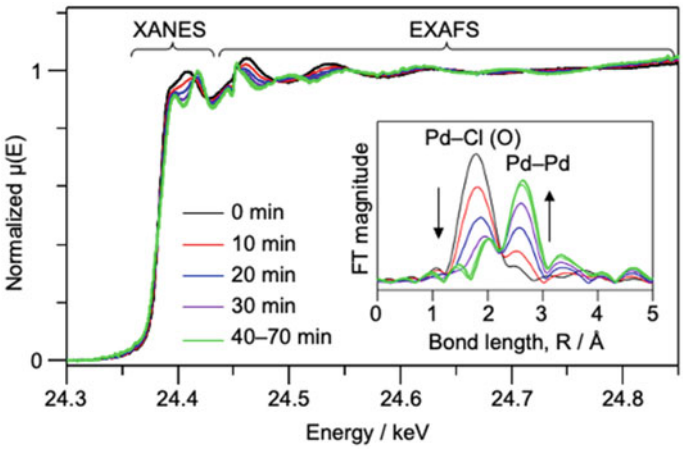


**Fig. 3.12** Time-resolved XAFS spectra at a laser fluence of 59.7 mJmJ/cm$^2$ from 0 to 70 min. The inset shows the temporal change in Fourier-transformed EXAFS oscillations. Adapted with permission from Ref. [9] ( Copyright 2019 American Chemical Society)

energy region beyond the absorption edge is called extended X-ray absorption fine structure (EXAFS). The EXAFS shows the oscillation created by the interference of waves between the outgoing photoelectron and the electron being backscattered by neighboring atoms. The analysis of the EXAFS oscillation provides structural information on the Pd–ligand bonds in the $Pd^{2+}$ ion complex and the Pd–Pd bonds in the Pd particle. The inset spectra in Fig. 3.12 present Fourier transforms (FTs) of the EXAFS oscillation. The FTs showed two bands in the R regions of 1.2−2.2 and 2.2−3.1 Å. The $Pd^{2+}$ ion complex is dissolved in the concentrated NaCl solution as $[Pd^{II}Cl_4]^{2-}$ and $[Pd^{II}Cl_3(H_2O)]^-$ [34]. The band in the range of 1.2−2.2 Å is attributed to the Pd−Cl and Pd–O bonds in $[PdCl_4]^{2-}$ and $[PdCl_3(H_2O)]^-$, which are indistinguishable owing to their similar bond lengths. The band in the range of 2.2−3.1 Å is attributed to the Pd−Pd bond in the Pd nanoparticle. The increase in irradiation time leads to the decrease in the Pd–Cl band and the increase in the Pd–Pd band. These changes reflect the dissociation of Pd–Cl and Pd–O bonds by the reduction of $[PdCl_4]^{2-}$ and $[PdCl_3(H_2O)]^-$ ions to $Pd^0$ neutral and the formation of Pd–Pd bonds in the Pd nanoparticle. A more detailed analysis of the EXAFS oscillations was described in Ref. [9].

The spectral shape around the Pd absorption edge is called X-ray absorption near edge structure (XANES). The XANES reflects the averaged oxidation state of Pd species during the LIPF process. Figure 3.13 presents the enlarged spectra of the XANES in Fig. 3.12. The increase in the irradiation time led to a decrease in the band intensity in the region of 24.38–24.41 keV, an increase in the band intensity in the region of 24.41–24.43 keV, and broadening of the edge width in the region of 24.36–24.40 keV. The band intensity and the edge width changed for 40 min and remain unchanged after 40 min. This suggests that the LIPF reaction was completed

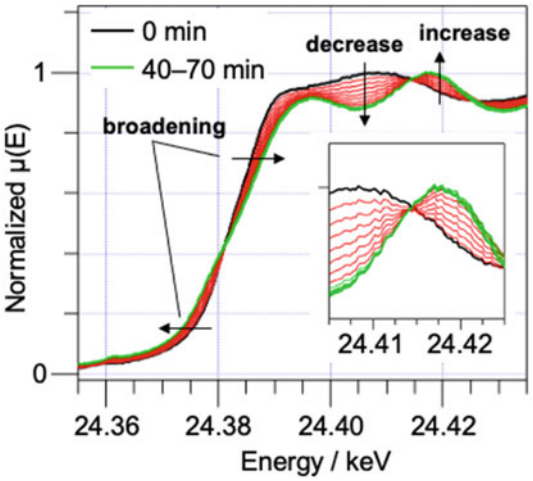


**Fig. 3.13** Temporal changes in the XANES spectra at a laser fluence of 59.7 mJmJ/cm$^2$. The inset shows the enlarged spectra around the isosbestic point at 24.41 keV. Adapted with permission from Ref. [9] ( Copyright 2019 American Chemical Society)

in 40 min. Further, the normalized μ(E) values were kept constant at 24.38, 24.41, and 24.43 keV during laser irradiation (inset of Fig. 3.13). The appearance of several isosbestic points indicated that the XANES spectra are dominated by two Pd species, $Pd^{2+}$ and $Pd^0$, without any intermediates.

As discussed in Ref. [9], the edge width and the band intensity of the XANES are correlated with the $Pd^{2+}$ concentration, [$Pd^{2+}$]. Figure 3.14 presents the temporal change in [$Pd^{2+}$] in LIPF with a fluence range of 0–59.7 mJ/cm$^2$, which was obtained from the analysis of the edge width. The temporal change at 0 mJ/cm$^2$ shows that [$Pd^{2+}$] was kept constant at 15 mM during the dispersive XAFS measurement. Thus, the $Pd^{2+}$ ion was not reduced only by X-ray irradiation. The temporal changes in [$Pd^{2+}$] in the fluence range of 19.9–59.7 mJ/cm$^2$ clearly indicate that the increase in the laser fluence promotes the laser-induced reduction of $Pd^{2+}$.

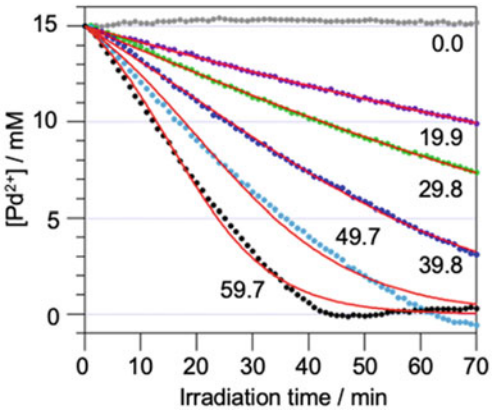


**Fig. 3.14** Temporal changes in [$Pd^{2+}$] obtained from the edge width of XANES at a fluence of 0–59.7 mJmJ/cm$^2$. The red lines indicate the simulated curves based on Eq. 3.13. Adapted with permission from Ref. [9] ( Copyright 2019 American Chemical Society)

To extract the information on the chemical kinetics of LIPF, the temporal changes in $[Pd^{2+}]$ were analyzed using a two-step reduction model, considering the autocatalytic growth described in Sect. 3.2. Based on Eqs. 3.1–3.4, the authors assumed the following elementary reactions:

$$Pd^{2+} + CH_3CH_2OH + h\nu \xrightarrow{k_1} Pd^0 + CH_3CHO + nH^+, \tag{3.8}$$

$$kPd^0 \rightarrow \left(Pd^0\right)_k, \tag{3.9}$$

and

$$\left(Pd^0\right)_m + Pd^{2+} + CH_3CH_2OH + h\nu \xrightarrow{k_2} \left(Pd^0\right)_{m+1} + CH_3CHO + nH^+. \tag{3.10}$$

$k_1$ and $k_2$ denote the reaction coefficients of Eqs. 3.8 and 3.10. Based on the elementary reactions 3.8 and 3.10, the rate equation of $[Pd^{2+}]$ is

$$\frac{d\left[Pd^{2+}\right]}{dt} = -k_1 \cdot \left[Pd^{2+}\right] \cdot [CH_3CH_2OH] - k_2 \cdot [\left(Pd^0\right)_m] \cdot [Pd^{2+}] \cdot [CH_3CH_2OH]. \tag{3.11}$$

$[CH_3CH_2OH]$ was assumed to be constant during the LIPF reaction because a large amount of EtOH was supplied in the sample solution. Thus, Eq. 3.11 is modified as.

$$\frac{d\left[Pd^{2+}\right]}{dt} = -k_1' \cdot \left[Pd^{2+}\right] - k_2' \cdot [\left(Pd^0\right)_m] \cdot [Pd^{2+}]. \tag{3.12}$$

The temporal change in $[Pd^{2+}]$ is described as.

$$\left[Pd^{2+}\right] = \frac{\frac{k_1'}{k_2'} + \left[Pd^{2+}\right]_0}{1 + \frac{k_1'}{k_2'\left[Pd^{2+}\right]_0} \exp\left\{\left(k_1' + k_2'\left[Pd^{2+}\right]_0\right)t\right\}}. \tag{3.13}$$

Here, $[Pd^{2+}]_0$ was 15 mM. By optimizing the $k_1$' and $k_2$' values in Eq. 3.13, we simulated the temporal changes in $[Pd^{2+}]$ at various fluences, as presented in Fig. 3.14. The good agreement between experimental and simulated curves suggests that the LIPF mechanism in the Pd solution can be explained by a two-step reaction model, considering the autocatalytic growth (Eqs. 3.8–3.10).

Figure 3.15 presents the log–log plot of the $k_1$' and $k_2$' values, which was obtained from the simulation of the temporal change in $[Pd^{2+}]$ (Fig. 3.14), against the laser fluence. The slopes of the plots, which reflect the number of UV photons that contribute to the reactions (Eqs. 3.8 and 3.10), are 1.03 for $k_1$' and 3.37 for $k_2$'.

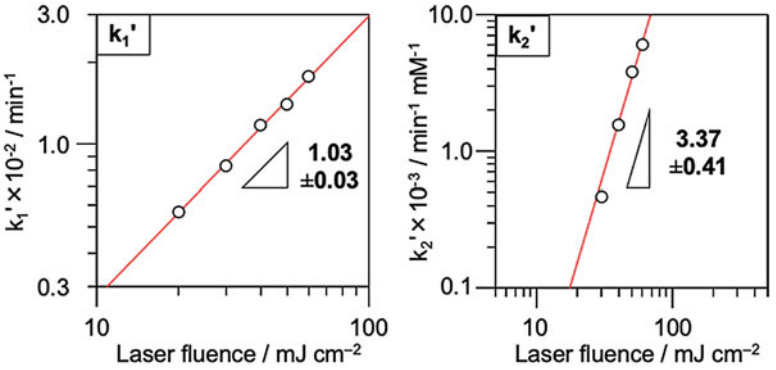


**Fig. 3.15** Log—log plots of the rate constants $k_1$' and $k_2$' (Eqs. 3.8 and 3.10) obtained from the simulation of the temporal changes in $[Pd^{2+}]$ (Fig. 3.14) against laser fluence. Adapted with permission from Ref. [9] ( Copyright 2019 American Chemical Society)

The $k_1$' and $k_2$' values indicate that the reduction of $Pd^{2+}$ proceeds via one UV photon absorption in Eq. 3.8 and via three-to-four UV photons in Eq. 3.10. Based on these results, we conclude that the nanosecond-pulsed UV laser contributes to not only the direct reduction of $Pd^{2+}$ by the one-photon process but also the autocatalytic reduction by the multiphoton process.

Figure 3.16 summarizes elementary reactions in the LIPF process in the Pd solution, which is speculated from the time-resolved XAFS results. Firstly, the $Pd^{2+}$ ion complexes are reduced to the $Pd^0$ neutrals by one-photon absorption. Spontaneous aggregation of the $Pd^0$ neutrals results in formation of the Pd nanoparticle, which grows up to be the Pd nanocatalyst by coalescence of the small Pd nanoparticles and so on. The Pd nanocatalyst promotes the photoreduction of the $Pd^{2+}$ ion by the multiphoton process and generates large Pd particle. The multiphoton process is a

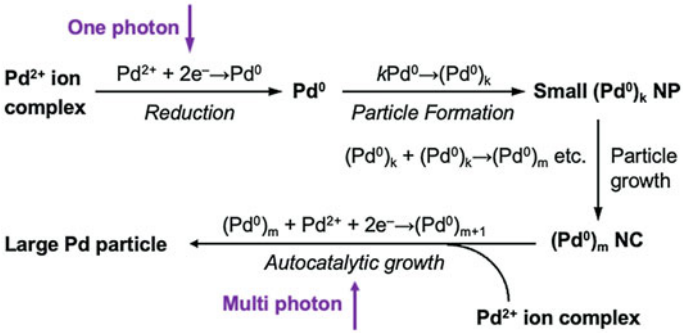


**Fig. 3.16** Summary of elementary reactions in the LIPF process in the Pd solution, which is speculated from the time-resolved XAFS study. NP and NC indicate nanoparticle and nanocrystal, respectively.

characteristic photochemical phenomenon observed when using an intense pulsed laser. It indicates that LIPF is effectively promoted by the irradiation of the pulsed UV laser. Note that Fig. 3.16 does not refer to the formation mechanism of the submicron Pd particle. To elucidate overall mechanism of the LIPF process, further research is necessary.

## 3.6 Summary

The basic principles, background, and applications of LIPF-based PM separation, as well as the fundamentals of the LIPF process, were described. It was demonstrated that the LIPF-based PM separation selectively recovered the Pd metal from the SNF solution, which contained more than 20 types of metals and radioactive actinides, and PMs other than Pd can be recovered by LIPF. In addition, pulsed laser conditions (pulse repetition rate and pulse fluence) changed the size of PM particles generated by LIPF even when the averaged laser fluence was kept constant. The autocatalytic growth in the LIPF process was promoted by the multiphoton process, which is typically observed when using an intense pulsed laser.

Finally, I refer to next development of the LIPF-based PM separation from the viewpoint of the applications and the fundamentals. Previous studies on LIPF-based PM separation have been conducted in batch-type reaction cells, which contain only several milliliters of the sample solution. When LIPF-based separation is implemented to the PM recycling process in the plant, it is applied to at least several liters of a waste solution per day. It means that the capabilities of the separation and recovery of PMs should be scaled up by at least 1,000 times for the implementation of LIPF-based PM separation. The LIPF-based PM separation parameters, such as the processing type (batch or flow), laser repetition rate, laser pulse fluence, and number of laser units, must be optimized. In particular, the selection of the processing type is important because flow processing has never been tested in LIPF-based PM separation. The most important development in LIPF-based PM separation would be the construction of flow processing and the comparison of the capabilities of flow processing and batch processing.

The fundamental study showed that the dependence of the reaction coefficients on the laser fluence is different between the reduction of $Pd^{2+}$ and the autocatalytic growth of the Pd particle, although this conclusion should be verified in comparison with other PM ions. Thus, dispersive XAFS measurements of PMs other than $Pd^{2+}$ are currently in progress. Moreover, we are also investigating the photoreduction mechanism of the $Pd^{2+}$ ion complex using ab initio multireference configuration interaction (MRCI) calculations [35, 36]. These works will elucidate overall mechanism of the LIPF process, paving the way for the development of LIPF-based PM separation in practical applications.

**Acknowledgements** The author would like to thank Dr. Hironori Ohba (QST), Dr. Shio Asai (AIST), Mr. Takumi Yomogida (JAEA), Dr. Tomitsugu Taguchi (QST), Dr. Ryuzo Nakanishi (QST),

Dr. Yuzuru Kurosaki (QST) and Dr. Fumitaka Esaka (JAEA) for their contribution to the applications of the LIPF separation to the SNF solution and the fundamental studies on the LIPF mechanism. The author would also like to thank Dr. Daiju Matsumura (JAEA), Dr. Takuya Tsuji (JAEA) and Dr. Hironori Saitoh (QST) for their cooperation in the study on the LIPF mechanism using X-ray absorption spectroscopy. The author express our sincere thanks to Prof. Emer. Nobuaki Nakashima (Osaka City Univ.) and Dr. Atsushi Yokoyama for their helpful comments to the LIPF researches. The author would like to thank Enago (www.enago.jp) for the English language review.

## References

1. H. Narita, R. Kasuya, T. Suzuki, R. Motokawa, M. Tanaka, Precious metal separations, in *Encyclopedia of Inorganic and Bioinorganic Chemistry*, ed by R.A. Scott (2020), pp. 1–28. https://doi.org/10.1002/9781119951438.eibc2756.
2. J. Shibata, A. Okuda, Recycling technology of precious metals. Shigen-to-sozai **118**, 1–8 (2002). https://doi.org/10.2473/shigentosozai.118.1 (inJapanese)
3. U. S. Geological Survey, Mineral commodity summaries 2021, https://doi.org/10.3133/mcs2021 (1 August 2021).
4. F.K. Crundwell, M.S. Moats, V. Ramachandran, T.G. Robinson, W.G. Davenport, Chapter 37—Refining of the platinum-group metals, in *Extractive Metallurgy of Nickel, Cobalt and Platinum Group Metals*, eds. by F.K. Crundwell, M.S. Moats, V. Ramachandran, T.G. Robinson, W.G. Davenport (Elsevier, Oxford, 2011), pp. 489–534. https://doi.org/10.1016/B978-0-08-096809-4.10037-1.
5. M. Saeki, F. Esaka, T. Taguchi, H. Ohba, Study on separation of platinum-group metals by using laser-induced particle formation. JAEA-Research 2012–030 (2012). https://doi.org/10.11484/jaea-research-2012-030 (in Japanese).
6. M. Saeki, T. Taguchi, N. Nakashima, H. Ohba, Wet separation between palladium(II) and molybdenum(IV) ions by using laser-induced particle formation: Enhancement of recovery efficiency of palladium by laser condition. J. Photochem. Photobiol A: Chem. **299**, 189–193 (2015). https://doi.org/10.1016/j.jphotochem.2014.11.022
7. S. Asai, T. Yomogida, M. Saeki, H. Ohba, Y. Hanzawa, T. Horita, Y. Kitatsuji, Determination of $^{107}$Pd in Pd recovered by laser-induced photoreduction with inductively coupled plasma mass spectrometry. Anal. Chem. **88**, 12227–12233 (2016). https://doi.org/10.1021/acs.analchem.6b03286
8. T. Yomogida, S. Asai, M. Saeki, Y. Hanzawa, T. Horita, F. Esaka, H. Ohba, Y. Kitatsuji, Non-contact and selective Pd separation based on laser-induced photoreduction for determination of $^{107}$Pd by ICP-MS-the relation between separation conditions and Pd recovery-. Bunseki Kagaku **66**, 647–652 (2017). https://doi.org/10.2116/bunsekikagaku.66.647 (inJapanese)
9. M. Saeki, D. Matsumura, T. Yomogida, T. Taguchi, T. Tsuji, H. Saitoh, H. Ohba, In situ time-resolved XAFS studies on laser-induced particle formation of palladium metal in an aqueous/EtOH solution. J. Phys. Chem. C **123**, 817–824 (2019). https://doi.org/10.1021/acs.jpcc.8b09532
10. S. Asai, M. Ohata, T. Yomogida, M. Saeki, H. Ohba, Y. Hanzawa, T. Horita, Y. Kitatsuji, Determination of $^{107}$Pd in Pd purified by selective precipitation from spent nuclear fuel by laser ablation ICP-MS. Anal. Bioanal. Chem. **411**, 973–983 (2019). https://doi.org/10.1007/s00216-018-1527-3
11. R. Nakanishi, M. Saeki, T. Taguchi, H. Ohba, Photoinduced gold recovery mediated by isopolymolybdate in strongly acidic HCl/NaCl solutions. J. Photochem. Photobiol A: Chem. **383**, 111994 (2019). https://doi.org/10.1016/j.jphotochem.2019.111994
12. M. Saeki, S. Asai, H. Ohba, Development of separation of platinum-group metals by using laser-induced particle formation. Bunseki **4**, 138–143 (2018). (in Japanese)

13. M. Sakamoto, T. Majima, Photochemistry for the synthesis of noble metal nanoparticles. Bull. Chem. Soc. Jpn. **83**, 1133–1154 (2010). https://doi.org/10.1246/bcsj.20100097
14. M. Sakamoto, M. Fujistuka, T. Majima, Light as a construction tool of metal nanoparticles: synthesis and mechanism. J. Photochem. Photobiol. C: Photochem. Rev. **10**, 33–56 (2009). https://doi.org/10.1016/j.jphotochemrev.2008.11.002
15. Committee of handbook on process and chemistry of nuclear fuel reprocessing, Handbook on process and chemistry of nuclear fuel reprocessing 3rd edition. JAEA-Rev 2015–002 (2015). https://doi.org/10.11484/jaea-review-2015-002 (in Japanese).
16. M.A. Watzky, R.G. Finke, Transition metal nanocluster formation kinetic and mechanistic studies. a wew mechanism when hydrogen is the reductant: slow, continuous nucleation and fast autocatalytic surface growth. J. Am. Chem. Soc. **119**, 10382–10400 (1997). https://doi.org/10.1021/ja9705102.
17. C.B. Whitehead, S. Özkar, R.G. Finke, LaMer's 1950 model for particle formation of instantaneous nucleation and diffusion-controlled growth: a historical look at the model's origins, assumptions, equations, and underlying sulfur sol formation kinetics data. Chem. Mater. **31**, 7116–7132 (2019). https://doi.org/10.1021/acs.chemmater.9b01273https://doi.org/10.1021/acs.chemmater.9b01273
18. C.B. Whitehead, S. Özkar, R.G. Finke, LaMer's 1950 model of particle formation: a review and critical analysis of its classical nucleation and fluctuation theory basis, of competing models and mechanisms for phase-changes and particle formation, and then of its application to silver halide, semiconductor, metal, and metal-oxide nanoparticles. Mater. Adv. **2**, 186–235 (2021). https://doi.org/10.1039/D0MA00439A
19. T. Yomogida, M. Saeki, S. Morii, H. Ohba, Y. Kitatsuji, Selective Pd separation from a simulated radioactive liquid waste by precipitation using a xenon lamp irradiation for simplified procedure. Anal. Sci. (2021). https://doi.org/10.2116/analsci.21N013
20. T. Donohue, Photochemical separation of metals in aqueous solution. Chem. Phys. Lett. **48**, 119 (1977). https://doi.org/10.1016/0009-2614(77)80228-5
21. D.R. Lide, *CRC Handbook of Chemistry and Physics*, 87th edn. (CRC Press, Boca Raton, FL, 2006)
22. T. Donohue, Photochemical separation of europium from lanthanide mixtures in aqueous solution. J. Chem. Phys. **67**, 5402–5404 (1977). https://doi.org/10.1063/1.434656
23. T. Donohue, Photochemical separation of cerium from rare earth mixtures in aqueous solution. Chem. Phys. Lett. **61**, 601–604 (1979). https://doi.org/10.1016/0009-2614(79)87181-X
24. M. Kusaba, N. Nakashima, Y. Izawa, C. Yamanaka, W. Kawamura, Two-photon reduction of $Eu^{3+}$ to $Eu^{2+}$ via the f-f transitions in methanol. Chem. Phys. Lett. **221**, 407–411 (1994). https://doi.org/10.1016/0009-2614(94)00279-7
25. N. Nakashima, S. Nakamura, S. Sakabe, H. Schillinger, Y. Hamanaka, C. Yamanaka, M. Kusaba, N. Ishihara, Y. Izawa, Multiphoton reduction of $Eu^{3+}$ to $Eu^{2+}$ in methanol using intense, short pulses from a Ti : Sapphire laser. J. Phys. Chem. A **103**, 3910–3916 (1999). https://doi.org/10.1021/jp984120t
26. D. Nishida, M. Kusaba, T. Yatsuhashi, N. Nakashima, Reduction of $Eu^{3+}$ to $Eu^{2+}$ by an intense femtosecond laser pulse in solution. Chem. Phys. Lett. **465**, 238–240 (2008). https://doi.org/10.1016/j.cplett.2008.10.005
27. M. Kusaba, Y. Tsunawaki, N. Nakashima, One-photon reduction of $Sm^{3+}$ to $Sm^{2+}$. J. Photochem. Photobiol. A **104**, 35–37 (1997). https://doi.org/10.1016/S1010-6030(97)00021-X
28. D. Nishida, E. Yamade, M. Kusaba, T. Yatsuhashi, N. Nakashima, Reduction of $Sm^{3+}$ to $Sm^{2+}$ by an intense femtosecond laser pulse in solution. J. Phys. Chem. A **114**, 5648–5654 (2010). https://doi.org/10.1021/jp9109089
29. N. Nakashima, K. Yamanaka, T. Yatsuhashi, Reduction of Yb(III) to Yb(II) by two-color two-photon excitation. J. Phys. Chem. A **117**, 8352–8359 (2013). https://doi.org/10.1021/jp402194g
30. K. Song, H. Cha, J. Lee, J.S. Choi, Y.I. Lee, K.S. Choi, Extraction of palladium metal from aqueous solution of palladium chloride by laser-induced photochemistry. Microchem. J. **68**, 121–126 (2001). https://doi.org/10.1016/S0026-265X(00)00138-7

31. Y. Toh, M. Segawa, M. Maeda, M. Tsuneyama, A. Kimura, S. Nakamura, S. Endo, M. Ebihara, Nondestructive quantitative analysis of difficult-to-measure radionuclides $^{107}$Pd and $^{99}$Tc. Anal. Chem. **93**, 9771–9777 (2021). https://doi.org/10.1021/acs.analchem.1c01233
32. M. Harada, Y. Kamigaito, Nucleation and aggregative growth process of platinum nanoparticles studied by in situ quick XAFS spectroscopy. Langmuir **28**, 2415–2428 (2012). https://doi.org/10.1021/la204031j
33. M. Harada, Y. Inada, In situ time-resolved XAFS studies of metal particle formation by photoreduction in polymer solutions. Langmuir **25**, 6049–6061 (2009). https://doi.org/10.1021/la900550t
34. J.J. Cruywagen, R.J. Kriek, Complexation of palladium(II) with chloride and hydroxide. J. Coord. Chem. **60**, 439–447 (2007). https://doi.org/10.1080/00958970600873588
35. Y. Kurosaki, R. Nakanishi, M. Saeki, H. Ohba, Ab initio MRCI study on potential energy surfaces for double Cl loss from the palladium tetrachloride anion $PdCl_4^{2-}$, Chem. Phys. Lett. **764**, 138247 (2021). https://doi.org/10.1016/j.cplett.2020.138247.
36. Y. Kurosaki, R. Nakanishi, M. Saeki, H. Ohba, Ab initio MRCI study on potential energy curves for a single Cl loss from the palladium tetrachloride anion $PdCl_4^{2-}$, Chem. Phys. Lett. **746**, 137288 (2020). https://doi.org/10.1016/j.cplett.2020.137288.

# Chapter 4
# Synthesis of Metal Nanoparticles Induced by Plasma-Assisted Electrolysis


**Naoki Shirai and Koichi Sasaki**

**Abstract** Plasma-assisted electrolysis was used to synthesize nanoparticles. Plasma-assisted electrolysis is a reaction that differs from conventional electrolysis due to plasma–liquid interaction. The synthesis of gold, silver, and magnetic particles was investigated as nanoparticle synthesis. For the synthesis of metal nanoparticles, aqueous solutions of $AgNO_3$, $HAuCl_4$, and their mixtures were used. In the plasma-assisted electrolysis using $AgNO_3$, Ag nanoparticles were synthesized only on the plasma cathode side. This means that the Ag nanoparticles were produced via the reduction of $Ag^+$ by electrons. In the $HAuCl_4$ solution, Au nanoparticles were synthesized at both the plasma anode and plasma cathode sides. Ion irradiation at the plasma anode is more effective than electron irradiation for the synthesis of Au nanoparticles. This result suggests that positive ions from the plasma cause dissociation reaction of $AuCl_4^-$ at the plasma–liquid interface. In the case of $AgNO_3$-$HAuCl_4$ mixture, the synthesized nanoparticles have the structure of Au core covered by Ag shell. Magnetic NPs were synthesized using an aqueous solution of $FeCl_2$ and an iron electrode immersed in the liquid, which supplied iron ions to the liquid. Magnetic NPs are synthesized at the interface between the plasma and the liquid by irradiating the surface of the liquid with an electron; in the case of the aqueous solution of $FeCl_2$, the synthesis conditions of magnetic NPs depend on the gas species of the plasma and the chemical agent in the liquid to control the oxidation.

**Keywords** Nanoparticle · Plasma–liquid interaction · Atmospheric pressure plasma · Plasma-assisted electrolysis

## 4.1 Introduction

Atmospheric pressure non-thermal plasmas can easily irradiate various materials such as liquids and living organisms in addition to conventional solids, and their applications in material processing, pollution control technology, biological and medical

N. Shirai (✉) · K. Sasaki
Graduate School of Engineering, Hokkaido University, Kita 13, Nishi 8, Kita-ku, Sapporo, Hokkaido 060-8628, Japan
e-mail: nshirai@qe.eng.hokudai.ac.jp



Y. Ishikawa et al. (eds.), *High-Energy Chemistry and Processing in Liquids*,
https://doi.org/10.1007/978-981-16-7798-4_4

fields have been widely studied [1, 2]. Research on the interaction between plasmas and liquids is expected to develop into a variety of applications [3–5]. In this chapter, we introduce the synthesis of metal nanoparticles using plasma-induced electrolysis. There are various methods of plasma generation using liquids, but here we describe a plasma process using a liquid as an electrode by DC voltage. An effective method for generating atmospheric pressure DC glow discharge using a liquid as an electrode is to introduce a miniature helium flow between the electrodes [6–8]. By using a miniature helium flow in open air, we were able to generate a stable DC glow discharge along the helium flow by cooling the electrodes and reducing the breakdown voltage.

Focusing on the reaction of the liquid, the discharge system can be considered as electrolysis using plasma electrodes. Plasma electrodes supply electrons and ions to the liquid, causing a reaction different from that of conventional electrolysis using metal electrodes [9, 10].

When a solution containing dissolved metal cations is irradiated with electrons and positive ions from the plasma, metal nanoparticles are synthesized on the surface of the liquid. Kaneko et al. reported the formation of Au nanoparticles by electron and positive ion irradiation using a low-pressure DC plasma with an ionic liquid containing $HAuCl_4$ as the liquid electrode [11, 12]. They suggest that Au cations are reduced by H atoms produced by energetic ions from the plasma in the ion irradiation mode and by electrons in the electron irradiation mode. Sankaran et al. also reported that Ag and Au nanoparticles can be synthesized in an atmospheric pressure DC microplasma with Ar flow using a dilute acid solution and a metal foil [13–16]. They mainly used electron irradiation from the plasma to reduce the metal cations in solution. In processes using liquid electrode discharges, such as the synthesis of metal nanoparticles, not only the reaction between the plasma and the liquid but also the electrolytic reaction in the liquid must be taken into account. Recently, Witzke et al. have confirmed that hydrogen gas is produced in the electrolysis of water using liquid anode discharge [17]. Although several synthesis processes of nanomaterials using plasma–liquid interactions have been reported, the details of the mechanisms are still not well understood due to the lack of understanding of plasma–liquid interactions. We will introduce the electrolysis reaction generated by the plasma–liquid interaction and the nanoparticle synthesis process using it. The experimental results are presented mainly based on the results of our previous papers [9, 10, 18–20]. Details of the experimental conditions are given in these references.

## 4.2 Plasma-Assisted Electrolysis

Figure 4.1 shows an example of an experimental setup for plasma-assisted electrolysis. When plasma is generated, an electrolytic reaction occurs in the liquid. Both discharges are in contact with the liquid and are stable. Without the helium flow, the discharges become unstable, and dual plasma electrolysis does not occur. For stable plasma electrolysis in air, the use of a small helium flow is effective. To verify that the typical characteristics of plasma electrolysis occurred, $Na_2SO_4$ solution with a

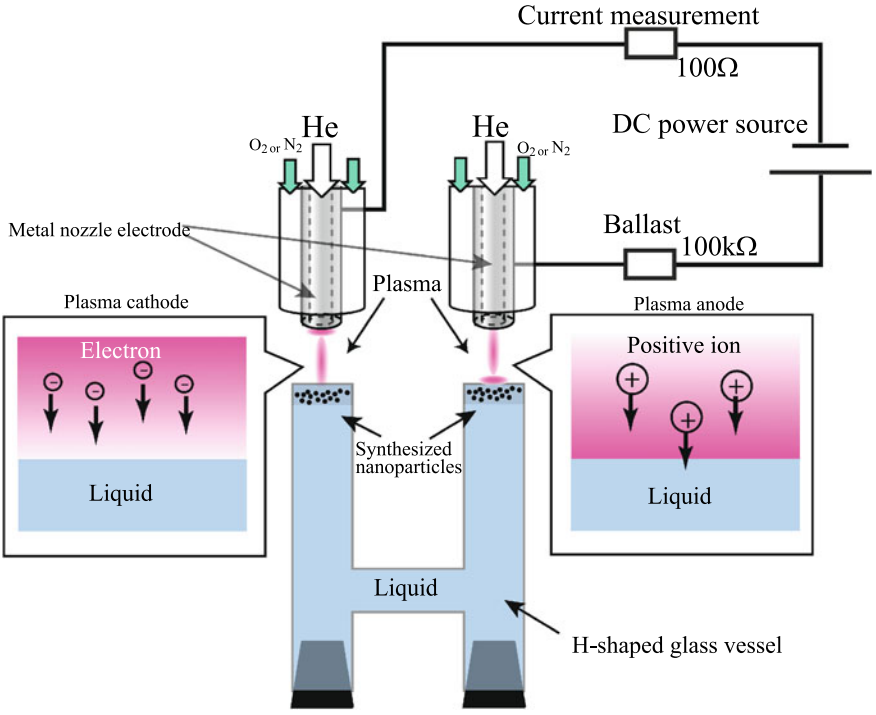


**Fig. 4.1** Experimental setup of plasma-assisted electrolysis

small amount of BTB solution was used as a chemical indicator. Figure 4.2 shows images of plasma electrolysis. The pH value of the solution, initially measured with a pH meter, was almost neutral. The solution in contact with the plasma cathode where electrons are irradiated onto the solution surface becomes alkaline, as indicated by the blue color of BTB. On the other hand, the solution in contact with the plasma anode, where positive ions are irradiated on the solution surface, becomes acidic, as shown by the yellow color. The change in pH value was similar when compared to conventional electrolysis under the same current conditions. The amount of gas bubbles ($O_2$ and $H_2$) generated in plasma electrolysis is less than that in conventional electrolysis. Using a commercially available vapor detector tube, we confirmed that the amount of gas generated by plasma electrolysis is small. The gas generation was also confirmed by using NaCl solution containing a small amount of BTB. In conventional electrolysis, $Cl_2$ gas is generated at the anode. This $Cl_2$ gas partially dissolves in water to produce HClO (hypochlorous acid). HClO, with its strong oxidizing power, readily decomposes BTB, so the solution around the anode is decolorized. We confirmed the gas generation of $Cl_2$ and HCl using a commercially available vapor detector tube. On the other hand, in plasma electrolysis, decolorization of the BTB solution could not be observed. The amount of $Cl_2$ gas generated in plasma electrolysis was lower than that in the case of using a commercial vapor detector tube. Although

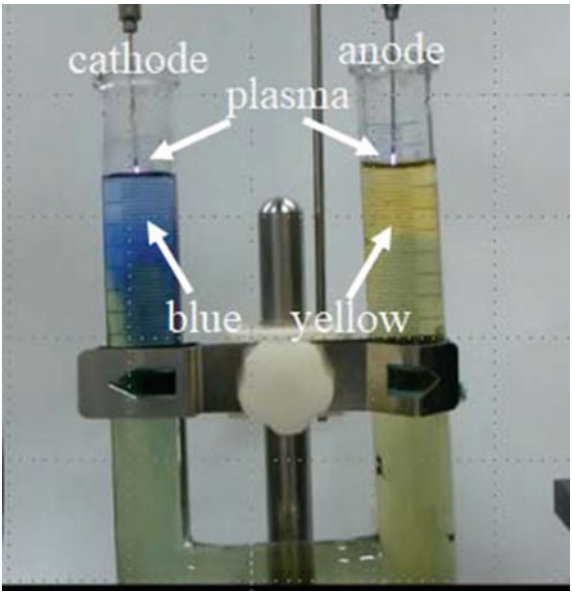


**Fig. 4.2** Images of plasma electrolysis using $Na_2SO_4$ solution with the addition of BTB (bromothymol blue) as a chemical pH indicator

this measurement of gas generation is not very accurate, it indicates the possibility that gas generation in plasma electrolysis is lower than in conventional electrolysis. In fact, Witzke et al. have confirmed hydrogen generation by plasma electrolysis by mass spectrometry [17]. In plasma electrolysis, the macroscopic change in pH appears to be the same as in conventional electrolysis, but the reactions are different from conventional electrolysis because the irradiation of electrons and positive ions on the surface of the liquid leads to dissociation, ionization, charge transfer, and evaporation. Electron irradiation from the plasma contributes to the formation of $OH^-$, while positive ion irradiation contributes to the formation of $H^+$.

## 4.3 Synthesis of Ag Nanoparticles

Figure 4.3 shows the time evolution of Ag nanoparticle synthesis using $AgNO_3$ solution. The color of the liquid on the plasma cathode side is yellowish. We confirmed that this yellow color comes from the surface plasmon resonance of the Ag nanoparticles which has an absorption spectrum around 400 nm. In other words, the Ag nanoparticles are synthesized at the interface between the plasma and the liquid by the electron irradiation from the plasma. On the other hand, the color of the liquid on the plasma anode side does not change. Therefore, Ag nanoparticles are not produced by the positive ion irradiation. When the solution surface is irradiated with electrons from the DC glow discharge, a significant number of hydrated electrons are generated near the interface between the plasma and the liquid. These hydrated electrons

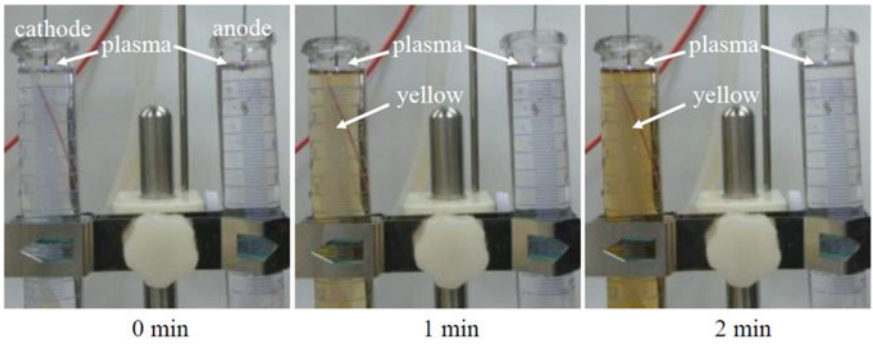


**Fig. 4.3** Time evolution of Ag nanoparticle synthesis by plasma electrolysis using aqueous solution of $AgNO_3$. Adapted with permission from [10]. Copyright 2014 The Japan Society of Applied Physics

then reduce $Ag^+$ to Ag and contribute to the formation of Ag nanoparticle nuclei.

$$Ag^+ + e_{aq}^- \rightarrow Ag \quad k = 3.3 \times 10^{10}\ M^{-1}s^{-1}$$

Since this reaction has a fast rate coefficient [21], the formation of Ag nanoparticles by electron irradiation from plasma is reasonable. H radicals can also reduce $Ag^+$, and H radicals are obtained from the dissociation of $H_2O$.

$$Ag^+ + H \rightarrow Ag + H^+ \quad k = 2.2 \times 10^{10}\ M^{-1}s^{-1}$$

This reaction also has a fast rate coefficient [22]. Kaneko et al. suggest that H radicals are the dominant reducing agents in the synthesis of Au nanoparticles. H radicals are effectively produced by high-energy positive ions accelerated in the cathode fall region through the dissociation of liquid molecules in a low-pressure glow discharge in contact with the liquid [11]. However, in this case, an atmospheric pressure DC glow discharge was used, and even though the discharge current was increased, the energy of the positive ions impacting the liquid surface is not sufficient to dissociate $H_2O$ [23]. Therefore, the plasma anode does not contribute to the synthesis of Ag nanoparticles.

## 4.4 Synthesis of Au Nanoparticles

Figure 4.4 shows the time variation of nanoparticle synthesis using $HAuCl_4$ solution. The color of the liquid on both the anode and cathode sides of the plasma is red. This red color is due to the surface plasmon resonance of Au nanoparticles, indicating that Au nanoparticles are being produced. The red color on the plasma anode side is darker than that on the plasma cathode side; using $HAuCl_4$ solution, Au

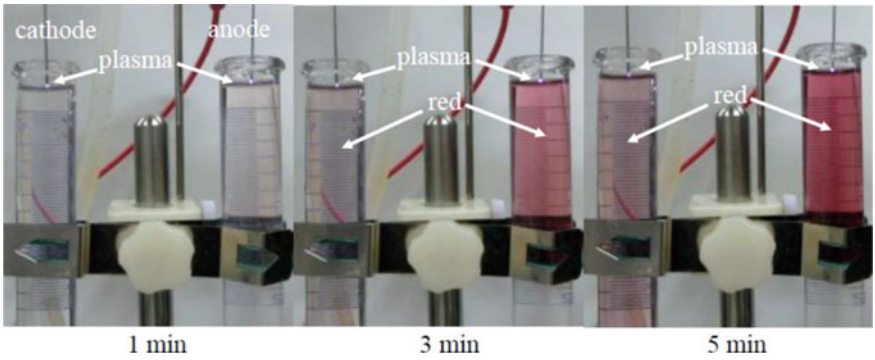


**Fig. 4.4** Time evolution of Ag nanoparticle synthesis by plasma electrolysis using aqueous solution of $HAuCl_4$ Adapted with permission from [10]. Copyright 2014 The Japan Society of Applied Physics

nanoparticles are produced not only by electron irradiation but also by positive ion irradiation. Figure 4.4 is a TEM image of the Au nanoparticles. It was confirmed by EDX that the nanoparticles were Au particles. The nanoparticles produced by electron irradiation at the plasma cathode have only a spherical structure with a diameter of about 10–30 nm, as shown in Fig. 4.5a. However, the nanoparticles produced by irradiating positive ions at the plasma anode have not only a spherical structure but also rod-like and triangular structures with a size of about 100 nm, as shown in Fig. 4.5b. The structure and size of the nanoparticles were found to be dependent on the reaction rate. From these results, it was found that the synthesis rate of nanoparticles by positive ion irradiation was higher than that by electron irradiation. The

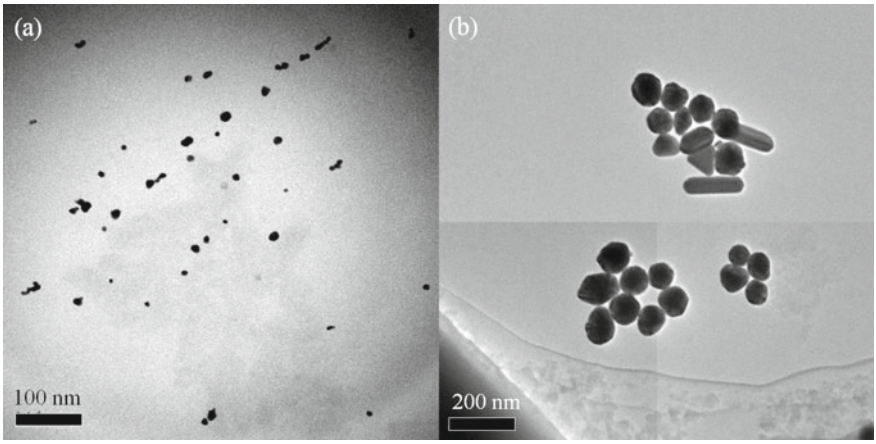


**Fig. 4.5** TEM images of Au nanoparticles synthesized by plasma electrode using aqueous solution of $HAuCl_4$: **a** plasma cathode and **b** plasma anode

reason why Au nanoparticles can be produced by both electron irradiation and positive ion irradiation is not clear. In most cases, the plasma-assisted synthesis process of Au nanoparticles in liquids has been discussed in terms of the reduction of $Au^{3+}$, $Au^{2+}$, and $Au^{+}$. Therefore, as in the case of Ag nanoparticle synthesis using $AgNO_3$ solution, hydrated electrons and H radicals are considered as promising candidates for the reducing agents. However, to the best of our knowledge, the reaction rates of "Au+e" and "Au+H" have not been reported. In previous section, we explained that Ag nanoparticles are not generated in $AgNO_3$ solution if the generation of H radicals by plasma anode is low. The same is true for $HAuCl_4$ solution when the generation of $H^-$ radicals by the plasma anode is low. Therefore, a different process is needed: $HAuCl_4$ dissociates into $H^+$ and $AuCl_4^-$ in solution. Our hypothesis for these phenomena is as follows. In electrolysis using a plasma electrode, an electrostatic double layer is formed in contact with the plasma electrode, and the density of $AuCl_4^-$ increases in the double layer facing the plasma anode. Therefore, when positive ions are irradiated from the plasma anode toward the liquid surface, even if the kinetic energy of the positive ions is small, the dissociation reaction of $AuCl_4^-$ can be triggered. This explains why positive ion irradiation is more effective than electron irradiation in the synthesis of Au nanoparticles in $HAuCl_4$ aqueous solution by electrolysis using plasma electrodes. Not all the plasma current goes to nanoparticle production, but some goes to other redox processes. The pH value is also an important factor in gold nanoparticle synthesis because it is a redox process; Bratescu et al. reported the pH dependence of Au nanoparticle size distribution in a solution plasma process [24]. Therefore, the hypothesis of gas generation, aqueous byproducts, and pH dependence needs to be confirmed.

## 4.5 Synthesis of Core–Shell Nanoparticles

Core–shell particles can also be synthesized by plasma-assisted electrolysis. As an example, we show the results using a mixture of $AgNO_3$ aqueous solution and $HAuCl_4$ aqueous solution with concentration $10^{-5}$ mol/l. Figure 4.6 shows the time evolution of nanoparticle synthesis using this mixture. First, the color of the liquid in contact with both plasma electrodes turns red. With the passage of time, the color of the liquid on the plasma cathode side changes from red to yellow, while the color of the liquid on the plasma anode side does not change. The nanoparticles synthesized on the plasma cathode side were examined by TEM observation and EDX mapping, and it was found that the structure consisted of a gold core covered with a silver shell, as shown in Fig. 4.7. Since the color of the liquid in Fig. 4.6 changes from red to yellow, it is presumed that the Au nanoparticles are first synthesized, and then Ag nanoparticles are synthesized around the Au nanoparticles. In general, the redox potential of Au (+1.52 V) is higher than that of Ag (+0.799 V), so Au is easily reduced first. This order depends on the redox potential of the metal cations. The ratio of Au to Ag is also an important factor in the synthesis of core–shell nanoparticles. The addition of a large amount of SDS to the liquid did not produce nanoparticles with

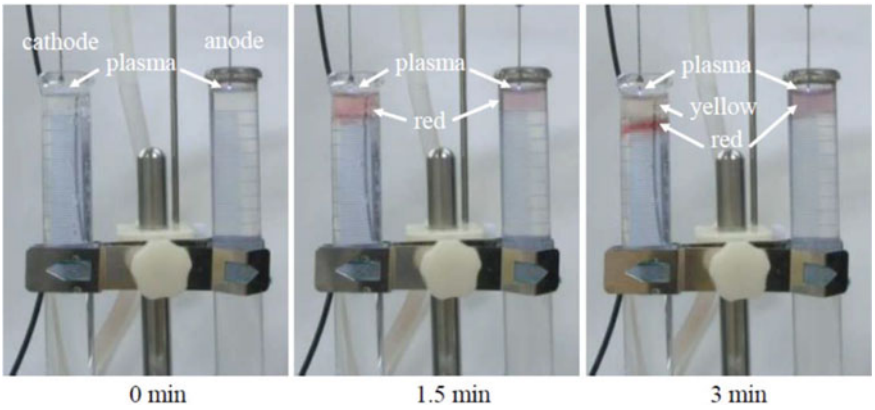


**Fig. 4.6** Time evolution of nanoparticle synthesis by plasma electrolysis using mixed aqueous solution of $AgNO_3$ and $HAuCl_4$. Adapted with permission from [10]. Copyright 2014 The Japan Society of Applied Physics

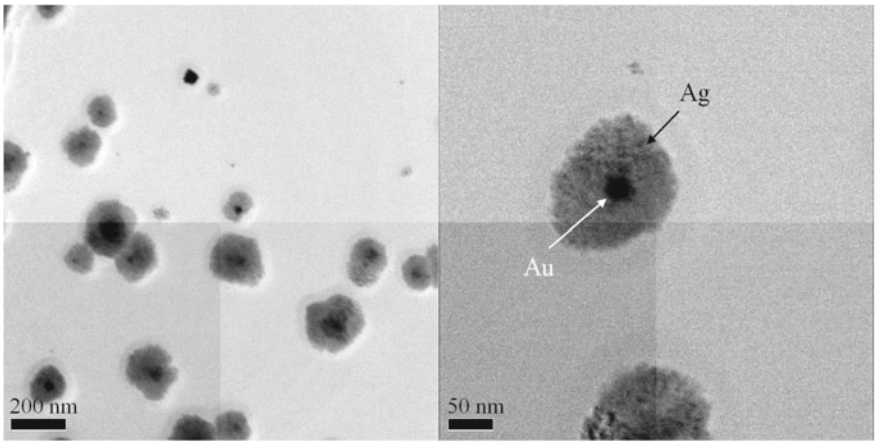


**Fig. 4.7** TEM image of nanoparticles with core–shell structure synthesized by plasma cathode of plasma electrolysis using $AgNO_3$-$HAuCl_4$ mixture

core–shell structure. Therefore, the use of surfactant is also an important factor to control the structure of core–shell nanoparticles. Although the detailed mechanism of nanoparticle synthesis is not yet fully understood, electrolysis using plasma electrodes has the potential to synthesize a wide variety of nanoparticles by controlling the plasma parameters and aqueous solution components.

## 4.6 Synthesis of Magnetic Nanoparticles

Plasma electrolysis can also be used to synthesize magnetic nanoparticles. Detailed experimental conditions are shown in the literature [18, 19]. Magnetic NPs are widely used for many applications in the fields of biotechnology, biomedical science, material science, engineering, and environmental science [25–27]. Magnetite NPs are one of the popular magnetic NPs, and they are typically synthesized by a coprecipitation method in which an alkali solution is added to an iron salt aqueous solution containing both $Fe^{2+}$ and $Fe^{3+}$. There are only a few papers about magnetic NP synthesis by plasma-assisted electrolysis.

Magnetite, a magnetic nanoparticle, is synthesized when plasma is irradiated to an aqueous solution of iron (II) chloride with ethanol. In this case, it is necessary to control the gas surrounding the plasma. When the surrounding gas is nitrogen, magnetite ($Fe_3O_4$) is synthesized, but when the surrounding gas is oxygen, hematite ($Fe_2O_3$) is synthesized. Both $Fe^{3+}$ and $Fe^{2+}$ are necessary for the synthesis of magnetite, but when the surrounding gas is oxygen, most of the $Fe^{2+}$ in the liquid is oxidized to $Fe^{3+}$, so hematite is synthesized. On the other hand, when the surrounding gas is nitrogen gas, some of the $Fe^{2+}$ in the solution is oxidized to $Fe^{3+}$, which is considered to be the synthesis of magnetite. To avoid excessive oxidation in the solution, the addition of ethanol is effective. Ethanol scavenges OH radicals as follows [28].

$$OH + C_2H_5OH \rightarrow H_2O + CH_3CHOH \quad k = 2.2^9\ M^{-1}s^{-1}$$

As an example, adding 10 ml of ethanol to 50 ml of 0.01 M $FeCl_2$ aqueous solution is an appropriate amount. Under these conditions, the amount of ethanol should not be too much or too little. If the amount of ethanol is too small, the number of NPs synthesized will be small. If the amount of ethanol is too large, the discharge operation becomes unstable, and the number of NPs synthesized decreases. The diameter of the magnetic NPs was 200–300 nm, and some of them were agglomerated. In general, both $Fe^{2+}$ and $Fe^{3+}$ are required to synthesize $Fe_3O_4$ by conventional methods such as coprecipitation. In the present experiment, only $Fe^{2+}$ is present in the $FeCl_2$ solution. When the solution is shielded with $N_2$ gas, some of the $Fe^{2+}$ are oxidized to $Fe^{3+}$ in the aqueous solution, and $Fe_3O_4$ is synthesized at the plasma–liquid interface with the appropriate molar ratio of $Fe^{2+}$ and $Fe^{3+}$ with or without $O_2$ shielding flow. The excess oxidation of $Fe^{2+}$ to $Fe^{3+}$ at the plasma–liquid interface does not result in the generation of ferromagnetic particles. These results indicate that the chemical reaction in the liquid can be controlled by adjusting the parameters of plasma generation such as gas composition.

A simpler method for synthesizing magnetite is plasma electrolysis, in which an iron electrode is submerged in a solution, as shown in Fig. 4.8. When plasma-assisted electrolysis is initiated, an electric current flows through the electrical circuit, dissolving the iron electrode and supplying $Fe^{2+}$ to the liquid, eliminating the need

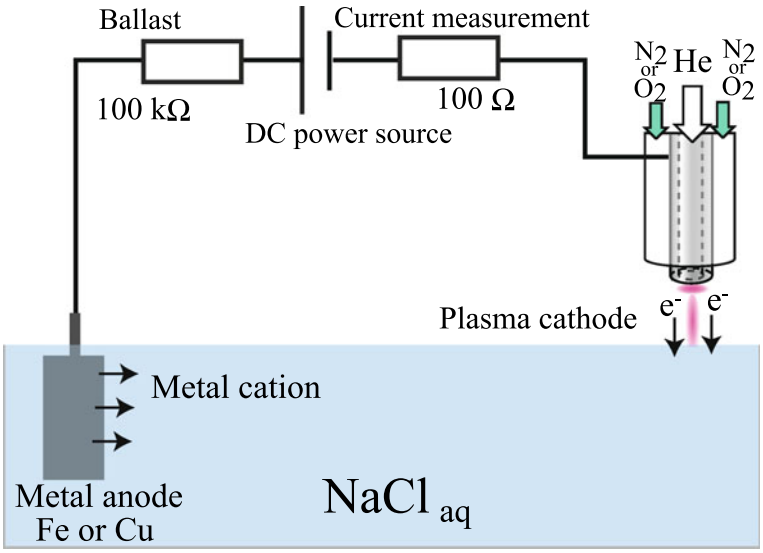


**Fig. 4.8** Experimental setup for synthesis of magnetite using plasma-assisted electrolysis plasma-assisted electrolysis with metal electrode dissolution

for additional chemicals. To control the conductivity of the liquid, NaCl is added to deionized water.

This technique can be applied not only to the synthesis of magnetite, but also to the synthesis of copper oxide [20]. When plasma electrolysis is generated by this method, a large amount of magnetite is synthesized more quickly than when using iron chloride solution. The magnetic susceptibility of particles synthesized using iron electrodes is higher than that using $FeCl_2$ aqueous solution, and the particle size is also smaller. It was shown that this method is a promising particle synthesis method.

Figure 4.9 shows a schematic of the mechanism of magnetite NP synthesis. Firstly, the Fe anode dissolves in the aqueous solution by electrolysis to supply $Fe^{2+}$. Subsequently, some of $Fe^{2+}$ are oxidized to $Fe^{3+}$. $Fe^{2+}$ is easily oxidized to $Fe^{3+}$ by reacting with oxygen. Using oxygen gas, a portion of oxygen might dissolve in liquid.

The amount of magnetite synthesized depends on the concentration of NaCl. When the concentration of NaCl solution is 1%, not much magnetite is synthesized. On the other hand, a lot of magnetite was synthesized when the concentration of NaCl solution was extremely high, 15%. In general, the concentration of NaCl solution depends on the amount of dissolved oxygen. In other words, the amount of dissolved oxygen in the solution affects the amount of $Fe^{2+}$ that is oxidized to $Fe^{3+}$. In fact, by adjusting the amount of dissolved oxygen in the solution, we have confirmed that magnetite can be synthesized even when the concentration of NaCl is not high [19]. Therefore, the rate of oxidation to $Fe^{3+}$ might decrease. At the plasma–liquid interface, $OH^-$ is generated by the reaction between electrons and $H_2O$ [9]. Therefore, magnetite is synthesized by the following reaction similar to the coprecipitation

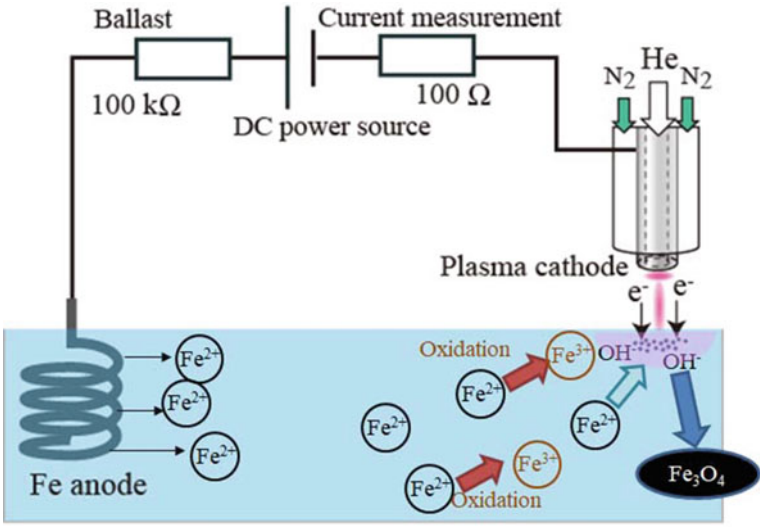


**Fig. 4.9** Schematic of the mechanism of magnetite NP synthesis by plasma-assisted electrolysis with Fe electrode dissolution. Adapted with permission from [18]. Copyright 2017 The Japan Society of Applied Physics

method:

$$Fe^{2+} + 2Fe^{3+} + 8OH^{-} \rightarrow Fe_3O_4 + 4H_2O$$

In conventional electrolysis, ferrous hydroxide $Fe(OH)_2$ or ferric hydroxide $Fe(OH)_3$ is generally synthesized as follows:

$$Fe^{2+} + 2OH \rightarrow Fe(OH)_2$$

$$Fe^{3+} + 3OH^{-} \rightarrow Fe(OH)_3$$

Black materials including a small amount of magnetite are synthesized by conventional electrolysis using Fe electrodes immersed in a liquid. These materials might be mainly $Fe(OH)_2$ or $Fe(OH)_3$. Therefore, the reaction involved in plasma-assisted electrolysis is different from that involved in conventional electrolysis. It is reported that some reactions in plasma-assisted electrolysis differ from those in conventional electrolysis [9]. Although the detailed mechanism of magnetite NP synthesis induced by plasma–liquid interactions is not yet understood completely, this study provides insight into the synthesis of magnetite NPs by plasma-assisted electrolysis.

## 4.7 Synthesis of Copper Oxide Nanoparticles

It is also possible to synthesize copper oxide ($Cu_2O$) using the same technique as the magnetite synthesis method using plasma-assisted electrolysis. Detailed experimental results are shown in reference [20]. $Cu_2O$ is a widely studied semiconductor material with a narrow band gap energy of 2.17 eV. Due to its unique optical, electronic, and magnetic properties, $Cu_2O$ is a promising material for many applications [29, 30].

$Cu_2O$ was synthesized when NaCl solution was used, but not when $NaNO_3$ solution was used. As in the case of magnetite synthesis, we considered the dissolved oxygen concentration to be important and conducted experiments by varying the dissolved oxygen content, but $Cu_2O$ was synthesized only when NaCl solution was used. Therefore, it became clear that NaCl solution was necessary for the synthesis of $Cu_2O$. The $Cl^-$ concentration and pH value of the electrolyte are dominant for the synthesis of $Cu_2O$ nanoparticles. The reaction between $CuCl_2^-$ produced by anodic dissolution of Cu and $OH^-$ produced by plasma irradiation is also involved in the formation of $Cu_2O$.

Based on the experimental results, we propose the synthesis mechanism of $Cu_2O$ nanoparticles as shown in Fig. 4.10. This synthesis mechanism consists of two steps. The first step is the formation of $CuCl_2^-$ [31]. When electrolysis is initiated, the Cu plate (anode) releases $Cu^+$ ions via anodic dissolution.

$$Cu^0 \rightarrow Cu^+ + e^-$$

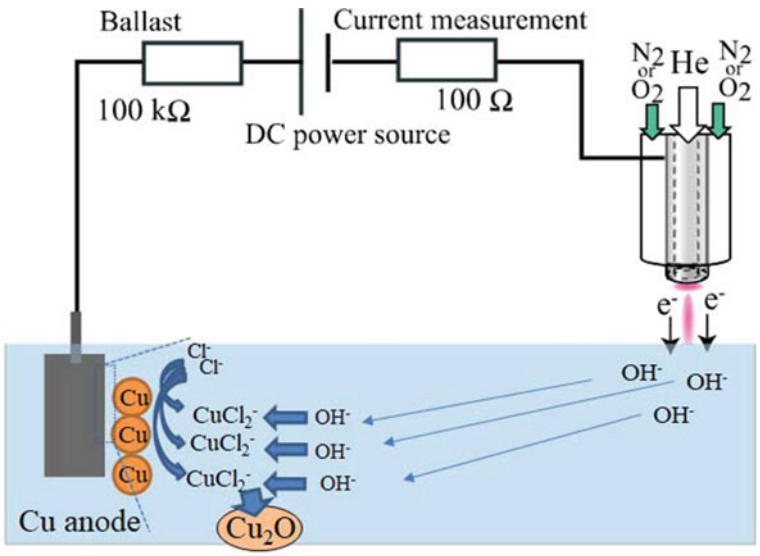


**Fig. 4.10** Schematic of possible synthesis mechanism of $Cu_2O$ nanoparticles

If the concentration of $Cl^-$ (i.e., the concentration of NaCl) is sufficiently high, $Cu^+$ will combine with $Cl^-$ immediately after formation to form $CuCl_2^-$.

$$Cu^0 + 2Cl^- \rightarrow CuCl_2^-$$

It should be noted that this reaction avoids the oxidation of $Cu^+$ to $Cu^{2+}$. Another way to produce $CuCl_2^-$ is directly from the electrode.

$$Cu^+ + 2Cl^- \rightarrow CuCl_2^-$$

and partial chlorination

$$Cu^0 + Cl^- \rightarrow CuCl + e^-$$

followed by

$$CuCl + Cl^- \rightarrow CuCl_2^-$$

High $Cl^-$ concentration is important in all production steps of $CuCl_2^-$.

The second step is the reaction of $OH^-$ with $CuCl_2^-$. $OH^-$ is generated under the irradiated point of the plasma. The formation of $OH^-$ is due to the reaction of OH radicals and solvated electrons at the interface between the plasma and the liquid. $OH^-$ ions are transported toward the copper anode. The $OH^-$ are transported toward the copper anode, and when the $OH^-$ reaches the anode, $Cu_2O$ is formed by the following reaction,

$$2CuCl_2^- + 2OH^- \rightarrow Cu_2O + H_2O + 4Cl^-$$

The importance of this reaction is that when $OH^-$ reaches the anode, $Cu_2O$ nanoparticles are produced; if the $OH^-$ concentration is insufficient, $Cu^+$ is oxidized to $Cu^{2+}$ by the following equation

$$CuCl_2^- \rightarrow Cu^{2+} + 2Cl^- + e^-$$

The formation of $Cu^{2+}$ results in the formation of $Cu_2(OH)_3Cl$ and CuO.

$$2Cu^{2+} + 3OH^- + Cl^- \rightarrow Cu_2(OH)_3Cl$$

and

$$Cu^{2+} + 2OH^- \rightarrow CuO + H_2O \tag{4.1}$$

These are the mechanisms by which the formation of $Cu_2(OH)_3Cl$ and CuO is promoted at low pH.

The anodic dissolution of Cu plates and the formation of $OH^-$ were also observed in conventional electrolysis, and the synthesis of $Cu_2O$ nanoparticles was also confirmed without plasma. However, there are differences between plasma and conventional electrolysis in the synthesis rate, minimum NaCl concentration, and the size and shape of the synthesized nanoparticles [20].

## 4.8 Conclusion

We have shown that metal nanoparticles can be synthesized by plasma-assisted electrolysis. Plasma-assisted electrolysis is a different reaction process from conventional electrolysis and has the potential to be used in a variety of material processes, including.

On the other hand, the synthesis of metal nanoparticles is almost an established technology in the field of chemistry; for example, gold nanoparticles have been commercialized and sold through chemical synthesis methods. Therefore, the mere synthesis of nanoparticles by plasma is of little value from the viewpoint of different fields, and it is necessary to show the superiority of high value-added particles that can be synthesized only by plasma, or high selectivity. At present, it is unclear whether this advantage exists, but first we need to fully understand the mechanism of nanoparticle synthesis and plasma–liquid interaction. Plasma is characterized by its ability to control reactions electrically, and this may be an advantage in particle synthesis.

## References

1. J. Ehlbeck, U. Schnabel, M. Polak, J. Winter, T. von Woedtke, R. Brandenburg, T. von dem Hagen, K.-D. Weltmann, Low temperature atmospheric pressure plasma sources for microbial decontamination. J. Phys. D **44**, 013002 (2011). https://doi.org/10.1088/0022-3727/44/1/013002
2. M. Laroussi, T. Akan, Arc-free atmospheric pressure cold plasma jets: A review. Plasma Process. Polym. **4**, 777 (2007). https://doi.org/10.1002/ppap.200700066
3. B.R. Locke, M. Sato, P. Sunka, M.R. Hoffmann, J.-S. Chang, Electrohydraulic discharge and nonthermal plasma for water treatment. Ind. Eng. Chem. Res. **45**, 882 (2006). https://doi.org/10.1021/ie050981u
4. P. Bruggeman, C. Leys, Non-thermal plasmas in and in contact with liquids. J. Phys. D **42**, 053001 (2009). https://doi.org/10.1088/0022-3727/42/5/053001
5. P. Bruggeman, M. Kushner, B. Locke, J. Gardeniers, W. Graham, D. Graves, R. Hofman-Caris, D. Maric, J. Reid, E. Ceriani, D. Fernandez Rivas, J. Foster, S. Garrick, Y. Gorbanev, S. Hamaguchi, F. Iza, H. Jablonowski, E. Klimova, J. Kolb, F. Krcma, P. Lukes, Z. Machala, I. Marinov, D. Mariotti, S. Mededovic Thagard, D. Minakata, E. Neyts, J. Pawlat, Z. Lj Petrovic, R. Pflieger, S. Reuter, D. Schram, S. Schroter, M. Shiraiwa, B. Tarabova, P. Tsai, J. Verlet, T. von Woedtke, K. Wilson, K. Yasui, G. Zvereva, Plasma–liquid interactions: a review and

roadmap. Plasma Sources Sci. Technol. **25**, 053002 (2016). https://doi.org/10.1088/0963-0252/25/5/053002
6. N. Shirai, M. Nakazawa, S. Ibuka, S. Ishii, Atmospheric DC glow microplasmas using miniature gas flow and electrolyte cathode. Jpn. J. Appl. Phys. **48**, 036002 (2009). https://doi.org/10.1143/JJAP.48.036002
7. N. Shirai, K. Ichinose, S. Uchida, F. Tochikubo, Influence of liquid temperature on the characteristics of an atmospheric dc glow discharge using a liquid electrode with a miniature helium flow. Plasma Sources Sci. Technol. **20**, 034013 (2011). https://doi.org/10.1088/0963-0252/20/3/034013
8. N. Shirai, S. Uchida, F. Tochikubo, Influence of oxygen gas on characteristics of self-organized luminous pattern formation observed in an atmospheric dc glow discharge using a liquid electrode. Plasma Sources Sci. Technol. **23**, 054010 (2014). https://doi.org/10.1088/0963-0252/23/5/054010
9. F. Tochikubo, Y. Shimokawa, N. Shirai, S. Uchida, Chemical reactions in liquid induced by atmospheric-pressure dc glow discharge in contact with liquid. Jpn. J. Appl. Phys. **53**, 126201 (2014). https://doi.org/10.7567/JJAP.53.126201
10. N. Shirai, S. Uchida, F. Tochikubo, Synthesis of metal nanoparticles by dual plasma electrolysis using atmospheric dc glow discharge in contact with liquid. Jpn. J. Appl. Phys. **53**, 046202 (2014). https://doi.org/10.7567/JJAP.53.046202
11. T. Kaneko, K. Baba, T. Harada, R. Hatakeyama, Novel gas-liquid interfacial plasmas for synthesis of metal nanoparticles. Plasma Process. Polym. **6**, 713 (2009). https://doi.org/10.1002/ppap.200900029
12. T. Kaneko, R. Hatakeyama, Creation of nanoparticle–nanotube conjugates for life-science application using gas–liquid interfacial plasmas. Jpn. J. Appl. Phys. **51**, 11PJ03 (2012). https://doi.org/10.1143/JJAP.51.11PJ03
13. D. Mariotti, R.M. Sankaran, Microplasmas for nanomaterials synthesis. J. Phys. D **43**, 323001 (2010). https://doi.org/10.1088/0022-3727/43/32/323001
14. C. Richmonds, R.M. Sankaran, Plasma-liquid electrochemistry: Rapid synthesis of colloidal metal nanoparticles by microplasma reduction of aqueous cations. Appl. Phys. Lett. **93**, 131501 (2008). https://doi.org/10.1063/1.2988283
15. W.H. Chiang, C. Richmonds, R.M. Sankaran, Continuous-flow, atmospheric-pressure microplasmas: A versatile source for metal nanoparticle synthesis in the gas or liquid phase. Plasma Sources Sci. Technol. **19**, 034011 (2010). https://doi.org/10.1088/0963-0252/19/3/034011
16. C. Richmonds, M. Witzke, B. Bartling, S.W. Lee, J. Wainright, C.-C. Liu, R.M. Sankaran, Electron-transfer reactions at the plasma–liquid interface. J. Am. Chem. Soc. **133**, 17582 (2011). https://doi.org/10.1021/ja207547b
17. M. Witzke, P. Rumbach, D.B. Go, R.M. Sankaran, Evidence for the electrolysis of water by atmospheric-pressure plasmas formed at the surface of aqueous solutions. J. Phys. D **45**, 442001 (2012). https://doi.org/10.1088/0022-3727/45/44/442001
18. N. Shirai, T. Yoshida, S. Uchida, F. Tochikubo, Synthesis of magnetic nanoparticles by atmospheric-pressure glow discharge plasma-assisted electrolysis. Jpn. J. Appl. Phys. **56**, 076201 (2017). https://doi.org/10.7567/JJAP.56.076201
19. Y. Yamazaki, N. Shirai, Y. Nakagawa, S. Uchida, F. Tochikubo, Chemical reaction process for magnetite nanoparticle synthesis by atmospheric-pressure DC glow-discharge electrolysis. Jpn. J. Appl. Phys. **57**, 096203 (2018). https://doi.org/10.7567/JJAP.57.096203
20. J. Liu, N. Shirai, K. Sasaki, Synthesis mechanism of cuprous oxide nanoparticles by atmospheric-pressure plasma electrolysis. J. Phys. D **54**, 105201 (2021). https://doi.org/10.1088/1361-6463/abca2a
21. S. Kapoor, D. Lawless, P. Kennepohl, D. Meisel, N. Serpone, Reduction and aggregation of silver ions in aqueous gelatin solutions. Langmuir **10**, 3018 (1994). https://doi.org/10.2172/10161032
22. G.V. Buxton, C.L. Greenstock, W.P. Helman, A.B. Ross, Critical Review of rate constants for reactions of hydrated electrons, hydrogen atoms and hydroxyl radicals (·OH/·$O^-$ in Aqueous Solution. J. Phys. Chem. Ref. Data **17**, 513 (1988). https://doi.org/10.1063/1.555805

23. J. Choi, F. Iza, J.K. Lee, C.-M. Ryu, Electron and ion kinetics in a DC microplasma at atmospheric pressure. IEEE Trans. Plasma Sci. **35**, 1274 (2007). https://doi.org/10.1109/TPS.2007.904827
24. M.A. Bratescu, S.-P. Cho, O. Takai, N. Saito, Size-controlled gold nanoparticles synthesized in solution plasma. J. Phys. Chem. C **115**, 24569 (2011). https://doi.org/10.1021/jp207447c
25. Q.A. Pankhurst, J. Connolly, S.K. Jones, J. Dobson, Applications of magnetic nanoparticles in biomedicine. J. Phys. D **36**, R167 (2003). https://doi.org/10.1088/0022-3727/36/13/201
26. F.E. Kruis, H. Fissan, A. Peled, Synthesis of nanoparticles in the gas phase for electronic, optical and magnetic applications—A review. J. Aerosol Sci. **29**, 511 (1998). https://doi.org/10.1016/S0021-8502(97)10032-5
27. Q.A. Pankhurst, N.T.K. Thanh, S.K. Jones, J. Dobson, Progress in applications of magnetic nanoparticles in biomedicine. J. Phys. D **42**, 224001 (2009). https://doi.org/10.1088/0022-3727/42/22/224001
28. N. Motohashi, Y. Saito, Competitive measurement of rate constants for hydroxyl radical reactions using radiolytic hydroxylation of benzoate. Chem. Pharm. Bull. **41**, 1842–1845 (1993). https://doi.org/10.1248/cpb.41.1842
29. M.Y. Shen, T. Yokouchi, S. Koyama, T. Goto, Dynamics associated with Bose-Einstein statistics of orthoexcitons generated by resonant excitations in cuprous oxide. Phys. Rev. B **56**, 13066 (1997). https://doi.org/10.1103/PhysRevB.56.13066
30. J. Ghijsen, L.H. Tjeng, J. van Elp, H. Eskes, J. Westerink, G.A. Sawatzky, M, T. Czyzyk, Electronic structure of $Cu_2O$ and CuO. Phys. Rev. B **38**, 11322 (1998). https://doi.org/10.1103/PhysRevB.38.11322
31. G. Kear, B.D. Barker, F.C. Walsh, Electrochemical corrosion of unalloyed copper in chloride media—A critical review. Corros. Sci. **46**, 109 (2004). https://doi.org/10.1016/S0010-938X(02)00257-3

# Chapter 5
# Controllable Surface Modification of Colloidal Nanoparticles Using Laser Ablation in Liquids and Its Utilization


**Takeshi Tsuji**

**Abstract** Laser ablation in liquids (LAL) is a powerful tool to prepare colloidal nanoparticles (NPs). LAL has attracted attention not only because of its simplicity and versatility, but also the unique characteristics of the colloidal NPs produced by the method. When we carried out LAL using a pure solvent, colloidal NPs adsorbing no chemical reagent can be obtained. Alternatively, when we carried out LAL using a solvent into which some protective reagents are added, NPs adsorbing these reagents very efficiently during the formation process can be obtained. In other words, surface modification of colloidal NPs can be carried out in a simple and controllable manner using LAL with protective reagents. Such a method is difficult to be applied for colloidal NPs prepared by chemical methods because various reagents necessary for the synthesis reaction are contained in the solution. In this chapter, some examples of surface modification of NPs using LAL for investigation of a photochemical property of NPs and for functionalizing NPs are introduced.

**Keywords** Laser ablation · Colloids · Nanoparticles · Agglomeration · Protective reagents

## 5.1 Introduction

As reported in comprehensive reviews [1–4], laser ablation in liquids (LAL) is well known as an alternative colloid processing technique, particularly because of the simplicity and versatility of the procedure. When a short pulsed (<nanosecond) laser is applied for a material in a liquid (Fig. 5.1a), a part of the material is ablated from the target and forms nanosized colloidal nanoparticles (NPs) in liquid (Fig. 5.1b).

In addition to its simplicity and versatility, a remarkable feature of LAL is that colloids obtained by LAL include no chemicals other than NPs and solvent (Fig. 5.2a). Such a condition of colloidal NPs prepared using LAL is markedly different from that of colloids obtained using chemical methods, with various substances such as

T. Tsuji (✉)
Department of Materials Science, Interdisciplinary Factory of Science and Engineering, Shimane University, Matsue, Shimane 690-8504, Japan
e-mail: tkstsuji@riko.shimane-u.ac.jp



Y. Ishikawa et al. (eds.), *High-Energy Chemistry and Processing in Liquids*,
https://doi.org/10.1007/978-981-16-7798-4_5

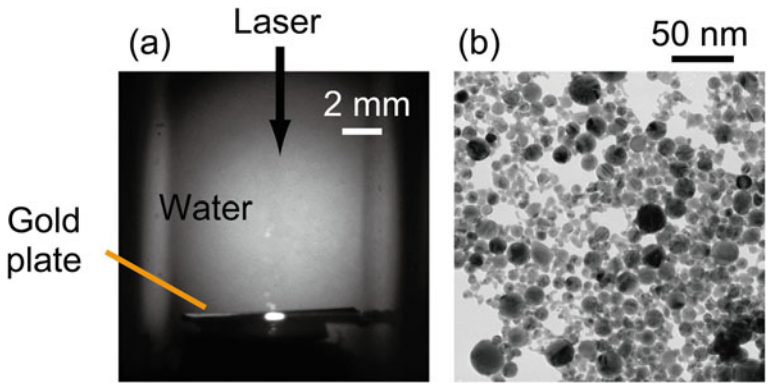


**Fig. 5.1** **a** Nanosecond-resolved shadowgraph observed for laser ablation of a gold plate in water. Plasma emissions are observed on the gold plate. **b** Gold NPs formed in water

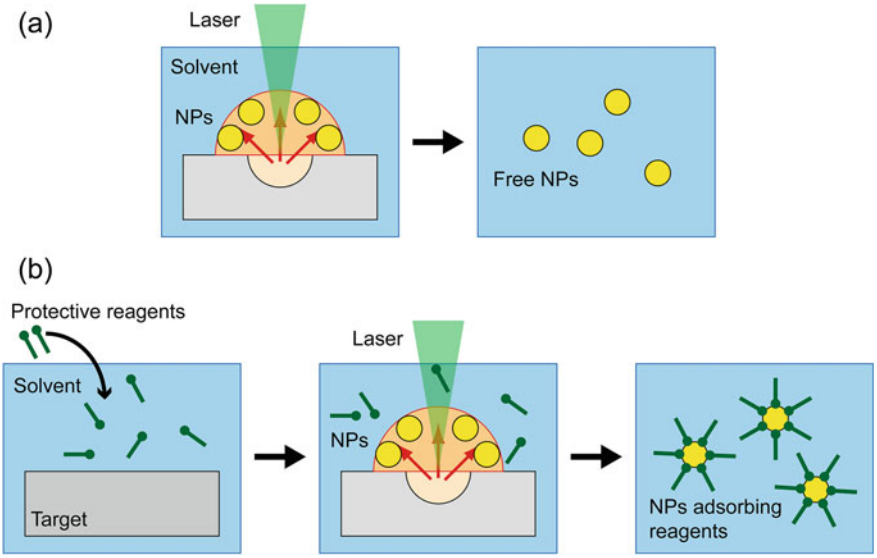


**Fig. 5.2** Surface conditions of nanoparticles obtained by LAL (**a**) in a pure solvent and (**b**) in a solution containing a protective reagent (ligands)

ions originating from the source compounds and protective reagents that are necessary to prevent NP agglomeration caused by these ions (salting out). Moreover, this beneficial feature of colloidal NPs is useful for biological and medical applications for which side effects derived from the supplemental reagents in colloidal solutions must be reduced.

When the amount and species of reagents are controlled properly, reagents can be useful to increase the usage of colloidal NPs. For example, protective reagents

improve the preservation property of colloids. In such cases, LAL becomes preferable to other methods. Protective reagents are adsorbed onto the NP surface, where they provide electric repulsion or special repulsion between NPs. Therefore, to use protective reagents efficiently, i.e., to minimize the reagent amount, adsorption of the protective agent onto NP surface must occur efficiently. Such efficient adsorption can be achieved using LAL because no other substance that can interfere with adsorption of the protective reagent is contained in the colloidal solution (Fig. 5.2b) [5, 6]. Furthermore, efficient adsorption presents interesting phenomena. An important example is that when LAL of a gold plate immersed in an aqueous solution containing NaCl, a typical compound that causes salting out acts as a protective agent [7, 8]. Figure 5.3 depicts temporal changes of relative adsorption intensity at 400 nm in UV–Vis spectra of gold NP colloids prepared using LAL in pure water and aqueous solutions of NaCl with different concentrations. The decrease in the absorption intensity is attributable to sedimentation of gold NPs. This figure shows that the gold colloid stability increases with increasing NaCl concentration. In this case, $Cl^-$ ions are adsorbed onto the gold NP surface, where they provide electric repulsive interaction among gold NPs [6].

This chapter explains some properties of the surface-modified NPs and introduces some examples of surface modification of NPs to functionalize NPs.

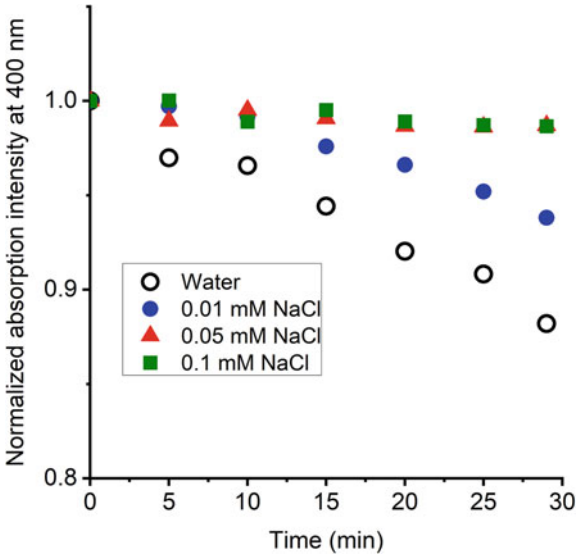


**Fig. 5.3** Temporal changes of relative adsorption intensity at 400 nm in UV–Vis spectra of gold NP colloids prepared using LAL in pure water and aqueous solutions of NaCl

## 5.2 Utilization of Colloidal Silver NPs Prepared Using LAL for Investigating Photo-Induced Shape Conversion

Shape control of metallic NPs has been a hot topic of NP synthesis because the optical property of metallic NPs depends strongly on the NP shape [9, 10]. In general, with chemical synthesis methods, NP shape control is achieved by adjusting various synthesis conditions such as temperature, reagents, and stabilizing agents. Mirkin's group reported a markedly different approach. They showed that room light irradiation for colloidal spherical silver NPs for about 100 h results in shape conversion to nanoprisms [11, 12].

The shape conversion mechanism is rather complex. It has been reported that dissolved oxygen, citrate ions used in the synthesis of silver NPs, and localized surface plasmon resonance (LSPR) caused by photoirradiation are crucially important factors [13–15]. However, because these colloids were prepared using a chemical synthesis method, the colloids used for these experiments reflected other factors such as ions and surfactants, which can affect shape conversion. Furthermore, only limited methods are available for preparation silver NP colloids in which photo-induced shape conversion occurs [11]. For that reason, we have investigated silver NP shape conversion using silver NPs prepared using LAL to clarify the important factors. As a result, we were able to reproduce similar shape conversion in silver NPs prepared using the experimental procedures shown in Fig. 5.4.

Procedure 1 is a basic procedure. In this procedure, the silver NP source was prepared using LAL in an aqueous solution containing sodium citrate, followed by pulsed laser irradiation (PLI) of those colloids to reduce the particle size. Using these treatments, silver NPs of less than 10 nm adsorbing citrate ions were prepared (Fig. 5.5a). After xenon lamp irradiation for 12 h with oxygen bubbling, the color of the colloids changed to green, and nanoprisms were formed (Fig. 5.5b). This result clarified the importance of the citrate ions and oxygen. Additionally, results indicated particle size (<10 nm) as another crucially important factor.

Procedures 2 and 3 in Fig. 5.4 were followed to investigate the role of citrate more precisely. Colloids prepared using these procedures contain sodium citrate and polyvinylpyrrolidone (PVP), although the order of the addition was different. Based on the discussion presented in Sect. 1, it is expected that silver NPs prepared using procedure 2 adsorbed citrate ions preferentially. Silver NPs prepared using procedure 3 were modified by PVP. Adsorption of citrate ions to the silver NPs was inhibited by PVP. Figure 5.6 portrays temporal changes of UV–Vis absorption spectra during photoirradiation for colloids prepared using procedures 2, 3. Bands of around 400 nm were attributed to spherical silver NPs, and those appearing around 600 nm were attributed to silver nanoprisms. These results demonstrate that citrate ion adsorption on the silver NP surface is important for shape conversion.

Based on these results, we propose the following factors as important for shape conversion.

(1) Size reduction of the source NPs: The stability of the atoms in the surface part of an NP decreases with decreasing particle size. Consequently, when the silver

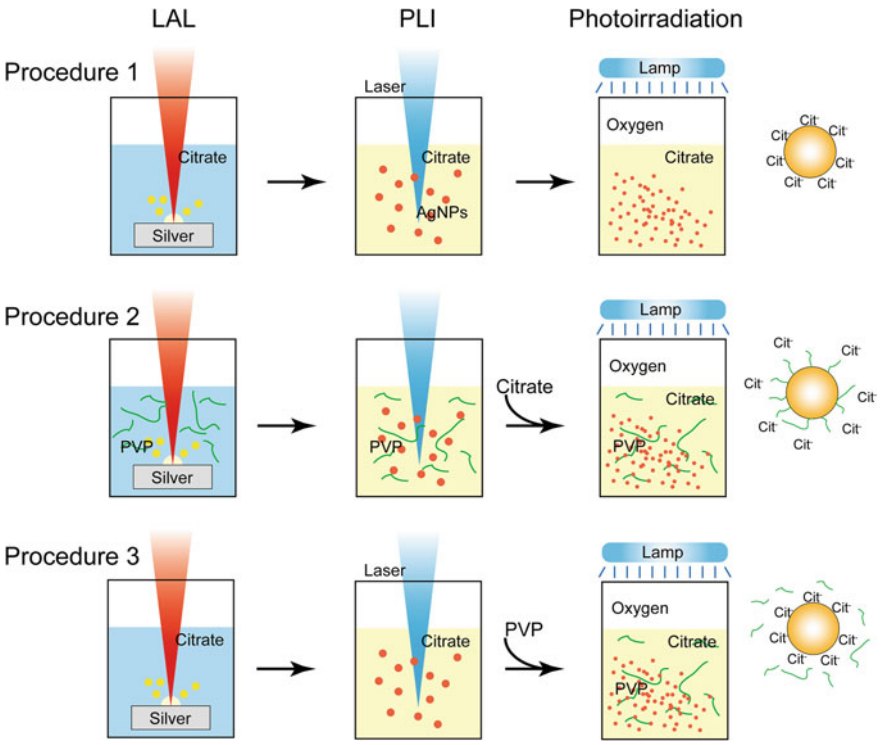


**Fig. 5.4** Preparation of silver NP colloids to observe photo-induced shape conversion using LAL. Oxygen bubbling was carried out during photoirradiation

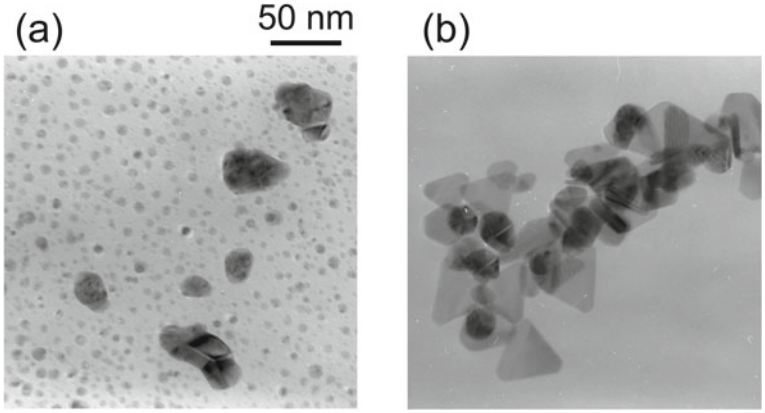


**Fig. 5.5** Silver NPs prepared using procedure 1 in Fig. 4: **a** before photoirradiation and **b** after photoirradiation for 12 h

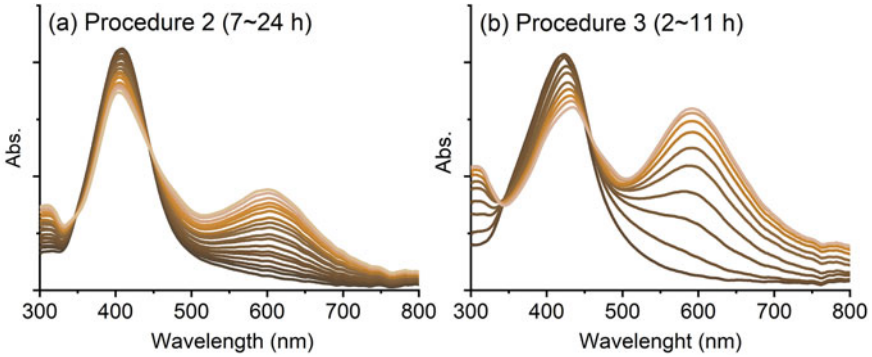


**Fig. 5.6** Temporal changes of UV–Vis spectra during photoirradiation of silver NP colloids prepared by **a** procedure 2 and **b** procedure 3 in Fig. 5.4. Absorption bands around 400 nm and those around 600 nm are assigned, respectively, to spherical NPs (Fig. 5.5a) and nanoprisms (Fig. 5.5b). For simplicity, only spectra in which the evolution of nanoprisms was observed are shown

NP size is reduced by laser irradiation, release of the silver atoms or ions from the surface of silver NPs is promoted.

(2) Oxygen: Oxygen can also promote the silver atom release from the NP surface by oxidation. Additionally, results suggest that silver ions (not atomic form) would be released.

(3) Photoirradiation: The role of the photoirradiation could not be clarified from the experiments described above. However, an earlier investigation of the relation between the illumination light wavelength and the result absorption spectra of the nanoprisms [16] indicated that photoirradiation promotes the oxidation of silver NPs, the release of silver ions, because the silver NPs able to absorb the irradiation light were diminished. Also, the silver NPs that were unable to absorb the irradiation light grew to nanoprisms.

(4) Sodium citrate: The reported result introduced in 3) above also suggests that silver ion reduction would occur on the NPs that do not absorb the irradiation light. Citrate ions adsorbed onto such NPs can be expected to reduce the silver ions derived from the NPs that undertake photooxidation on the surface of the NPs. Our experiment results showing that adsorption of citrate ions onto the silver NP surface is important for shape conversion strongly support this idea. The nanoprisms can be expected to form in the crystallization of silver atoms derived from reduction of the silver ions.

Finally, it is noteworthy that the discussion presented above became possible because of the simple contents of colloids prepared using LAL. Colloidal NPs prepared using LAL are appropriate to investigate substances that can interfere with nanosized materials' intrinsic properties unavoidable using chemical methods.

## 5.3 Utilization of LAL for Efficient Preparation of Submicrometer-Sized Spherical Particles

One important application of metal NPs is conductive inks. A colloidal solution containing NPs can be patterned on a substrate using an inkjet to form wiring. The NPs are sintered at low temperature. Through this process, atoms on the surface of the highly curved NPs are unstable and diffuse even at temperatures lower than the melting point, filling gaps between NPs. Recently, submicrometer-sized spherical particles (SMPs) are attracting attention as a material that is suitable for such applications. At approximately submicrometer size, the property of low-temperature sintering is maintained as with NPs, but the gaps separating SMPs are larger than those of NPs. Therefore, irreversible agglomeration of SMPs is unlikely to occur, even when no protective agent is added. This is a salient advantage of SMPs over NPs, particularly when considering industrial production.

To use low-temperature sintering of SMPs, SMPs with a smooth surface are necessary. However, synthesis of SMPs with a smooth surface is difficult to achieve using chemical methods. Particles with a faceted surface tend to be formed as the particle size increases [17]. Ishikawa and Koshizaki's group found an alternative method to obtain SMP in a very simple manner. They demonstrated that nanosecond-pulsed laser irradiation at moderate intensity to colloidal NPs induced SMP formation via the melting and fusion of NPs [18–20]. This technique is designated as "pulsed laser melting in liquids (PLML)." Fig. 5.7 shows a typical example of gold SMPs obtained by this technique. Spherical-shaped gold SMPs with a smooth surface are formed form colloidal gold NPs.

When forming SMPs that are larger than NPs in PLML, results showed that the NP agglomeration can be expected to occur before laser irradiation: the SMP formation does not occur via collision of the melted NPs [21]. However, NP agglomeration in colloids entails a possible shortcoming. The agglomeration of colloidal

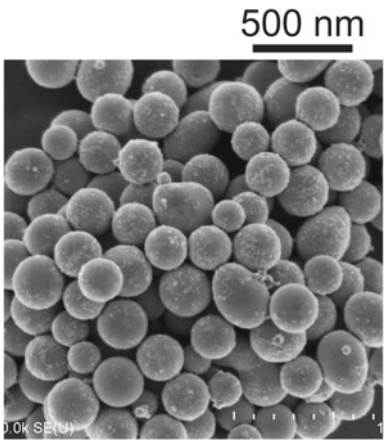


**Fig. 5.7** SEM image of gold SMPs prepared by PLML for gold NPs in an aqueous solution containing 0.005 mM sodium citrate. The average diameter is 234 nm

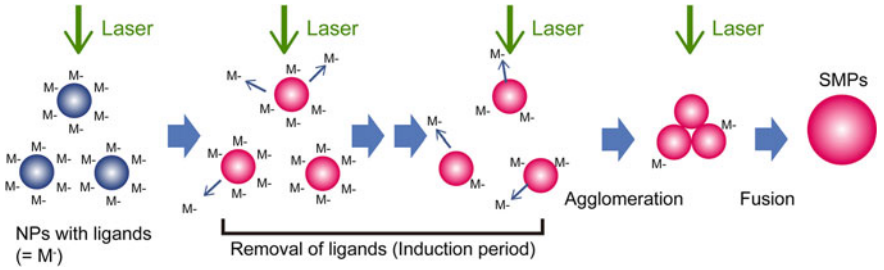


**Fig. 5.8** SMPs via the laser-induced agglomeration of the source NPs adsorbing protective reagent (ligands)

NPs usually engenders NP sedimentation. If sedimentation occurs in the source NPs of SMPs before laser irradiation, then those NPs will not absorb laser irradiation. No melting will occur, leading to a decrease in SMP formation efficiency. Therefore, NP agglomeration control is necessary to obtain SMPs efficiently.

We proposed an NP agglomeration control method that is appropriate for the PLML process, as shown by Fig. 5.8 [22]. In this method, the source NPs with ligands (protective reagent molecules) such as sodium citrate are used to avoid NP agglomeration and sedimentation before laser irradiation. Upon laser irradiation, NPs are heated by laser energy. The ligands adsorbed onto the NPs are removed via the decomposition and/or generation of mechanical force such as shock waves and cavitation bubbles. As laser irradiation continues, the number of ligands on the NPs is decreased. Eventually, NP agglomeration occurs when the number of ligands becomes insufficient to avoid NP agglomeration. These agglomerated NPs are fused following laser irradiation and thereby form SMPs. The "laser-induced agglomeration" occurs immediately before NP fusion. Therefore, we can suppress their sedimentation before laser irradiation.

Although this method is simple, two key conditions must be adjusted to use laser-induced agglomeration efficiently. One key condition is the protective reagent concentration, i.e., the number of ligands adsorbed onto a gold NP. As shown in Fig. 5.9, an increase in the protective reagent concentration leads to an increase in the induction period, consequently leading to a reduction of the production efficiency, although the stability of colloids is increased. Furthermore, our results demonstrated that the protective reagent concentration also influences the SMP size [23]. Using LAL, the protective reagent concentration in the source colloids can be adjusted simply by adjusting the concentration of a protective agent added to the solvent in which the LAL is conducted.

Another key condition is the protective reagent species. Figures 5.10 and 5.11 show that laser-induced agglomeration behavior and SMP size depend on the protective reagent species [24, 25]. Using LAL, selection of the protective reagent species can be conducted in a simple manner. The LAL is conducted in the solution containing a selected protective reagent. Such a wide range of choice of protective reagents is useful when the application of SMPs is considered. For example, if one wants to

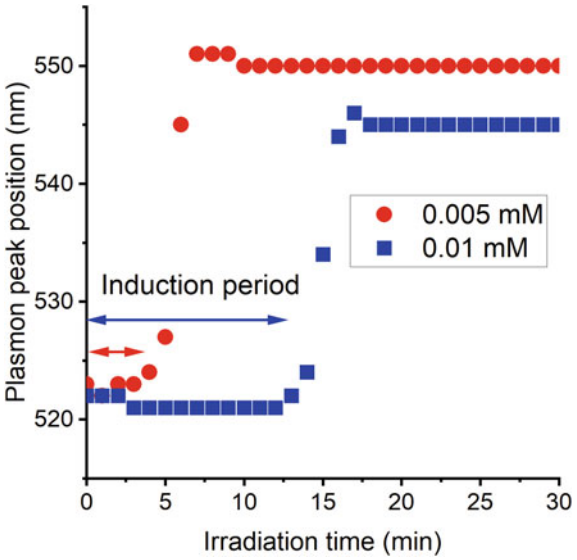


**Fig. 5.9** Temporal changes of plasmon peak position in UV–Vis spectra of gold colloids in the aqueous solution of sodium citrate during laser irradiation to produce SMPs. The plasmon band peak position of gold NP colloids is red-shifted when NP agglomeration and fusion (size increase) occur. Therefore, the plasmon peak position can be used to monitor the NP agglomeration. Observations of the induction period indicate that NP agglomeration occurs via the scheme shown in Fig. 5.8. The induction period is increased with the increasing sodium citrate concentration. These colloids were prepared using LAL for gold plate in an aqueous solution containing 0.005 mM or 0.01 mM sodium citrate

**Fig. 5.10** Temporal changes of plasmon peak position in UV–Vis spectra during laser irradiation for gold colloids in aqueous solutions of 0.005 mM sodium citrate, 0.01 mM NaCl, and 0.01 mM $Na_2CO_3$

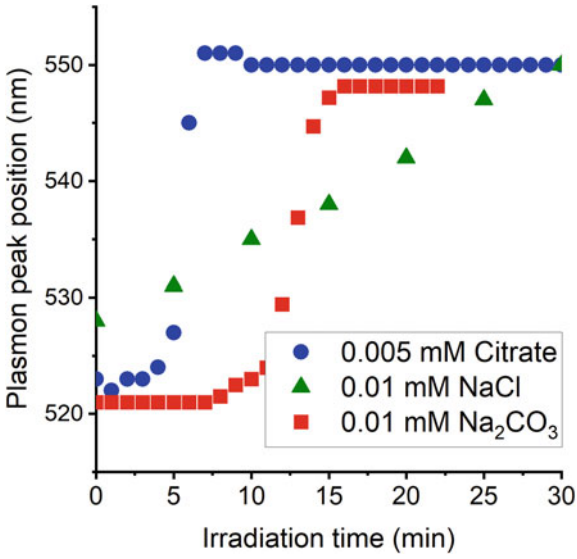

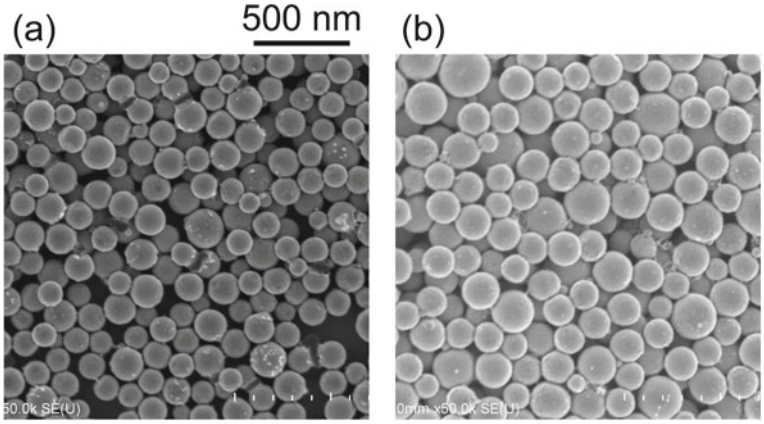


**Fig. 5.11** SEM image of gold SMPs prepared by PLML for gold NPs in an aqueous solution containing 0.01 mM NaCl (**a**) and 0.01 mM $Na_2CO_3$ (**b**). The average diameter of the SMPs is 146 nm for NaCl and 184 nm for $Na_2CO_3$

use SMPs for biological application such as a cell marker, then non-toxic reagents such as NaCl are useful. If one wants to use SMPs for electric devices, then reagents containing halides cannot be used. Organic reagents such as sodium citrate should be chosen. For these reasons, using LAL to prepare PLML source NPs is efficient for improving the usability of SMPs.

## 5.4 Control of Electric Properties of Colloidal NPs Using LAL in Organic Solvents

An interesting point is that NPs formed in some organic solvents are much more stable than NPs formed in pure water [26]. Table 5.1 shows the zeta potential of gold NPs formed in water and in some organic solvents [27]. The gold NPs formed in these organic solvents are more strongly negatively charged than those formed in water. Such electric charging of NPs occurring in LAL is apparent for other materials such as $TiO_2$ [28], suggesting that this phenomenon is a common feature of LAL. The origin of the negative charge provided by these organic solvents remains unclear.

**Table 5.1** Zeta potentials of gold NPs prepared by laser ablation in various solvents

| Solvent | Zeta potential (mV) |
|---|---|
| Water | –10 ~ 10 |
| Ethanol | –20 |
| 1-Propanol | –50 |
| Acetone | –90 |

Acetone in the enol form [26] and alcohols can have a negative charge when they release a proton. Nevertheless, explaining the negative charge of the NPs is difficult in terms of the ionization because their ionization degree is low. Interaction between the solvent molecule and the NP surface is inferred as playing an important role. From another perspective, clarifying the origin of the negative charge would provide useful information about interaction between substances and NPs.

We have demonstrated that the negative charge of NPs is useful for application of NPs prepared using LAL as functional materials. For example, when a pair of electrode plates is set in an NP colloidal solution prepared in those organic solvents and an electric field is applied between the electrodes, then negatively charged NPs are attracted onto the positive electrode (Fig. 5.12). This phenomenon is useful to collect NPs in a colloidal solution efficiently and to form NP deposit films (Fig. 5.13a). Such an NP deposit film is useful as a battery electrode (Fig. 5.13b) [28], and as a substrate for the surface-assisted laser desorption ionization (SALDI) technique for mass spectrometry (Fig. 5.14a) because deposit films have a nano-sized surface structure (Fig. 5.14a).

Very recently, we identified another interesting phenomenon by LAL in which a negative charge provided by alcohols plays an important role. Figure 5.15 presents photographs of CaO particle colloids observed during LAL. In less than 60 min, the colloidal solution became cloudier, indicating that fragmentation of the CaO power progressed by focused laser irradiation. However, at ca. 60 min, the colloidal solution became clear; larger gel-like structures were formed. As depicted in the SEM image, the gel-like structures have complex morphology. Such structures are useful as a substrate of catalysis when metal NPs are deposited on them. Additionally, it is remarkable that such complex structures were formed by strong laser irradiation

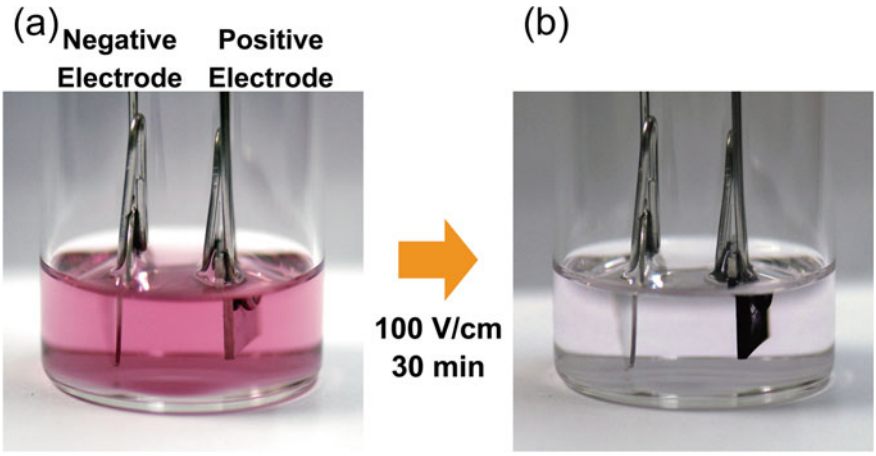


**Fig. 5.12** Appearance change of gold NP colloids (**a**) before and (**b**) after electrophoresis at 100 V/cm for 30 min. Gold colloids were prepared using LAL in acetone

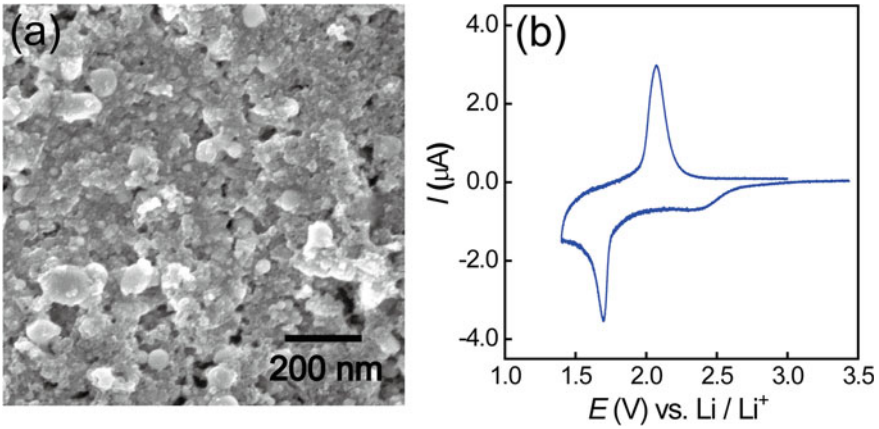


**Fig. 5.13** **a** SEM images of $TiO_2$ NPs deposited on a Pt substrate by electrophoresis. **b** A CV curve measured using the deposited $TiO_2$ NPs. The $TiO_2$ NPs were prepared using LAL for $TiO_2$ powder in acetone

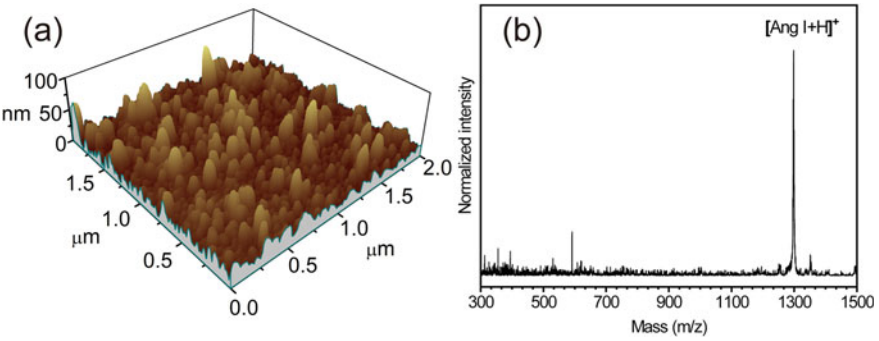


**Fig. 5.14** **a** Surface morphology of a gold NP deposit film formed by electrophoresis. **b** Typical SALDI spectrum of angiotensin I obtained using a gold NP deposit film. The gold NPs were prepared using LAL in acetone

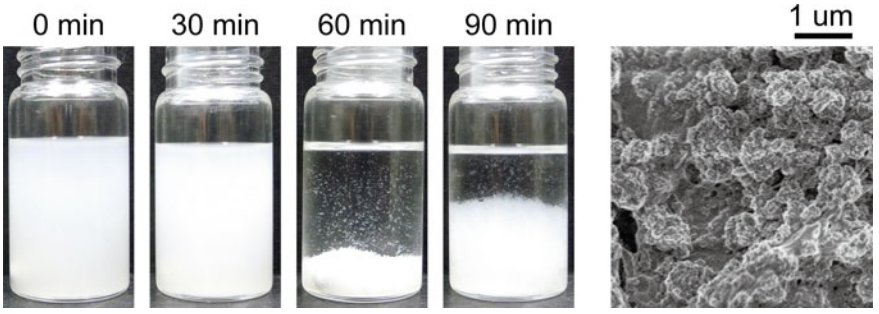


**Fig. 5.15** Appearance changes of CaO particle colloid dispersed in ethanol during LAL, with an SEM image of gel-like structures observed at 30 and 60 min after they were dried

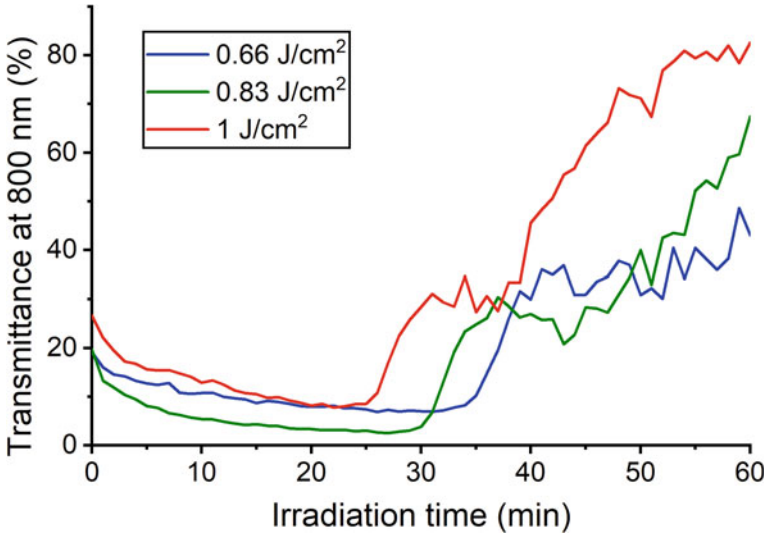


**Fig. 5.16** Temporal optical transmittance changes of CaO colloidal solutions during LAL and its changes by laser fluences. The time of the gel-like structure formation is different from that shown in Fig. 5.15 because this observation was carried out using 3 mL solutions: the volume of the colloids in Fig. 5.15 was 10 mL

that usually induces only NP fragmentation. For these reasons, we have undertaken further investigation of this phenomenon.

Figure 5.16 shows temporal optical transmittance changes of CaO colloidal solutions during LAL. The gel-like structure formation can be detected by observing the optical transmittance of the colloidal solutions. Figure 5.16 presents two important pieces of information.

(1) The gel-like structures are formed rapidly after an induction period lasting a few tens of minutes, not from the beginning of laser irradiation.
(2) The induction period length decreases concomitantly with increasing laser intensity, suggesting that gel-like structure formation is correlated to the NP concentration.

These facts suggest that gel-like structures were formed via NP agglomeration because NP agglomeration can occur abruptly. Its efficiency increases with increasing NP concentration.

How does NP agglomeration occur in CaO NP colloids? One can reasonably infer that the NP agglomeration occurs via a mechanism similar to the formation process of SMP; stabilizer adsorbed onto NPs is removed by laser irradiation. In CaO NP colloids, ethanol can be a stabilizer of NPs, as described earlier in this section. However, differing from the SMP formation process, removing ethanol from CaO NPs to induce agglomeration is impossible because ethanol is the solvent used for this system and ethanol molecules removed by laser irradiation will be compensated

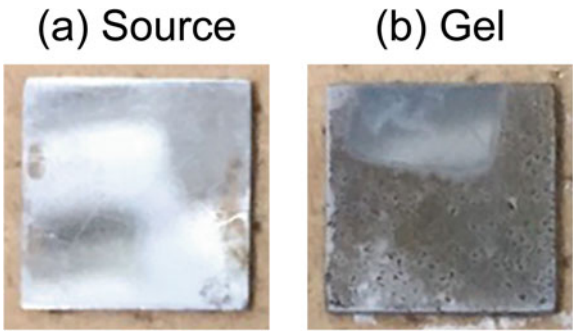


**Fig. 5.17** Photographs of negative electrode plates after electrophoresis of **a** source powder colloids in ethanol and **b** colloids with gel-like structures formed by laser irradiation

by surrounding molecules. Consequently, the CaO NP agglomeration conditions in this system must be controlled by another factor.

We conducted electrophoresis of the source particles in ethanol (Fig. 5.17a). It is remarkable that the source CaO particles were positively charged. We also confirmed that the source CaO powder (before it is dispersed into ethanol) was positively charged. Such electric charging of powder materials is suggested to be generated by friction among particles and that between particles and container wall, although the origin of the electric charge of CaO powder used in our experiment has not been clarified. This positive charge can prevent CaO particle agglomeration.

When LAL is conducted for CaO particles in ethanol, it will be possible that ethanol molecules are adsorbed onto the CaO NP surface during their generation process and that it will provide a negative charge, as observed for gold NPs. The donation of a negative charge by ethanol for positively charged CaO particles causes electric neutralization, which can engender colloid agglomeration. In other words, results suggest that the gel-like structures would be generated by neutralization of positively charged CaO NPs by ethanol. In addition, considering that the gel-like structures still have a negative charge (Fig. 5.17b), partial neutralization will be necessary to obtain gel-like structures, namely the gel-like structures are weakly agglomerated NPs. The formation scheme of the gel-like structures explained above is shown in Fig. 5.18.

In addition, using the positive charge of the gel-like structure, we demonstrated that metal–CaO nanocomposites can be prepared by a simple manner. As shown in Fig. 5.19, when a gold or platinum NP colloidal solution prepared using LAL in ethanol (NPs were negatively charged) and a colloidal solution containing gel-like structures (positively charged) were mixed, red or brown gel-like structures were obtained. Such nanocomposites can be model materials of the catalyst. For that reason, gel-like structure formation by LAL is anticipated as a novel method for synthesizing functional materials.

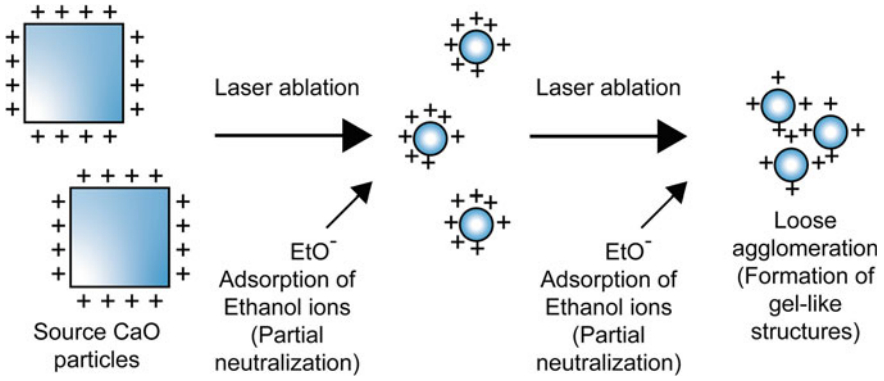


**Fig. 5.18** Proposed formation mechanism of gel-like structures formed by LAL for CaO dispersed in ethanol

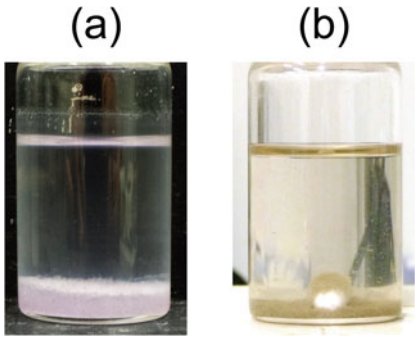


**Fig. 5.19** Solutions obtained by mixing a colloidal solution containing CaO gel-like structures and a colloidal solution of **a** gold NPs or **b** platinum NPs prepared using LAL in ethanol

## 5.5 Summary

Surface modification of colloidal NPs is crucially important for control of the stabilization and functionalization of colloidal NPs. This review illustrates that the surface modification of NPs is conducted controllably using the LAL technique. Actually, LAL can be conducted in a solvent in which a target material and a protective reagent are contained. Therefore, only the protective reagent contained can be adsorbed onto the NPs of the target material without interference from other compounds. Furthermore, the reagent adsorption can be controlled by adjusting the reagent amount and the order of addition. It is also remarkable that some organic solvents themselves modify the NPs surface. Such surface modification is difficult for colloidal NPs prepared using chemical synthesis methods because colloids prepared using chemical methods contain various substances. The results achieved through surface modification using LAL are expected to provide important information not only for material fabrication but also for colloid science.

**Acknowledgements** The experiment results introduced in this article were obtained with the assistance of many collaborators. Especially the author would like to thank Prof. Masaharu Tsuji (Kyushu Univ.), Prof. Naoto Koshizaki (Hokkaido Univ.), Dr. Yoshie Ishikawa (National Institute of Advanced Industrial Science), Prof. Shuichi Hashimoto (Tokushima Univ.) and Prof. Yasuyuki Tsuboi (Osaka City Univ.) for their cooperation.

## References

1. V. Amendola, M. Meneghetti, Laser ablation synthesis in solution and size manipulation of noble metal nanoparticles. Phys. Chem. Chem. Phys. **11**, 3805–3821 (2009). https://doi.org/10.1039/B900654k
2. G. Yang, *Laser Ablation in Liquids Principles and Applications in the Preparation of Nanomaterials* (Pan Stanford Publishing, Singapore, 2012), p. 1151
3. D. Zhang, B. Gökce, S. Barcikowski, Laser synthesis and processing of colloids: fundamentals and applications. Chem. Rev. **117**, 3990–4103 (2017). https://doi.org/10.1021/acs.chemrev.6b00468
4. V. Amendola, D. Amans, Y. Ishikawa, N. Koshizaki, S. Scirè, G. Compagnini, S. Reichenberger, S. Barcikowski, Room-temperature laser synthesis in liquid of oxide, metal-oxide core-shells, and doped oxide nanoparticles. Chemistry (Weinheim an der Bergstrasse, Germany) **26**, 9206–9242 (2020). https://doi.org/10.1002/chem.202000686
5. P. Wagener, A. Schwenke, S. Barcikowski, How citrate ligands affect nanoparticle adsorption to microparticle supports. Langmuir **28**, 6132–6140 (2012). https://doi.org/10.1021/la204839m
6. V. Merk, C. Rehbock, F. Becker, U. Hagemann, H. Nienhaus, S. Barcikowski, In situ non-DLVO stabilization of surfactant-free, plasmonic gold nanoparticles: effect of Hofmeister's anions. Langmuir **30**, 4213–4222 (2014). https://doi.org/10.1021/la404556a
7. C.H. Bae, S.H. Nam, S.M. Park, Formation of silver nanoparticles by laser ablation of a silver target in NaCl solution. Appl. Surf. Sci. **197–198**, 628–634 (2002). https://doi.org/10.1016/S0169-4332(02)00430-0
8. T. Tsuji, Y. Higashi, M. Tsuji, Y. Ishikawa, N. Koshizaki, Preparation of submicron-sized spherical particles of gold using laser-induced melting in liquids and low-toxic stabilizing reagent. Appl. Surf. Sci. **348**, 10–15 (2015). https://doi.org/10.1016/j.apsusc.2015.02.057
9. C.J. Murphy, T.K. San, A.M. Gole, C.J. Orendorff, J.X. Gao, L. Gou, S.E. Hunyadi, T. Li, Anisotropic metal nanoparticles: synthesis, assembly, and optical applications. J. Phys. Chem. B **109**, 13857–13870 (2005). https://doi.org/10.1021/jp0516846
10. B. Wiley, Y.G. Sun, B. Mayers, Y.N. Xia, Shape-controlled synthesis of metal nanostructures: the case of silver. Chem. Eur. J. **11**, 454–463 (2005). https://doi.org/10.1002/chem.200400927
11. R.C. Jin, Y.W. Cao, C.A. Mirkin, K.L. Kelly, G.C. Schatz, J.G. Zheng, Photoinduced conversion of silver nanospheres to nanoprisms. Science **294**, 1901–1903 (2001). https://doi.org/10.1126/science.1066541
12. R.C. Jin, Y.C. Cao, E.C. Hao, G.S. Metraux, G.C. Schatz, C.A. Mirkin, Controlling anisotropic nanoparticle growth through plasmon excitation. Nature **425**, 487–490 (2003). https://doi.org/10.1038/nature02020
13. M. Maillard, P.R. Huang, L. Brus, Silver nanodisk growth by surface plasmon enhanced photoreduction of adsorbed [$Ag^+$]. Nano Lett. **3**, 1611–1615 (2003). https://doi.org/10.1021/nl034666d
14. X.M. Wu, P.L. Redmond, H.T. Liu, Y.H. Chen, M. Steigerwald, L. Brus, Photovoltage mechanism for room light conversion of citrate stabilized silver nanocrystal seeds to large nanoprisms. J. Am. Chem. Soc. **130**, 9500–9506 (2008). https://doi.org/10.1021/ja8018669
15. C. Xue, G.S. Metraux, J.E. Millstone, C.A. Mirkin, Mechanistic study of photomediated triangular silver nanoprism growth. J. Am. Chem. Soc. **130**, 8337–8344 (2008). https://doi.org/10.1021/ja8005258

16. A. Callegari, D. Tonti, M. Chergui, Photochemically grown silver nanoparticles with wavelength-controlled size and shape. Nano Lett. **3**, 1565–1568 (2003). https://doi.org/10.1021/nl034757a
17. X.H. Ji, X.N. Song, J. Li, Y.B. Bai, W.S. Yang, X.G. Peng, Size control of gold nanocrystals in citrate reduction: the third role of citrate. J. Am. Chem. Soc. **129**, 13939–13948 (2007). https://doi.org/10.1021/ja074447k
18. Y. Ishikawa, Q. Feng, N. Koshizaki, Growth fusion of submicron spherical boron carbide particles by repetitive pulsed laser irradiation in liquid media. Appl. Phys. A **99**, 797–803 (2010). https://doi.org/10.1007/s00339-010-5745-6
19. Y. Ishikawa, T. Sasaki, N. Koshizaki, Submicron-sized boron carbide particles encapsulated in turbostratic graphite prepared by laser fragmentation in liquid medium. J. Nanosci. Nanotechnol. **10**, 5467–5470 (2010). https://doi.org/10.1166/jnn.2010.1947
20. H.Q. Wang, A. Pyatenko, K. Kawaguchi, X. Li, Z. Swiatkowska-Warkocka, N. Koshizaki, Selective pulsed heating for the synthesis of semiconductor and metal submicrometer spheres. Angew. Chem. Int. Ed. **49**, 6361–6364 (2010). https://doi.org/10.1002/anie.201002963
21. Y. Ishikawa, Y. Katou, N. Koshizaki, Q. Feng, Raw particle aggregation control for fabricating submicrometer-sized spherical particles by pulsed-laser melting in liquid. Chem. Lett. **42**, 530–531 (2013). https://doi.org/10.1246/cl.130044
22. T. Tsuji, T. Yahata, M. Yasutomo, K. Igawa, M. Tsuji, Y. Ishikawa, N. Koshizaki, Preparation and investigation of the formation mechanism of submicron-sized spherical particles of gold using laser ablation and laser irradiation in liquids. Phys. Chem. Chem. Phys. **15**, 3099–3107 (2013). https://doi.org/10.1039/c2cp44159d
23. T. Tsuji, S. Sakaki, H. Fujiwara, H. Kikuchi, M. Tsuji, Y. Ishikawa, N. Koshizaki, Stabilizer-concentration effects on the size of gold submicrometer-sized spherical particles prepared using laser-induced agglomeration and melting of colloidal nanoparticles. J. Phys. Chem. C **122**, 21659–21666 (2018). https://doi.org/10.1021/acs.jpcc.8b05911
24. T. Tsuji, Y. Higashi, M. Tsuji, H. Fujiwara, Y. Ishikawa, N. Koshizaki, Fabrication of spherical-shaped submicron particles of ZnO using laser-induced melting of submicron-sized source materials. J. Laser Micro/Nano Eng. **8**, 292–295 (2013). https://doi.org/10.2961/jlmn.2013.03.0017
25. T. Tsuji, I. Takade, M. Tsuji, Y. Ishikawa, N. Koshizaki, Preparation of gold submicron-sized particles using laser irradiation for gold nanoparticles stabilized by carbonate. Electr. Commun. Jpn. **99**, 64–70 (2016). https://doi.org/10.1002/ecj.11875
26. E. Giorgetti, M. Muniz-Miranda, P. Marsili, D. Scarpellini, F. Giammanco, Stable gold nanoparticles obtained in pure acetone by laser ablation with different wavelengths. J. Nanopart. Res. **14**, 649 (2012). https://doi.org/10.1007/s11051-011-0648-9
27. T. Tsuji, T. Mizuki, M. Yasutomo, M. Tsuji, H. Kawasaki, T. Yonezawa, F. Mafune, Efficient fabrication of substrates for surface-assisted laser desorption/ionization mass spectrometry using laser ablation in liquids. Appl. Surf. Sci. **257**, 2046–2050 (2011). https://doi.org/10.1016/j.apsusc.2010.08.128
28. T. Tsuji, M. Nakanishi, T. Mizuki, M. Tsuji, T. Doi, T. Yahiro, J. Yamaki, Preparation of nano-sized functional materials using laser ablation in liquids. Appl. Surf. Sci. **255**, 9626–9629 (2009). https://doi.org/10.1016/j.apsusc.2009.04.075

# Part II
# High-Energy Processing of Nonmetals

# Chapter 6
# Fabrication and Control of Semiconductor Random Lasers Using Laser Processing Techniques


**Hideki Fujiwara**

**Abstract** In this chapter, I introduce a novel method for fabricating random lasers using various types of laser processing techniques. Random lasers, in which laser oscillation is induced by random feedback based on multiple light scattering, can achieve low threshold and oscillation mode control by optimizing the size and shape of scatterers. On the other hand, laser processing techniques enable us to realize surface processing, photochemical synthesis, nanoparticle fabrication, and so on, by means of phenomena such as ablation and photo-heating due to laser irradiation and also to fabricate structures of various shapes by controlling the laser irradiation conditions. Utilizing these advantages, I can achieve not only the fabrication of various types of random lasers but also the realization of low-threshold laser oscillation and lasing wavelength control by optimizing the fabrication conditions. This chapter covers three laser processing methods: (1) laser-induced melting method, (2) laser-induced hydrothermal synthesis, and (3) laser-induced surface roughness structures, and introduces the features and advantages of these methods for realizing low-cost and low-threshold random lasers.

**Keywords** Random laser · Laser-induced melting method · Laser-induced hydrothermal synthesis · Laser-induced periodic surface structures

## 6.1 Introduction

Lasers are widely used as light sources that contribute to basic technologies in many industries such as in processing/manufacturing, information/communication, medical care, plant cultivation, and illumination. Because lasers have characteristics that differ from conventional thermal light sources (e.g., high monochromaticity, high spatial and temporal coherence, good directivity, and high light density), these properties are suitable for laser processing and scanning-type imaging. However, in the case of full-field imaging or sensors, which require light sources that can uniformly

H. Fujiwara (✉)
Faculty of Engineering, Hokkai-Gakuen University, 1-1, S26W11, Chuo-ku, Sapporo 064-0926, Japan
e-mail: h-fujiwara@hgu.jp



Y. Ishikawa et al. (eds.), *High-Energy Chemistry and Processing in Liquids*,
https://doi.org/10.1007/978-981-16-7798-4_6

irradiate the entire field of view, conventional lasers are not suitable because intensity speckles owing to high coherence will degrade the imaging quality. Additionally, because conventional lasers require a well-defined cavity structure that provides feedback to cause laser oscillation, advanced material processing technology, and precise adjustment mechanism are basically indispensable.

In contrast, random lasers that I focus on in this chapter has been attracting interest since 1994 when Lawandy et al. reported the observation of amplified spontaneous emission in a nanoparticle-dispersed dye solution [1]. From the late 1990s to the early 2000s, random laser has been actively studied by several groups, which determined that random lasers without clear cavity structures can be characterized as a "laser" with temporal coherence that is similar to that of conventional lasers [2–7]. Then, the application of random lasers has been rapidly attracting attention using various materials and morphologies, since Redding et al. had proposed light source applications for the full-field imaging in 2012 [8]. Laser oscillation in a random laser occurs owing to random feedback within an irregular refractive index distribution, which is induced by the multiple light scattering and its interference effect. Therefore, random lasers have the advantage that they do not require a well-defined cavity structure and they can be fabricated relatively easily and inexpensively. Owing to this random feedback (because laser oscillation can be induced accidentally in frequency and space domains), random laser has low spatial coherence and maintains temporal coherence, which means random lasers have the properties both of thermal light and laser properties can be obtained. These characteristics make random laser a high-brightness, pseudo-monochromatic, speckle-free laser light source, which provides a uniformly high intensity light over the entire field of view. Therefore, these properties may enable us to develop light source applications for high-speed, high-accuracy full-field imaging, sensors, and intense UV germicidal irradiation. However, although random laser has industrially important advantages (e.g., it can be easily and inexpensively produced), because of randomness, it is not suitable for electric drive, which is important for its practical applications; additionally, it is difficult to control the oscillation mode in space and frequency, which results in high thresholds. Additionally, considering the realization of electrically driven solid-state random lasers, random lasers made of semiconductor materials are important candidates. However, although zinc oxide and gallium nitride have been widely used for semiconductor random lasers, there are fewer reports that use other semiconductor materials for random lasers [9–11].

In my research on such problems, I aimed to develop novel laser processes for fabricating semiconductor random lasers with various morphologies by focusing on the following points: (1) lower threshold by controlling lasing modes (structural control), (2) device fabrication using semiconductor materials that can be electrically driven, (3) switching and control mechanism of lasing modes by external stimuli. For this purpose, I paid attention to the laser processing technique because this technique can easily fabricate random structures in a large area while maintaining the advantage of easy and low-cost fabrication. Additionally, during laser processing, because a structure can be manufactured in a noncontact manner, it allows us to fabricate the structures in a vacuum, solution, and gas atmosphere. Furthermore, by controlling

the irradiation laser conditions, structures can be controlled which allows to control lasing modes to lower the thresholds. In this chapter, I introduce three fabrication methods that I developed thus far and their achievements with the aim of establishing a new method of fabricating a semiconductor random laser that can control the lasing mode and structure for the practical application of random laser.

## 6.2 Realization of Single Mode Random Lasing Using a Laser-Induced Melting Method

In a conventional nanoparticle aggregation film, because the nanoparticles are irregularly arranged and the shapes and sizes of individual nanoparticles are varied, the frequency response of individual nanoparticles is canceled out and the film does not have resonance at a particular wavelength. Therefore, it is not possible to provide strong random feedback at a specific wavelength region that matches the maximum gain wavelength of the gain medium.

In contrast, if the size and shape of the nanoparticles are uniform, although the particles are randomly distributed, a certain periodicity can be introduced into the structure to enhance the resonance of individual nanoparticles and make the scattering of specific wavelengths stronger. This idea has been first reported as a photonic glass and structural coloration, in which a specific wavelength of the reflection spectrum is strongly scattered [12–14]. Lasing wavelength tuning was achieved by filling the photonic glass with a dye solution and changing the particle size [13, 14]. However, because mono-dispersed polymer particles with low refractive index were used, only an incoherent random laser (amplified spontaneous emission) was produced owing to low scattering efficiency. To control coherent random laser in a similar fashion, mono-dispersed scatterers with high refractive index (e.g., semiconductors) are indispensable; however, such nanoparticles cannot be obtained as a commercial product.

On the contrary, using numerical analysis, I had been searching for a way to control the oscillation modes of a random laser and proposed a simple method to control random lasing modes using resonances of size mono-dispersed scatterers and create a defect region where no scatterers are placed in the structure [15–19]. In the proposed method, because a defect region is surrounded by size mono-dispersed scatterers, a random structure strongly scatters light at a specific wavelength depending on the resonance of individual uniform scatterers and strongly localized at the defect regions. Thus, effective photon localization can be achieved at the defect and random lasing can be controlled spatially and spectrally using resonant scatterers and intentionally introduced defects, which results in low-threshold random lasing.

To fabricate mono-dispersed scattering nanoparticles, I focused on the laser melting method in liquid developed by Koshizaki et al. [20–23]. In this method, initial nanoparticles dispersed in liquid are irradiated with a laser to melt aggregated nanoparticles to produce spherical nanoparticles with a sub-micron meter size. The

size can be controlled by adjusting the sizes of initial particles and aggregations and the irradiated laser intensity and time. In this section, I introduce the experimental results of random lasing mode control using mono-dispersed zinc oxide (ZnO) spherical nanoparticles fabricated by this laser melting method [15–19].

ZnO nanoparticles were selected as scatters because they have already been reported as scatterers and gain materials in many experiments on random lasers. Because the emission wavelength of ZnO is 380–390 nm, considering the optical resonance of particles from the Mie scattering theory, the optimal particle size is estimated to be ~200 nm. Using the laser melting method [23], commercially available ZnO particles (average particle size: 100 nm) were used to prepare ZnO spherical particles with an average particle size of ~200 nm. Initial nanoparticles have irregular shapes and various sizes; however, after laser melting, I was able to obtain uniform spherical nanoparticles (average size: 212 nm) (see Fig. 6.1). After adding green fluorescent polystyrene particles (average size: 900 nm) as defect particles to the spherical nanoparticles dispersed solution, the solution was deposited on a glass substrate and dried to form a thin film with a thickness of ~100 μm. Samples with commercial ZnO particles and fluorescent particles were also prepared for comparison. In the experiments, fluorescent particles were used as a defect because the position of defect in thin film could be identified from the green fluorescence image.

The sample was placed on the piezo stage of the microscope, and UV laser pulses (355 nm, 300 ps, 1 kHz) were irradiated on the sample with a 100 × objective lens (NA 0.9, spot diameter ~65 μm). The emission from the sample is collected by the same objective lens and filtered with an excitation light cut-off filter. After passing through a pinhole (5 μm diameter at the sample surface), the emission was introduced into a spectrophotometer. A photomultiplier tube attached to the spectrophotometer was used to measure the intensity distribution at a specific wavelength by scanning the sample stage. Then, the emission spectra at arbitrary positions were measured by a cooled CCD camera attached to the spectrophotometer. The position of defect fluorescent particles was confirmed by acquiring a green fluorescence image with a color CCD camera after the excitation laser intensity was sufficiently reduced.

Figure 6.2 shows the green fluorescence image of defect particles in an untreated ZnO nanoparticle films (left panel) and the UV emission intensity distribution of the same region (right panel). Based on the fluorescence image, the excitation region (including a defect for measuring the UV emission intensity distribution) was determined and the excitation intensity was set to 90 MW/cm$^2$ which was approximately

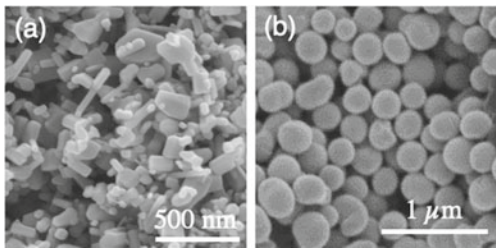


**Fig. 6.1** SEM images of submicrometer-sized ZnO particles **a** before and **b** after laser-induced melting

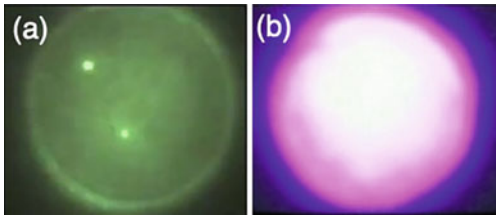


**Fig. 6.2** **a** Fluorescence and **b** UV emission images of an untreated ZnO particle film including polymer particles

twice the threshold. Although a fluorescent particle (defects) was confirmed from the fluorescence image, the UV emission intensity was uniformly distributed in the entire sample regardless of the defect position. Figure 6.3 shows the emission spectrum measured around the defect in this nanoparticle film, and the multi-peak laser oscillation with a threshold of ~50 MW/cm$^2$ was induced near the emission peak (387 nm). Such behavior was also observed in other places regardless of the presence or absence of defects, which was in good agreement with the behavior of conventional random lasers reported thus far.

However, Fig. 6.4 shows the results of a similar experiment using a laser-treated ZnO nanoparticle film including defects. The excitation intensity of the emission intensity distribution measurement was set to 10 MW/cm$^2$, which was almost 10 times weaker than the excitation intensity used in Fig. 6.2. Despite the uniform intensity in the excitation area, higher emission intensity was observed at the defect

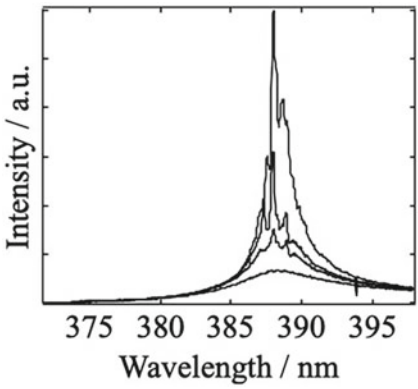


**Fig. 6.3** Emission spectra measured at a defect site in an untreated ZnO particle film. The excitation intensities were 0.5, 1.0, 1.5, and 2.0 times of the threshold from bottom to top

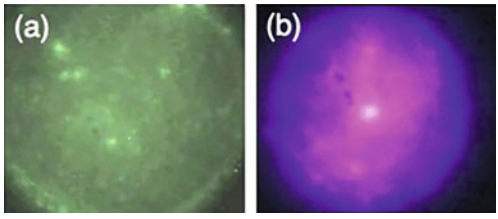


**Fig. 6.4** **a** Fluorescence and **b** UV emission images of a laser-treated ZnO particle film including polymer particles

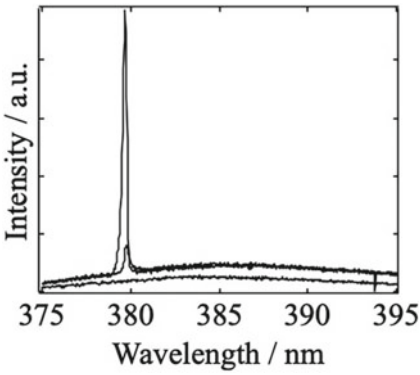


**Fig. 6.5** Emission spectra measured at a defect site in a laser-treated ZnO particle film. The excitation intensities were 0.5, 1.1, and 2.0 times of the threshold from bottom to top

region than that in the defect-free region, which suggested that laser oscillation was efficiently induced and confined around the defect region (Fig. 6.4b). The emission spectra in Fig. 6.5 show that almost a single lasing peak was observed, which clearly differs from conventional random lasers. Additionally, it was confirmed that while the peak intensity changed with a change in the excitation intensity, the wavelength remained almost unchanged and appeared on the shorter wavelength side (~380 nm) compared with the results in Fig. 6.3. Thus, the spectrum at the defect region was also significantly different from conventional random lasers.

Figure 6.6 shows the excitation intensity dependence of the lasing peak intensity at defect and defect-free regions. These results confirmed that the threshold value was 80 MW/cm$^2$ at the defect-free region, whereas the threshold value was 6 MW/cm$^2$ at the defect, which was ~10 times lower. Furthermore, it was ~8 times lower than the threshold value (50 MW/cm$^2$) of the commercially available (non-treated) ZnO nanoparticle film. Based on my previously reported numerical results [15], a reduction in the lasing threshold at the defect could be attributed to the resonant scattering of individual uniform ZnO nanoparticles that would enhance photon confinement at the defect. On the contrary, because the random structure composed of resonant

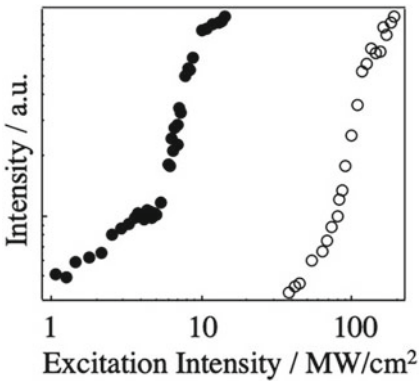


**Fig. 6.6** Excitation intensity dependence of peak intensities measured at defect (solid circles) and defect-free (open circles) regions in a laser-treated ZnO nanoparticle film

scatterers produces a stop band near the resonant wavelength (380–390 nm) of scatterers owing to strong light scattering, UV emission was less likely to exist inside the structure at the defect-free regions and the threshold value increased compared to that of a commercially available ZnO nanoparticle film that was composed of irregularly shaped poly-dispersed nanoparticles. Additionally, I repeatedly performed the same experiments in other samples composed of mono-dispersed ZnO spherical nanoparticles and confirmed the reproducibility. Approximately, half of them showed few lasing peaks and ~ 30% showed single lasing peaks.

From the abovementioned results, using the mono-dispersed spherical nanoparticles fabricated by the laser-induced melting method as scatterers, I succeeded in enhancing the feedback at a specific wavelength band and localized in the defect region. Thus, by optimizing the structure, quasi-single mode, low-threshold, and wavelength-controllable random lasers can be realized.

## 6.3 Nanorod Array Random Lasers Fabricated by Laser-Induced Hydrothermal Synthesis

In the previous section, I showed that the homogenization of nanoparticles (resonant scatterers) allows to lower thresholds and control lasing modes. However, in nanoparticle films, because the lasing region with high optical confinement efficiency exists deep inside the film, the extraction efficiency is deteriorated. Furthermore, because the film is composed of nanoparticle aggregates, it is hard to form electrodes on both sides of the film and to conduct electrical current. Therefore, although the realization of an electrically driven random laser is an important subject for light source applications, a nanoparticle aggregate film is not suitable for such applications. As one of the methods for overcoming such problems, I focused on a two-dimensional random laser that was directly fabricated on a semiconductor substrate. Recently, random lasers with a two-dimensional structure have been attracting attention; using such structure, it is possible to realize electrically driven random lasers [24–27]. However, although several approaches exist for producing two-dimensional random lasers, in which lattice disorder in photonic crystals and spontaneously formed defect pits in a semiconductor substrate were used for random feedback, lasing mode control was realized only by a top-down processing approach using expensive apparatuses [26, 27].

In contrast, I focused on two laser processing methods that can directly fabricate a random laser on a semiconductor surface: (1) laser-induced hydrothermal synthesis [28, 29] and (2) laser-induced periodic surface structure [30, 31]. In this section, I introduce a laser-induced hydrothermal synthesis of zinc oxide nanorod array random lasers and present the results of optimizing the fabrication conditions to achieve lower threshold.

This laser-induced hydrothermal synthesis is a method used for fabricating nanorod arrays (NRAs); the method has been proposed by Ko et al. [28, 29].

Conventional methods for fabricating nanorod array structures (e.g., vapor–liquid–solid (VLS) growth method and metal organic chemical vapor deposition) are well-known [32, 33]. However, because these approaches require expensive apparatuses and are time-consuming, they are not suitable compared to the methods used for making random lasers, which can be fabricated easily and at low cost. Although the hydrothermal synthesis method is relatively inexpensive, the fabrication time is typically long (i.e., from several hours to several days) and the nanorod array structure cannot be fabricated locally and selectively. On the contrary, laser-induced hydrothermal synthesis is a method that can fabricate semiconductor nanorod arrays using local heating through laser light absorption by the substrate instead of heating the entire precursor solution with a heater. Because this approach is based on the conventional hydrothermal synthesis, it can fabricate nanorod arrays at relatively low temperature and low cost. Additionally, owing to laser heating, nanorod arrays can be selectively fabricated only in the laser-irradiated area and can be easily controlled by controlling laser irradiation conditions. Furthermore, this method is applicable to various substrates that can be heated by light absorption. Ko et al. [28, 29] have synthesized nanorod arrays and proposed applications such as a structure to enhance Raman scattering of cells and an ultraviolet light detection. In this section, I introduce the results of applying this method to the fabrication of zinc oxide nanorod array random lasers and trying to lower the threshold by optimizing the laser irradiation conditions [34].

ZnO, which can be hydrothermally synthesized under mild conditions and is known as a laser gain material, was used in the experiments. To prepare zinc oxide nanorod arrays, an aqueous solution of zinc nitrate hexahydrate and hexamethylenetetramine at the same concentration was prepared and mixed in equal amounts to make a precursor solution. In the experiments, the precursor solution concentration was varied in the range of 25–150 mM to fabricate the optimal structure. To suppress the impurity emission of ZnO nanorod arrays to be synthesized, high-purity Teflon containers were used to reduce contamination that reduces UV emission. This precursor solution was deposited onto a bottom dish and covered by a cover glass coated with 50-nm-thick gold as a light absorbing substrate. This gold-coated substrate was irradiated with a CW laser with a wavelength of 405 nm from the substrate side using a planoconvex lens (irradiation spot diameter ~75 μm). ZnO nanorod array was fabricated by changing the laser irradiation intensity and time, and the obtained structure on the gold thin film was confirmed by a microscope equipped with a CCD camera. After the fabrication of the nanorod array structure, the sample was washed with ultrapure water and dried. Then, the sample was set on a microscope stage; the sample was irradiated with ultraviolet laser pulses (355 nm, 300 ps, 1 kHz) through an objective lens (NA = 0.9, 100 × , Air) to excite the ZnO nanorod array (spot size diameter ~ 70 μm). The emission from the sample was collected by the same objective lens and introduced into a spectrophotometer equipped with a high-sensitivity CCD camera to measure the emission spectrum. To confirm random laser oscillation, emission spectra were repeatedly measured by changing the excitation intensity. Moreover, to confirm the influence of fabrication

conditions on the nanorod array structure, the fabricated samples were observed by an electron microscope.

Figure 6.7a and b show the SEM images of the sample fabricated using the laser intensity of 1.25 kW/cm$^2$ (maximum intensity of my apparatus) and the precursor concentration of 25 mM, while the irradiation time was 5 and 20 min. With an increase in the irradiation time (from 5 to 20 min), the average diameter of nanorods increased from 47 to 60 nm (Fig. 6.8a) and the number density decreased from ~ 23 to 10 $\mu m^{-2}$. However, the rough estimate of the surface filling factor from the average diameter and number density indicated that although the nanorod size increased with an increase in the growth time, the surface filling factor remained approximately constant (30%). Additionally, the SEM images of ZnO nanorod arrays with different growth times confirmed that the nanorod length did not considerably change (~2 $\mu m$),

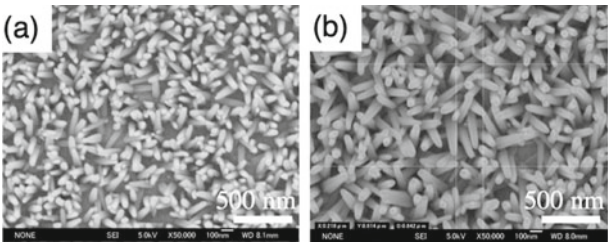


**Fig. 6.7** SEM images of fabricated ZnO NRAs with different growth times of **a** 5 and **b** 20 min. Irradiation laser intensity and precursor solution concentration were fixed at 1.25 kW cm$^2$ and 25 mM, respectively

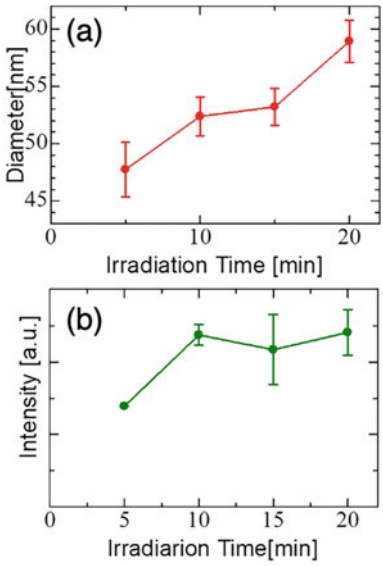


**Fig. 6.8** Growth time dependence of mean diameters and UV emission intensities of ZnO nanorods. Irradiation laser intensity and precursor solution concentration were fixed at 1.25 kW cm$^2$ and 25 mM, respectively

while the average diameter of ZnO nanorods changed. The length of nanorods was limited according to the temperature distribution because the temperature decreases as it moves away from the gold-coated substrate (heat source) [28, 29, 34]. Additionally, Fig. 6.8b shows the UV emission intensity of the samples fabricated using different laser irradiation times. The UV emission intensity increased with respect to the irradiation time up to ~10 min, but the emission intensity remained almost constant for the irradiation longer than 10 min. I considered that this result was also attributed to the temperature distribution from a gold-coated substrate. As the nanorod growth progressed and the apex of the nanorods moved away from the gold substrate, the nanorods with good crystallinity could not be formed owing to temperature decrease; ultraviolet emission became constant and visible emission increased. From the emission spectrum of the sample fabricated using the laser irradiation time of 10 min, UV emission peculiar to ZnO was much stronger than visible emission. In the previous studies using conventional hydrothermal synthesis, the UV emission was typically weak owing to the influence of impurities and lower quality of their crystal structures; in most cases, the UV emission was recovered by annealing treatment. However, I confirmed strong UV emission from a ZnO nanorod array grown without post-annealing by suppressing impurities during the preparation of precursor solution and adjusting laser irradiation intensity. These results showed that the laser irradiation time longer than 10 min was necessary to improve emission characteristics; in the experiments described below, the irradiation time was fixed at 10 min.

Figure 6.9 shows the plots of nanorod diameters and UV emission intensities versus irradiation intensity when the precursor concentration and time were fixed at 25 mM and 10 min. With an increase in the irradiation intensity to ~0.8 kW/cm$^2$, the

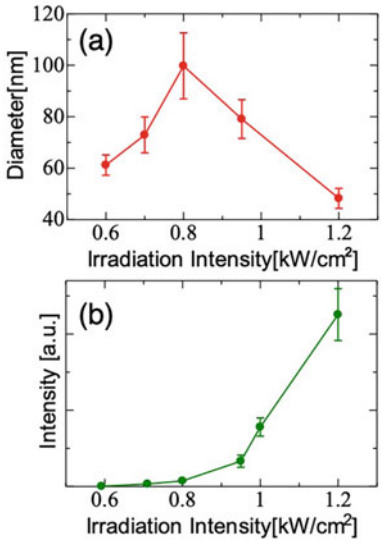


**Fig. 6.9** Irradiation intensity dependence of mean diameters and UV emission intensities of ZnO nanorods. Growth time and precursor solution concentration were fixed at 10 min and 25 mM, respectively

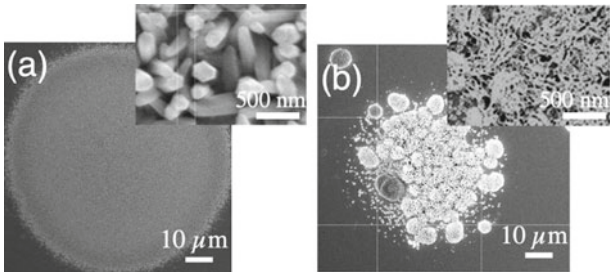


**Fig. 6.10** SEM images of fabricated ZnO NRAs with different irradiation intensities (**a** 1.25 and **b** 0.4 kW $cm^2$). Growth time and precursor solution concentration were fixed at 10 min and 25 mM, respectively. Insets show the enlarged views of each image

rod diameter increased but decreased for the irradiation intensity above 0.8 kW/$cm^2$. This behavior has been also reported in [35], where the hydrothermal growth of ZnO nanorods was performed using a heater. The authors reported that nanorod size decreased at certain temperature and then increased with an increase in temperature. At this temperature, the authors indicated that high quality nanorods started to grow. The SEM images in Fig. 6.10 show that only the rod shape was confirmed when the irradiation laser intensity was stronger than 0.8 kW/$cm^2$ (Fig. 6.10a), while at lower irradiation intensities (<0.8 kW/$cm^2$), structures other than nanorods were formed. Especially, at the intensity of 0.4 kW/$cm^2$, the structures were completely different from the nanorod array structure (Fig. 6.10b). Furthermore, from the results of the UV emission intensity, the UV emission intensity increases when the irradiation laser intensity is stronger than 0.8 kW/$cm^2$. From these results, it is considered that when the irradiation light intensity was smaller than 0.8 kW/$cm^2$, the induced heat was not sufficient to increase the temperature and to synthesize high quality ZnO nanorods. Therefore, to fabricate a sample with high UV emission intensity, the irradiation laser intensity must be sufficiently high. Because the maximum intensity of my apparatus was 1.25 kW/$cm^2$, the irradiation laser intensity was set to 1.25 kW/$cm^2$ in the experiments.

Finally, based on the abovementioned results, when the irradiation intensity and time were fixed at 1.25 kW/$cm^2$ and 10 min, respectively, the dependence of the precursor solution concentrations was examined. Figure 6.11 shows the precursor concentration dependence of UV intensity and nanorod diameter. Figure 6.11a shows that because the synthesis rate increases with an increase in concentration, the rod diameter tends to sharply increase compared to the cases with change in the laser irradiation time and intensity. However, at concentrations higher than 120 mM, deposits with irregular shapes were formed on the nanorods (Fig. 6.12). As mentioned above, this phenomenon occurs because the temperature decreases far from the surface of the heated gold thin film. If the nanorods rapidly grow to a certain length within the irradiation time, the temperature becomes insufficient at the apex of nanorods and irregularly shaped products other than ZnO nanorods will be synthesized. The UV emission intensity was highest at 75 mM and when the concentration became higher

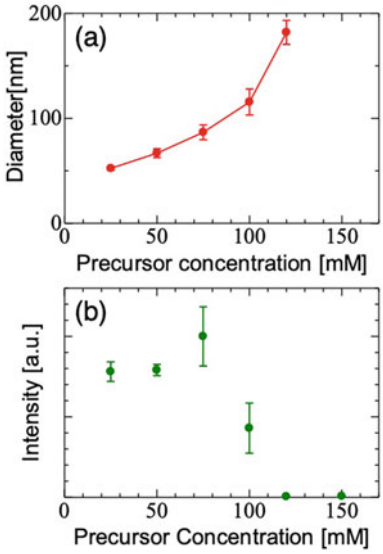


**Fig. 6.11** Precursor concentration dependence of mean diameters and UV emission intensities of ZnO nanorods. Irradiation laser intensity and growth time were fixed at 1.25 kW cm$^2$ and 10 min, respectively

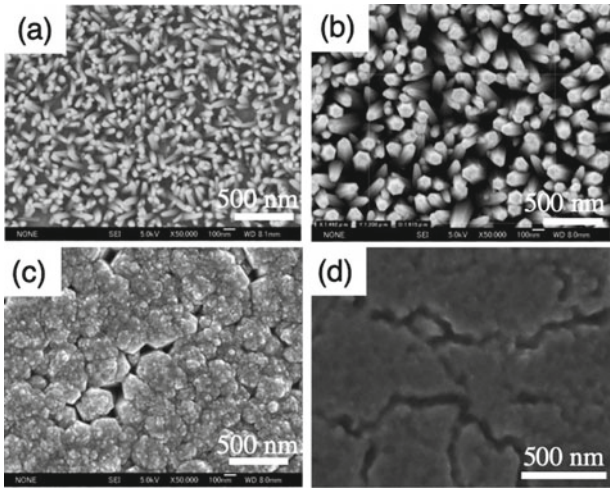


**Fig. 6.12** SEM images of fabricated ZnO NRAs with different precursor concentrations (**a** 25, **b** 100, **c** 125, and **d** 150 mM). Irradiation intensity and growth time were fixed at 1.25 kW cm$^2$ and 10 min, respectively

than 120 mM and no UV emission and an increase in visible emission owing to structural defects and impurities was confirmed (Fig. 6.11b). These results suggest that ZnO growth in the high-concentration solution within the irradiation time was too rapid to fabricate the structure with good crystallinity.

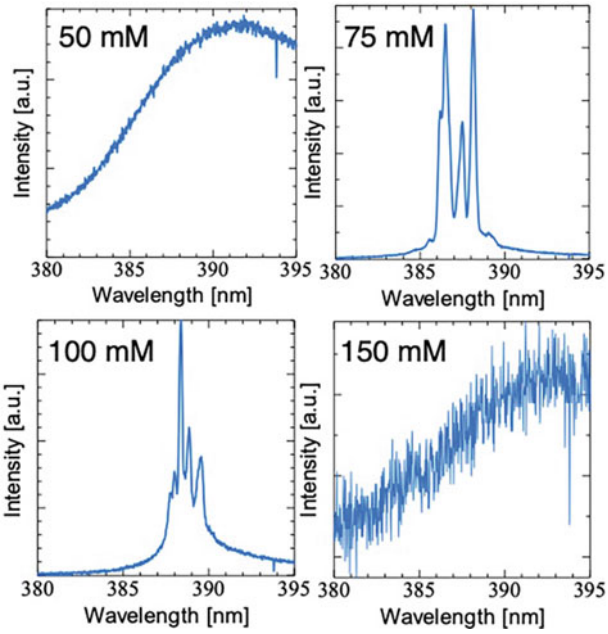


**Fig. 6.13** Emission spectra of ZnO NRAs fabricated using different precursor concentrations when irradiation intensity and growth time were fixed at 1.25 kW $cm^2$ and 10 min, respectively

Based on the abovementioned results, I examined random laser oscillations of the nanorod array structures fabricated at each concentration. Because the precursor solution concentration at ~75–100 mM maximizes UV emission and the obtained nanorod size matches the expected size for the resonance of ZnO emission wavelength (~100 nm), it is expected that random lasers can be induced at this concentration. Figure 6.13 shows the emission spectra of the nanorod arrays, which were fabricated using different precursor concentrations and excited by the constant excitation intensity (the laser irradiation intensity and time were fixed at 1.25 kW/$cm^2$ and 10 min, respectively). In the spectra, multi-mode discrete sharp peaks peculiar to random lasers was observed only when the precursor concentrations were 75 and 100 mM while only broad and weak emission was observed for the concentration of 50 and 150 mM. Additionally, by measuring the dependence of emission peak intensity on the excitation intensity (Fig. 6.14), I confirmed that the emission peak intensity rapidly increased from the excitation intensity of several tens MW/$cm^2$ (~45 MW/$cm^2$ for 75 mM and ~60 MW/$cm^2$ for 100 mM) which indicated that laser oscillation was induced. This threshold has almost the same order of magnitude compared to the threshold values for a commercially available ZnO nanoparticle aggregate film. This means that considering that the height of nanorod arrays is only few μm, and the structure is an open system in the vertical direction, I can say that the observed threshold value is sufficiently low, and the obtained nanorod arrays can efficiently confine light in the plane direction to induce laser oscillation by

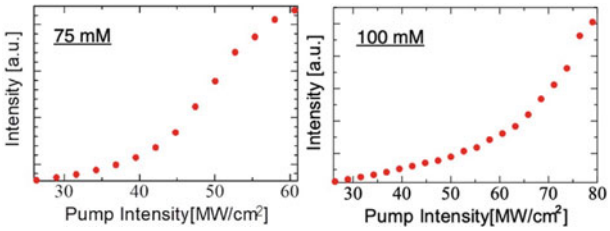


**Fig. 6.14** Excitation intensity dependence of UV peak intensities from ZnO NRAs fabricated using different precursor concentrations of 75 and 100 mM

controlling the fabrication conditions. Additionally, when similar experiments were repeatedly performed and the probability of inducing laser oscillations was estimated, I succeeded in improving the probabilities, which were ~70% and 45% for 75 and 100 mM concentrations, respectively, by optimizing the fabrication conditions.

## 6.4 Random Lasers Fabricated by a Laser-Induced Periodic Surface Structures

In the previous section, the laser-induced hydrothermal synthesis method was introduced as a novel fabrication technique for low-threshold random lasers with nanorod array structures aiming at the realization of an electrically driven random laser. However, although this method can be applied to nanorod array structures that can be fabricated under mild conditions (e.g., zinc oxide and titanium oxide, which do not require pressurization and can be hydrothermally synthesized at less than 100 °C), other emissive semiconductors cannot be readily synthesized under such mild conditions, and materials that this method is applicable to are limited. The number of semiconductor types that can be synthesized increases using conventional solvothermal synthesis; however, many of them require high temperature, high pressure, and an organic solvent and are not suitable for random lasers that can be fabricated easily and inexpensively.

In this section, instead of the laser-induced hydrothermal synthesis [30, 31], I focused on the laser-induced surface periodic structure fabrication method as the second method to fabricate a random structure directly on a semiconductor substrate. In this laser-induced surface periodic structure fabrication method, when an intense linearly-polarized pulsed laser is focused and irradiated on the substrate surface for a few seconds, a quasi-periodic surface structure is fabricated in the direction orthogonal to the polarization direction. Regarding this mechanism, it has been reported that when the surface is ablated by the laser irradiation and turned into plasma, the interference fringe is formed by the plasmon excitation by laser irradiation and a quasi-periodic surface structure is created in the direction perpendicular to the polarized light [30, 31, 36]. Thus, because a pseudo-periodic structure is formed by

the interference, there is an advantage that shapes (e.g., period, pitch, and groove depth) can be controlled by controlling the irradiation laser conditions such as irradiation intensity, time, wavelength, and focusing angle. Additionally, because a quasi-periodic structure has been confirmed not only for metals and semiconductors but also with various materials such as polymers and glasses (as long as substrate can be ablated by laser pulses), it is expected that this method will be highly versatile for the fabrication of various types of random lasers. Although many studies have already been conducted on laser-induced periodic surface structures, most of them have been focused on the elucidation of structure formation mechanism or applied to passive devices such as structural coloring and diffraction grating elements [37–39].

In this study, I focused on the advantages that a random laser can be directly fabricated on the surface of a semiconductor substrate only by irradiating intense pulsed laser without the need for costly and time-consuming equipment and chemical treatment. Using this method, I aimed to establish a new random laser fabrication method directly on a semiconductor substrate toward the realization of electrical-driven random lasers [40]. The obtained knowledge will also be applicable to the fields such as photocatalysts, photovoltaic devices, sensors, and light emitting devices. From the experimental results, by establishing the structural control technique by laser irradiation, I will provide an important step toward the realization of electrically driven low-threshold semiconductor random laser sources.

In the experiments, gallium nitride (GaN, 4 μm thickness) grown on a sapphire substrate was used because GaN is a semiconductor material that is well-known as a laser medium [41–43]. This substrate was set on a microscope stage, and a linearly-polarized pulsed laser (300 ps, 1 kHz) with a wavelength of 355 nm was irradiated through an objective lens (40 × (NA 0.75) or 10 × (NA 0.5)) (spot diameter 50 μm). A quasi-periodic structure on the substrate surface was fabricated by adjusting the irradiation intensity and time. After the fabrication, the same pulsed laser was weakened by ~10 times or lower and the emission spectra were measured. To discuss the surface morphology, the SEM images of the surface were measured. Additionally, to show the effectiveness of this method using different materials, the same experiment was conducted on a GaAs substrate used as a laser medium in the near-infrared region.

Figure 6.15a shows the SEM image of structures fabricated using the irradiation intensity of ~500 MW/cm$^2$ with the irradiation time fixed at 10 s. There were fine structures on the surface (quasi-periodic structures). Because the direction of the period was perpendicular to the polarization direction, it is considered that the structure was fabricated via the same mechanism as the previously reported laser-induced surface periodic structures [30, 31, 36–39]. The observed periodicity was more disturbed than previously reported structures, which would be attributed to the use of a sub-nanosecond pulsed laser in my experiments, while femtosecond pulsed lasers were mainly used in the previous reports. It is considered that a clear periodicity could not be confirmed owing to the influence of heat generation when the pulse duration time becomes longer, which may destroy the structure. Furthermore, when the laser irradiation intensity decreased (< ~ 300 MW/cm$^2$), any structure on the surface was not observed, and the broad spectrum was the same as that of the

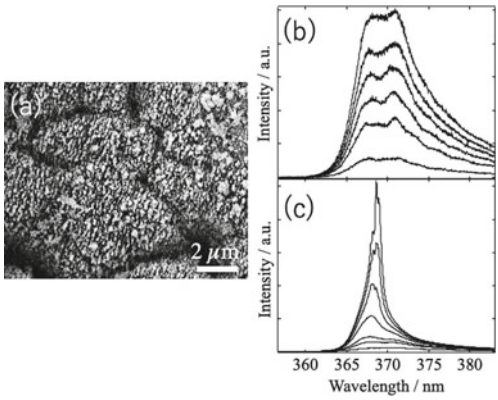


**Fig. 6.15** **a** SEM image of a roughened GaN surface after irradiating linearly-polarized UV pulses. Emission spectra of GaN substrate **b** before and **c** after the irradiation of linearly-polarized UV pulses. The excitation intensities in **b** and **c** were increased from bottom to top

flat substrate (Fig. 6.15b). However, when the irradiation intensity and time reached certain values (~600 MW/cm$^2$, 10 s), a strong emission peak could be observed in the structure (Fig. 6.15c). When the irradiation intensity increased further, a GaN layer was ablated and removed, which resulted in the reduction of emission intensity. The obtained results show that at moderate irradiation intensity, a clear quasi-periodic structure can be fabricated on the surface, and strong emission peak can be confirmed. It is necessary to optimize the laser irradiation intensity and time to form optimum quasi-periodic structures for random lasers.

Figure 6.16a shows the excitation laser intensity dependence of the emission spectra of the sample fabricated using the irradiation intensity of 0.8 GW/cm$^2$ and irradiation time of 10 s, in which a quasi-periodic structure was fabricated on the surface. When the excitation intensity was close to 70 MW/cm$^2$, the spectral intensity at the wavelength of ~ 368 nm sharply increased and was accompanied by spectral narrowing and discrete peaks. Additionally, when the dependence of the emission intensity on the excitation laser intensity was plotted (solid circles in Fig. 6.16b), a

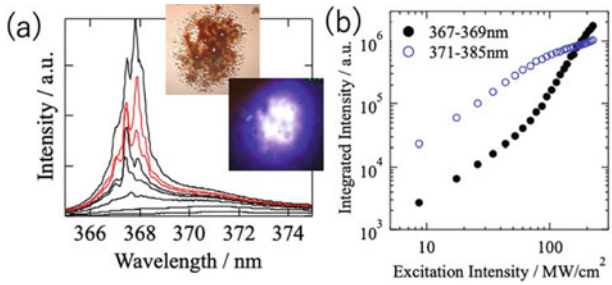


**Fig. 6.16** **a** Emission spectra from a roughened GaN substrate and **b** excitation intensity dependences of integrated emission intensities. Solid circles: wavelengths from 366 to 369 nm, open circles: wavelengths from 371 to 385 nm. The excitation intensity in **a** was increased from bottom to top. The insets in **a** show the microscope image of the roughened GaN surface and its emission image

clear threshold behavior was confirmed, which indicated that random laser oscillation was induced by surface roughness. However, of note, in the place without a periodic structure, laser oscillation could not be confirmed (open circles in Fig. 6.16b). Based on these results, it is concluded that owing to the effect of the quasi-periodic structure, random feedback was formed, and laser oscillation could be induced. Thus, it is expected that a low-threshold random laser can be realized when a high-contrast surface structure is fabricated by adjusting the fabrication conditions.

To realize low-threshold random lasers, I repeatedly performed the same experiments under different conditions and the dependence of their thresholds on the fabrication laser intensity and irradiation time was confirmed (Fig. 6.17). I found that when the irradiation time was changed to 0.1, 1, 10, and 100 s, the fabrication intensity that achieved the minimum threshold value at each irradiation time also changed. The shaded region in the figures indicates the area where a quasi-periodic structure was not formed at lower irradiation intensity and where the sample was destroyed at higher irradiation intensity. Under both conditions, laser oscillation was not confirmed. The obtained results confirmed that there was an appropriate irradiation time and intensity for the fabrication of low-threshold random lasers, and the minimum threshold value (~60 MW/cm$^2$) was realized when the structure was fabricated using the irradiation intensity of ~0.8 GW/cm$^2$ (~8 mW) for 10 s.

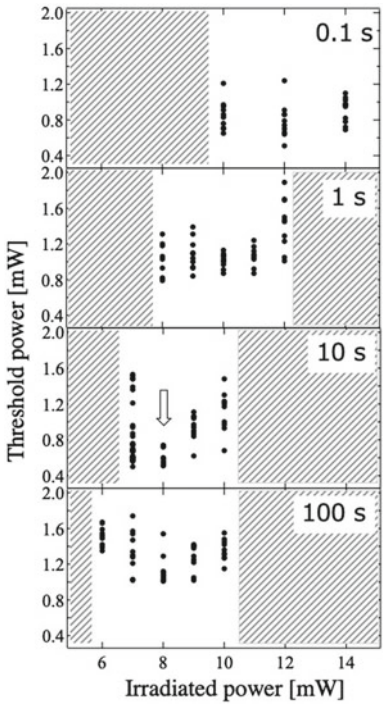


**Fig. 6.17** Thresholds versus irradiation intensities for different irradiation times. Shaded areas: lasing behavior was not observed. White arrow indicates the optimal fabrication condition where minimum thresholds were observed

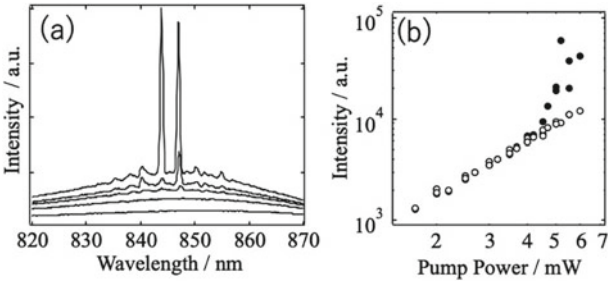


**Fig. 6.18** **a** Emission spectra from a roughened GaAs substrate and **b** excitation intensity dependences of emission intensities. Solid and open circles indicate the intensity at the wavelengths of 847 and 855 nm. The excitation intensity in **a** was increased from bottom to top

To confirm the versatility of this method, I applied this method to other semiconductor materials and tried to realize a random laser in different wavelength regions. A commercially available undoped gallium arsenide (GaAs) substrate, which is known as a laser material operating in the near-infrared region [44, 45], was selected. Although I first tried using a UV pulsed laser, any high-contrast quasi-periodic structure was not observed. This occurs because the gap energy of GaAs is smaller than that of GaN; thus, the excess of absorbed UV energy generates heat and periodic structures melt. Therefore, the fabrication laser was changed from UV to 532 nm pulsed laser (532 nm, 700 ps, 5 kHz), whose wavelength was closer to the band-gap energy and conducted similar experiments. As a result, I successfully observed the quasi-periodic structures and their random lasing behaviors, although the fabrication conditions were not optimized (Fig. 6.18). The figure shows clear discrete peaks at ~840 nm, as well as the threshold behavior (~35 MW/cm$^2$ (~4 mW)). This result suggested the versatility of this method, which is applicable to various types of semiconductor materials. Further, using a laser with wavelength that matches the band-gap energy and with shorter pulse duration time, I believe that heat generation can be sufficiently suppressed and a high-contrast quasi-periodic structure can be formed, which allows to realize low-threshold random lasers that are directly fabricated on a semiconductor surface.

## 6.5 Conclusions

In this chapter, I introduced three laser processes for fabricating random lasers with low thresholds. In Sect. 2, using resonant nanoparticles fabricated by the laser melting method, I experimentally verified that the random feedback at specific wavelength band could be enhanced based on resonant scattering of individual nanoparticles. Thus, by optimizing laser irradiation conditions to fabricate scatterers with optimal size, I achieved a resonance-driven, low-threshold, and quasi-single mode random laser, which had never been reported. In Sect. 3, I showed that a low-threshold nanorod

array random laser can be synthesized on a gold thin film using the laser-induced hydrothermal synthesis method. Because this method is based on the irradiation laser absorption by a substrate, nanorod arrays can be selectively synthesized within the laser irradiation spot in a short period of time. I experimentally investigated the effect on the rod diameter and UV emission characteristics when the fabrication conditions (e.g., laser irradiation time, intensity, and precursor solution concentration) were changed. The rod diameter and UV emission characteristics were improved by optimizing the fabrication conditions which allowed realizing a low-threshold nanorod array random laser. In Sect. 4, because the laser-induced surface quasi-periodic structure fabrication method is a surface structure fabrication method that utilizes ablation by a pulsed laser irradiation of the substrate, it is possible to easily obtain optimal quasi-periodic structures to realize low-threshold random lasers by controlling the laser irradiation conditions. Additionally, this method is applicable to various semiconductor substrates using lasers that match the absorption characteristics of the substrates. In this section, I showed the successful fabrication of low-threshold UV and near-infrared random lasers on GaN and GaAs substrates, respectively.

All of the abovementioned methods are processing/synthesis methods that use lasers and have the advantage of being applicable to any materials as long as the material has optical absorption. Furthermore, owing to the use of a laser, the fabrication conditions can be easily controlled in a noncontact and highly accurate manner; therefore, it is possible to fabricate structures that are optimal for laser oscillation without them being affected by the environmental conditions such as in liquid, vacuum, or gas phases. Therefore, by combining with existing semiconductor processes, I expect that this work can pave the way for the development of new practical applications that are based on random structures such as photosensors, photoelectric conversion elements, and electrical-driven random laser sources.

**Acknowledgements** The author thank Prof. T. Tsuji, Prof. N. Koshizaki, Prof. Y. Ishikawa, Prof. T. Nakamura, and Prof. K. Sasaki for their helpful discussions and sample preparations. The authors also thank Dr. R. Niyuki, Mr. T. Suzuki, Mr. T. Shintaku, Dr. J. Kuitunen, Mr. S. Kawaguchi, and Mr. D. Yonekawa for their experimental assistances. This work was partially supported by JSPS KAKENHI (Grant Numbers JP19H04529, JP20K05290, JP21H04657), NIFS Collaboration Research Program (NIFS20KBAH029), the Cooperative Research Program of "Network Joint Research Center for Materials and Devices" (20201005, 20211002), Amada Foundation (AF-2021226-B3) and Nippon Sheet Glass Foundation for Materials Science and Engineering. SEM images were measured using a field emission scanning electron microscope system (JEOL, JSM-6700FT) at the Open Facility, Hokkaido University Sousei Hall.

## References

1. N.M. Lawandy, R.M. Balachandran, A.S.L. Gomes, E. Sauvain, Laser action in strongly scattering media. Nature **368**, 436–438 (1994). https://doi.org/10.1038/368436a0
2. H. Cao, Lasing in random media. Wave Random Media **13**, R1–R39 (2003). https://doi.org/10.1088/0959-7174/13/3/201

3. H. Cao, Y.G. Zhao, S.T. Ho, E.W. Seelig, Q.H. Wang, R.P.H. Chang, Random laser action in semiconductor powder. Phys. Rev. Lett. **82**, 2278–2281 (1999). https://doi.org/10.1103/PhysRevLett.82.2278
4. D.S. Wiersma, The physics and applications of random lasers. Nat. Phys. **4**, 359–367 (2008). https://doi.org/10.1038/nphys971
5. D.S. Wiersma, Disordered photonics. Nat. Photon. **7**, 188–196 (2013). https://doi.org/10.1038/nphoton.2013.29
6. M.A. Noginov, *Solid-State Random Lasers* (Springer, New York, 2005)
7. G. van Soest, F.J. Poelwijk, R. Sprik, A. Lagendijk, Dynamics of a random laser above threshold. Phys. Rev. Lett. **86**, 1522–1525 (2001). https://doi.org/10.1103/PhysRevLett.86.1522
8. B. Redding, M.A. Choma, H. Cao, Speckle-free laser imaging using random laser illumination. Nat. Photon. **6**, 355–359 (2012). https://doi.org/10.1038/nphoton.2012.90
9. M.A. Noginov, G. Zhu, I. Fowlkes, M. Bahoura, GaAs random laser. Laser Phys. Lett. **1**, 291–293 (2004). https://doi.org/10.1002/lapl.200410068
10. D.V. Martyshkin, V.V. Fedorov, C. Kim, I.S. Moskalev, S.B. Mirov, Mid-IR random lasing of Cr-doped ZnS nanocrystals. J. Opt. **12**, 024005 (2010). https://doi.org/10.1088/2040-8978/12/2/024005
11. T. Takahashi, T. Nakamura, S. Adachi, Blue-light-emitting ZnSe random laser. Opt. Lett. **34**, 3923–3925 (2009). https://doi.org/10.1364/OL.34.003923
12. C. Rockstuhl, F. Lederer, Suppression of the local density of states in a medium made of randomly arranged dielectric spheres. Phys. Rev. B **79**, 132202 (2009). https://doi.org/10.1103/PhysRevB.79.132202
13. P.D. García, R. Sapienza, C. López, Photonic glasses: a step beyond white paint. Adv. Mater. **22**, 12–19 (2010). https://doi.org/10.1002/adma.200900827
14. S. Gottardo, R. Sapienza, P.D. García, A. Blanco, D.S. Wiersma, C. López, Resonance-driven random lasing. Nat. Photon. **2**, 429–432 (2008). https://doi.org/10.1038/nphoton.2008.102
15. H. Fujiwara, Y. Hamabata, K. Sasaki, Numerical analysis of resonant and lasing properties at a defect region within a random structure. Opt. Express **17**, 3970–3977 (2009). https://doi.org/10.1364/OE.17.003970
16. H. Fujiwara, R. Niyuki, Y. Ishikawa, N. Koshizaki, T. Tsuji, K. Sasaki, Low-threshold and quasi-single-mode random laser within a submicrometer-sized ZnO spherical particle film. Appl. Phys. Lett. **102**, 061110 (2013). https://doi.org/10.1063/1.4792349
17. T. Nakamura, H. Fujiwara, R. Niyuki, K. Sasaki, Y. Ishikawa, N. Koshizaki, T. Tsuji, S. Adachi, Origins of lasing emission in resonance-controlled ZnO random laser. New J. Phys. **16**, 093054 (2014). https://doi.org/10.1088/1367-2630/16/9/093054
18. R. Niyuki, H. Fujiwara, Y. Ishikawa, N. Koshizaki, T. Tsuji, K. Sasaki, Toward single-mode random lasing within a submicrometre-sized spherical ZnO particle film. J. Opt. 18, 035202 (2016). https://doi.org/10.1088/2040-8978/18/3/035202
19. R. Niyuki, H. Fujiwara, T. Nakamura, Y. Ishikawa, N. Koshizaki, T. Tsuji, K. Sasaki, Double threshold behavior from a resonance-controlled ZnO random laser. APL Photonics **2**, 036101 (2017). https://doi.org/10.1063/1.4974334
20. Y. Ishikawa, Q. Feng, N. Koshizaki, Growth fusion of submicron spherical boron carbide particles by repetitive pulsed laser irradiation in liquid media. Appl. Phys. A **99**, 797–803 (2010). https://doi.org/10.1007/s00339-010-5745-6
21. H.Q. Wang, N. Koshizaki, L. Li, L.C. Jia, K. Kawaguchi, X.Y. Li, A. Pyatenko, Z. Swiatkowska-Warkocka, Y. Bando, D. Golberg, Size-tailored ZnO submicrometer spheres: bottom-up construction, size-related optical extinction, and selective aniline trapping. Adv. Mater. **23**, 1865–1870 (2011). https://doi.org/10.1002/adma.201100078
22. T. Tsuji, S. Sakaki, H. Fujiwara, H. Kikuchi, M. Tsuji, Y. Ishikawa, N. Koshizaki, Stabilizer-concentration effects on the size of gold submicrometer-sized spherical particles prepared using laser-induced agglomeration and melting of colloidal nanoparticles. J. Phys. Chem. C **122**, 21659–21666 (2018). https://doi.org/10.1021/acs.jpcc.8b05911
23. T. Tsuji, Y. Higashi, M. Tsuji, H. Fujiwara, Y. Ishikawa, N. Koshizaki, Fabrication of spherical-shaped submicron particles of ZnO using laser-induced melting of submicron-sized source

materials. J. Laser Micro Nanoen. **8**, 292–295 (2013). https://doi.org/10.2961/jlmn.2013.03.0017
24. F. Gao, M.M. Morshed, S.B. Bashar, Y. Zheng, Y. Shi, J. Liu, Electrically pumped random lasing based on an Au–ZnO nanowire Schottky junction. Nanoscale **7**, 9505–9509 (2015). https://doi.org/10.1039/C5NR01349F
25. H. Zhu, A. Chen, Y. Wu, X. Ji, Y. He, Z. Qiu, Z. Tang, S. Yu, Low-threshold GaN thin-film random laser through the weak scattering feedback. J. Phys. D **50**, 045107 (2017). https://doi.org/10.1088/1361-6463/aa4f66
26. M. Lee, S. Callard, C. Seassal, H. Jeon, Taming of random lasers. Nat. Photon. **13**, 445–448 (2019). https://doi.org/10.1038/s41566-019-0407-5
27. H. Noh, J.-K. Yang, S. F. Liew, M. J. Rooks, G. S. Solomon, H. Cao, Control of lasing in biomimetic structures with short-range order. Phys. Rev. Lett. **106**, 183901 (2011). https://doi.org/10.1103/PhysRevLett.106.183901
28. J. Yeo, S. Hong, M. Wanit, H.W. Kang, D. Lee, C.P. Grigoropoulos, H.J. Sung, S.H. Ko, Rapid, one-step, digital selective growth of ZnO nanowires on 3D structures using laser induced hydrothermal growth. Adv. Funct. Mater. **23**, 3316–3323 (2013). https://doi.org/10.1002/adfm.201203863
29. S. Hong, H. Lee, J. Yeo, S.H. Ko, Digital selective laser methods for nanomaterials: from synthesis to processing. Nano Today **11**, 547–564 (2016). https://doi.org/10.1016/j.nantod.2016.08.007
30. P.M. Fauchet, A.E. Siegman, Surface ripples on silicon and gallium arsenide under picosecond laser illumination. Appl. Phys. Lett. **40**, 824–826 (1982). https://doi.org/10.1063/1.93274
31. L. Wang, B.-B. Xu, X.-W. Cao, Q.-K. Li, W.-J. Tian, Q.-D. Chen, S. Juodkazis, H.-B. Sun, Competition between subwavelength and deep-subwavelength structures ablated by ultrashort laser pulses. Optica **4**, 637–642 (2017). https://doi.org/10.1364/OPTICA.4.000637
32. M.H. Huang, S. Mao, H. Feick, H. Yan, Y. Wu, H. Kind, E. Weber, R. Russo, P. Yang, Room-temperature ultraviolet nanowire nanolasers. Science **292**, 1897–1899 (2001). https://doi.org/
33. J.-J. Wu, S.-C. Liu, Low-temperature growth of well-aligned ZnO Nanorods by chemical vapor deposition. Adv. Mater. **14**, 215–218 (2002). https://doi.org/
34. H. Fujiwara, T. Suzuki, R. Niyuki, K. Sasaki, ZnO nanorod array random lasers fabricated by a laser-induced hydrothermal growth. New J. Phys. **18**, 103046 (2016). https://doi.org/10.1088/1367-2630/18/10/103046
35. M. Guo, P. Diao, X. Wang, S. Cai, The effect of hydrothermal growth temperature on preparation and photoelectrochemical performance of ZnO nanorod array films. J. Solid State Chem. **178**, 3210–3215 (2005). https://doi.org/10.1016/j.jssc.2005.07.013
36. J. Bonse, S. Höhm, S.V. Kirner, A. Rosenfeld, J. Krüger, Laser-induced periodic surface structures—a scientific evergreen. IEEE J. Sel. Top. Quantum Electron. **23**, 9000615 (2017). https://doi.org/10.1109/JSTQE.2016.2614183
37. L. Xu, J. Zhang, H. Zhao, H. Sun, C. Xu, Enhanced photoluminescence intensity by modifying the surface nanostructure of $Nd^{3+}$-doped (Pb, La)(Zr, Ti)$O_3$ ceramics. Opt. Lett. **42**, 3303–3306 (2017). https://doi.org/10.1364/OL.42.003303
38. X. Wang, C. Li, C. Ma, J. Feng, W. Hong, Z. Zhang, Formation of laser induced periodic structures on stainless steel using multi-burst picosecond pulses. Opt. Express **26**, 6325–6330 (2018). https://doi.org/10.1364/OE.26.006325
39. Y. Fuentes-Edfuf, J.A. Sańchez-Gil, C. Florian, V. Giannini, J. Solis, J. Siegel, Surface plasmon polaritons on rough metal surfaces: role in the formation of laser-induced periodic surface structures. ACS Omega **4**, 6939–6946 (2019). https://doi.org/10.1021/acsomega.9b00546
40. H. Fujiwara, K. Sasaki, Amplified spontaneous emission from a surface-modified GaN film fabricated under pulsed intense UV laser irradiation. Appl. Phys. Lett. **113**, 171606 (2018). https://doi.org/10.1063/1.5040551
41. H.W. Choi, K.N. Hui, P.T. Lai, P. Chen, X.H. Zhang, S. Tripathy, J.H. Teng, S.J. Chua, Lasing in GaN microdisks pivoted on Si. Appl. Phys. Lett. **89**, 211101 (2006). https://doi.org/10.1063/1.2392673

42. A. Das, J. Heo, M. Jankowski, W. Guo, L. Zhang, H. Deng, P. Bhattacharya, Room temperature ultralow threshold GaN nanowire polariton laser. Phys. Rev. Lett. **107**, 066405 (2011). https://doi.org/10.1103/PhysRevLett.107.066405
43. C. Cachoncinlle, E. Millon, A. Petit, High-resolution emission spectroscopy of random lasing in GaN films pumped by UV-pulsed laser. Opt. Commun. **368**, 49–53 (2016). https://doi.org/10.1016/j.optcom.2016.01.085
44. G. Zhu, C.E. Small, M.A. Noginov, Single- and two-photon excitation of a GaAs random laser. Opt. Lett. **33**, 920–922 (2008). https://doi.org/10.1364/OL.33.000920
45. T. Nakamura, T. Takahashi, S. Adachi, Temperature dependence of GaAs random laser characteristics. Phys. Rev. Lett. **81**, 125324 (2010). https://doi.org/10.1103/PhysRevB.81.125324

# Chapter 7
# Formation Mechanism of Spherical Submicrometer Particles by Pulsed Laser Melting in Liquid


**Naoto Koshizaki and Yoshie Ishikawa**

**Abstract** Pulsed laser melting in liquid (PLML) has been developed to fabricate crystalline spherical submicrometer particles by irradiating lasers onto raw particles dispersed in a liquid. This technique is based on photothermal processing of particles dispersed in a liquid and is similar to the reshaping of noble metals nanoparticles such as Au and Ag. However, this phenomenon can be extended beyond Au and Ag using appropriate laser fluences to reshape or melt agglomerated or aggregated particles from raw particles of various materials (semiconductors, oxides, carbides, etc.) to form large submicrometer particles. The produced particles have a submicrometer size range due to the heating efficiency of raw particles caused by laser irradiation. The formation of spherical particles is controlled by rapid heating above melting points, and the instantaneously formed vapor layers (thermally induced nanobubbles) play a significant role in inducing rapid temperature increase. This chapter discusses how thermally induced nanobubbles enhance the rapid temperature increase as well as the maximum attained temperature. A novel technique for monitoring the formation of thermally induced nanobubbles and the effect of transiently formed chemical species for particle reaction are also discussed.

**Keywords** Pulsed laser melting in liquid · Submicrometers · Spherical particles · Thermally induced nanobubbles · Rapid vaporization · High-temperature reaction · Heat dissipation barrier

## 7.1 Pulsed Laser Melting in Liquid

Pulsed laser ablation in liquid (PLAL) has been intensively investigated owing to its simple process, contamination-free nanoparticle production, and highly energetic

N. Koshizaki (✉)
Graduate School of Engineering, Hokkaido University, Kita 13 Nishi 8, Kita-ku, Sapporo 060-8623, Japan
e-mail: koshizaki.naoto@eng.hokudai.ac.jp

Y. Ishikawa
Research Institute for Advanced Electronics and Photonics, National Institute of Advanced Industrial Science and Technology (AIST), Tsukuba 305-8565, Japan



Y. Ishikawa et al. (eds.), *High-Energy Chemistry and Processing in Liquids*,
https://doi.org/10.1007/978-981-16-7798-4_7

particle fabrication process [1, 2]. Therefore, some chapters in this book deal with PLAL as high-energy processing in liquids involving chemistry from various aspects. Pulsed laser melting in liquid (PLML), the main subject in this and the subsequent chapters, is also a laser process for particle fabrication and appears to be controlled by a similar process. However, the mechanism, processing conditions, and products are different from those of PLAL. This chapter discusses how high-energy chemistry and processing are involved in PLML, particularly in comparison with the PLAL process.

PLML is a technique for fabricating spherical submicrometer particles by irradiating pulsed (generally nanoseconds) laser onto liquid dispersing raw nanoparticles [3–7]. Figure 7.1 presents a schematic illustration of the PLML process. The target is typically nanoparticles with low heat capacity, enabling absorbed laser energy to be used by raw particles to rapidly elevate the particle temperature without heat dissipation. When the temperature exceeds the melting point of materials, particles melt to form molten droplets and quench to form spherical particles.

The main products of PLML are submicrometer spherical particles, demonstrating a size increase caused by laser irradiation. This is completely different from the PLAL process, which is obtained by fragmenting bulk materials or larger particles. The increase in particle size is caused by the fact that the particles dispersed in a liquid are generally aggregated or agglomerated in liquid. Aggregated particles in the liquid are melted by laser irradiation and merge to form larger particles. However, the particles will not grow further to a micrometer scale or larger, which will be discussed later.

Another important feature of PLML is the laser fluence range of the process. A typical PLAL process uses several J $cm^{-2}$ $pulse^{-1}$ to several tens of J $cm^{-2}$ $pulse^{-1}$, which is larger by one or two orders of magnitude than that of PLML (several tens to hundreds of mJ $cm^{-2}$ $pulse^{-1}$). Thus, plasma is generated during the PLAL process whereas PLML is a thermal process. Therefore, the main chemical processes in PLML are based on high-temperature thermodynamic processes, which

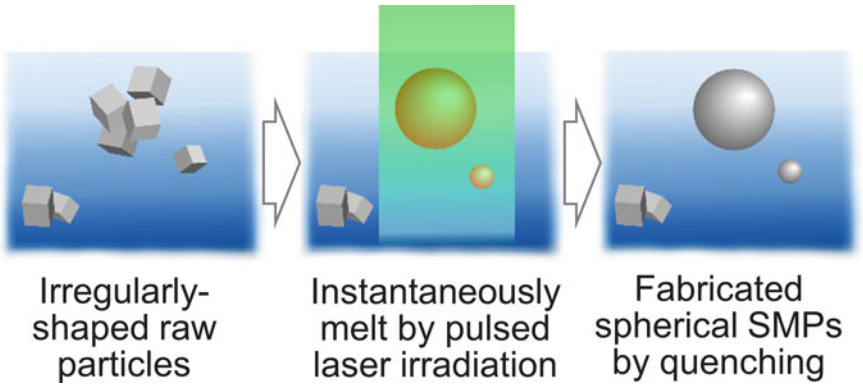


**Fig. 7.1** Schematic illustration of a typical particle formation process by PLML

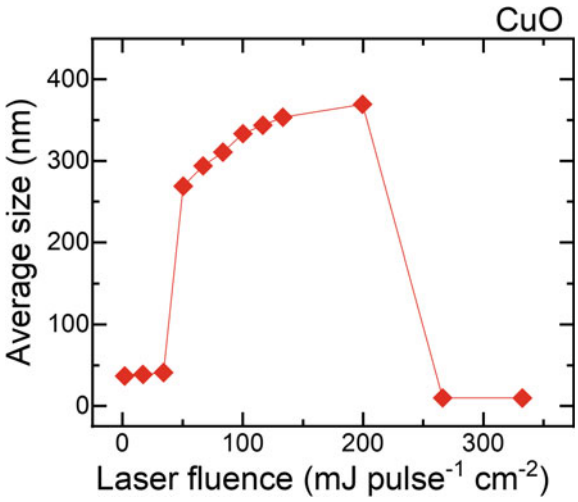


**Fig. 7.2** Laser fluence dependence of average particle size of CuO generated under PLML conditions. Reprinted from reference [5] with the permission from John Wiley and Sons

are typically used for metallurgical or ceramic processes at 1000 K–4000 K, even though the temporal and spatial scales of PLML are short-term and small-sized scales.

Figure 7.2 presents the obtained particle size of CuO under typical fluence conditions for PLML [5], indicating the clear energy window for submicrometer spherical particle formation induced by melt droplet generation. This fluence dependence of particle size corresponds to the phase change of the target particles during laser heating, from solid (no size change), liquid (melt droplet of aggregated raw particles), and vapor (nanoparticle formation from evaporated particles).

The energy input process to raw particles for PLML is optical absorption, which is different from typical metallurgical or ceramic processing for bulk materials by heat conduction from the surrounding environment. In a metallic particle, laser light is shielded by free electrons in the particle. Smaller metallic nanoparticles can still be heated by laser light that slightly penetrates the surface, and smaller spherical metallic nanoparticles can be fabricated through melting, as in the case of noble metal nanoparticle reshaping [8]. Ceramic particles cannot efficiently absorb laser energy when the particle size is smaller than the laser wavelength. When the particle size is in the submicrometer range, which is equivalent to the laser wavelength, spherical submicrometer ceramic particles can be generated if ceramic materials have a sufficient optical absorption band close to the laser wavelength. A more quantitative explanation will be discussed in the next section.

Submicrometer particles were occasionally found as minor byproducts in various PLAL processes. However, our group successfully observed the formation of nonmetallic spherical submicrometer particles as main products (yield >90%), a decade ago for B and $B_4C$ only by reducing the laser fluence to avoid oxidation during PLAL experiments [3, 4]. Later on, these approaches for $B_4C$ particle fabrication can be extended to various oxides, semiconductors, and metals through low-fluence laser irradiation. Typical examples of various spherical submicrometer particles generated

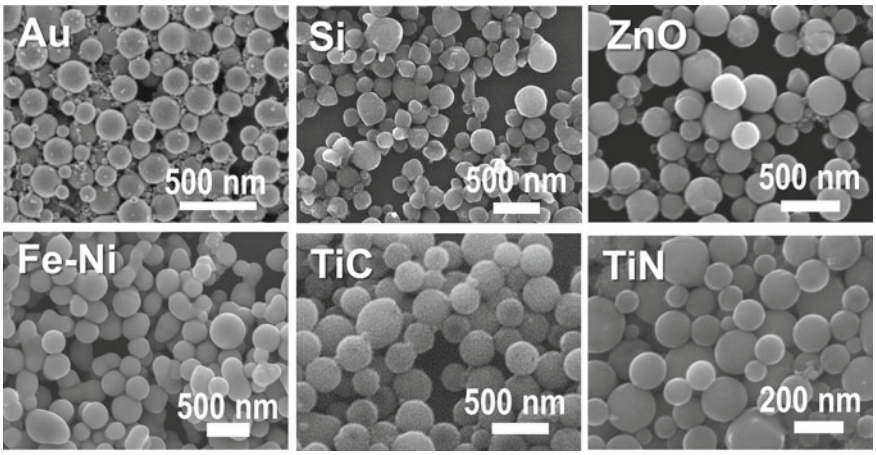


**Fig. 7.3** Submicrometer spherical particles of various materials

by the PLML process are presented in Fig. 7.3, suggesting the versatility of this technique.

## 7.2 Adiabatic Approach

A simple model to describe the PLML process is developed by Pyatenko et al. [9, 10], assuming that energy conversion from optically absorbed energy to thermal energy for the temperature increase occurs without heat dissipation to the surrounding environment (adiabatic assumption). Nanosecond lasers with pulse frequencies of 10–100 Hz are commonly used for the PLML process, and each pulse can be regarded as an individual pulse with no inter-pulse interaction during processing. Based on this assumption, the energy of a particle absorbed by a single laser shot can be equated with the energy required to heat the particle to a specific temperature $T$, as expressed by Eq. (7.1).

$$J \cdot \frac{\pi d^2}{4} Q_{abs}^{\lambda}(d) = \frac{\pi}{6} d^3 \rho_p \Delta \tilde{H}(T) \tag{7.1}$$

The left-hand side of Eq. (7.1) denotes the energy absorbed by a particle, where $J$ represents the laser fluence of a single pulse; $d$ is the particle diameter; and $Q_{abs}^{\lambda}(d)$ is the dimensionless absorption efficiency (absorption cross section normalized by geometrical cross section) deduced from the Mie theory, assuming spherical particles. $Q_{abs}^{\lambda}(d)$ is a value representing the material- and wavelength-dependent optical absorption property. The right-hand side of Eq. (7.1) denotes the energy used to elevate the temperature, where $\rho_p$ denotes the particle density, and $\Delta \tilde{H}(T)$ denotes

the enthalpy per unit weight required for the particle to reach a specific temperature from surrounding liquid temperature (generally at room temperature).

Equation (7.2), which is derived from Eq. (7.1), represents the required fluence $J$ to reach a specific temperature by a single laser shot. For the PLML process, $\Delta\tilde{H}$ must be a required enthalpy from room temperature to the melting point. However, depending on the enthalpy used for the calculation, the phase state of the particle influenced by laser irradiation at fixed fluence can be estimated. Thus, by plotting the phase boundary $J(d)$ curve on a $J$-$d$ plane, a phase diagram (often called a size-fluence diagram) can be obtained.

$$J = \frac{2}{3}\rho_p \Delta\tilde{H} \frac{d}{Q^{\lambda}_{abs}(d)} \tag{7.2}$$

The size-fluence diagrams were already calculated for various materials and laser wavelengths to understand the produced phase (melting starts with solid–liquid coexistence; melting ends only when the solid is completely melted, etc.) of a particle with a fixed size by laser irradiation with a fixed fluence. Figure 7.4 presents examples of size-fluence diagrams, indicating only the melting start phase boundary curves at different wavelengths.

When $d$ increases, $Q^{\lambda}_{abs}(d)$ remains almost constant, and $J$ is nearly proportional to $d$ from Eq. (7.2). Larger fluence is required to melt larger particles, and thus, the

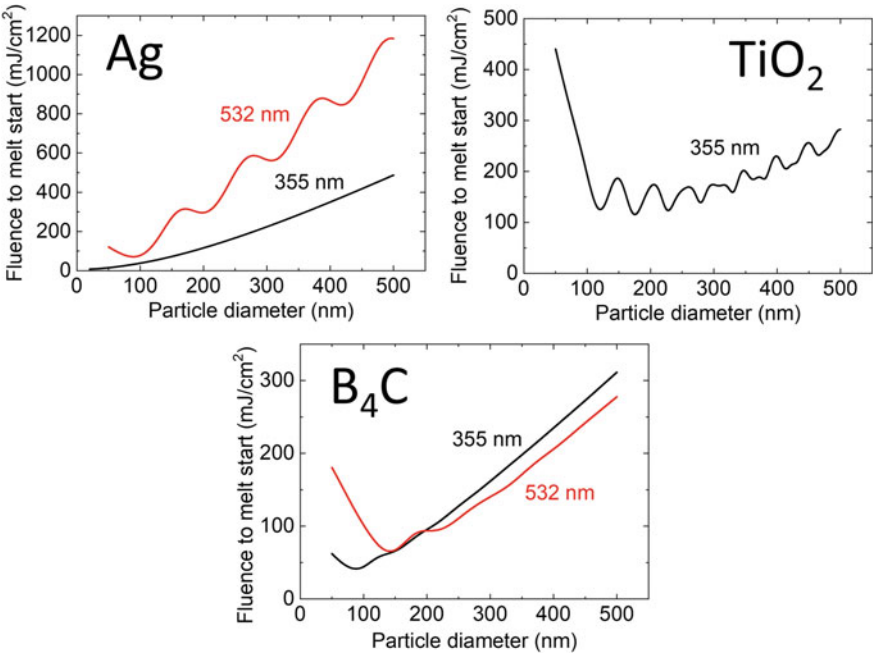


**Fig. 7.4** Size-fluence phase diagram of Ag, $TiO_2$, and $B_4C$

size increase caused by the PLML process is autonomously stopped at a fixed laser fluence. Contrarily, when the particle size decreases, $Q_{abs}^{\lambda}(d)$ drastically decreases, especially for ceramic materials, such as $TiO_2$ and $B_4C$, increasing the required laser fluence to melt a particle smaller than 100 nm.

From these diagrams based on this simple model, the experimental conditions for spherical submicrometer particle formation can be easily estimated and systematic PLML experiments can be conducted to fabricate various spherical submicrometer particles.

## 7.3 Heat Dissipation Effect

Size-fluence diagrams calculated on the basis of adiabatic assumption are fairly well verified for various material systems by comparing laser fluence conditions with clear particle shape modification at the melting point through the PLML process. However, discrepancies were found in several PLML systems using long-pulse laser irradiation or smaller raw particle experiments. Figure 7.5 presents long-pulse laser irradiation using the excimer laser for ZnO submicrometer particle fabrication [11]. The adiabatic assumption described in Sect. 2 does not contain any pulse width term, and therefore, the laser fluence threshold for forming submicrometer particles should not depend on the pulse width. However, the data in Fig. 7.5 indicate that the laser fluence threshold changed with pulse width. This suggests that these discrepancies appear to be caused by heat dissipation during laser heating or from particle surfaces

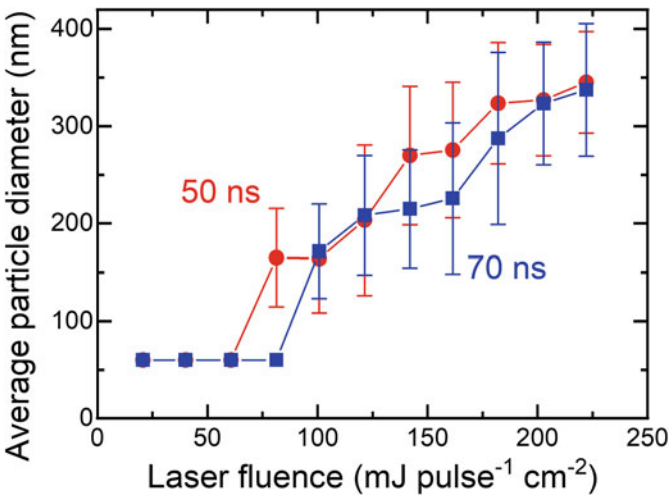


**Fig. 7.5** Laser-fluence dependence of the average particle size of ZnO particles obtained by nanosecond pulsed KrF excimer laser irradiation with a pulse width of 50 (red circles) or 70 ns (blue squares). Reprinted from reference [11] with the permission from John Wiley and Sons

with high-specific surface areas. Thus, a particle heating–melting–cooling model has been developed to include the heat dissipation term.

The time derivative of energy $E(t)$ stored in a particle changes with time considering that heat dissipation is expressed by Eq. (7.3) [11].

$$\frac{dE(t)}{dt} = Q_{abs}^{\lambda}(d) \cdot \frac{\pi d^2}{4} \cdot J(t) - h \cdot \pi d^2 \cdot \{T(t) - T_0\} \tag{7.3}$$

The first term on the right-hand side is the energy increase rate caused by laser irradiation, where $J(t)$ denotes the time-dependent laser fluence temporal profile, which is typically in the form of a Gaussian function and dependent on the laser pulse width. The second term represents heat transfer to the surrounding liquid based on the thermal engineering formulation, in which heat dissipation is proportional to the temperature difference between the particle $T(t)$ and surrounding liquid $T_0$. Conductive heat transfer is solely considered for heat dissipation, and convection around a submicrometer particle is negligible in the PLML conditions. The time-dependent energy $E(t)$ stored in the particle can be numerically calculated by integrating Eq. (7.3). The temperature of the particle is thermodynamically calculated using the stored energy $E(t)$ and thermodynamic parameters of material from the database.

The $h$ in the second term on the right-hand side of Eq. (7.3) denotes the heat transfer coefficient, as expressed by Eq. (7.4):

$$h = \frac{Nu_d \cdot \kappa_m}{d} \tag{7.4}$$

$Nu_d$, Nusselt number, indicating the ratio of convective heat transfer to conductive heat transfer, approximately equals two for submicrometer-scale heating [12]. $\kappa_m$ denotes the heat conductivity of the surrounding medium.

In the initial heating stage, particles are in direct contact and are cooled with liquid. Therefore, the heat conductivity $\kappa_m$ of the liquid is used to calculate Eq. (7.3). Spherical particle formation indicates that the maximum attained temperature during laser heating is above the melting point. In the PLAL process, a liquid that interfaces laser-heated materials is known to be vaporized at the spinodal temperature (~573 K) at a rapid heating rate. Similarly, bubbles generated by the rapid vaporization of the liquid at the interface are assumed to be formed, even for the PLML process, though PLML is slower and milder than PLAL. This effect is included in Eqs. (3) and (4) as a switch of heat conductivity $\kappa_m$ from liquid to vapor at the spinodal temperature, expressing the formation of a transient thermal resistance vapor layer. This thermal barrier further induces rapid heat accumulation within the particles.

Figure 7.6 presents the temporal temperature profile of the ZnO particle (200 nm in diameter) irradiated by laser pulses (wavelength: 355 nm, pulse width: 8 ns) with different laser fluences [11]. The plateau range for 80 mJ pulse$^{-1}$ cm$^{-2}$ indicates that the ZnO particle is at the melting point, and it melts to form spherical particles. From these temporal temperature profiles obtained from Eq. (7.3), the maximum attained

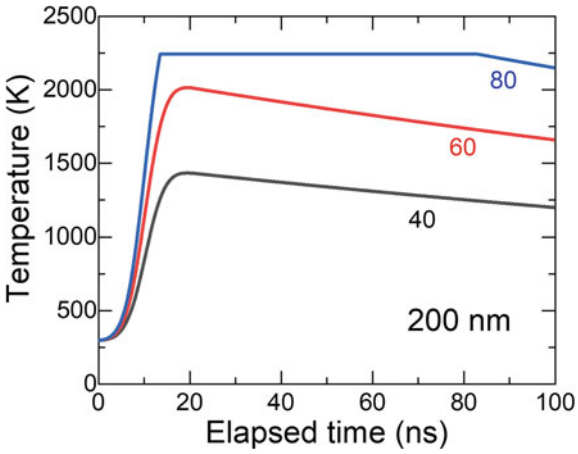


**Fig. 7.6** Calculated temporal temperature profiles for ZnO particles (200 nm in diameter) irradiated by 355 nm laser (8 ns pulse width). Numbers near the curves correspond to the laser fluences in mJ pulse$^{-1}$ cm$^{-2}$

temperature at the respective conditions can be obtained and the phase state of the particle at the maximum temperature can be estimated. The size-fluence diagram, as presented in Sect. 2, can be plotted using the maximum attained temperature as a function of particle size $d$ and applied total laser fluence $\int J(t)dt$.

Figure 7.7 presents the size-fluence diagram of ZnO melting start for 248 nm laser irradiation with different laser pulse widths of 7 and 70 ns using Eq. (7.3). Phase boundary curve under the adiabatic assumption by Eq. (7.2) is also presented

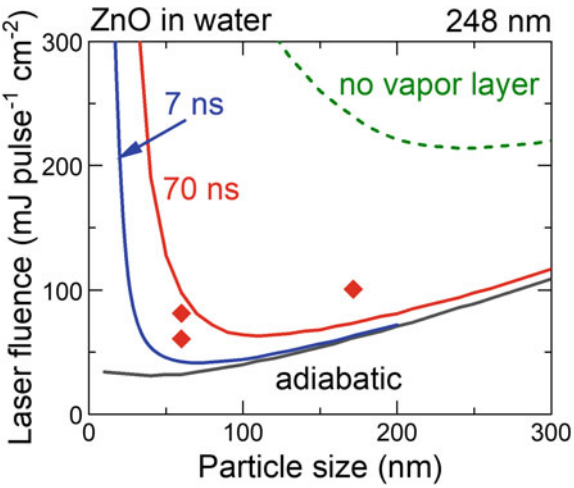


**Fig. 7.7** Size-fluence diagram of ZnO to melt start in water for adiabatic conditions and laser pulse widths of 7 and 70 ns considering the heat dissipation process. Experimental data marked as red diamonds are generated by excimer laser (248 nm, 70 ns pulse width). Required fluence assuming that particle keeps contacting water without forming vapor layer is also plotted in green broken line. Reprinted from reference [11] with the permission from John Wiley and Sons

in Fig. 7.7. For a smaller particle size, the required laser fluences to reach the ZnO melting point are significantly increased with an increase in the pulse width. This is due to heat dissipation during longer laser pulse, and additional laser energy is required to compensate for the energy dissipated to the surroundings to reach the melting point. The red diamonds in Fig. 7.7 indicate experimental data points obtained at 70 ns laser pulses. When the laser fluence exceeds the red curve of the phase boundary to reach the melting point, the particle size suddenly increases to form submicrometer spherical particles from aggregated raw particles, suggesting that this model well explains the experimental data, even for a long-pulse laser case.

Furthermore, the phase boundary curve is plotted in Fig. 7.7 as a green broken line, assuming that the liquid interfacing the laser-heated particle does not vaporize and remains in a liquid phase. Due to the difference in thermal conductivities of liquid and water vapor, the required laser fluence to reach the ZnO melting point is increased in this case. However, this calculation data did not match the experimental data, indicating that spherical particle formation occurred at fluences lower than 100 mJ pulse$^{-1}$ cm$^{-2}$.

Figure 7.8 presents another example of a size-fluence diagram for metallic Pd case (60 nm in diameter) caused by 355 nm laser irradiation (pulse width: 8 ns) compared with and without considering the heat dissipation effect. The required fluence to melt the Pd particle is small for particle sizes less than 30 nm based on the adiabatic assumption. However, by considering heat dissipation from the particle surface, the temperature of the particle will not be easily elevated by laser irradiation and large laser fluence is required for smaller particles. Thus, a particle size window is formed for 40–70 nm particles that are easily melted compared with other particle size ranges. A similar effect is experimentally observed for spherical particle formation of Au nanoparticles [13].

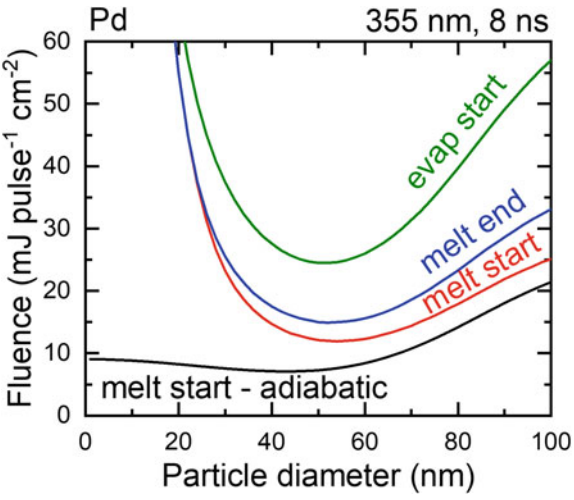


**Fig. 7.8** Size-fluence diagram of Pd to melt start with and without considering heat dissipation process

Thus, transient vapor layer formation is reasonable for spherical submicrometer particle formation through the PLML process, which well explains the many experimental results.

## 7.4 Observation of Thermally Induced Nanobubbles

PLML is a simple thermal process and distinctly different from the well-studied PLAL process. As discussed in the previous section, a transiently formed vapor phase is deduced to act as a thermal barrier coating on the particle produced by liquid vaporization. Due to the rapid thermal barrier formation and the small thermal conductivity of the vapor phase, the adiabatic approach in Sect. 2 can be a good approximation.

Cavitation bubble formation during the PLAL process has been intensively investigated to understand the nanoparticle formation process using various spectroscopic techniques [14–18]. However, thermally induced vapor bubbles during the PLML process are smaller than cavitation bubbles, non-emissive without plasma formation, and are produced close to the particle surface. Therefore, analyzing them using techniques used for cavitation bubble analysis is difficult. Plasmonic nanobubbles that are reported to form during the plasmonic heating of Au nanoparticles by pulsed laser irradiation appear to have the same size, temperature, and duration range as those observed in the PLML process [19–21]. However, bubbles in PLML processes are formed even without plasmonic heating. Therefore, bubbles in PLML processes and the plasmonic nanobubbles should be called thermally induced nanobubbles since the origin of these bubbles is the same as the thermal process.

When particles dispersed in liquid are irradiated by laser and a vapor layer is formed at the particle liquid interface, a laser beam may be slightly deflected by the surrounding vapor layer and light transmittance through the liquid may be affected. The transient optical transmittance change of a liquid dispersing particle by laser irradiation is monitored to confirm the possibility of analyzing the formation process of thermally induced nanobubbles during the PLML process. Optical measurement data are compared with the morphology of the produced particles and Mie calculation results of bubble-coated spherical particles.

Figure 7.9 presents a schematic illustration of the experimental setup for the transient optical transmittance measurements during Nd:YAG laser irradiation [22]. A continuous probe laser was used to irradiate the four-face cell filled with colloidal solution orthogonally to the optical path of the processing Nd:YAG laser for PLML. A photodetector was used to collect the temporal probe laser signal transmitted through the optical cell, triggered by the processing laser.

Figure 7.10 presents the calculated bubble thickness dependence of the extinction cross section for air-coated ZnO particles placed in water by irradiation with 640 nm light, assuming that the refractive indices of core (ZnO) and shell (air) have a stepwise variation at the interface. When the particle diameter is 300 nm, the extinction cross section decreases and then increases with the bubble thickness. In this case, the

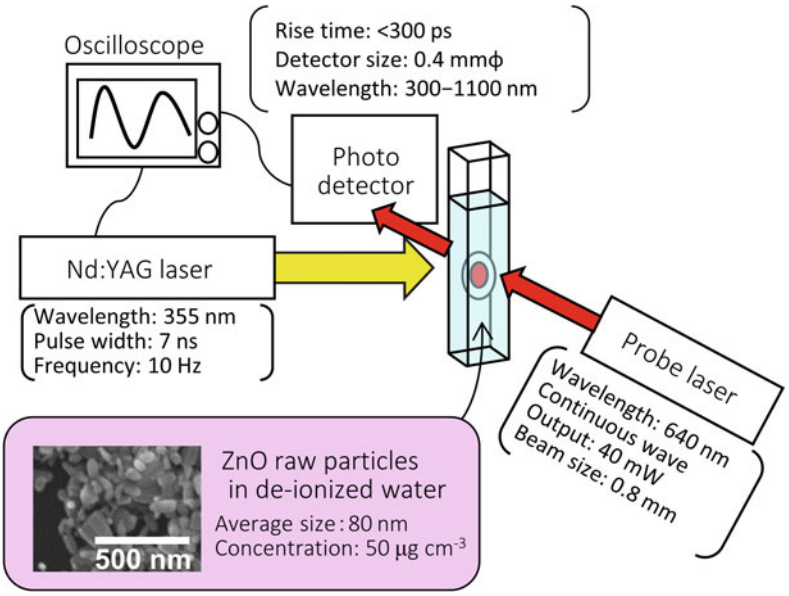


**Fig. 7.9** Experimental setup to measure the change in optical extinction caused by the formation of thermally induced nanobubbles. Reprinted from reference [22] with the permission from American Chemical Society

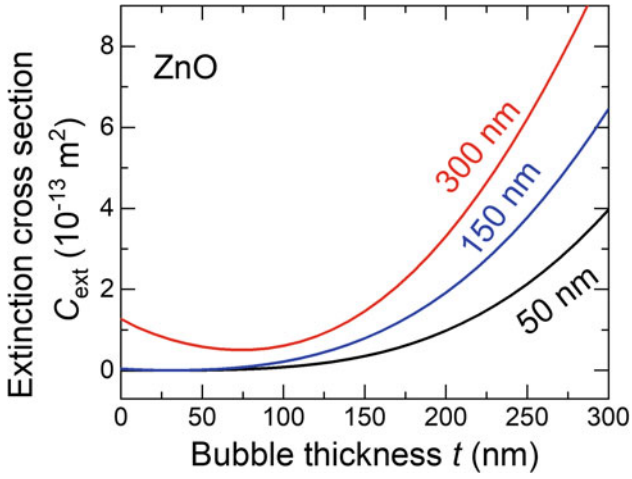


**Fig. 7.10** Calculated bubble thickness dependence of the extinction cross section of ZnO particles with diameters of 50, 150, and 300 nm. Reprinted from reference [22] with the permission from American Chemical Society

bubble formation process can be monitored by monitoring the optical transmittance increase and decrease with bubble expansion. Contrarily, when the particle size is small, as in typical raw particles of a PLML process, the formation of a thin bubble layer during the initial stage of laser irradiation is difficult to monitor and only thick thermally induced nanobubbles with a size larger than 100 nm can be monitored by the transmittance decrease.

Figure 7.11 presents the photodetector output generated by irradiation with a 640 nm probe laser into a colloidal solution of raw ZnO nanoparticles during and after irradiation with a 355 nm processing Nd:YAG laser (7 ns pulse width). It is difficult to quantitatively explain the data since raw ZnO particles and their aggregates have wide size distribution, and therefore, the photodetector signal change cannot be as simple as in Fig. 7.10. However, the initial increase in the photodetector output may be due to the contribution of large-sized raw particles. By increasing the processing laser fluence to 20 mJ pulse$^{-1}$ cm$^{-2}$ or more, a decrease in the photodetector output is observed at 20–80 ns after the laser irradiation. This behavior may be related to the formation of a thick bubble with a size larger than 100 nm, as presented in Fig. 7.10. Thus, bubbles are formed and act as a thermal barrier to elevate the temperature and to delay cooling, even at lower fluences of approximately 20 mJ pulse$^{-1}$ cm$^{-2}$.

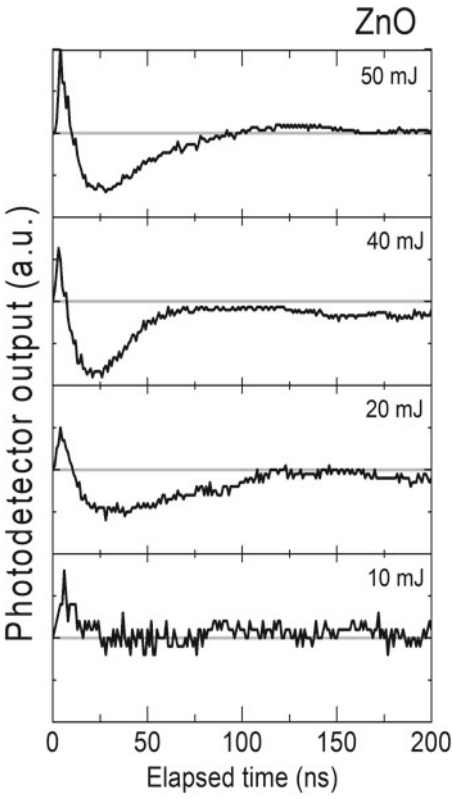


**Fig. 7.11** Temporal dependence of photodetector output caused by the transmitted light intensity through a colloidal solution of raw ZnO nanoparticles irradiated with different laser fluences. Reprinted from reference [22] with the permission from American Chemical Society

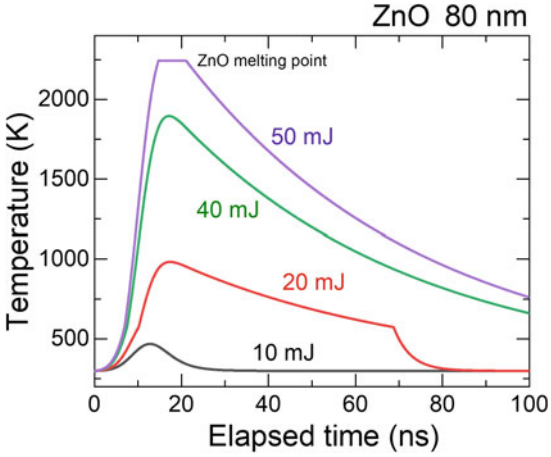


**Fig. 7.12** Estimated temperature temporal profile of ZnO NPs (80 nm) after initiating laser irradiation. Reprinted from reference [22] with the permission from American Chemical Society

Figure 7.12 presents temporal temperature profiles calculated on the basis of the procedures described in Sect. 3. Compared with Fig. 7.6 for the 200 nm ZnO particle, the cooling rate for 80 nm ZnO particles is fast even though smaller laser fluence is sufficient to reach the melting point due to the difference in the heat capacity of the particles.

Figure 7.13 presents the corresponding scanning electron microscopy (SEM) images of particles obtained using the PLML process. At 10 mJ pulse$^{-1}$ cm$^{-2}$, the applied laser fluence is below the estimated bubble formation threshold and a corresponding transmittance change that could indicate the formation of thermally induced nanobubbles was not detected as presented in Fig. 7.11. At 20–40 mJ pulse$^{-1}$ cm$^{-2}$, thermally induced nanobubbles are formed as can be seen from Fig. 7.12. Aggregated raw particles can interact by interdiffusion when the particle temperature is close to the melting point, but the formation of large spherical particles was not frequent without melting. At 50 mJ pulse$^{-1}$ cm$^{-2}$, raw particles (80 nm in diameter) can reach the melting point of ZnO (2243 K) to form spherical particles and merge with adjacent molten particles to form larger submicrometer particles as presented in Fig. 7.13.

Thus, in typical PLML processing conditions for materials with a high melting point, raw particles must be heated to form thermally induced nanobubbles above the spinodal temperature. The thermally induced nanobubbles act as a thermal barrier between particles and the surrounding liquid to enhance rapid heating of particles up to the melting point of the material. The formation of thermally induced nanobubbles not only promotes the formation of submicrometer spherical particles but also induces the process of interparticle sintering by merging, as in the bulk scale material processing.

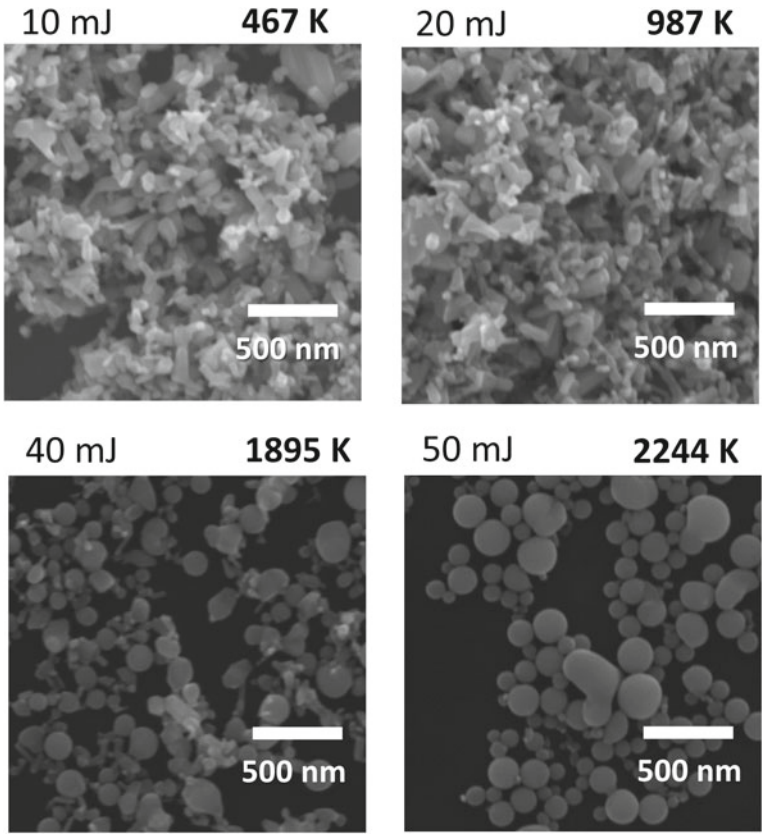


**Fig. 7.13** SEM images of ZnO particles obtained under various laser fluences by the PLML process (Nd:YAG laser, wavelength: 355 nm, in water, 30 min) from raw ZnO nanoparticles (80 nm in nominal size) with the estimated highest particle temperatures. Reprinted from reference [22] with the permission from American Chemical Society

## 7.5 Chemical Reaction Mediated by Thermally Induced Nanobubbles

Chemical reactions in PLML processes can be seen in the following examples, in which an organic solvent is used as the surrounding liquid medium. The reduction reaction proceeds from a transition metal oxide to metal or metal oxide with a lower oxidation state than raw particles, as in the case of raw $Fe_3O_4$ particles to Fe and FeO particles in ethanol [23]. The carbonization reaction from raw B particles to $B_4C$ submicrometer particles is also reported in ethanol [3, 4]. Thermally induced nanobubbles, where particles and liquid interface, may play an important role in these high-temperature chemical reactions. However, the details of these chemical reactions have not been elucidated until now.

Figure 7.14 presents a schematic of a laser-irradiated particle, the surrounding ethanol, and the vapor layer at the interface [24], as suggested on the basis of the discussion in the previous sections. When a particle is irradiated by laser light, the particle temperature exceeds the melting point when the PLML condition is applied. Ethanol, interfacing with the heated particle, cannot be in the liquid phase and thus transforms into the vapor phase. The particle temperature can easily exceed the decomposition temperature of ethanol due to the formation of a heat-insulating ethanol vapor layer. However, the heating time is on the order of tens or hundreds of nanoseconds during the PLML process due to nanosecond laser irradiation. Therefore, it is unclear how the thermal decomposition process of ethanol proceeds in such a short time, even though the temperature of the particle is around several thousand kelvins.

Particle reduction appeared difficult to achieve using a simple thermal decomposition process under typical PLML laser irradiation conditions ($\leq$200 mJ pulse$^{-1}$ cm$^{-2}$) in ethanol. In addition, in the PLML process, the product in ethanol is reduced compared with that in water. Therefore, another chemical process mediated by the decomposed products of the surrounding ethanol in the thermally induced nanobubbles has to be involved as presented in Fig. 7.14. However, it is difficult to probe the chemical reaction process, including the formation process of reaction intermediates by thermal decomposition in a transiently short time and small nanobubble space.

Here, the ethanol thermal decomposition process in a transient time scale is computationally calculated using the Chemkin-Pro (ANSYS Japan) software. This

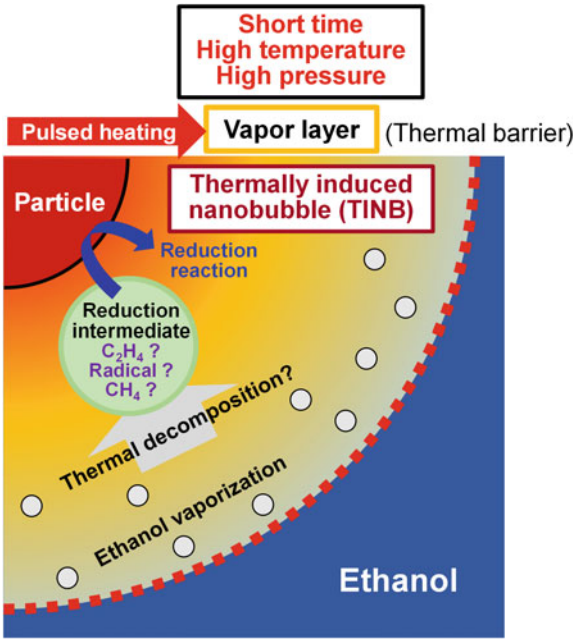


**Fig. 7.14** Schematic illustration of a laser-irradiated particle, the surrounding ethanol, and the thermally induced nanobubble at the interface. Reprinted from reference [24] with the permission from John Wiley and Sons

software can simulate the temporal change in the molar chemical composition and chemical reaction path of gas molecules using reaction rate constants of elementary reactions, the thermodynamic functions of various chemical species, and reaction conditions (temperature, pressure, and time) [25]. The calculation conditions were based on the typical range in the PLML process (1000 K–4000 K, 1 atm to the critical pressure of ethanol (60 atm)) [11].

Figure 7.15 presents the initial thermal decomposition process of ethanol at 2500 K [24]. $C_2H_4$ and $H_2O$ are increased to a 0.2 mol fraction until 40 ns. The minor components with a fraction of 5% or less, such as $CH_3$, $CH_4$, and $H_2$, are also generated via thermal decomposition. According to the pressure dependence calculation (not shown here), a higher pressure at 2500 K further accelerates the $C_2H_4$ production rate. Higher pressure is possibly attained in the thermally induced nanobubbles even though the actual pressure during the PLML process is unknown. Thus, $C_2H_4$ is suggested to promote rapid and efficient chemical reactions in thermally induced nanobubbles.

Figure 7.16 presents the temperature dependence of the mole fraction of components generated by ethanol thermal decomposition after 100 ns heating at 1 atm. $C_2H_4$ and $H_2O$ are major components at 2500 K–3500 K, and $H_2$ and $C_2H_2$ are generated at a higher temperature of 4000 K. Thus, $C_2H_4$ may play an important role in the chemical reactions mediated by the thermal decomposition of ethanol by the PLML process since the typical temperature range for the PLML process is 2000 K–4000 K.

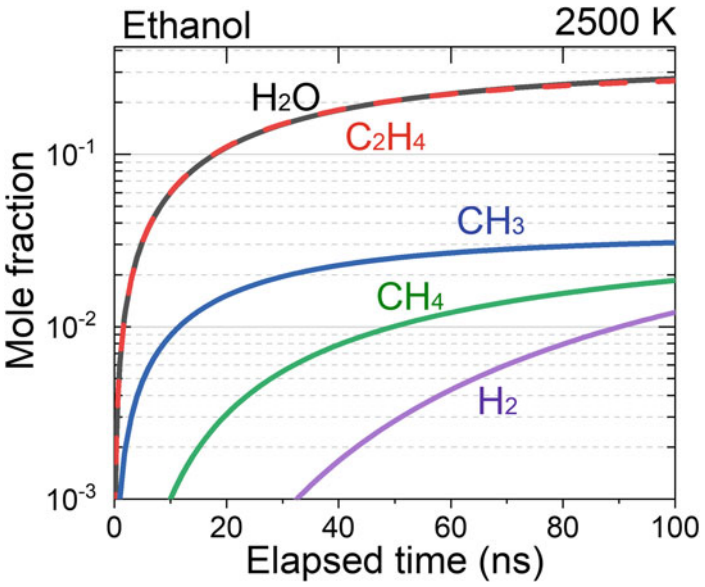


**Fig. 7.15** Calculated time evolution of chemical composition change when ethanol is introduced into a container at 2500 K for 100 ns. Reprinted from reference [24] with the permission from John Wiley and Sons

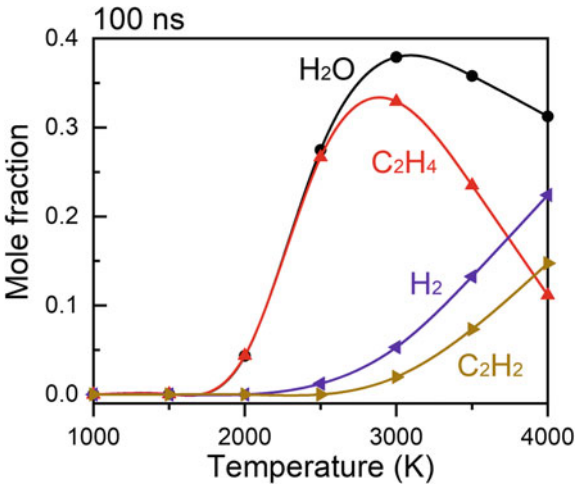


**Fig. 7.16** Temperature dependence of the mole fraction of components generated by ethanol thermal decomposition. Elapsed time: 100 ns. Pressure: 1 atm. Reprinted from reference [24] with the permission from John Wiley and Sons

Figure 7.17 presents the long-term change in the mole fraction for components thermally decomposed from ethanol at 2500 K and 1 atm. This graph shows that $C_2H_4$ and $H_2O$ are the major components only for a short time, whereas $H_2$ and CO dominate the products after a longer heating time. Thus, this result indicates that the PLML process preferentially produces $C_2H_4$ by nanosecond pulsed laser heating with a low-frequency laser, which may be different from the case using a MHz laser with a high repetition rate or the conventional thermal process by continuous heating.

Computational research on ethanol thermal decomposition suggested that $C_2H_4$ is a possible reaction intermediate of ethanol decomposition in the PLML process (<100 ns) with rapid heating and long cooling. $C_2H_4$ may also mediate reduction

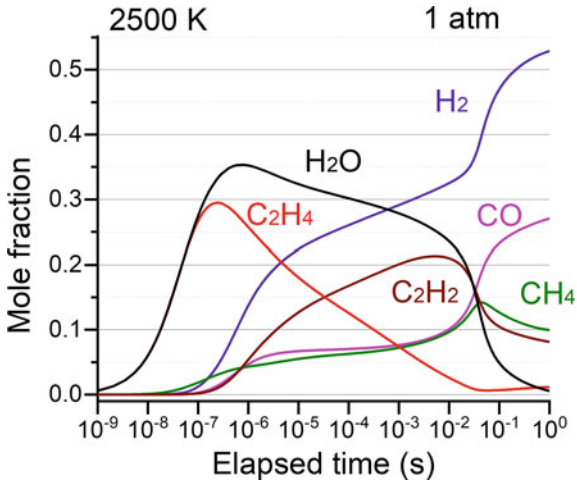


**Fig. 7.17** Long-term evolution of mole fraction for components generated by ethanol thermal decomposition. Temperature: 2500 K. Pressure: 1 atm. Reprinted from reference [24] with the permission from John Wiley and Sons

reactions of oxides, such as $Fe_3O_4$ and other transition metal oxides, to the less-oxidized phase, such as FeO or metallic Fe. The formation of low-valence oxides or metallic phases is more thermodynamically advantageous than simple thermal reduction when $C_2H_4$ is transiently formed in the PLML process. These analyses were previously reported in detail by comparing the thermodynamic calculations with the experimental data of product morphology for various transition metal oxide reductions [24]. Here, another chemical reaction by PLML for the carbonization of B to form $B_4C$ is discussed.

$C_2H_4$ is generated via ethanol decomposition in the following equation under the PLML condition from Fig. 7.15.

$$C_2H_5OH \rightleftarrows C_2H_4 + H_2O \tag{7.5}$$

$C_2H_4$ can produce a carbon source to react with boron atoms in the particles.

$$C_2H_4 \rightleftarrows 2C + 2H_2 \tag{7.6}$$

The simple thermal carbonization reaction of B for one mole of B is

$$B + \frac{1}{4}C \rightleftarrows \frac{1}{4}B_4C \tag{7.7}$$

If the thermal carbonization reaction in Eq. (7.7) is mediated by the decomposition reaction of $C_2H_4$ in Eq. (7.6), the overall reduction reaction of B to $B_4C$ is

$$B + \frac{1}{8}C_2H_4 \rightleftarrows \frac{1}{4}B_4C + \frac{1}{4}H_2 \tag{7.8}$$

The temperature dependence of $\Delta G$ for the simple thermal carbonization reaction in Eq. (7.7) and $C_2H_4$-mediated carbonization reaction in Eq. (7.8) is plotted in Fig. 7.18.

The black line in Fig. 7.18 indicates the $\Delta G$ curve of a simple thermal decomposition reaction, indicating that the reaction is thermodynamically possible. However, for the $C_2H_4$-mediated carbonization reaction (red line), the $\Delta G$ value is less than that for the simple thermal decomposition reaction, especially at the melting point of B (indicated by dots), where spherical particles are formed. This suggests that the carbonization reaction to form $B_4C$ submicrometer spherical particles proceeds through the mediation of $C_2H_4$ generated by the thermal decomposition of ethanol.

The reaction products of submicrometer particles can be predicted from thermodynamic calculations, even without considering the catalytic effect of nanoparticles, and are mediated by molecules decomposed from ethanol. Thus, chemical reactions are mainly controlled by thermodynamic relations, even by short-term laser heating, and the kinetic effects during the PLML process are less effective.

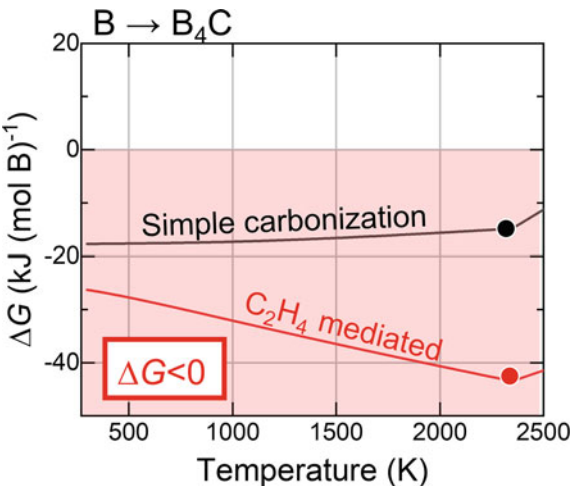


**Fig. 7.18** Temperature dependence of $\Delta G$ for the carbonization reaction of boron and that mediated with $C_2H_4$ generated by thermal decomposition of ethanol. Black and red solid circles correspond to the melting point of B

## 7.6 Summary

In this chapter, the basic mechanism of PLML is discussed compared with that of PLAL. Cavitation bubbles are important for nanoparticle generation in the PLAL process, whereas thermally induced nanobubbles play a significant role in the generation of submicrometer spherical particles by the PLML process. However, these bubbles have different sizes, temperatures, and generation times. The generation of thermally induced nanobubbles that has never been examined can be monitored by newly developed transient optical transmittance measurements. The chemical reactions in the PLML process are considered to be mediated by chemicals generated in thermally induced nanobubbles. Especially, metal oxides can be reduced and boron can be carbonized by laser irradiation for a short time using the PLML process in ethanol and this process can be thermodynamically explained with a mediation of $C_2H_4$ thermally decomposed from ethanol.

## References

1. D. Zhang, B. Gökce, S. Barcikowski, Laser synthesis and processing of colloids: fundamentals and applications. Chem. Rev. **117**, 3990–4103 (2017). https://doi.org/10.1021/acs.chemrev.6b00468
2. V. Amendola, D. Amans, Y. Ishikawa, N. Koshizaki, S. Scirè, G. Compagnini, S. Reichenberger, S. Barcikowski, Room-temperature laser synthesis in liquid of oxide, metal-oxide core-shells, and doped oxide nanoparticles. Chem. Eur. J. **26**, 9206–9242 (2020). https://doi.org/10.1002/chem.202000686
3. Y. Ishikawa, Y. Shimizu, T. Sasaki, N. Koshizaki, Boron carbide spherical particles encapsulated in graphite prepared by pulsed laser irradiation of boron in liquid medium. Appl. Phys. Lett. **91** (2007) 161110. https://doi.org/10.1063/1.2799786

4. Y. Ishikawa, Q. Feng, N. Koshizaki, Growth fusion of submicron spherical boron carbide particles by repetitive pulsed laser irradiation in liquid media. Appl. Phys. A **99**, 797–803 (2010). https://doi.org/10.1007/s00339-010-5745-6
5. H. Wang, A. Pyatenko, K. Kawaguchi, X. Li, Z. Swiatkowska-Warkocka, N. Koshizaki, Selective pulsed heating for the synthesis of semiconductor and metal submicrometer spheres. Angew. Chem. Int. Ed. Engl. **49**, 6361–6364 (2010). https://doi.org/10.1002/anie.201002963
6. H. Wang, N. Koshizaki, L. Li, L. Jia, K. Kawaguchi, X. Li, A. Pyatenko, Z. Swiatkowska-Warkocka, Y. Bando, D. Golberg, Size-tailored ZnO submicrometer spheres: bottom-up construction, size-related optical extinction, and selective aniline trapping. Adv. Mater. **23**, 1865–1870 (2011). https://doi.org/10.1002/adma.201100078
7. H. Wang, M. Miyauchi, Y. Ishikawa, A. Pyatenko, N. Koshizaki, Y. Li, L. Li, X. Li, Y. Bando, D. Golberg, Single-crystalline rutile $TiO_2$ hollow spheres: room-temperature synthesis, tailored visible-light-extinction, and effective scattering layer for quantum dot-sensitized solar cells. J. Am. Chem. Soc. **133**, 19102–19109 (2011). https://doi.org/10.1021/ja2049463
8. G. González-Rubio, A. Guerrero-Martínez, L.M. Liz-Marzán, Reshaping, fragmentation, and assembly of gold nanoparticles assisted by pulse lasers. Acc. Chem. Res. **49**, 678–686 (2016). https://doi.org/10.1021/acs.accounts.6b00041
9. A. Pyatenko, H. Wang, N. Koshizaki, T. Tsuji, Mechanism of pulse laser interaction with colloidal nanoparticles. Laser Photonics Rev. **7**, 596–604 (2013). https://doi.org/10.1002/lpor.201300013
10. A. Pyatenko, H. Wang, N. Koshizaki, Growth mechanism of monodisperse spherical particles under nanosecond pulsed laser irradiation. J. Phys. Chem. C **118**, 4495–4500 (2014). https://doi.org/10.1021/jp411958v
11. S. Sakaki, H. Ikenoue, T. Tsuji, Y. Ishikawa, N. Koshizaki, Pulse-width dependence of the cooling effect on sub-micrometer ZnO spherical particle formation by pulsed-laser melting in a liquid. ChemPhysChem **18**, 1101–1107 (2017). https://doi.org/10.1002/cphc.201601175
12. A. F. Mills, Heat Transfer, 2nd ed. 1998, New York: Prentice Hall.
13. T. Tsuji, S. Sakaki, H. Fujiwara, H. Kikuchi, M. Tsuji, Y. Ishikawa, N. Koshizaki, Stabilizer-concentration effects on the size of gold submicrometer-sized spherical particles prepared using laser-induced agglomeration and melting of colloidal nanoparticles. J. Phys. Chem. C **122**, 21659–21666 (2018). https://doi.org/10.1021/acs.jpcc.8b05911
14. A. Kanitz, M.R. Kalus, E.L. Gurevich, A. Ostendorf, S. Barcikowski, D. Amans, Review on experimental and theoretical investigations of the early stage, femtoseconds to microseconds processes during laser ablation in liquid-phase for the synthesis of colloidal nanoparticles. Plasma Sources Sci. Technol. **28** (2019) 103001. https://doi.org/10.1088/1361-6595/ab3dbe
15. T. Tsuji, D.H. Thang, Y. Okazaki, M. Nakanishi, Y. Tsuboi, M. Tsuji, Preparation of silver nanoparticles by laser ablation in polyvinylpyrrolidone solutions. Appl. Surf. Sci. **254**, 5224–5230 (2008). https://doi.org/10.1016/j.apsusc.2008.02.048
16. K. Sasaki, N. Takada, Liquid-phase laser ablation. Pure Appl. Chem. **82**, 1317–1327 (2010). https://doi.org/10.1351/PAC-CON-09-10-23
17. M. Dell'Aglio, R. Gaudiuso, O. De Pascale, A. De Giacomo, Mechanisms and processes of pulsed laser ablation in liquids during nanoparticle production. Appl. Surf. Sci. **348**, 4–9 (2015). https://doi.org/10.1016/j.apsusc.2015.01.082
18. S. Reich, A. Letzel, A. Menzel, N. Kretzschmar, B. Gökce, S. Barcikowski, A. Plech, Early appearance of crystalline nanoparticles in pulsed laser ablation in liquids dynamics. Nanoscale **11**, 6962–6969 (2019). https://doi.org/10.1039/C9NR01203F
19. E.Y. Lukianova-Hleb, A.N. Volkov, D.O. Lapotko, Laser pulse duration is critical for the generation of plasmonic nanobubbles. Langmuir **30**, 7425–7434 (2014). https://doi.org/10.1021/la5015362
20. T. Katayama, K. Setoura, D. Werner, H. Miyasaka, S. Hashimoto, Picosecond-to-nanosecond dynamics of plasmonic nanobubbles from pump-probe spectral measurements of aqueous colloidal gold nanoparticles. Langmuir **30**, 9504–9513 (2014). https://doi.org/10.1021/la500663x

21. D. Lohse, X. Zhang, Surface nanobubbles and nanodroplets. Rev. Mod. Phys. **87**, 981–1035 (2015). https://doi.org/10.1103/RevModPhys.87.981
22. Y. Tabayashi, S. Sakaki, N. Koshizaki, Y. Yamauchi, Y. Ishikawa, Behavior of thermally induced nanobubbles during instantaneous particle heating by pulsed laser melting in liquid. Langmuir **37**, 7167–7175 (2021). https://doi.org/10.1021/acs.langmuir.1c00736
23. Y. Ishikawa, N. Koshizaki, A. Pyatenko, Submicrometer-sized spherical iron oxide particles fabricated by pulsed laser melting in liquid. Electr. Commun. Jpn. **99**, 37–42 (2016). https://doi.org/10.1002/ecj.11898
24. K. Suehara, R. Takai, Y. Ishikawa, N. Koshizaki, K. Omura, H. Nagata, Y. Yamauchi, Reduction mechanism of transition metal oxide particles in thermally induced nanobubbles by pulsed laser melting in ethanol. ChemPhysChem **22**, 675–683 (2021). https://doi.org/10.1002/cphc.202001000
25. M. Sieradzka, P. Rajca, M. Zajemska, A. Mlonka-Mędrala, A. Magdziarz, Prediction of gaseous products from refuse derived fuel pyrolysis using chemical modelling software - Ansys Chemkin-Pro J. Clean. Prod. **248** (2020) 119277. https://doi.org/10.1016/j.jclepro.2019.119277

# Chapter 8
# Mass Production of Spherical Submicrometer Particles by Pulsed Laser Melting in Liquid


**Yoshie Ishikawa and Naoto Koshizaki**

**Abstract** Pulsed laser melting in liquid (PLML) can produce crystalline spherical submicrometer particles that are impossible to obtain using traditional particle fabrication methods. The mass production technology of these submicrometer particles is essential for various promising applications. However, the laser process generally has low productivity due to the fine laser beam and unidirectional energy input. PLML process requires the adequate fluence range for submicrometer particle formation, and therefore, the effective depth where the PLML can proceed must be well utilized. A guided slit nozzle for a continuous flow system, suitable for a laser with a high pulse energy and low pulse frequency (several tens of Hz), is developed for the PLML process. By single flow passage irradiation of an adequately slow continuous suspension flow through the slit nozzle, the spherical submicrometer particle formation rate exceeded 90%. This new slit nozzle flow can further provide information on the pulse-to-pulse particle formation process in PLML. An automated iterative batch processing system is also developed for the PLML process to produce submicrometer particles through the chemical reaction between particles and liquid.

**Keywords** Spherical submicrometer particles · Pulsed laser melting in liquid · Mass production · Slit nozzle · Continuous flow · Formation mechanism

Y. Ishikawa (✉)
Research Institute for Advanced Electronics and Photonics, National Institute of Advanced Industrial Science and Technology (AIST), Tsukuba Central 5, 1-1-1 Higashi, Tsukuba 305-8565, Ibaraki, Japan
e-mail: ishikawa.yoshie@aist.go.jp

N. Koshizaki
Graduate School of Engineering, Hokkaido University, Kita 13 Nishi 8, Kita-ku, Sapporo, Hokkaido 060-8628, Japan
e-mail: koshizaki.naoto@eng.hokudai.ac.jp



Y. Ishikawa et al. (eds.), *High-Energy Chemistry and Processing in Liquids*,
https://doi.org/10.1007/978-981-16-7798-4_8

## 8.1 Uniqueness and Functions of Spherical Submicrometer Particles Obtained by PLML

As described in Chap. 7, pulsed laser melting in liquid (PLML) is a unique particle fabrication technique using less energetic laser beam irradiation (several tens to hundreds of mJ $cm^{-2}$ $pulse^{-1}$). The main products of the PLML process are spherical submicrometer particles, different from the nanoparticles obtained using pulsed laser ablation in liquid (PLAL) process. Furthermore, particles obtained by PLML are usually crystalline and relatively size-homogeneous.

Submicrometer is the size range that divides the two general particle fabrication processes, top-down and bottom-up. The lower size limit of the top-down approach, such as pulverization or jet milling, is in micrometers or submicrometers at larger side. Alternatively, the bottom-up process is difficult to fabricate submicrometer particles by extending the common nucleation and growth methods typically used for nanoparticle fabrication. However, the PLML process can produce particles of the intervening submicrometer range, particularly at the smaller side (Fig. 8.1).

Size-homogeneous spherical submicrometer particles of polymer and glass fabricated are commercially available, though they are generally amorphous [1]. Spherical submicrometer particles composed of aggregated nanoparticles have also been reported, though these particles and their calcined particles are mostly polycrystalline, porous, or less crystallized [2–4]. Thus, conventional particle fabrication methods cannot easily obtain crystalline and non-aggregated spherical submicrometer particles of various materials.

Submicrometer particles can be used in size-specific functions (Fig. 8.1), such as optical scatterers for random lasers [5] and solar cell back reflectors [6]; medical

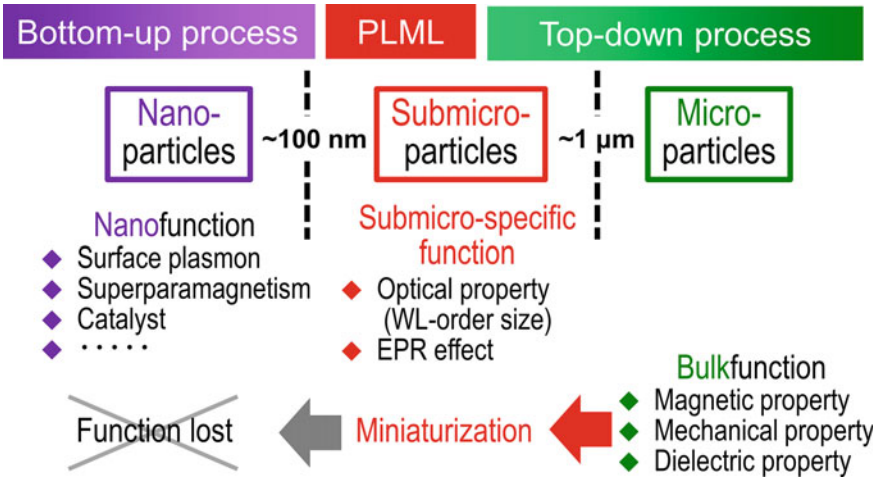


**Fig. 8.1** Relationship between particle size range, processing, and size-derived functions

applications as boron neutron capture therapy agents based on the enhanced permeability and retention effect [7]; enhanced magnetization due to the size-dependent superpara-/ferromagnetic transitions [8]; and high fracture strength property for lubricant additives [9]. These functions are different from size-specific nanoparticle functions, such as surface plasmon resonance, superparamagnetism, and catalyst [10]. Spherical particles have a smooth surface and can be easily disaggregated due to the point contact aggregation, practically important for actual particle applications. Furthermore, bulk functions based on the crystal structure, such as magnetic and dielectric properties, can be miniaturized into submicrometer range without losing their bulk functions (Fig. 8.1).

Thus, the functions of unique crystalline spherical submicrometer particles obtained by the PLML process appear promising for various applications. However, a large amount of submicrometer spherical particles are demanded for actual particle property tests and their real applications, though the production rate of laser processing is generally limited due to the small laser beam size and unidirectional energy input. This chapter discusses the approaches for mass production of spherical submicrometer particles by PLML based on the understanding of particle generation process.

## 8.2 Process Parameters Affecting the Productivity

### *8.2.1 Unfocused Laser Irradiation*

A decade ago, spherical submicrometer particles of boron and boron carbide were generated (yield > 90%) based on the PLML process during the experiment of boron nanoparticle fabrication by pulsed laser fragmentation process [11, 12]. A focused laser beam with a low fluence was irradiated onto boron raw nanoparticles dispersed in water or an organic solvent to avoid oxidation, resulting in the formation of spherical submicrometer particles of amorphous B in water via a simple melting process and $B_4C$ in organic solvent via a reactive PLML process.

Subsequently, an unfocused low fluence laser beam instead of a focused high fluence laser beam is irradiated since the required fluence for spherical submicrometer particle formation is one order of magnitude smaller than typical PLAL conditions. Figure 8.2 shows the changes in the fraction of $B_4C$ spherical submicrometer particles produced by the PLML process in an organic solvent as a function of laser irradiation time. The required time for $B_4C$ generation is significantly shortened by unfocused laser irradiation, indicating the production efficiency improvement by enlarging reaction space using an unfocused laser beam. This appears beneficial in the productivity compared with the other laser processing techniques using the focused laser beam, such as PLAL.

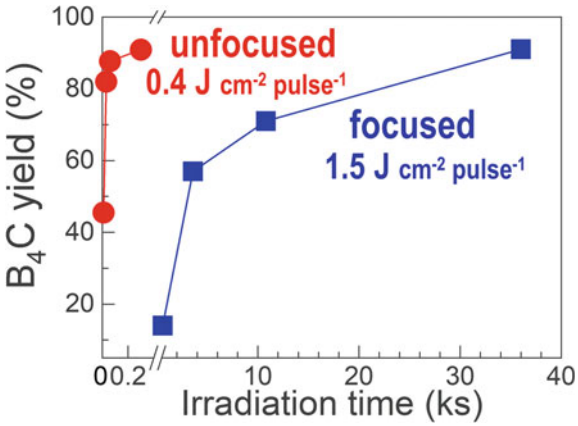


**Fig. 8.2** Temporal yield change for $B_4C$ spherical submicrometer particles by PLML in ethanol from B raw nanoparticles using a focused and unfocused laser beam

### *8.2.2 Requirement of Lasers*

Figure 8.3a shows the relationship between laser pulse energy and pulse frequency for different laser power from 1 W to 1 kW. High-frequency lasers are generally based on the laser diode pumping, and respective laser pulses have smaller energy. In contrast, low-frequency lasers commercially available are operated by flash-lamp pumping with high pulse energy. A suitable laser fluence range for the PLML process is presented as a red rectangle, assuming that the laser beam size is 1 $cm^2$.

Figure 8.3b shows the suitable laser fluence range for the PLML process as a function of pulse energy and beam size. When a low pulse energy laser is used, laser beam may have to be focused for the PLML process to increase the laser fluence,

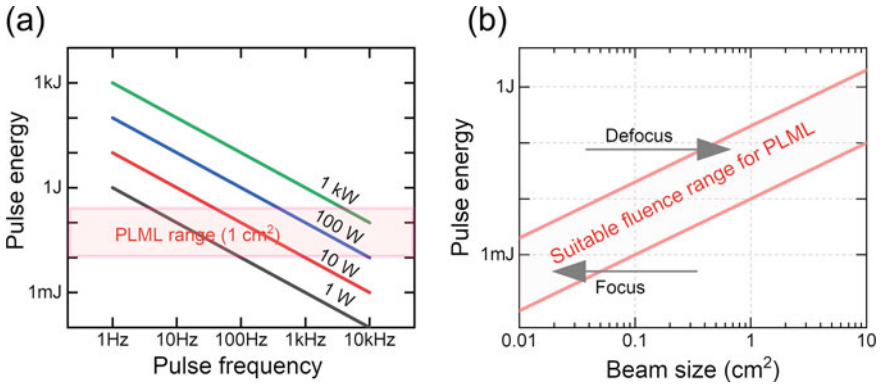


**Fig. 8.3** **a** Relationship between pulse energy and pulse frequency for different power (1 W to 1 kW) of pulsed lasers. A suitable range for PLML is presented in red zone when laser beam size is 1 $cm^2$. **b** A suitable fluence range for PLML process as a function of beam size and pulse energy of pulsed laser.

resulting in the decrease in production rate. For mass production, high pulse power laser is advantageous when used in unfocused or defocused mode to illuminate large area of a liquid containing raw particles.

### *8.2.3 Required Pulse Number*

As explained in Sect. 7.2, the adiabatic assumption well explains the laser fluence conditions for spherical submicrometer particle formation. In this assumption, inter-pulse interaction is ignored for particle melting, and the required fluence to melt a particle is calculated as a single laser pulse event. This indicates that the spherical submicrometer particles are possibly obtained just by single laser pulse irradiation.

To experimentally confirm the required number of laser pulses to obtain spherical particles, micro-batch cell experiments were performed with a fixed-number laser pulse irradiation onto the whole micro-cell filled with diluted boron raw particle suspension (2.5 ppm) to ensure that all particles are irradiated without a shadowing effect [13]. Figure 8.4 shows SEM images of the boron particles irradiated with different numbers of laser pulses in the micro-batch cells, demonstrating that only a few laser pulses yielded spherical particles over 90%.

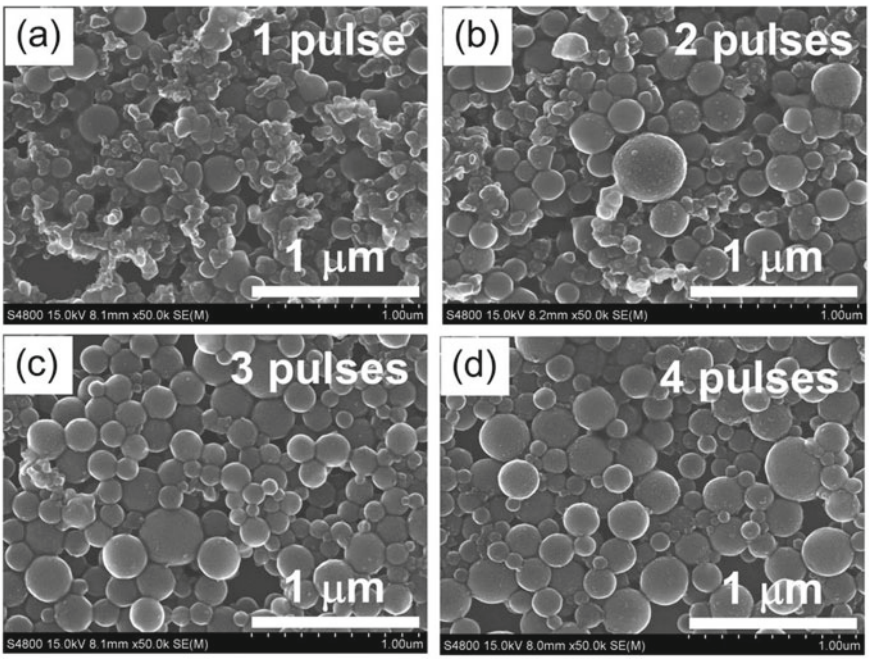


**Fig. 8.4** SEM images of boron particles dispersed in water after the irradiation with various laser pulses in the micro-batch cells. Reprinted from Reference [13]

### 8.2.4 *Effective Depth for Spherical Submicrometer Particle Formation*

Another critical parameter to affect the productivity of spherical submicrometer particles is laser fluence, as discussed in Chap. 7. Even when the applied laser fluence $J_{app}$ is sufficiently larger than the threshold fluence $J_{th}$ for spherical particle formation, the submicrometer particles are only generated in the surface region of the liquid. The fluence gradually decreases from the liquid surface to the liquid inside due to the optical absorption of raw particles dispersed in liquid and becomes lower than the threshold fluence. Effective depth $d_{eff}$ for spherical submicrometer particle formation where the fluence is over the threshold fluence $J_{th}$ is calculated by Eq. (8.1).

$$d_{eff} = \frac{1}{\alpha}\ln\left(\frac{J_{app}}{J_{th}}\right) \tag{8.1}$$

where the absorption coefficient $\alpha$ can be estimated by optical transmittance measurement of raw particle colloidal solution, assuming that liquid medium is homogeneous and that scattering process is negligible. Figure 8.5 demonstrates the procedure to estimate the effective depth for spherical submicrometer particle formation for Ag colloidal solution (200 ppm) as an example. The laser fluence required to fabricate spherical particles was calculated to be 50 mJ pulse$^{-1}$ cm$^{-2}$ for Ag at a wavelength of 355 nm (see Chap. 7). The incident laser fluence was 67 mJ pulse$^{-1}$ cm$^{-2}$ in this experiment. The effective depth estimated from the absorption coefficient obtained by optical transmittance measurement using Eq. (8.1) is 1.1 mm, indicating that spherical submicrometer particles can be generated in the surface layer of 1.1 mm thickness. The effective depth $d_{eff}$ depends on the laser fluence through the $J_{app}$ term; on the material, particle size, and laser wavelength through the $J_{th}$ term; and on the concentration and dispersion of colloidal solution through the absorption coefficient

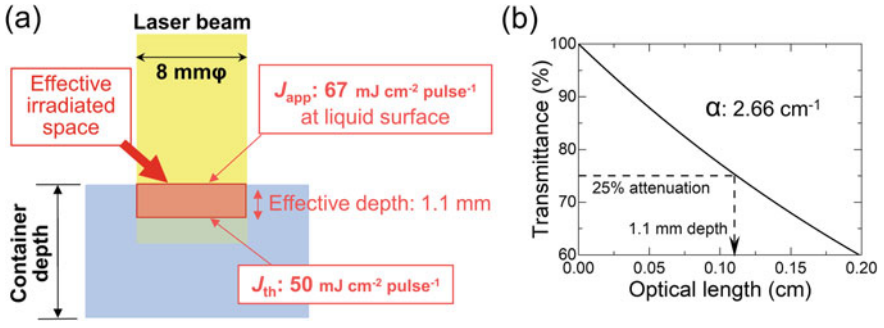


**Fig. 8.5** **a** A schematic illustration of laser irradiation and effective irradiation depth for the PLML process. **b** The procedure to estimate optical length from the photo absorption curve derived from the optical absorption coefficient. Adopted from Chem. Eng. Sci., 219 (2020) 115,580. Copyright 2020, with permission from Elsevier

$\alpha$ term. The $d_{\text{eff}}$ is around 1 mm under the typical experimental conditions smaller than a typical liquid container size for the PLML process.

The decrease in laser fluence along the effective depth could be suppressed by decreasing the suspension concentration. However, it is disadvantageous for mass production because it decreases the throughput per unit time and requires more post-processing treatment, such as condensation or particle collection. In addition, incident angle to the liquid surface or shape of the liquid surface may also affect the effective depth.

Based on these considerations, the best way to increase the productivity is to equally irradiate laser onto all respective particles dispersed in liquid only a few times and reduce the excessive multiple laser irradiation onto all particles as little as possible. The following sections discuss approaches to improve productivity by realizing this requirement separately for the flow and batch processes.

## 8.3 Flow System for Continuous Particle Production by PLML

### *8.3.1 PLAL Versus PLML*

Mass production of nanoparticles by PLAL, using flowing liquid media and scanning of the laser beam on a target, has been intensively studied by Barcikowski's group and recently achieved a production rate of 4 g $h^{-1}$ [14]. This value is much larger than 550 mg $h^{-1}$, the threshold production rate more economical than the typical wet chemical synthesis method for gold nanoparticles [15]. Thus, laser irradiation onto liquid can potentially be a practical particle fabrication technique. However, PLAL generally uses a bulk target, whereas PLML uses particles as a target. Thus, a suitable mass production setup designed for laser irradiation in a PLML process has to be developed.

When a laser beam is irradiated onto a liquid containing raw particles through the walls of the container in a PLML process, the generated submicrometer particles frequently adhere to the inner surface due to the transient high temperature of the particles, interfering with the PLML process through optical absorption of adhered substances. Thus, the open surface of the liquid must be directly irradiated with the laser in the PLML process.

### *8.3.2 Cylindrical Liquid Flow with Low Pulse Energy*

Laser irradiation on a suspension of raw particles flowing at an adequate rate should continuously produce submicrometer spherical particles with a high submicrometer particle formation ratio. Barcikowski et al. attempted high pulse frequency, low pulse

energy laser fragmentation of dispersed particles in a suspension flow [16, 17] and applied this approach to the PLML process [18, 19]. A cylindrical suspension flow (1 mm diameter) with a high flow rate (60 cm $s^{-1}$) and a high-frequency (100 kHz) pulsed laser were used [19]. However, submicrometer spheres were obtained in high yield after repeating laser irradiation 50 times onto flow passage through the system.

PLML processes usually require 10–200 mJ $cm^{-2}$ per pulse for submicrometer particle fabrication [20–22]. Therefore, the laser beam must be focused to a diameter of 0.6 mm or smaller since a typical high-frequency laser has pulse power of ~ 300 μJ. Thus, the beam size is smaller than the diameter of the cylindrical suspension flow in this experimental setup for PLML mass production, resulting in the multiple flow passage irradiation.

### *8.3.3 Cylindrical Liquid Flow with High Pulse Energy*

High pulse energy, low pulse frequency laser (532 nm, 30 Hz, 8 ns pulse width) instead of low pulse energy laser were irradiated on cylindrical suspension flow released from a Pasteur pipette (1.4 mm in inner diameter), aiming for eliminating the mismatch in laser irradiation area with high fluence for the PLML. Deionized water dispersed with raw B nanoparticles (0.2 g $L^{-1}$) flowed from the pipette nozzle into free space.

Figure 8.6a, b presents the appearances of downward suspension flow just after being released from a Pasteur pipette [13]. Due to surface tension, a liquid flow ejected as a laminar jet from a tube nozzle into free space at a low flow rate (0.29 mL $s^{-1}$) transforms into a drip flow (Fig. 8.6a). Droplets generated in a drip flow by this morphological change were 3–5 mm in size (larger than the diameter of the laminar jet) and released from the pipette nozzle tip at 0.33 s intervals. In contrast, when liquid flow is ejected as a laminar jet at a high flow rate (0.73 mL $s^{-1}$), the continuous flow (Fig. 8.6b) was observed.

Figure 8.6c, d presents SEM images of produced particles by only one passage of the flow tube obtained at respective conditions. The drip flow (Fig. 8.6a) was irradiated just below the tip of the pipette nozzle by the unshaped laser beam (diameter: 8 mm) at 300 mJ $cm^{-2}$ $pulse^{-1}$. Due to the large size of droplets, the laser fluence within the droplet is significantly reduced, and spherical particles were rarely observed (Fig. 8.6 c). For irradiating the liquid continuous film flow (Fig. 8.6 b), the laser beam was shaped into a line beam (2 or 3 mm wide, 30 mm long) by cylindrical lenses and also irradiated at 300 mJ $cm^{-2}$ $pulse^{-1}$. The obtained particles were not well converted to spheres by a single passage through the capillary tube (Fig. 8.6 d).

Continuous flow is beneficial for the constant generation of submicrometer particles, though a higher flowing rate is necessary to have stable continuous laminar cylindrical flow. However, all raw particles may not be irradiated by laser pulses at a higher flow rate during the flow tube passage. Furthermore, the 1.4 mm diameter of cylindrical liquid flow is thicker than the effective depth in this case. Thus, the

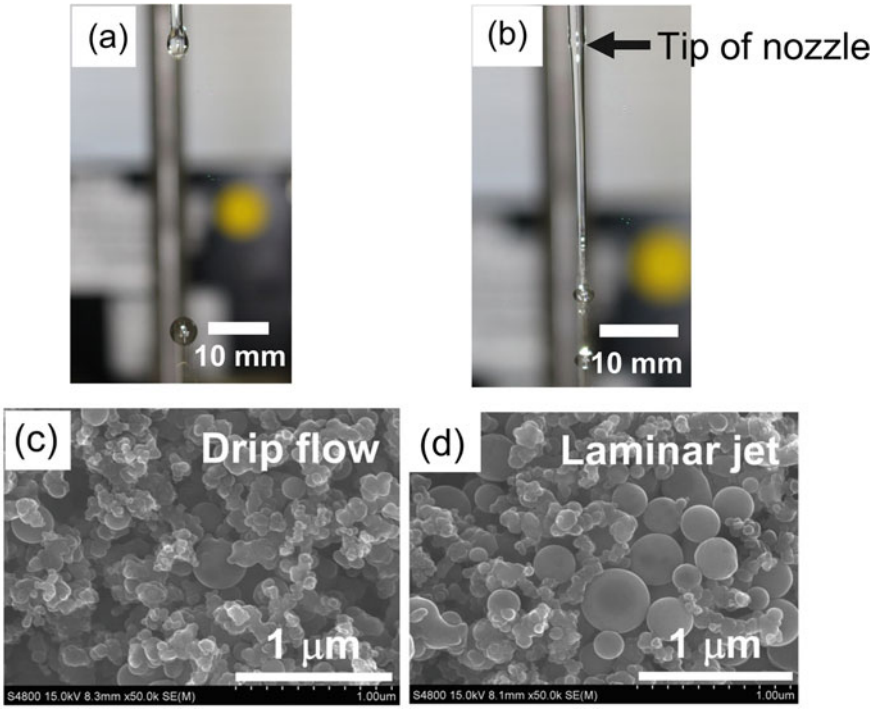


**Fig. 8.6** **a** A drip flow at 0.29 mL $s^{-1}$ and **b** a laminar jet at 0.73 mL $s^{-1}$ using a Pasteur pipette nozzle with an inner nozzle diameter of 1.4 mm. SEM images of boron particles after laser irradiation of boron suspension by single liquid flow passage through the Pasteur pipette nozzle. **c** at 0.29 ml $s^{-1}$ volume flow rate in drip flow, and **d** at 0.73 mL $s^{-1}$ volume flow rate in a laminar jet. Reprinted from Reference [13]

fraction of particles in liquid flow is not irradiated by a laser with sufficient fluence for spherical particle formation.

### *8.3.4 Thin Liquid Film Flow with High Pulse Energy*

Thin liquid flow with a stable low flow rate is advantageous for efficient spherical particle production. For this purpose, a new slit nozzle to guide thin liquid flow is developed (Fig. 8.7) [13]. The liquid film guided by the 30 mm long slit (1 mm or 1.5 mm gap) made of quartz was entirely irradiated with a line-shaped laser beam during a single passage of the flow.

Figure 8.8 presents the appearances of developed slit-guided liquid flow at 0.29 mL $s^{-1}$ and 0.73 mL $s^{-1}$ and corresponding SEM images of particles obtained by laser irradiation under PLML conditions by only one passage in the slit flow. SEM images indicate that particles released from the slit nozzle are mainly spherical

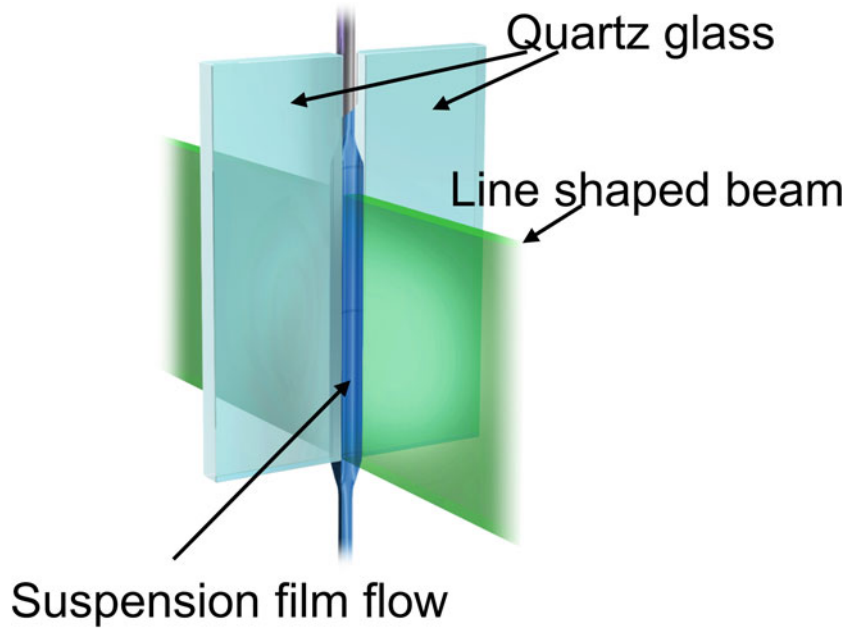


**Fig. 8.7** Schematic illustration of a developed slit nozzle. Reprinted from Ref. [13]

particles. Thus, the liquid film flow guided by the slit nozzle is more advantageous for spherical particle formation than cylindrical suspension flow into free space. This is owing to the shortened thickness of the produced liquid film in the slit nozzle. The concept of thin film liquid flow is extended to the pulsed laser fragmentation process [23].

### *8.3.5 Flow Rate Dependence and Yield*

Figure 8.9 presents the irradiated average pulse numbers by one passage through the slit-guided nozzle and spherical particle formation ratios for various volume flow rates. The irradiated average pulse numbers were larger than the two pulses at 0.20 mL $s^{-1}$ and 0.29 mL $s^{-1}$ volume flow rates. Therefore, the spherical particle ratios exceeded 90% after a single liquid flow passage through the slit nozzle. Thus, the slit nozzle is advantageous compared with the cylindrical liquid flow since the slit nozzle can generate non-droplet continuous liquid flow even at a low flow rate. At 0.37 mL $s^{-1}$, the spherical particle ratio decreased to 63% due to the decrease in the received average pulse numbers.

The spherical particle yield was evaluated to be 195 mg $h^{-1}$ at a suspension volume flow rate of 0.29 mL $s^{-1}$ (1 mm wide, 1 mm thick slit nozzle) by extrapolating the data from the 20 mL suspension. Furthermore, the high spherical particle ratio

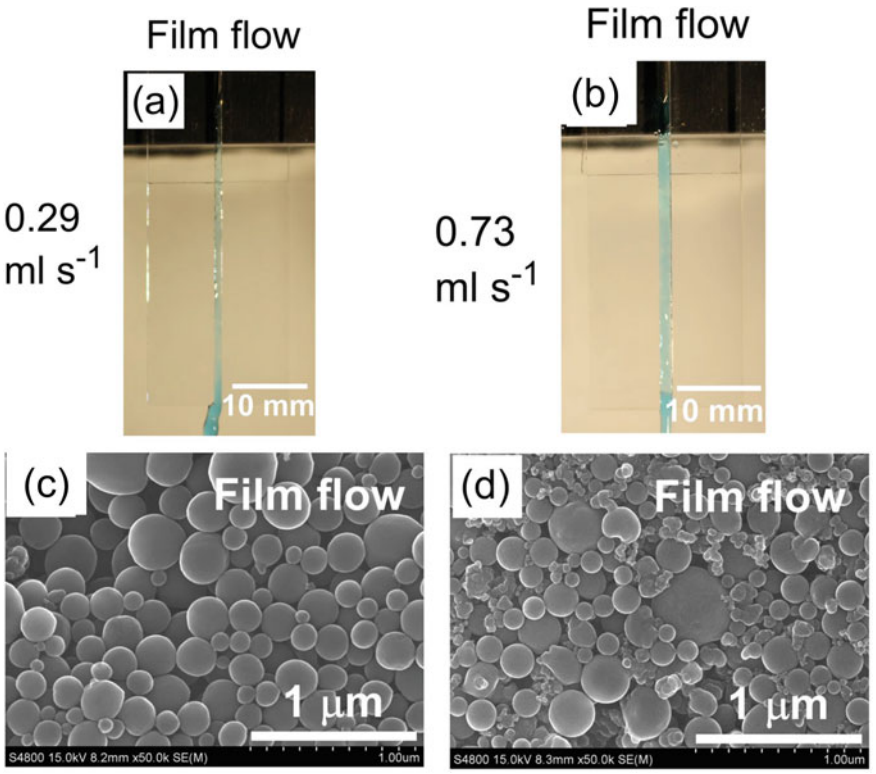


**Fig. 8.8** Liquid flows of the slit nozzle at different volume flow rates at **a** 0.29 mL $s^{-1}$ and **b** 0.73 mL $s^{-1}$. Flows were visualized by methylene blue aqueous solution. SEM images of boron particles obtained by laser irradiation through the slit nozzle at the volume flow rate of **c** 0.29 mL $s^{-1}$, and **d** 0.73 mL $s^{-1}$. Reprinted from Ref. [13]

and high yield by irradiation through single passage flow were confirmed using the unique continuous slow flow realized by the slit nozzle. Thus, laser irradiation of a suspension film flowing through this new slit nozzle is promising for mass production by PLML.

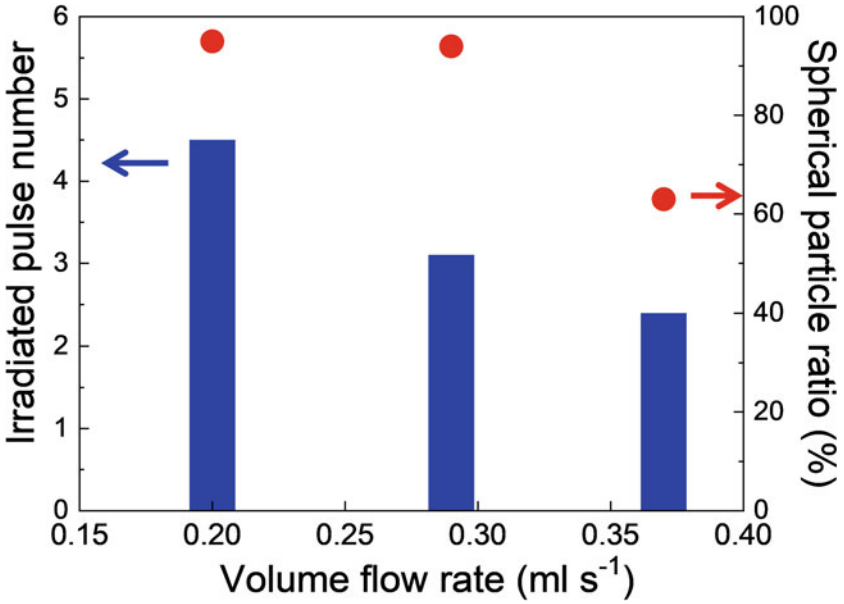


**Fig. 8.9** Relationship of irradiated average pulse number (blue bars) and spherical particle ratios (red dots) at various volume flow rates of boron suspension through the 1 mm wide, 1 mm thick slit nozzle. Reprinted from Ref. [13]

## 8.4 Controlled Pulse Number Irradiation in Flow System for PLML Process Analysis

### *8.4.1 Controlled Pulse Number Irradiation by Viscosity Change*

Randomly shaped raw particles in a liquid flow were irradiated through the developed slit nozzle, resulting in a 95% spherical particle formation ratio with only single passage irradiation (Sect. 8.3) [13]. This means that controlled number of pulses can be used to irradiate most particles passing through the slit nozzle. As a result, the slit nozzle, which was originally designed for mass production, can be used to deduce detailed PLML mechanisms, such as particle shape modification and chemical reduction process from the product analysis.

Raw cube-shaped $Fe_3O_4$ powder with 200 nm in diameter (0.1 g $L^{-1}$) was suspended in deionized water and aqueous solution of glycerol mass-30% or -60% to control the flow rate by viscosity change. The suspension flow through the slit nozzle generated a liquid film flow guided by the slit nozzle. The liquid film flow was irradiated by a Nd:YAG laser (wavelength: 532 nm, pulse frequency: 30 Hz, pulse width: 8 ns) at 300 mJ $cm^{-2}$ $pulse^{-1}$. Figure 8.10 shows SEM images of (a) raw $Fe_3O_4$ particles and particles obtained by irradiation onto suspensions of (b) deionized water,

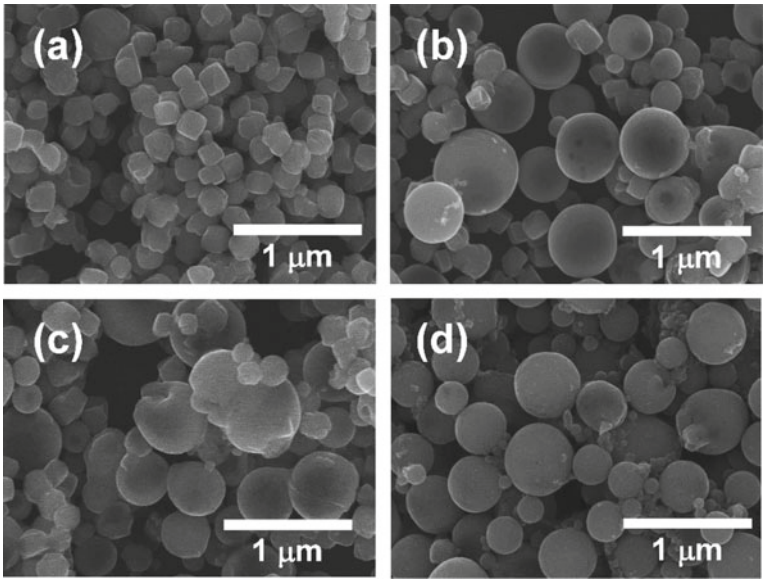


**Fig. 8.10** SEM images of **a** raw $Fe_3O_4$ particles and particles obtained by irradiation of a suspension of **b** deionized water and a **c** 30 wt % and **d** 60 wt % aqueous solution of glycerol with a single passage through the slit nozzle. Reprinted with permission from Reference [24]. Copyright 2019 American Chemical Society

aqueous glycerol solution at (c) mass-30%, and (d) mass-60% passing through the slit nozzle only one passage [24]. Most particles were converted to spherical particles (conversion rate: 92%) in aqueous glycerol solution at mass-60%, although many unconverted raw particles were observed in deionized water and aqueous glycerol solution at mass-30%.

According to the linear flow rate measurements by high-speed particle tracking and the numerical analysis of flow rate distribution in the slit nozzle, irradiated pulse number distribution of the particles during one passage of the slit nozzle can be calculated. Figure 8.11 presents cumulative frequencies of irradiated pulse number of individual particles through the slit nozzle with one passage for the deionized water suspension and the 60 wt % aqueous glycerol solution suspension. The irradiating pulse number is narrow-ranged, suggesting that step-by-step laser irradiation by a few pulses is possible. However, the suspension viscosity may affect the cross-sectional liquid film shape (Fig. 8.12), reducing the conversion efficiency when the film thickness is larger than the effective depth.

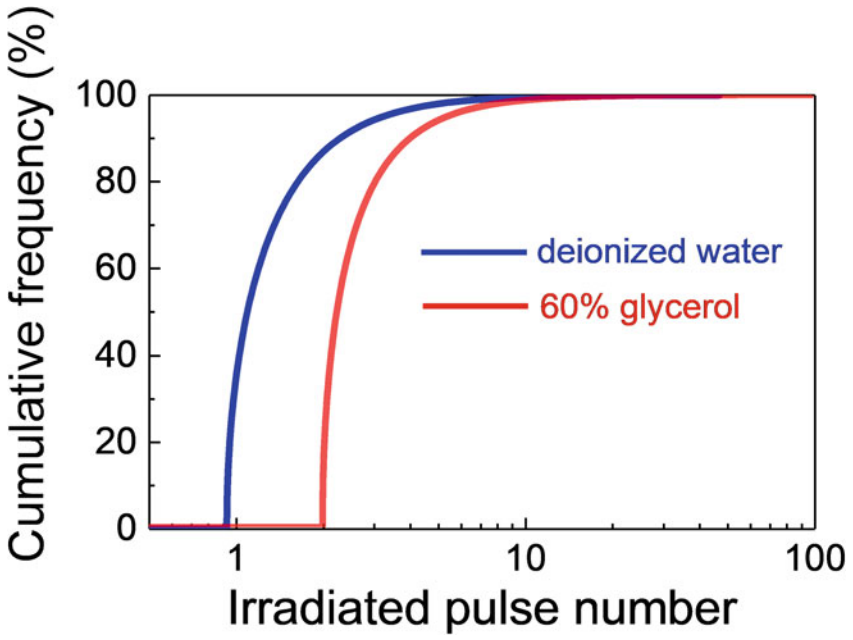


**Fig. 8.11** Numerically calculated cumulative frequencies of irradiated pulse number of particles through the slit nozzle. Reprinted with permission from Ref. [24]. Copyright 2019 American Chemical Society

### *8.4.2 PLML Process Analysis by Controlled Pulse Number Irradiation*

PLML process analysis by laser irradiation using conventional batch cells was difficult due to uncontrolled and broad pulse numbers irradiated on the particles. However, the number of irradiating pulses during the slit nozzle passage could be precisely controlled by altering experimental conditions such as volume flow rate, suspension viscosity, and slit nozzle dimensions. This enables tracing phenomena with every specific pulse irradiation and clarifying the detailed mechanism of PLML.

Figure 8.13 shows SEM images of irradiated $Fe_3O_4$ particles in 60% aqueous glycerol solution suspension through the slit nozzle (a) one passage and (c) four passages. Particles with dark contrast at the center were frequently observed in particles after one passage flow, suggesting that these particles have low-density structures inside. Figure 8.13 also shows corresponding SEM images of cross sections (b) from (a) and (d) from (c) obtained by a focused ion beam processing of particles. Hollow particles were formed at the initial laser irradiation stage. The formed voids in hollow spherical particles are gradually excluded from the melted droplet by repetitive pulse irradiation.

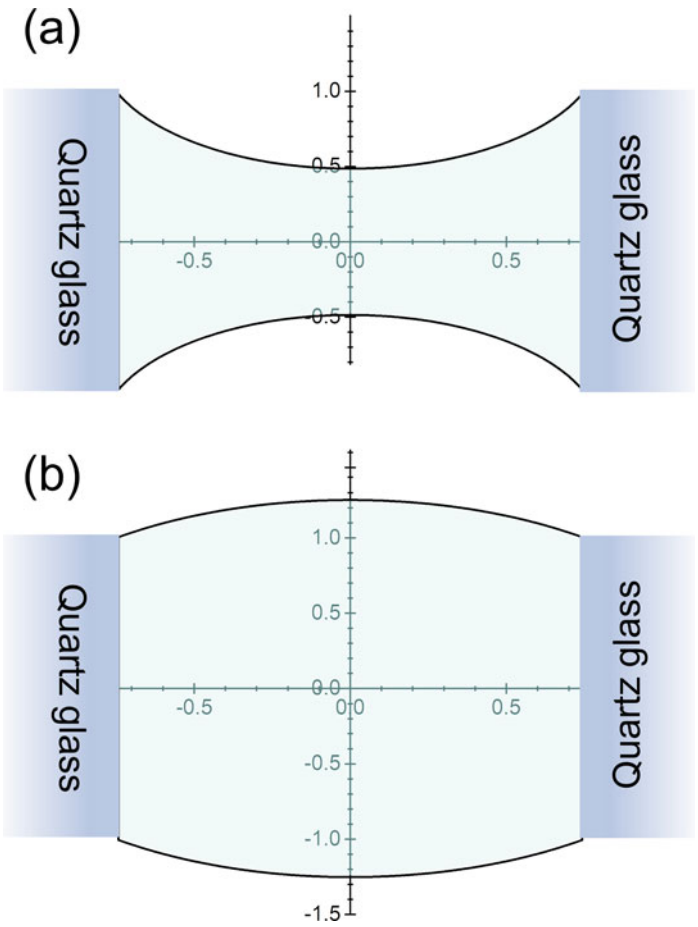


**Fig. 8.12** Cross-sectional figures of film flow calculated numerically on the basis of the linear flow rate distribution for **a** a deionized water suspension and **b** 60 wt % glycerol aqueous solution suspension. Adopted with permission from Reference [24]. Copyright 2019 American Chemical Society

Figure 8.14 shows XRD patterns of particles before and after irradiation in 60% aqueous glycerol solution suspension at various flow passages. FeO peaks gradually appeared as the number of passages increased, as previously reported [25]. While the raw particle shape conversion took 2 to 3 pulses of irradiation, the reduction of $Fe_3O_4$ to FeO took longer, probably due to the interface reduction reaction between the melted particle and pyrolyzed gas species, as well as diffusion of oxygen from the inside to the interface [21, 26].

Thus, flow type irradiation using the slit nozzle enables detailed pulse-by-pulse observation of the spherical particle formation process, especially in the earlier stages of spherical particle formation. Furthermore, by changing the viscosity of the liquid,

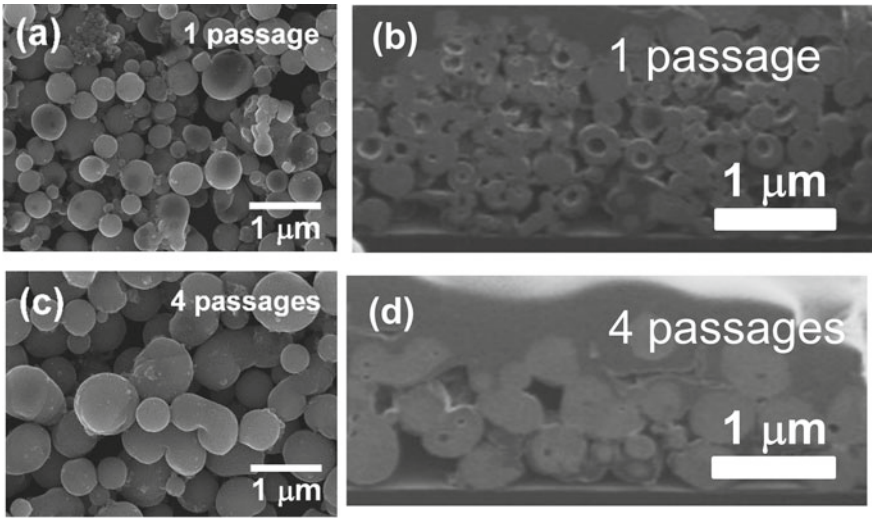


**Fig. 8.13** SEM images of $Fe_3O_4$ particles suspended in 60 wt % glycerol aqueous solution and irradiated through the slit nozzle for **a** one and **c** four passages. Corresponding SEM images of cross sections of $Fe_3O_4$ particles irradiated with **b** one and **d** four passages and cut out with focused ion beam. Reprinted with permission from Reference [24]. Copyright 2019 American Chemical Society

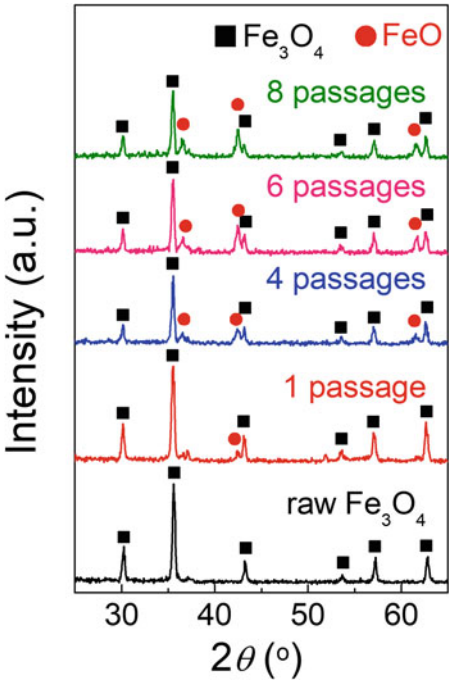


**Fig. 8.14** XRD patterns of raw $Fe_3O_4$ and particles obtained with various number passage irradiation in 60% glycerol aqueous solution. Reprinted with permission from Ref. [24]. Copyright 2019 American Chemical Society

the highest spherical particle formation ratio 92% and spherical particle productivity 361 mg $h^{-1}$ were simultaneously achieved in the glycerol mass-60% aqueous solution suspension of $Fe_3O_4$ (0.1 g $L^{-1}$) at 1.1 mL $s^{-1}$ volume flow rate with single flow passage.

## 8.5 Batch-Type Iterative Particle Production

### *8.5.1 Advantages and Disadvantages of PLML Batch Process*

Over 90% of raw particles can be converted to spherical submicrometer particles with just a few laser pulses during a single passage of the liquid film flow guided by a slit nozzle, as explained in Sect. 8.3. However, a small number of laser pulses is insufficient to grow spherical submicrometer particles through a chemical reaction between the particles and liquid, such as the formation of FeO particles from $Fe_3O_4$ particles in ethanol [25], as explained in Sect. 8.4.2. In such cases, batch-type laser irradiation is practically feasible to fabricate submicrometer particles through the PLML process by irradiating plural laser pulses for high-temperature chemical reactions.

To irradiate laser pulses by plural times onto most of the particles dispersed in a liquid vessel, laser pulse frequency can be a simple parameter to reduce the total irradiation time and increase the production rate by the PLML process. Figure 8.15 presents the SEM images of ZnO particles after laser irradiation using the same pulses with different laser pulse frequencies [27]. Up to 200 Hz, spherical submicrometer particles were generated, and the production rate is proportionally increased with the pulse frequency. However, when the pulse frequency is over 200 Hz, particles with smaller sizes were simultaneously generated, suggesting that the particles are partially vaporized by overheating the particles. This is possibly due to the heat accumulation in the surrounding liquid and a short inter-pulse cooling time.

To achieve a high conversion rate of irradiated particles in the vessel, the PLML batch process requires stirring process and a long irradiation time to compensate the short effective depth for spherical submicrometer particle fabrication. Thus, to ensure that all particles suspended in the batch vessel are converted to spherical particles, the vessel is irradiated by an excessive number of laser pulses.

### *8.5.2 Numerical Simulation of PLML Batch Process*

Figure 8.16 presents a schematic of the cell configuration and the parameters used to quantitatively calculate spherical particle formation efficiency in the batch process [28]. $f = V_c / V_i$ where $V_c$ is the total liquid volume in a container, and $V_i$ is the laser-irradiated volume in the batch cell derived from the effective depth discussed in

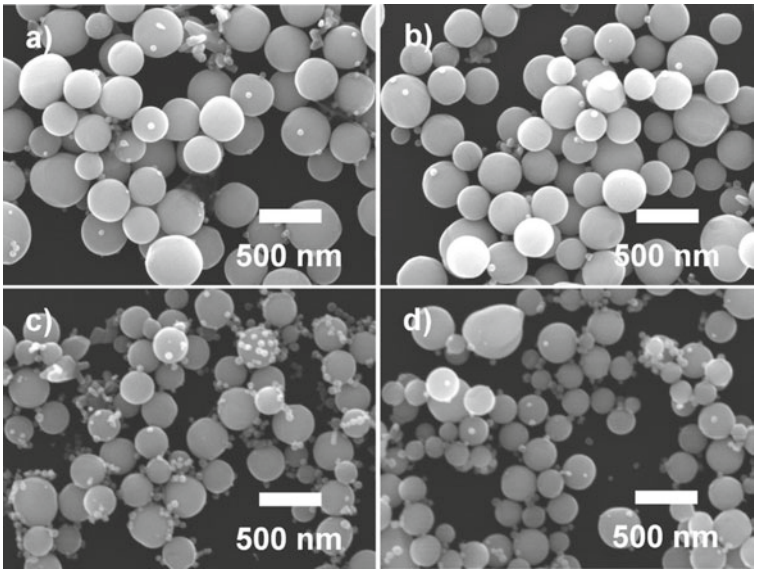


**Fig. 8.15** SEM images of obtained ZnO particles irradiated with a KrF excimer laser irradiation at a laser fluence of 182 mJ pulse$^{-1}$ cm$^{-2}$ by 48 000 pulses. Pulse frequencies are **a** 25 Hz, **b** 200 Hz, **c** 400 Hz, and **d** 800 Hz. Reprinted from [27], Copyright 2018, with permission from Elsevier

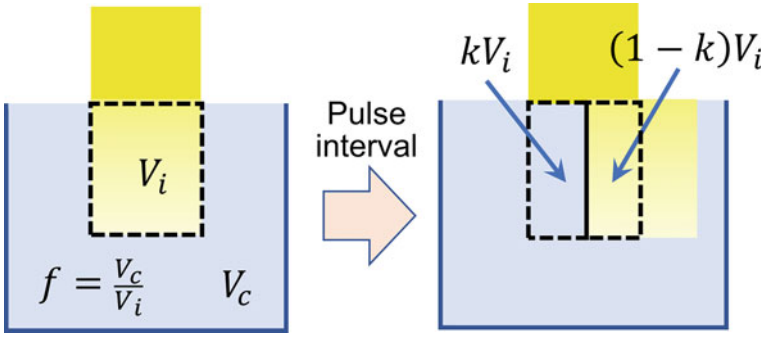


**Fig. 8.16** Schematic images of the cell configuration and the parameters used to calculate formation rates. $V_c$ is the total liquid volume in a container. $V_i$ is the laser-irradiated volume in the batch cell, which depends on the concentration and absorption efficiency of the raw particles. $k$ is the laser-irradiated volume exchange ratio of the pulse interval. Reprinted from [28], Copyright 2020, with permission from Elsevier

Sect. 8.2.4, which depends on the laser fluence and the concentration and absorption efficiency of the raw particles. When raw particle concentration is high, $V_i$ decreases, and hence, $f$ increases. $k$ is the exchange ratio of laser-irradiated volume during the pulse interval depending on stirrer condition and liquid viscosity.

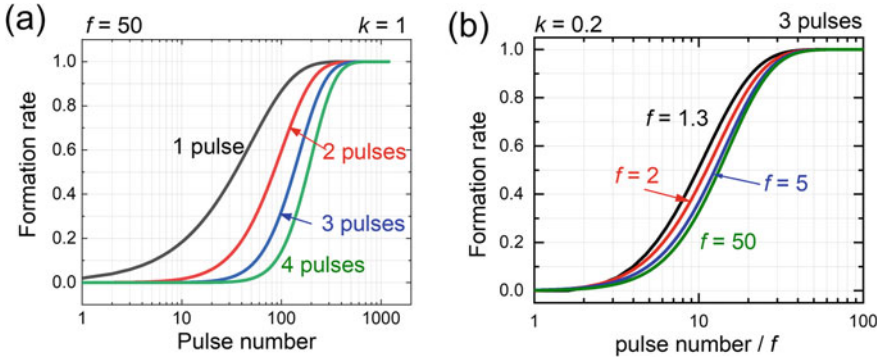


**Fig. 8.17** Simulated calculation results for the PLML process. **a** Change in the formation rate as a function of pulse number when $k = 1$ (complete mixing) and $f = 50$. **b** The liquid volume effect on the spherical particle formation rate when the laser-irradiated volume exchange ratio is $k = 0.2$, the number of pulses required for spherical particle formation is 3, and the effective irradiation space is constant. Reprinted from [28], Copyright 2020, with permission from Elsevier

Figure 8.17a shows the changes in conversion rates to spherical particles as a function of pulse number when $k = 1$ (complete mixing) and $f = 50$ (a typical value in a batch cell). If only a few laser pulses were required to convert a raw aggregate to a submicrometer particle, approximately 600 pulses (1 min for a 10 Hz laser) were sufficient to convert all of the particles, though several tens of minutes were generally required to convert over 90% in yields. This suggests $k < 1$ (incomplete mixing), and the actual $k$ value can be roughly estimated from the experiment data to be $k = 0.2$ under a typical liquid cell condition ($f = 50$). Figure 8.17b shows the effect of liquid volume on the particle formation rate when $k = 0.2$, and three pulses were required for particle formation. If the complete mixing is true ($k = 1$), the pulse number for conversion proportionally increases with the liquid volume increase, and all curves in Fig. 8.17(b) overlap. However, Fig. 8.17b presents that the curves shift toward the large pulse number side with the liquid volume increase. This is due to the extra laser pulses required to compensate for the incomplete mixing of a large liquid volume. Thus, owing to the thin-layer reaction region (thin effective depth) in the optical process and incomplete mixing in the liquid container during pulse interval, a small liquid volume cell (small $f$) with a smaller number of laser pulses is efficient in fabricating submicrometer particles.

### *8.5.3 Automated Iterative Batch Process for PLML Process*

The calculated results suggested that automated iterative short-term laser irradiation with a small volume of the raw particle suspension would be more efficient for mass production than large cells if a liquid container exchange was performed as quickly as possible. The estimated production rate under these conditions was 5.15 mg $h^{-1}$.

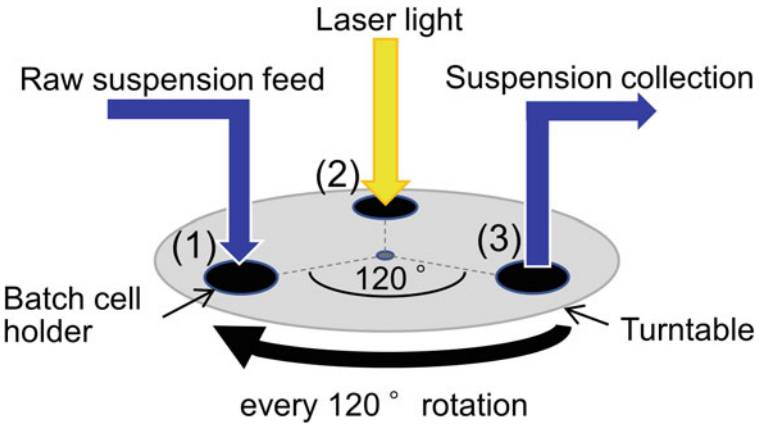


**Fig. 8.18** Schematic illustration of a developed automated iterative batch system for the production of submicrometer spherical particles, consisting of a circular turntable with three spots for batch cell holders located at 120° intervals, with a raw suspension feed, a laser irradiation spot, and a suspension collection port. Reprinted from [28], Copyright 2020, with permission from Elsevier

Thus, an automated iterative batch system for the production of submicrometer spherical particles is developed as illustrated in Fig. 8.18, consisting of a circular turntable with three spots for batch cell holders located at 120° intervals, with a raw suspension feed, a laser irradiation spot, and a suspension collection port. However, the system with too small cells had difficulty in stirring during processing, and therefore, the cell size should be at least ~3 $cm^3$.

## 8.6 Summary

Submicrometer particles obtained by PLML are spherical, crystalline, and show great promise in a variety of applications. However, mass production by laser process is difficult due to the fine laser beam and unidirectional energy input. PLML can use unfocused laser beams and appears to be suitable for mass production, though actual industrial use will necessitate a further increase in production rate. The laser specifications and a liquid dispersed with raw particles are relevant to PLML productivity. In the case of lasers, a single laser pulse must melt particles efficiently, so the laser pulse energy should be several tens to hundreds of mJ $cm^{-2}$ $pulse^{-1}$. Therefore, the nanosecond pulsed laser with low pulse frequency (10–200 Hz) is preferable, and high pulse frequency (~MHz) laser is not suitable. Furthermore, the applied laser fluence gradually decreases from the surface to the interior of the liquid by the optical absorption of raw particles. The effective depth with sufficient laser fluence for the PLML process is typically around 1 mm and must be well considered to increase productivity.

As an efficient flow system for PLML, a guided slit flow nozzle for a continuous flow system is developed. This nozzle generates a thin film flow close to the effective depth for spherical submicrometer particle fabrication. The spherical particle ratios exceeded 90% after a single liquid flow passage through the slit nozzle. The slit nozzle can also be utilized to analyze the initial particle formation process from the pulse-to-pulse product variation. As an efficient batch system for PLML, an automated iterative batch processing system is developed utilizing thin-layered small cells (equivalent to the effective depth) with a small number of laser pulse irradiation and frequent automatic cell exchange.

Thus, the method to increase the productivity of the PLML process is examined. The production yield now approaches the practical level by an appropriate design of laser irradiation system by adopting the concept of the effective depth for spherical submicrometer particle fabrication. Laser specification design with high pulse power further improves the productivity of spherical submicrometer particles.

## References


1. Y. Li, T. Sasaki, Y. Shimizu, N. Koshizaki, Hexagonal-Close-Packed, Hierarchical Amorphous $TiO_2$ Nanocolumn Arrays: Transferability, Enhanced Photocatalytic Activity, and Superamphiphilicity without UV Irradiation. J. Am. Chem. Soc. **130**, 14755–14762 (2008). https://doi.org/10.1021/ja805077q
2. P. Murugavel, M. Kalaiselvam, A.R. Raju, C.N.R. Rao, Sub-micrometre spherical particles of $TiO_2$, $ZrO_2$ and PZT by nebulized spray pyrolysis of metal–organic precursors. J. Mater. Chem. **7**, 1433–1438 (1997). https://doi.org/10.1039/A700301C
3. T. Kojima, T. Baba, K. Ota, C. Yukita, K. Inamoto, N. Uekawa, Preparation of porous titania particles by partial dissolution and heat treatment of hydrous titania. J. Ceram. Soc. Jpn. **124**, 1226–1228 (2016). https://doi.org/10.2109/jcersj2.16208
4. R.L. Dong, S.Y. Liu, Z.Y. Li, Z.D. Chen, H.P. Zhang, $TiO_2$ microspheres with variable morphology, size and density synthesized by a facile emulsion-mediated hydrothermal process. Mater. Lett. **123**, 135–137 (2014). https://doi.org/10.1016/j.matlet.2014.03.008
5. H. Fujiwara, R. Niyuki, Y. Ishikawa, N. Koshizaki, T. Tsuji, K. Sasaki, Low-threshold and quasi-single-mode random laser within a submicrometer-sized ZnO spherical particle film, Appl. Phys. Lett., 102 (2013) 061110. https://doi.org/10.1063/1.4792349
6. H. Wang, M. Miyauchi, Y. Ishikawa, A. Pyatenko, N. Koshizaki, Y. Li, L. Li, X. Li, Y. Bando, D. Golberg, Single-crystalline rutile $TiO_2$ hollow spheres: room-temperature synthesis, tailored visible-light-extinction, and effective scattering layer for quantum dot-sensitized solar cells. J. Am. Chem. Soc. **133**, 19102–19109 (2011). https://doi.org/10.1021/ja2049463
7. T. Tsuji, H. Yoshitomi, Y. Ishikawa, N. Koshizaki, M. Suzuki, J. Usukura, A method to selectively internalise submicrometer boron carbide particles into cancer cells using surface transferrin conjugation for developing a new boron neutron capture therapy agent. J. Exp. Nanosci. **15**, 1–11 (2019). https://doi.org/10.1080/17458080.2019.1692178
8. G.C. Papaefthymiou, Nanoparticle magnetism. Nano Today **4**, 438–447 (2009). https://doi.org/10.1016/j.nantod.2009.08.006
9. X. Hu, H. Gong, Y. Wang, Q. Chen, J. Zhang, S. Zheng, S. Yang, B. Cao, Laser-induced reshaping of particles aiming at energy-saving applications. J. Mater. Chem. **22**, 15947–15952 (2012). https://doi.org/10.1039/c2jm32041j
10. D. Vollath, Nanomaterials: An Introduction to Synthesis, Properties and Applications, 2nd Edition. 2013: Wiley.

11. Y. Ishikawa, Y. Shimizu, T. Sasaki, N. Koshizaki, Boron carbide spherical particles encapsulated in graphite prepared by pulsed laser irradiation of boron in liquid medium, Appl. Phys. Lett., 91 (2007) 161110. https://doi.org/10.1063/1.2799786
12. Y. Ishikawa, Q. Feng, N. Koshizaki, Growth fusion of submicron spherical boron carbide particles by repetitive pulsed laser irradiation in liquid media. Appl. Phys. A **99**, 797–803 (2010). https://doi.org/10.1007/s00339-010-5745-6
13. Y. Ishikawa, N. Koshizaki, Guided Slow Continuous Suspension Film Flow for Mass Production of Submicrometer Spherical Particles by Pulsed Laser Melting in Liquid. Sci. Rep. **8**, 14208 (2018). https://doi.org/10.1038/s41598-018-32528-6
14. P. Wagener, A. Schwenke, B.N. Chichkov, S. Barcikowski, Pulsed Laser Ablation of Zinc in Tetrahydrofuran: Bypassing the Cavitation Bubble. J. Phys. Chem. C **114**, 7618–7625 (2010). https://doi.org/10.1021/jp911243a
15. R. Streubel, G. Bendt, B. Gökce, Pilot-scale synthesis of metal nanoparticles by high-speed pulsed laser ablation in liquids, Nanotechnology, 27 (2016) 205602. https://doi.org/10.1088/0957-4484/27/20/205602
16. P. Wagener, S. Barcikowski, Laser fragmentation of organic microparticles into colloidal nanoparticles in a free liquid jet. Appl. Phys. A **101**, 435–439 (2010). https://doi.org/10.1007/s00339-010-5814-x
17. S. Siebeneicher, F. Waag, M. Escobar Castillo, V.V. Shvartsman, D.C. Lupascu, B. Gokce, Laser Fragmentation Synthesis of Colloidal Bismuth Ferrite Particles, Nanomaterials, 10 (2020) 359. https://doi.org/10.3390/nano10020359.
18. M. Lau, S. Barcikowski, Quantification of mass-specific laser energy input converted into particle properties during picosecond pulsed laser fragmentation of zinc oxide and boron carbide in liquids. Appl. Surf. Sci. **348**, 22–29 (2015). https://doi.org/10.1016/j.apsusc.2014.07.053
19. D.S. Zhang, M. Lau, S.W. Lu, S. Barcikowski, B. Gökce, Germanium Sub-Microspheres Synthesized by Picosecond Pulsed Laser Melting in Liquids: Educt Size Effects. Sci. Rep. **7**, 40355 (2017). https://doi.org/10.1038/srep40355
20. A. Pyatenko, H. Wang, N. Koshizaki, T. Tsuji, Mechanism of pulse laser interaction with colloidal nanoparticles. Laser Photonics Rev. **7**, 596–604 (2013). https://doi.org/10.1002/lpor.201300013
21. A. Pyatenko, H. Wang, N. Koshizaki, Growth Mechanism of Monodisperse Spherical Particles under Nanosecond Pulsed Laser Irradiation. J. Phys. Chem. C **118**, 4495–4500 (2014). https://doi.org/10.1021/jp411958v
22. Y. Ishikawa, N. Koshizaki, A. Pyatenko, N. Saitoh, N. Yoshizawa, Y. Shimizu, Nano- and Submicrometer-Sized Spherical Particle Fabrication Using a Submicroscopic Droplet Formed Using Selective Laser Heating. J. Phys. Chem. C **120**, 2439–2446 (2016). https://doi.org/10.1021/acs.jpcc.5b10691
23. S. Zerebecki, S. Reichenberger, S. Barcikowski, Continuous-Flow Flat Jet Setup for Uniform Pulsed Laser Postprocessing of Colloids. J. Phys. Chem. A **124**, 11125–11132 (2020). https://doi.org/10.1021/acs.jpca.0c08787
24. Y. Ishikawa, N. Koshizaki, S. Sakaki, Spherical Particle Formation Mechanism in Pulsed Laser Melting in Liquid under Controlled-Pulse-Number Irradiation using a Slit Nozzle Flow System. J. Phys. Chem. C **123**, 24934–24942 (2019). https://doi.org/10.1021/acs.jpcc.9b06949
25. Y. Ishikawa, N. Koshizaki, A. Pyatenko, Submicrometer-Sized Spherical Iron Oxide Particles Fabricated by Pulsed Laser Melting in Liquid. Electr. Commun. Jpn. **99**, 37–42 (2016). https://doi.org/10.1002/ecj.11898
26. K. Suehara, R. Takai, Y. Ishikawa, N. Koshizaki, K. Omura, H. Nagata, Y. Yamauchi, Reduction Mechanism of Transition Metal Oxide Particles in Thermally Induced Nanobubbles by Pulsed Laser Melting in Ethanol. ChemPhysChem **22**, 675–683 (2021). https://doi.org/10.1002/cphc.202001000
27. S. Sakaki, H. Ikenoue, T. Tsuji, Y. Ishikawa, N. Koshizaki, Influence of pulse frequency on synthesis of nano and submicrometer spherical particles by pulsed laser melting in liquid. Appl. Surf. Sci. **435**, 529–534 (2018). https://doi.org/10.1016/j.apsusc.2017.10.235

28. R. Takai, N. Koshizaki, Y. Ishikawa, Y. Hakuta, Automated iterative batch processing of submicrometer spherical particles by pulsed laser melting in liquid, Chem. Eng. Sci., 219 (2020) 115580. https://doi.org/10.1016/j.ces.2020.115580

# Chapter 9
# Material Processing for Colloidal Silicon Quantum Dot Formation


**Toshihiro Nakamura**

**Abstract** Semiconductor quantum dot is a nanoparticle-based future building block for optoelectronics because of quantum confinement-induced exotic optical properties such as a size-dependent luminescence color. Among the semiconductor quantum dots, silicon quantum dot has striking features, not like compound semiconductor-based quantum dots such as cadmium selenide dots, non-toxicity, earth abundancy, and scalability in the production of the raw material originating from silicon-industrial technology. In particular, solution dispersible colloidal silicon dot has been paid much attention due to demands in novel solution-based electronic devices. In this chapter, it is reviewed that processing for fragmentation induced formation of luminescent colloidal silicon quantum dots from condensed silicon targets including bulk silicon, quantum dots-embedded silica matrix, and porous silicon. A wide variety of processing such as pulsed laser irradiation, mechanical fragmentation, chemical etching, and low-temperature heat treatments are employed to fragmentate the silicon targets. The present review highlights the features of the processing, the production yields: and luminescence properties of colloidal dots, revealing the advantages of each processing to develop future industrial production system of silicon dots for applying practical electronic devices.

**Keywords** Luminescence · Laser processing · Chemical etching · Quantum confinement · Semiconductor nanomaterial

## 9.1 Introduction

Semiconductor quantum dot is a zero-dimensional quantum-confined system consisting of semiconductor single crystalline nanoparticle with a size of around exciton Bohr radius. The quantum-confined effects in the quantum dot allow us to control their electronic structures through size tuning [1]. Because of the controllability, the quantum dot is a nanoparticle-based future building block for electronics

T. Nakamura (✉)
Department of Electrical and Electronic Engineering, Hosei University, Kajino 3-7-2, Koganei 184-8584, Tokyo, Japan
e-mail: nakamura@hosei.ac.jp



Y. Ishikawa et al. (eds.), *High-Energy Chemistry and Processing in Liquids*,
https://doi.org/10.1007/978-981-16-7798-4_9

and optoelectronics [2, 3]. Semiconductor quantum dots have exotic luminescence properties such as emission color tuning and bright emission compared to bulk semiconductors. Luminescence in quantum dots is usually attributed to confined electron–hole recombination at their electronic bandgap. Smaller quantum dots have higher bandgap energies due to stronger confinement-induced discrete electronic states, resulting in shorter emission wavelength luminescence. Simultaneously, stronger confinement of excited carriers in smaller quantum dots leads to the enhancement of radiative recombination probability due to carrier localizations.

There are various forms of the quantum dots, e.g., quantum dots deposited on a semiconductor substrate [4, 5] and free-standing (colloidal) dots dispersed in a solvent [6–8]. High-quality quantum dots are formed on a lattice matched semiconductor substrate by an epitaxial semiconductor growth process. By using this quantum dot system, commercial grade excellent light-emitting devices such as a laser diode are reported [9–11], although expensive vacuum instruments are needed. On the other hand, colloidal quantum dots are prepared by relatively cost-effective processes such as a solution-based synthesis. Furthermore, the colloidal dots are compatible to rapidly developing solution-based organic light-emitting devices [12–14].

Direct bandgap semiconductors are usually employed as a colloidal quantum dot material in optoelectronic applications because of their intrinsic large radiative recombination coefficient (e.g., $2 \times 10^{-10}$ $cm^3/s$ for GaAs and InP [15]) compared to indirect bandgap semiconductors (3.4 and $0.2 \times 10^{-14}$ $cm^3/s$ for germanium and silicon [16]). Among direct gap semiconductors, CdSe is one of the most excellent luminescent quantum dot materials, and CdSe-based quantum dots have been intensively investigated since Murray et al. synthesized well-monodispersed CdX (X = Se, S, Te) quantum dots [6]. This is because of their luminescence color controllability in a wide visible range via size changes. There are various types of the quantum dots such as core–shell dots [17] and impurity doped dots [18]. Furthermore, CdSe-based quantum dots are employed for lighting devices such as light-emitting diodes [19] and lasers [20]. However, their toxicity originated from cadmium [21] is problematic in the aspect of practical applications for commercial uses.

One of promising cadmium free quantum dot materials is silicon. It is non-toxic to human and cost-effective because of its earth abundancy (the value of earth's crust abundant for silicon is 28.2% [22]). While silicon is an excellent electronic device material, its indirect bandgap nature, i.e., the phonon assist is essentially needed to occur radiative recombination between electrons and holes at band edge, prevents it to apply in light-emitting devices. However, the quantum confinement of electron–hole pair in a silicon quantum dot partly allows the pair to radiatively recombine without phonons, called quasi-direct radiative recombination [23]. This effect leads to the strong enhancement of radiative recombination rate ($w_r$) up to $w_r \sim 10^6$ $s^{-1}$ depending on the size of quantum dots [24] from $w_r \sim 4 \times 10^2$ $s^{-1}$ for $10^{17}$ $cm^{-3}$ of majority carriers in bulk silicon [16].

The small bandgap energy of bulk silicon at room temperature, $E_g^b = 1.12$eV (~1050 nm) [25], which is far from visible light wavelengths (~400–800 nm), indicates that it is inappropriate to lighting applications. However, in the case of silicon quantum dots, the quantum confinement makes the bandgap energy shift to a high

energy side, resulting in the use of the silicon dot as a visible light emission material. The quantum confinement can be divided in two different regimes, i.e., strong confinement or weak confinement regimes, usually meaning that the radius of a spherical quantum dot is smaller or larger than exciton Bohr radius. A simple effective medium theory can predict the size dependence of bandgap energies $E_g$ in quantum dots including silicon quantum dot as [26]

$$E_g = E_g^{\text{bulk}} + \pi^2 Ry^* \left(\frac{a_B}{a}\right)^2 - 1.786 Ry^* \frac{a_B}{a} \tag{9.1}$$

where $E_g^{\text{bulk}}$ is bulk bandgap energy, and $Ry^*$ represents exciton Rydberg energy. $a$ and $a_B$ are the radius of quantum dot and the exciton of bulk material. Using the bulk silicon values of $a_B = 4.3\,\text{nm}$ and $Ry^* = 0.015\text{eV}$ [26], the bandgap energy of silicon quantum dots with their diameters from 4.8 to 2.3 nm is expected to be tuned in a whole visible light energy range (~1.55–3.10 eV). These quantum confinement effects induced luminescent property changes in the dot are schematically summarized in Fig. 9.1.

The quantum confinement effects (the enhancement of radiative recombination rate and visible luminescence) as mentioned above have been firstly reported in porous silicon by Canham [27, 28], which is a wire-like assembly of silicon quantum dots [29]. The porous silicon is typically prepared by electrochemical etching of a silicon wafer in hydrofluoric acid (HF) solution. The porous layer is formed on the

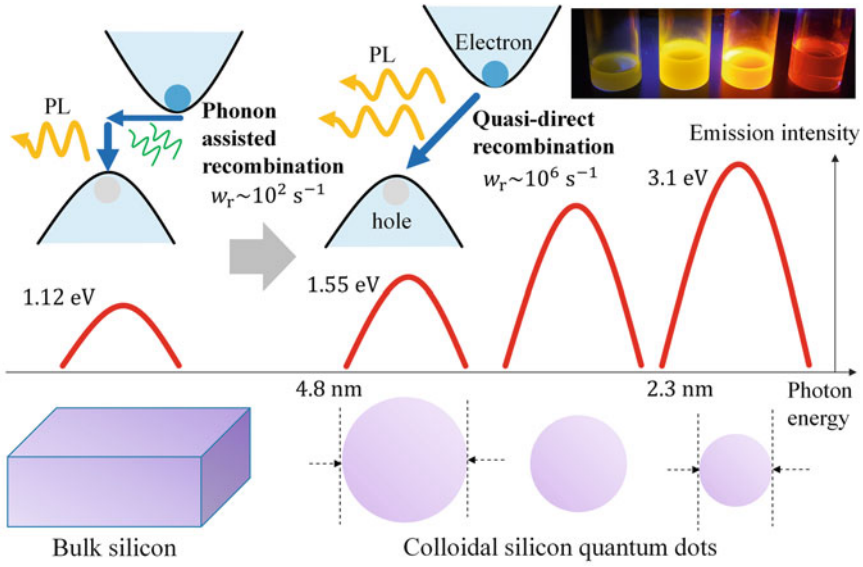


**Fig. 9.1** Schematic illustration of quantum confinement effects on the luminescence properties in silicon quantum dots

silicon wafer through the anodization of silicon and subsequent etching of silicon oxides [30]. The actual formation process and properties of porous layer such as porosity which influences the optical and electronic properties of porous silicon are determined by various etching conditions, e.g., doping levels and types of wafers, current density, etching time, and the addition of surfactant [31]. For example, a heavily p-type doping is required to form the porous layer without hole injection process such as light illumination. An alcohol-based surfactant such as ethanol is used for preventing hydrogen bubble formation in the etching reaction. The higher current density and/or longer etching time the wafer is applied, the higher porosity the porous layer has, resulting in the larger average pore diameter.

The luminescence of porous silicon originating from the recombination of quantum-confined electron–hole pairs at indirect gaps can be tuned in a wide emission energy range (1.1–2.2 eV) [32], corresponding to the color range from blue to near-infrared (NIR). The emission wavelength usually becomes shorter with increasing the porosity of porous silicon. This is due to the size reduction of each silicon core (silicon dot) consisting of wire-like interconnected porous network because of the increase in the pore (void) sizes.

The luminescence efficiency of porous silicon strongly depends on the quality of surface passivation, which means that unsaturated (dangling) bonds of silicon crystal surface atoms are covalently terminated with non-silicon atoms such as hydrogen or oxygen. This is because the dangling bonds of silicon surface trap the photo-excited electrons. As-prepared porous silicon by HF-based etching solution is naturally passivated with hydrogen atoms [33]. Some surface modification treatments can improve the luminescence efficiency. For example, high-pressure vapor thermal annealing treatment forms the high-quality oxide passivation layers, resulting in considerable increase in the photoluminescence (PL) absolute quantum efficiency from ~1% to 23% [34–36]. The analysis by PL decay dynamics indicates that this strong PL enhancement is due to the suppression of non-radiative decay route because of the decreasing in the surface dangling bonds. Thus, in a silicon quantum dot system including porous silicon, the degree of the surface termination is essential for the luminescence efficiency.

After the discovery of quantum confinement effects in porous silicon, different forms of silicon quantum dots have been reported: silicon dots embedded in silica matrix prepared by annealing of silicon rich silica [37–39], and colloidal (free standing) quantum dot [40–42]. The silica matrix-embedded silicon dots have stable luminescent in different ambient conditions because they are naturally covered with robust silicon dioxide network. On the other hand, the luminescence properties of colloidal dots are strongly dependent on their surface passivation [43], as like porous silicon and other semiconductor colloidal dots. Hydrogen-passivated silicon dots purely reflect the properties of silicon cores, although they are easily suffered from oxidation effects [44] because of the lower bond dissociation energy. On the contrary, the oxide covered dots have stable luminescent properties, i.e., its luminescence intensity is durable against continuous light illumination [45]. Another stable passivation is organic ligands, such as alkyl [46, 47] and amine [48, 49] groups. The organically

passivated silicon dots occasionally show some different properties from hydrogen-passivated dots, e.g., the surface-related bright luminescence [50] and direct-like optical transitions [51–53] due to ligand effects. In these silicon dots, the dispersibility in polar or nonpolar solvents can be also tuned by kinds of organic ligands [54]. Because of these excellent properties, organic terminated silicon dots are expected to be applied in bio-imaging fields [55–57] and solution-based light-emitting diodes [58, 59].

There are various formation routes for colloidal silicon quantum dots formation. A traditional route for compound semiconductor quantum dots, i.e. the solution synthesis, is used for the formation of silicon quantum dots [42, 53, 60]. Furthermore, another approaches, such as laser pyrolysis [61–63] or plasma synthesis via decomposition of silane, are commonly employed for the silicon dots formation [64–66]. These routes can be categorized in the bottom-up processes [67] which means that the colloidal dos are formed by coalescent and crystallization of silicon precursors and subsequent surface passivation. Other interesting routes are that colloidal dots are formed through some fragmentation of various types of condensed silicon targets including bulk crystalline silicon. Typical routes are mechanical ball milling and liquid-based laser processing of bulk silicon, which are obviously categorized in so-called top-down processes. Another route is the formation of quantum dots from the fragmentation of the condensed assembly targets of silicon crystal cores (quantum dots), i.e., porous silicon and quantum dots-embedded silica matrix. In the case of porous silicon target, the chemical etching of bulk silicon is performed. On the contrary, the quantum dot-embedded silica matrix is formed from silicon precursors such as sol–gel precursors and sputtered film. Former can be categorized in top-down process, and the latter can be categorized in bottom-up process [67]. In both cases, after the formation of silicon-condensed assembly targets, silicon crystal cores liberate from the targets via various low or high energy processing depending on their structural features. In this chapter, we review these material processing for the formation of luminescent colloidal silicon quantum dots from condensed silicon targets. The focused targets in this review are (i) bulk silicon (e.g., wafer and chunk), (ii) quantum dots-embedded silica, and (iii) porous silicon, as schematically shown in Fig. 9.2. We compare these processing in the views of the quality of colloidal silicon dots as a luminescence material (i.e., the controllability of luminescence properties) and of the productivity, to reveal advantages of each processing.

## 9.2 Bulk Silicon Targets

Mechanical ball milling of bulk silicon targets can directly generate nanometer-sized silicon nanoparticles. Lam et al. used silica powder as a target and showed mechanical ball milling formation of Si quantum dots [68], combining the thermal annealing process to reduce the silica to crystalline silicon. This process yields ~10 g per experimental batch of silicon quantum dots exhibiting red to near-infrared PL emission. Heintz et al. performed the ball milling of a silicon chunk target to directly

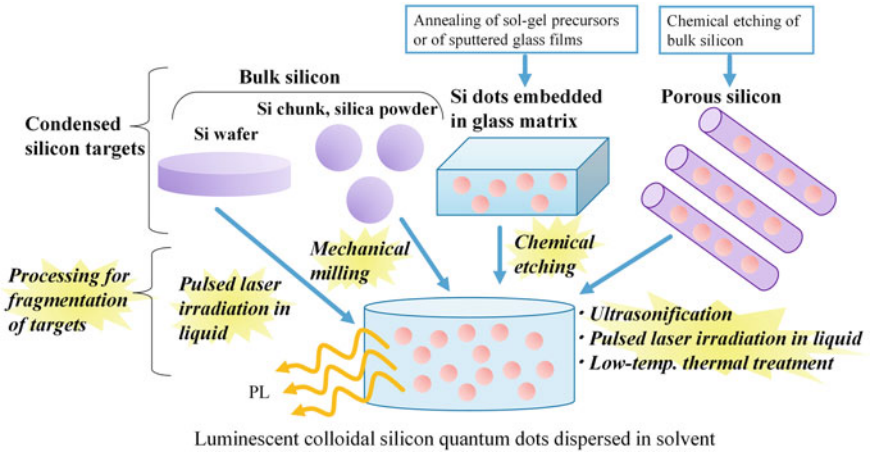


**Fig. 9.2** Material processing flows for colloidal luminescent silicon quantum dot formation from condensed silicon targets

generate silicon quantum dots [69]. The obtained dots are the diameters of several nanometers without additional process such as annealing. One of the original points in their milling processing is the addition of an alkyne organic solvent during the milling, since the surface of milled silicon is not passivated. A chemical reaction occurs between silicon surface and alkynes, and then, the surfaces of quantum dots are passivated with alkyl species. Their silicon dot samples have a broad PL emission band peaked at 430 nm. They treated the 1.5 g of silicon chunk for the formation of quantum dots. Although both milling processes need relatively long periods from 1 to 10 days to obtain the quantum dot samples, the quantity of the treating sample per experimental batch is a gram scale order. Furthermore, Bose et al. demonstrated silicon quantum dot formation from a biomass-condensed silicon-based material, i.e., rise husk which consists of mainly silica, toward future green scalable synthesis [70]. They milled rise husk and then, performed microwave irradiation of milled rice husk to reduce the silicon oxides for 1 h, resulting in the formation of green light-emitting silicon quantum dots. In this process, 2 g of raw rice husk powders were used per batch, and the yield of quantum dots was 5%, i.e., 10 mg of colloidal sample was produced.

Semiconductor-grade silicon wafer is extremely high-purity single crystal. Because of the excellent purity and high crystallinity, it can be an ideal silicon target for the formation of quantum dots. Pulsed laser irradiation in liquid is one of the most successful and concise techniques to produce quantum dots from silicon wafer. In traditional semiconductor industry, laser processing is known to be utilized for annealing to recovery crystalline quality and/or recrystallize the wafer [71]. Umezu et al. firstly demonstrated that the pulsed laser irradiation in water and hexane generates silicon quantum dots exhibiting PL emission in a blue to near-UV region [72]. Švrček et al. investigated the dependence of the morphology of the formed quantum

dots and PL properties on the irradiation conditions in detail [73]. They revealed that the intensity of PL band at ~400 nm increases with laser fluence and the smaller aggregates of the quantum dots are formed at higher fluence. The formation mechanism of the laser processing in liquid for silicon quantum dot formation is the laser ablation of the silicon wafer and subsequent condensed growth of nanocrystalline silicon from vaporized silicon at the liquid interface. After these works, many elaborate works have been published to control PL properties; Saitow et al. demonstrated the formation of the silicon quantum dots and the control of their emission color via an interesting approach [74, 75], i.e., they employed supercritical $CO_2$ fluid as a liquid medium. By changing the supercritical fluid pressure, the formed quantum dots exhibited wide range visible PL emissions such as blue, green, and red in addition to UV emission via size changes of dots as shown in Fig. 9.3.

The size control is also attained via other various irradiation conditions such as laser fluence and laser wavelength. For example, Yan et al. demonstrated that higher laser fluence the wafer target is irradiated, the smaller silicon quantum dots they obtained [76]. As another interesting approach to control the size they showed, a post size selection treatment after the laser processing in liquid has been proposed; silicon quantum dot samples with different mean diameters were obtained by centrifugation of an as-prepared sample with mixture of water and ethanol. Furthermore, Shirahata et al. demonstrated the size separation using a column chromatography technique [77], which is also utilized in pyrolysis synthesized silicon quantum dots [41]. They obtained clear green and blue silicon quantum dots samples. Using the same approach, well size-separated germanium quantum dots were prepared [78]. Moreover, an ultrasonification treatment in HF solution of the silicon nanoparticles with diameters of ~20–100 nm prepared by laser-induced fragmentation was demonstrated to further reduce their size [79]. The liberation of aggregated quantum dots consisted in prepared nanoparticles and the chemical etching of silicon oxides on their surfaces generate smaller size-distributed quantum dots sample with a mean diameter of ~4.5 nm. This silicon dot sample exhibits a relatively broad PL emission band peaked at 550 nm with a full width half maximum (FWHM) of ~120 nm.

One of the most notable merits in the laser processing in liquid for silicon quantum dot formation, in addition to the use of concise process instruments, is that the surface passivation spontaneously occurs during the processing [80, 81]. As-formed quantum dots after the condensation of ablated material vapor have radical surfaces. This surface instantly reacts with surrounding medium. In the case of organic molecules such an unsaturated hydrocarbon as a liquid medium, quantum dot surfaces are passivated with organic ligands. The stable and high-quality organic surface passivation leads to a relatively high absolute quantum efficiency of up to ~10%, in spite of no surface passivation treatments [77].

The reported yield of quantum dot samples in the laser irradiation process in liquid per experimental batch is reported to be 50 μg/min with respective to laser irradiation time [76]. Of course, with increasing irradiation area, the yield of this process would be increased. Furthermore, as summarized in the reviews [82], various interesting approaches to improve the productivity such as a scan of laser irradiation spot over target substrate have been demonstrated, and thus, further improvements for the

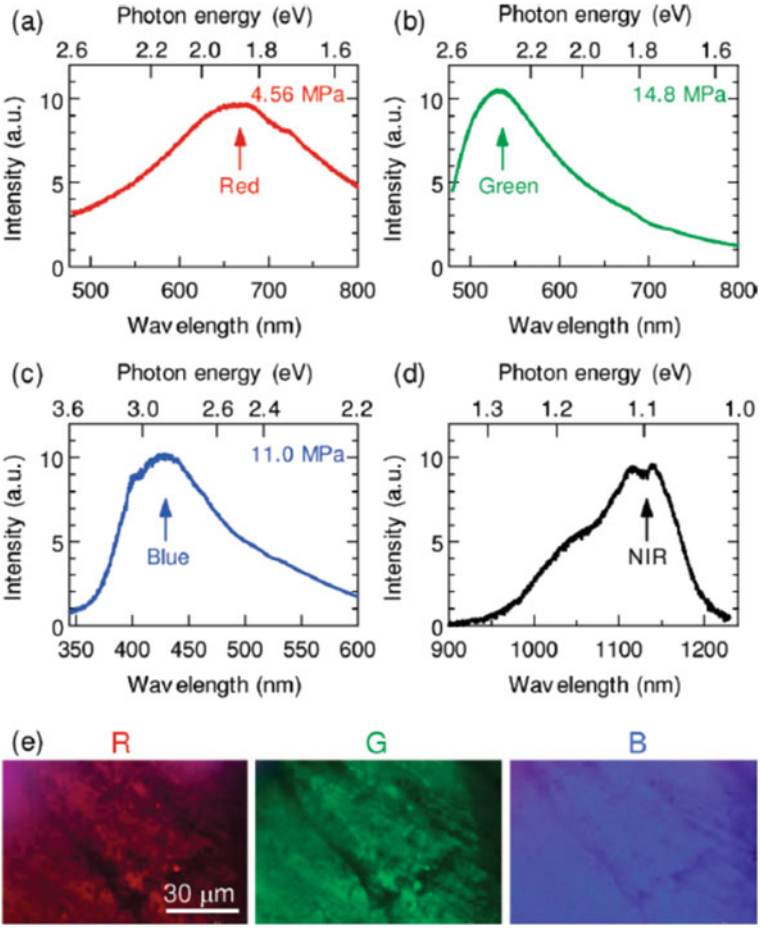


**Fig. 9.3** PL spectra of colloidal silicon dots by pulsed laser irradiation in supercritical fluid and their luminescent color images. The different color PL emissions are shown for different pressures of the fluid. Reprinted with permission from Ref. [75]. Copyright 2009 American Chemical Society

silicon quantum dot formation by laser processing in liquid are interesting future works.

## 9.3 Silica Matrix Targets

The silicon quantum dot system where the dots are embedded in silica matrix has excellent controllability of optical properties as well as stable luminescence, as mentioned in Sec. 9.1. Crystalline silicon quantum dots in this system are formed via aggregation and crystallization of excess silicon atoms by annealing silicon-rich silica

matrix. The silicon-rich silica matrix films are traditionally prepared by ion implantation [38, 83, 84] and sputtering techniques [39, 85–87]. By changing the contents of silicon and annealing conditions such as temperature and time, the size of silicon dots is controlled, e.g., when silica matrix has the larger content of excess silicon, the prepared sample has larger size distribution of silicon quantum dots, leading to PL emission at longer wavelength [39, 87]. These quantum dots systems also have the easiness of doping with different ions, n- and p-type dopants ions such as boron and phosphorus [88–90] and rare-earth metal ions [91–94]. In addition to these silica films, a commercially available molecular precursor, i.e., hydrogen silsequoxane, is employed as a starting material for quantum dots [95, 96]. The thermal annealing of hydrogen silsequoxane in reduced atmosphere forms the size-controlled silicon quantum dots in silica powders and as similar to silica matrix film samples, and the size of quantum dots can be changed through the annealing temperatures.

The free-standing dots generation from above silicon dots-embedded silica matrix samples were firstly reported by Shinoda et al. [97]. They chemically etched quantum dots-embedded $SiO_2$ film in HF aqueous solution and then showed that the removal of silica matrix produces free-standing colloidal dots dispersed ethanol solution. As-prepared dots are mainly passivated with hydrogen atoms due to the HF treatment, and its PL emission band peak is at ~700 nm. It should be noted that with aging the prepared dot sample at air ambient, its PL emission degrades due to partially surface passivation changes from hydrogen to oxygen.

It was also demonstrated that stable colloidal silicon dot samples are formed from phosphorus and boron codoped silicon dot-embedded silica matrix [98–102]. The silica matrix films were grown by co-sputtering of Si and $SiO_2$ targets with $P_2O_5$ and $B_2O_3$ and the subsequent annealing of the grown film. By changing the annealing temperature, PL emission energy can be controlled in a wide NIR region from ~0.8 to ~1.6 eV, which extends below bandgap energy of bulk silicon. This below bandgap PL emission is due to the recombination of electrons and holes between donor and acceptor impurity states. The colloidal codoped silicon dots are stably dispersed in polar solvents such as methanol and water without any photodegradation and aggregation for one year because of the formation of the subsurface consisting of doped phosphorus and boron leading to negative surface potential.

Hessel et al. firstly reported that the formation of the colloidal quantum dots by etching of quantum dot embedded in silica powder obtained from hydrogen silsesquioxane [95]. One of the merits of the hydrogen silsesquioxane route for the colloidal dot formation is its relatively large-scale production yield. Typically, the etching of 300 mg of quantum dot-embedded silica powder generates 30 mg of liberated quantum dot sample for 1 ~ 2 h etching time per experimental batch. Of course, both annealing and etching processes can be scalable, and this route potentially has a high productivity. The PL emission band of the silsesquioxane-originated colloidal dots can be controlled from a green to red spectral region by changing the etching time as shown in Fig. 9.4a. This is due to the size reduction via chemical etching of dots. The external PL quantum efficiency of as-prepared hydrogen-passivated quantum dots is reported to be ~4% [95]. To improve PL emission color quality

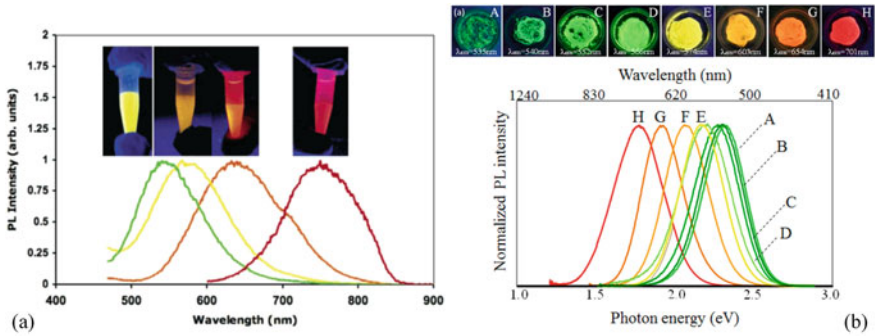


**Fig. 9.4** PL emission spectra of hydrogen-passivated colloidal silicon quantum dots prepared by chemical etching of silicon dot-embedded silica matrix. The different color PL emissions are shown for different processing conditions. Adapted with permission from **a** Ref. [95] and **b** Ref. [104]. Copyright **a** 2006 and **b** 2020 American Chemical Society

toward light-emitting device applications, a size separation technique using ultra-centrifugation [103] was demonstrated. Moreover, the etching of another silicon dots-embedded silica matrix formed by triethoxysilane-derived sol–gel precursor also generates hydrogen-terminated colloidal dots which exhibit PL emission in a green to red region as shown in Fig. 9.4b without any bleaching for ~20 days [104].

The silsesquioxane-originated hydrogen-passivated colloidal silicon dots have a capability of controlling surface termination with organic ligands [105]. Because the as-prepared silicon dots are passivated with hydrogen, the organic ligands can be effectively attached on the silicon surface via hydrosilylation reaction, which is a chemical reaction between hydrogen silicon surface and unsaturated hydrocarbon molecules. The hydrosilylation reaction can be assisted by various treatments such as the addition of radical initiator [106], heat treatment [107], and light illumination [108]. In particular, the addition of a radical initiator ($PCl_5$) is demonstrated to be more effective for the formation of organic ligands than thermal treatment [106]. The colloidal dots treated with the radical initiators show a relatively high absolute PL quantum efficiency up to 68%. Yang et al. interestingly reported that the treatments (heat or light illumination) for assisting hydrosilylation reaction affect PL properties [109] such as the luminescence decay dynamics and PL emission peak of silicon dots, because of the inclusions of oxygen species during the hydrosilylation treatment.

Various types of organic ligands are passivated to the silicon quantum dots via hydrosilylation, leading to different solubility in various types of solution. For example, hydrocarbons-passivated quantum dots are only dispersed in nonpolar solution, such as chloroform and toluene [108]. On the contrary, when amphiphilic ligands are passivated by thermally assisted hydrosilylation at 180 °C, the dots are well soluble in polar solvent (i.e., water) without any PL property changes, and the dots have long-term PL stability for several months [107]. In this case, an aqueous water solution up to 98 mg/ml of colloidal dots can be prepared. Such a dense solution can be useful for bio-imaging application. Similar ligand-induced solubility control has

been also demonstrated via room temperature hydrosilylation treatment, where the passivation efficiency is strongly dependent on the size of silicon dots and the kinds of organic spices [54].

## 9.4 Porous Silicon Targets

Porous silicon has various specific properties different from bulk silicon crystal due to its sponge structure, in addition to quantum confinement-induced room temperature visible luminescence as mentioned in Sect. 9.1. In the view of the silicon-condensed target for quantum dots formation, an important property is its mechanical fragility [110]. Porous silicon has different mechanical properties compared to bulk silicon. For example, the yield strength, which is an index for measuring the resistance for stretching or compressing without breaking, is lower than bulk silicon, depending on the porosity. This low yield strength indicates that porous silicon is relatively fragile against mechanical stress, leading to an advantage point for fragmentation treatment in quantum dot formation processing. Another important property of porous silicon for quantum dot formation is its peculiar thermal characteristics [31]. The porous silicon has a low thermal conductivity (0.025–1.2 W/mK) comparative to polymer materials such as rubber, accompanying low volumetric heat capacity (0.18–0.96 $MJ/m^3K$). These thermal features of porous silicon are preferable for thermal insulation as like air, resulting in a thermal confinement effect inside porous silicon by heating. Thus, some thermally induced fragmentation processing to porous silicon target such as laser irradiation or heat treatment as described below are expected to be enhanced compared to bulk silicon target.

There are several mechanical fragmentation processing for the generation of the colloidal silicon quantum dots from porous silicon, i.e., the mechanical grind and ultrasonification. The ultrasonification is typical and concise processing for the fragmentation of porous silicon because of its fragility. Heinrich et al. firstly demonstrated that the colloidal luminescent solution consisting of silicon quantum dots can be prepared by ultrasonification of porous silicon on silicon [111]. In their process, the electrochemically prepared porous layer on silicon wafer is directly ultrasonificated in various solutions for 0.25 to 2 h. The obtained colloidal solutions show the essentially same PL emission as original porous silicon samples. From TEM analysis, the obtained colloids are crystalline silicon and inherit original irregularity of the shape and sizes of the porous silicon, i.e., the size variation is micrometers to nanometers. This indicates that the porous structures are not fully fragmented, and the obtained colloids consist of both free-standing quantum dots and the interconnected assemblies of the quantum dots.

To purely obtain the free-standing colloidal dots, the sedimentation and filtering treatments have been tried: Valenta et al. prepared luminescent colloidal solutions consisting of free-standing silicon quantum dots by the procedure [112] as schematically shown in Fig. 9.5a. Porous silicon powder is firstly dispersed in solvent, and the ultrasonification treatment is performed for the dispersed solvent. Then, after the

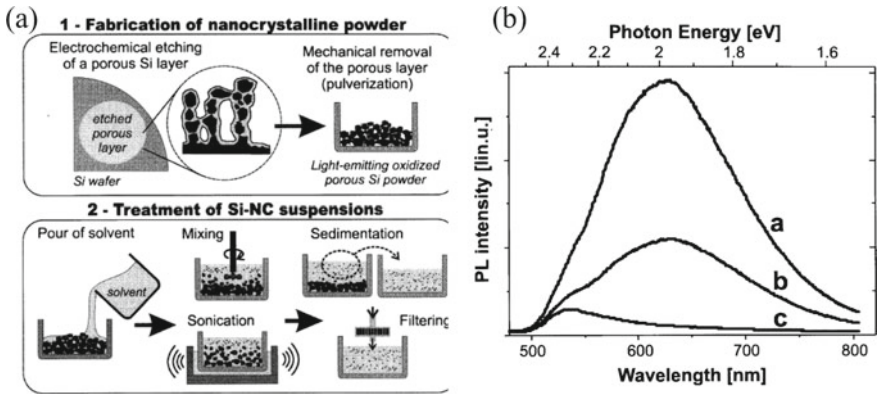


**Fig. 9.5** Schematic illustration of the ultrasonification processing (**a** left figure). **b** Right figure shows the PL spectra of (a) original porous silicon, (b) the sample after ultrasonification and sedimentation treatment, and (c) the sample after filtering treatment of (b). Reproduced with permissions from Ref. [112]

sedimentation of larger particles, the supernatant solution is extracted, and it is filtered with the Teflon membrane with pores of 200 nm. Figure 9.5b shows the PL spectra of their samples after each treatment. The colloidal samples after sedimentation and filtering show blue-shifted green PL emission with respect to original porous silicon powders, indicating that larger particles such as porous silicon assembly particles or larger sized free-standing quantum dots are removed. The atomic force microscope measurements revealed that the diameter of obtained colloidal dots is 1–2 nm [113]. It should be noted that, as shown in Fig. 9.5b, PL intensity considerably decreases from the original porous powder PL intensity, since a larger part of luminescent dots is filtered out even after sedimentation treatments. Thus, the throughput of the ultrasonification processing is poor and the processing generates larger wastes.

To further improve or control luminescence properties, Kůsová et al. performed light-induced hydrosilylation treatment to the quantum dot samples prepared by ultrasonification processing [114, 115]. After the ultrasonification for 15 min and sedimentation of porous silicon powder for the fragmentation and size selection of the powder, a continuous-wave laser light at 325 nm from He-Cd laser was irradiated to the sample for light-induced hydrosilylation for 30 min twice a week. Then, bright yellow-emitting alkyl-passivated colloidal dots were obtained. The absolute quantum efficiency of the colloid sample is 20% which is larger than original porous silicon (2%), and the decay times considerably change from microsecond range for original porous silicon to nanosecond range for the colloidal sample, indicating that the recombination mechanism is strongly modified by the alkyl passivation [51].

In the laser processing in liquid, it is known that the target morphology strongly influences the size and production yield of nanoparticles due to different laser-induced heating profile and resultant different fragmentation mechanisms [82]. Because the porous silicon has a complex morphology completely different from

bulk silicon, the characteristics of quantum dots formation from porous silicon target by laser processing can be expected to differ from that of bulk silicon targets.

Švrček et al. firstly demonstrated the formation of colloidal silicon dots by the laser irradiation of a porous silicon target in a spin on silica solution [116]. The obtained dots prepared at higher laser fluence exhibit blue emission as the same as those in the use of bulk silicon targets [73]. Nakamura et al. also demonstrated the formation of silicon quantum dots from porous silicon target by laser ablation in an organic solution [117, 118]. They prepared the porous silicon targets by the stain etching of relatively inexpensive metallurgical grade silicon powder [119] in mixed aqueous solution of nitric acid and HF. The stain-etched porous silicon powder consists of porous silicon and bulk layers [120]. The porous powder was dispersed in 1-octene, which acts as a dispersed liquid medium, as well as the surface passivation species. Then, the irradiation of nanosecond pulsed laser light at 532 nm generates blue emitting colloidal silicon dots. As expected, the luminescence properties and surface chemistry of the prepared dots are essentially the same as those in the use of bulk silicon targets [77], indicating that the formation mechanism is the laser ablation of target silicon and subsequent condensation in the nanoparticles with simultaneous surface passivation by organic molecules.

An advantage of the use of porous silicon targets is high yield formation of colloidal dots [117]. The production yield of colloidal samples in the use of porous silicon, which was estimated from the comparison with the PL emission intensities, is 40 times higher than bulk silicon target used. This high yield formation is attributed to the specific thermal properties of porous silicon, i.e., the low thermal conductivity and volumetric thermal capacity, leading to a heat confinement of the porous silicon target.

It should be noted that the optical properties of formed colloidal dots are completely different from the original porous silicon [117]. The PL emission peak energies for the colloidal dots and porous silicon are 2.9 eV and 1.65 eV, respectively, and the PL band has relatively wider emission width (~500 meV) than original porous silicon targets (~300 meV). From these data, the size of the silicon quantum dots is estimated to be 1.3–1.8 nm, while for porous silicon, the silicon core size is 3–5 nm. These different sizes strongly support that the formation of the dots is through laser ablation mechanism as described above.

It was also demonstrated that the colloidal dots exhibiting different luminescence colors are generated via laser-induced fragmentation from the different porous silicon samples, which means that the silicon quantum dots consisted in porous silicon simply liberate from the porous network without any changes in their sizes [121]. In that work, porous silicon samples with different silicon core sizes were, firstly, prepared by changing the stain-etching condition of porous silicon. Then, the irradiation of UV pulsed laser light at 266 nm to the porous silicon samples in 1 octene generates the orange and red luminescent colloidal dots as shown in Fig. 9.6, which are well passivated with alkyl ligands. The luminescence spectral features of colloidal dot samples, i.e., peak wavelength and band width, are very similar to those of original porous silicon samples (Fig. 9.6), indicating that the colloidal dots arise from the fragmentation of porous silicon assembly targets and resultant liberation

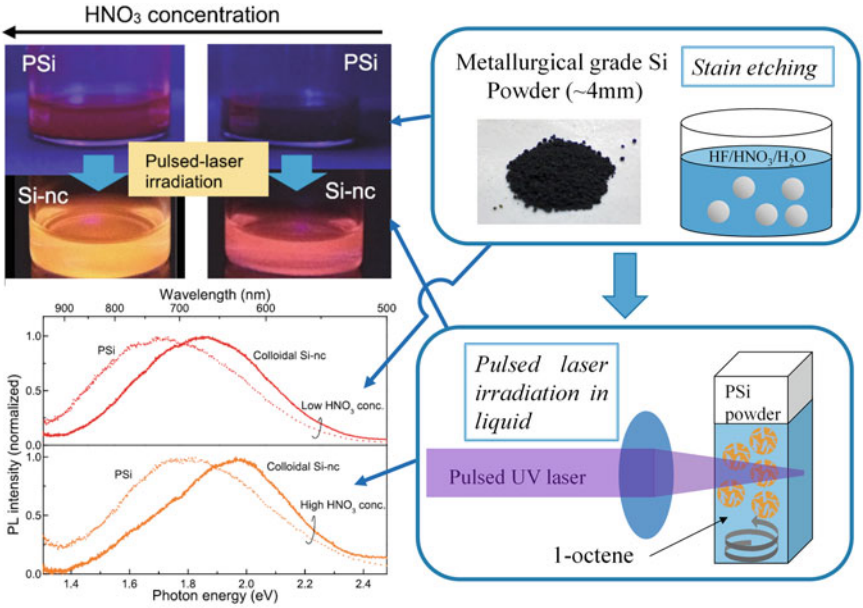


**Fig. 9.6** Pictures of PL emission colors and corresponding PL spectra of porous silicon powder and colloidal silicon dots (left figures). Right figure shows preparation processing of each sample. Reproduced with permissions from Ref. [121]

of corresponding silicon cores. Despite similar core sizes between porous silicon and colloidal dots, the luminescent efficiencies of colloidal dots (~20%) are much higher than that of original porous silicon (~3%). This is due to higher coverage of surface alkyl ligands and the ligand-induced radiative recombination rate changes. By using a solvent with HF, a considerable improvement of the absolute PL quantum efficiency up to ~70% is observed [122].

The differences between the formation mechanisms in Refs. [117] and [121] results are probably due to the different degrees of the absorbed light energy of the porous silicon target. The incident fluence of incident pulsed lights at 532 nm and 266 nm is ~2.5 and ~0.5 J/cm$^2$, respectively. In contrast, the absorption coefficient of silicon at 266 nm is, at least, two orders of magnitude higher than that at 532 nm [123]. These differences cause the vaporization of porous silicon or fragmentation of silicon cores. In fact, the different absorbed energies of incident light in metal colloidal particles are reported to result in the different fragmentation mechanisms such as thermal evaporation and Coulomb explosion [82]. To further analyze the mechanisms, some numerical simulations with considering the specific thermal and optical properties of porous silicon will be needed.

Švrček et al. demonstrated that different pulse width laser irradiation in liquid for porous silicon target generates different sized silicon particles [124]: Nanosecond laser pulse irradiation to porous silicon generates the submicrometer spherical silicon

particles with a mean diameter of ~350 nm due to laser-induced melting effect, leading to the agglomeration of fragmentated silicon particles. While for femtosecond laser pulse irradiation, well dispersed colloidal silicon dots with diameters of 1–7 nm. Interestingly, the femtosecond laser irradiation also leads to the passivation of colloidal dots with OH bonds, resulting in preventing the re-agglomeration of formed colloidal dots and stable dispersibility in water. Because this surfactant-free femtosecond laser processing to porous silicon does not need any toxic materials, the prepared water-dispersed colloidal dots are beneficial for various bio-applications.

Recently, Nakamura et al. demonstrate a facile formation processing of colloidal dots from porous silicon, i.e., low-temperature heat treatment [125] as depicted Fig. 9.7. They electrochemically etched the silicon wafer and lift porous layer only from the wafer by applying a high electronic current. The lifted porous layer, of which the shape is flake, is dispersed in a reactive solvent, unsaturated hydrocarbon solution (1-decene) mixed with small amount HF aqueous solution, was heated at ~50 °C for 2 h. Such a moderate heat treatment surprisingly leads to the efficient formation of luminescent colloidal silicon quantum dots. The yield of the colloidal dots is very high, i.e., 60–100% of the original porous silicon flake targets, depending on the quantity of flakes, transform into colloidal dots. The typical yielded quantity of colloidal dots per experimental batch is 30 mg from 50 mg of porous silicon targets. Because the PL peak energy of dots is like the original porous silicon, the obtained colloids are formed via the fragmentation of porous assembly and resultant liberation

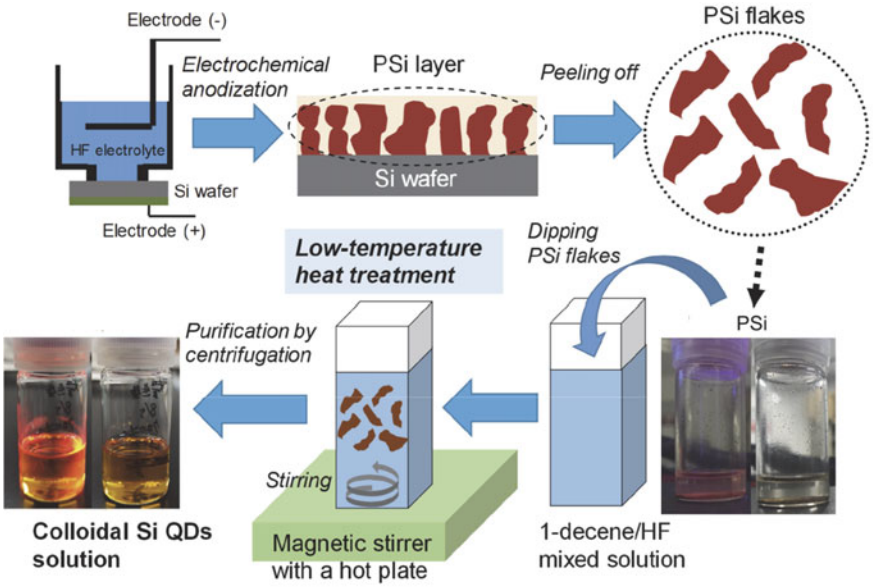


**Fig. 9.7** Schematic illustration of low-temperature heat treatment of porous silicon flakes for the luminescent colloidal silicon dots. Reproduced with the license under a Creative Commons Attribution (CC BY) license of [121]

of silicon cores consisting of porous silicon. Obviously, such a low-temperature heat treatment to bulk silicon target never causes any fragmentation of the targets. The efficient fragmentation by low-temperature treatment results from thermally induced cracking, i.e., a thermal stress induces mechanical cracking to the porous silicon target, due to the specific thermal properties [31] and the mechanical fragility [110] of porous silicon, as mentioned above. In fact, the activation energy of the colloidal formation yield is the similar value for the cracking energy of porous silicon estimated from the crack resistance energy of bulk silicon [125]. In addition to thermal-induced cracking, chemical reaction, i.e., the hydrosilylation between hydrogen-terminated silicon surface and unsaturated hydrocarbon molecules, also causes a mechanical stress. This chemically induced stress is partly attributed to the fragmentation of porous silicon [46]. It should be noted that this low-temperature heat treatment is scalable, i.e., scaling up of processing instruments is easier to be attained. Thus, by optimizing the treatment condition, gram to kilogram scale productions of colloidal quantum dots can be expected to be realized.

The luminescent properties of colloidal dots by low-temperature heat treatment are essentially the same as those formed by pulse laser irradiation; the absolute quantum efficiency is ~20%, which is larger than the original porous silicon (~1%), due to alkyl passivation via hydrosilylation and the luminescence colors for both colloidal dots are red. Furthermore, the yield of colloidal sample in low-temperature treatment (50–100%) is equivalent to that of pulse laser processing (~50%). Thus, the low-temperature treatment is more energy cost-effective compared to the laser processing. As well as its cost-effectiveness, it is more scalable than the laser processing since its active volume for the colloidal formation is limited within the laser spot area.

## 9.5 Summary

In this chapter, the material processing of various condensed silicon material targets for the luminescent colloidal silicon dot formation via fragmentation of targets was reviewed. The focused targets are bulk silicon, the quantum dots assemblies such as quantum dots-embedded silica matrix and porous silicon. The features of each processing reviewed, such as formation yield, and luminescence properties, are summarized in Table 9.1. Among the processing shown in the table, the laser irradiation to bulk silicon targets in liquid is the simplest processing to obtain the silicon quantum dots with exhibiting a whole visible wavelength (blue to NIR) range PL emission, since the quantum dot formation and the surface passivation are simultaneously attained by laser irradiation. By applying various advanced techniques (e.g., scanning of laser irradiation spot), the productivity of the quantum dots is expected to be considerably improved. The gram scale quantum dot formation by the laser processing in liquid utilizing such a technique is a future interesting and challenging task. The processing of silicon dot assembly target, such as chemical etching treatment of silicon dots-embedded silica or low-temperature heat treatment of porous silicon, allows us to produce the quantum dots of several tens of milligram. Such more

**Table 9.1** Summary of the features of the material processing for the fragmentation of a condensed silicon targets (bulk silicon, quantum dots-embedded silica matrix, and porous silicon)

| | Condensed silicon targets | | | | | |
|---|---|---|---|---|---|---|
| | Bulk silicon | | Silicon quantum dot-embedded silica matrix | Porous silicon | | |
| Target forms | Si chunks or silica powders | wafer | Film or powder | Mixture of porous and bulk layers | Free-standing porous layer | |
| Processing for fragmentation of targets | Mechanical milling | Laser irradiation in liquid | Chemical etching | Laser irradiation in liquid | Ultrasonification | Low-temp. heat treatment |
| Target weight | 1–15 g [68–70] | - | 200 mg [95] | 100 mg [117] | 2.5 mg [114] | 50 mg [125] |
| Colloid formation yield | 10 mg [70] | 50 μg/min [76] | 20 mg | < 1 mg | - | 30 mg [125] |
| Processing period for fragmentation | 1–10 days [68, 69] | - | 30–135 min [95] | 2 h [117, 121] | 15 min [114] | 2 h [125] |
| PL color | Blue [69], green [70] and near-infrared [68] | Blue to near-infrared [75] | Green to Red [95, 104], NIR [99] | Blue [117], Orange and red [121] | Blue [113], Yellow [114, 115], Red [112] | Orange to red [125] |
| PL efficiency | - | ≤ 10% [77] | ≤ 60% [106] | ≤ 70% [122] | ≤ 20% [115] | ≤ 40% [125] |

scalable routes via fragmentation of silicon dot assemblies open the possibility in the industrial production of silicon quantum dot-based electronic devices where a large quantity of quantum dots is needed. In the view of controllability of luminescence properties, PL emission colors in the route via silica matrix target are controllable in a wide visible range from green to NIR by varying the preparation conditions of the target. In addition, there are some reports on the size separation technique using ultra-centrifugation after colloidal dots formation to improve luminescence color quality. On the other hand, for the porous silicon processing route, PL emission bands are limited in an orange to red color region. Thus, in this processing, further development of silicon dot size control during the process or a size separation after colloidal dot formation is needed for enhancing the luminescence color controllability.

## References

1. A.P. Alivisatos, Semiconductor Clusters, Nanocrystals, and Quantum Dots. Science **271**, 933–937 (1996). https://doi.org/10.1126/science.271.5251.933
2. J.M. Pietryga, Y.S. Park, J. Lim, A.F. Fidler, W.K. Bae, S. Brovelli, V.I. Klimov, Spectroscopic and device aspects of nanocrystal quantum dots. Chem. Rev. **116**, 10513–10622 (2016). https://doi.org/10.1021/acs.chemrev.6b00169
3. F.P. García de Arquer, D. V. Talapin, V.I. Klimov, Y. Arakawa, M. Bayer, E.H. Sargent, Semiconductor quantum dots: Technological progress and future challenges, Science. 373 (2021) eaaz8541. https://doi.org/10.1126/science.aaz8541.
4. P.W. Fry, I.E. Itskevich, D.J. Mowbray, M.S. Skolnick, J.J. Finley, J.A. Barker, E.P. O'Reilly, L.R. Wilson, I.A. Larkin, P.A. Maksym, M. Hopkinson, M. Al-Khafaji, J.P.R. David, A.G. Cullis, G. Hill, J.C. Clark, Inverted electron-hole alignment in inas-gaas self-assembled quantum dots. Phys. Rev. Lett. **84**, 733–736 (2000). https://doi.org/10.1103/PhysRevLett.84.733
5. J. Oshinowo, M. Nishioka, S. Ishida, Y. Arakawa, Highly uniform InGaAs/GaAs quantum dots (∼15 nm) by metalorganic chemical vapor deposition. Appl. Phys. Lett. **65**, 1421–1423 (1994). https://doi.org/10.1063/1.112070
6. C.B. Murray, D.J. Norris, M.G. Bawendi, Synthesis and characterization of nearly monodisperse CdE (E = sulfur, selenium, tellurium) semiconductor nanocrystallites. J. Am. Chem. Soc. **115**, 8706–8715 (1993). https://doi.org/10.1021/ja00072a025
7. A.A. Guzelian, U. Banin, A.V. Kadavanich, X. Peng, A.P. Alivisatos, Colloidal chemical synthesis and characterization of InAs nanocrystal quantum dots. Appl. Phys. Lett. **69**, 1432–1434 (1996). https://doi.org/10.1063/1.117605
8. R. Rossetti, S. Nakahara, L.E. Brus, Quantum size effects in the redox potentials, resonance Raman spectra, and electronic spectra of CdS crystallites in aqueous solution. J. Chem. Phys. **79**, 1086–1088 (1983). https://doi.org/10.1063/1.445834
9. K. Tachibana, T. Someya, Y. Arakawa, R. Werner, A. Forchel, Room-temperature lasing oscillation in an InGan self-assembled quantum dot laser. Appl. Phys. Lett. **75**, 2605–2607 (1999). https://doi.org/10.1063/1.125092
10. T. Kageyama, K. Nishi, M. Yamaguchi, R. Mochida, Y. Maeda, K. Takemasa, Y. Tanaka, T. Yamamoto, M. Sugawara, Y. Arakawa, Extremely high temperature (220°C) continuous-wave operation of 1300-nm-range quantum-dot lasers, 2011 Conf. Lasers Electro-Optics Eur. 12th Eur. Quantum Electron. Conf. CLEO Eur. 2011. 1163 (2011) 2021. https://doi.org/10.1109/CLEOE.2011.5943701.

11. J. Kwoen, B. Jang, K. Watanabe, Y. Arakawa, High-temperature continuous-wave operation of directly grown InAs/GaAs quantum dot lasers on on-axis Si (001). Opt. Express. **27**, 2681 (2019). https://doi.org/10.1364/oe.27.002681
12. B.H. Kim, M.S. Onses, J. Bin Lim, S. Nam, N. Oh, H. Kim, K.J. Yu, J.W. Lee, J.-H. Kim, S.-K. Kang, C.H. Lee, J. Lee, J.H. Shin, N.H. Kim, C. Leal, M. Shim, J. a. Rogers, High-Resolution Patterns of Quantum Dots Formed by Electrohydrodynamic Jet Printing for Light-Emitting Diodes, Nano Lett. 15 (2015) 969–973. https://doi.org/10.1021/nl503779e.
13. J. Yang, M.K. Choi, U.J. Yang, S.Y. Kim, Y.S. Kim, J.H. Kim, D.H. Kim, T. Hyeon, Toward Full-Color Electroluminescent Quantum Dot Displays. Nano Lett. **21**, 26–33 (2021). https://doi.org/10.1021/acs.nanolett.0c03939
14. M. Kawamura, H. Kuwae, T. Kamibayashi, J. Oshima, T. Kasahara, S. Shoji, J. Mizuno, Liquid/solution-based microfluidic quantum dots light-emitting diodes for high-colour-purity light emission. Sci. Rep. **10**, 1–9 (2020). https://doi.org/10.1038/s41598-020-70838-w
15. R.K. Ahrenkiel, B.M. Keyes, S.M. Durbin, J.L. Gray, Recombination lifetime and performance of III-V compound photovoltaic devices, in: Conf. Rec. Twenty Third IEEE Photovolt. Spec. Conf. - 1993 (Cat. No.93CH3283–9), IEEE, 1993: pp. 42–51. https://doi.org/10.1109/PVSC.1993.347081.
16. R.N. Hall, Recombination processes in semiconductors, Proc. IEE - Part B Electron. Commun. Eng. 106 (1959) 923–931. https://doi.org/10.1049/pi-b-2.1959.0171.
17. P. Reiss, M. Protière, L. Li, Core/Shell semiconductor nanocrystals. Small **5**, 154–168 (2009). https://doi.org/10.1002/smll.200800841
18. D.J. Norris, A.L. Efros, S.C. Erwin, Doped nanocrystals. Science **319**, 1776–1779 (2008). https://doi.org/10.1126/science.1143802
19. V.L. Colvin, M.C. Schlamp, A.P. Alivisatos, Light-emitting diodes made from cadmium selenide nanocrystals and a semiconducting polymer. Nature **370**, 354–357 (1994). https://doi.org/10.1038/370354a0
20. F. Fan, O. Voznyy, R.P. Sabatini, K.T. Bicanic, M.M. Adachi, J.R. McBride, K.R. Reid, Y.S. Park, X. Li, A. Jain, R. Quintero-Bermudez, M. Saravanapavanantham, M. Liu, M. Korkusinski, P. Hawrylak, V.I. Klimov, S.J. Rosenthal, S. Hoogland, E.H. Sargent, Continuous-wave lasing in colloidal quantum dot solids enabled by facet-selective epitaxy. Nature **544**, 75–79 (2017). https://doi.org/10.1038/nature21424
21. N. Chen, Y. He, Y. Su, X. Li, Q. Huang, H. Wang, X. Zhang, R. Tai, C. Fan, The cytotoxicity of cadmium-based quantum dots. Biomaterials **33**, 1238–1244 (2012). https://doi.org/10.1016/j.biomaterials.2011.10.070
22. S. Adachi, *Earth-Abundant Materials for Solar Cells: Cu2-II-IV-VI4 Semiconductors* (John Wiley & Sons, West Sussex, 2015)
23. T. Takagahara, K. Takeda, Theory of the quantum confinement effect on excitons in quantum dots of indirect-gap materials. Phys. Rev. B. **46**, 15578–15581 (1992). https://doi.org/10.1103/PhysRevB.46.15578
24. C. Delerue, G. Allan, C. Reynaud, O. Guillois, G. Ledoux, F. Huisken, Multiexponential photoluminescence decay in indirect-gap semiconductor nanocrystals. Phys. Rev. B. **73**, 1–4 (2006). https://doi.org/10.1103/PhysRevB.73.235318
25. S. Adachi, *Handbook on Physical Properties of Semiconductors* (Kluer Academic Publishers, Massachusetts, 2004)
26. S.V. Gaponenko, *Optical Properties of Semiconductor Nanocrystals* (Cambridge University Press, Cambridge, 1998)
27. L.T. Canham, Silicon quantum wire array fabrication by electrochemical and chemical dissolution of wafers. Appl. Phys. Lett. **57**, 1046–1048 (1990). https://doi.org/10.1063/1.103561
28. A.G. Cullis, L.T. Canham, Visible light emission due to quantum size effects in highly porous crystalline silicon. Nature **353**, 335–338 (1991). https://doi.org/10.1038/353335a0
29. A.G. Cullis, L.T. Canham, P.D.J. Calcott, The structural and luminescence properties of porous silicon. J. Appl. Phys. **82**, 909–965 (1997). https://doi.org/10.1063/1.366536

30. A. Loni, Porous Silicon Formation by Anodization, in: Handb. Porous Silicon, Springer International Publishing, Cham, 2014: pp. 1–12. https://doi.org/10.1007/978-3-319-04508-5_2-1.
31. N. Koshida, L.T. Canham, Thermal Properties of Porous Silicon, in: L.T. Canham (Ed.), Handb. Porous Silicon, 2nd ed., Springer, New York, 2017: pp. 309–318. https://doi.org/10.1007/978-3-319-05744-6.
32. D. Kovalev, H. Heckler, G. Polisski, F. Koch, Optical Properties of Si Nanocrystals. Phys. Status Solidi. **215**, 871–932 (1999). https://doi.org/10.1002/(SICI)1521-3951(199910)215:2%3c871::AID-PSSB871%3e3.0.CO;2-9
33. M.J. Sailor, E.J. Lee, Surface chemistry of Luminescent Silicon Nanocrystallites. Adv. Mater. **9**, 783–793 (1997). https://doi.org/10.1002/adma.19970091004
34. B. Gelloz, A. Kojima, N. Koshida, Highly efficient and stable luminescence of nanocrystalline porous silicon treated by high-pressure water vapor annealing, Appl. Phys. Lett. 87 (2005) 031107. https://doi.org/10.1063/1.2001136
35. B. Gelloz, N. Koshida, Mechanism of a remarkable enhancement in the light emission from nanocrystalline porous silicon annealed in high-pressure water vapor, J. Appl. Phys. 98 (2005) 123509. https://doi.org/10.1063/1.2147847
36. B. Gelloz, T. Shibata, N. Koshida, Stable electroluminescence of nanocrystalline silicon device activated by high pressure water vapor annealing, Appl. Phys. Lett. 89 (2006) 191103. https://doi.org/10.1063/1.2385206
37. A.J. Kenyon, P.F. Trwoga, C.W. Pitt, G. Rehm, The origin of photoluminescence from thin films of silicon-rich silica. J. Appl. Phys. **79**, 9291–9300 (1996). https://doi.org/10.1063/1.362605
38. T. Shimizu-Iwayama, S. Nakao, K. Saitoh, Visible photoluminescence in Si + -implanted thermal oxide films on crystalline Si. Appl. Phys. Lett. **65**, 1814–1816 (1994). https://doi.org/10.1063/1.112852
39. S. Takeoka, M. Fujii, S. Hayashi, Size-dependent photoluminescence from surface-oxidized Si nanocrystals in a weak confinement regime. Phys. Rev. B. **62**, 16820–16825 (2000). https://doi.org/10.1103/PhysRevB.62.16820
40. S. Schuppler, S.L. Friedman, M.A. Marcus, D.L. Adler, Y.H. Xie, F.M. Ross, Y.J. Chabal, T.D. Harris, L.E. Brus, W.L. Brown, E.E. Chaban, P.F. Szajowski, S.B. Christman, P.H. Citrin, Size, shape, and composition of luminescent species in oxidized Si nanocrystals and H-passivated porous Si. Phys. Rev. B. **52**, 4910–4925 (1995). https://doi.org/10.1103/PhysRevB.52.4910
41. W.L. Wilson, P.F. Szajowski, L.E. Brus, Quantum confinement in size-selected, surface-oxidized silicon nanocrystals. Science **262**, 1242–1244 (1993). https://doi.org/10.1126/science.262.5137.1242
42. J.R. Heath, A Liquid-Solution-Phase Synthesis of Crystalline Silicon, Science (80-. ). 258 (1992) 1131–1133. https://doi.org/10.1126/science.258.5085.1131.
43. K. Dohnalová, T. Gregorkiewicz, K. Kůsová, K. Dohnalova, T. Gregorkiewicz, K. Kusova, Silicon quantum dots: surface matters., J. Phys. Condens. Matter. 26 (2014) 173201. https://doi.org/10.1088/0953-8984/26/17/173201.
44. D.B. Mawhinney, J.A. Glass, J.T. Yates, FTIR Study of the Oxidation of Porous Silicon. J. Phys. Chem. B. **101**, 1202–1206 (1997). https://doi.org/10.1021/jp963322r
45. B. Gelloz, F.B. Juangsa, T. Nozaki, K. Asaka, N. Koshida, L. Jin, Si/SiO2 Core/Shell Luminescent Silicon Nanocrystals and Porous Silicon Powders With High Quantum Yield, Long Lifetime, and Good Stability. Front. Phys. **7**, 1–7 (2019). https://doi.org/10.3389/fphy.2019.00047
46. L.H. Lie, M. Duerdin, E.M. Tuite, A. Houlton, B.R. Horrocks, Preparation and characterisation of luminescent alkylated silicon quantum dots. J. Electroanal. Chem. **538**, 183–190 (2002)
47. M. Rosso-Vasic, E. Spruijt, B. Van Lagen, L. De Cola, H. Zuilhof, Alkyl-Functionalized Oxide-Free Silicon Nanoparticles: Synthesis and Optical Properties. Small **4**, 1835–1841 (2008). https://doi.org/10.1002/smll.200800066
48. J.H. Ahire, Q. Wang, P.R. Coxon, G. Malhotra, R. Brydson, R. Chen, Y. Chao, Highly luminescent and nontoxic amine-capped nanoparticles from porous silicon: Synthesis and their

use in biomedical imaging. ACS Appl. Mater. Interfaces. **4**, 3285–3292 (2012). https://doi.org/10.1021/am300642m
49. M. Rosso-Vasic, E. Spruijt, Z. Popović, K. Overgaag, B. Van Lagen, B. Grandidier, D. Vanmaekelbergh, D. Domínguez-Gutiérrez, L. De Cola, H. Zuilhof, Amine-terminated silicon nanoparticles: Synthesis, optical properties and their use in bioimaging. J. Mater. Chem. **19**, 5926–5933 (2009). https://doi.org/10.1039/b902671a
50. Q. Li, T.-Y. Luo, M. Zhou, H. Abroshan, J. Huang, H.J. Kim, N.L. Rosi, Z. Shao, R. Jin, Silicon Nanoparticles with Surface Nitrogen: 90% Quantum Yield with Narrow Luminescence Bandwidth and the Ligand Structure Based Energy Law, ACS Nano. (2016) acsnano.6b03113. https://doi.org/10.1021/acsnano.6b03113.
51. K. Kůsová, P. Hapala, J. Valenta, P. Jelínek, O. Cibulka, L. Ondič, I. Pelant, Direct Bandgap Silicon: Tensile-Strained Silicon Nanocrystals. Adv. Mater. Interfaces. **1**, 1300042 (2014). https://doi.org/10.1002/admi.201300042
52. J.D. Holmes, K.J. Ziegler, R.C. Doty, L.E. Pell, K.P. Johnston, B.A. Korgel, Highly Luminescent Silicon Nanocrystals with Discrete Optical Transitions. J. Am. Chem. Soc. **123**, 3743–3748 (2001). https://doi.org/10.1021/ja002956f
53. K. Dohnalová, A.N. Poddubny, A. a Prokofiev, W.D. de Boer, C.P. Umesh, J.M. Paulusse, H. Zuilhof, T. Gregorkiewicz, Surface brightens up Si quantum dots: direct bandgap-like size-tunable emission, Light Sci. Appl. 2 (2013) e47. https://doi.org/10.1038/lsa.2013.3.
54. Y. Yu, C.M. Hessel, T.D. Bogart, M.G. Panthani, M.R. Rasch, B.A. Korgel, Room temperature hydrosilylation of silicon nanocrystals with bifunctional terminal alkenes. Langmuir **29**, 1533–1540 (2013). https://doi.org/10.1021/la304874y
55. P.D. Howes, R. Chandrawati, M.M. Stevens, Colloidal nanoparticles as advanced biological sensors, Science (80-. ). 346 (2014) 1247390. https://doi.org/10.1016/0250-6874(86)80002-6.
56. S. Chandra, B. Ghosh, G. Beaune, U. Nagarajan, T. Yasui, J. Nakamura, T. Tsuruoka, Y. Baba, N. Shirahata, F.M. Winnik, Functional double-shelled silicon nanocrystals for two-photon fluorescence cell imaging: spectral evolution and tuning. Nanoscale **8**, 9009–9019 (2016). https://doi.org/10.1039/c6nr01437b
57. Y. Zhong, X. Sun, S. Wang, F. Peng, F. Bao, Y. Su, Y. Li, S.T. Lee, Y. He, Facile, Large-Quantity Synthesis of Stable, Tunable-Color Silicon Nanoparticles and Their Application for Long-Term Cellular Imaging. ACS Nano **9**, 5958–5967 (2015). https://doi.org/10.1021/acsnano.5b00683
58. F. Maier-Flaig, J. Rinck, M. Stephan, T. Bocksrocker, M. Bruns, C. Kübel, A.K. Powell, G.A. Ozin, U. Lemmer, Multicolor silicon light-emitting diodes (SiLEDs). Nano Lett. **13**, 475–480 (2013). https://doi.org/10.1021/nl3038689
59. B. Ghosh, Y. Masuda, Y. Wakayama, Y. Imanaka, J. Inoue, K. Hashi, K. Deguchi, H. Yamada, Y. Sakka, S. Ohki, T. Shimizu, N. Shirahata, Hybrid White Light Emitting Diode Based on Silicon Nanocrystals. Adv. Funct. Mater. **24**, 7151 (2014). https://doi.org/10.1002/adfm.201401795
60. Y. Zhong, F. Peng, F. Bao, S. Wang, X. Ji, L. Yang, Y. Su, S.T. Lee, Y. He, Large-scale aqueous synthesis of fluorescent and biocompatible silicon nanoparticles and their use as highly photostable biological probes. J. Am. Chem. Soc. **135**, 8350–8356 (2013). https://doi.org/10.1021/ja4026227
61. M. Ehbrecht, B. Kohn, F. Huisken, M. Laguna, V. Paillard, Photoluminescence and resonant Raman spectra of silicon films produced by size-selected cluster beam deposition. Phys. Rev. B. **56**, 6958–6964 (1997). https://doi.org/10.1103/PhysRevB.56.6958
62. F. Huisken, G. Ledoux, O. Guillois, C. Reynaud, Light-emitting silicon nanocrystals from laser pyrolysis. Adv. Mater. **14**, 1861–1865 (2002). https://doi.org/10.1002/adma.200290021
63. F. Hua, F. Erogbogbo, M.T. Swihart, E. Ruckenstein, Organically capped silicon nanoparticles with blue photoluminescence prepared by hydrosilylation followed by oxidation. Langmuir **22**, 4363–4370 (2006). https://doi.org/10.1021/la0529106
64. L. Mangolini, E. Thimsen, U. Kortshagen, High-yield plasma synthesis of luminescent silicon nanocrystals. Nano Lett. **5**, 655–659 (2005). https://doi.org/10.1021/nl050066y

65. K. Nozaki, S. Kita, T. Baba, Room temperature continuous wave operation and controlled spontaneous emission in ultrasmall photonic crystal nanolaser. Opt. Express. **15**, 7506–7514 (2007). https://doi.org/10.1364/OE.15.007506
66. R. Anthony, U. Kortshagen, Photoluminescence quantum yields of amorphous and crystalline silicon nanoparticles. Phys. Rev. B. **80**, 1–6 (2009). https://doi.org/10.1103/PhysRevB.80.115407
67. N. Koshida, T. Nakamura, Emerging Functions of Nanostructured Porous Silicon—With a Focus on the Emissive Properties of Photons, Electrons, and Ultrasound. Front. Chem. **7**, 1–15 (2019). https://doi.org/10.3389/fchem.2019.00273
68. C. Lam, Y.F. Zhang, Y.H. Tang, C.S. Lee, I. Bello, S.T. Lee, Large-scale synthesis of ultrafine Si nanoparticles by ball milling. J. Cryst. Growth. **220**, 466–470 (2000). https://doi.org/10.1016/S0022-0248(00)00882-4
69. A. Heintz, M. Fink, Mechanochemical synthesis of blue luminescent alkyl/alkenyl-passivated silicon nanoparticles. Adv. Mater. **19**, 3984–3988 (2007). https://doi.org/10.1002/adma.200602752
70. S. Bose, M.A. Ganayee, B. Mondal, A. Baidya, S. Chennu, J.S. Mohanty, T. Pradeep, Synthesis of Silicon Nanoparticles from Rice Husk and their Use as Sustainable Fluorophores for White Light Emission. ACS Sustain. Chem. Eng. **6**, 6203–6210 (2018). https://doi.org/10.1021/acssuschemeng.7b04911
71. I.W. Boyd, J.I.B. Wilson, Laser processing of silicon. Nature **303**, 481–486 (1983). https://doi.org/10.1038/303481a0
72. I. Umezu, H. Minami, H. Senoo, A. Sugimura, Synthesis of photoluminescent colloidal silicon nanoparticles by pulsed laser ablation in liquids. J. Phys. Conf. Ser. **59**, 392–395 (2007). https://doi.org/10.1088/1742-6596/59/1/083
73. V. Svrcek, T. Sasaki, N. Koshizaki, V. Švrček, T. Sasaki, Y. Shimizu, N. Koshizaki, Blue luminescent silicon nanocrystals prepared by ns pulsed laser ablation in water, Appl. Phys. Lett. 89 (2006) 213113. https://doi.org/10.1063/1.2397014
74. K. Saitow, Silicon Nanoclusters Selectively Generated by Laser Ablation in Supercritical Fluid. J. Phys. Chem. B. **109**, 3731–3733 (2005). https://doi.org/10.1021/jp0442551
75. K. Saitow, T. Yamamura, Effective Cooling Generates Efficient Emission: Blue, Green, and Red Light-Emitting Si Nanocrystals. J. Phys. Chem. C. **113**, 8465–8470 (2009). https://doi.org/10.1021/jp900067s
76. S. Yang, W. Cai, H. Zhang, X. Xu, H. Zeng, Size and structure control of Si nanoparticles by laser ablation in different liquid media and further centrifugation classification. J. Phys. Chem. C. **113**, 19091–19095 (2009). https://doi.org/10.1021/jp907285f
77. N. Shirahata, D. Hirakawa, Y. Sakka, Interfacial-related color tuning of colloidal Si nanocrystals. Green Chem. **12**, 2139–2141 (2010). https://doi.org/10.1039/c0gc00502a
78. N. Shirahata, D. Hirakawa, Y. Masuda, Y. Sakka, Size-Dependent Color Tuning of Efficiently Luminescent Germanium Nanoparticles., Langmuir. (2012). https://doi.org/10.1021/la303482s.
79. K. Abderrafi, R. García Calzada, M.B. Gongalsky, I. Suárez, R. Abarques, V.S. Chirvony, V.Y. Timoshenko, R. Ibáñez, J.P. Martínez-Pastor, Silicon nanocrystals produced by nanosecond laser ablation in an organic liquid, J. Phys. Chem. C. 115 (2011) 5147. https://doi.org/10.1021/jp109400v.
80. N. Shirahata, M.R. Linford, S. Furumi, L. Pei, Y. Sakka, R.J. Gates, M.C. Asplund, Laser-derived one-pot synthesis of silicon nanocrystals terminated with organic monolayers, Chem. Commun. (2009) 4684. https://doi.org/10.1039/b905777c.
81. D. Tan, Z. Ma, B. Xu, Y. Dai, G. Ma, M. He, Z. Jin, J. Qiu, Surface passivated silicon nanocrystals with stable luminescence synthesized by femtosecond laser ablation in solution. Phys. Chem. Chem. Phys. **13**, 20255–20261 (2011). https://doi.org/10.1039/c1cp21366k
82. D. Zhang, B. Gökce, S. Barcikowski, B. Gokce, S. Barcikowski, Laser Synthesis and Processing of Colloids: Fundamentals and Applications. Chem. Rev. **117**, 3990–4103 (2017). https://doi.org/10.1021/acs.chemrev.6b00468

83. K.S.K. Min, K.V. Shcheglov, C.M. Yang, H.A. Atwater, M.L. Brongersma, A. Polman, Defect-related versus excitonic visible light emission from ion beam synthesized Si nanocrystals in $SiO_2$. Appl. Phys. Lett. **69**, 2033–2035 (1996). https://doi.org/10.1063/1.116870
84. M.L. Brongersma, P.G. Kik, a. Polman, K.S. Min, H. a. Atwater, Size-dependent electron-hole exchange interaction in Si nanocrystals, Appl. Phys. Lett. 76 (2000) 351. https://doi.org/10.1063/1.125751.
85. Y. Osaka, K. Tsunetomo, F. Toyomura, H.M. Kohno, Y. Osaka, K. Tsunetomo, F. Toyomura, H.M. Kohno, Visible Photoluminescence from Si Microcrystals Embedded in SiO2 Glass Films. Jpn. J. Appl. Phys. **31**, L365–L366 (1992). https://doi.org/10.1143/JJAP.31.L365
86. S. Hayashi, T. Nagareda, Y. Kanzawa, K. Yamamoto, Photoluminescence of si-rich sio2 films: Si clusters as luminescent centers. Jpn. J. Appl. Phys. **32**, 3840–3845 (1993). https://doi.org/10.1143/JJAP.32.3840
87. Y. Kanzawa, T. Kageyama, S. Takeoka, M. Fujii, S. Hayashi, K. Yamamoto, Size-dependent near-infrared photoluminescence spectra of Si nanocrystals embedded in SiO2 matrices. Solid State Commun. **102**, 533–537 (1997). https://doi.org/10.1016/S0038-1098(96)00774-0
88. M. Fujii, A. Mimura, S. Hayashi, K. Yamamoto, Photoluminescence from Si nanocrystals dispersed in phosphosilicate glass thin films: Improvement of photoluminescence efficiency. Appl. Phys. Lett. **75**, 184 (1999). https://doi.org/10.1063/1.124313
89. M. Fujii, A. Mimura, S. Hayashi, Hyperfine structure of the electron spin resonance of phosphorus-doped Si nanocrystals, Phys. Rev. Lett. 89 (2002) 206805. https://doi.org/10.1103/PhysRevLett.89.206805
90. M. Fujii, K. Toshikiyo, Y. Takase, Y. Yamaguchi, S. Hayashi, Below bulk-band-gap photoluminescence at room temperature from heavily P- and B-doped Si nanocrystals. J. Appl. Phys. **94**, 1990 (2003). https://doi.org/10.1063/1.1590409
91. M. Fujii, M. Yoshida, Y. Kanzawa, S. Hayashi, K. Yamamoto, 1.54 μm photoluminescence of Er3+ doped into SiO2 films containing Si nanocrystals: Evidence for energy transfer from Si nanocrystals to Er3+, Appl. Phys. Lett. 71 (1997) 1198–1200. https://doi.org/10.1063/1.119624.
92. S.Y. Seo, J.H. Shin, Carrier-induced Er3+ luminescence quenching of erbium-doped silicon-rich silicon oxide. Appl. Phys. Lett. **75**, 4070–4072 (1999). https://doi.org/10.1063/1.125539
93. P.G. Kik, a. Polman, Exciton–erbium interactions in Si nanocrystal-doped SiO[sub 2], J. Appl. Phys. 88 (2000) 1992. https://doi.org/10.1063/1.1305930.
94. K. Watanabe, M. Fujii, S. Hayashi, Resonant excitation of Er by the energy transfer from Si nanocrystals. J. Appl. Phys. **90**, 4761–4767 (2001). https://doi.org/10.1063/1.1409572
95. C.M. Hessel, E.J. Henderson, J.G.C. Veinot, Hydrogen silsesquioxane: A molecular precursor for nanocrystalline Si-SiO2 composites and freestanding hydride-surface-terminated silicon nanoparticles. Chem. Mater. **18**, 6139–6146 (2006). https://doi.org/10.1021/cm0602803
96. J.A. Kelly, E.J. Henderson, J.G.C. Veinot, Sol–gel precursors for group 14 nanocrystals. Chem. Commun. **46**, 8704 (2010). https://doi.org/10.1039/c0cc02609c
97. K. Shinoda, S. Yanagisawa, K. Sato, K. Hirakuri, Stability of nanocrystalline silicon particles in solution. J. Cryst. Growth. **288**, 84–86 (2006). https://doi.org/10.1016/j.jcrysgro.2005.12.035
98. M. Fukuda, M. Fujii, H. Sugimoto, K. Imakita, S. Hayashi, Surfactant-free solution-dispersible Si nanocrystals surface modification by impurity control. Opt. Lett. **36**, 4026 (2011). https://doi.org/10.1364/ol.36.004026
99. H. Sugimoto, M. Fujii, K. Imakita, S. Hayashi, K. Akamatsu, All-Inorganic Near-Infrared Luminescent Colloidal Silicon Nanocrystals: High Dispersibility in Polar Liquid by Phosphorus and Boron Codoping. J. Phys. Chem. C. **116**, 17969–17974 (2012). https://doi.org/10.1021/jp305832x
100. H. Sugimoto, M. Fujii, K. Imakita, S. Hayashi, K. Akamatsu, Codoping n- and p-Type Impurities in Colloidal Silicon Nanocrystals: Controlling Luminescence Energy from below Bulk Band Gap to Visible Range. J. Phys. Chem. C. **117**, 11850–11857 (2013). https://doi.org/10.1021/jp4027767

101. H. Sugimoto, M. Fujii, M. Fukuda, K. Imakita, Acceptor-related low-energy photoluminescence from boron-doped Si nanocrystals, J. Appl. Phys. 110 (2011) 063528. https://doi.org/10.1063/1.3642952
102. H. Sugimoto, M. Fujii, K. Imakita, S. Hayashi, K. Akamatsu, Phosphorus and Boron Codoped Colloidal Silicon Nanocrystals with Inorganic Atomic Ligands. J. Phys. Chem. C. **117**, 6807–6813 (2013). https://doi.org/10.1021/jp312788k
103. M.L. Mastronardi, F. Hennrich, E.J. Henderson, F. Maier-Flaig, C. Blum, J. Reichenbach, U. Lemmer, C. Kubel, D. Wang, M.M. Kappes, G. a Ozin, Preparation of monodisperse silicon nanocrystals using density gradient ultracentrifugation, J. Am. Chem. Soc. 133 (2011) 11928–11931. https://doi.org/10.1021/ja204865t.
104. N. Shirahata, J. Nakamura, J.I. Inoue, B. Ghosh, K. Nemoto, Y. Nemoto, M. Takeguchi, Y. Masuda, M. Tanaka, G.A. Ozin, Emerging Atomic Energy Levels in Zero-Dimensional Silicon Quantum Dots. Nano Lett. **20**, 1491–1498 (2020). https://doi.org/10.1021/acs.nanolett.9b03157
105. J.G.C. Veinot, Synthesis, surface functionalization, and properties of freestanding silicon nanocrystals, Chem. Commun. (2006) 4160–4168. https://doi.org/10.1039/b607476f.
106. M.A. Islam, H. Mobarok, R. Sinelnikov, T.K. Purkait, J.G.C. Veinot, Phosphorous Pentachloride Initiated Functionalization of Silicon, Langmuir. (2017) 1–14. https://doi.org/10.1021/acs.langmuir.7b00518.
107. M.A. Islam, R. Sinelnikov, M.A. Howlader, A. Faramus, J.G.C. Veinot, Mixed Surface Chemistry: An Approach to Highly Luminescent Biocompatible Amphiphilic Silicon Nanocrystals. Chem. Mater. **30**, 8925–8931 (2018). https://doi.org/10.1021/acs.chemmater.8b04227
108. J. a. Kelly, J.G.C. Veinot, An investigation into near-UV hydrosilylation of freestanding silicon nanocrystals, ACS Nano. 4 (2010) 4645–4656. https://doi.org/10.1021/nn101022b.
109. Z. Yang, G.B. De los Reyes, L. V Titova, I. Sychugov, M. Dasog, J. Linnros, F.A. Hegmann, J.G.C. Veinot, Evolution of the Ultrafast Photoluminescence of Colloidal Silicon Nanocrystals with Changing Surface Chemistry., ACS Photonics. 2 (2015) 595–605. https://doi.org/10.1021/acsphotonics.5b00143.
110. L. Canham, Mechanical Properties of Porous Silicon, in: L.T. Canham (Ed.), Handb. Porous Silicon, 2nd ed., Springer International Publishing, Cham, 2014: pp. 213–220. https://doi.org/10.1007/978-3-319-05744-6_21.
111. J.L. Heinrich, C.L. Curtis, G.M. Credo, M.J. Sailor, K.L. Kavanagh, Luminescent colloidal silicon suspensions from porous silicon. Science **255**, 66–68 (1992). https://doi.org/10.1126/science.255.5040.66
112. J. Valenta, P. Janda, K. Dohnalová, D. Nižňansky, F. Vácha, J. Linnros, Colloidal suspensions of silicon nanocrystals: From single nanocrystals to photonic structures. Opt. Mater. **27**, 1046–1049 (2005). https://doi.org/10.1016/j.optmat.2004.08.060
113. J. Valenta, A. Fucikova, I. Pelant, On the origin of the fast photoluminescence band in small silicon nanoparticles, New J. Phys. 10 (2008) 073022. http://iopscience.iop.org/1367-2630/10/7/073022 (accessed October 15, 2013).
114. K. Kůsová, O. Cibulka, K. Dohnalová, I. Pelant, A. Fučíková, J. Valenta, Yellow-emitting colloidal suspensions of silicon nanocrystals: Fabrication technology, luminescence performance and application prospects. Phys. E Low-Dimensional Syst. Nanostructures. **41**, 982–985 (2009). https://doi.org/10.1016/j.physe.2008.08.022
115. K. Kůsová, O. Cibulka, K. Dohnalová, I. Pelant, J. Valenta, A. Fűcíková, K. Žídek, J. Lang, J. Englich, P. Matějka, P. Štěpánek, S. Bakardjieva, Brightly luminescent organically capped silicon nanocrystals fabricated at room temperature and atmospheric pressure. ACS Nano **4**, 4495–4504 (2010). https://doi.org/10.1021/nn1005182
116. V. Svrcek, T. Sasaki, Y. Shimizu, N. Koshizaki, Silicon nanocrystals formed by pulsed laser-induced fragmentation of electrochemically etched Si micrograins, Chem. Phys. Lett. 429 (2006) 483. http://www.sciencedirect.com/science/article/pii/S0009261406011675 (accessed March 25, 2013).
117. T. Nakamura, Z. Yuan, S. Adachi, High-yield preparation of blue-emitting colloidal Si nanocrystals by selective laser ablation of porous silicon in liquid., Nanotechnology. 25 (2014) 275602. https://doi.org/10.1088/0957-4484/25/27/275602.

118. Z. Yuan, T. Nakamura, S. Adachi, K. Matsuishi, Luminescence color control and quantum-efficiency enhancement of colloidal Si nanocrystals by pulsed laser irradiation in liquid. Nanoscale **9**, 1193–1200 (2017). https://doi.org/10.1039/c6nr08757d
119. S. Limaye, S. Subramanian, B. Goller, J. Diener, D. Kovalev, Scaleable synthesis route for silicon nanocrystal assemblies, Phys. Status Solidi(A). 204 (2007) 1297–1301. https://doi.org/10.1002/pssa.200674320.
120. K.W. Kolasinski, N.J. Gimbar, H. Yu, M. Aindow, E. M??kil??, J. Salonen, Regenerative Electroless Etching of Silicon, Angew. Chemie - Int. Ed. 56 (2017) 624–627. https://doi.org/10.1002/anie.201610162.
121. T. Nakamura, Z. Yuan, K. Watanabe, S. Adachi, Bright and multicolor luminescent colloidal Si nanocrystals prepared by pulsed laser irradiation in liquid, Appl. Phys. Lett. 108 (2016) 023105. https://doi.org/10.1063/1.4939902
122. Z. Yuan, T. Nakamura, S. Adachi, K. Matsuishi, Improvement of Laser Processing for Colloidal Silicon Nanocrystal Formation in a Reactive Solvent. J. Phys. Chem. C. **121**, 8623–8629 (2017). https://doi.org/10.1021/acs.jpcc.7b00288
123. D. Kovalev, J. Diener, H. Heckler, G. Polisski, N. Künzner, F. Koch, Optical absorption cross sections of Si nanocrystals. Phys. Rev. B. **61**, 4485–4487 (2000). https://doi.org/10.1103/PhysRevB.61.4485
124. V. Svrcek, D. Mariotti, U. Cvelbar, G. Filipič, M. Lozac'h, C. McDonald, T. Tayagaki, K. Matsubara, Environmentally Friendly Processing Technology for Engineering Silicon Nanocrystals in Water with Laser Pulses, J. Phys. Chem. C. 120 (2016) 18822–18830. https://doi.org/10.1021/acs.jpcc.6b04405.
125. T. Nakamura, N. Koshida, Z. Yuan, J. Otsubo, High-yield green fabrication of colloidal silicon quantum dots by low-temperature thermal cracking of porous silicon, APL Mater. 8 (2020) 081105. https://doi.org/10.1063/5.0014206.

# Chapter 10
# Processing of Transparent Materials Using Laser-Induced High-Energy State in Liquid


**Tadatake Sato**

**Abstract** High-energy states formed upon focused laser irradiation are a basic phenomenon in laser material processing. The high-energy states formed in liquid can also contribute to material processing. When laser pulses are focused onto the solid–liquid interface through solid materials, a high-energy state is generated at the interface. More precisely, it is generated in a thin liquid layer in contact with solid materials. Laser-induced backside wet etching (LIBWE) is a laser micromachining technique that utilizes the action of such high-energy states at the solid–liquid interface. Precise micromachining of hard and brittle transparent materials was achieved using this technique. The simple concept of this technique allows a variety of combinations of lasers, materials, and experimental setups for processing. While the concept for processing is relatively simple, the mechanism of the material removal is rather complex and has not yet been fully elucidated. A variety of material combination and conditions of laser irradiation is a factor making it more complex. Several attempts have been made to address the action of the high-energy state in liquid for material removal. Studies regarding LIBWE are overviewed in the context of the action of high-energy state generated in liquid.

**Keywords** Laser processing · Micromachining · Transparent materials · Laser-induced backside wet etching (LIBWE) · Laser-absorbing liquid

## 10.1 Introduction: High-Energy States in Liquid for Laser Processing

The formation of local high-energy states upon focused irradiation of laser pulses is a basic phenomenon in processing of various materials with lasers [1]. Upon absorbing the energy of laser light, the irradiated part is instantaneously heated; thus, the formed local high-energy state results in the removal of materials by melting,

T. Sato (✉)
National Institute of Advanced Industrial Science and Technology (AIST), Tsukuba Central 2, 1-1-1 Umezono, Tsukuba 305-8568, Ibaraki, Japan
e-mail: sato-tadatake@aist.go.jp



Y. Ishikawa et al. (eds.), *High-Energy Chemistry and Processing in Liquids*,
https://doi.org/10.1007/978-981-16-7798-4_10

evaporation, or ablation. The recent development of high-power lasers with kW-classes has contributed to high-speed processing in the industry. Moreover, laser light can be focused into a small spot at the micrometer scale. Therefore, the precise micromachining of solid material surfaces is executable. This type of laser micro-processing can be applied to various materials ranging from hard materials such as metals and ceramics, to soft materials, such as organic materials and biological tissues.

Similar phenomena can be induced on the surfaces of liquids. Laser ablation from the liquid surface has been studied to obtain a better understanding of the mechanisms of laser ablation in more complex solid systems [2, 3]. Material ejection from the free surfaces of liquid has been observed similarly to solid materials when the fluence of the irradiation exceeds the threshold [4–6]. Laser ablation of liquid was investigated using a nanosecond imaging technique, as shown in Fig. 10.1. The threshold was evaluated at 100 mJ/cm$^2$ for benzene irradiated by ultraviolet (UV) pulses of a KrF excimer laser [4]. The difference in threshold values for several benzene derivatives was revealed to be correlated to the efficiency of photochemical bond dissociation [5]. On the other hand, the ablation of diluted solutions of benzene derivatives showing relatively larger thresholds was discussed based on the photothermal mechanism [6]. Thus, the high-energy states used in laser material processing can be formed on the surface of liquids. Note, laser ablation of laser-absorbing liquids should be distinguished from laser-induced breakdown in transparent liquids, which are often used

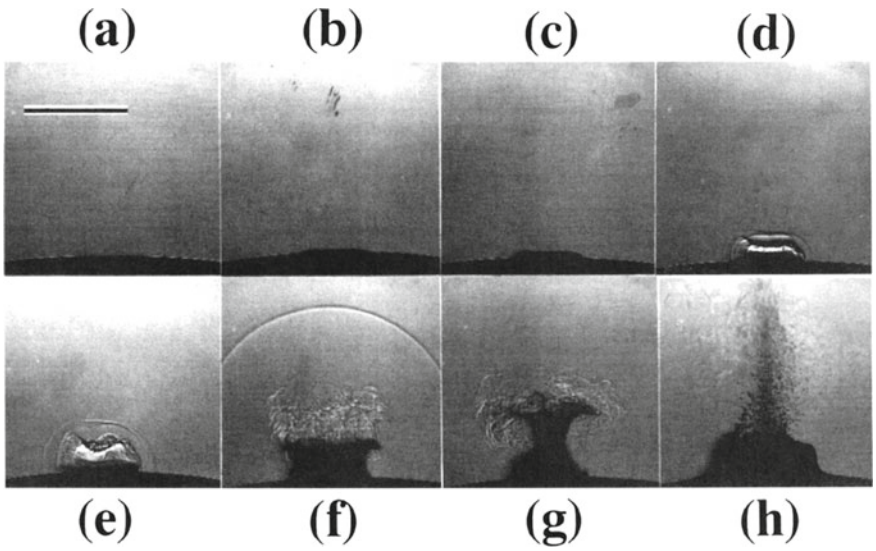


**Fig. 10.1** Nanosecond images of laser ablation of liquid toluene. The scale bar represents 2 mm. Delay time: **a** 0 ns, **b** 35 ns, **c** 100 ns, **d** 500 ns, **e** 1 μs, **f** 5 μs, **g** 10 μs, and **h** 100 μs. Reprinted with permission from Ref [5], Copyright 1994 American Chemical Society

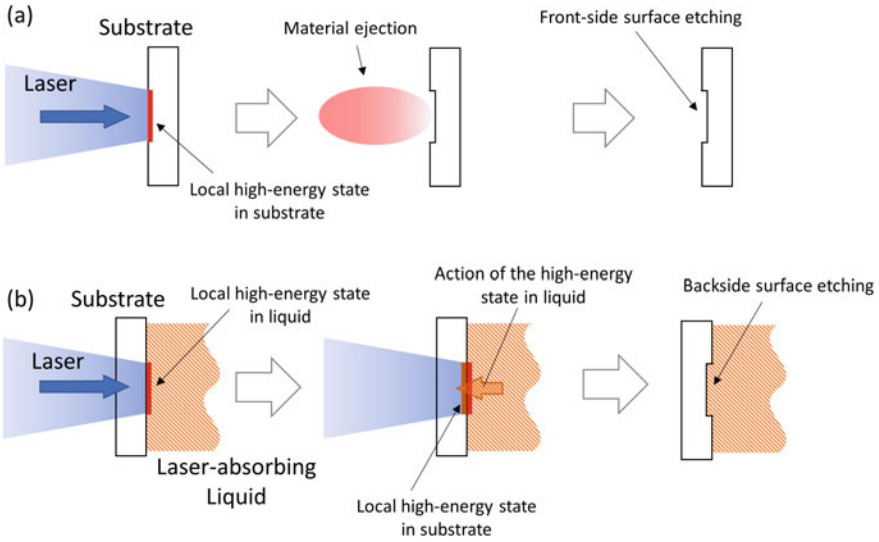


**Fig. 10.2** Schematic drawing of **a** direct and **b** indirect laser processes

for laser-induced breakdown spectroscopy (LIBS) measurements for the elemental analysis [7].

When a substrate that can transmit laser light is set on the laser-absorbing liquid, a high-energy state can be formed at the solid–liquid interface by irradiating the liquid through the transparent substrates (Fig. 10.2). More precisely, a high-energy state is formed in the thin liquid layer in contact with the transparent materials. When the liquid presents a higher absorbance at the laser wavelength, the liquid layer where the laser light is absorbed becomes thinner, resulting in a higher energy density. This high-energy state can act on the backside surface of the substrate and etch the surface gently. Wang et al. developed a surface micromachining technique employing this phenomenon and named it "Laser-induced backside wet etching (LIBWE)" [8].

## 10.2 Laser-Induced Backside Wet Etching (LIBWE) in the Initial Study

LIBWE is a technique for the laser surface micromachining of transparent materials, such as glasses. Because transparent materials are generally hard and brittle, precise micromachining is challenging; for example, cracks are easily formed. The same issue exists for laser processing. Moreover, the transparency of the materials makes laser processing inherently difficult, which is based on the energy deposition upon the optical absorption of materials. One important characteristic of LIBWE is the crack-free micromachining of the transparent materials. The indirect action of a

laser enables precise micromachining without crack formation; the laser energy is not absorbed directly by the transparent materials to be etched, but instead by the laser-absorbing liquid in contact with the transparent materials. A diagram of the LIBWE apparatus is shown in the Fig. 10.3.

In a study by Wang et al. [8], fused silica was etched by a KrF excimer laser ($\lambda = 248$ nm, FWHM 30 ns, pulse repetition 2 Hz) by employing an acetone solution containing pyrene with a concentration of 0.4 mol/dm$^3$. The laser light was patterned by a metal stencil mask and projected at the liquid–solid interface. The laser energy passing through the fused silica plate was absorbed by the solution at the interface. The concentration of the solution was nearly saturated, demonstrating a high absorbance at the laser wavelength. The optical penetration depth was evaluated as 0.7 μm. Etching showed the threshold for applied fluence similarly to the laser ablation; etching was observed at a fluence higher than the threshold of 240 mJ/cm$^2$. Therefore, the LIBWE has often been described as the etching based on the laser ablation of liquid. The threshold of LIBWE is significantly lower than the fluence required for direct laser ablation (>14 J/cm$^2$) [9]. The surface of the irradiated area was etched pulse by pulse above the threshold, as shown in Fig. 10.4. The etch rate was ranged from 5 to 25 nm/pulse for the applied laser fluence ranging from 400 to 1300 mJ/cm$^2$. Additionally, the fabrication of crack-free and debris-free microstructures was demonstrated on patterned irradiation, as shown in Fig. 10.5.

Several research groups have developed the LIBWE technique. The important characteristics of this technique are as follows:

(1) Micrometer-scale structures can be fabricated on the surface of hard and brittle transparent materials without debris or crack formation.
(2) Etching can be performed at a significantly lower fluence compared to that required for the direct ablation of materials.

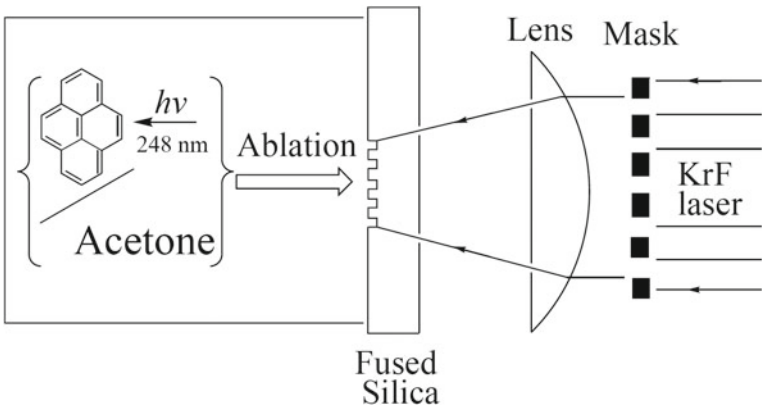


**Fig. 10.3** Diagram of LIBWE apparatus used in Ref. [8]. Reprinted by permission from Springer: Ref [8], Copyright 1999.

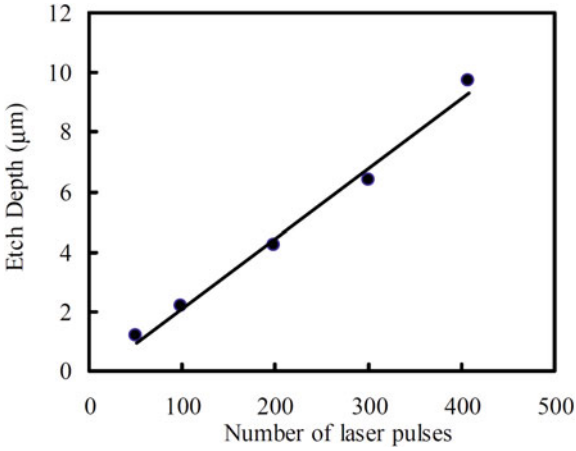


**Fig. 10.4** Etch depths increased linearly with the number of applied laser pulses. Reprinted by permission from Springer: Ref [8], Copyright 1999.

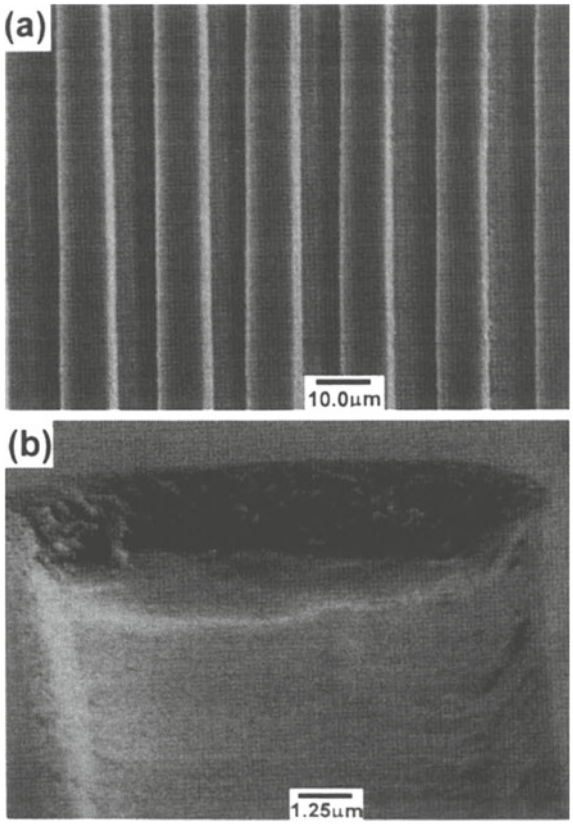


**Fig. 10.5** Micrometer-scale lines and spaces pattern fabricated on the surface of fused silica. Reprinted by permission from Springer: Ref [8], Copyright 1999.

(3) The depth of etching increases linearly with the applied pulse numbers, enabling the fabrication of structures with high aspect ratios, whose depths can be precisely controlled.
(4) A smooth etched surface can be obtained.
(5) The apparatus used for general laser processing can be applied to this technique.
(6) Stable and reproducible processing can be executed upon accumulation of pulse irradiation.
(7) Various lasers and laser-absorbing liquids can be applied for the processing of various transparent materials.

Utilization of the indirect action of lasers is an effective method for the crack-free micromachining of hard and brittle transparent materials. Another indirect processing techniques utilizing the action of laser-induced plasma have been developed as the laser-induced plasma-assisted ablation (LIPAA) technique [10–14]. Additionally, laser etching at a surface-adsorbed layer (LESAL) [15] and laser-induced backside dry etching (LIBDE) [14, 16, 17] have been developed based on studies regarding LIBWE.

## 10.3 Variation in Combination of Lasers and Materials

The LIBWE process is based on the formation of the laser-induced high-energy state at the liquid–solid interface and its action on transparent materials. This simple concept of LIBWE has resulted in a wide variety of laser and material selection. However, a substantial limitation is that the laser energy sufficient for etching must reach the interface. Therefore, the optical transmittance at the laser wavelength is a key factor in the LIBWE process. Figure 10.6 presents the optical transmittance spectra of several transparent materials with indications of the wavelengths of typical lasers.

In a study by Wang et al. [8], a KrF excimer laser and fused silica plates were employed as the light source and the material to be etched, respectively. This combination came from the experiments on laser ablation of polymeric materials enhanced by dye molecules [18], where the transparent polymeric films containing dye molecules were ablated by UV pulses of a KrF excimer laser. Pyrene, a popular dye molecule used by photochemists, was chosen as the dye molecule for the experiments. Transparent polymeric films containing pyrene were prepared on fused silica substrates. When the polymer film was unintentionally irradiated through the substrate, the fused silica plate was unexpectedly damaged, despite the irradiated fluence being significantly below the damage threshold. To apply this phenomenon to the etching of fused silica, polymer films were replaced by an acetone solution containing pyrene. By employing the solution, the liquid–solid interface can be regenerated after each laser pulse irradiation, and deeper etching can be attained by repeated pulse irradiation. Acetone was selected as a solvent to dissolve pyrene at high concentrations. Note, similar damage formation had already been realized in an early study regarding the laser ablation of molecular liquids [2]. In this section, the

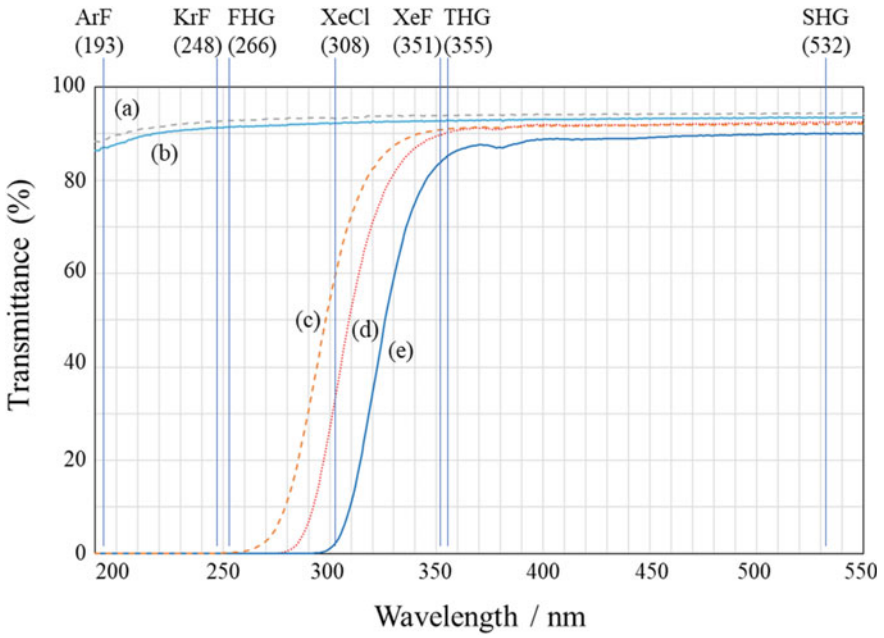


**Fig. 10.6** Optical transmission spectra of representative transparent materials: **a** $CaF_2$ (2 mm), **b** fused silica (2 mm), **c** Corning gorilla glass, aluminosilicate glass (1 mm), **d** Corning Pyrex, borosilicate glass (2 mm), **e** soda-lime glass (1.75 mm); thickness indicated in parentheses

combinations of lasers and materials are discussed. Lasers, laser-absorbing liquids, and materials to be etched are listed with the types of experimental setups in Table 10.1. Note, the studies reporting the first usage of the combination are listed.

Precedent to the naming of LIBWE, there were several reports regarding the laser machining of transparent materials assisted by liquid media. Ikeno et al. had reported the etching of fused silica using a Nd:YAG laser ($\lambda = 1064$ nm, $\tau = 1$ ms, pulse energy 3 J/pulse) with a $NiSO_4$ aqueous solution (~2 mol/l) [19]. Hole drilling at the millimeter to sub-millimeter scale was performed by the focused irradiation of near-infrared (NIR) laser pulses. Dolgaev et al. reported the drilling of sapphire using a copper-vapor laser ($\lambda = 510$ nm, $\tau = 10$ ns, pulse repetition 8 kHz) [20, 21] combined with aqueous solutions of $CrO_3$, $KMnO_3$, and $FeCl_3$ or a highly dispersed suspension of carbon in toluene as a laser-absorbing liquid. These drilling processes originate from the high-energy states formed in the liquid layer. In these studies, it was concluded that the first action of the high-energy state is not the etching of the transparent materials, but the formation of absorbing oxide layers on the surface of the transparent materials [21]. The contributions of the deposited and/or modified layers for the LIBWE process are presented in a later section. Recently, similar processes were reported as LIBWE processes employing aqueous solutions of inorganic compounds combined with fundamental or second harmonic generation (SHG) pulses of diode-pumped solid-state (DPSS) lasers [22–28].

**Table 10.1** Combinations of lasers, laser-absorbing liquids, materials to be etched, and types of the experimental setups in the LIBWE processes

| Laser (wavelength) | Laser-absorbing liquid | Material to be etched | Type of experimental setup | References |
|---|---|---|---|---|
| ArF excimer (193) | Naphthalene/methylmethacrylate | Fused silica | Focused | [29] |
| KrF excimer (248) | Pyrene/acetone | Fused silica | Mask projection | [8] |
| | Pyrene/acetone | Quartz(c-$SiO_2$) | Mask projection | [30] |
| | Pyrene/acetone | $CaF_2$ | Mask projection | [31] |
| | Pyrene/$C_2Cl_4$<br>Pyrene/cyclohexane | Fused silica<br>Sapphire<br>$CaF_2$<br>$MgF_2$ | Mask projection<br>Scanning counter mask | [32] |
| | Pyrene/toluene | Fused silica | Phase grating projection | [33] |
| | Pyrene/$C_6H_5Cl$<br>Pyrene/$C_6H_4Cl_2$<br>Pyrene/$C_6H_5F$ | Fused silica | Mask projection | [34] |
| | Toluene | Fused silica | Mask projection | [35] |
| | Toluene | Sapphire | Mask projection | [36] |
| | Phenolphthalein/N-methyl-2-pyrrolidone | Sapphire | Mask projection | [37] |
| | Naphthalene /methylmethacrylate | Fused silica | Focused | [38] |
| | Pyranine/water | Fused silica | Mask projection | [39] |
| | Naphthalene $(SO_3)_3Na_3$/water | Fused silica | Mask projection | [40] |
| | Liquid Ga | Fused silica | Mask projection | [41] |
| | Hg | Fused silica | Mask projection | [42] |
| | liquid Sn | Fused silica | Mask projection | [17] |

(continued)

**Table 10.1** (continued)

| Laser (wavelength) | Laser-absorbing liquid | Material to be etched | Type of experimental setup | References |
|---|---|---|---|---|
| FHG of Solid Laser (266) | Pyrene/acetone<br>Toluene<br>*t*-butylbenzene<br>Trimethylbenzene<br>Naphthalene/Acetone<br>Phenanthrene/acetone<br>Anthracene/acetone<br>9-methylanthrathene/acetone<br>9,10-dimethylanthrathene/acetone<br>Fluoranthene/acetone<br>9-phenylanthracene/acetone | Schott Borofloat33 (borosilicate glass) | Stage scan | [43] |
| | Toluene | Fused silica | Galvano scan | [44] |
| | $C_6H_5Cl$ | Sapphire | Phase grating (interference) | [45] |
| | Naphthalene/methylmethacrylate | Fused silica | Beam interference | [46] |
| | Naphthalene/methylmethacrylate | $SiO_2$ film/fused silica<br>$Al_2O_3$ film/fused silica<br>$Y_2O_3$ film/fused silica | Beam interference | [47] |
| | Naphthalene/methylmethacrylate | $HfO_2$ film/fused silica<br>$ZrO_2$ film/fused silica | Beam interference | [48] |
| XeCl excimer (308) | Pyrene/THF | FEP | Mask projection | [49] |
| | Pyrene/THF | Quartz | Mask projection | [50] |
| | Pyrene/acetone | Fused silica | Mask projection | [51] |
| | Pyrene/acetone | Quartz | Mask projection | [52] |

(continued)

**Table 10.1** (continued)

| Laser (wavelength) | Laser-absorbing liquid | Material to be etched | Type of experimental setup | References |
|---|---|---|---|---|
| | Pyrene/acetone | $CaF_2$<br>$BaF_2$<br>Sapphire | Mask projection | [53] |
| XeF excimer (351) | Pyrene/acetone<br>Pyrene/$C_2Cl_4$<br>Pyrene/cyclohexane | Corning pyrex, 7059<br>Schott D263, AF45<br>(borosilicate glass) | Mask projection | [54] |
| | Pyranine/water | Fused silica | Mask projection | [39] |
| THG of Solid Laser (355) | Pyrene/toluene<br>Toluene | Quartz | Galvano scan | [55] |
| | Toluene | Fused silica | Galvano scan | [56] |
| | Toluene | Sapphire<br>$MgF_2$<br>$CaF_2$ | Galvano scan | [57] |
| Cu vapor (510) | $CrO_3$/water<br>$KMnO_4$/water<br>Carbon (suspended)/toluene | Sapphire | Stage scan | [20] |
| | $FeCl_3$/water | Sapphire | Stage scan | [21] |
| SHG of Solid Laser (515) | $KMnO_4$ / water | $SiO_2$ | Galvano scan | [22] |
| SHG of Solid Laser (527) | $AgNO_3$/water<br>Amaranth/water | Silicate glass | Stage scan | [23] |
| | Amaranth + PEG/water | Silicate glass | Focused | [58] |
| | $AgNO_3$ / water | Sapphire | Stage scan | [24] |

(continued)

**Table 10.1** (continued)

| Laser (wavelength) | Laser-absorbing liquid | Material to be etched | Type of experimental setup | References |
|---|---|---|---|---|
| SHG of Solid Laser (532) | Rose bengal/acetone | Soda-lime glass | Stage scan | [59] |
| | Rose bengal/water | ITO-coated glass | Stage scan | [60] |
| | Rhodamine 6G/ethanol–toluene | Fused silica | Galvano scan | [61] |
| | Oil-Red-O/*p*-xylene | Borosilicate glass | Stage scan | [62] |
| | Sudan IV/toluene | Soda-lime glass | Galvano scan with beam interference | [63] |
| | $KMnO_4$ / water | PMMA | Stage scan | [25] |
| | Liquid Ga<br>In–Ga | Soda-lime glass<br>Quartz | Stage scan | [64] |
| | Liquid Ga | Fused silica fiber | Dipping | [65] |
| | In–Ga | Zerodur | Stage scan | [66] |
| | In–Ga | PMMA | Stage scan | [67] |
| Fundamental of Solid Laser (1064) | $NiSO_4$ / water | Fused silica | Focused | [19] |
| | $CuSO_4$ /water | Soda-lime glass | Galvano scan | [26] |
| | $CuSO_4$ /water | Sapphire | Galvano scan | [27] |
| | $CuSO_4$ + phosphoric acid /water | Soda-lime glass | Galvano scan | [28] |
| | Liquid Ga | Fused silica | Focused | [68] |
| | In–Ga | NaCl | Focused | [69] |

After the naming of LIBWE, etching employing excimer lasers (ArF ($\lambda$ = 193 nm), KrF ($\lambda$ = 248 nm), XeCl ($\lambda$ = 308 nm), and XeF ($\lambda$ = 351 nm)) has been reported by several research groups. The number of studies employing a KrF excimer laser is larger than that using other excimer lasers, which may be due to the fact that the optical absorption ascribed to the $\pi$-$\pi^*$ transition of the benzene ring is located at approximately 250 nm, and a wide variety of molecules containing benzene rings can be used as absorbers. The materials to be etched were fused silica, quartz ($SiO_2$ crystal), sapphire, and fluoride crystals ($CaF_2$, $MgF_2$, and $BaF_2$). These materials can transmit laser pulses at UV wavelengths. Wang et al. reported the etching of a UV-transparent fluoropolymer (FEP) film [49]. One exceptional case is the study by Cheng et al., who reported the etching of Borofloat33 (Schott), which is a type of borosilicate glass, with the fourth harmonic generation (FHG) pulses ($\lambda$ = 266 nm) of a DPSS laser [43]. As shown in Fig. 10.6, pyrex classified to borosilicate glasses presents an absorption edge at approximately 350 nm, and no transmittance at 266 nm. It was reported that a Borofloat33 glass with a thickness of 0.7 mm absorbed 50% of the laser energy. Thus, the remaining 50% reached the interface and was used for the crack-free fabrication of microtrenches. This study revealed that the LIBWE of the materials that weakly absorbs the laser energy is executable if sufficient energy reaches the interface without causing damage to the substrates. When a XeF excimer laser that emits laser pulses with the wavelength of 351 nm is used for LIBWE, the etching of borosilicate glasses (Corning, Pyrex, 7059, Schott D263, AF45) can be performed as a processing of highly transparent materials [54].

Pyrene is a major dye molecule used in LIBWE. Several organic solvents such as acetone, tetrahydrofuran, toluene, cyclohexane, and tetrachloroethylene ($C_2Cl_4$) are used to dissolve it. Because molecules with benzene rings present an optical absorption near 250 nm, toluene and other substituted benzenes can be used as laser-absorbing dye molecules [35, 36, 43–45]. Cheng et al. investigated the threshold fluences of LIBWE for 11 organic laser-absorbing liquids and confirmed that the unit length absorbance, which is related to the optical penetration lengths, correlated with the obtained threshold values [43]. Vass et al. used a solution of naphthalene dissolved in methylmethacrylate for LIBWE with ArF [29] and KrF [38] excimer lasers as well as FHG pulses of the Nd:YAG laser [46–48]. Fujito et al. employed a solution of phenolphthalein dissolved in N-methyl-2-pyrrolidone for the etching of sapphire [37]. Aqueous dye solutions have adapted for LIBWE by Ding et al.; pyranine [39] and naphthalene-1,3,5-trisulfonic acid trisodium salt ($Np(SO_3)_3Na_3$) [40] were employed as dye molecules. Thus, a wide variety of dye molecules can be used in the LIBWE employing the UV lasers.

The green emission of SHG pulses of solid lasers in visible range ($\lambda$ = 515, 527, and 532 nm) can be used for LIBWE. As shown in Fig. 10.6, all transparent materials present a sufficient transmittance at this wavelength. Cheng et al. developed the LIBWE employing SHG pulses and named it visible LIBWE [59]. Soda-lime glasses, the most commonly available glass used for windows in buildings, whose absorption edges are located near 380 nm, can be etched by employing the visible wavelengths. Tsvetkov et al. employed an aqueous solution containing Amaranth, a red food dye [23, 58]. Moreover, polyethylene glycol (PEG) was added to the solution

to reduce the surface tension of the liquid, which affected the cavitation behavior, which will be described later.

Liquid metal was also used for etching. Etching using liquid-phase gallium combined with a KrF excimer laser was first reported by Zimmer et al., which presents one-order higher etch rates than the LIBWE employing an organic dye solution [41]. The low melting point of gallium (29.76 ºC) enables its use in the liquid phase upon heating. Although high reflectivity causes energy loss, the penetration depth of light is relatively small. Therefore, metals in the liquid phase can be good laser-absorbing liquids for the LIBWE process, which can be used for a wide range of wavelengths. Zimmer et al. reported the etching of fused silica by fundamental laser pulses of the Nd:YAG laser ($\lambda = 1064$ nm) [68]. Studies employing mercury [42] and molten tin [17] have been reported. Eutectic indium/gallium alloy (In–Ga) can be used for visible LIBWE without heating [64, 66, 67, 69].

## 10.4 Variation in Experimental Setups for LIBWE

In addition to the combination of lasers and materials, the simple concept of LIBWE also results in variation of the setups for irradiation. In this section, the experimental setups for LIBWE are reviewed.

### *10.4.1 Mask Projection with Excimer Laser*

Because excimer lasers can emit laser pulses with large areas, they can be used for patterned irradiation by mask projection. This technique is similar to that used in the photolithography processes for semiconductor device production. Therefore, setups for patterned irradiation with homogeneous light intensity have been established and enable precise surface micromachining. It was reported that smooth surface with low roughness of 50 nm could be obtained by employing this type of apparatus [52, 70]. The fabrication of micro-optical devices has been demonstrated [32, 52, 70, 71].

Initially, we used simple experimental setups equipped by ourselves with a metal stencil mask and a planoconvex lens for each experiment. Although the fabrication of microstructures can be demonstrated, the quality of fabrication is occasionally not exceptional [51]. Beam shaping and the precise positioning of samples to match the liquid–solid interface with the imaging plane of the optical system enable high-quality machining, as shown in Fig. 10.7; for fabricating the structure, Böhme et al. used an irradiation setup with projection optics having a resolution of 5.0 and 1.5 μm [32].

We introduced a machining setup composed of beam homogenizer, dielectric attenuator, chromium-on-quartz-masks, as well as an × 8 demagnification objective (MicroLas Lasersystem GmbH), and a motorized x–y-z stage for the sample positioning (Fig. 10.8). The resolution limit of this system was specified as 3 μm lines

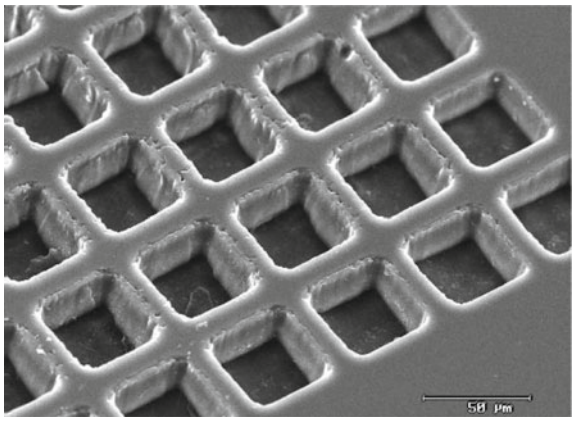


**Fig. 10.7** Surface structure of fused silica fabricated by Böhme et al. Reprinted from Ref. [32], Copyright (2002), with permission from Elsevier.

(a)

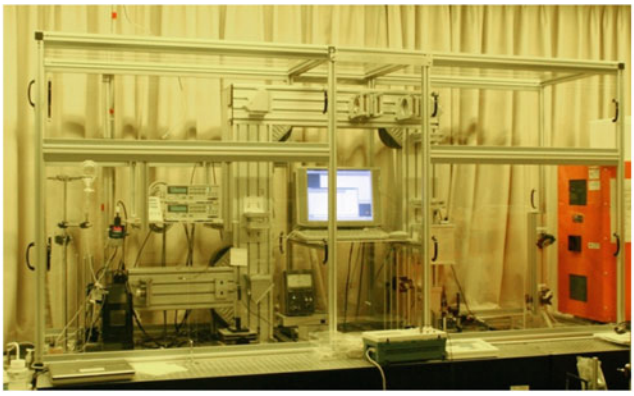

(b)

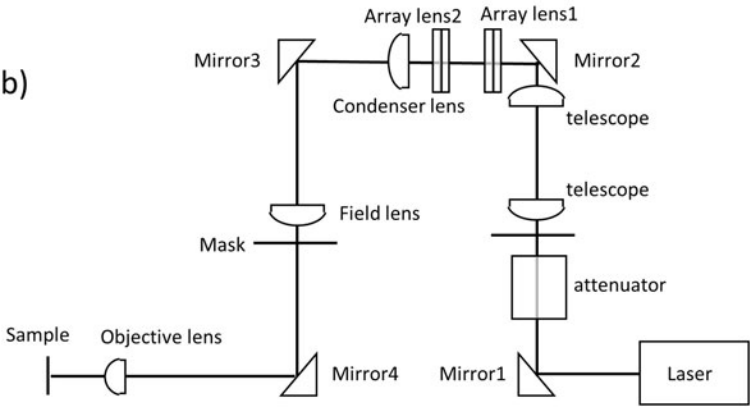


**Fig. 10.8** **a** An image and **b** layout of the new setup for the mask projection LIBWE

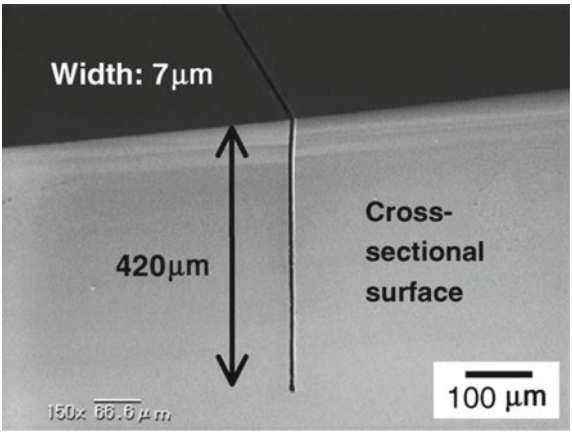


**Fig. 10.9** Cross-sectional SEM image of deep microtrench fabricated with adjusting dynamically the sample position for matching the etch front to the imaging plane of the optical system. Reprinted from Ref. [74], Copyright (2006), with permission from Elsevier.

and spaces. The quality and reproducibility of microfabrication improved by using this system [36]. A precise control of the sample position within ± 15 μm to match the liquid–solid interface with the imaging plane of the optical system is required for precise etching [72]. We developed a system to compensate for the inclination of the surface and the displacement induced by the surrounding temperature change; the fabrication of microstructures with homogeneous quality over a wide area on the fused silica plates was then attained. Based on the precise positioning of samples, the fabrication of deep microtrenches and holes with high aspect ratios was performed (Fig. 10.9) [72–77]. This type of fabrication can be achieved by locating dynamically the etch front, which in this case was the bottom of the trenches, at the imaging plane of the optical system.

### *10.4.2 Etching on Interference*

The spatial resolution of the mask projection systems is limited by optical systems. To achieve a higher resolution, the interference of laser beams was applied for etching. Zimmer et al. reported the fabrication of a surface relief grating with a period of 780 nm by phase grating projection using a Schwarzschild objective [33]. The submicron resolution of LIBWE was proven in this study. Vass et al. demonstrated the fabrication of surface relief grating with a shorter period by a two-beam interference of FHG pulses of the Nd:YAG laser with incident angles up to 60° [46]. They named this method TWIN-LIBWE and fabricated surface relief gratings with various periods, the smallest period was 104 nm (Fig. 10.10) [47, 48, 78–81].

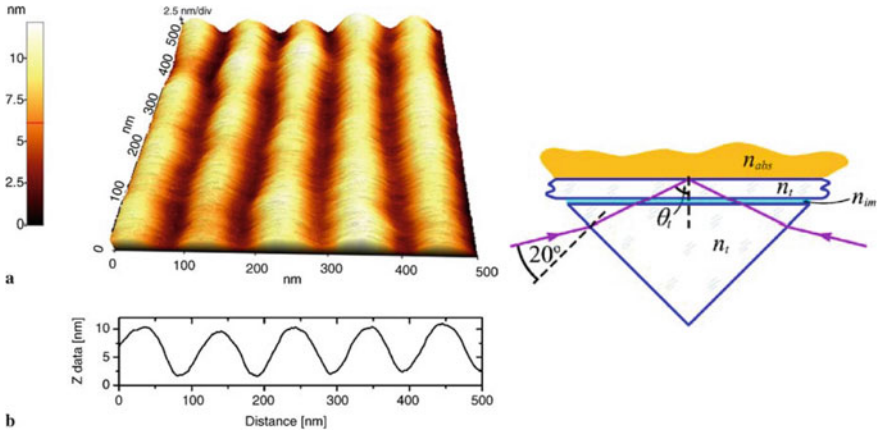


**Fig. 10.10** Surface relief grating with period of 104 nm fabricated by the immersion TWIN-LIBWE. Reprinted by permission from Springer: Ref [78], Copyright 2007.

### *10.4.3 Direct-Writing by Scanning with High Repetition*

Laser-Direct-Write (LDW) is an attractive technique that enables versatile material processing with patterns in scales ranging from nanometers to millimeters [82], where lasers with a high pulse repetition (~100 kHz) are employed for computer-controlled two- and three-dimensional pattern formation in a serial fashion. LDW with LIBWE was first demonstrated by Cheng et al. using computer numerical control (CNC) stages and a DPSS laser operated with a pulse repetition of 4.5 kHz [43]. Microchannel structures for microfluidic chips were fabricated on borosilicate glass. A direct write with beam scanning by a galvanometer-based point scanning system was demonstrated by Niino et al. [44, 83] (Fig. 10.11), where a DPSS laser was operated at a 10 kHz pulse repetition and used for flexible mask-less processing. This type of LIBWE can be used for the laser marking of glass materials (Fig. 10.12) [44, 63, 84].

## 10.5 Various Studies Regarding the Elucidation of the LIBWE Mechanisms

While the basic concept of the LIBWE is simple, the mechanisms involved are complex. The mechanism of material removal has not yet been fully understood. Several processes would be involved in the etching phenomena, and their contributions may be altered by the applied materials and conditions of laser irradiation. The wide variety of materials and conditions for LIBWE makes the situation more

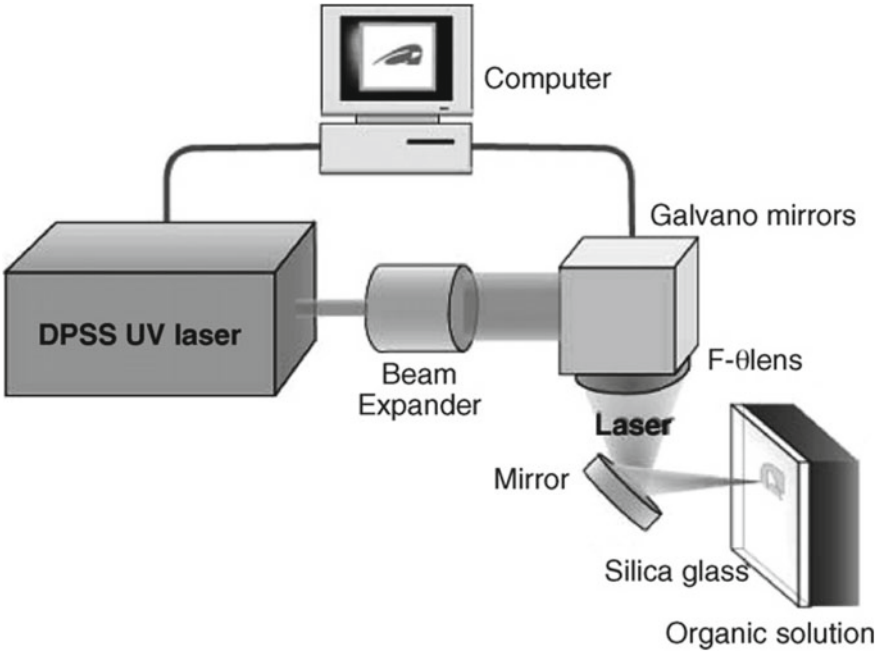


**Fig. 11** Setup for LDW LIBWE employing the galvanometer-based point scanning system with a DPSS laser. Reprinted from Ref. [83], Copyright (2007), with permission from Elsevier.

complex. Discussions and diagnostic studies addressing the elemental phenomena are overviewed.

### *10.5.1 Estimation of Temperature Rise*

In the initial studies, the temperature increase in the thin liquid layers was evaluated using the absorbed laser energy, liquid volume that absorbed laser light obtained from the optical penetration depth, and the heat capacity of the solvent [8, 52]. The maximum temperatures of the liquid layer were evaluated as 1900–2300 K, which is above the softening and melting temperatures of fused silica. Wang et al. discussed on the involvement of super-heated liquid [31] produced by heating within a pulse duration based on a cyclic multiphotonic absorption mechanism [85]. Note, the transient imaging of the interface indicated that the initial flat bubbles before expansion were observed at a delay time of 100 ns [35, 40, 86]. Organic molecules are decomposed at such high temperature. Partial decomposition of organic molecules was indicated by emission of gas bubbles with the distinctive odor of sulfur-containing gas [39], or by production of carbon soot from photolyzed toluene [35]. Note, the emitted gas bubbles should be distinguished from the cavitation bubbles that will be

described later. Kopitkovas et al. reported that the difference in the threshold fluences obtained for the LIBWE by KrF and XeCl lasers can be explained by the calculated induced temperatures reaching the melting point of quartz (1880 K) as shown in Fig. 10.13 [52]. However, as indicated by Vass et al., the temperature of the solid target was not calculated in these studies. They evaluated the temperature of a solid target by numerical calculations using the method of finite differences [29, 86]. The surface of the solid target was concluded to reach the melting point; the depths of the melting layers formed upon irradiation at various fluences were also evaluated (Fig. 10.14). The difference between etch depth and calculated maximum depth of the melted layer was ascribed to the partial removal of the melted fused silica. On

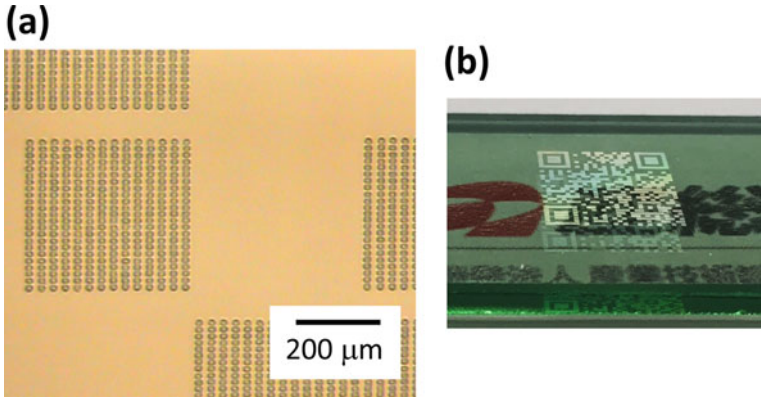


**Fig. 10.12** Laser marking on glass by LIBWE with **a** micropit array structures for writing **b** a QR code on a soda-lime glass plate. Reproduced from Ref. [84] with permission from Japan Laser Processing Society.

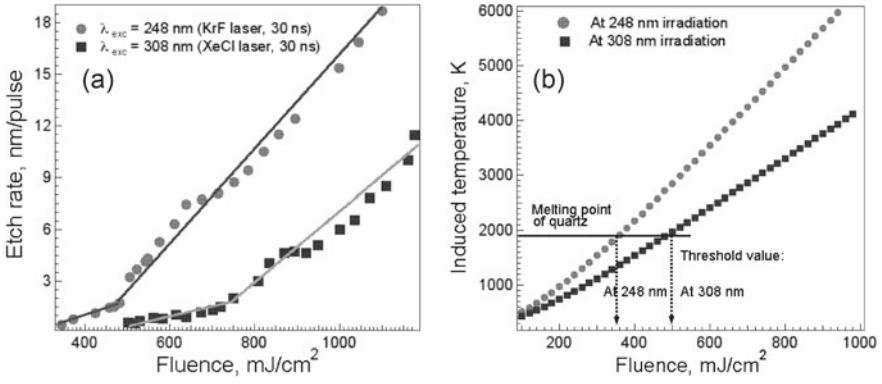


**Fig. 10.13** **a** Etch rates dependent on the laser fluence presenting two-stage behaviors in the LIBWE employing the KrF and XeCl laser. **b** Calculated temperature at the quartz-liquid interface as a function of the laser fluence. Reprinted from Ref. [52], Copyright (2003), with permission from Elsevier.

the other hand, an analytical solution of the laser-induced temperature distribution was evaluated by Zimmer [87]. He argued that the temperature of the surface of the solid target did not reach the melting point without the existence of the interface absorption. The existence of a modified layer with interface absorption was proven, which will be described later.

### *10.5.2 Etch Rates and Threshold Values*

The threshold fluence and the etch rate have been focused in the studies on LIBWE as the parameters characterizing the processes. Böhme et al. first realized that the etch rates dependent on the fluence were fitted by two lines in different fluence ranges [32]. As shown in Fig. 10.13, similar two-stage behaviors were confirmed in different studies [40, 52, 53, 70, 86]. This appears to be a general behavior for LIBWE, indicating that different mechanisms are involved in the etching process. Note, the etch rate of LIBWE can be varied with spot size for irradiation, as shown in Fig. 10.15 [88]. The experimental results obtained under different conditions should be treated with care.

The incubation effect in the LIBWE is shown in Fig. 10.15. The existence of this effect was first reported by Yasui et al. [51] in the etching of fused silica with a XeCl excimer laser at the fluence of 0.4 J/cm$^2$; etching was not discerned upon irradiation with 3000 pulses, while etching with the depth of 0.4 μm was observed upon irradiation with 5000 pulses. Similar behavior was observed for the etching of quartz by a XeCl excimer laser at low fluences (1.18 J/cm$^2$), just above the threshold; start of the etching was observed upon irradiation with more than 150 laser pulses [53]. The existence of the incubation effect revealed the involvement of an initial process causing the generation of absorbing sites, such as defects. Ding et al. confirmed that

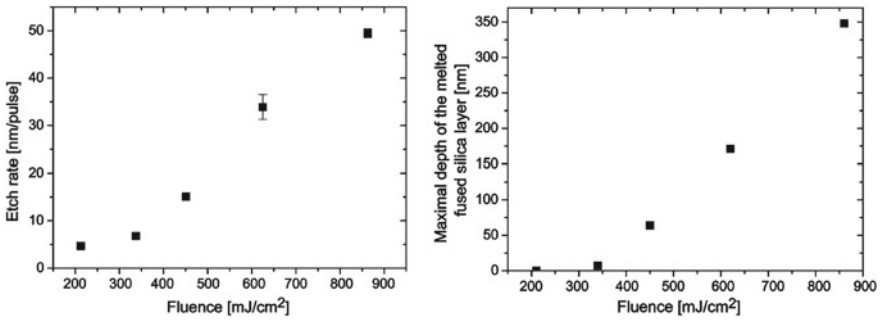


**Fig. 10.14** (left) Etch rates versus laser fluence for LIBWE employing an ArF excimer laser and naphthalene/methylmethacrylate, (right) the maximum depth of the melted fused silica layer calculated by the method of finite differences. Reprinted from Ref. [29], Copyright (2004), with permission from Elsevier.

the etching of sapphire started after the etched area was covered with black particles of amorphous carbon [36]. On the other hand, the etching from a single laser pulse was confirmed at a sufficiently high fluence [53]. Single-shot etching was also confirmed in LIBWE employing focused laser pulses of DPSS lasers [84, 89].

### *10.5.3 Characterization of Etched Surface.*

Etched surfaces were evaluated using Rutherford backscattering spectroscopy (RBS) [90], X-ray photoelectron spectroscopy (XPS) [90–92], Raman scattering spectroscopy [90, 91], fiber-tip ATR-IR spectroscopy [91], and ellipsometry [92]. The Raman spectra of the etched surface indicated the presence of amorphous carbon deposits, while chemical modification of fused silica was indicated by the XPS and fiber-tip ATR-IR results. Thus, not only the adhered amorphous carbon deposit layer, but also the formation of a modified layer in LIBWE was indicated. RBS measurements indicated the generation of an amorphization layer on quartz crystals with a thickness of up to 60 nm. The formation of a modified layer on fused silica with a thickness of 10–30 nm with an absorption coefficient of 100,000–180,000 $cm^{-1}$ was indicated by ellipsometry. Zimmer et al. evaluated the absorption coefficient of the modified layer by local absorption measurements for a surface prepared by the ion beam beveling technique (Fig. 10.16) [93]. The existence of a modified layer on fused silica with a thickness less than 25 nm with a high absorption coefficient of $40 \times 10^4$ $cm^{-1}$ was indicated. The thickness of a few tens nm was indicated in several observations and coincident with the typical etch rates obtained for LIBWE with excimer lasers. Based on the confirmation of the existence of a modified layer, they proposed a new mechanism of LIBWE composed of the formation of a modified layer and its direct ablation [94].

### *10.5.4 Diagnostic Studies on LIBWE*

To address the mechanism of LIBWE, diagnostic studies using several in situ measurements have been applied. As previously indicated, a rapid temperature increase in the liquid layer causes cavitation in the liquid. The cavitation behaviors were observed by transient imaging using the shadow graph technique, as shown in Fig. 10.17 [35, 40, 86, 95–97], and in situ reflectivity measurements [61, 98]. Based on the dynamics of a bubble, the pressure inside of a bubble can be evaluated based on the following physical model [99]:

$$p\left(R, \frac{dR}{dt}\right) = \left(p_{stat} + \frac{2\sigma}{R_n}\right)\left(\frac{R_n}{R}\right)^{3\kappa} - \frac{2\sigma}{R} - \frac{4\mu}{R}\frac{dR}{dt} \tag{10.1}$$

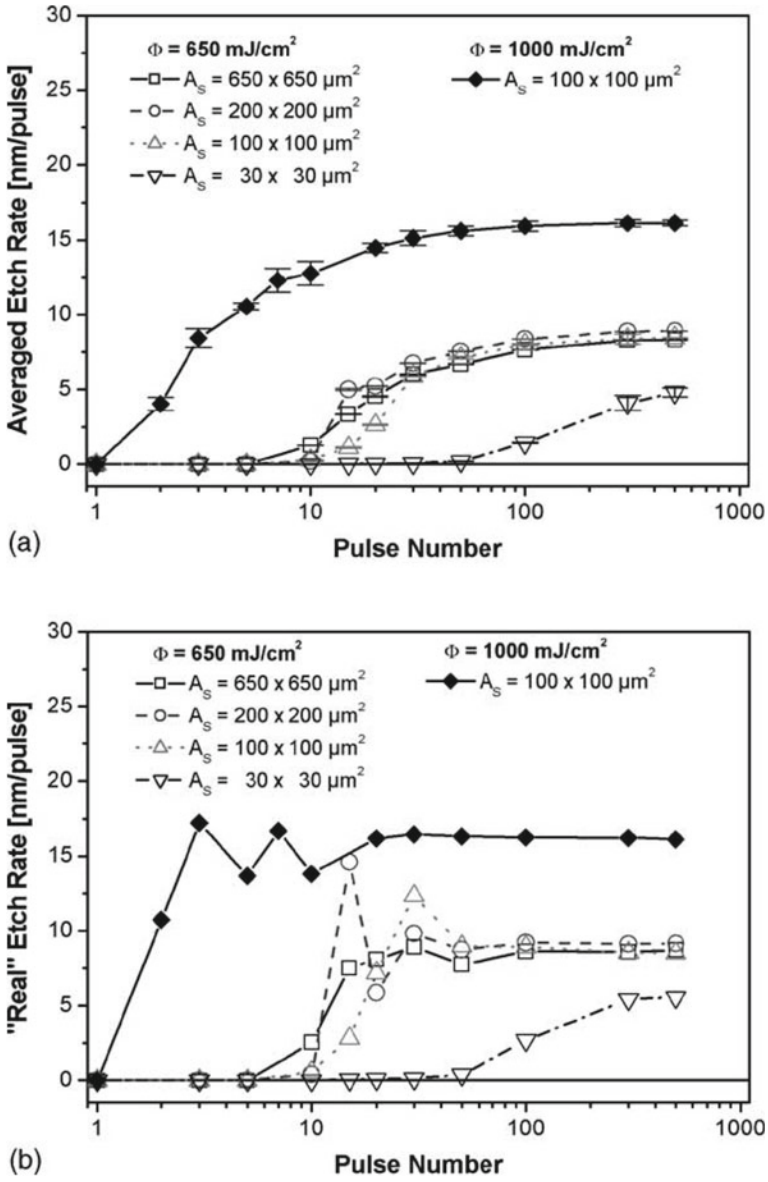


**Fig. 10.15** **a** Averaged etch rate in dependent on the applied pulse number for difference spot sizes. **b** Calculated "real" etch rate per laser pulse. Reprinted from Ref. [88], Copyright (2005), with permission from Elsevier.

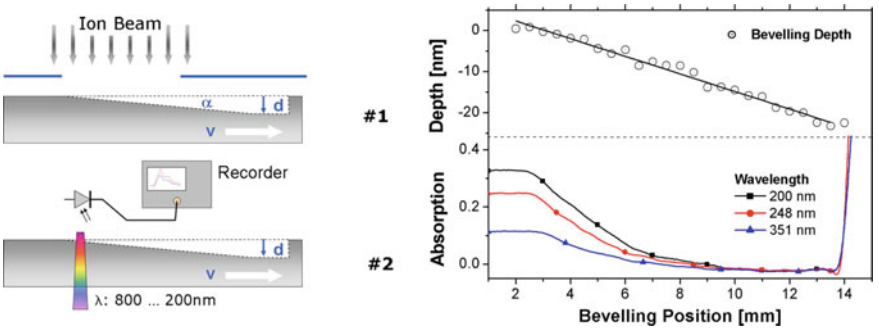


**Fig. 10.16** (left) Schematic illustration of the preparation of the sample by ion beam beveling (#1) and the near-surface local absorption measurement (#2). (right) Measured etch depth and absorption at different positions of beveling. Reprinted from Ref. [93] with permission from AIP Publishing.

where $R$ is the radius, $R_n$ is the equilibrium radius of the bubble, $p_{stat}$ is the statistic ambient air pressure, $\sigma$ is the surface tension, $\mu$ is the dynamic shear viscosity, and $\kappa$ is the polytropic exponent of the solvent. Vass et al. calculated an initial high pressure of approximately 70 MPa, which decreased instantly with the expansion of the bubble [86]. This initial high pressure was considered to remove the melted material from the surface. The generated initial high pressure propagates in the liquid as a shockwave, which can be detected using a piezoelectric pressure gauge [44, 58, 84, 89, 96, 97]. The initial pressure of 65 MPa deduced from the distance dependence was in the same order with the pressure obtained from the cavitation dynamics [97]. Meanwhile, cavitation dynamics indicate that the high-pressure is generated once again when cavitation bubble collapsed. Pairs of pressure signals corresponding to the formation and collapse of the cavitation bubble were observed (Fig. 10.18) [44, 84, 89]. The single-shot etching behavior was confirmed to be correlated to the cavitation behavior [84]. A micropit with a diameter of approximately 30 μm and the maximum depth up to 0.35 μm was fabricated by single-pulse irradiation. The maximum depths of micropits fabricated by two laser pulses with different time intervals are shown in Fig. 10.19; the etching with depth of approximately 0.6 μm was confirmed at the time interval larger than 125 μs, while etch depths became the half of them at the time interval less than 60 μs. Because the lifetime of cavitation bubble was evaluated as 63.2 ± 0.9 μs for the applied pulse energy of 44.0 μJ/pulse, these results revealed that the etching by the second pulse irradiated before collapsing of the cavitation bubble was completely suppressed. Moreover, decreased etch depths at the time intervals between 70 and 120 μs indicated partial suppression due to the formation of the second bubble [95]. The suppression of the etching by the second pulse in the successive two pulses was clearly observed in the etching with beam scanning. Figure 10.20 shows the micropit array fabricated with pulse repetition and scan speed of (a) 10 kHz and 750 mm/s and (b) 20 kHz and 1500 mm/s, respectively; laser pulses were delivered at every 75 μm in both cases. When the pulse repetition was 20 kHz, time interval of laser pulses of 50 μs was shorter than the lifetime

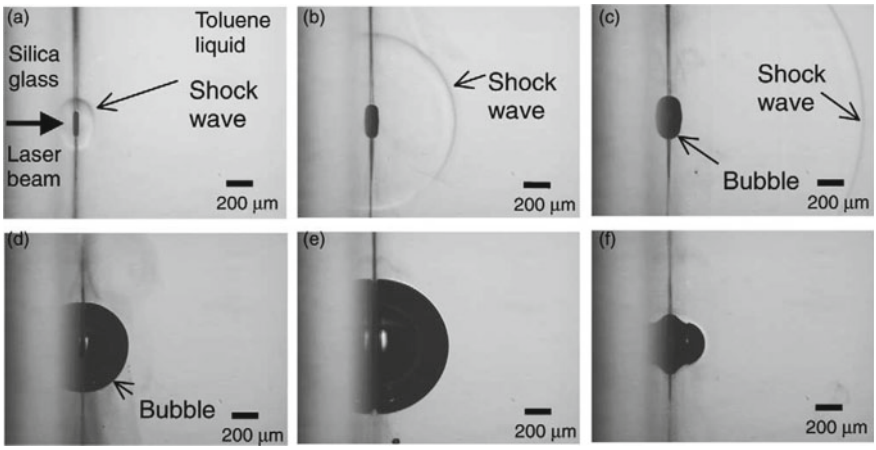


**Fig. 10.17** Time-resolved optical images of the cavitation bubble formed by a KrF excimer laser irradiation on the interface between toluene and fused silica at the delay time of **a** 100 ns, **b** 500 ns, **c** 1.2 μs, **d** 10 μs, **e** 50 μs, and **f** 100 μs. Reprinted from Ref. [35], Copyright (2003), with permission from Elsevier.

of the cavitation bubble. As shown in Fig. 10.17, the bubble expands to out of the irradiated area. Thus, the suppression of the etching by every second pulse was induced (Fig. 10.20). Given the results that the self-assembled monolayer (SAM) on the fused silica around the irradiated area kept their function as reported by Ding et al. [100, 101], gas phase chemicals inside the bubble induced minor effect on the surface around the irradiated areas.

Although the results on single-shot LIBWE indicated the required action of liquid for etching, the involvement of the surface modification was not ruled out. The modified layer generation within the pulse duration was detected by time-resolved reflection measurements, as shown in Fig. 10.21 [94]. An increase in reflectivity observed within 15 ns indicated the generation of the modified layer within the pulse duration. Meanwhile, the etch depth of up to 0.35 μm in the single-shot LIBWE [84] would be larger than the thickness of the modified layer, that are coincident with the typical etch rates of a few tens nanometer. There should be additional mechanisms for material removal. In a similar single-shot LIBWE, the decrease in etch rates by adding PEG to the laser-absorbing liquid was confirmed [58]. The addition of PEG as a surfactant reduces the surface tension of the liquid and results in a decrease in the cavitation pressure as indicated by the measured pressure signal. The results indicate that the removal of melted material by the initial high pressure of cavitation is a possible additional mechanism. In the same study, the authors discussed the role of etching with supercritical water. However, given the etching is relatively slow, an etch rate of ca. 1 μm/min was observed in the etching of glass with supercritical water [102], the role of etching with supercritical water would be minor.

The blue light plasma emission, including the atomic lines of Ca and Al, was detected by Cheng et al., which indicated the direct ablation of glass materials [103].

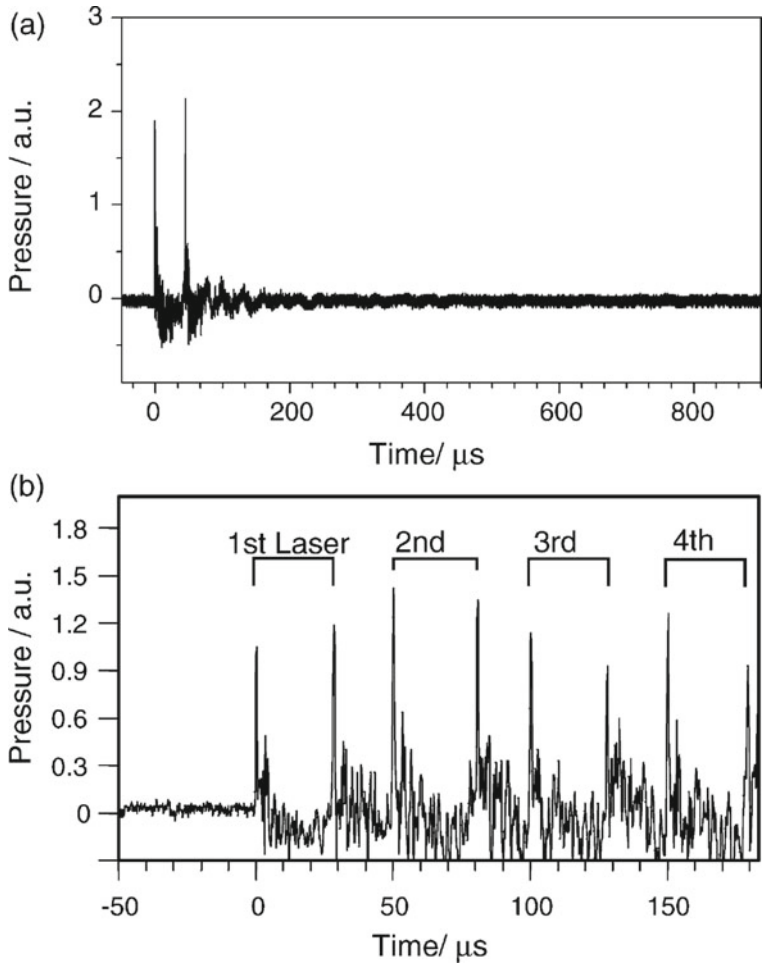


**Fig. 10.18** Transient pressure signals observed in LIBWE using toluene and DPSS UV lasers at **a** 1 kHz (fluence: 520 mJ $cm^{-2}$, laser spot: 50 μm) and **b** 20 kHz (fluence: 5.7 J $cm^{-2}$, laser spot: 12 μm). Reprinted from Ref. [44], Copyright (2006), with permission from Elsevier.

Meanwhile, in the visible LIBWE of PMMA with In–Ga, the plasma emission of In and Ga was observed [67], which indicated plasma formation from the liquid media. The etching of transparent materials assisted by laser-induced plasma has been studied as LIPAA. In these studies, it was confirmed that the major role of plasma in LIPAA was the creation of an absorption site at the surface of the material [13, 14]. In the LIBWE process, the laser-induced plasma may contribute to the generation of an absorption site.

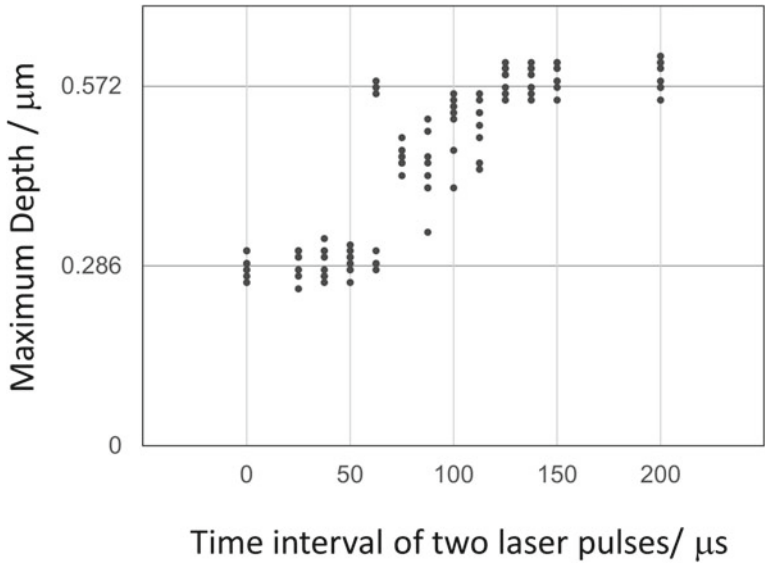


**Fig. 10.19** Maximum depths of the micropits fabricated with two laser pulses with different time intervals. Reproduced from Ref. [84] with permission from Japan Laser Processing Society.

## 10.6 Summary

In this chapter, studies regarding the LIBWE process, that is the laser processing based on the action of high-energy states formed in liquid layer, are reviewed. This process achieves crack-free and debris-free precise micromachining of transparent materials. Therefore, it can be applied to fabricate micro-optical and microfluidic devices. The simple concept of this technique for utilizing the high-energy state in liquid allows a variety of combinations of lasers and materials as well as a variety of experimental setups for processing. While the concept for processing is simple, the mechanism of material removal, the action of the generated high-energy states, is rather complex. Several studies have been conducted to elucidate the actions of the high-energy states for material removal, which revealed that several mechanisms with different contribution ratios are involved in this process. One important mechanism is that the surface layer of the materials is modified by the chemical species formed in the high-energy state, and direct laser ablation of the laser-absorbing modified layer is induced. This phenomenon can be induced within a single-pulse duration. This process would be a major mechanism in the fabrication of microstructures on silica-based transparent materials with organic laser-absorbing liquid that shows a low etch rate up to a few tens of nanometers per pulse. For the etching of sapphire, the adhered amorphous carbon layer would be act as the interface absorbing layer. However, it is not clear that similar mechanism is involved in the etching of fluoride crystals or polymeric materials, or the etching employing liquid metallic absorbers. In addition

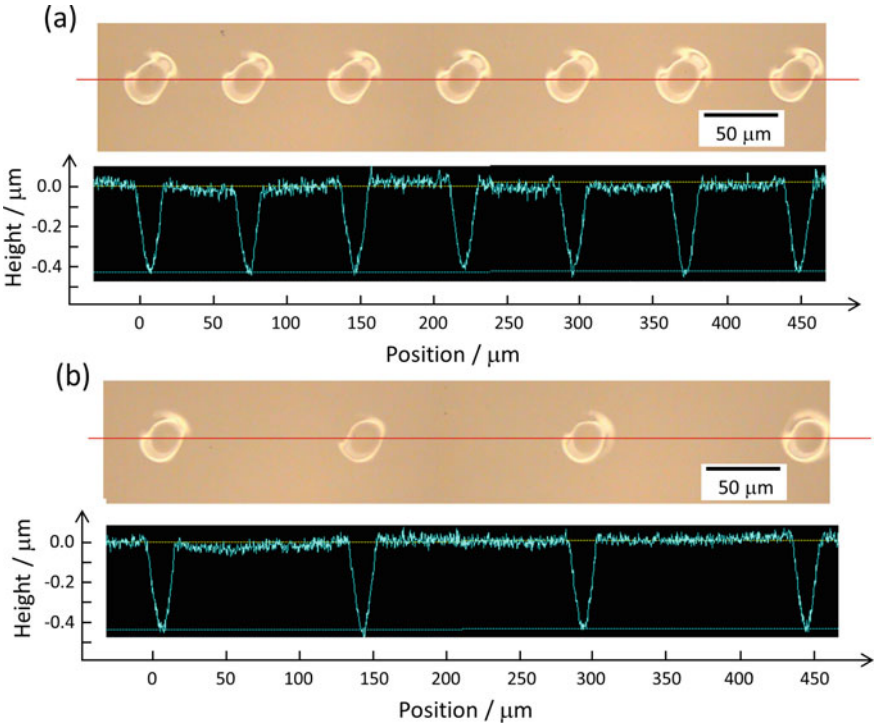


**Fig. 10.20** Micropit array structures fabricated with pulse repetition and scan speed of **a** 10 kHz and 750 mm/s, **b** 20 kHz and 1500 mm/s, respectively. Reproduced from Ref. [84] with permission from Japan Laser Processing Society.

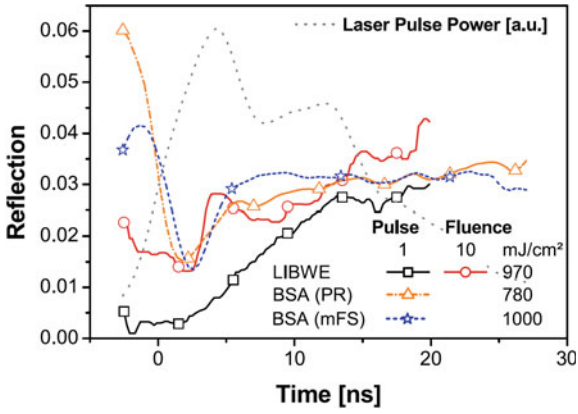


**Fig. 10.21** Time-resolved reflection measurements at 248 nm for LIBWE and the backside ablation (BSA) of a 100-nm thick photoresist film on fused silica (PR) and LIBWE-modified fused silica (mFS). Reprinted by permission from Springer: Ref [94], Copyright 2010.

to the direct ablation of the modified layer, the mechanical removal of melted material by the high pressure induced in the initial stage of cavitation would be involved in the etching process induced at a higher fluence. An increased contribution of the latter mechanism was observed in the LDW-type LIBWE demonstrating incubation-free etching.

## References


1. W. M. Steen, J. Mazumder, Laser Materials Processing, 4th ed., Springer-Verlog London, 2010
2. R. Srinivasan, A.P. Ghosh, Ablation of liquid benzene by pulsed ultraviolet (248 or 308 nm) laser radiation. Chem. Phys. Lett. **143**, 546–550 (1988). https://doi.org/10.1016/0009-2614(88)87064-7
3. S. Georgiou, A. Koubenakis, Laser-induced material ejection from model molecular solids and liquids: mechanisms, implications, and applications. Chem. Rev. **103**, 349–394 (2003). https://doi.org/10.1021/cr010429o
4. Y. Tsuboi, H. Fukumura, H. Masuhara, Nanosecond imaging study on laser ablation of liquid benzene. Appl. Phys. Lett. **64**, 2745–2747 (1994). https://doi.org/10.1063/1.111461
5. Y. Tsuboi, K. Hatanaka, H. Fukumura, H. Masuhara, The 248 nm excimer laser ablation of liquid benzene derivatives: a relation between ablation threshold and molecular photochemical reactivity. J. Phys. Chem. **98**, 11237–11241 (1994). https://doi.org/10.1021/j100095a001
6. K. Hatanaka, M. Kawao, Y. Tsuboi, H. Fukumura, H. Masuhara, Switching from photochemical to photothermal mechanism in laser ablation of benzene solutions. J. Appl. Phys. **82**, 5799–5806 (1997). https://doi.org/10.1063/1.366447
7. K. Toyota, S. Nakashima, T. Okada, Near-infrared laser-induced breakdown of liquid benzene. Chem. Phys. Lett. **323**, 323–328 (2000). https://doi.org/10.1016/S0009-2614(00)00532-7
8. J. Wang, H. Niino, A. Yabe, One-step microfabrication of fused silica by laser ablation of an organic solution. Appl. Phys. A **68**, 111–113 (1999). https://doi.org/10.1007/s003390050863
9. J. Ihlemann, B. Wolff-Rottke, Excimer laser micro machining of inorganic dielectrics. Appl. Surf. Sci. **106**, 282–286 (1996). https://doi.org/10.1016/S0169-4332(96)00422-9
10. J. Zhang, K. Sugioka, K. Midorikawa, High-speed machining of glass materials by laser-induced plasma-assisted ablation using a 532-nm laser. Appl. Phys. A **67**, 499–501 (1998). https://doi.org/10.1007/s003390050810
11. J. Zhang, K. Sugioka, K. Midorikawa, High-quality and high-efficiency machining of glass materials by laser-induced plasma-assisted ablation using conventional nanosecond UV, visible, and infrared lasers. Appl. Phys. A **69**, S876–S882 (1999). https://doi.org/10.1007/s003390051551
12. Y. Hanada, K. Sugioka, I. Miyamoto, K. Midorikawa, Double-pulse irradiation by laser-induced plasma-assisted ablation (LIPAA) and mechanisms study. Appl. Surf. Sci. **248**, 276–280 (2005). https://doi.org/10.1016/j.apsusc.2005.03.050
13. Y. Hanada, K. Sugioka, K. Obata, S. V. Garnov, I. Miyamoto, K. Midorikawa, Transient electron excitation in laser-induced plasma-assisted ablation of transparent materials, J. Appl. Phys. **99**, 043301 (2006). https://doi.org/10.1063/1.2171769
14. B. Hopp, T. Smausz, T. Csizmadia, C. Vass, T. Csákó, G. Szabó, Comparative study of different indirect laser-based methods developed for microprocessing of transparent materials. J. Laser Micro/Nanoeng. **5**, 80–85 (2010). https://doi.org/10.2961/jlmn.2010.01.0017
15. K. Zimmer, R. Böhme, B. Rauschenbach, Laser etching of fused silica using an adsorbed toluene layer. Appl. Phys. A **79**, 1883–1885 (2004). https://doi.org/10.1007/s00339-004-2961-y

16. B. Hopp, Cs. Vass, T. Smausz, Laser induced backside dry etching of transparent materials, Appl. Surf. Sci. **253**, 7922–7925 (2007). https://doi.org/10.1016/j.apsusc.2007.02.068
17. B. Hopp, T. Smausz, C. Vass, G. Szabó, R. Böhme, D. Hirsch, K. Zimmer, Laser-induced backside dry and wet etching of transparent materials using solid and molten tin as absorbers. Appl. Phys. A **94**, 899–904 (2009). https://doi.org/10.1007/s00339-009-5078-5
18. J. Wang, H. Niino, A. Yabe, Laser ablation of poly(methylmethacrylate) doped with aromatic compounds: Laser intensity dependence of absorption coefficient. Jpn. J. Appl. Phys. **38**, 871–876 (1999). https://doi.org/10.1143/JJAP.38.871
19. J. Ikeno, A. Kobayashi, T. Kasai, YAG laser processing of fused silica glass with the aid of solution, Jpn. Soc. Precis. Eng. **55**, 335–340 (1989) (in Japanese). https://doi.org/10.2493/jjspe.55.335
20. S.I. Dolgaev, A.A. Lyalin, A.V. Simakin, G.A. Shafeev, Etching of sapphire assisted by copper-vapour laser radiation. Quantum Electron. **26**, 65–68 (1996). https://doi.org/10.1070/QE1996v026n01ABEH000590
21. S.I. Dolgaev, A.A. Lyalin, A.V. Simakin, V.V. Voronov, G.A. Shafeev, Fast etching and metallization of via-holes in sapphire with the help of radiation by copper vapor laser. Appl. Surf. Sci. **109–110**, 201–205 (1997). https://doi.org/10.1016/S0169-4332(96)00660-5
22. M. Ehrhardt, P. Lorenz, B. Han, R. Zhu, K. Zimmer, Laser-induced backside wet etching of $SiO_2$ with a visible ultrashort laser pulse by using $KMnO_4$ solution as an absorber liquid. J. Laser Micro/Nanoeng. **13**, 47–54 (2018). https://doi.org/10.2961/jlmn.2018.02.0001
23. M. Y. Tsvetkov, V. I. Yusupov, N. V. Minaev, P. S. Timashev, K. M. Golant, V. N. Bagratashvili, Effects of thermo-plasmonics on laser-induced backside wet etching of silicate glass, Laser Phys. Lett. **13**, 106001 (2016). https://doi.org/10.1088/1612-2011/13/10/106001
24. O.M. Zhigalina, D.N. Khmelenin, A.V. Atanova, N.V. Minaev, A.P. Sviridov, M.Y. Tsvetkov, A nanoscale modification of materials at thermoplasmonic laser-induced backside wet etching of sapphire. Plasmonics **15**, 599–608 (2020). https://doi.org/10.1007/s11468-019-01091-9
25. H. F. Chang, W. K. Yeung, W. C. Kao, M. Ehrhardt, K. Zimmer, J. Y. Cheng, Surface micromachining on a polymethylmethacrylate substrate using visible laser-induced backside wet etching with a $KMnO_4$ solution as an absorber, J. Laser Appl. **32**, 022014 (2020). https://doi.org/10.2351/1.5114659
26. Z.Q. Huang, M.H. Hong, T.B.M. Do, Q.Y. Lin, Laser etching of glass substrates by 1064 nm laser irradiation. Appl. Phys. A **93**, 159–163 (2008). https://doi.org/10.1007/s00339-008-4674-0
27. X.Z. Xie, M.F. Hu, W.F. Chen, X. Wei, W. Hu, X.Y. Gao, X.R. Yuan, M.H. Hong, Cavitation bubble dynamics during laser wet etching of transparent sapphire substrates by 1064 nm laser irradiation. J. Laser Micro/Nanoeng. **8**, 259–265 (2013). https://doi.org/10.2961/jlmn.2013.03.0012
28. K.-K. Kwon, H. Kim, T. Kim, C. N. Chu, High aspect ratio channel fabrication with near-infrared laser-induced backside wet etching, J. Mater. Proc. Tech. **278**, 116505 (2020). https://doi.org/10.1016/j.jmatprotec.2019.116505
29. Cs. Vass, B. Hopp, T. Smausz, F. Ignácz, Experiments and numerical calculations for the interpretation of the backside wet etching of fused silica, Thin Solid Films **453–454** 121–126 (2004). https://doi.org/10.1016/j.tsf.2003.11.081
30. J. Wang, H. Niino, A. Yabe, Micromachining of quartz crystal with excimer lasers by laser-induced backside wet etching. Appl. Phys. A **69**, S271–S273 (1999). https://doi.org/10.1007/s003390051398
31. J. Wang, H. Niino, A. Yabe, Micromachining of transparent materials with super-heated liquid generated by multiphotonic absorption of organic molecule. Appl. Surf. Sci. **154–155**, 571–576 (2000). https://doi.org/10.1016/S0169-4332(99)00462-6
32. R. Böhme, A. Braun, K. Zimmer, Backside etching of UV-transparent materials at the interface to liquids. Appl. Surf. Sci. **186**, 276–281 (2002). https://doi.org/10.1016/S0169-4332(01)00630-4
33. K. Zimmer, R. Böhme, A. Braun, B. Rauschenbach, F. Bigl, Excimer laser-induced etching of sub-micron surface relief gratings in fused silica using phase grating projection. Appl. Phys. A **74**, 453–456 (2002). https://doi.org/10.1007/s003390101184

34. R. Böhme, K. Zimmer, Effect of halogenated organic solvents on laser-induced backside wet etching of fused silica. Appl. Phys. A **83**, 9–12 (2006). https://doi.org/10.1007/s00339-006-3483-6
35. H. Niino, Y. Yasui, X. Ding, A. Narazaki, T. Sato, Y. Kawaguchi, A. Yabe, Surface microfabrication of silica glass by excimer laser irradiation of organic solvent. J. Photochem. Photobiol. A: Chem. **158**, 179–182 (2003). https://doi.org/10.1016/S1010-6030(03)00032-7
36. X. Ding, T. Sato, Y. Kawaguchi, H. Niino, Laser-induced backside wet etching of sapphire. Jpn. J. Appl. Phys. **42**, L176–L178 (2003). https://doi.org/10.1143/JJAP.42.L176
37. K. Fujito, T. Hashimoto, K. Samonji, J.S. Speck, S. Nakamura, Growth of AlN by the chemical vapor reaction process and its application to lateral overgrowth on patterned sapphire substrates. J. Cryst. Growth **272**, 370–376 (2004). https://doi.org/10.1016/j.jcrysgro.2004.08.079
38. Cs. Vass, D. Sebők, B. Hopp, Comparing study of subpicosecond and nanosecond wet etching of fused silica, Appl. Surf. Sci. **252**, 4768–4772 (2006). https://doi.org/10.1016/j.apsusc.2005.07.118
39. X. Ding, Y. Yasui, Y. Kawaguchi, H. Niino, A. Yabe, Laser-induced back-side wet etching of fused silica with an aqueous solution containing organic molecules. Appl. Phys. A **75**, 437–440 (2002). https://doi.org/10.1007/s003390101131
40. X. Ding, Y. Kawaguchi, H. Niino, A. Yabe, Laser-induced high-quality etching of fused silica using a novel aqueous medium. Appl. Phys. A **75**, 641–645 (2002). https://doi.org/10.1007/s00339-002-1453-1
41. K. Zimmer, R. Böhme, D. Ruthe, B. Rauschenbach, Backside laser etching of fused silica using liquid gallium. Appl. Phys. A **84**, 455–458 (2006). https://doi.org/10.1007/s00339-006-3630-0
42. K. Zimmer, R. Böhme, D. Hirsch, B. Rauschenbach, Backside etching of fused silica with UV laser pulses using mercury. J. Phys. D: Appl. Phys. **39**, 4651–4655 (2006). https://doi.org/10.1088/0022-3727/39/21/022
43. J.Y. Cheng, M.H. Yen, C.W. Wei, Y.C. Chuang, T.H. Young, Crack-free direct-writing on glass using a low-power UV laser in the manufacture of a microfluidic chip. J. Micromech. Microeng. **15**, 1147–1156 (2005). https://doi.org/10.1088/0960-1317/15/6/005
44. H. Niino, Y. Kawaguchi, T. Sato, A. Narazaki, T. Gumpenberger, R. Kurosaki, Laser ablation of toluene liquid for surface micro-structuring of silica glass. Appl. Surf. Sci. **252**, 4387–4391 (2006). https://doi.org/10.1016/j.apsusc.2005.07.084
45. S. Pissadakis, R. Böhme, K. Zimmer, Sub-micron periodic structuring of sapphire by laser induced backside wet etching technique. Opt. Exp. **15**, 1428–1433 (2007). https://doi.org/10.1364/OE.15.001428
46. Cs. Vass, K. Osvay, Fabrication of 150 nm period grating in fused silica by two-beam interferometric laser induced backside wet etching method, Opt. Exp. **14**, 8354–8359 (2006). https://doi.org/10.1364/OE.14.008354
47. B. Kiss, F. Ujhelyi, Á. Sipos, B. Farkas, P. Dombi, K. Osvay, C. Vass, Microstructuring of transparent dielectric films by twin-LIBWE method for OWLS applications. J. Laser Micro/Nanoeng. **8**, 271–275 (2013). https://doi.org/10.2961/jlmn.2013.03.0014
48. C. Vass, B. Kiss, R. Flender, Z. Felházi, P. Lorenz, M. Ehrhardt, K. Zimmer, Comparative study on grating fabrication in transparent materials by TWIN-LIBWE and ultrashort pulsed ablation techniques. J. Laser Micro/Nanoeng. **10**, 38–42 (2015). https://doi.org/10.2961/jlmn.2015.01.0008
49. J. Wang, H. Niino, A. Yabe, Microfabrication of a fluoropolymer film using conventional XeCl excimer laser by laser-induced backside wet etching. Jpn. J. Appl. Phys. **38**, L761–L763 (1999). https://doi.org/10.1143/JJAP.38.L761
50. G. Kopitkovas, T. Lippert, N. Murazawa, C. David, A. Wokaun, J. Gobrecht, R. Winfield, Laser processing of micro-optical components in quartz. Appl. Surf. Sci. **254**, 1073–1078 (2007). https://doi.org/10.1016/j.apsusc.2007.09.048
51. Y. Yasui, H. Niino, Y. Kawaguchi, A. Yabe, Microetching of fused silica by laser ablation of organic solution with XeCl excimer laser. Appl. Surf. Sci. **186**, 552–555 (2002). https://doi.org/10.1016/S0169-4332(01)00635-3

52. G. Kopitkovas, T. Lippert, C. David, A. Wokaun, J. Gobrecht, Fabrication of micro-optical elements in quartz by laser induced backside wet etching. Microelectron. Eng. **67–68**, 438–444 (2003). https://doi.org/10.1016/S0167-9317(03)00099-6
53. G. Kopitkovas, T. Lippert, C. David, A. Wokaun, J. Gobrecht, Surface micromachining of UV transparent materials. Thin Solid Films **453–454**, 31–35 (2004). https://doi.org/10.1016/j.tsf.2003.11.074
54. K. Zimmer, A. Braun, R. Böhme, Etching of fused silica and glass with excimer laser at 351 nm. Appl. Surf. Sci. **208–209**, 199–204 (2003). https://doi.org/10.1016/S0169-4332(02)01372-7
55. Z.Q. Huang, M.H. Hong, K.S. Tiaw, Q.Y. Lin, Quality glass processing by laser induced backside wet etching. J. Laser Micro/Nanoeng. **2**, 194–199 (2007). https://doi.org/10.2961/jlmn.2007.03.0006
56. M. Ehrhardt, G. Raciukaitis, P. Gecys, K. Zimmer, Microstructuring of fused silica by laser-induced backside wet etching using picosecond laser pulses. Appl. Surf. Sci. **256**, 7222–7227 (2010). https://doi.org/10.1016/j.apsusc.2010.05.055
57. M. Ehrhardt, G. Raciukaitis, P. Gecys, K. Zimmer, Laser-induced backside wet etching of fluoride and sapphire using picosecond laser pulses. Appl. Phys. A **101**, 399–404 (2010). https://doi.org/10.1007/s00339-010-5833-7
58. M.Y. Tsvetkov, V.I. Yusupov, P.S. Timashev, K.M. Golant, N.V. Minaev, S.I. Tsypina, V.N. Bagratashvili, On the role of supercritical water in laser-induced backside wet etching of glass. Russ. J. Phys. Chem. B **11**, 1061–1069 (2017). https://doi.org/10.1134/S1990793117070181
59. J.Y. Cheng, M.H. Yen, T.H. Young, Crack-free micromachining on glass using an economic Q-switched 532 nm laser. J. Micromech. Microeng. **16**, 2420–2424 (2006). https://doi.org/10.1088/0960-1317/16/11/024
60. J.Y. Cheng, M.H. Yen, W.C. Hsu, J.H. Jhang, T.H. Young, ITO patterning by a low power Q-switched green laser and its use in the fabrication of a transparent flow meter. J. Micromech. Microeng. **17**, 2316–2323 (2007). https://doi.org/10.1088/0960-1317/17/11/019
61. T. Sato, Y. Kawaguchi, R. Kurosaki, A. Narazaki, W. Watanabe, H. Niino, Laser-induced backside wet etching employing green DPSS laser and liquid metallic absorber. J. Laser Micro/Nanoeng. **6**, 204–208 (2011). https://doi.org/10.2961/jlmn.2011.03.0006
62. J. Y. Cheng, M. Z. Mousavi, C. Y. Wu, H. F. Tsai, Blue light emission from a glass/liquid interface for real-time monitoring of a laser-induced etching process, J. Micromech. Microeng. **21**, 075019 (2011). https://doi.org/10.1088/0960-1317/21/7/075019
63. T. Nakazumi, T. Sato, A. Narazaki, H. Niino, Laser marking on soda-lime glass by laser-induced backside wet etching with two-beam interference, J. Micromech. Microeng. **26**, 095015 (2016). https://doi.org/10.1088/0960-1317/26/9/095015
64. M.H. Yen, C.W. Huang, W.C. Hsu, T.H. Young, K. Zimmer, J.Y. Cheng, Crack-free micromachining on glass substrates by visible LIBWE using liquid metallic absorbers. Appl. Surf. Sci. **257**, 87–92 (2010). https://doi.org/10.1016/j.apsusc.2010.06.041
65. Cs. Vass, B. Kiss, J. Kopniczky, B. Hopp, Etching of fused silica fiber by metallic laser-induced backside wet etching technique, Appl. Surf. Sci. **278**, 241–244 (2013). https://doi.org/10.1016/j.apsusc.2012.11.163
66. J.Y. Cheng, H.Y. Chen, M.Z. Mousavi, C.Y.Y. Chang, Crack-free micromachining of glass ceramic using visible LIBWE. J. Laser Micro/Nanoeng. **8**, 253–258 (2013). https://doi.org/10.2961/jlmn.2013.03.0011
67. J.Y. Cheng, W.C. Kao, M.Z. Mousavi, H.F. Chang, W.C. Hsu, M.H. Yen, M. Ehrhardt, K. Zimmer, High-quality surface micromachining on polymer using visible-LIBWE. J. Laser Micro/Nanoeng. **11**, 117–123 (2016). https://doi.org/10.2961/jlmn.2016.01.0022
68. K. Zimmer, R. Böhme, S. Pissadakis, L. Hartwig, G. Reisse, B. Rauschenbach, Backside etching of fused silica with Nd:YAG laser. Appl. Surf. Sci. **253**, 2796–2800 (2006). https://doi.org/10.1016/j.apsusc.2006.05.059
69. X. Zhao, M. Ehrhardt, P. Lorenz, B. Han, K. Zimmer, L. Xu, X. Ni, Nanosecond Nd:YAG laser induced backside wet etching of NaCl with eutectic gallium-indium alloy as absorbing liquid, Surf. Interfaces **17**, 100353 (2019). https://doi.org/10.1016/j.surfin.2019.100353

70. G. Kopitkovas, T. Lippert, C. David, S. Canulescu, A. Wokaun, J. Gobrecht, Fabrication of beam homogenizers in quartz by laser micromachining. J. Photochem. Photobiol. A: Chem. **166**, 135–140 (2004). https://doi.org/10.1016/j.jphotochem.2004.05.001
71. K. Zimmer, R. Böhme, Precise etching of fused silica for micro-optical applications. Appl. Surf. Sci. **243**, 415–420 (2005). https://doi.org/10.1016/j.apsusc.2004.09.118
72. T. Sato, Y. Kawaguchi, T. Kurosaki, A. Narazaki, W. Watanabe, H. Niino, Variation in the etch rate of LIBWE fabricating deep microtrenches. J. Laser Micro/Nanoeng. **7**, 81–86 (2012). https://doi.org/10.2961/jlmn.2012.01.0016
73. Y. Kawaguchi, T. Sato, A. Narazaki, R. Kurosaki, H. Niino, Etching a micro-trench with a maximum aspect ratio of 60 on silica glass by laser-induced backside wet etching (LIBWE). Jpn. J. Appl. Phys. **44**, L176–L178 (2005). https://doi.org/10.1143/JJAP.44.L176
74. Y. Kawaguchi, T. Sato, A. Narazaki, R. Kurosaki, H. Niino, Rapid prototyping of silica glass microstructures by the LIBWE method: Fabrication of deep microtrenches. J. Photochem. Photobiol. A: Chem. **182**, 319–324 (2006). https://doi.org/10.1016/j.jphotochem.2006.05.033
75. T. Sato, R. Kurosaki, A. Narazaki, Y. Kawaguchi, H. Niino, Flexible 3D deep microstructures of silica glass by laser-induced backside wet etching. Appl. Phys. A **101**, 319–323 (2010). https://doi.org/10.1007/s00339-010-5790-1
76. T. Sato, R. Kurosaki, Y. Kawaguchi, A. Narazaki, H. Niino, Fabrication of multiple slanted microstructures on silica glass by laser-induced backside wet etching. J. Laser Micro/Nanoeng. **5**, 256–262 (2010). https://doi.org/10.2961/jlmn.2010.03.0014
77. T. Sato, R. Kurosaki, A. Narazaki, Y. Kawaguchi, H. Niino, Flexible fabrication of deep microstructures by laser-induced backside wet etching, Proc. SPIE **7584**, 758408 (2010). https://doi.org/10.1117/12.841583
78. C. Vass, K. Osvay, B. Hopp, Z. Bor, 104 nm period grating fabrication in fused silica by immersion two-beam interferometric laser induced backside wet etching technique. Appl. Phys. A **87**, 611–613 (2007). https://doi.org/10.1007/s00339-007-3891-2
79. Cs. Vass, K. Osvay, M. Csete, B. Hopp, Fabrication of 550 nm gratings in fused silica by laser induced backside wet etching technique, Appl. Surf. Sci. **253**, 8059–8063 (2007). https://doi.org/10.1016/j.apsusc.2007.02.087
80. C. Vass, K. Osvay, T. Véső, B. Hopp, Z. Bor, Submicrometer grating fabrication in fused silica by interferometric laser-induced backside wet etching technique. Appl. Phys. A **93**, 69–73 (2008). https://doi.org/10.1007/s00339-008-4636-6
81. B. Kiss, Cs. Vass, P. Heck, P. Dombi, K. Osvay, Fabrication and analysis of transmission gratings produced by the indirect laser etching technique, J. Phys. D: Appl. Phys. **44**, 415103 (2011). https://doi.org/10.1088/0022-3727/44/41/415103
82. C.B. Arnold, A. Piqué, Laser Direct-Write Processing. MRS Bull. **32**, 9–11 (2007). https://doi.org/10.1557/mrs2007.9
83. H. Niino, Y. Kawaguchi, T. Sato, A. Narazaki, R. Kurosaki, Surface microstructuring of silica glass by laser-induced backside wet etching with a DPSS UV laser. Appl. Surf. Sci. **253**, 8287–8291 (2007). https://doi.org/10.1016/j.apsusc.2007.02.099
84. T. Sato, A. Narazaki, H. Niino, Fabrication of micropits by LIBWE for laser marking of glass materials. J. Laser Micro/Nanoeng. **12**, 248–253 (2017). https://doi.org/10.2961/jlmn.2017.03.0013
85. H. Fukumura, H. Masuhara, The mechanism of dopant-induced laser ablation. Possibility of cyclic multiphotonic absorption in excited states, Chem. Phys. Lett. **221**, 373–378 (1994). https://doi.org/10.1016/0009-2614(94)00277-0
86. Cs. Vass, T. Smausz, B. Hopp, Wet etching of fused silica: a multiplex study, J. Phys. D: Appl. Phys. **37**, 2449–2454 (2004). https://doi.org/10.1088/0022-3727/37/17/018
87. K. Zimmer, Analytical solution of the laser-induced temperature distribution across internal material interfaces. Int. J. Heat Mass Trans. **52**, 497–503 (2009). https://doi.org/10.1016/j.ijheatmasstransfer.2008.03.034
88. R. Böhme, K. Zimmer, The influence of the laser spot size and the pulse number on laser-induced backside wet etching. Appl. Surf. Sci. **247**, 256–261 (2005). https://doi.org/10.1016/j.apsusc.2005.01.058

89. M.Y. Tsvetkov, V.I. Yusupov, N.V. Minaev, A.A. Akovantseva, P.S. Timashev, K.M. Golant, B.N. Chichkov, V.N. Bagratashvili, On the mechanisms of single-pulse laser-induced backside wet etching. Opt. Laser Technol. **88**, 17–23 (2017) https://doi.org/10.1016/j.optlastec.2016.05.020
90. R. Böhme, D. Spemann, K. Zimmer, Surface characterization of backside-etched transparent dielectrics. Thin Solid Films **453–454**, 127–132 (2004). https://doi.org/10.1016/j.tsf.2003.11.083
91. G. Kopitkovas, V. Deckert, T. Lippert, F. Raimondi, C.W. Schneider, A. Wokaun, Chemical and structural changes of quartz surfaces due to structuring by laser-induced backside wet etching. Phys. Chem. Chem. Phys. **10**, 3195–3202 (2008). https://doi.org/10.1039/B800090E
92. C. Vass, J. Budai, Z. Schay, B. Hopp, Interpretation and modeling of laser-induced backside wet etching procedure. J. Laser Micro/Nanoeng. **5**, 43–47 (2010). https://doi.org/10.2961/jlmn.2010.01.0010
93. K. Zimmer, M. Ehrhardt, R. Böhme, Simulation of laser-induced backside wet etching of fused silica with hydrocarbon liquids, J. Appl. Phys. **107**, 034908 (2010). https://doi.org/10.1063/1.3276204
94. K. Zimmer, R. Böhme, M. Ehrhardt, B. Rauschenbach, Mechanism of backside etching of transparent materials with nanosecond UV-lasers. Appl. Phys. A **101**, 405–410 (2010). https://doi.org/10.1007/s00339-010-5878-7
95. T. Lee, D. Jang, D. Ahn, D. Kim, Effect of liquid environment on laser-induced backside wet etching of fused silica, J. Appl. Phys. **107**, 033112 (2010). https://doi.org/10.1063/1.3294615
96. Y. Kawaguchi, X. Ding, A. Narazaki, T. Sato, H. Niino, Transient pressure induced by laser ablation of liquid toluene: toward the understanding of laser-induced backside wet etching. Appl. Phys. A **79**, 883–885 (2004). https://doi.org/10.1007/s00339-004-2580-7
97. Y. Kawaguchi, X. Ding, A. Narazaki, T. Sato, H. Niino, Transient pressure induced by laser ablation of toluene, a highly laser-absorbing liquid. Appl. Phys. A **80**, 275–281 (2005). https://doi.org/10.1007/s00339-003-2347-6
98. R. Böhme, T. Otto, K. Zimmer, In situ reflectivity investigations of solid/liquid interface during laser backside etching. Appl. Surf. Sci. **252**, 4392–4396 (2006). https://doi.org/10.1016/j.apsusc.2005.06.044
99. A. Vogel, R. Engelhardt, U. Behnle, U. Parlitz, Minimization of cavitation effects in pulsed laser ablation illustrated on laser angioplasty. Appl. Phys. B **62**, 173–182 (1996). https://doi.org/10.1007/BF01081122
100. X. Ding, Y. Kawaguchi, T. Sato, A. Narazaki, H. Niino, Site-selective dye deposition on microstructures of fused silica fabricated using the LIBWE method, Chem. Commun. 2168–2169 (2003). https://doi.org/10.1039/B306770J
101. X. Ding, Y. Kawaguchi, T. Sato, A. Narazaki, H. Niino, Fabrication of microarrays on fused silica plates using the laser-induced backside wet etching method. Langmuir **20**, 9769–9774 (2004). https://doi.org/10.1021/la0498004
102. P. Karásek, J. Grym, M. Roth, J. Planeta, F. Foret, Etching of glass microchips with supercritical water. Lab Chip **15**, 311–318 (2015). https://doi.org/10.1039/C4LC00843J
103. J.Y. Cheng, M.Z. Mousavi, C.Y. Wu, H.F. Tsai, Blue light plasma emission during LIBWE using 532 nm Q-switched nanosecond laser. J. Laser Micro/Nanoeng. **7**, 87–92 (2012). https://doi.org/10.2961/jlmn.2012.01.0017

# Chapter 11
# Functional Nanomaterials Synthesized by Femtosecond Laser Pulses


**Yasuhiko Shimotsuma and Kiyotaka Miura**

**Abstract** Femtosecond laser ablation in solution is a simple technique to synthesize nanomaterials from any solid materials in various solvent molecules. In typical setups for laser ablation of solid-state target in liquid, the laser pulses have to propagate through the solution layer before hitting the target. In this process, not only Fresnel reflection at the boundaries, but also vaporization of the liquid, self-focusing and optical breakdown will occur. In this chapter, appropriate parameters for laser ablation in liquid are discussed to achieve efficient nanomaterials generation. Furthermore, characteristic advantages of this technique can apply to synthesize functional nanomaterials such as fluorescent nanodiamonds. We demonstrated synthesis of fluorescent nanodiamonds with interesting luminescent properties, which are controllable by kind of solvent molecules.

**Keywords** Femtosecond laser · Double-pulse · Laser ablation in liquid · Nanoparticle · Nanodiamond

## 11.1 Introduction

The size, shape, structure, and composition of nanoscale materials extremely important in controlling their physical and chemical properties, including electrical and thermal conductivity, magnetic properties, luminescence, and catalytic activity. The fabrication method of nanomaterials can be generally classified the following two processes: (1) breakdown process of mechanically crushing particles and (2) buildup process by physical and chemical reactions. In particular, the various liquid-phase methods such as sol–gel [1], reduction [2], hydrothermal [3] and solvothermal [4], spray pyrolysis [5], supersonic [6], and laser ablation [7] are widely used for synthesis of various functional nanomaterials. Recent progress in high-power ultrashort pulse lasers has opened new frontiers in technology of material processing including nanoparticle synthesis [8–13], because of its advantages, such as the applicability to

Y. Shimotsuma (✉) · K. Miura
Kyoto University, Kyotodaigaku-katsura, Nishikyo-ku, Kyoto 615-8510, Japan
e-mail: shimotsuma.yasuhiko.3m@kyoto-u.ac.jp



Y. Ishikawa et al. (eds.), *High-Energy Chemistry and Processing in Liquids*,
https://doi.org/10.1007/978-981-16-7798-4_11

various target materials in an ambient atmosphere. More recently, ultrashort pulse laser ablation in liquid has become an increasingly popular approach for preparing nanoparticles from the viewpoint of the concise procedures and ease of handling [14]. Meanwhile, the biggest drawback of this technique is the low productivity. In this chapter, the laser irradiation conditions for effective synthesis of nanoparticles by femtosecond laser ablation in liquid are discussed. Furthermore, synthesis of functional nanomaterials such as fluorescent nanodiamonds is also demonstrated.

## 11.2 Effective Synthesis of Nanoparticles by Femtosecond Laser Ablation in Liquid

Our previous investigations have revealed that variety of nanoparticles ranging from metal Cu nanorod and nanowire [15–17], ZnO nanorod and nanowire [18–20], $Nd_2Fe_{14}B$ single-domain nanoparticle [21], from fluorescent nanodiamond [22–26] can be successfully synthesized by laser ablation in liquid. However, since the plasma generation leading to ablation occurs only in the vicinity of the focus, the reaction volume to generate nanoparticles is very small. Furthermore, the cavitation bubbles and nanoparticles are generated during the ablation process block the laser beam propagation, the number of nanoparticles synthesized by femtosecond laser ablation in liquid is extremely small. To eliminate the influence of cavitation bubbles and generated nanoparticles, the solvent was flowed with various rate during laser ablation. The Si wafer in a quartz vessel filled with 30 mL of ethanol was set on a XYZ stage under an optical microscope. Figure 11.1 shows an optical system for femtosecond laser ablation in liquid. The liquid flow rate was tuned by a syringe pump (Harvard, PHD2000-P). Typical amount of flow was fixed to be 7 mL. A mode-locked, regeneratively amplified femtosecond laser pulse (Coherent, Legend), operating at 800 nm with 120 fs pulse-width and 1 kHz repetition rate was focused via a 20 × (NA = 0.40) microscope objective lens on the wafer surface through quartz window. The laser focus was moved perpendicularly to the direction of laser propagation with

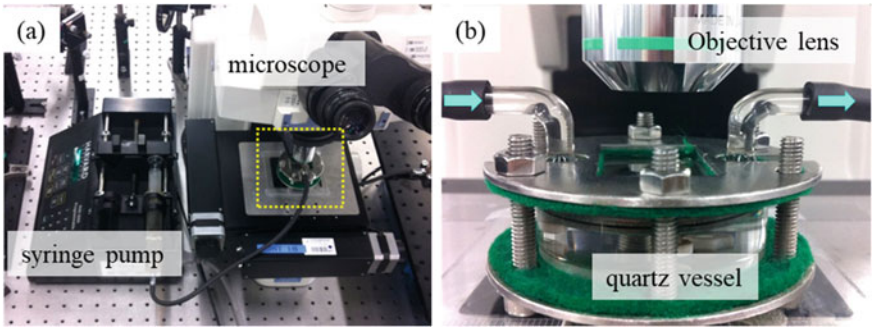


**Fig. 11.1** **a** Optical system for femtosecond laser ablation in liquid, **b** flow quartz vessel

writing speed of 100 μm/s. Typical pulse energy was 500 μJ, corresponding to a laser fluence of $1.1 \times 10^4$ J/cm$^2$. To estimate particle concentration during laser irradiation, the changes in the transmission spectra were monitored using spectrometer (Ocean Optics, USB2000 + ) and used to evaluate the particle concentration based on the calibration curve. The morphology of resultant Si nanoparticles was observed with FE-SEM (JEOL, JSM-6705F). In order to extrapolate the number of Si nanoparticles produced by laser ablation in ethanol, the transmission at 800 nm of an ethanol suspension with a different amount of Si nanoparticles (US Research Nanomaterials, US1128) with an average size of 49.6 nm was measured (Fig. 11.2). In order to estimate the effect of liquid flow rate on the laser ablation process, the Si nanoparticle concentration was observed while changing liquid flow rate. The nanoparticle concentration was saturated at the liquid flow rate more than 20 mL/min; finally, the concentration attains 3 times (Fig. 11.3). Such improvement mainly due to removing the interruption of laser beam propagation by the generated cavitation bubbles and the ablated particles.

Although it should be generally considered the influence of the melt film and the convective instabilities [27], assuming that the penetration depth of laser pulse is sufficiently smaller than its wavelength, it is well known that the efficiency of laser cutting depends on the absorption coefficient calculated from the Fresnel Eq. (11.1) [28, 29].

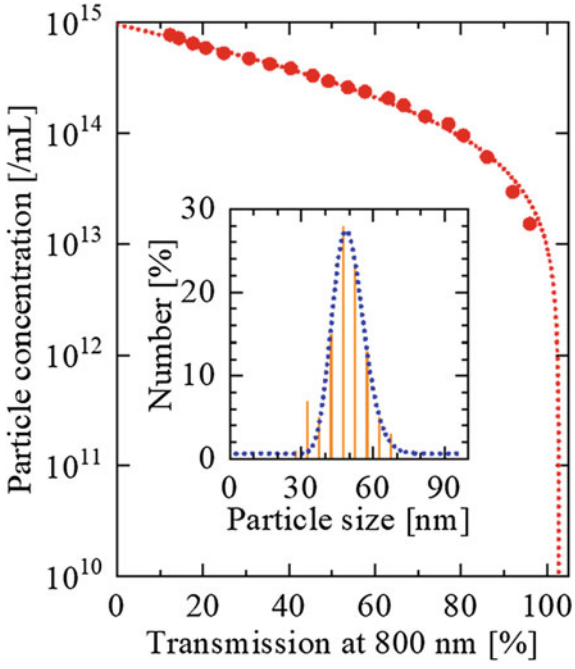


**Fig. 11.2** Calibration curve of Si nanoparticle concentration as a function of transmission at 800 nm. Inset shows the size distribution of the reference Si nanoparticles

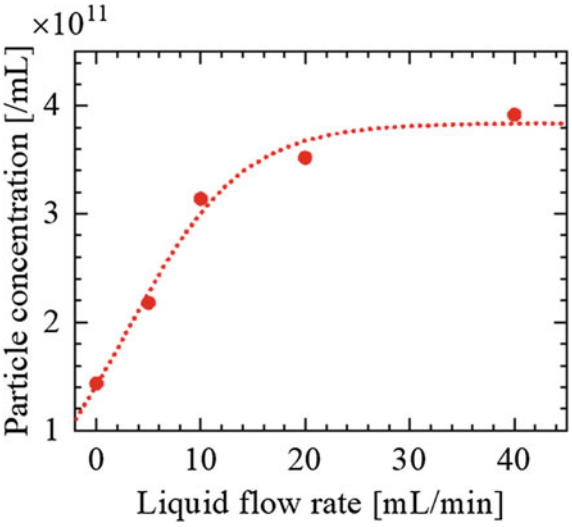


**Fig. 11.3** Si nanoparticle concentration as a function of liquid flow rate. Dotted line is guide for the eye

$$R_{\mathrm{p}} = \left| \frac{\tilde{n}^2 \cos\theta - \sqrt{\tilde{n}^2 - \sin^2\theta}}{\tilde{n}^2 \cos\theta + \sqrt{\tilde{n}^2 - \sin^2\theta}} \right|^2, \; R_{\mathrm{s}} = \left| \frac{\cos\theta - \sqrt{\tilde{n}^2 - \sin^2\theta}}{\cos\theta + \sqrt{\tilde{n}^2 - \sin^2\theta}} \right|^2 \tag{11.1}$$

where $R_{\mathrm{p}}$ and $R_{\mathrm{s}}$ are the reflectivity of power for the perpendicular and parallel component of the polarization, respectively. The angle $\theta$ is defined between the surface normal and the laser incidence. $\tilde{n}$ is the complex refractive index of material. Figure 11.4 shows the Si nanoparticle concentration as a function of laser irradiation time without liquid flow. The laser polarization was set to be parallel or perpendicular to the writing direction. This graph indicates that amount of the Si nanoparticle production in the case of the polarization parallel to the writing direction was approximately twice as much as that in the case of the perpendicular direction. This is due to the fact that the ablated surface is tilted to the laser incidence; therefore, the next pulse is in an oblique incident state. Considering Fresnel reflection, the reflectance of p-polarized light is lower than that of s-polarized light; consequently, the absorbed laser energy becomes large leading to efficient laser ablation [27].

It is known that the femtosecond double-pulse train with a suitable delay time improves the interaction with a material compared to that for the conventional single-pulse train, although the irradiated total laser energy is the same [30, 31]. To enhance the light–matter interaction, we configured the Mach–Zehnder type of double-pulse optical setup [32]. The delay time between femtosecond double pulses was controlled by using an optical delay line. The total pulse energy of the equally divided double pulses was set to be 500 μJ. The laser writing speed and the liquid flow rate were set to be 100 μm/s and 40 mL/min, respectively. In addition, to clarify the effect on the nanoparticle generation of the laser polarization, the double-pulse train with

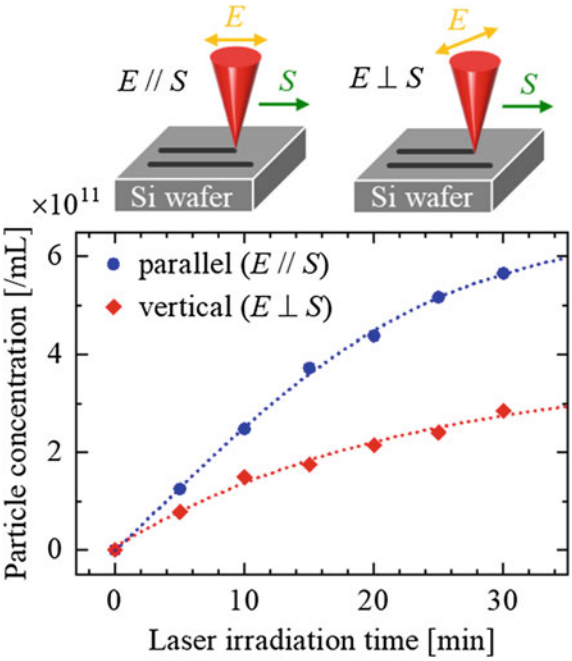


**Fig. 11.4** Si nanoparticle concentration as a function of laser irradiation time without liquid flow. Schematic illustration of the laser polarization direction ($E$) and writing direction ($S$) is also shown. The laser polarization was set to be parallel ($E//S$) or perpendicular ($E \perp S$) to the writing direction

four different polarization states was irradiated on the Si wafer surface in ethanol solution.

Figure 11.5 shows Si nanoparticle concentration as a function of the delay time between femtosecond double pulses. The polarization directions of the first ($E^{1st}$) and second ($E^{2nd}$) pulse were set to be parallel or perpendicular to the laser writing direction ($S$). For comparison, the results of single-pulse train are also shown. Similar to Fig. 11.4, the amount of generated Si nanoparticles was large in the double-pulse train parallel to the writing direction. Particularly, the amount of Si nanoparticles generated by the double-pulse train was larger than that of the single-pulse train if the delay time was 100 ps or less, independent of polarization direction. Compared to the results of the single-pulse train, about 2.5 times as many Si nanoparticles were generated at the delay time of 10 ps. Assuming the lifetime of the plasma is considered to be several tens of ps, the second pulse can interact with the electron plasma generated by the first pulse before the electron plasma is relaxed. Such electrons are accelerated by the ponderomotive force, and the kinetic energy of the electrons is increased by the inverse bremsstrahlung, leading to enhance the ionization [33]. Finally, the Si nanoparticles can be efficiently generated by the double-pulse train compared to that for the single-pulse train. It should be noted that there is no big difference in the size distribution of Si nanoparticles between produced by the single-pulse train and the double-pulse train.

Furthermore, symmetric variation of the particle concentration to the delay time between orthogonally polarized femtosecond double pulse was also observed

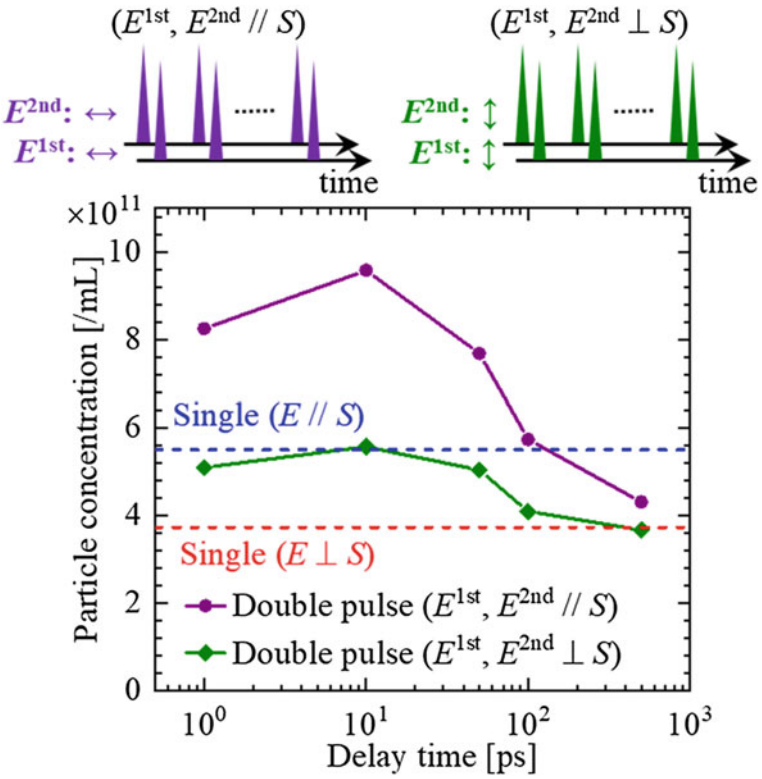


**Fig. 11.5** Si nanoparticle concentration as a function of the delay time between femtosecond double-pulses with different polarization directions ($S//E$ or $S \perp E$), where $S$ is the writing direction. $E^{1st}$ and $E^{2nd}$ show the polarization direction of the first and second pulses, respectively. Dotted lines indicate the results of single-pulse train experiments. Schematics of double-pulse sequence with different polarization direction are also shown. © IEEE. Reprinted, with permission, from [38]

(Fig. 11.6). When the delay time is 100 ps or less, the amount of generated Si nanoparticles was increased compared to that for the single-pulse train, regardless of the polarization directions of the first and second pulses. After about 100 ps, the amount of generated Si nanoparticles was decreased and asymptotically approached that for the single-pulse train in the polarization direction parallel to the writing direction. This phenomenon was in good agreement with the result of Fig. 11.5. On the other hand, when the delay time was 10 ps or less, the amount of generated Si nanoparticles was dramatically decreased, and the amount of production was close to the result of the single-pulse train in the polarization direction perpendicular to the writing direction. Since the time resolution is $70 \pm 40$ fs in our experiments, assuming the double-pulse trains are overlapped in time, it is considered that the polarization direction was tilted to be 45° to the writing direction. From the above results, it is

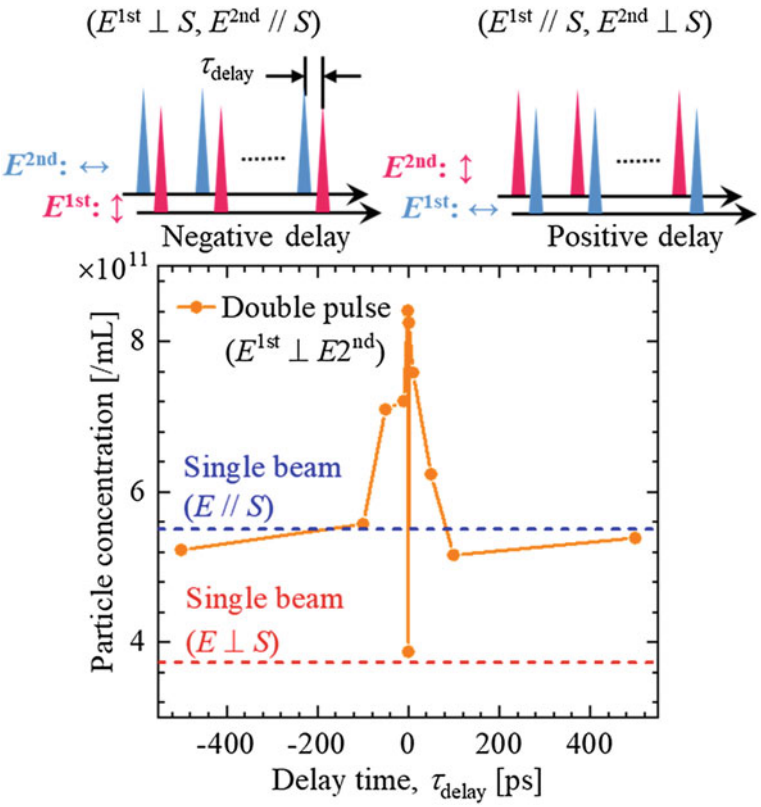


**Fig. 11.6** Si nanoparticle concentration as a function of the delay time between orthogonally polarized femtosecond double-pulse. Negative delay indicates that the first (second) pulses are polarized perpendicular (parallel) to the writing direction, respectively. Positive delay indicates vice versa. Dotted lines indicate the results of single-pulse train experiments. Schematics of orthogonally-polarized double-pulse sequence are also shown. © IEEE. Reprinted, with permission, from [38]

ideally possible to produce Si nanoparticles about 8 times as much as a conventional single-pulse train experiment by flowing a solvent and using femtosecond double-pulse configuration with suitable polarization direction.

## 11.3 Synthesis of Fluorescent Nanodiamonds by Femtosecond Laser Ablation in Liquid

### *11.3.1 Nanodiamond Synthesis from Solid-State Carbon Source*

The technique of pulsed laser ablation in liquid has become attractive as the method to synthesize nanodiamond [34, 35]. Recently, Nee et al. reported that nanodiamonds with the size of <5 nm can be directly synthesized from the dissociation of ethanol ($C_2H_5OH$) by femtosecond laser irradiation [36]. More recently, Hao et al. also showed a one-step synthesis method for fluorescent nanodiamonds by femtosecond pulsed laser ablation of bulk diamond in water [37]. The maximum yield in this technique can be reached to 8.2 mg/h under 828 mW. Based on the previously mentioned efficient liquid-phase laser ablation method, we applied to various solid-state carbon sources [38]. We used the following three types of solid-state carbon sources: (1) graphite carbon (10 × 10 × 0.5 mm), (2) glassy carbon (15 × 15 × 1 mm), and (3) bagasse charcoal, which is a strained lee of sugarcane. The carbonized bagasse powder was sintered by spark plasma sintering (SPS) equipment, and then a pellet-like sample ($\phi = 10$ mm) was obtained. As the solvent, ethanol, cyclohexane, and acetone were used in the experiments. Transmission electron microscopic (TEM) observation of the produced nanoparticles was performed by a high-resolution transmission electron microscope (JEOL, JEM2100F). Figure 11.7 shows TEM images and electron diffraction patterns of nanoparticles produced from different solid-state carbon sources of graphite carbon, glassy carbon, and bagasse charcoal by laser ablation in ethanol. Sugarcane bagasse is a waste material, which is fibrous production in large quantities after sugar juice extraction from sugarcane stalks [39]. Therefore, it is known that the crystal structure of carbonized bagasse is an amorphous and includes many kinds of functional group derived from cellulose, hemicellulose, and lignin [40]. Interestingly, clear crystal lattices are observed in the TEM images, with interplanar spacing of 0.21 nm, which is assigned to (111) planes of cubic diamond structure. These results clearly indicate that the produced nanoparticles have a diamond structure with high crystallinity, regardless of the crystallinity of starting carbon source. The size distributions of nanodiamonds produced from different solid-state carbon sources by laser ablation in ethanol were estimated by TEM observation (Fig. 11.8). The average size of nanodiamonds synthesized from glassy carbon (~2.9 nm) was smaller than these of graphite carbon (~4.5 nm) and bagasse charcoal (~5.4 nm). Further experiments should be needed to understand the difference in the size distribution.

To clarify the influence of the solvent molecule, photoluminescence (PL) spectra of the nanodiamonds produced from glassy carbon after liquid-phase laser ablation in ethanol, cyclohexane, and acetone were measured (Fig. 11.9). The PL spectra were measured by using a fluorescence spectrophotometer (Horiba Jobin Yvon Inc., FluoroMax-3).

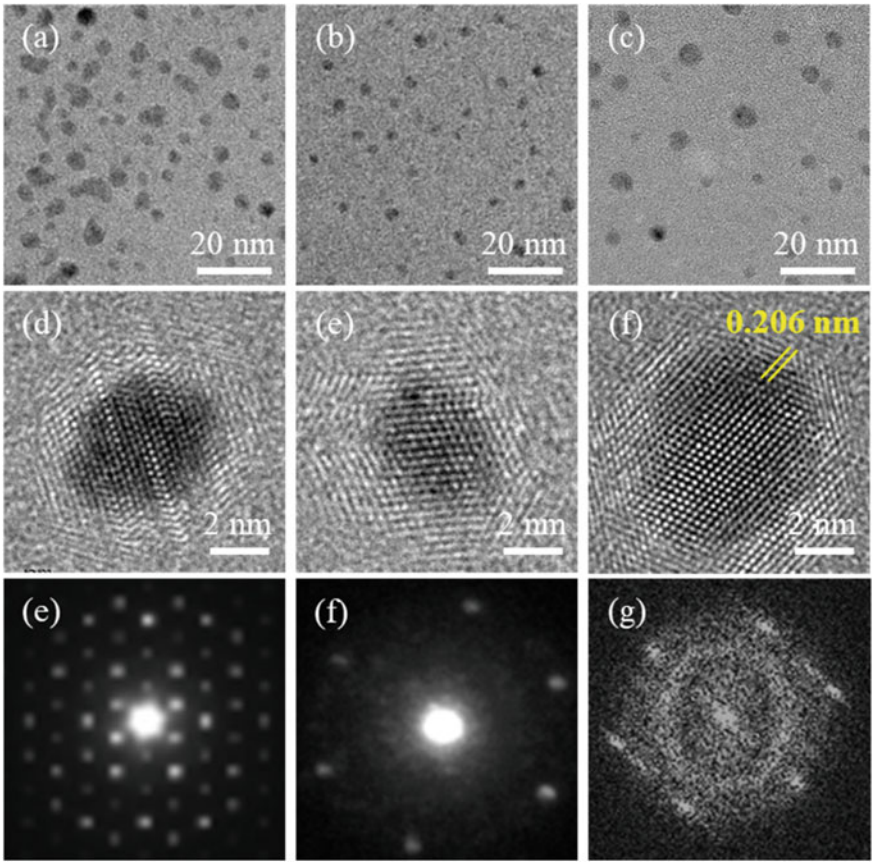


**Fig. 11.7** TEM images and electron diffraction patterns of nanoparticles produced from different solid-state carbon sources (a, d, e) graphite carbon, (b, e, f) glassy carbon, and (c, f, g) bagasse charcoal by laser ablation in ethanol. Low (a, b, c) and high (d, e, f) magnification images are shown. © Elsevier. Reprinted, with permission, from [23, 24]

The PL spectra of the nanodiamonds are dependent on the excitation wavelengths. The emission of nanodiamonds produced in ethanol is mainly in the UV region with the maximum intensity at 440 nm with an excitation wavelength of 360 nm. Increasing the excitation wavelengths, the PL peak is red-shifted and the PL intensity is gradually decreased. Although the PL spectra in the case of cyclohexane are similar to that for ethanol, the main emission at green region from 500 to 600 nm is slightly weak. The maximum emission of nanodiamonds produced in acetone is observed at about 520 nm when excited by 420 nm. The red-shifted PL with increase of excitation wavelengths is also observed. These results show that the optimal PL peak of nanodiamonds can be tailored by changing the solvent molecule.

Different oxygen-containing functional groups of solvent molecule result in different oxidation defect states on the surface of nanodiamonds, which are reflected

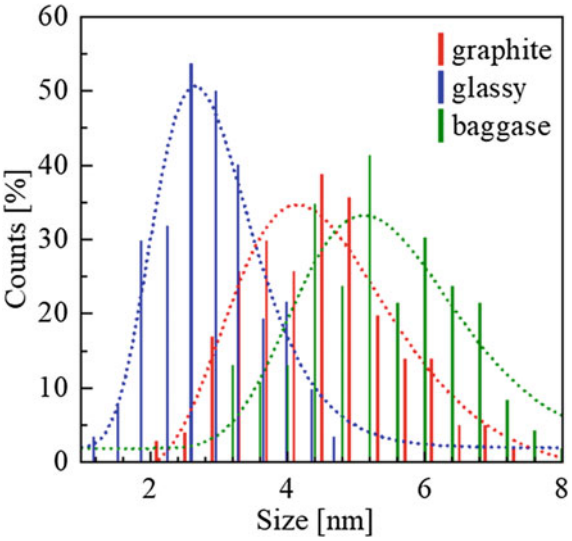


**Fig. 11.8** Size distribution of the nanoparticles produced from different solid-state carbon sources by laser ablation in ethanol

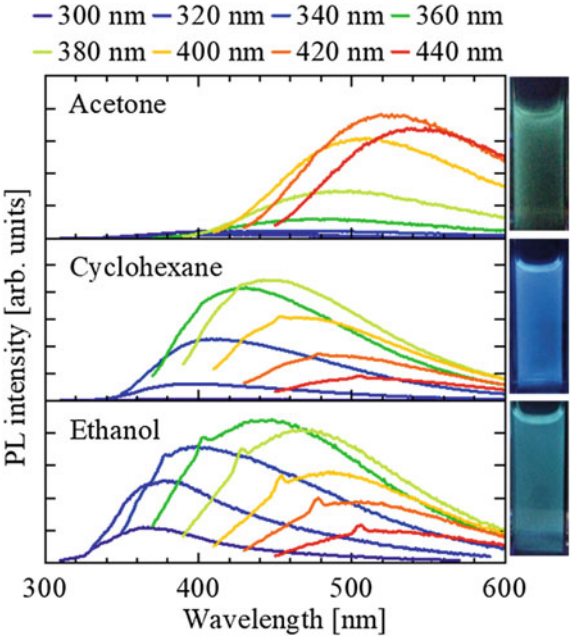


**Fig. 11.9** PL spectra of nanodiamond produced from glassy carbon by laser ablation in various solvent (ethanol, cyclohexane and acetone). Excitation wavelength was varied from 300 to 440 nm. The right-hand photos show luminescence from nanodiamonds in various solvent under 365 nm excitation

in the excitation spectra [23, 26, 38]. Well-defined peaks are also observed in the excitation spectra. In the case of ethanol, there are several excitation peaks in the range from 270 to 320 nm which are assigned to n-π* transition of carbonyl groups [41, 42]. For cyclohexane, there is no big difference in the excitation spectra compared to that for ethanol. For acetone, the main excitation shoulders exist in the range from 380 to 500 nm with a common peak at 420 nm. These obvious π transitions indicate the existence of highly localized π states and oxidation defect states, between which two possible ways of radiative recombination, intrinsic direct transitions and defect energy trapping (DET) state-related transitions could take place [43–45]. Here, we suggest that more DET states are created with enhancement of surface oxidation degree, resulting in red-shifted PL. As discussed previously, from cyclohexane, ethanol to acetone, the optimal PL wavelengths increase with the enhancement of oxidation degree, which confirm the above hypothesis.

In order to evaluate the functional groups on the surface of nanodiamonds produced from glassy carbon by laser ablation in various solvent, an infrared absorption spectroscopy was inspected by a FT-IR (Perkin Elmer, Spectrum Two) attached with a diamond attenuated total reflection (ATR) unit. The dispersion solutions of nanodiamonds were dropped and dried on the metal Cu plate, and then, FT-IR spectra were measured by ATR method (Fig. 11.10). The FT-IR spectra for each solvent without nanodiamonds are also shown in Fig. 11.10. From the comparison between the FT-IR spectra of nanodiamonds and that of solvent, some characteristic peaks of 1633 $cm^{-1}$ (C = O) and 1659 $cm^{-1}$ (OH) for ethanol, 1081 $cm^{-1}$ (C = O, OH) and 1712 $cm^{-1}$ (C = O) for cyclohexane, 1659 $cm^{-1}$ (C = O, OH), 3200 $cm^{-1}$ (OH) and 3358 $cm^{-1}$ (OH) for acetone were observed on the surface of nanodiamonds. These

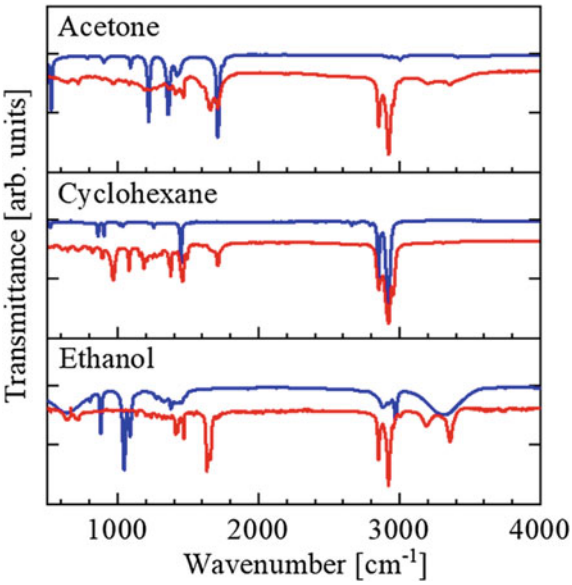


**Fig. 11.10** FT-IR spectra of nanodiamond produced from glassy carbon by laser ablation in various solvent (ethanol, cyclohexane and acetone). These spectra were measured by the attenuated total reflection (ATR) method. The blue curves show FT-IR spectra for each solvent without nanodiamonds

results support the change of fluorescence spectrum of nanodiamonds according to solvent.

### *11.3.2 Nanodiamond Synthesis from Solvent Molecules*

The laser ablation process in liquid is capable of removing the layer of amorphous carbon and covalent bonds from detonation nanodiamonds, which were first produced from detonation of explosives [46]. Furthermore, the use of starting carbon source other than diamond may possibility include impurities derived from starting carbon source and solvent molecules [36, 37]. Therefore, the purification and the dispersion of nanodiamonds produced by laser ablation in liquid still need to be improved. In this section, we used graphene oxide aqueous solution (Graphene Supermarket; 0.5 ~5 μm in diameter), which was diluted by the two kinds of solvents of water or ethanol. The concentration of graphene oxide was 0.5 mg/ml. Detailed laser ablation experiments were reported in [26]. The laser ablation of ethanol or cyclohexane without any solid-state carbon sources was also performed. The PL spectra and PL excitation (PLE) spectra were measured by using a fluorescence spectrophotometer (Horiba Jobin Yvon Inc., FluoroMax-3). Transmission electron microscopy (TEM) and electron energy-loss spectroscopy (EELS) were performed by a high-resolution transmission electron microscope (JEOL, JEM2100F).

Figure 11a, b show PL and PLE spectra maps of nanodiamonds produced from graphene oxide by laser ablation in ethanol or water. PL and PLE spectra maps of nanodiamonds produced from ethanol or cyclohexane without solid-state carbon source by laser ablation are also shown in Fig. 11.11c, d. The nanodiamonds produced from graphene oxide by laser ablation in ethanol show colorful luminescence, such phenomenon is similar to the results of laser ablation of various solid-state carbon sources in ethanol (Fig. 11.9). While in the case of graphene oxide in water, narrow PL and PLE peaking at 450 nm and 350 nm, respectively, was apparently observed, compared to that of graphene oxide in ethanol. Figure 11.11e show TEM image obtained from of nanodiamonds produced from graphene oxide by laser ablation in water. The nanodiamonds contain many point defects and multiple twins. Such defects also play an important role on PL properties of nanodiamonds. TEM image shows that nanodiamonds produced from graphene oxide by laser ablation in water consist of polycrystalline diamond structure. The three different values (0.206 nm, 0.193 nm and 0.218 nm) of crystal lattice spacing in nanodiamonds were observed. The crystal lattice spacing of 0.206 nm corresponds to that of (111) planes of cubic diamond. On the other hand, the crystal lattice spacing of 0.193 nm and 0.218 nm is considered to be attributed to the hexagonal diamond, which is known as lonsdaleite [47]. The crystal lattice spacing of 0.193 nm and 0.218 nm correspond to that of (101) and (110) planes of hexagonal diamond, respectively.

Figure 11.11f shows the electron energy-loss spectroscopy (EELS) spectrum of carbon K-edge obtained from nanodiamonds produced from glassy carbon by laser ablation in ethanol or graphene oxide by laser ablation in water. Reference EELS

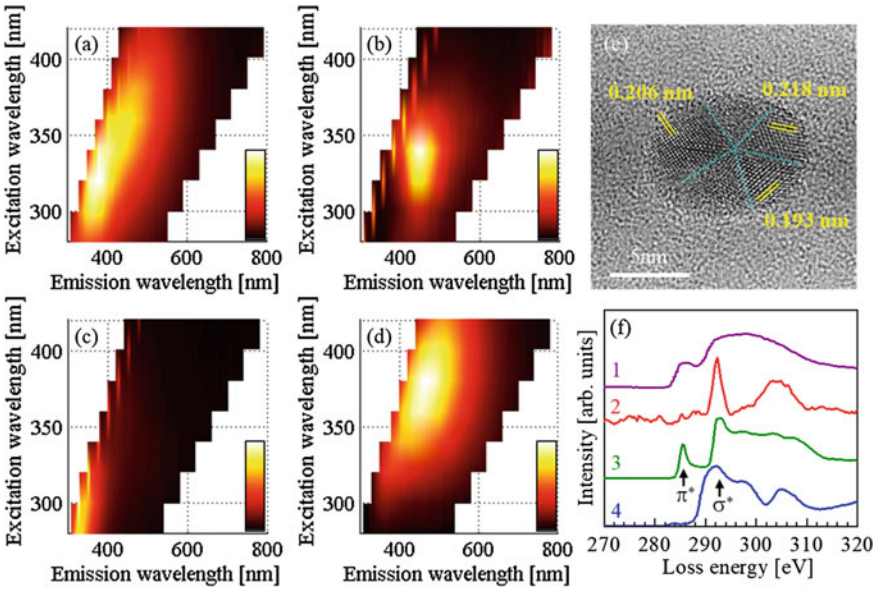


**Fig. 11.11** PL and PLE spectra map of nanodiamonds produced from graphene oxide by laser ablation in **a** ethanol or **b** water. PL and PLE spectra map of nanodiamonds produced from **c** ethanol or **d** cyclohexane without solid-state carbon source by laser ablation are also shown. **e** TEM image of nanodiamonds produced from graphene oxide by laser ablation in water. Light-blue lines show multiple twins. **f** Carbon K-edge EELS spectra of nanodiamonds produced from (1) glassy carbon by laser ablation in ethanol, (2) graphene oxide by laser ablation in water. Reference spectra of (3) graphite and (4) diamond were also shown. © SPIE Publications. Reprinted, with permission, from [26]

spectra of graphite and diamond were also shown. The EELS spectrum of nanodiamonds produced from glassy carbon by laser ablation in ethanol shows π* peak at 285 eV followed by a relatively featureless, broad σ* peak at around 295 eV, suggesting that nanodiamonds are hybridized with $sp^2$ and $sp^3$ carbon similar to diamond-like carbon. The π* peak existence could be explained by the $sp^2$ carbon located in the structural defects and/or the surface. This diamond-like crystalline character of nanodiamonds is also shown in electron diffraction pattern and Raman spectra in the previous report [48]. On the other hand, it is suggested that nanodiamonds produced from graphene oxide in water does not contain almost $sp^2$ carbon leading to the relatively homogeneous production.

Interestingly, ethanol and cyclohexane solvent without any solid-state carbon sources after the femtosecond laser irradiation also indicates PL emission. It should be noted that no PL peaks were observed before laser irradiation. In the case of ethanol, weak PL was observed in bluer region below 400 nm (Fig. 11.11c). These PL peaks suggest that any fluorescent molecules were generated from degradation of ethanol molecules by the femtosecond laser irradiation. That is also confirmed by the smell of the ethanol sample after laser irradiation, which obviously differed

from the initial ethanol. While, the tendency of PL and PLE spectra map for cyclohexane was quite different from that of ethanol, the maximum PL intensity was obtained at about 470 nm (Fig. 11.11d). This result could indicate that fluorescent carbon molecules with different PL properties were generated from cyclohexane. It is known that polyyne molecules, which are linear carbon chains with alternating triple and single sp-hybridized C–C bonds terminated by atoms or groups, are directly synthesized in various solvent by dissociation using femtosecond laser irradiation [49, 50]. We assumed that such polyyne molecules and/or nanodiamonds have been generated from degradation of cyclohexane molecules. It should be noted that PLE properties derived from the polyyne molecules and nanodiamonds are clearly different, compared between Fig. 11.11b, d. Detailed investigations should be needed to understand such differences in PL and PLE properties.

## 11.4 Conclusion

In summary, by using the femtosecond laser ablation in liquid, we have successfully produced nanoparticles with higher yield by the double pulse with shorter delay time than electron–ion relaxation time (<100 ps), considering polarization direction regarding laser writing direction. We have also demonstrated nanodiamonds with interesting fluorescent properties can be produced by this technique. The hexagonal diamond was also synthesized. More interestingly, cyclohexane after femtosecond laser irradiation without any solid-state carbon sources is suggested to undergo transformation to fluorescent material such as polyyne molecules and/or nanodiamonds. These techniques for nanoparticle preparation by femtosecond laser ablation in liquid will open the door to the improvement of flexibility and productivity of functional nanomaterials fabrication.

## References

1. W. Stöber, A. Fink, E. Bohn, Controlled growth of monodisperse silica spheres in the micron size range. J. Colloid Interface Sci. **26**, 62–69 (1968). https://doi.org/10.1016/0021-9797(68)90272-5
2. M. Faraday, Experimental relations of gold (and other metals) to light. Philos. Mag. **147**, 145–181 (1857). https://doi.org/10.1098/rstl.1857.0011
3. K. Byrappa, T. Adschiri, Hydrothermal technology for nanotechnology. Prog. Cryst. Growth Charact. Mater. **53**, 117–166 (2007). https://doi.org/10.1016/j.pcrysgrow.2007.04.001
4. J. Li, Q. Wu, J. Wu, Synthesis of nanoparticles via solvothermal and hydrothermal methods, in *Handbook of Nanoparticles*. ed. by M. Aliofkhazraei (Springer International Publishing, Switzerland, 2016), pp. 295–328
5. G.L. Messing, S.-C. Zhang, G.V. Jayanthi, Ceramic powder synthesis by spray pyrolysis. J. Am. Ceram. Soc. **76**, 2707–2726 (1993). https://doi.org/10.1111/j.1151-2916.1993.tb04007.x
6. M. Kakati, B. Bora, S. Sarma, B.J. Saikia, T. Shripathi, U. Deshpande, A. Dubey, G. Ghosh, A.K. Das, Synthesis of titanium oxide and titanium nitride nano-particles with narrow size

distribution by supersonic thermal plasma expansion. Vacuum **82**, 833–841 (2008). https://doi.org/10.1016/j.vacuum.2007.11.014
7. J. Neddersen, G. Chumanov, T.M. Cotton, Laser ablation of metals: a new method for preparing SERS active colloids. Appl. Spectrosc. **47**, 1959–1964 (1993). https://doi.org/10.1366/0003702934066460
8. F. Mafuné, J. Kohno, Y. Takeda, T. Kondow, H. Sawabe, Formation and size control of silver nanoparticles by laser ablation in aqueous solution. J. Phys. Chem. B **104**, 9111–9117 (2000). https://doi.org/10.1021/jp001336y
9. H. Harada, S. Shimizu, T. Yatsuhashi, S. Sakabe, Y. Izawa, N. Nakashima, A key factor in parent and fragment ion formation on irradiation with an intense femtosecond laser pulse. Chem. Phys. Lett. **342**, 563–570 (2001). https://doi.org/10.1016/S0009-2614(01)00662-5
10. Y. Tamaki, T. Asahi, H. Masuhara, Nanoparticle formation of vanadyl phthalocyanine by laser ablation of its crystalline powder in a poor solvent. J. Phys. Chem. A **106**, 2135–2139 (2002). https://doi.org/10.1021/jp012518a
11. T. Tsuji, K. Iryo, N. Watanabe, M. Tsuji, Preparation of silver nanoparticles by laser ablation in solution: influence of laser wavelength on particle size. Appl. Surf. Sci. **202**, 80–85 (2002). https://doi.org/10.1016/S0169-4332(02)00936-4
12. K. Sasaki, N. Takada, Liquid-phase laser ablation. Pure Appl. Chem. **82**, 1317–1327 (2010). https://doi.org/10.1351/PAC-CON-09-10-23
13. X. Li, H. Wang, Y. Shimizu, A. Pyatenko, K. Kawaguchi, N. Koshizaki, Preparation of carbon quantum dots with tunable photoluminescence by rapid laser passivation in ordinary organic solvents. Chem. Commun. **47**, 932–934 (2011). https://doi.org/10.1039/C0CC03552A
14. J. Xiao, P. Liu, C.X. Wang, G.W. Yang, External field-assisted laser ablation in liquid: An efficient strategy for nanocrystal synthesis and nanostructure assembly. Prog. Mater. Sci. **87**, 140–220 (2017). https://doi.org/10.1016/j.pmatsci.2017.02.004
15. Y. Shimotsuma, T. Yuasa, H. Homma, M. Sakakura, A. Nakao, K. Miura, K. Hirao, M. Kawasaki, J. Qiu, P.G. Kazansky, Photoconversion of copper flakes to nanowires with ultrashort pulse laser irradiation. Chem. Mater. **19**, 1206–1208 (2007). https://doi.org/10.1021/cm062592b
16. G. Chang, Y. Shimotsuma, M. Sakakura, T. Yuasa, H. Homma, M. Oyama, K. Miura, J. Qiu, P.G. Kazansky, K. Hirao, Photo-conversion and evolution of one-dimensional Cu nanoparticles under femtosecond laser irradiation. Appl. Surf. Sci. **254**, 4992–4998 (2008). https://doi.org/10.1016/j.apsusc.2008.01.172
17. A. Nakao, Y. Shimotsuma, M. Nishi, K. Miura, K. Hirao, Morphological control of nanoparticles by femtosecond laser irradiation, J. Ceram. Process. Res. 9 (2008) 425–429. https://doi.org/10.36410/jcpr.2008.9.4.425.
18. E.T.Y. Lee, Y. Shimotsuma, M. Sakakura, M. Nishi, K. Miura, K. Hirao, Photo-initiated growth of zinc oxide (ZnO) nanorods. Mater. Lett. **62**, 4044–4046 (2008). https://doi.org/10.1016/j.matlet.2008.05.066
19. E.T.Y. Lee, Y. Shimotsuma, M. Sakakura, M. Nishi, K. Miura, K. Hirao, Ultrashort pulse manipulation of ZnO nanowire growth. J. Nanosci. Nanotechnol. **9**, 618–626 (2009). https://doi.org/10.1166/jnn.2009.j069
20. N. Wu, Y. Shimotsuma, M. Nishi, M. Sakakura, K. Miura, K. Hirao, Photo-initiation of ZnO nanorod formation by femtosecond laser irradiation. J. Ceram. Soc. Jpn. **118**, 147–151 (2010). https://doi.org/10.2109/jcersj2.118.147
21. T. Yamamoto, Y. Shimotsuma, M. Sakakura, M. Nishi, K. Miura, K. Hirao, Intermetallic magnetic nanoparticle precipitation by femtosecond laser fragmentation in liquid. Langmuir **27**, 8359–8364 (2011). https://doi.org/10.1021/la201211e
22. D. Tan, Y. Yamada, S. Zhou, Y. Shimotsuma, K. Miura, J. Qiu, Photoinduced luminescent carbon nanostructures with ultra-broadly tailored size ranges. Nanoscale **5**, 12092–12097 (2013). https://doi.org/10.1039/C3NR04392D
23. D. Tan, S. Zhou, B. Xu, P. Chen, Y. Shimotsuma, K. Miura, J. Qiu, Simple synthesis of ultrasmall nanodiamonds with tunable size and photoluminescence. Carbon **62**, 374–381 (2013). https://doi.org/10.1016/j.carbon.2013.06.019

24. D. Tan, Y. Yamada, S. Zhou, Y. Shimotsuma, K. Miura, J. Qiu, Carbon nanodots with strong nonlinear optical response. Carbon **69**, 638–640 (2014). https://doi.org/10.1016/j.carbon.2013.12.056
25. D. Tan, S. Zhou, Y. Shimotsuma, K. Miura, J. Qiu, Effect of UV irradiation on photoluminescence of carbon dots. Opt. Mater. Express **4**, 213–219 (2014). https://doi.org/10.1364/OME.4.000213
26. N. Agatsuma, Y. Fujimatsu, Y. Shimotsuma, M. Sakakura, K. Miura, Synthesis of fluorescent nanocarbons by femtosecond laser induced plasma in liquid. Proc. SPIE **9983**, 99831C (2016). https://doi.org/10.1117/12.2235727
27. V.G. Niziev, A.V. Nesterov, Influence of beam polarization on laser cutting efficiency. J. Phys. D: Appl. Phys. **32**, 1455–1461 (1999). https://doi.org/10.1088/0022-3727/32/13/304
28. A. Mahrle, E. Beyer, Theoretical aspects of fibre laser cutting. J. Phys. D: Appl. Phys. **42**(2009). https://doi.org/10.1088/0022-3727/42/17/175507
29. M. Zubair, Y.S. Ang, K.J.A. Ooi, L.K. Ang, Fractional Fresnel coefficients for optical absorption in femtosecond laser-induced rough metal surfaces. J. Appl. Phys. **124**(2018). https://doi.org/10.1063/1.5039811
30. K. Sugioka, M. Iida, H. Takai, K. Micorikawa, Efficient microwelding of glass substrates by ultrafast laser irradiation using a double-pulse train. Opt. Lett. **36**, 2734–2736 (2011). https://doi.org/10.1364/OL.36.002734
31. M. Mori, Y. Shimotsuma, T. Sei, M. Sakakura, K. Miura, H. Udono, Tailoring thermoelectric properties of nanostructured crystal silicon fabricated by infrared femtosecond laser direct writing. Phys. Status Solidi A **212**, 715–721 (2015). https://doi.org/10.1002/pssa.201431777
32. E. Kim, Y. Shimotsuma, M. Sakakura, K. Miura, 4H-SiC wafer slicing by using femtosecond laser double-pulses. Opt. Mater. Express **7**, 2450–2460 (2017). https://doi.org/10.1364/OME.7.002450
33. D.E. Roberts, A. du Plessis, L.R. Botha, Femtosecond laser ablation of silver foil with single and double pulses. Appl. Surf. Sci. **256**, 1784–1792 (2010). https://doi.org/10.1016/j.apsusc.2009.10.004
34. S.R.J. Pearce, S.J. Henley, F. Claeyssens, P.W. May, K.R. Hallam, J.A. Smith, K.N. Rosser, Production of nanocrystalline diamond by laser ablation at the solid/liquid interface. Diam. Relat. Mater. **13**, 661–665 (2004). https://doi.org/10.1016/j.diamond.2003.08.027
35. L. Yang, P.W. May, L. Yin, J.A. Smith, K.N. Rosser, Growth of diamond nanocrystals by pulsed laser ablation of graphite in liquid. Diam. Relat. Mater. **16**, 725–729 (2007). https://doi.org/10.1016/j.diamond.2006.11.010
36. C.-H. Nee, S.-L. Yap, T.-Y. Tou, H.-C. Chang, S.-S. Yap, Direct synthesis of nanodiamonds by femtosecond laser irradiation of ethanol. Sci. Rep. **6**, 33966 (2016). https://doi.org/10.1038/srep33966
37. J. Hao, L. Pan, S. Gao, H. Fan, B. Gao, Production of fluorescent nano-diamonds through femtosecond pulsed laser ablation. Opt. Mater. Express **9**, 4734–4741 (2019). https://doi.org/10.1364/OME.9.004734
38. Y. Shimotsuma, Y. Yamada, M. Sakakura, K. Hirao, K. Miura, Nanoparticle synthesis by femtosecond laser ablation in liquid, Proc. CLEOPR (2013) TuE3–3. https://doi.org/10.1109/CLEOPR.2013.6600108.
39. C.A. Cardona, J.A. Quintero, I.C. Paz, Production of bioethanol from sugarcane bagasse: status and perspectives. Bioresour. Technol. **101**, 4754–4766 (2010). https://doi.org/10.1016/j.biortech.2009.10.097
40. H.A. Baloch, S. Nizamuddin, M.T.H. Siddiqui, N.M. Mubarak, D.K. Dumbre, M.P. Srinivasan, G.J. Griffin, Sub-supercritical liquefaction of sugarcane bagasse for production of bio-oil and char: Effect of two solvents. J. Environ. Chem. Eng. **6**, 6589–6601 (2018). https://doi.org/10.1016/j.jece.2018.10.017
41. Z. Luo, Y. Lu, L.A. Somers, A.T.C. Johnson, High yield preparation of macroscopic graphene oxide membranes. J. Am. Chem. Soc. **131**, 898–899 (2009). https://doi.org/10.1021/ja807934n
42. G. Eda, Y.-Y. Lin, C. Mattevi, H. Yamaguchi, H.-A. Chen, I.-S. Chen, C.-W. Chen, M. Chhowalla, Blue photoluminescence from chemically derived graphene oxide. Adv. Mater. **22**, 505–509 (2010). https://doi.org/10.1002/adma.200901996

43. J. Robertson, Electronic structure of diamond-like carbon. Diam. Relat. Mater. **6**, 212–218 (1997). https://doi.org/10.1016/S0925-9635(96)00627-9
44. K.B. Holt, Undoped diamond nanoparticles: origins of surface redox chemistry. Phys. Chem. Chem. Phys. **12**, 2048–2058 (2010). https://doi.org/10.1039/B920075D
45. C.-T. Chien, S.-S. Li, W.-J. Lai, Y.-C. Yeh, H.-A. Chen, I.-S. Chen, L.-C. Chen, K.-H. Chen, T. Nemoto, S. Isoda, M. Chen, T. Fujita, G. Eda, H. Yamaguchi, M. Chhowalla, C.-W. Chen, Tunable photoluminescence from graphene oxide. Angew. Chem. Int. Ed. **51**, 6662–6666 (2012). https://doi.org/10.1002/anie.201200474
46. K.-Y. Niu, H.-M. Zheng, Z.-Q. Li, J. Yang, J. Sun, X.-W. Du, Laser dispersion of detonation nanodiamonds. Angew. Chem. Int. Ed. **50**, 4099–4102 (2011). https://doi.org/10.1002/anie.201007731
47. A. Kumar, P.A. Lin, A. Xue, B. Hao, Y.K. Yap, R.M. Sankaran, Formation of nanodiamonds at near-ambient conditions via microplasma dissociation of ethanol vapour. Nat. Commun. **4**, 2618 (2013). https://doi.org/10.1038/ncomms3618
48. J. Xiao, G. Ouyang, P. Liu, C.X. Wang, G.W. Yang, Reversible nanodiamond-carbon onion phase transformations. Nao Lett. **14**, 3645–3652 (2014). https://doi.org/10.1021/nl5014234
49. A. Hu, W.W. Duley, Synthesis of nanocrystalline hexagonal diamond films in organic solvents by femtosecond laser irradiation. Mater. Res. Soc. Symp. Proc. **1039**, 1508 (2007). https://doi.org/10.1557/PROC-1039-P15-08

# Chapter 12
# Preparation of Functional Nanoparticles by Laser Process in Liquid and Their Optical Applications


**Hiroyuki Wada**

**Abstract** Laser ablation in liquid is one of unique laser processing techniques which has been studied recently. Functional nanoparticles such as metal, semiconductor, inorganic, and organic materials can be created easily. This easiness is very useful for the researches about applications of nanoparticles. In this chapter, preparation of nanoparticles of various materials by this method and their applications are explained. Firstly upconversion nanoparticles, $Y_2O_3$:Er,Yb, are reported. Upconversion material emits visible light by irradiation with infrared (IR) light. This material is very useful for bioimaging and cancer therapy. Next one is afterglow material, $Sr_2MgSi_2O_7$:Eu,Dy. Afterglow material emits visible light even after blocking excitation light. This material is also useful for bioimaging. Semiconductor nanoparticles of Si are another important material. These nanoparticles are utilized for next generation's solar cell. Last nanoparticle is organic material, naphthalocyanine. Because naphthalocyanine absorbs IR light, it is also very attractive for next generation's bioimaging. These various nanoparticles easily prepared by laser ablation in liquid are promising material for biomedical, electrical and energy fields.

**Keywords** Ablation · Nanoparticle · Cancer therapy · Bioimaging · Solar cell

## 12.1 Introduction

Recently nanoparticles have been studied extensively because of unique properties and the potentiality of wide application in biomedical, electronics, and energy research fields. The materials of nanoparticles are various, e.g., metal, semiconductor, ceramics, and organic compounds. Metal nanoparticles are widely studied in many fields due to the easiness of synthesis. Ceramics nanoparticles can be applied with various doping and expand their applications, although not so many researches on ceramics nanoparticles have been done.

H. Wada (✉)
Department of Chemical Science and Engineering, School of Materials and Chemical Technology, Tokyo Institute of Technology, 4259 Nagatsuta-cho, Midori-ku, Yokohama 226-8582, Japan
e-mail: wada.h.ac@m.titech.ac.jp



Y. Ishikawa et al. (eds.), *High-Energy Chemistry and Processing in Liquids*,
https://doi.org/10.1007/978-981-16-7798-4_12

In general, the preparation of nanoparticles is classified into gas-phase method, liquid-phase method, and solid-phase method. Gas-phase method includes CVD, which synthesizes nanoparticles through chemical reaction, and spray pyrolysis, which synthesizes nanoparticles through thermal decomposition. Liquid-phase method can create nanoparticles-dispersed liquid. These liquids can be utilized in various research fields. Sol–gel method and co-precipitation method are classified in the liquid-phase method. Solid-state reaction represents solid-phase method, which usually synthesizes aggregated nanoparticles.

However, nanoparticles prepared by these conventional methods suffer from several problems. (1) In the case of high temperature process, nanoparticles are aggregated and secondary particle size is increased. Large particles cause many problems. (2) In the case of liquid-phase method such as sol–gel method and co-precipitation method used widely to obtain nanoparticles-dispersed liquid, and the preparation of multi-elements nanoparticles is difficult. It is critical to prepare the doped ceramics nanoparticles which include several elements. (3) The preparation of highly crystalline nanoparticles is also difficult. The crystallinity of nanoparticles is closely related to physical properties such as fluorescent intensity. (4) If the nanoparticles prepared by the liquid-phase method are used for biomedical applications, the unreacted starting materials included in the liquid often cause the problem such as cell death.

To solve these problems, study on laser ablation in liquid was started. Figure 12.1 shows the schematic of laser ablation in liquid [1]. In this method, target in liquid is irradiated with focused pulse laser beam to obtain nanoparticles-dispersed liquid. Extensive researches on preparation of nanoparticles by laser ablation in liquid have been carried out in past decades [2–14]. The studies about laser ablation in gas phase were started from the middle of the twentieth century [15], and the various researches have been done, which was mainly related to preparation of thin films. In contrast, the research on laser ablation in liquid was started recently, which generated nanoparticles in liquid [2–4].

Advantage of this method is the followings;

(1) Nanoparticles-dispersed liquid can be prepared easily.
(2) Unreacted starting materials are not included in the liquid.
(3) Multi-elements nanoparticles such as doped phosphor can be prepared.
(4) Preparation of highly crystalline ceramics nanoparticles is possible.
(5) Particle size hardly increases because the duration of high temperature is short.
(6) Prepared nanoparticles are collected with high efficiency.

The advantage from two to four is attributed to the fact that the fragmentation of highly crystalline target occurs by laser irradiation.

In the case of inorganic nanoparticle, preparation methods were classified to two categories. One is nanosizing of target material, and the other one is usage of chemical reaction between target and solvent. The former is similar to the preparation of metal nanoparticles to irradiate a bulk target with laser beam. Preparation of $TiO_2$ nanoparticles as a photocatalyst from a colloidal solution of $TiO_2$ powder has been studied widely, and the formation mechanism though thermal melting process was

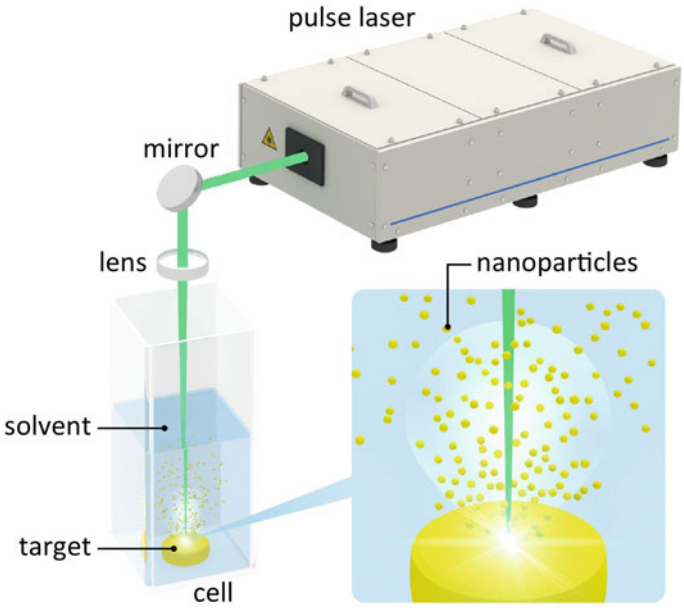


**Fig. 12.1** Schematic of laser ablation in liquid [1]. Copyright (2015) The Chemical Society of Japan

investigated [16]. The latter is preparation of oxide by the reaction between metal and water. For example, the irradiation to Zn plate created ZnO nanoparticles and the irradiation to Ti plate created $TiO_2$ nanoparticles [17].

Generation of high temperature and pressure at the interface between target and solvent has been discussed and chemical reaction and phase change would proceed. Preparation of nanodiamonds at high pressure was reported [18]. Method to control the shape of nanoparticles was to apply voltage during laser irradiation [19]. Although pulse duration of laser which was used for laser ablation in liquid was usually nanosecond, femtosecond laser was used for the reduction of thermal effect. Millisecond and continuous wave (CW) lasers were also used [20].

In the early stage of laser ablation in liquid, metal target such as gold and silver was used [2–4, 6–8, 10–12, 14]. A metal plate held with tweezers in liquid was irradiated with focused laser beam [2]. Gold nanoparticles-dispersed liquid indicates wine red color because of absorption of green related to surface plasmon resonance (SPR). After the report that particle size of prepared nanoparticles was controlled by the addition of surfactant [4], many researchers in various field started to utilize this method. Ceramics nanoparticles were also prepared [9, 13, 21, 22]. Because solvent was usually water, most of the ceramic nanoparticles were oxide. Nitride nanoparticles were prepared by using aqueous ammonia [23] or liquid nitrogen [24] as solvent. Sulfide nanoparticles prepared by laser ablation of CdS in acetone [25] and chloride nanoparticles prepared by laser ablation of Ag in NaCl solution [26]

were also prepared. In the case of ceramics, ceramics target was generally used for the preparation of nanoparticles although some researchers utilized the oxidation of metal in water. Semiconductor nanoparticles such as compound semiconductor were prepared, which would be useful in electronics and energy fields [27]. Although nanoparticles of semiconductors such as Si [7] and Ge [28] were investigated due to easiness to obtain a wafer as target or various applications of nanoparticles, surface of the prepared nanoparticles was usually oxidized. If ethanol was used as solvent, the oxidation was prevented due to reduction effect [29]. Laser ablation in liquid using carbon as target has been investigated because of the extension of research of carbon nanotube. Preparation of nanodiamond by this method was reported [18]. High temperature and pressure in cavitation bubble created by laser irradiation were indicated [30]. Recently, preparation of quantum dots such as ZnSe and CdS has been tried [31]. Biomaterials such as apatite were also prepared [32]. Organic nanoparticles were prepared, which is promising materials in biomedical field [5].

The shapes of prepared nanoparticles were polygon, which was related to crystal structure, or sphere, which was related to surface tension. Although prepared nanoparticle is usually single material, core/shell structure is prepared under some experimental conditions. Metal nanoparticles, surface of which was oxidized, were easily prepared [33]. In this case, the source of oxygen such as dissolved oxygen or water was not discussed well. Laser ablation in organic solvent which contains thiol group created nanoparticle with metal core and metal sulfide shell. If alloy such as brass (Cu 60%, Zn 40%) was used for target, core/shell structure was also prepared [34]. Hollow nanoparticles were prepared by removal of core from core/shell structure. Nanoparticles were absorbed to polystyrene as a mold, and then mold was removed to prepare hollow nanoparticles. Leaf-like $WO_3$ nanoparticles were prepared by laser ablation in liquid [35].

## 12.2 Upconversion Nanoparticle

$Y_2O_3$:Er,Yb is upconversion material, which is a kind of phosphor. In the case of upconversion, visible luminescence is observed by the excitation of infrared (IR) light with low photon energy, while visible luminescence is observed by the excitation of ultraviolet (UV) light with high photon energy in the case of normal phosphor. Upconversion nanoparticles have the potentiality of promising practical usage [35–37]. The potential applications of the upconversion nanoparticles are bioimaging and cancer therapy in biomedical field.

The bioimaging is key technique for diagnosis, research, and development in this field because of understanding of the position and the pathway of specific cells or materials [38, 39]. Water which is one of the main components of a living body has absorption in far-IR region, and hemoglobin in blood has absorption in visible region. Near-IR region is called ‘optical window’ in biomedical field because of low absorption [40]. Low absorption decreases thermal damage of a living body. Moreover, it reduces autofluorescence related to phosphor derived from a living body such

as NADH. Autofluorescence is one of critical issues in bioimaging. Thus, the advantages of upconversion nanoparticle in the biomedical field are high transparency, low damage of a living body, and low autofluorescence.

The other important application of the upconversion nanoparticles is cancer therapy. Photodynamic therapy (PDT) is one of the promising cancer therapies because of less invasiveness. However, the large cancer and the non-dermatological cancer cannot be cured by this therapy. The combination of PDT and upconversion nanoparticles would solve these problems because of high transparency of a living body [41, 42].

Moreover, the application of upconversion nanoparticles to solar cells increased the energy conversion efficiency because of the effective utilization of IR light which was not used in conventional solar cells [43].

$Y_2O_3$:Er,Yb is chemically and physically stable. The emissions attributed to $Er^{3+}$ ion are green $\left({}^2H_{11/2}, {}^4S_{3/2} \rightarrow {}^4I_{15/2}\right)$ and red $\left({}^4F_{9/2} \rightarrow {}^4I_{15/2}\right)$ [44]. The fluorescent intensity is increased by co-doping of $Yb^{3+}$ ion. In the case of biomedical usage, the particle size with the range from several tens nanometers to 200 nm is desirable. This is because particles with particle size of less than several tens nanometers are excreted through kidney, and particles with particle size of more than 200 nm are ingested by Kupffer's cells in a liver; these nanoparticles cannot stay in blood vessel for the circulation in a living body [45, 46]. Moreover, these particles are passively ingested by cancer cells (EPR effect) [47]. Since solid-phase method and co-precipitation method include high temperature process, the primary particle size was increased and nanoparticles were connected each other. These high temperature processes create the particles with the secondary particle size of micrometers to millimeters scale. Therefore, we used laser ablation in liquid to obtain the liquid in which upconversion nanoparticles with desirable particle size were dispersed.

Upconversion nanoparticles were prepared by laser ablation in liquid. $Y_2O_3$:Er,Yb ceramics target in deionized (DI) water was irradiated with laser beam. Laser was Nd:YAG (SHG, wavelength: 532 nm, pulse duration: 13 ns, repetition rate: 10 Hz). Target was synthesized by co-precipitation method. Ammonia was added to nitrate solution, and then the powder was calcined. Pelletized powder was sintered to obtain highly crystalline $Y_2O_3$:Er,Yb target as a precursor of upconversion nanoparticle dispersed in water.

The synthesized target placed in DI water was irradiated with focused pulse laser beam to obtain upconversion nanoparticles dispersed in water. Prepared nanoparticles were identified with single phase matrix $Y_2O_3$ which is the same as target material. The target did not react with the liquid in this case, although some targets reacted with the liquid in previous cases [22, 27]. Relation between particle size and energy density of irradiated laser beam was investigated by the secondary particle size measured by dynamic light scattering (DLS) [48]. Particle size was reduced with the decrease in energy density. Nanoparticles were observed by scanning electron microscope (SEM) after the nanoparticles-dispersed liquid was dropped on Cu grid with carbon membrane and dried [48]. These nanoparticles were mixture of fine nanoparticles, particle size of which was several tens nanometers, and coarse nanoparticles, particle size of which was several hundred nanometers. Figure 12.2 shows SEM images of

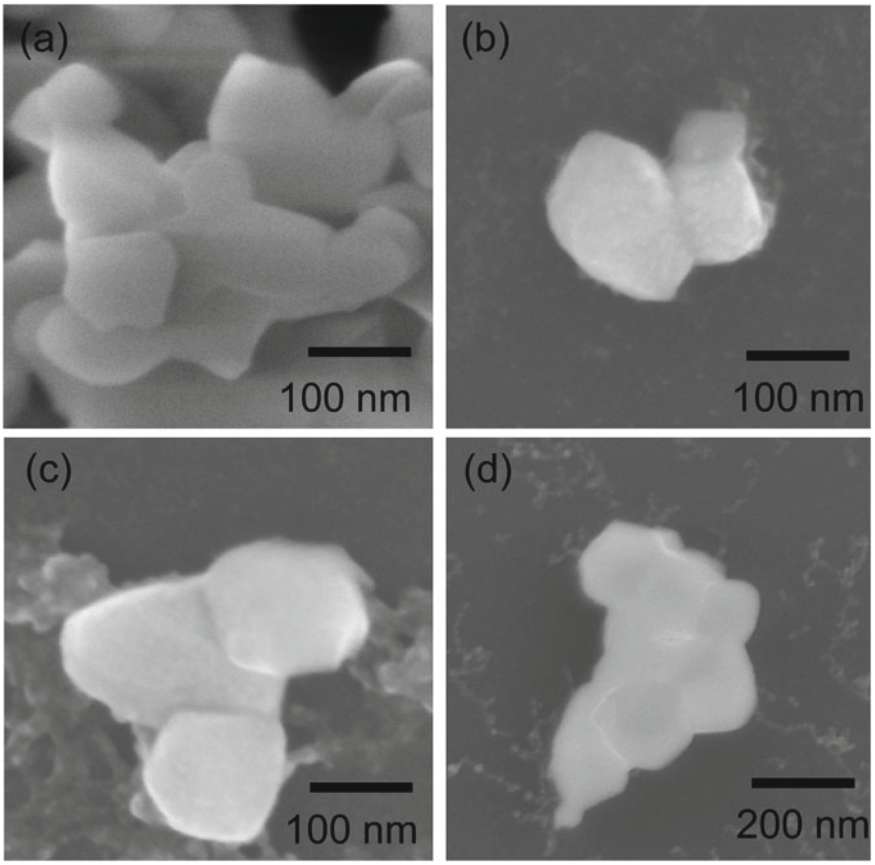


**Fig. 12.2** SEM images of target (**a**) and coarse nanoparticles (**b**–**d**). Energy density: **b** 0.59 J/cm$^2$, **c** 1.06 J/cm$^2$, **d** 1.61 J/cm$^2$. Reprinted from [48], Copyright 2012, with permission from Elsevier

target (a) and coarse nanoparticles (b-d). Secondary particle size was decreased with the reduction of laser energy density, as shown in Fig. 12.2b-d. These results support that of DLS. Primary particles size and morphology of nanoparticles in target shown in Fig. 12.2a are almost same as those of coarse nanoparticles prepared by laser ablation in liquid. Therefore, these coarse nanoparticles would be created by the fragmentation of ceramics target by the effects of thermal expansion and shock wave of laser irradiation. Figure 12.3 shows SEM images of fine nanoparticles [48]. Dot-like nanostructures were observed at low laser energy density as shown in Fig. 12.3a, while string-like nanostructures were observed at high laser energy density as shown in Fig. 12.3b. The dot-like nanostructures, particle size of which are several tens nanometers, were created from target, particle size of which are several hundred nanometers. According to transmission electron microscope (TEM) images of string-like nanostructures shown in Fig. 12.3b, lattice fringes in TEM

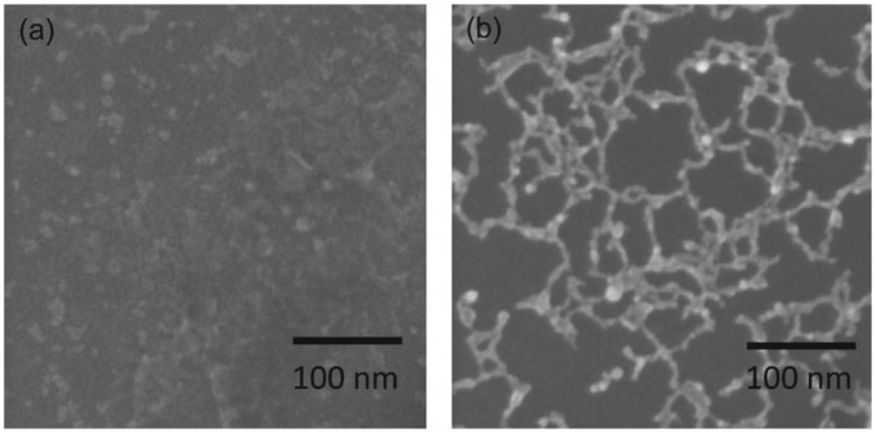


**Fig. 12.3** SEM images of fine nanoparticles. Energy density: **a** 0.59 J/cm$^2$, **b** 1.61 J/cm$^2$. Reprinted from [48], Copyright 2012, with permission from Elsevier

image indicate polycrystal [48]. And the results of energy dispersive X-ray analysis (EDX) indicate that string-like nanostructures consisted of Y, O, Er, and Yb which are elements of $Y_2O_3$:Er,Yb [48]. The dot-like nanostructures created firstly would be aggregated and then melted at high energy density to form polycrystalline string-like nanostructures.

PL spectra of the target material with excitation wavelength of 380 nm and upconversion spectra of them with excitation wavelength of 980 nm were measured. Observed green and red emissions are attributed to $Er^{3+}$ ion as shown in Fig. 12.4. According to energy diagram of $Er^{3+}$ ion [44], the luminescence process with excitation wavelength of 980 nm is the following;

$$
\begin{aligned}
&{}^4I_{15/2} \rightarrow {}^4I_{11/2}\\
&{}^4I_{11/2} \rightarrow {}^4F_{7/2}\\
&{}^4F_{7/2} \rightarrow {}^2H_{11/2},\ {}^4S_{3/2}\ (\text{non - radiative relaxation})\\
&{}^2H_{11/2},\ {}^4S_{3/2} \rightarrow {}^4I_{15/2}.
\end{aligned}
$$

In this case, the fluorescent intensity is increased by co-doping $Yb^{3+}$ ion because the excitation occurs by the energy transfer from $Yb^{3+}$ ion$\left({}^2F_{5/2} \rightarrow {}^2F_{7/2}\right)$. In contrast, red emission is the following:

$$
\begin{aligned}
&{}^4I_{15/2} \rightarrow {}^4I_{11/2}\\
&{}^4I_{11/2} \rightarrow {}^4I_{13/2}(\text{non} - \text{radiative relaxation})\\
&{}^4I_{13/2} \rightarrow {}^4F_{9/2}\\
&{}^4F_{9/2} \rightarrow {}^4I_{15/2}.
\end{aligned}
$$

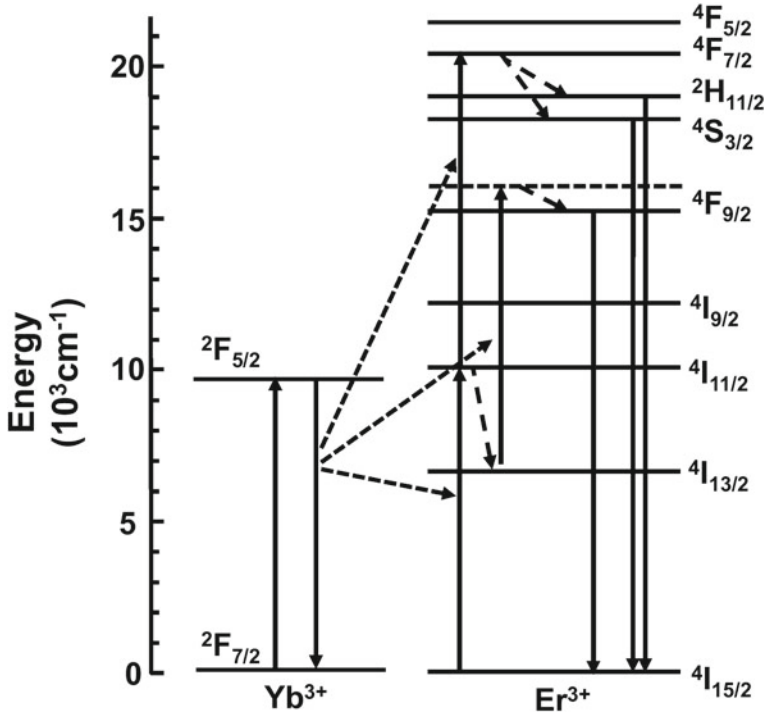


**Fig. 12.4** Energy level diagrams of $Er^{3+}$ and $Yb^{3+}$. Reprinted from [48], Copyright 2012, with permission from Elsevier

This emission is also increased by co-doping $Yb^{3+}$ ion. In the photoluminescence (PL) spectra, green emission is dominant because excitation by UV light increases population at higher energy level.

Upconversion spectra of prepared nanoparticles with excitation at 980 nm were measured [48]. Green and red emissions were observed, which was the same as those of target material. Increase in energy density of irradiated laser beam in the preparation process increased fluorescent intensity. In general, the increase in fluorescent intensity is related to the increase in luminescent efficiency or the increase in amount of phosphor. In general, the increase in energy density of irradiated laser increases the amount of prepared nanoparticle. In this study, the amount of upconversion nanoparticles would also be increased by the increase in laser energy density, and then upconversion intensity was increased.

The relation between excitation intensity $I_{ex}$ and emission intensity $I_{em}$ of upconversion nanoparticles was investigated. The relation is given by the following Eq. (12.1) [49].

$$I_{em} \propto I_{ex}^{n} \tag{12.1}$$

where n is the number of photons related to the upconversion process, which is the slope of double logarithmic plot between excitation and emission intensity. Therefore, upconversion intensity should be continuously increased with increase in excitation intensity. However, it was discontinuously increased at excitation intensity of about 100 mW [50]. In the case of bulk material, similar phenomena were observed previously and called a photon avalanche [51–54]. The observed drastic increase in upconversion intensity is ascribed to the photon-avalanche effect, induced by cross-relaxation as explained below. According to the energy diagram of $Er^{3+}$ ion as shown in Fig. 12.5, excited $Er^{3+}$ ion from $^4F_{9/2}$ to $^2H_{9/2}$ undergoes a non-radiative transition to $^4F_{9/2}$ accompanied by a cross-relaxation transition from $^4I_{13/2}$ to $^4F_{9/2}$. These transitions increase the population of $^4F_{9/2}$ and then red emission increases significantly. By this effect, upconversion efficiency is increased. The photon-avalanche is very useful for practical usage of upconversion nanoparticles because emission is usually reduced by nanosizing due to the increase in specific surface area.

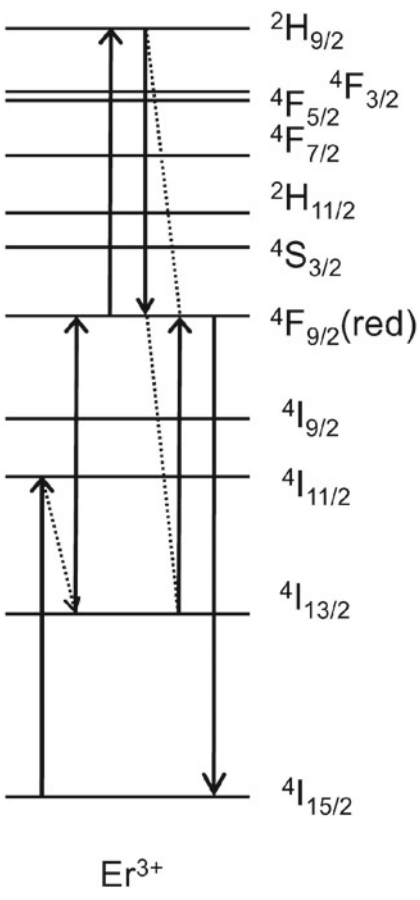


**Fig. 12.5** Energy level diagram of $Er^{3+}$. Reprinted from [50], Copyright 2013, with permission from Trans. Mat. Res. Soc. Japan

Single particle level spectroscopy was investigated with an optical microscopy for bioimaging as future biomedical application [55]. Upconversion nanoparticles on glass slide with excitation of femtosecond laser (wavelength: 793 nm, pulse duration: 100 fs, repetition rate: 80 MHz) were observed by CCD through objective lens. Emission of nanoparticles was detected by this setup. The size of emission observed in the microscope image was larger than that of SEM images. The fluorescent intensities of each particle varied significantly due to the differences of crystallinity, particle size, aggregation size, and surface condition. Next, we measured upconversion spectra of single nanoparticle level by using a pinhole and a spectrometer instead of CCD [55]. The spectra of each emission were measured. Upconversion intensity around 800 nm showed the maximum at 793 nm which was similar to energy level of $^4I_{15/2} \rightarrow {}^4 I_{9/2}$. The reason of variation of upconversion intensity ratio of green emission to red emission would be the same as that of the microscopic image. The ratio was $0.27 \pm 0.12$. Luminescence process with excitation wavelength of 793 nm was investigated by using energy diagram of $Er^{3+}$ ion. The specific surface area is increased by nanoparticle generation and/or disaggregation by laser ablation in liquid. In general, there are many surface defects and the substances, which induce the energy transfer, on the surface. These accelerate non-radiative transition. Red emission is more related to non-radiative transition than green one. Therefore, the ratio of red would be increased in the case of nanoparticles prepared by laser ablation in liquid.

Upconversion nanoparticles are useful for biomedical field. One of the applications is bioimaging to know a lesion such as a tumor for diagnosis and to examine molecular pathways within living organisms [56, 57]. If upconversion nanoparticles are used as a marker for bioimaging, they can be excited by IR light and emit visible light to recognize the position. Especially absorption at near-IR light to a living body is very low, while strong absorption at visible and far-IR regions is due to the existence of hemoglobin and water [40].

Another attractive application of upconversion nanoparticle is cancer therapy. PDT is one of the promissing less invasive treatments. In the case of normal PDT, a photosensitizer such as porphyrin compound accumulated in a cancer cell is irradiated with visible light and then singlet oxygen ($^1O_2$), one of reactive oxygen species (ROS), is generated. The singlet oxygen kills cancer cells. The problem of this method is that a large cancer and a cancer at deep portion from skin surface cannot be cured because of low transparency of visible light to a living body. To solve these problems, upconversion nanoparticles would be used [42, 58–61]. The irradiation with near-IR light to upconversion nanoparticles in a cancer cell emits red light, and it excites photosensitizer to generate singlet oxygen. This process can kill a large cancer and a cancer at deep portion.

Generation of singlet oxygen by upconversion nanoparticles and photosensitizer was examined [62]. Because 1,3-diphenylisobenzofuran (DPBF) is decomposed by singlet oxygen, DPBF can detect singlet oxygen generation. Absorbance of upconversion nanoparticles, photosensitizer, and DPBF in solvent was measured by changing the irradiation time with near-IR light (Fig. 12.6). Absorbance peak of DPBF is observed at 410 nm. Increase in irradiation time decreased absorbance of DPBF.

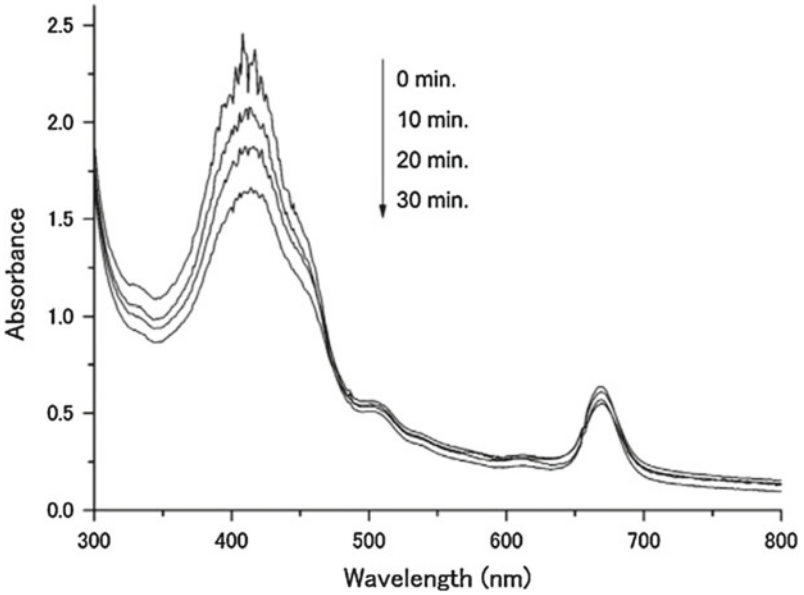


**Fig. 12.6** Absorbance of solution containing upconversion nanoparticles, photosensitizer, and DPBF after irradiation with near-IR light. Reprinted from [62], Copyright 2015, with permission from Elsevier

Control experiments were also performed by measuring time course of normalized absorbance. Data (A) is result of above experiment. Data (B) is the case without upconversion nanoparticle. Data (C) is the case without the irradiation with near-IR light. The slight decrease in control experiments, (B) and (C), was observed, and it would be attributed to the decomposition of DPBF by natural light. The decreasing ratio of (A) is greater than those of (B) and (C). Therefore, singlet oxygen would be generated by the irradiation with near-IR light to upconversion nanoparticles and photosensitizer.

To examine the PDT effect by using upconversion nanoparticles, cytotoxicities of upconversion nanoparticle and photosensitizer to cancer cells were investigated firstly [62]. Cell viabilities as a function of concentrations of these materials were investigated. Cell viability was measured by MTT assay. Under the existence of a living cell, 3-(4,5-dimethylthiazol-2-yl)-2,5-diphenyltetrazolium bromide (MTT) is transformed to formazan, which is purple color. Therefore, absorbance of sample indicates cell viability. When the concentration of upconversion nanoparticles was 1 mg/ml, cancer cells were killed. Cancer cells were also killed at the photosensitizer concentration more than 10 μM. Experimental condition of PDT was decided by these results. Because the number of cancer cells was decreased by the irradiation with near-IR light to upconversion nanoparticles and photosensitizer, PDT effect was confirmed by this experiment.

Surface capping of nanoparticles is important for biomedical application because problems in immune system such as nonspecific adhesion occur. Polyethylene glycol (PEG) is one of biocompatible materials for surface capping [63–65]. Another reason for surface capping is prevention of aggregation of nanoparticles by the steric effect [66]. $Y_2O_3$:Er,Yb nanoparticles were capped with PEG by using silane coupling agent, (3-aminopropyl)triethoxysilane (APTES) [67]. After the nanoparticles were dispersed in 2-propanol, APTES was added to the solution and stirred to obtain APTES-capped nanoparticles, on the surface of which amino groups existed. And then they were dried. After the powder of nanoparticle was dispersed in dimethyl sulfoxide (DMSO), N-Hydroxysuccinimide–PEG (NHS–PEG) with activated ester was added to the solution and then stirred to obtain the PEG capped nanoparticles by amide binding reaction. According to FT-IR spectra of prepared nanoparticles, stretching mode of C–H bonding was observed at 2900 $cm^{-1}$ and asymmetric stretching mode of C–O–C bonding was observed at 1100 $cm^{-1}$. The peaks correspond to the PEG chain. Therefore, nanoparticles would be capped with PEG by APTES as a linker. Turbidity of nanoparticle-dispersed solution as a function of time was measured. Because absorbance is proportional to the concentration of nanoparticles according to the Lambert–Beer law, increase in the concentration increases turbidity. If nanoparticles are aggregated and then precipitated, the solution is clear and the turbidity is decreased. Thus, the stability of nanoparticle-dispersed solution can be examined. The solution of PEG-capped nanoparticles was stable, while the other ones were not stable, showing decrease in turbidity. The stability of nanoparticle-dispersed solution is improved by the electrostatic and steric effects [66]. In this case, the steric effect of the PEG chain would improve the stability.

## 12.3 Afterglow Nanoparticle

Afterglow nanoparticles have the potentiality of promising practical usage [68, 69]. $Sr_2MgSi_2O_7$:Eu,Dy was found as an afterglow material. In the case of afterglow, luminescence is observed after blocking excitation light, while luminescence is not observed after blocking excitation in the case of normal phosphor. Afterglow nanoparticles will be useful in biomedical research field. If we use an afterglow nanoparticle as a marker for bioimaging, autofluorescence problem would be solved [21, 22]. Autofluorescence makes the recognition of fluorescent markers of bioimaging difficult because the fluorescence derived from a living body increases background light in imaging. Afterglow nanoparticle is also useful for security, energy saving, and dark place operation.

Afterglow nanoparticles-dispersed liquid was prepared by above-mentioned laser ablation. Irradiated laser wavelength was 355 nm (Nd:YAG/THG). Target was $Sr_2MgSi_2O_7$:Eu,Dy, which was water-insoluble afterglow material. The pellet of a target was fabricated by spark plasma sintering (SPS) [21].

The effect of liquid on the composition of nanoparticles prepared by laser ablation in liquid was investigated [21]. According to the X-ray diffraction (XRD) patterns

of target and nanoparticles prepared in DI water and ethanol, by-products depended on the sort of liquid. Strontium carbonate was formed as by-product in the case of DI water, while strontium formate was formed as by-product in the case of ethanol. These results indicate chemical reaction between target and the liquid during laser ablation. Relative intensity ratio (RIR) method indicated the by-product in DI water was less than that in ethanol at same energy density.

The energy density of irradiated laser was varied and then the composition, particle size, and optical properties of nanoparticles prepared by laser ablation in liquid were investigated [21]. According to RIR method of XRD pattern of nanoparticles at each energy density, the decrease in energy density reduced the by-products. The secondary particle size measured by DLS as a function of energy density was measured; the decrease in energy density decreased the particle size.

PL spectra of the nanoparticles were almost same as that of target, which was a broad peak at 467 nm [21]. Figure 12.7 shows afterglow properties of nanoparticles prepared at each energy density. The increase in the energy density improved the afterglow properties. In general, nanoparticles have large specific surface area. Defects on the surface increase non-radiative transition and decrease photoluminescence. Therefore, the afterglow properties of the nanoparticles prepared at high energy density, particle size of which was large, would be improved. Surface coating of nanoparticles, which would decrease the surface defects and would increase photoluminescence, was important for the application of nanoparticles.

As mentioned before, surface capping of nanoparticle is important. It improves biocompatibility and dispersibility in solvent due to steric effect. At the same time, optical properties are also improved because defects exist on the surface of material. Defects decrease optical properties as mentioned before. Specific surface area of nanoparticle is larger than that of bulk material. These defects would be passivated by capping material and optical properties are improved. The capping material is classified to organic and inorganic material. Typical organic material is PEG and inorganic material is silicon dioxide.

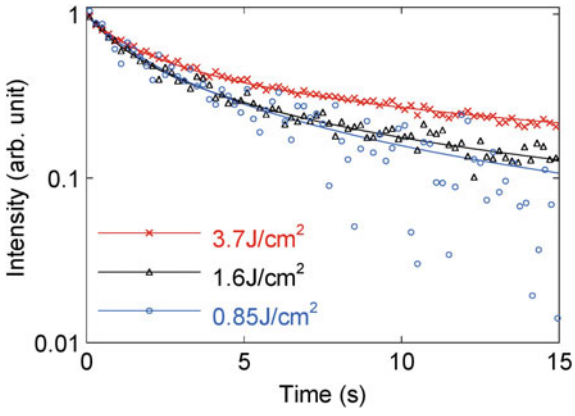


**Fig. 12.7** Afterglow properties of nanoparticles prepared at each energy density. Reprinted from [21], Copyright 2011, with permission from Elsevier

For the capping, PEG was added to solvent for laser ablation in liquid [22]. Physical adsorption would progress PEG capping. According to PL spectra of afterglow nanoparticles with changing concentration of PEG, the shape and peak wavelength of spectra were not changed. This emission would be attributed to $Eu^{2+}$ ion because it is broad peak related to f-d transition [70]. Meanwhile, emission of $Eu^{3+}$ ion is usually sharp around 600 nm related to f-f transition shielded by the outer 5 s and 5p electrons [70]. The shielding makes the peak wavelength of $Eu^{3+}$ ion insensitive [70]. In contrast, the peak wavelength of $Eu^{2+}$ ion is sensitive to the crystal [70]. Because each spectrum of $Eu^{2+}$ ion is almost same, the luminescent center, $Eu^{2+}$, and the host material were not transformed by the addition of PEG. According to quantum yield of the nanoparticles as a function of the PEG concentration, an increase in the PEG concentration increased the quantum yield of photoluminescence. At a high PEG concentration, saturation of luminescent efficiency occurred because photoluminescence would not be increased after the complete passivation of defect. Previously scientists reported that passivation of phosphor by polymers increased PL intensity [71–73].

Decay curves of afterglow luminescence with changing concentration of PEG were measured. Origin of afterglow luminescence is the recombination of the trapped carriers [69, 74–78]. After a trapped hole is excited to the valence band by thermal energy of room temperature, recombination of electron and hole occurs [69]. Afterglow intensity I(t) is given by the following Eqs. (12.2–12.3) [79]:

$$I_{(t)} = \frac{I_0}{(1+\gamma t)^n}, \tag{12.2}$$

$$\gamma = \frac{N}{an_t}, \tag{12.3}$$

where $I_0$ is the initial value, $t$ is time, $N$ is the trap concentration, $a$ is the probability of a trapped carrier's transition to the band, $n_t$ is the number of carriers per unit volume in the trap level, and $n$ is the value approximately 0.5–2. The values of $n$ and $\gamma$ were calculated by the curve fitting of afterglow intensity. Relation between the value of $\gamma$ and the PEG concentration indicated that addition of PEG to solvent significantly decreased the value of $\gamma$. Decrease in $\gamma$ value improves the afterglow luminescence as shown in Eqs. (12.2–12.3). PEG capping would passivate the surface defects and increase the afterglow properties.

## 12.4 Semiconductor Nanoparticle

Semiconductor nanoparticle is called quantum dot. There are many applications for quantum dots due to unique properties related to quantum confinement effect [80, 81]. One of the promising applications is solar cell. The structure of quantum-dot-sensitized solar cell (QDSSCs) is the followings; the space between a transparent

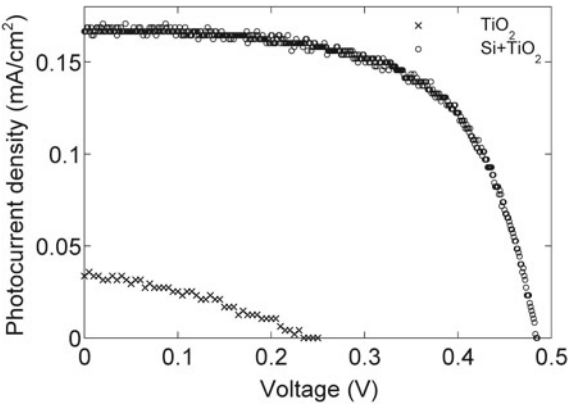


**Fig. 12.8** I–V characteristics of the QDSSCs [86]. Copyright (2014) The Japan Society of Applied Physics

conducting oxide (TCO) electrode, on which $TiO_2$ and Si nanoparticles are placed, and Pt electrode is filled with electrolyte. The advantages of QDSSCs are low cost production and high energy conversion efficiency by multiexciton generation (MEG) [82].

Si nanoparticles were prepared by laser ablation in liquid. Properties of prepared nanoparticles were changed by changing wavelength of laser [83]. According to TEM, decrease in wavelength from 1064 to 532 nm decreased size of prepared nanoparticles from 7 to 3 nm. Same tendency was also observed by Raman spectroscopy. Raman peak position shift is a function of crystal size of silicon [84]. Blue shift was observed in PL spectra because quantum confinement increased the bandgap of silicon. According to absorbance spectrum of the obtained colloidal solution, decrease in wavelength from 1064 to 532 nm increased the amount of prepared nanoparticle because absorbance is proportional to the concentration by Beer–Lambert law.

The particle size of Si nanoparticles (less than 10 nm) was smaller than that of inorganic nanoparticles in Sects. 12.2 and 12.3. It would be attributed to the difference of target of laser ablation in liquid. The target of $Y_2O_3$:Er,Yb, which was a sintered compact, was aggregate of coarse nanoparticle with the particle size of a few hundred nanometer. The irradiation with laser beam to the aggregate partially created the dispersed coarse nanoparticles by shock wave or thermal shock of laser irradiation as I mentioned before. However, the ablation of a single-crystal wafer of Si created the very fine nanoparticle.

According to TEM, size of prepared nanoparticle was not significantly changed with the increase in energy density of laser from 0.17 J/cm$^2$ to 0.45 J/cm$^2$ [85]. According to inductively coupled plasma mass spectrometry (ICP-MS), the increase in energy density proportionally increased the concentration of prepared Si nanoparticles. The increase in energy density also increased it. According to absorbance spectrum, the bandgap of prepared Si nanoparticle was 2.2 eV, which was higher than that of bulk silicon, 1.1 eV, because of quantum confinement.

QDSSC was fabricated by using iodide electrolyte [86]. Figure 12.8 shows the I–V characteristics of the QDSSCs. The energy conversion efficiency of the QDSSCs with

Si nanoparticles and $TiO_2$ was 17 times greater than that of QDSSCs with only $TiO_2$. The short-circuit current density ($J_{SC}$) significantly increased, while open-circuit voltage ($V_{OC}$) and fill factor ($FF$) were approximately constant during operation. The phenomena would be related to the reduction of the series resistance due to the removal of native silicon dioxide layer on the Si nanoparticle through electrochemical reduction and photocorrosion dissolution.

QDSSC was fabricated by using polysulfide electrolyte [87]. In the case of polysulfide electrolyte, $J_{SC}$ was higher than that of iodide electrolyte, although $V_{OC}$ and $FF$ were lower. The comparatively high stability was also obtained because of nonreactivity of polysulfide with Si. QDSSCs with/without Si nanoparticles were investigated by electrical impedance spectroscopy (EIS). The intercept at high frequency region means the series resistance at electrolyte and conducting electrode. The semicircle at high-frequency region means the charge transfer resistance at the interface between counter electrode and electrolyte, while that at low-frequency region means the charge transfer resistance by ions in electrolyte [88–90]. Because the electrolyte and counter electrode in iodide system were the same as those in polysulfide system, the series resistances of both QDSSCs were almost equal. Because the resistances of QDSSC with Si nanoparticles at low and middle frequency were decreased, the current density would be increased.

## 12.5 Organic Nanoparticle

Naphthalocyanine nanoparticle is one of potential organic materials because of absorption at IR light. One of important imaging methods in biomedical field is photoacoustic imaging [91]. If contrast agent is IR-light-absorbing material, inside of a living body can be observed without surgery. Naphthalocyanine nanoparticle is IR-light-absorption material, which is suitable for contrast agent of the photoacoustic imaging.

Naphthalocyanine nanoparticles were prepared by laser ablation in liquid [92]. According to SEM as shown in Fig. 12.9, nanoparticles were prepared by this method from micron-size columnar powder. Increase in energy density of laser from 50 mJ/cm$^2$ to 200 mJ/cm$^2$ decreased the size of nanoparticle from 444 to 285 nm. Same tendency was observed by DLS. According to FT-IR spectroscopy, the increase in energy density of laser increased peaks at 1420 and 1575 cm$^{-1}$, which would be asymmetrical and symmetrical stretching vibration of the carboxylate anion [93–95]. According to absorbance spectra nanoparticles, two peaks were observed at 700 nm and 800 nm. Increase in energy density of laser decreased peak intensity at 800 nm. The Q bands of naphthalocyanine and phthalocyanine are split into two peaks by Davidov splitting [96, 97]. The intensity ratio of the two peaks is changed by the crystal structure change [98–101]. Therefore, crystal structure of the nanoparticles would be changed by laser irradiation.

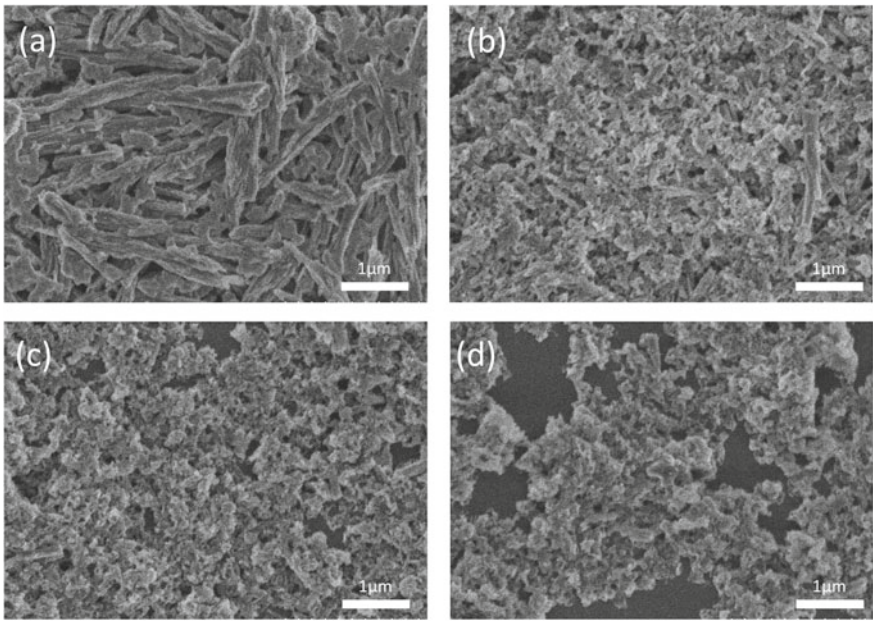


**Fig. 12.9** SEM images of **a** the target and nanoparticles obtained at each fluence: **b** 50, **c** 100, and **d** 200 mJ/cm$^2$ [92]. Copyright (2018) The Japan Society of Applied Physics

Photoacoustic imaging was performed successfully by using by naphthalocyanine nanoparticle as contrast agent, as shown in Fig. 12.10 [92]. Nanosizing increased photoacoustic signal. It would be attributed to increase in the specific surface area.

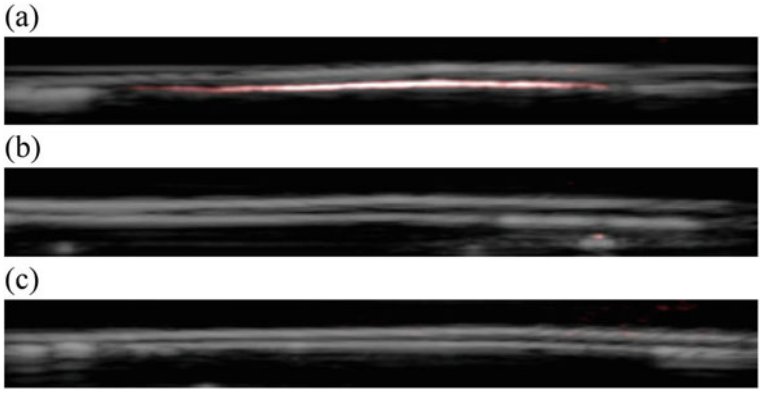


**Fig. 12.10** Photoacoustic image of **a** naphthalocyanine nanoparticle colloidal solution prepared by laser ablation in liquid, **b** suspension of naphthalocyanine before laser ablation in liquid, and **c** DI water [92]. Copyright (2018) The Japan Society of Applied Physics

## 12.6 Summary

Various functional nanoparticles were prepared by laser ablation in liquid and were applied to applications in several research fields. The optical properties of these nanoparticles such as inorganic, organic, and semiconductor materials are useful for biomedical, electrical, and energy fields.

## References

1. H. Wada, Preparation of functional inorganic nanoparticles and their applications. Chem. Chem. Indus. (in Japanese) **68**, 137–139 (2015)
2. J. Neddersen, G. Chumanov, T. Cotton, Laser ablation of metals: A new method for preparing SERS active colloids. Appl. Spectrosc. **47**, 1959–1964 (1993). https://doi.org/10.1366/0003702934066460
3. A. Fojtik, A. Henglein, Laser ablation of films and suspended particles in a solvent: formation of cluster and colloid solutions. Berichte der Bunsen-Gesellschaft **97**, 252–254 (1993)
4. F. Mafune, J.Y. Kohno, Y. Takeda, T. Kondow, H. Sawabe, Structure and stability of silver nanoparticles in aqueous solution produced by laser ablation. J. Phys. Chem. B **104**, 8333–8337 (2000). https://doi.org/10.1021/jp001803b
5. Y. Tamaki, T. Asahi, H. Masuhara, Tailoring nanoparticles of aromatic and dye molecules by excimer laser irradiation. Appl. Surf. Sci. **168**, 85–88 (2000). https://doi.org/10.1016/S0169-4332(00)00596-1
6. G. Compagnini, A.A. Scalisi, O. Puglisi, Ablation of noble metals in liquids: a method to obtain nanoparticles in a thin polymeric film. Phys. Chem. Chem. Phys. **4**, 2787–2791 (2002). https://doi.org/10.1039/B109490D
7. S.I. Dolgaev, A.V. Simakin, V.V. Voronov, G.A. Shafeev, F. Bozon-Verduraz, Nanoparticles produced by laser ablation of solids in liquid environment. Appl. Surf. Sci. **186**, 546–551 (2002). https://doi.org/10.1016/S0169-4332(01)00634-1
8. T. Tsuji, K. Iryo, N. Watanabe, M. Tsuji, Preparation of silver nanoparticles by laser ablation in solution: influence of laser wavelength on particle size. Appl. Surf. Sci. **202**, 80–85 (2002). https://doi.org/10.1016/S0169-4332(02)00936-4
9. C. Liang, Y. Shimizu, T. Sasaki, N. Koshizaki, Synthesis, characterization, and phase stability of ultrafine $TiO_2$ nanoparticles by pulsed laser ablation in liquid media. J. Mater. Res. **19**, 1551–1557 (2004). https://doi.org/10.1557/JMR.2004.0208
10. N.V. Tarasenko, A.V. Butsen, E.A. Nevar, Laser-induced modification of metal nanoparticles formed by laser ablation technique in liquids. Appl. Surf. Sci. **247**, 418–422 (2005). https://doi.org/10.1016/j.apsusc.2005.01.093
11. C. Tabor, W. Qian, M. El-Sayed, Dependence of the treshold energy of femtosecond laser ejection of gold nanoprisms from quartz substrates on the nanoparticle environment. J. Phys. Chem. C **111**, 8934–8941 (2007). https://doi.org/10.1021/jp070282q
12. S. Salmaso, P. Caliceti, V. Amendola, M. Meneghetti, J.P. Magnusson, G. Pasparakis, C. Alexander, Cell up-take control of gold nanoparticles functionalized with a thermoresponsive polymer. J. Mater. Chem. **19**, 1608–1615 (2009). https://doi.org/10.1039/B816603J
13. C.L. Sajti, R. Sattari, B.N. Chichkov, S. Barcikowski, Gram scale synthesis of pure ceramic nanoparticles by laser ablation in liquid. J. Phys. Chem. C **114**, 2421–2427 (2010). https://doi.org/10.1021/jp906960g
14. D. Werner, A. Furube, T. Okamoto, S. Hashimoto, Femtosecond laser-induced size reduction of aqueous gold nanoparticles: In situ and pump−probe spectroscopy investigations revealing coulomb explosion. J. Phys. Chem. C **115**, 8503–8512 (2011). https://doi.org/10.1021/jp112262u

15. J.J. Muray, Photoelectric effect induced by high-intensity laser light beam from quartz and borosilicateglass. Bull. Am. Phys. Soc. **8**, 77 (1963)
16. M. Sugiyama, H. Okazaki, S. Koda, Size and shape transformation of $TiO_2$ nanoparticles by irradiation of 308-nm laser beam. Jpn. J. Appl. Phys. **41**, 4666–4674 (2002). https://doi.org/10.1143/JJAP.41.4666
17. H. Usui, Y. Shimizu, T. Sasaki, N. Koshizaki, Photoluminescence of ZnO nanoparticles prepared by laser ablation in different surfactant solutions. J Phys. Chem. B **109**, 120–124 (2005). https://doi.org/10.1021/jp046747j
18. G.-W. Yang, J.-B. Wang, Q.-X. Liu, Preparation of nano-crystalline diamonds using pulsed laser induced reactive quenching. J. Phys.: Condens. Matter **10**, 7923–7928 (1998). https://doi.org/10.1088/0953-8984/10/35/024
19. P. Liu, C.X. Wang, X.Y. Chen, G.W. Yang, Controllable fabrication and cathodoluminescence performance of high-index facets $GeO_2$ micro- and nanocubes and spindles upon electrical-field-assisted laser ablation in liquid. J. Phys. Chem. C **112**, 13450–13456 (2008). https://doi.org/10.1021/jp802529r
20. A. Abdolvand, S.Z. Khan, Y. Yuan, P.L. Crouse, M.J.J. Schmidt, M. Sharp, Z. Liu, L. Li, Generation of titanium-oxide nanoparticles in liquid using a high-power, high-brightness continuous-wave fiber laser. Appl. Phys. A **91**, 365–368 (2008). https://doi.org/10.1007/s00339-008-4448-8
21. F. Yoshimura, K. Nakamura, F. Wakai, M. Hara, M. Yoshimoto, O. Odawara, H. Wada, Preparation of long-afterglow colloidal solution of $Sr_2MgSi_2O_7:Eu^{2+}$, $D^{y3}+$ by laser ablation in liquid. Appl. Surf. Sci. **257**, 2170–2175 (2011). https://doi.org/10.1016/j.apsusc.2010.09.067
22. F. Yoshimura, M. Ishizaki, F. Wakai, M. Hara, O. Odawara, H. Wada, Optical properties of afterglow nanoparticles $Sr_2MgSi_2O_7:Eu^{2+}$, $D^{y3}+$ Capped with polyethylene glycol. Adv. Opt. Technol. **2012**, 814745 (2012). https://doi.org/10.1155/2012/814745
23. L. Yang, P.W. May, L. Yin, R. Brown, T.B. Scott, Direct growth of highly organized crystalline carbon nitride from liquid-phase pulsed laser ablation. Chem. Mater. **18**, 5058–5064 (2006). https://doi.org/10.1021/cm061485e
24. N. Takada, T. Sasaki, K. Sasaki, Synthesis of crystalline TiN and Si particles by laser ablation in liquid nitrogen. Appl. Phys. A **93**, 833–836 (2008). https://doi.org/10.1007/s00339-008-4748-z
25. A.V. Simakin, V.V. Voronov, N.A. Kirichenko, G.A. Shafeeva, Nanoparticles produced by laser ablation of solids in liquid environment. Proc. SPIE **5121**, 212–221 (2003). https://doi.org/10.1117/12.515574
26. C. Dong, Z. Yan, J. Kokx, D.B. Chrisey, C.Z. Dinu, Antibacterial and surface-enhanced Raman scattering (SERS) activities of AgCl cubes synthesized by pulsed laser ablation in liquid. Appl. Surf. Sci. **258**, 9218–9222 (2012). https://doi.org/10.1016/j.apsusc.2011.07.076
27. S. Kagaya, Y. Ehara, Y. Kitamoto, H. Funakubo, M. Hara, Y. Yamazaki, O. Odawara, H. Wada, Preparation of InP Nanoparticles by Laser Ablation in Liquid. Rev. Laser Eng. (in Japanese) **40**, 117–121 (2012). https://doi.org/10.2184/lsj.40.2_117
28. P. Liu, Y.L. Cao, X.Y. Chen, G.W. Yang, Trapping high-pressure nanophase of Ge upon laser ablation in liquid. Cryst. Growth Des. **9**, 1390–1393 (2009). https://doi.org/10.1021/cg800633j
29. S. Yang, W. Cai, G. Liu, H. Zeng, P. Liu, Optical study of redox behavior of silicon nanoparticles induced by laser ablation in liquid. J. Phys. Chem. C **113**, 6480–6484 (2009). https://doi.org/10.1021/jp810787d
30. W. Soliman, T. Nakano, N. Takada, K. Sasaki, Modification of Rayleigh-Plesset theory for reproducing dynamics of cavitation bubbles in liquid-phase laser ablation. Jpn. J. Appl. Phys. **49**, 116202 (2010). https://doi.org/10.1143/JJAP.49.116202
31. K.V. Anikin, N.N. Melnik, A.V. Simakin, G.A. Shafeev, V.V. Voronov, A.G. Vitukhnovsky, Formation of ZnSe and CdS quantum dots via laser ablation in liquids. Chem. Phys. Lett. **366**, 357–360 (2002). https://doi.org/10.1016/S0009-2614(02)01534-8
32. S. Mhin, J.H. Ryu, K.M. Kim, G.S. Park, H. Ryu, K.B. Shim, T. Sasaki, N. Koshizaki, Simple synthetic route for hydroxyapatite colloidal nanoparticles via a Nd:YAG laser ablation in liquid medium. Appl Phys A **96**, 435–440 (2009). https://doi.org/10.1007/s00339-009-5219-x

33. H. Zeng, W. Cai, Y. Li, J. Hu, P. Liu, Composition/structural evolution and optical properties of ZnO/Zn nanoparticles by laser ablation in liquid media. J. Phys. Chem. B **109**, 18260–18266 (2005). https://doi.org/10.1021/jp052258n
34. P.V. Kazakevich, A.V. Simakin, V.V. Voronov, G.A. Shafeev, D. Starikov, A. Bensaoula, Formation of core-shell nanoparticles by laser ablation of copper and brass in siquids. Solid State Phenom. **106**, 23–26 (2005). https://doi.org/10.4028/www.scientific.net/SSP.106.23
35. H. Zhang, G. Duan, Y. Li, X. Xu, Z. Dai, W. Cai, Leaf-like tungsten oxide nanoplatelets induced by laser ablation in liquid and subsequent aging. Cryst. Growth Des. **12**, 2646–2652 (2012). https://doi.org/10.1021/cg300226r
36. F. Auzel., Upconversion and anti-stokes processes with f and d ions in solids. Chem. Rev. **104**, 139–174 (2004). https://doi.org/10.1021/cr020357g
37. F. Auzel, Compteur quantique par transfert d'énergie entre deux ions de terres rares dans un tungstate mixte et dans un verre. C.R. Acad. Sci. **262**, 1016–1019 (1966)
38. V.V. Ovsyankin, P.P. Feofilov, Cooperative sensitization of luminescnece in crystals acrivated with rare earth ions. Sov. Phys. JETP Lett. **3**, 317–318 (1966)
39. M. Bruchez, M. Moronne, P. Gin, S. Weiss, A.P. Alivisatos, Semiconductor nanocrystals as fluorescent biological labels. Science **281**, 2013–2016 (1998). https://doi.org/10.1126/science.281.5385.2013
40. W.C.W. Chan, S. Nie, Quantum dot bioconjugates for ultrasensitive nonisotopic detection. Science **281**, 2016–2018 (1998). https://doi.org/10.1126/science.281.5385.2016
41. M.S. Patterson, B.C. Wilson, D.R. Wyman, The propagation of optical radiation in tissue. II: Optical properties of tissues and resulting fluence distributions. Lasers Med. Sci. **6**, 379–390 (1991). https://doi.org/10.1007/BF02042460
42. P. Zhang, W. Steelant, M. Kumar, M. Scholfield, Versatile photosensitizers for photodynamic therapy at infrared excitation. J. Am. Chem. Soc. **129**, 4526–4527 (2007). https://doi.org/10.1021/ja0700707
43. Y. Guo, M. Kumar, P. Zhang, Nanoparticle-based photosensitizers under CW infrared excitation. Chem. Mater. **19**, 6071–6072 (2007). https://doi.org/10.1021/cm7028454
44. A. Shalav, B.S. Richards, T. Trupke, K.W. Krämer, H.U. Güdel, Application of $NaYF_4:Er^{3+}$ up-converting phosphors for enhanced near-infrared silicon solar cell response. Appl. Phys. Lett. **86**, 013505 (2005). https://doi.org/10.1063/1.1844592
45. G.H. Dieke, H.M. Crosswhite, The spectra of the doubly and triply ionized rare earths. Appl. Opt. **2**, 675–686 (1963). https://doi.org/10.1364/AO.2.000675
46. A. Schadlich, H. Caysa, T. Mueller, F. Tenambergen, C. Rose, A. Gopferich, J. Kuntsche, K. Mader, Tumor accumulation of NIR fluorescent PEG–PLA nanoparticles: Impact of particle size and human xenograft tumor model. ACS Nano **5**, 8710–8720 (2011). https://doi.org/10.1021/nn2026353
47. M. Ohlson, J. Sorensson, B. Haraldsson, A gel-membrane model of glomerular charge and size selectivity in series. Am. J. Physiol. Renal Physiol. **280**, F396–F405 (2001). https://doi.org/10.1152/ajprenal.2001.280.3.F396
48. Y. Matsumura, H. Maeda, A new concept for macromolecular therapeutics in cancer chemotherapy: Mechanism of tumoritropic accumulation of proteins and the antitumor agent smancs. Cancer Res. **46**, 6387–6392 (1986)
49. T. Nunokawa, Y. Onodera, M. Hara, Y. Kitamoto, O. Odawara, H. Wada, Preparation of $Y_2O_3$:Er, Yb nanoparticles by laser ablation in liquid. Appl. Surf. Sci. **261**, 118–122 (2012). https://doi.org/10.1016/j.apsusc.2012.07.110
50. M. Pollnau, D.R. Gamelin, S.R. Luthi, H.U. Gudel, Power dependence of upconversion luminescence in lanthanide and transition-metal-ion systems. Phys. Rev. B **61**, 3337 (2000). https://doi.org/10.1103/PhysRevB.61.3337
51. Y. Onodera, T. Nunokawa, O. Odawara, H. Wada, Photon-avalanche effect of $Y_2O_3$:Er,Yb nanoparticles prepared by laser ablation in liquid. Trans. Mat. Res. Soc. Jpn **38**, 317–320 (2013). https://doi.org/10.14723/tmrsj.38.317
52. J.S. Chivian, W.E. Case, D.D. Eden, The photon avalanche: A new phenomenon in $Pr^{3+}$-based infrared quantum counters. Appl. Phys. Lett. **35**, 124–125 (1979). https://doi.org/10.1063/1.91044

53. T. Hebert, R. Wannemacher, R.M. Macfarlane, W. Lenth, Blue continuously pumped upconversion lasing in Tm:$YLiF_4$. Appl. Phys. Lett. **60**, 2592–2594 (1992). https://doi.org/10.1063/1.106919
54. M.F. Joubert, S. Guy, B. Jacquier, Model of the photon-avalanche effect. Phys. Rev. B **48**, 10031–10037 (1993). https://doi.org/10.1103/PhysRevB.48.10031
55. S. Guy, M.F. Joubert, B. Jacquier, Photon avalanche and the mean-field approximation. Phys. Rev. B **55**, 8240–8248 (1997). https://doi.org/10.1103/PhysRevB.55.8240
56. T. Nunokawa, Y. Onodera, H. Kobayashi, T. Asahi, O. Odawara, H. Wada, Upconversion luminescence properties of $Y_2O_3$:Er, Yb colloid prepared by laser ablation in liquid. J. Ceram. Processing Res. **14**, s1-4 (2013)
57. M.G. Bawendi, M.L. Steigerwald, L.E. Brus, The quantum mechanics of larger semiconductor clusters ("quantum dots"). Annu. Rev. Phys. Chem. **41**, 477–496 (1990). https://doi.org/10.1146/annurev.pc.41.100190.002401
58. A.P. Alivisatos, Semiconductor clusters, nanocrystals, and quantum dots. Science **271**, 933–937 (1996). https://doi.org/10.1126/science.271.5251.933
59. H.S. Qian, H.C. Guo, P.C.L. Ho, R. Mahendran, Y. Zhang, Mesoporous-silica-coated upconversion fluorescent nanoparticles for photodynamic therapy. Small **5**, 2285–2290 (2009). https://doi.org/10.1002/smll.200900692
60. J.N. Shan, S.J. Budijono, G.H. Hu, N. Yao, Y.B. Kang, Y.G. Ju, R.K. Prud'homme, Pegylated composite nanoparticles containing upconverting phosphors and meso-tetraphenyl porphine (TPP) for photodynamic therapy. Adv. Funct. Mater. **21**, 2488–2495 (2011). https://doi.org/10.1002/adfm.201002516
61. C. Wang, H.Q. Tao, L. Cheng, Z. Liu, Near-infrared light induced in vivo photodynamic therapy of cancer based on upconversion nanoparticles. Biomaterials **32**, 6145–6154 (2011). https://doi.org/10.1016/j.biomaterials.2011.05.007
62. B. Ungun, R.K. Prud'homme, S.J. Budijon, J. Shan, S.F. Lim, Y. Ju, R. Austin, Nanofabricated upconversion nanoparticles for photodynamic therapy. Opt. Express **17**, 80–86 (2009). https://doi.org/10.1364/OE.17.000080
63. T. Ikehata, Y. Onodera, T. Nunokawa, T. Hirano, S. Ogura, T. Kamachi, O. Odawara, H. Wada, Photodynamic therapy using upconversion nanoparticles prepared by laser ablation in liquid. Appl. Surf. Sci. **348**, 54–59 (2015). https://doi.org/10.1016/j.apsusc.2014.12.097
64. K. Uchida, H. Otsuka, M. Kaneko, K. Kataoka, Y. Nagasaki, A reactive poly(ethylene glycol) layer to achieve specific surface plasmon resonance sensing with a high S/N ratio: the substantial role of a short underbrushed PEG layer in minimizing nonspecific adsorption. Anal. Chem. **77**, 1075–1080 (2005). https://doi.org/10.1021/ac0486140
65. J. Blümmel, N. Perschmann, D. Aydin, J. Drinjakovic, T. Surrey, M. Lopez-Garcia, H. Kessler, J.P. Spatz, Protein repellent properties of covalently attached PEG coatings on nanostructured $SiO_2$-based interfaces. Biomaterials **28**, 4739–4747 (2007). https://doi.org/10.1016/j.biomaterials.2007.07.038
66. T. Zako, H. Nagata, N. Terada, M. Sakono, K. Soga, M. Maeda, Improvement of dispersion stability and characterization of upconversion nanophosphors covalently modified with PEG as a fluorescence bioimaging probe. J. Mater. Sci. **43**, 5325–5330 (2008). https://doi.org/10.1007/s10853-008-2776-x
67. G. Gao, Nanostructures and Nanomaterials (Imperial College Press, London, 2004) Chap. 2.
68. H. Kobayashi, K. Fujii, T. Nunokawa, O. Odawara, H. Wada, Surface modification of $Y_2O_3$:Er,Yb upconversion nanoparticles prepared by laser ablation in water. Jpn. J. Appl. Phys. **53**, 05FK04 (2014). https://doi.org/10.7567/JJAP.53.05FK04
69. T. Matsuzawa, Y. Aoki, N. Takeuchi, Y. Murayama, A new long phosphorescent phosphor with high brightness, $SrAl_2O_4$:$Eu^{2+}$, $D^{y3}$+. J. Electrocem. Soc. **143**, 2670–2673 (1996). https://doi.org/10.1149/1.1837067
70. N. Kodama, T. Takahashi, M. Yamaga, Y. Tanii, J. Qiu, K. Hirao, Long-lasting phosphorescence in $Ce^{3+}$-doped $Ca_2Al_2SiO_7$ and $CaYAl_3O_7$ crystals. Appl. Phys. Lett. **75**, 1715–1717 (1999). https://doi.org/10.1063/1.124799

71. T. Kano, Luminescence center of rare-earth ions, in *Phosphor Handbook*, eds. by W. M. Yen, S. Shionoya, H. Yamamoto (Chapyer 3.3, CRC Press, Boca Raton, Fla, USA, 2206)
72. J.I. Pankove, *Optical Processes in Semiconductors* (Dover, New York, NY, USA, 1971)
73. O. I.Mi´ci´c, J. Sprague, Z. Lu, A.J. Nozik, Highly efficient band-edge emission from InP quantum dots. Appl. Phys. Lett. **68**, 3150–3152 (1996). https://doi.org/10.1063/1.115807
74. M. Kuno, J.K. Lee, B.O. Dabbousi, F.V. Mikulec, M.G. Bawendi, The band edge luminescence of surface modified CdSe nanocrystallites: Probing the luminescing state. J. Chem. Phys. **106**, 9869–9882 (1997). https://doi.org/10.1063/1.473875
75. A.A. Setlur, A.M. Srivastava, H.L. Pham, M.E. Hannah, U. Happek, Charge creation, trapping, and long phosphorescence in $Sr_2MgSi_2O_7$:$Eu^{2+}$, $R^{E3}$+. J. Appl. Phys. **103**, 053513 (2008). https://doi.org/10.1063/1.2844473
76. M. Yamaga, Y. Tanii, N. Kodama, T. Takahashi, M. Honda, Mechanism of long-lasting phosphorescence process of $Ce^{3+}$-doped $Ca_2Al_2SiO_7$ melilite crystals. Phys. Rev. B **65**, 235108 (2002). https://doi.org/10.1103/PhysRevB.65.235108
77. T. Kinoshita, M. Yamazaki, H. Kawazoe, H. Hosono, Long lasting phosphorescence and photostimulated luminescence in Tb-ion-activated reduced calcium aluminate glasses. J. Appl. Phys. **86**, 3729–3733 (1999). https://doi.org/10.1063/1.371243
78. J. Qiu, A. Makishima, Ultraviolet-radiation-induced structure and longlasting phosphorescence in $Sn^{2+}$–$Cu^{2+}$ co-doped silicate glass. Sci. Technol. Adv. Mater. **4**, 35–38 (2003). https://doi.org/10.1016/S1468-6996(03)00008-1
79. M. Yamaga, N. Kodama, Fluorescence of $Ce^{3+}$ in fluorides and long-lasting phosphorescence of $Ce^{3+}$ in oxides. J. Alloy. Comp. **408–412**, 706–710 (2006). https://doi.org/10.1016/j.jallcom.2005.01.092
80. E. Nakazawa, Transient characteristics of luminescence, in *Phosphor Handbook*, eds. by W.M. Yen, S. Shionoya, H. Yamamoto, (Chapter 2.7, CRC Press, Boca Raton, Fla, USA, 2006)
81. L. Al, A.L. Efros, Efros, Interband light absorption in semiconductor spheres. Sov. Phys. Semicond. **16**, 772–775 (1982)
82. L.E. Brus, Electron–electron and electron-hole interactions in small semiconductor crystallites: The size dependence of the lowest excited electronic state. J. Chem. Phys. **80**, 4403–4409 (1984). https://doi.org/10.1063/1.447218
83. A.J. Nozik, Quantum dot solar cells. Physica E **14**, 115–120 (2002). https://doi.org/10.1016/S1386-9477(02)00374-0
84. P. Chewchinda, T. Tsuge, H. Funakubo, O. Odawara, H. Wada, Laser wavelength effect on size and morphology of silicon nanoparticles prepared by laser ablation in liquid. Jpn. J. Appl. Phys. **52**, 025001 (2013). https://doi.org/10.7567/JJAP.52.025001
85. R. Intartaglia, K. Bagga, F. Brandi, G. Das, A. Genovese, E. Di Fabrizio, A. Diaspro, Optical properties of femtosecond laser-synthesized silicon nanoparticles in deionized water. J. Phys. Chem. C **115**, 5102–5107 (2011). https://doi.org/10.1021/jp109351t
86. H. Kobayashi, P. Chewchinda, H. Ohtani, O. Odawara, H. Wada, Effects of laser energy density on silicon nanoparticles produced using laser ablation in liquid. J. Phys.: Conf. Series **441**, 012035 (2013). https://doi.org/10.1088/1742-6596/441/1/012035
87. H. Kobayashi, P. Chewchinda, Y. Inoue, H. Funakubo, M. Hara, M. Fujino, O. Odawara, H. Wada, Photovoltaic properties of Si-based quantum-dot-sensitized solar cells prepared using laser plasma in liquid. Jpn. J. Appl. Phys. **53**, 010208 (2014). https://doi.org/10.7567/JJAP.53.010208
88. P. Chewchinda, K. Hayashi, D. Ichida, H. Seo, G. Uchida, M. Shiratani, O. Odawara, H. Wada, Preparation of Si nanoparticles by laser ablation in liquid and their application as photovoltaic material in quantum dot sensitized solar cell. J. Phys.: Conf. Series **518**, 012023 (2014). https://doi.org/10.1088/1742-6596/518/1/012023
89. X.M. Li, Y. Qiu, S.S. Wang, S. Lu, R.I. Gruar, X.H. Zhang, J.A. Darr, T. He, Electrophoretically deposited $TiO_2$ compact layers using aqueous suspension for dye-sensitized solar cells. Phys. Chem. Chem. Phys. **15**, 14729–14735 (2013). https://doi.org/10.1039/C3CP51705E
90. H. Chen, L. Zhu, H. Liu, W. Li, ITO porous film-supported metal sulfide counter electrodes for high-performance quantum-dot-sensitized solar cells. J. Phys. Chem C **117**, 3739–3746 (2013). https://doi.org/10.1021/jp309967w

91. H.W. Seo, Y.T. Wang, G. Uchida, K. Kamataki, N. Itagaki, K. Koga, M. Shiratani, Analysis on the effect of polysulfide electrolyte composition for higher performance of Si quantum dot-sensitized solar cells. Electrochim. Acta **95**, 43–47 (2013). https://doi.org/10.1016/j.electacta.2013.02.026
92. G. Ku, L.V. Wang, Deeply penetrating photoacoustic tomography in biological tissues enhanced with an optical contrast agent. Opt. Lett. **30**, 507–509 (2005). https://doi.org/10.1364/OL.30.000507
93. R. Yanagihara, T. Asahi, Y. Ishibashi, O. Odawara, H. Wada, Fabrication of naphthalocyanine nanoparticles by laser ablation in liquid and application to contrast agents for photoacoustic imaging. Jpn. J. Appl. Phys. **57**, 035001 (2018). https://doi.org/10.7567/JJAP.57.035001
94. C. Tranquilan-Aranilla, N. Nagasawa, A. Bayquen, A.D. Rosa, Synthesis and characterization of carboxymethyl derivatives of kappa-carrageenan. Carbohydr. Polym. **87**, 1810–1816 (2012). https://doi.org/10.1016/j.carbpol.2011.10.009
95. R.A. Mereu, A. Mesaros, T. Petrisor Jr., M. Gabor, M. Popa, L. Ciontea, T. Petrisor, Synthesis, characterization and thermal decomposition study of zinc propionate as a precursor for ZnO nano-powders and thin films. J. Anal. Appl. Pyrolysis **104**, 653–659 (2013). https://doi.org/10.1016/j.jaap.2013.05.001
96. O. Stefanescu, T. Vlase, S. Sorescu, P. Barvinschi, M. Stefanescu, Thermal behavior of Co(II) and Ni(II) hydroxycarboxylate complexes obtained by two original synthesis methods. J. Therm. Anal. Calorimetry **113**, 1345–1354 (2013). https://doi.org/10.1007/s10973-013-2951-4
97. D. Roy, N.M. Das, N. Shakti, P.S. Gupta, Comparative study of optical, structural and electrical properties of zinc phthalocyanine Langmuir-Blodgett thin film on annealing. RSC Adv. **4**, 42514–42522 (2014). https://doi.org/10.1039/C4RA05417B
98. A.A.M. Farag, I.S. Yahia, S. AlFaify, A.A. Al-Ghamdi, Nano-flower 2,3-naphthalocyanine heterojunction for optoelectronic applications. Synth. Met. **203**, 261–268 (2015). https://doi.org/10.1016/j.synthmet.2015.02.040
99. S. Karan, B. Mallik, Effects of annealing on the morphology and optical property of copper (II) phthalocyanine nanostructured thin films. Solid State Commun. **143**, 289–294 (2007). https://doi.org/10.1016/j.ssc.2007.05.043
100. T.V. Basova, I.V. Jushina, A.K. Ray, Influence of post-deposition annealing under magnetic field on the structure of phthalocyanine thin films. J. Mater. Sci.: Mater. Electron. **26**, 4716–4721 (2015). https://doi.org/10.1007/s10854-015-2924-4
101. M. Hosoda, T. Wada, A. Yamada, A.F. Garito, H. Sasabe, Phases and third-order optical nonlinearities in tetravalent metallophthalocyanine thin films. Jpn. J. Appl. Phys. **30**, L1486–L1488 (1991). https://doi.org/10.1143/JJAP.30.L1486
102. A. Zawadzka, P. Płóciennik, J. Strzelecki, M. Pranaitis, S. Dabos-Seignon, B. Sahraoui, Structural and nonlinear optical properties of as-grown and annealed metallophthalocyanine thin films. Thin Solid Films **545**, 429–437 (2013). https://doi.org/10.1016/j.tsf.2013.07.042
103. P. Zhang, W. Steelant, M. Kumar, M. Scholfield, Versatile photosensitizers for photodynamic therapy at infrared excitation, J. Am. Chem. Soc. 129, 4526-4527 (2007). https://doi.org/10.1021/ja0700707

# Part III
# High-Energy Chemistry of Nonmetals

# Chapter 13
# Novel Ingenious and High-Quality Utilization of Microwave High Energy in Chemical Reactions: Heterogeneous Microscopic Heating, Promoted Electron Transfer by Electromagnetic Wave Energy, and Generation of In-Liquid Plasma


**Satoshi Horikoshi and Nick Serpone**

**Abstract** The purpose of this chapter is to introduce the effective use of microwave energy in chemical reactions. When microwave energy is effectively used in chemical reactions, it can be used in the following roles, expected to have effects that cannot be obtained with existing thermal energy: (a) conversion of microwave energy into microscopic distributed thermal energy (microwave heterogeneous microscopic thermal effects: MHMEs), (b) direct use of microwave electromagnetic waves (microwave electromagnetic effects: MEMEs), and (c) conversion of microwave energy into in-liquid plasma energy (microwave-induced in-liquid plasma: MILP). Three concrete examples are discussed to elaborate on the effective use of microwaves in chemical reactions: (i) how to generate hydrogen via a catalytic dehydrogenation reaction of organic hydrides (for MHMEs), (ii) how to enhance a photocatalytic reaction (for MEMEs), and (iii) how to synthesize a gel of considerable interest to Green Chemistry (by the MILP method).

**Keywords** Microwave chemistry · Microwave Heterogeneous Microscopic Thermal Effects (MHMEs) · Microwave Electromagnetic Wave Effects (MEMEs) · $TiO_2$ Photocatalyst · Hydrogen energy · Microwave-Induced In-Liquid Plasma (MILP)

S. Horikoshi (✉)
Faculty of Science and Technology, Department of Materials and Life Sciences, Sophia University, 7–1 Kioicho, Chiyodaku, Tokyo 102–8554, Japan
e-mail: horikosi@sophia.ac.jp

N. Serpone
Visiting Professor, Dipartimento di Chimica, PhotoGreen Laboratory, Università di Pavia, via Taramelli 12, Pavia 27100, Italy
e-mail: nick.serpone@unipv.it



Y. Ishikawa et al. (eds.), *High-Energy Chemistry and Processing in Liquids*,
https://doi.org/10.1007/978-981-16-7798-4_13

## 13.1 Microwaves and Microwave Energy

Before entertaining an explanation of microwave chemistry, it is best and foremost to explain the nature and characteristics of microwaves. So, what are microwaves? Electromagnetic waves? Or for some, some horrible energy source? …… Unmistakably, people have different images and viewpoints of microwaves. Simply stated, microwave radiation represents electromagnetic radiation that spans the frequencies between 30 GHz and 300 MHz; that is, it spans the range of wavelengths from 1 cm to 1 m. Electromagnetic waves in these frequencies are referred to as "radio waves", and even those who are not familiar with "microwaves" they are certainly familiar with "radio waves". These radio waves are used daily: for example, in microwave ovens (frequency, 2.45 GHz) and in wireless LANs communications (frequency, 2.4 GHz). That is, the frequencies used are similar to radio waves.

Though these devices use radio waves of the same frequency, their design concepts are very different. If microwaves were used for communication purposes, they would typically use adjusted waves in terms of phase, amplitude and frequency in order to carry the information. They do not require large microwave output power. On the one hand, what is a device's utility when microwaves are used as a thermal energy source? The heating rate by microwaves depends on the output power, so that development of "high-power microwave sources" and improvement of conversion efficiencies from electricity to microwaves are required. Knowledge of how to prevent leakages of high-power microwaves from an applicator in a given device is also very important. In other words, the "quality" of microwaves as electromagnetic waves is an important aspect whenever they are used in communications. On the other hand, when using microwaves as a thermal/heat energy source, then the "amount" as electromagnetic waves is important.

In the early days, radio waves were used to send electrical energy wirelessly (World Wireless System). This idea was proposed long ago by Nikola Tesla [1]. It was a very good idea, but the capabilities of the equipment at the time were either insufficient or unavailable to make it happen. Today, the idea is being used as a wireless charging technology for smartphones and charging electric toothbrushes. And as the number of electrical vehicles (EV; cars) becomes more widespread, the tests on wireless charging of EV cars are being continued with the power supply buried underground. However, because of the failure of Tesla's experiment, the attempt to use radio waves as an energy source was forgotten by everyone for decades. In other words, Tesla's research has only recently resurfaced as a result of recent developments in wireless power supply systems.

Originally, utilization of microwave energy was accidentally conceived from the interaction of microwaves with chocolate after more than 30 years. This discovery is frequently regarded as an example of serendipity. The first commercial microwave oven was developed in 1952 by the Raytheon Company [2]. Nonetheless, there were reports of microwaves being used to heat food well before this date: for instance, during World War II, it was reported that placing sweet potatoes near

a microwave device during radar development produced cooked/roasted sweet potatoes. A commercial-based microwave device became available only after 1952.

Prior to using microwaves in chemical reactions, attempts were made to use microwaves to sinter ceramics. A study was carried out in the early 1970s on the calcination and sintering of ceramics by microwaves [3], with fundamental and application studies following thereafter around 1980. Perhaps this was a natural way to progress in the utilization of microwaves. The sintering of many ceramics is a process that proceeds under high-temperature conditions exceeding 1000 °C. To the extent that the structure of the electric furnace heats the refractory inside the electric furnace and heats the sample with the radiant heat, only about 20–30% of the input energy is used [4]. Modern electric furnaces with improved heat insulation and energy savings are no big change. In contrast, microwaves can heat ceramics directly that contributes to significant energy savings. The early industrial use of microwaves as a heat source was to remove water from inorganic materials. In this regard, a Symposium held at a Conference on Materials Science in 1989 by the Materials Research Society (MRS) revealed that materials processing by microwaves was a topic that drew a great deal of interest [5]. Basic interactions between the microwaves and materials were also widely discussed. Various kinds of ceramics have since been treated by the microwave method (see, e.g., ref. [6]). In recent years, calcination of special ceramics with a specific microwave method has been reported [7]. This microwave sintering technology has led to the application of microwaves to environmental purification of contaminated ecosystems and to organic syntheses implicating solid catalysts. Several interesting review articles have appeared in the last few years that describe the use of microwave radiation in several processes [8–10].

## 13.2 Microwave Chemistry Rules

When microwaves are directly incorporated into chemical reactions, two types of phenomena {microwave heterogeneous microscopic thermal effects (MHMEs) and microwave electromagnetic effects (MEMEs)} develop depending on the chemicals used. The first is a chemical reaction in which microwave energy interacts with a substance to convert the microwave energy into heat, as occurs in the daily use of domestic microwave ovens. However, in the case of microwave chemistry, as microwaves are electromagnetic waves, their absorption by substances is an important factor that determines heat generation efficiency.

Organic chemical reactions typically involve the breaking and formation of chemical bonds and so need external energy to overcome inherent barriers/obstacles. Generally, microwaves deliver thermal energy to the whole bulk. Delivery of energy by conventional means transfers the energy from heating sources via various media, thereby losing efficiency and inducing side reactions. It has frequently been reported that the use of microwaves shortens reaction times and improves the yield. If one were to carry out microwave chemistry with a small amount of reaction substrate in a solvent, with the latter being a highly absorber of microwaves, then the consequence

**Table 13.1** Relationships between microwave absorption rate for reaction substrates, solvent, and catalyst; and promotion of chemical reactions (especially organic reactions)

| | Promotion of chemical reaction[a] | | | Chemical reactions not promoted | | |
|---|---|---|---|---|---|---|
| Reaction substrate | High abs[b] | Low abs | High abs | High abs | Low abs | Low abs |
| Solvent | Low abs | Low abs | Low abs | High abs | High abs | High abs |
| Catalyst | none | High abs | High abs | none | none | Low abs |

[a]Tendency with some exceptions
[b]When it comes to a certain cluster size in a solvent [11, 12]

would be the generation of heat. In this case, the use of microwaves would be no different than conventional heating using an oil bath, for example, because the heat of the solvent heats the reaction substrates by heat conduction. Accordingly, there would be no advantage in using microwaves.

In contrast, microwave heating is known to be highly efficient through dipole interactions of the microwaves with polar media. For this reason, if a reaction substrate that is a strong absorber of microwaves (e.g., polar or ionic molecules) were placed in a solvent with low microwave absorption (e.g., non-polar solvents) and irradiated with microwaves, only the reaction substrate will generate heat as microwave heterogeneous microscopic thermal effects (MHMEs). Such selective heating can be said to be the original microwave phenomenon. However, the presence of one polar molecule in a non-polar solvent cannot be heated [11], as it would require a cluster of polar molecules [12]. To clarify this MHME phenomenon, it is more important to consider separating the intermolecular distances by means of using different phases, namely solid/liquid, solid/gas, and liquid/gas systems (see Sect. 13.3 for a detailed explanation). If you created such conditions, then you could benefit more on the use of microwaves in chemical reactions. These combinations are organized in Table 13.1. Note that these arrangements show trends, as there are exceptions in every rule. On the other hand, in some catalytic systems driven by energy other than heat (photocatalysts, etc.), the energy from the electromagnetic waves can be quite effective (see Sect. 13.4 for a further explanation).

## 13.3 Microwave Heterogeneous Microscopic-Thermal Effects (MHMEs) in Catalytic Chemistry

When microwave non-absorbing substrates, such as a non-polar solvent or non-polar sample or gas sample, are involved in a catalyzed chemical process, only the solid catalyst is selectively heated. Figure 13.1 illustrates the results of a simulation experiment of the temperature distributions in water and in cyclohexane (a poor microwave absorber) in the presence of an activated carbon (AC) catalyst support (a strong microwave absorber) exposed to microwave radiation [13]. The activated carbon was selectively heated in cyclohexane. However, selective heating of activated

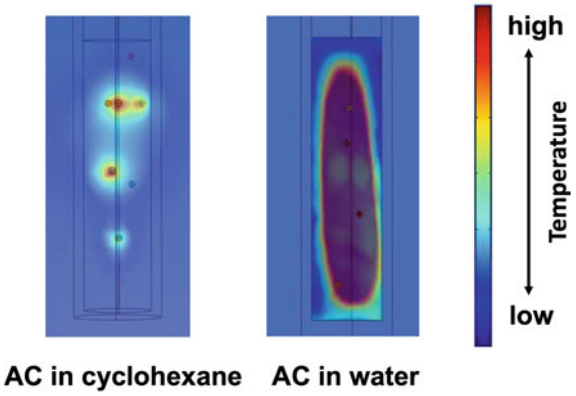


**Fig. 13.1** Simulated temperature distribution in water and cyclohexane solvents in the presence of Pt/activated carbon (AC) catalyst particles subjected to microwave radiation. The simulation was carried out using an RF module and the COMSOL Multiphysics software Version 4.3a. Reproduced with permission from Horikoshi and coworkers [13]. Copyright 2014 by the Royal Society of Chemistry

carbon did not occur in aqueous media as water is a strong microwave absorber. Chemical reactions typically occur at the catalyst particle surface so that when only dispersed catalyst particles are selectively heated by the microwaves, not only does the reaction take place but significant energy conservation can be achieved.

Parenthetically, why is activated carbon heated by microwaves? Books that describe introduces microwave ovens state that microwave heating is derived from the vibration of water molecules. If that is the case, is the heat generated by the activated carbon in Fig. 13.1 affected by the water contained in the activated carbon? The heating of substances by microwaves is based on three types of heating phenomena caused by microwaves: (a) conduction heating, (b) dielectric heating, and (c) magnetic heating [4]. In this regard, the thermal energy $P$ produced per unit volume originating from microwave radiation can be estimated from Eq. 13.1 [14],

$$P = \frac{1}{2}\sigma|E|^2 + \pi f \varepsilon_0 \varepsilon_r''|E|^2 + \pi f \mu_0 \mu_r''|H|^2 \tag{13.1}$$

where $|\boldsymbol{E}|$ and $|\boldsymbol{H}|$ denote the strength of the microwaves' electric and magnetic fields, respectively; $\boldsymbol{\sigma}$ is the electrical conductivity; $\boldsymbol{f}$ is the frequency of the microwaves; $\boldsymbol{\varepsilon_0}$ is the permittivity in vacuum; $\boldsymbol{\varepsilon''}$ is the relative dielectric loss factor; $\boldsymbol{\mu_0}$ is the magnetic permeability in vacuum; and $\boldsymbol{\mu''}$ is the relative magnetic loss factor.

The first term in Eq. 13.1 expresses ***Joule heating*** (conduction heating), the second term denotes ***dielectric heating***, whereas ***magnetic heating*** is given by the third term. Microwave heating of solutions is governed mostly by dielectric heating, whereas conduction heating involves mostly, but not exclusively (see below), solid materials. Generation of heat by magnetic heating is expected only in magnetic (solid)

materials. Consequently, it is instructive to consider each of these forms of heating. For example, when heating a saline aqueous solution with microwaves, Joule heating, and dielectric heating take place at the same time. At this time, it is relevant to note that the rate-determining factor is not the heating of water but the ***Joule heating*** of $Na^+$ and $Cl^-$ ions dissolved in water. In other words, Joule heating is a very effective method of microwave heating.

What can we do then with this selective heat generation? For example, selective heating of microwaves can be used to store and transfer hydrogen energy through chemical reactions. As an example, reaction of 1 mols of hydrogen ($H_2$) with 1/2 mol of oxygen ($O_2$) yields 1 mol of water ($H_2O$) exothermally with a standard Gibbs free energy of 237 kJ $mol^{-1}$ at 298 K (Eq. 13.2).

$$H_2 + 1/2O_2 \rightarrow H_2O \quad \Delta G_0 = -237\,\mathrm{KJ\ mol^{-1}} \tag{13.2}$$

From this point of view, hydrogen has attracted considerable attention as a clean energy source. Additionally, the energy density per weight of hydrogen gas is high (142 MJ $kg^{-1}$) compared with other fuels (e.g., gasoline, 49 MJ $kg^{-1}$), whereas the energy density per volume is rather low (11.9 MJ $m^{-3}$ versus 34.6 MJ $m^{-3}$ for gasoline) [15].

However, hydrogen energy has problems in terms of volume and safety in transportation and storage because hydrogen is a gas at room temperature. Therefore, there has been substantial interest in using organic hydrides as energy carriers, whose volumetric energy density is higher than high-pressure hydrogen, in adition to which these hydrides can be transported rather safely in liquid form under normal operating conditions of temperature and pressure [16–19]. This technology solves the problems of storage and transportation by chemically bonding hydrogen to liquid organic molecules. There is also the advantage that the existing oil infrastructure can be used to transport these hydrides; expectations for its practical application are increasing. For instance, methylcyclohexane (MCH: $C_7H_{14}$) is a hydrogen carrier molecule, and after the necessary hydrogen ($3H_2$) is extracted by a catalytic dehydrogenation reaction, the resulting toluene ($C_7H_8$) can subsequently be re-hydrogenated (recycled) with hydrogen to regenerate MCH. However, the problem with this method is that the removal of hydrogen from the MCH is an endothermic catalytic reaction, which requires palladium (Pd) as a catalyst while being heated to a high temperature. Since the purpose is to obtain hydrogen energy, the energy balance with the thermal energy used for the catalyst is important. In the actual case, as the energy balance is low, considerations are being given to extract the thermal energy required to drive the reaction from the exhaust heat of an incinerator (or the like). Can this problem be solved with selective heating by microwaves? To this question, a dehydrogenation catalytic reaction was carried out using microwave selective heating. Note that MCH and toluene are non-polar liquids, and there is no energy loss (no heat generation) even when irradiated with microwaves. Accordingly, activated carbon particles were used to support the Pd catalyst (Pd/AC) required for the reaction to occur with the microwave absorbing AC generating the necessary heat. When this reaction system

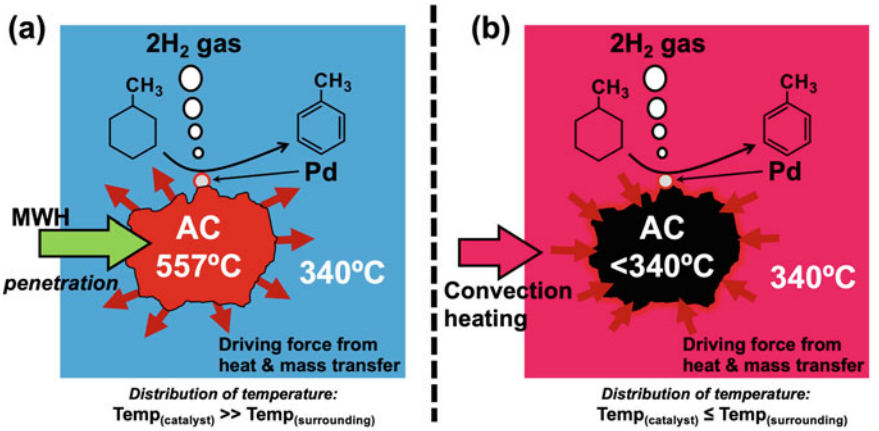


**Fig. 13.2** Model of heat transfer direction: **a** under microwave heating (MWH): $T_{catalyst} > T_{surrounding}$, heat transfers from the catalyst to the surroundings; mass also transfers in the same direction because of the coupling vector, and **b** under classical convection heating (CH): $T_{catalyst} \leq T_{surrounding}$, heat transfers from the surroundings to the catalyst. Reproduced from ref. [20]. Copyright 2016 by Elsevier B.V.

is irradiated with microwaves, only Pd/AC is selectively heated, so hydrogen can be extracted with the minimum energy required for the reaction (Fig. 13.2a) [20].

The microscopic distribution of temperature of the Pd/AC catalyst and the MCH (surrounding) from the simulation is illustrated in the cartoons of Fig. 13.2a. The advantageous effect of microwaves on increasing species transport (Fig. 13.2a, which demonstrates that to bring MCH from ambient temperature to 340 °C necessitates the temperature of the Pd/AC particles to be at 557 °C, resulting in a temperature gradient of 217 °C. On the other hand, the existing heat transfer requires heating the entire system (Fig. 13.2b), which wastes most of the energy, owing to the direction of conventional heating (Fig. 13.2b; for $T_{cat} < T_{surrounding}$) – see Fig. 13.2b. Under microwave irradiation then, the Pd/AC particles are continuously heated by the microwave radiation field, with much of the resulting thermal energy in the catalyst bed being spent to heat methylcyclohexane.

The amount of hydrogen produced was analyzed by immobilizing the Pd/AC catalyst in a flow-type reaction vessel, continuously irradiating it with microwaves, and circulating the MCH organic hydride. MCH and Pd/AC were placed in a test tube, and the effects of microwaves on Pd/AC during the reaction were observed using a high-speed camera (Fig. 13.3a) [22]; based on the emission spectrum, the temperatures reached were 600 °C to 1200 °C. Hydrogen was rapidly generated at the initial stage of microwave irradiation, but decreased sharply when microwave irradiation was continued, which was attributed to the presence of hot spots in the solid catalysts [21]. This microplasma Is a negative characteristic peculiar to microwaves, which causes particle aggregation and deactivation of the nano-sized Pd catalyst (Fig. 13.3b). Accordingly, it was relevant to examine which factors were responsible

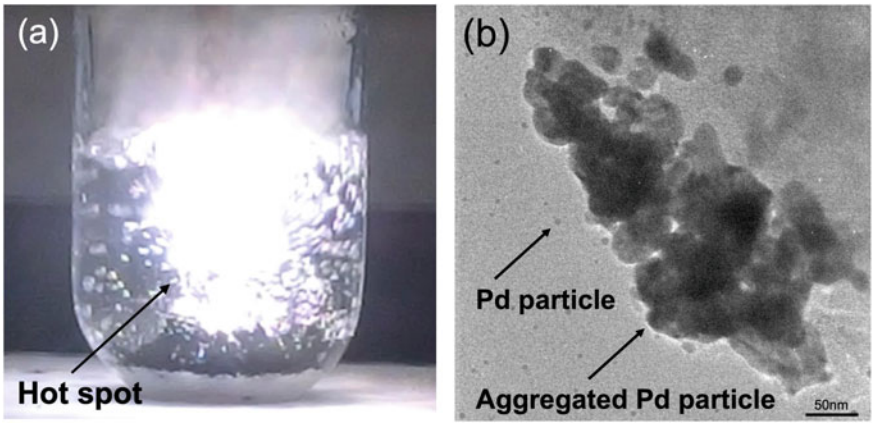


**Fig. 13.3** **a** High-speed-camera photographs of electrical arc discharge occurring on Pd/AC catalyst surface during a reaction in the 25 mm wide tube reactor under microwave irradiation. **b** TEM images of aggregated Pd particles on activated carbon surface after 30 min of microwave irradiation. Reproduced from ref. [22]. Copyright 2014 by American Chemical Society

and to find ways to suppress the generation of hot spots, also a problem peculiar to microwaves.

Consequently, a prototype microwave heating (MWH) device was developed that did not generate hot spots. This permitted the continuous generation of hydrogen with the MCH ⇔ toluene system using the microwave organic hydride method [20]. For comparison, studies were also carried out, under otherwise identical conditions, by a conventional heating method (CH method) using a ceramic heater and a heat insulating material. The rate of hydrogen generation of each method was 95% or more, except that the CH method required 136 W of power consumption for heating, whereas the MWH method could keep it at 15 W. Hence, energy saving by the latter method was nearly tenfold through selective heating. As well, the residual time for heating the catalyst was kept to within 10 s with the MWH method (Fig. 13.4), in addition to which cooling could be performed immediately after termination of microwave irradiation. This suggests that hydrogen generation of hydrogen can be turned ON and OFF as needed, just like tap water.

Interestingly, microwaves can also be used as an energy source for extracting hydrogen energy from water. n this regard, when activated carbon packed in a flow-type reaction vessel was microwave-heated and water was passed through it, hydrogen was generated in yields of 80% [23]. The hydrogen is generated after water encounters the microwave-hot activated carbon causing the gasification reaction to proceed yielding carbon monoxide and hydrogen (syngas; Eq. 13.3). No doubt, water was also involved with carbon monoxide in the water–gas shift reaction (Eq. 13.4 ) to generate additional hydrogen, together with carbon dioxide. Note that generation of carbon monoxide was not detected by gas chromatographic analysis, which suggested that CO was a short-lived transient intermediate.

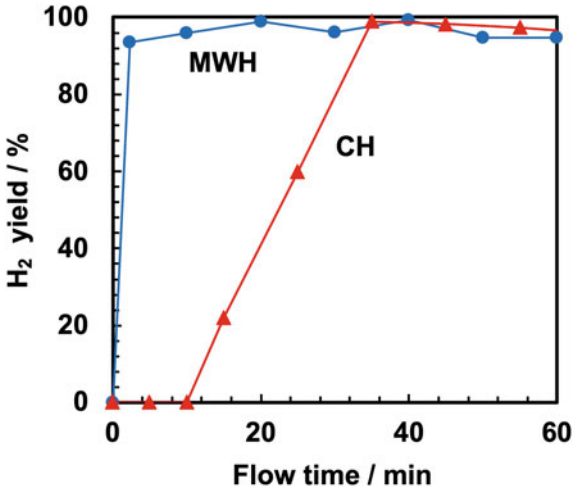


**Fig. 13.4** Hydrogen gas generation yields with a 16-mm quartz flow reactor in the presence of Pd/AC under microwave heating (MWH) and under traditional convection heating (CH)

$$C + H_2O \rightarrow H_2 + CO \tag{13.3}$$

$$CO + H_2O \rightarrow H_2 + CO_2 \tag{13.4}$$

or else (Eq. 13.5):

$$C + 2H_2O \rightarrow 2H_2 + CO_2 \tag{13.5}$$

The temperature of activated carbon can be set to ca. 600 °C even with a weak microwave output power of about 30 W, which allows a process that mimics the steam reforming and water–gas shift processes to occur albeit at lower temperatures. Hydrogen generation by the conventional steam reforming method is not particularly efficient at reaction temperatures around 600 °C, while the microwave method performed efficiently at 600 °C to produce hydrogen in the presence of activated carbon through microscopic local microwave heating of the Pd catalyst on the activated carbon particulate surface.

Further clarification of the advantages of the microwave method (MWH) was obtained using waste activated carbons that had been used in water and sewage treatments [23]. Even with the waste activated carbons, the same amount of hydrogen was generated from pure water. As well, hydrogen was also extracted from contaminated water containing macromolecules and pesticides, as well as from seawater [23]. Even with these problematic waters, more than 80% of hydrogen could be extracted in an energy-saving manner by using selective heating with microwaves.

## 13.4 Microwave Electromagnetic Wave Effects (MEMEs) in Photocatalytic Reactions

Irradiation of the photocatalyst $TiO_2$ with UV light leads to the generation and separation of charge carriers (electrons in the conduction band and holes in the valence band of this semiconductor) such that redox reactions can take place to yield reactive oxygen species such as the $^{\bullet}OH$ radicals via the oxidation of the hydroxyl ($OH^-$) functions on the surface of $TiO_2$ or else from the surface-adsorbed water. This knowledge stems from the hundreds of studies into the fundamentals of semiconductor-based photocatalysis, particularly with the $TiO_2$ photocatalyst, among others, since the early 1980s as part of efforts in environmental detoxification [24]. However, when used for water treatments and with catalyst nanoparticles, it was important to immobilize the particles onto some suitable supports, which makes contact efficiency with the pollutants a serious problem. The reason is that the lifetime of generated $^{\bullet}OH$ radicals is short (e.g., the lifetime of $^{\bullet}OH$ radicals are less than 2.7 μs [25]), and the decomposition of pollutants proceeds on the $TiO_2$ surface. In addition, the rate of degradation of the pollutants is slower vis-à-vis other chemical treatment methods (e.g., ozone oxidation). The $TiO_2$ catalyst works well even with sunlight UV radiation; there are very few cases where this technology has been put into practical use.

A relevant question then is: can microwaves improve/enhance the photocatalytic activity of $TiO_2$, a non-insignificant problem with photocatalysts? The UV light required to drive the photocatalyst (anatase polymorph) is at wavelengths $\leq$ 387 nm (i.e., at energies $\geq$ 3.2 eV). Domestic and industrial microwave ovens generally operate at a frequency of 2.45 GHz, which corresponds to a wavelength of 12.24 cm and a quantum energy of only $1.02 \times 10^{-5}$ eV; that is, microwaves are $10^{-5}$ times weaker than the energy required to drive/activate the photocatalyst. If a contaminated aqueous dispersion of the photocatalyst $TiO_2$ were irradiated with microwaves, the only effect would therefore be an increase of the water temperature without any effect on the photocatalyst. Part of our initiation into microwave chemistry involved the question: What if the dispersion were simultaneously irradiated with microwaves and with UV light? What then?

To answer such a query, our earlier studies [26, 27] explored the photocatalytic degradation of the cationic dye rhodamine-B (Rh-B) in ion-exchanged water in the presence of $TiO_2$—the suspension was irradiated with both UV and microwave radiations (Fig. 13.5). Irradiation with only UV light—the conventional photocatalytic method—brought about but a slight discoloration of the Rh-B aqueous suspension ($TiO_2$/UV). Of course, continued irradiation for longer periods would ultimately lead to a fuller discoloration of Rh-B. In contrast, simultaneous irradiation with both microwaves and UV light ($TiO_2$/UV/MW) led to complete discoloration of the Rh-B suspension and to the decomposition of Rh-B, as evidenced by the red aqueous solution turning completely colorless and transparent; the temperature of the Rh-B aqueous suspension reached 100 °C. Was the role of microwave irradiation only to heat the Rh-B aqueous solution? To examine this query, the Rh-B/$TiO_2$

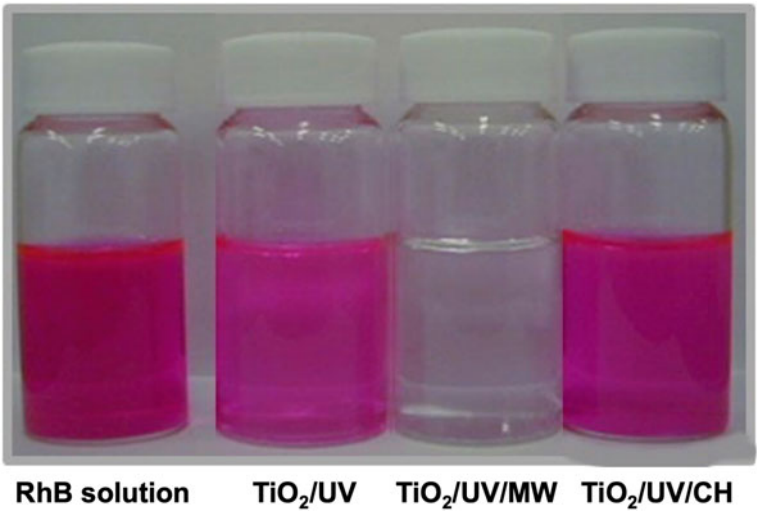


**Fig. 13.5** Visual comparison of color fading in the degradation of RhB solutions (0.05 mM) after being subjected to various degradation methods for 150 min. From left to right: initial RhB solution; photo-assisted degradation ($TiO_2$/UV); integrated microwave-/photo-assisted degradation ($TiO_2$/UV/MW); thermal- and photo-assisted degradation ($TiO_2$/UV/CH). Reproduced from ref. [28]. Copyright 2009 by Elsevier B.V.

aqueous suspension was then subjected to UV radiation at a temperature of 100 °C obtained through conventional heating with a heater ($TiO_2$/UV/CH) under the same conditions as when irradiating with microwaves. Under the latter conditions, there was no accelerating effect on the photocatalytic decomposition of RhB. Obviously, the photocatalytic reaction did not respond to heat, but to microwave energy as an electromagnetic wave.

Why then did irradiation with microwaves at the same time as UV light promote the decomposition of RhB? The amount of $^{\bullet}OH$ radicals (active species) produced by the decomposition of water by $TiO_2$ is a factor that determines the decomposition rate of pollutants using the photocatalyst $TiO_2$. Therefore, generation of $^{\bullet}OH$ radicals during $TiO_2$-photooxidations driven simultaneously by UV light and microwave radiation was probed by electron spin resonance spectroscopy employing a novel setup in which the EPR sample (containing the DMPO spin-trapping agent and $TiO_2$ particles in aqueous media) could be irradiated by both UV light and microwave radiation (UV/MW) [29, 30]. Microwave radiation was produced with a magnetron microwave generator (frequency, 2.45 GHz), a three-stub tuner, a power monitor, and an isolator (Fig. 13.6). The setup was coupled to a monopole antenna with a microwave coaxial cable via a power monitor. The input power of the microwave radiation was about 3 and 16 W incident on the sample solution in the flat cell located in the EPR cavity. The irradiation source was an Ushio 250-W Hg lamp, whose UV light irradiated the sample at an angle to the horizontal plane using a fiber-optic light guide (see Fig. 13.6).

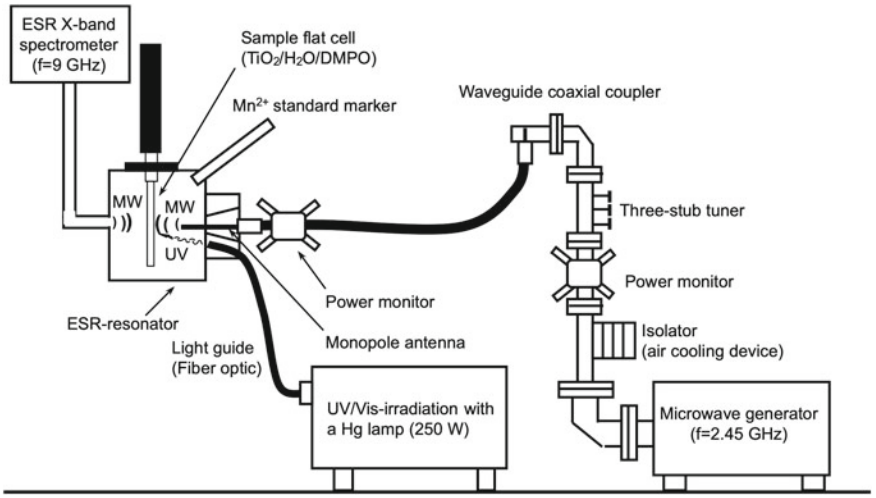


**Fig. 13.6** Setup used to generate •OH radicals in water alone under MW irradiation, in an aqueous $TiO_2$ dispersion by MW irradiation alone, and by the UV and UV/MW methods. Reproduced from ref. [30]. Copyright 2003 by Elsevier B.V.

The number of •OH radicals produced by the UV/MW method was nearly 30% greater than the quantity generated by the UV method alone. A fivefold increase in incident microwave power from 3 to 16 W caused an increase (ca. 40%) in the number of •OH radicals produced. Such an increase was significant enough to increase the efficiency of photooxidation of the organic pollutant in water. Nonetheless, the temperature of the aqueous solution hardly increased even if it were irradiated with 3-W microwaves. In addition, the amount of •OH radicals decreased even when the sample was heated with hot air during the EPR measurement. Evidently, an increase in temperature reduced the lifetime of the •OH radicals. Thus, the role of microwaves (electromagnetic waves) seems to be the effect on the photocatalyst $TiO_2$.

Another question that has been elusive for some time is: what are the microwave electromagnetic effects (MEMEs) in photocatalytic reactions? Most major ceramics such as $TiO_2$, ZnO and $SiO_2$ tend to be rather poor absorbers of microwaves, as observed for $TiO_2$ [31]. On the other hand, if impurities or oxygen vacancies were introduced in $TiO_2$ particles, the microwaves would then be concentrated at those irregular places in the $TiO_2$ crystallites. This phenomenon has been observed by *in-situ* Raman spectroscopy [32, 33]. As a result, $TiO_2$ with imperfect crystals is heated by microwaves. That is, a perfect crystal $TiO_2$ transmits the microwaves, while the problematic crystalline $TiO_2$ converts the microwave energy into thermal energy. Note that these phenomena do not improve the activity of the photocatalyst. What then is the interaction between microwaves and $TiO_2$ that promotes photocatalytic reactions? The MEMEs were related to the degree of lattice distortions in the $TiO_2$ crystallites [34] that depended on the amount of "impurities" in the $TiO_2$ [32] and

on the number of oxygen vacancies [33]. Consequently, the efficiency of electron transfer in photocatalytic reactions will increase by the MEMEs. In our experience, the commercially available photocatalyst $TiO_2$ that responded to microwaves was the Evonik P-25 $TiO_2$ [31] as the crystallites show some oxygen deficiency. In this regard, if a stoichiometric $TiO_2$ system that does not respond to microwaves were reduced to generate the same number of oxygen deficiencies, then it would respond to microwaves as demonstrated earlier by Horikoshi and coworkers [33, 34]. In other words, $TiO_2$ is a microwave- and photo-driven catalyst that responds to the microwaves' electromagnetic fields. It seems that the use of microwave energy in chemical reactions is either the use of heat generated by interaction with molecules or the use of its electromagnetic energy.

## 13.5 Microwave-Induced In-Liquid Plasma (MILP) in Green Gel Synthesis

People routinely use microwave energy in the kitchen to convert it into thermal energy to cook or re-heat foods. On the other hand, we have shown in Sect. 13.4 that microwaves can also be used in the form of electromagnetic waves in photocatalytic reactions without converting the microwave energy into heat. Is there another novel way to use microwave energy? For example, can it be used to generate submerged plasma (i.e., in-liquid plasma) [35]. When you hear someone mention the word plasma, you will likely think of plasma as being generated in the gas phase such as in semiconductor manufacturing and in air purifiers, or more likely as in "blood plasma." However, this submerged plasma can be generated even in liquids, although it requires a conductive aqueous medium, which can severely limit its range of applications. However, plasma can now also be generated in pure water using microwaves as the energy source. Therefore, various applications are now being envisioned in countless chemical reactions within this new high-energy field.

As an example, this section will now describe the synthesis of a gel using microwave-induced in-liquid plasma (MILP) that may be important in Green Chemistry. For instance, dissolving polyvinylpyrrolidone (PVP) in water and subsequently irradiating the transparent aqueous PVP solution (Fig. 13.7b) with in-liquid plasma (Fig. 13.7a) for 5 min yielded a fluffy yellow fine solid in the aqueous medium (Fig. 13.7c). When this aqueous solution was dried and the solid placed in a variety of solvents, from polar to non-polar, it swelled without dissolving in the solvent with the PVP taking on a typical gel structure. Normally, to gel PVP, cross-linking gelation is performed chemically in an organic solvent using an initiator and/or a cross-linking agent. However, if submerged plasma were used, there would be no need for these chemicals nor the organic solvents, as the initiators and cross-linking agents are often highly toxic and the organic solvents my cause formation of volatile organic chemicals (VOCs). Thus, it is possible to gel the polymer using a method favored by green chemistry.

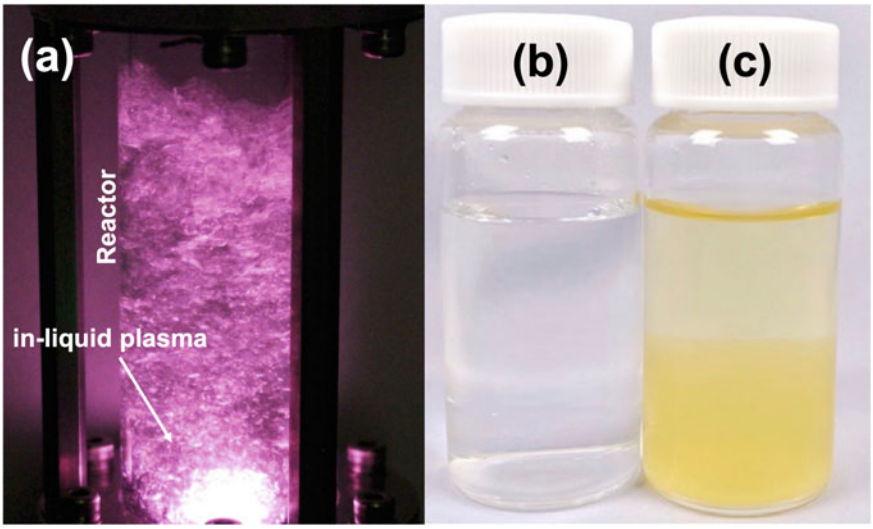


**Fig. 13.7** Photographs of **a** the generated in-liquid plasma in the quartz reactor, poly- vinylpyrrolidone (PVP) in aqueous media **b** initial solution and **c** by the microwave-induced in- liquid-plasma (MILP) method

As well, gelation of water-insoluble polymers, such as silicone, can also be performed with the submerged plasma. Silicone is a hydrophobic liquid, and when mixed in ion-exchanged water, the silicone is present in a separated form (Fig. 13.8a). Irradiation of the latter by the MILP method causes the transparent silicone to turn (Fig. 13.8b) [35]. When the generated silicone gel was added to various kinds of solvents, swelling occurred without dissolving.

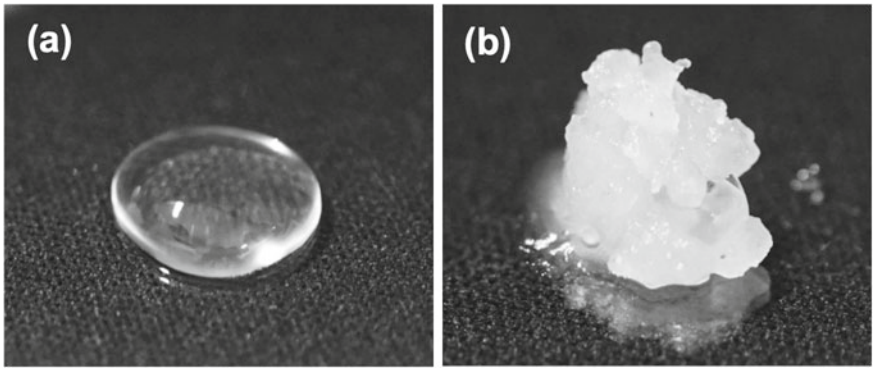


**Fig. 13.8** Photographs of **a** dimethylpolysiloxane (silicone) and **b** a silicone gel produced after a 5 min MILP irradiation period. Reproduced from ref. [35]. Copyright 2021 by the Royal Society of Chemistry

The viscosity of this silicone gel was about 62 times higher than the existing silicone synthesized in an organic solvent using an initiator and/or a cross-linking agent. The molecular chain of the silicone can be sufficiently crosslinked, even when carrying out the gel synthesis with submerged plasma.

## 13.6 Concluding Remarks

This chapter has described three examples of chemical processes that made use of microwaves as a specific thermal energy source, as electromagnetic waves, and their conversion into other energy forms. Although the complete scientific principles of these phenomena have yet to be fully elucidated, microwaves can nonetheless be used as an energy source for new chemical reactions. We heat food daily in the microwave oven, but we seldom consider the details of what happens within the oven. In Japan, there is a saying—"develop new ideas based on studies of the past". Accordingly, if you could envision the outcome of "**familiar energy coupled to chemistry**", then you might be able to create yet undiscovered chemistry.

**Acknowledgements** This article would not have been possible without the fruitful collaboration of many academic and industrial researchers, and not least without the cooperation of many students whose names appear in many of the earlier publications. S.H. is grateful to the Japan Society for the Promotion of Science (JSPS; Grant-in-aid for Scientific Research No. C-25420820) for financial support. A grant from the Sophia University-wide Collaborative Research Fund to S.H is also appreciated. One of us (NS) thanks the staff of the PhotoGreen Laboratory of the University of Pavia (Italy) for their continued hospitality.

## References

1. N. Tesla, The true wireless. Electr. Exp. **61–63**, 28–30 (1919)
2. P.L. Spencer, Method of treating foodstuff, *U.S. Patent* No. 2,495,429, January 24, 1950.
3. K. Shimomura, T. Miyazaki, N. Taniguchi, A. Tutiya, Study of ceramics processing. Ann. Rep. RIKEN, Jpn. **48**, 11–19 (1972)
4. S. Horikoshi, R.F. Schiffmann, J. Fukushima, N. Serpone. (Eds. and Authors), Microwave chemical and materials processing: A tutorial, Springer Japan, 2017.
5. W.H. Sutton, Microwave processing of ceramic materials. Am. Ceram. Soc. Bull. **68**, 376–386 (1989)
6. D.C. Folz, J.H. Booske, D.E. Clark, J.F. Gerling (Eds.) Microwave and radio frequency applications, Proceedings from the third world congress on microwave and rf processing. Am. Ceramic Soc., Westerville, OH, 2003.
7. H. Takizawa, Microwave non-equilibrium chemistry in an inorganic chemistry and material chemistry (in Japanese). Institute Elect. Eng. Jpn. **132**, 17–19 (2012). https://doi.org/10.1541/ieejjournal.132.17
8. R. Luque, A.M. Balu, D.J. MacQuarrie, Microwave-assisted heterogeneously catalyzed processes. in Microwaves in organic synthesis, Hoz A. De la, Loupy A. (Eds.), 3rd Edn., vol. 2, pp. 811–842, Chapter 18, 2012, Wiley-VCH Verlag GmbH & Co. KGaA, Germany.

9. A. Mazubert, M. Poux, J. Aubin, Intensified processes for FAME production from waste cooking oil: A technological review. Chem. Engin. J. **233**, 201–223 (2013). https://doi.org/10.1016/j.cej.2013.07.063
10. L.N. Protasova, M. Bulut, D. Ormerod, A. Buekenhoudt, J. Berton, C.V. Stevens, Latest highlights in liquid-phase reactions for organic synthesis in microreactors. Org. Proc. Res. Dev. **17**, 760–791 (2013). https://doi.org/10.1021/op4000169
11. D. Sakemi, S. Horikoshi, Verification of microwave effects on molecular clusters by using supersonic molecular jets. J. Oleo Sci. 2021 in press.
12. T. Sumi, R. Dillert, S. Horikoshi, Novel microwave thermodynamic model for alcohol with clustering structure in nonpolar solution. J. Phys. Chem. B **119**, 14479–14485 (2015). https://doi.org/10.1021/acs.jpcb.5b06168
13. S. Horikoshi, N. Serpone, Role of microwaves in heterogeneous catalytic systems, Catal. Sci. Technol. **4**, 1197–1210 (2014). https://doi.org/10.1039/C3CY00753G
14. S. Horikoshi, N. Serpone, Microwave frequency effect(s) in organic chemistry. Mini-Rev. Org. Chem. **8**, 299–305 (2011). https://doi.org/10.2174/157019311796197436
15. A. Zuüttel, Hydrogen storage methods. Natur Wissenschaften **91**, 157–172 (2004). https://doi.org/10.1007/s00114-004-0516-x
16. M. Taube, D.W.T. Rippin, D.L. Cresswell, W. Knecht, A system of hydrogen powered vehicles with liquid organic hydrides. Int. J. Hydrogen Energy **8**, 213–225 (1983). https://doi.org/10.1016/0360-3199(83)90067-8
17. J. Gretz, J.P. Baselt, O. Ullmann, H. Wendt, The 100 MW Euro-Quebec hydro-hydrogen pilot project. Int. J. Hydrogen Energy **15**, 419–424 (1990). https://doi.org/10.1016/0360-3199(90)90199-9
18. E. Newson, T.H. Haueter, P. Hottinger, F. Von Roth, G.W.H. Scherer, T.H.H. Schucan, Seasonal storage of hydrogen in stationary systems with liquid organic hydrides. Int. J. Hydrogen Energy **23**, 905–909 (1998). https://doi.org/10.1016/S0360-3199(97)00134-1
19. A. Shukla, S. Karmakar, R.B. Biniwale, Hydrogen delivery through liquid organic hydrides: considerations for a potential technology. Int. J. Hydrogen Energy **37**, 3719–3726 (2012). https://doi.org/10.1016/j.ijhydene.2011.04.107
20. S. Horikoshi, M. Kamata, T. Sumi, N. Serpone, Selective heating of Pd/AC catalyst in heterogeneous systems for the microwave- assisted continuous hydrogen evolution from organic hydrides: Temperature distribution in the fixed-bed reactor. Int. J. Hydrogen Energy **41**, 12029–12037 (2016). https://doi.org/10.1016/j.ijhydene.2016.05.139
21. S. Horikoshia, A. Osawa, S. Sakamoto, N. Serpone, Control of microwave-generated hot spots. Part V. Mechanisms of hot-spot generation and aggregation of catalyst in a microwave-assisted reaction in toluene catalyzed by Pd-loaded AC particulates, Appl. Catal. A **460–461**, 52–60 (2013). https://doi.org/10.1016/j.apcata.2013.04.022
22. S. Horikoshi, M. Kamata, T. Mitani, N. Serpone, Control of microwave-generated hot spots. 6. Generation of hot spots in dispersed catalyst particulates and factors that affect catalyzed organic syntheses in heterogeneous media. Ind. Eng. Chem. Res. **53**, 14941−14947 (2014). https://doi.org/10.1021/ie502169z
23. S. Horikoshi, R. Takahashi, K. Sueishi, H. Tanizawa, N. Serpone, Microwave-induced hydrogen production from wastewaters and seawater with spent activated carbons, RSC Adv. **11**, 31590–31600 (2021). https://doi.org/10.1039/D1RA05977G
24. S. Horikoshi, N. Serpone, Can the photocatalyst $TiO_2$ be incorporated into a wastewater treatment method? Background and prospects. Catal. Today **340**, 334–346 (2020). https://doi.org/10.1016/j.cattod.2018.10.020
25. P. Attri, Y.H. Kim, D.H. Park, J.H. Park, Y.J. Hong, H.S. Uhm, K.-N. Kim, A. Fridman, E.H. Choi, Generation mechanism of hydroxyl radical species and its lifetime prediction during the plasma-initiated ultraviolet (UV) photolysis. Sci. Rep. **5**, 9332 (2015). https://doi.org/10.1038/srep09332
26. S. Horikoshi, H. Hidaka, N. Serpone, Environmental remediation by an integrated microwave/UV illumination method. 1. Microwave-assisted degradation of rhodamine-B dye in aqueous $TiO_2$ dispersions, Environ. Sci. Technol. **36**, 1357–1366 (2002). https://doi.org/10.1021/es030326i

27. S. Horikoshi H. Hidaka, N. Serpone, Environmental remediation by an integrated microwave/UV illumination method. V. Thermal and nonthermal effects of microwave radiation on the photocatalyst and on the photodegradation of rhodamine-B under UV/Vis radiation, Environ. Sci. Technol. **37**, 5813–5822 (2002). https://doi.org/10.1021/es030326i
28. S. Horikoshi, N. Serpone, Photochemistry with microwaves. Catalysts and environmental applications, J. Photochem. Photobiol. C **10**, 96–110 (2009). https://doi.org/10.1016/j.jphotochemrev.2009.06.001
29. S. Horikoshi, F. Sakai, M. Kajitani, M. Abe, A.V. Emeline, N. Serpone, Microwave specific effects in various $TiO_2$ specimens. Dielectric properties and degradation of 4-chlorophenol, J. Phys. Chem. C **113**, 5649–5657 (2009). https://doi.org/10.1021/jp810002z
30. S. Horikoshi, H. Hidaka, N. Serpone, Hydroxyl radicals in microwave photocatalysis. Enhanced formation of •OH radicals probed by ESR techniques in microwave-assisted photocatalysis in aqueous $TiO_2$ dispersions, Chem. Phys. Lett. **376**, 475–480 (2003). https://doi.org/10.1016/S0009-2614(03)01007-8
31. H.M. Kingston, S.J. Haswell, Microwave-Enhanced Chemistry. Fundamentals, Sample Preparation and Applications Edited by American Chemical Society: Washington, D.C. 1997, ISBN 0–8412–3375–6.
32. S. Horikoshi, Y. Minatodani, H. Sakai, M. Abe, N. Serpone, Characteristics of microwaves on second generation nitrogen-doped $TiO_2$ nanoparticles and their effect on photoassisted processes. J. Photochem. Photobiol. A **217**, 191–200 (2011). https://doi.org/10.1016/j.jphotochem.2010.10.008
33. S. Horikoshi, M. Abe, S. Sato, N. Serpone, Effect of microwave radiation on the (Raman) lattice phonons in selected titanium dioxide solid specimens. J. Photochem. Photobiol. A **220**, 94–101 (2011). https://doi.org/10.1016/j.jphotochem.2011.03.025
34. S. Horikoshi, Y. Minatodani, H. Tsutsumi, H. Uchida, M. Abe, N. Serpone, Influence of lattice distortion and oxygen vacancies on the UV-driven/microwave-assisted $TiO_2$ photocatalysis. J. Photochem. Photobiol. A **265**, 20–28 (2013). https://doi.org/10.1016/j.jphotochem.2013.05.010
35. S. Horikoshi, N. Serpone, In-liquid plasma: a novel tool in the fabrication of nanomaterials and in the treatment of wastewaters. RSC Adv. **7**, 47196–47218 (2017). https://doi.org/10.1039/C7RA09600C

# Chapter 14
# Defect Engineering Using the High-Energy Laser-Processing Techniques and Their Application to Photocatalysis


**Yoshinori Murakami**

**Abstract** Laser processing to the photocatalytic powders in water was performed for the $BiVO_4$-based photocatalyst as well as metal oxide photocatalyst. For $BiZn_2VO_6$ and $BiCu_2VO_6$ photocatalysts, photocurrent enhancement was observed after a few hours' irradiations to those photocatalytic powders. The particle size distribution after the irradiation of the focused laser beams was also investigated, and it was suggested that not only the size reduction but also the defect formation on the photocatalytic surfaces played important roles in the enhancement of photocurrents. Defect formation of metal oxide photocatalysts such as $TiO_2$, $SnO_2$, ZnO, and $SrTiO_3$ using the laser-processing techniques was also carried out. It was suggested that active oxygen species formed by the oxidation reaction on the defect sites of black $TiO_2$ photocatalyst might be different from those formed by $TiO_2$ without any laser modification. The amount of OH radicals formed by UV irradiation to the photocatalytic reactions for all of the laser-irradiated defect-rich photocatalytic powers of $SnO_2$, ZnO, and $SrTiO_3$ was also investigated and it was confirmed that the amount of OH radicals were increased by the laser processing and defect formation to these photocatalytic powders.

**Keywords** Laser processing · Photocatalysis · Defect formation · Photocurrent · OH radicals

## 14.1 Introduction

Since the pioneering work of Honda and Fujishima on the photo-induced splitting of water into hydrogen and oxygen by the irradiation of $TiO_2$ with UV light in water [1], numerous works have been carried out in the fields of semiconductor photoelectrochemistry and photocatalysis from fundamental research to their applications. The

Y. Murakami (✉)
National Institute of Technology, Nagaoka College, 888 Nishikatakai, Nagaoka 940-8532, Niigata, Japan
e-mail: murakami_mb@nagaoka-ct.ac.jp



Y. Ishikawa et al. (eds.), *High-Energy Chemistry and Processing in Liquids*,
https://doi.org/10.1007/978-981-16-7798-4_14

use of photocatalysis not only for solar energy conversion but also for the degradation of harmful organic contaminants is also an intriguing concept. However, $TiO_2$ is a high bandgap material that can only be excited by high-energy UV radiation with a wavelength of no longer than 380 nm. This practically rules out the use of sunlight as an energy source. Therefore, attempts to extend the absorption range of the photocatalyst have been performed using bulk or surface modification using metal ion implantation [2] and anion doping such as nitrogen [3], sulfur [4], and carbon [5] to the semiconductor photocatalyst. Recently, the effects of the surface oxygen vacancies of photocatalyst, especially of $TiO_2$, on the photocatalytic activities have been extensively investigated by several researchers, and successful fabrication of the visible-light responsive photocatalysts by the bandgap narrowing was reported by several researchers [6, 7].

In addition to those techniques mentioned above, modification of materials using the process under extreme conditions created by the focused laser beams is also another candidate to improve the chemical and physical properties of materials. Although laser annealing techniques are now commonly used for the melting and explosive crystallization of the metal [8] or semiconductor materials [9], very few works have been done for the modification of the photocatalytic materials probably due to the expected negative effects of the generation of defect sites which act as the recombination centers, which will also promote the charge recombination of the photogenerated holes and electrons. In our previous work [10], it was observed by the pulsed laser irradiation to aerosol metal nanoparticles that were irradiated by the pulsed 1064-nm laser beams were initiated with the absorption of the photon energy, followed by the evaporation of metal and heat release to the surrounding medium, which was unique to the pulsed laser heating techniques. Laser fragmentation or size reduction of metal nanoparticles by the pulsed laser irradiation to the solid metal in the solution was also observed by several authors [11, 12]. It would be expected that new phenomena would be expected by the pulsed laser irradiation to the photocatalytic materials. In this chapter, our previous investigations about the effects of the pulsed laser irradiation to the photocatalytic materials on the photocatalytic activities such as photocurrent and degradation mechanism were summarized.

## 14.2 Experimental Methods

Similar to the laser ablation of metals [13] or organic crystals [14] in solution, which was extensively investigated by many researchers, focused laser beams were irradiated to the suspension of the photocatalytic powders from the top for up to several hours. The focus of the lens was 150 mm, and the typical laser fluence of the laser was 200 mJ/pulse. 2nd (532 nm) or 3rd (355 nm) harmonic of the Nd: YAG laser with the repetition rate of 10 Hz was used for the laser ablation of photocatalysis. To avoid the precipitation at the bottom of the cell, the suspension of the photocatalytic powers was continuously stirred by the magnetic stirrer until the termination of the irradiation of the focused laser beam. A typical example of the experimental

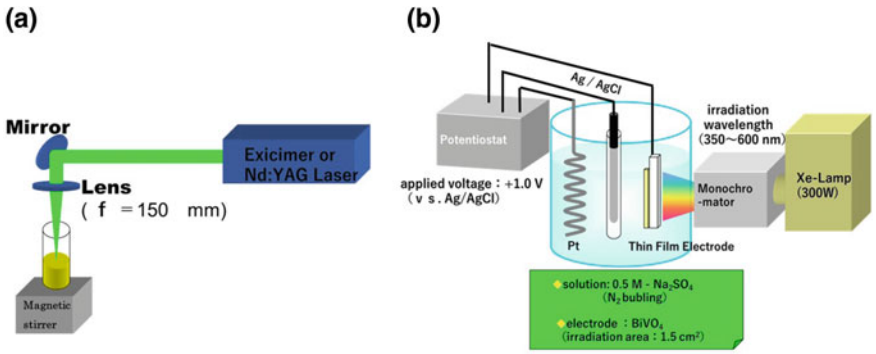


**Fig. 14.1** **a** Schematic figure of the experimental setup of the laser ablation for the water-splitting photocatalysis. **b** Schematic figure of the photocurrent measurements

setups for the laser ablation system was shown in Fig. 14.1a. After the few hours' focused laser beam irradiation to the suspension of the photocatalytic powders, the laser-ablated suspensions were pasted to the glass plate coated with F-doped $SnO_2$ (FTO) films repeatedly for six times and heated at 450 °C for 30 min. The surfactants (Kao, POIX532A) were added to the colloidal solution of the laser-ablated photocatalytic suspensions. Typical experimental setups for the photocurrent measurements were shown in Fig. 14.1b. Pt plate was employed as a counter electrode, and an Ag/AgCl/sat KCl was used as a reference electrode. The photocurrent of this laser-ablated photocatalysis was measured at the applied voltage of +1.0 V (vs. Ag/AgCl) as a function of the wavelength of the 300 W Xe lamp, which was equipped with a single monochromator. The 0.5 M $Na_2SO_4$ solution was used as an electrolyte solution and removed oxygen by bubbling with $N_2$ gas in advance.

Recently, several researchers [15, 16] reported that oxygen vacancies could be easily introduced to the $TiO_2$ photocatalyst by the unfocused UV laser beam to the suspension containing the $TiO_2$ photocatalytic powders in water. Our group also attempted the experiment on the laser-induced formation of the oxygen vacancies of several photocatalytic powders in similar techniques. In such experiments, the laser beam was directly irradiated to the suspension of the photocatalytic powders in the quartz cell without any focusing lens in the course of the laser light beam as shown in Fig. 14.2. Then the laser-irradiated photocatalytic powders were centrifuged and dried in vacuum or air for several hours and then used for the photocatalytic activity tests.

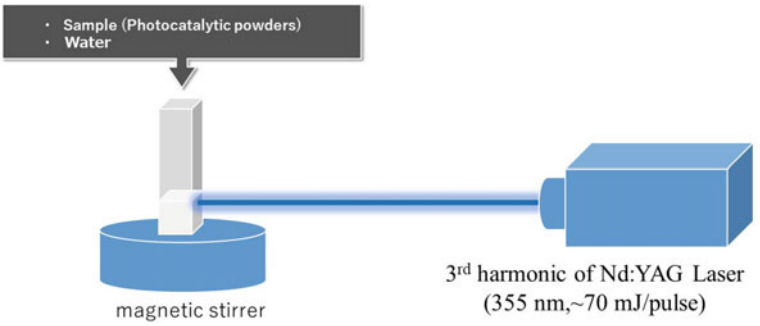


**Fig. 14.2** Schematic figure of the experimental setup of the laser ablation for the water-splitting photocatalysis

## 14.3 Laser Ablation to the Water-Splitting Photocatalysts and Photocurrent Measurements

As was previously reported in [17], $BiVO_4$, which was well known as the highly efficient water-splitting photocatalyst that was able to evolve oxygen, was used as a target material for the laser ablation. Here, our group synthesized another water-splitting photocatalyst of $BiZn_2VO_6$ and $BiCu_2VO_6$ and investigated the effects of the photocurrent efficiencies on the irradiation of the focused laser beams. Figure 14.3 was the XRD pattern and the absorption spectra of $BiZn_2VO_6$ photocatalysts synthesized in our laboratory. By comparing the XRD patterns and UV–VIS absorption spectra of the $BiZn_2VO_6$ photocatalysts reported by Liu et al. [18], it was confirmed that $BiZn_2VO_6$ photocatalysts were properly synthesized in our laboratory. As shown in Fig. 14.3, $BiZn_2VO_6$ photocatalysts absorbed below 550 nm, attempts to irradiate to the $BiZn_2VO_6$ photocatalytic powders with two different wavelengths of 355 nm and 532 nm using the third and second harmonic of Nd:YAG laser, respectively.

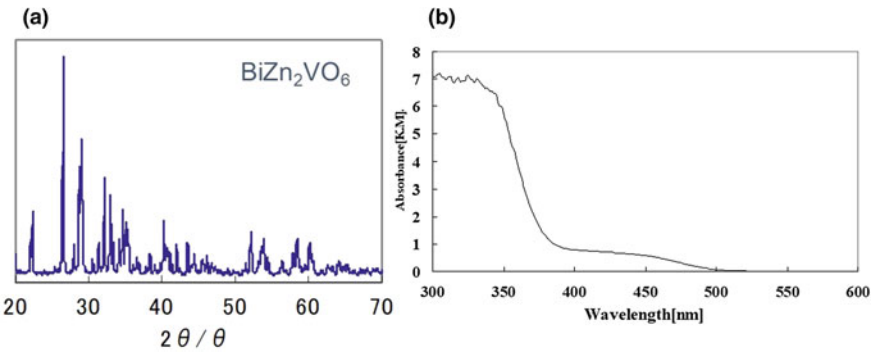


**Fig. 14.3** **a** XRD patterns of $BiZn_2VO_6$ photocatalytic powders. **b** Diffuse reflectance spectra of $BiZn_2VO_6$

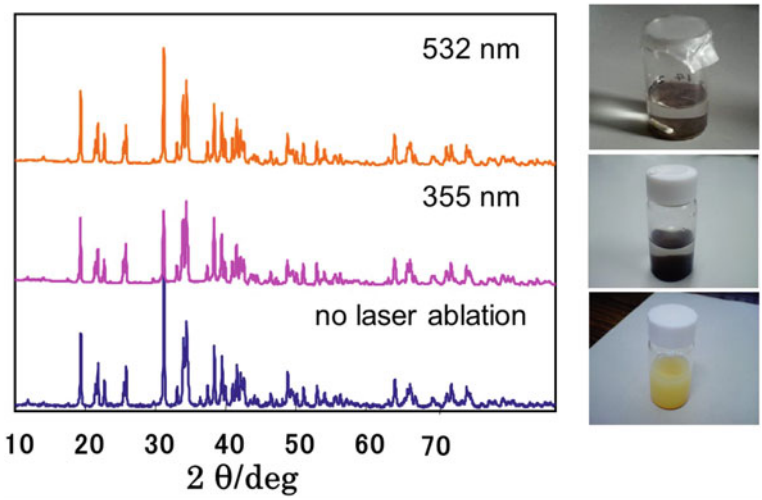


**Fig. 14.4** XRD patterns (left) and photos of the susupension (right) of $BiZn_2VO_6$ photocatalytic powders for **a** 532-nm laser irradiation, **b** 355-nm laser irradiation, and **c** no laser irradiation. The time for the laser irradiation was 1 h

The results were shown in Fig. 14.4. Suspension of the $BiZn_2VO_6$ photocatalytic powders was yellowish similarly to that of $BiVO_4$ photocatalytic powders, but when the focused laser light of 532 or 355 nm was irradiated to the $BiZn_2VO_6$ photocatalytic powders the color of the suspension was changed from yellow to dark gray, and the suspension was precipitated to the bottom of the container, which indicated the electrostatic repulsions between the $BiZn_2VO_6$ photocatalytic powders became weaker due to the focused laser irradiation, regardless of the wavelength of the laser lights. For the focused laser beam irradiation to $BiVO_4$ photocatalytic powders previously reported in [17], the color of the suspension became from yellow to green, which was resembled the results of $BiZn_2VO_6$ photocatalysis that the color was changed from yellow to dark gray. However, although $BiVO_4$ photocatalytic powders were suspended even after the focused laser beam irradiation of 532 nm laser light for few hours, precipitation to the bottom of the container was observed in the case of the laser ablation to the suspension of the $BiZn_2VO_6$ photocatalytic powders. The XRD patterns of $BiZn_2VO_6$ photocatalytic powders before and after the laser irradiation processed were investigated but no distinct differences were observed between the $BiZn_2VO_6$ photocatalytic powders and those after a few hours' irradiations of the focused 355-nm or 532-nm laser lights. Since laser fragmentation of metal nanoparticles by irradiation of the focused laser light has already been reported by several researchers [11, 12, 19], fragmentation of $BiZn_2VO_6$ by the laser ablation was expected. To investigate whether the laser fragmentation occurred for the laser ablation process to the $BiZn_2VO_6$ photocatalytic powders, measurement of particle size distribution using the laser diffraction and optical scattering particle size analyzer. The results are given in Fig. 14.5. Change for the particle diameter distribution of the

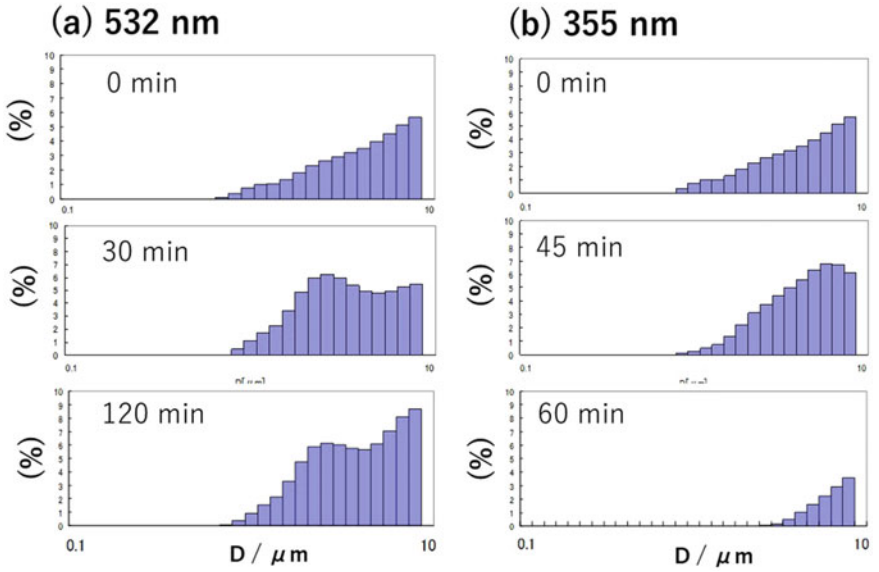


**Fig. 14.5** Time evolution of particle diameter distributions of $BiZn_2VO_6$ photocatalytic powders for **a** 532-nm laser irradiation, **b** 355-nm laser irradiation measured by the laser diffraction and scattering analyzer

$BiZn_2VO_6$ photocatalytic powders by the 355-nm laser ablation was larger than that of 532-laser irradiation, which was consistent with the fact that the absorbance of $BiZn_2VO_6$ at 355 nm was larger than that at 532 nm as was illustrated in the absorption spectra of Fig. 14.3. Finally, the photocurrent measurements of the $BiZn_2VO_6$ photocatalytic powders with and without the focused laser beam irradiation were investigated. The result was given in Fig. 14.6. As shown in Fig. 14.6, photocurrent efficiency was increased by the focused laser beam irradiation to $BiZn_2VO_6$ photocatalytic powders irrelevant to the wavelength of the laser light between 400 and 500 nm. It is an interesting point that the photocurrent efficiency of 532-nm laser irradiation was slightly larger than that of 355-nm laser irradiation, although the particle diameter distribution of the $BiZn_2VO_6$ photocatalytic powders by the 532-nm laser ablation was smaller than that by the 355-nm laser ablation process. Furthermore, the photocurrent efficiency of the $BiZn_2VO_6$ photocatalytic powders by the 532-nm laser ablation showed a small peak around 470 nm. The reason for such a small shoulder was not clear, but it was not due to the increase of absorbance and not due to the size reduction of the $BiZn_2VO_6$ photocatalytic powders by the 532-nm laser irradiation. Thus, it was suggested that not only the size reduction but also the defect sites on the $BiZn_2VO_6$ photocatalytic surfaces played key roles in such enhancement of the photocurrent efficiencies.

To further confirm that effects, $BiCu_2VO_6$ photocatalytic powders were also synthesized and investigated the effects of the photocurrent efficiencies on the focused laser beam irradiation to the $BiCu_2VO_6$ photocatalytic powders. The

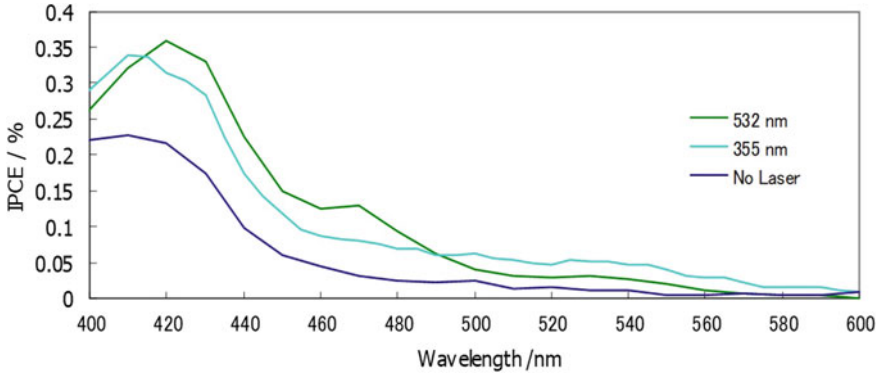


**Fig. 14.6** Photocurrent efficiency versus wavelength of $BiZn_2VO_6$ photocatalytic powders for 532-nm laser irradiation (green), 355-nm laser irradiation (blue), and no laser irradiation (purple). The laser was irradiated for 1 h

synthesis of $BiCu_2VO_6$ photocatalysis was carried out using the synthetic procedure previously reported by Liu et al. [20]. Using the same procedure for preparing the $BiZn_2VO_6$ photocatalytic electrode with and without focused laser beam irradiation, the thin-film electrode of $BiCu_2VO_6$ photocatalytic powders was prepared and these photocurrent efficiencies were measured. In this study, 532 nm laser was used, and it was also confirmed that the particle size of $BiCu_2VO_6$ photocatalytic powders was nearly the same particle size distribution as those before the 532-nm focused laser irradiation from the laser diffraction and scattering particle size analyzer, which was consistent with the fact that $BiCu_2VO_6$ photocatalysis has very small absorbance at 532 nm, which resembled the case of $BiZn_2VO_6$ photocatalysis. Figure 14.7 is the results of the photocurrent efficiencies of the $BiCu_2VO_6$ photocatalytic thin-film electrodes. Photocurrent efficiencies of the $BiCu_2VO_6$ thin-film electrode were

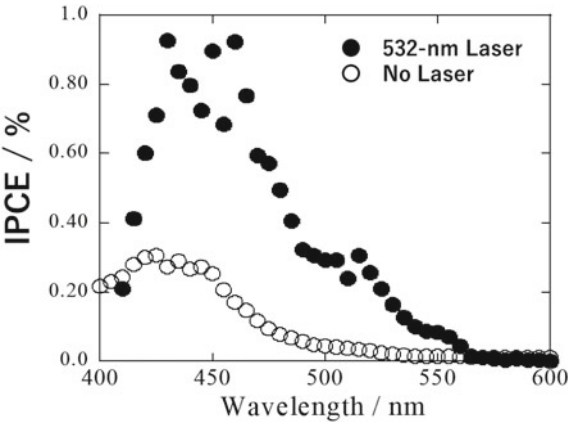


**Fig. 14.7** Photocurrent efficiency versus wavelength of $BiCu_2VO_6$ photocatalytic powders for 532-nm laser irradiation (closed circle) and no laser irradiation (open circle). The laser was irradiated for 30 min

increased when the $BiCu_2VO_6$ photocatalytic powders were irradiated by the 532-nm laser light with a focused lens in advance. Analogous to the experimental results of the $BiZn_2VO_6$ photocatalysis, it was suggested that not only the particle size but the defect sites on the $BiCu_2VO_6$ photocatalytic surfaces played key roles in such enhancement of the photocurrent efficiencies.

## 14.4 Preparation of Black $TiO_2$ Using the Laser Ablation Techniques and the Photocatalytic Activity

Black $TiO_2$ is now extensively investigated by numerous researchers because black $TiO_2$ has also very high visible light absorption and can be easily fabricated by the reduction reaction such as hydrogen thermal treatment and chemical reduction method. Black $TiO_2$ is defined as defective crystals, and therefore, experimental and theoretical studies on the roles of such defective sites in photocatalytic activities were also intrigued by a lot of researchers so far. Recently, Song et al. [21] reported that black $TiO_2$ showed efficient solar-driven water-splitting reactions and they speculated that the reason for the increase of the hydrogen evolution in black $TiO_2$ was the existence of oxygen vacancies in black $TiO_2$ nanostructures, which could increase the donor density and effectively promote the separation and transportation of photogenerated electron−hole pairs. Thus, attempts to generate visible-light responsive high-efficient photocatalysts with oxygen vacancies using high-energetic techniques such as plasma and laser were also performed by several researchers. For example, Chen et al. [22] reported that black $TiO_2$ prepared 355-mn laser irradiation to the $TiO_2$ suspended solution. They have also reported that the particle size became smaller and enhancement of photocatalytic degradation of Rhodamine B with green LED (533 nm). Zuniga-Ibarra et al. [23] prepared black $TiO_2$ using the 532-nm laser light and characterized these black $TiO_2$ using various analytical techniques. Thus, our group also attempted to fabricate black $TiO_2$ using the 355-nm laser irradiation to the suspension of $TiO_2$ photocatalytic powders. Anatase form of $TiO_2$ powders was purchased from Kanto Chemicals and used as received. 355-nm laser irradiation for 2 h made the color of $TiO_2$ black as was previously reported by Chen et al. [22]. Figure 14.8a was the diffuse reflectance spectra of $TiO_2$ and black $TiO_2$ prepared by the 355-nm laser irradiation. It was confirmed that laser irradiation to the $TiO_2$ photocatalytic powders changes the color of $TiO_2$ from white to black, suggesting that oxygen vacancies of $TiO_2$ were generated by the unfocused 355-nm laser light. The crystal phase of $TiO_2$ after the 355-nm laser irradiation was investigated by measuring the XRD patterns before and after the laser irradiation. The results are given in Fig. 14.8b. $TiO_2$ photocatalysts are known to have three crystal phases of anatase, rutile, and brookite [24]. As shown in Fig. 14.8b, it was observed that XRD peaks of anatase $TiO_2$ decreased and those of rutile $TiO_2$ increased, suggesting that anatase $TiO_2$ was changed to rutile $TiO_2$ by the 355-nm laser irradiation. High-temperature anatase–rutile transformation of $TiO_2$ photocatalyst is a well-known

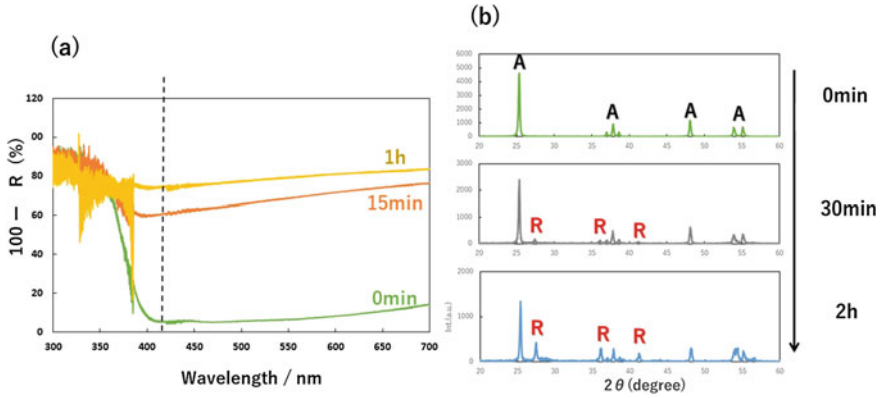


**Fig. 14.8** **a** Diffuse reflectance spectra of $TiO_2$ with 355-nm laser irradiation from 0 min to 1 h. **b** XRD patterns of $TiO_2$ with 355-nm laser irradiation from 0 min to 2 h. The designation of "A" and "R" indicate the anatase and rutile phase, respectively

phenomenon, and there are several reviews on this phase transition of $TiO_2$ [25]. The present anatase to rutile transformation was due to the photothermal conversion and the temperature jump of $TiO_2$ particles irradiated by the 355-nm laser light. Finally, the photocatalytic activities were investigated for the present black $TiO_2$ prepared by 355-nm laser irradiation in water. To investigate the photocatalytic activities of black $TiO_2$, the amount of OH radicals formed by the 355-nm laser-irradiated $TiO_2$ (namely, Black $TiO_2$) were investigated using the coumarin fluorescence probe techniques since OH radicals were known as the key species in the photocatalytic reactions. This coumarin probe method is now accepted as one of the standard methods used as the probe of OH radicals formed in various environments [26, 27]. Since coumarin is easily oxidized by OH radicals to form 7-hydroxycoumarin by the following reaction scheme

$$\text{Coumarin} + \text{OH} \rightarrow \text{7-hydroxycoumarin} \tag{14.1}$$

and 7-hydroxycoumarin is much more fluorescent than coumarin, the amount of OH radicals can be easily monitored via the fluorescence of 7-hydroxycoumarin around 450 nm formed by the reaction (1) in a coumarin solution. As you can see in Fig. 14.9a, OH radical formation by the UV-irradiated $TiO_2$ or black $TiO_2$ made by the 355-nm laser irradiation showed the formation of 7-hydroxycoumarin around 450 nm with nearly the same tendency. On the other hand, black $TiO_2$ photocatalyst with visible light excitation gave another fluorescence peak around 530 nm, which was not observed in $TiO_2$ without any laser modification (see Fig. 14.9b). Defects in $TiO_2$ narrow the bandgap as shown in Fig. 14.10, but active oxygen species formed from the defect sites might be different from those formed by $TiO_2$ without any laser modification.

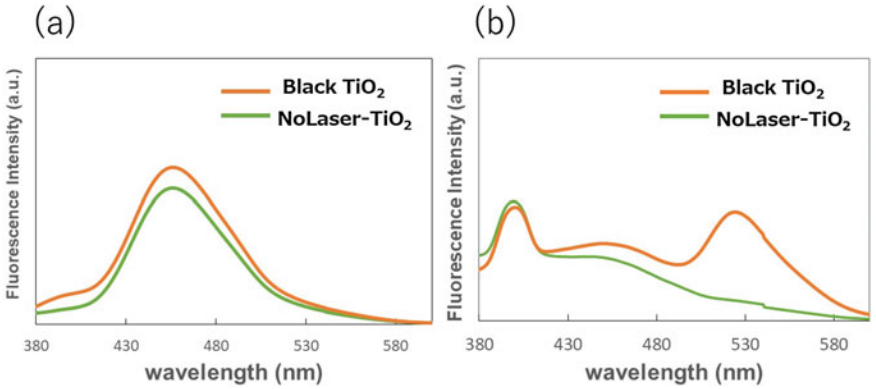


**Fig. 14.9** Fluorescence spectra of coumarin solution obtained by the 30-min irradiation to to the black $TiO_2$ and $TiO_2$ photocatalytic powders. **a** UV light and **b** visible light irradiation

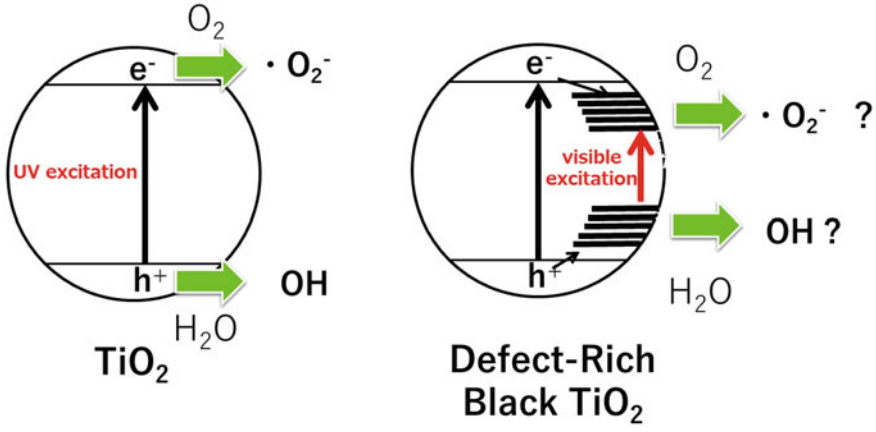


**Fig. 14.10** Schematic figure of $TiO_2$ and black $TiO_2$ and the mechanism of $O_2^-$ and OH radical formation

## 14.5 Laser Ablation to the Photocatalytic Oxide Semiconductors: Defect Formation Versus Photocatalytic Activities

In the previous section, oxygen defect formation of $TiO_2$ by the 355-nm laser irradiation and the effects on the photocatalytic activities were reported. Although several studies have been done for the black $TiO_2$ photocatalyst, very few works have been done for the other photocatalytic oxide semiconductors. Here, 355-nm laser irradiation to the ZnO, $SnO_2$, and $SrTiO_3$ photocatalytic powders was performed and investigated the effects of the amount of OH radicals for such laser irradiation. The

results of the color change by the 355-nm laser irradiation were shown in Fig. 14.11. The color for the photocatalysis of $SnO_2$ became black as the 355-nm laser was irradiated for more than 1 h, but the color for the photocatalysis of ZnO became yellow as the 355-nm laser was irradiated for more than 1 h. By the diffuse reflectance spectra of ZnO photocatalytic powders irradiated by the 355-nm laser light for 1 h, the edge of absorption spectra was found to extend from around 380 to 450 nm. The effects of the defects for the diffuse reflectance spectra of ZnO were investigated by Chen et al. [28]. They formed the defects of ZnO using ball-milling, but their results of the diffuse reflectance spectra of the ZnO after the ball-milling were very similar to those of our laser-irradiated ZnO photocatalytic powers. Thus, it was suggested that not only $TiO_2$ [29, 30] but also other oxide semiconductor photocatalytic powders generate defects by the 355-nm laser irradiation to the suspension of the photocatalytic powders in water. For the $SrTiO_3$ photocatalytic powders, on the other hand, 355-nm laser irradiation did not change the color. Thus, the effects of the laser irradiation on the color change, that is absorption spectra of the semiconductor materials, were found to be different from each other.

To further investigate the effects of the OH-radical formation by the UV irradiation to these laser-modified photocatalysts, coumarin fluorescence probe techniques were applied to these photocatalysts. The light source for these experiments was a high-pressure mercury lamp and was used without any cut-off filters. The results were given in Fig. 14.12. For all of the photocatalytic powers of $SnO_2$, ZnO, and $SrTiO_3$, the amount of OH radicals formed by UV irradiation to the photocatalytic reactions were increased. Techniques for generating defect sites in photocatalysis are now investigated by a lot of researchers to develop new strategies for visible light-responsive photocatalysts. Comparisons of the characteristics of the defects on the surface or inner part of the photocatalysis between the present laser irradiation techniques and the other techniques are still unknown. Thus, application of the laser

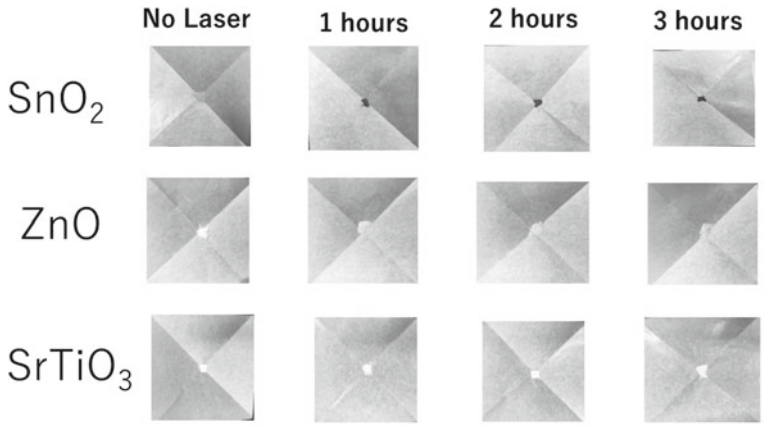


**Fig. 14.11** Photos for the $SnO_2$, ZnO, and $SrTiO_3$ photocatalytic powders after the 355-nm laser irradiation up to 3 h

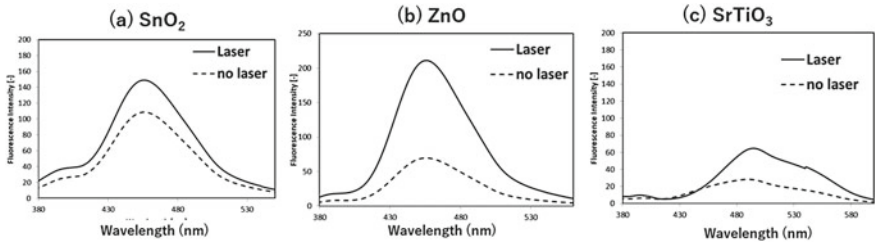


**Fig. 14.12** Detection of OH radicals with coumarin fluorescence method. Fluorescence spectra (wavelength of excitation is 350 nm) of coumarin solution after 30 min of the UV irradiation to **a** $SnO_2$, **b** ZnO and **c** $SrTiO_3$ photocatalytic powders. Solid lines: the 355-nm laser-irradiated, Dashed lines: no laser irradiation

ablation to photocatalysis is still unexplored so far and, indeed, further works are still open for researchers.

## 14.6 Conclusions

Laser ablations to the Bi-containing photocatalysts that can water-splitting under visible light irradiation were performed, and the enhancement of the photocurrent efficiencies was observed. It was also confirmed that not only the size reduction but also the surface defect formation played key roles in such photocurrent enhancement.

Unfocused laser beam irradiation to the metal oxide photocatalysts such as $TiO_2$, $SnO_2$, ZnO, and $SrTiO_3$ was performed, and it was observed that some of the photocatalysts showed the change of the color as well as the absorption spectra. Thus, it was concluded that defects of the photocatalysts were easily generated even in the unfocused laser beam irradiation. The photocatalytic activity of these laser-modified photocatalysts was checked by monitoring the amount of OH radicals, and it was found that laser irradiation to the photocatalysts changes or enhances the photocatalytic activities.

**Acknowledgements** This work was partly supported by a Core Research for Evolution Science grant and technology from the Japan Science and Technology Agency and the Uchida Energy Science Promotion Foundation. The author acknowledges Prof. Yoshio Nosaka for supervising and helpfully supports for summarizing the results of the research on the laser ablation of water-splitting photocatalysis. The author also likes to express thanks to Prof. Nobuo Saito, Mr. Igarashi, Mr. Hashizume, Mr. Sakamoto, Nagaoka University of Technology, and Ms. Murayama, Ms. Lee, and Mr. Suzuki, National Institute of Technology, Nagaoka College for the measurements and discussion of the data analysis used for the present manuscript.

## References


1. A. Fujishima, K. Honda, Electrochemical photolysis of water at a semiconductor electrode, Nature **238**, 37−38 (1972). https://doi.org/10.1038/238037a0
2. M. Anpo, Use of visible light. Second-generation titanium oxide photocatalysts prepared by the application of an advanced metal ion-implantation method. Pure Appl. Chem. **72**, 1787−1792 (2000). https://doi.org/10.1351/pac200072091787
3. R. Asahi, T. Morikawa, K. Ohwaki, Y. Aoki, Y. Taga, Visible-light photocatalysis in nitrogen-doped titanium oxides. Science **293**, 269–271 (2001). https://doi.org/10.1126/science.1061051
4. O. Teruhisa, M. Takahiro, M. Mochio, Photocatalytic activity of S-doped $TiO_2$ photocatalyst under visible light. Chem. Lett. **32**, 364–365 (2003). https://doi.org/10.1246/cl.2003.364
5. S. Sakthivel, H. Kisch, Daylight photocatalysis by carbon-modified titanium dioxide. Angew. Chem. Int. Ed. **42**, 4908–4911 (2003). https://doi.org/10.1002/anie.200351577
6. A. Naldoni, M. Allieta, S. Santangelo, M. Marelli, F. Fabbri, S. Cappelli, C.L. Bianchi, R. Psaro, V.D. Santo, Effect of nature and location of defects on bandgap narrowing in black $TiO_2$ nanoparticles. J. Am. Chem. Soc. **134**, 7600–7603 (2012). https://doi.org/10.1021/ja3012676
7. X. Pan, Y.J. Xu, Defect-mediated growth of noble-metal (Ag, Pt, and Pd) nanoparticles on $TiO_2$ with oxygen vacancies for photocatalytic redox reactions under visible light. J. Phys. Chem. C **117**, 17996–18005 (2013). https://doi.org/10.1021/jp4064802
8. S.J. Henley, J.D. Carey, S.R.P. Silva, Pulsed-laser-induced nanoscale island formation in thin metal-on-oxide films. Phys. Rev. B. **72**, 195408 (2005). https://doi.org/10.1103/PhysRevB.72.195408
9. J. Narayan, J. Fletcher, C.W. White, W.H. Christie, Melting phenomena and pulsed-laser annealing in semiconductor. J. Appl. Phys. **52**, 7121–7128 (1981). https://doi.org/10.1063/1.328685
10. Y. Murakami, T. Sugatani, Y. Nosaka, Laser-induced incandescence study on the metal aerosol particles as the effect of the surrounding gas medium. J. Phys. Chem. A **109**, 8994–9000 (2005). https://doi.org/10.1021/jp058044n
11. P.V. Kamat, M. Flumiani, G.V. Hartland, Picosecond dynamics of silver nanoclusters. Photoejection of electrons and fragmentation. J. Phys. Chem. B **102**, 3123−3128 (1998). https://doi.org/10.1021/jp980009b
12. A. Tamaki, H. Kurita, S. Koda, Laser-induced size reduction of noble netal particles. J. Phys. Chem. B **103**, 1226–1232 (1999). https://doi.org/10.1021/jp983503o
13. T. Sasaki, Y. Shimizu, N. Koshizaki, Preparation of metal oxide-based nanomaterials using nanosecond pulsed laser ablation in liquids. J. Photochem. Photobiol. A **182**, 335–341 (2006). https://doi.org/10.1016/j.jphotochem.2006.05.031
14. T. Asahi, T. Sugiyama, H. Masuhara, Laser fabrication and spectroscopy of organic nanoparticles. Acc. Chem. Res. **41**, 1790–1798 (2008). https://doi.org/10.1021/ar800125s
15. S. Filice, G. Compagnini, R. Fiorenza, S. Scire, L. D'Urso, M.E. Fragala, P. Russo, E. Fazio, S. Scalese, Laser processing of $TiO_2$ colloids for an enhanced photocatalytic water splitting activity. Colloid. Int. Sci. **489**, 131–137 (2017). https://doi.org/10.1016/j.jcis.2016.08.013
16. M. Lau, S. Reichenberger, I. Haxhiaj, S. Barcikowski, A.M. Muller, Mechanism of laser-induced bulk and surface defect generation in ZnO and $TiO_2$ nanoparticles: effect on photoelectrochemical performance. ACS Appl. Energy. Mater. **1**, 5366–5385 (2018). https://doi.org/10.1021/acsaem.8b00977
17. Y. Murakami, M. Ikarashi, M. Hashizume, A.Y. Nosaka, Y. Nosaka, Laser ablation of the photocatalytic $BiVO_4$ and $BiZn_2VO_6$ powders in water and their photocurrent properties. Electrochem. Solid-State Lett. **11**, H42–H46 (2007). https://doi.org/10.1149/1.2821237
18. H. Liu, R. Nakamura, Y. Nakato, A visible-light responsive photocatalyst, $BiZn_2VO_6$, for efficient oxygen photoevolution from aqueous particulate suspensions. Electrochem. Solid-State Lett. **9**, G187–G190 (2006). https://doi.org/10.1149/1.2184496
19. D. Werner, A. Furube, T. Okamoto, S. Hashimoto, Femtosecond laser-induced size reduction of aqueous gold nanoparticles: in situ and pump-probe spectroscopy investigations revealing

coulomb explosion. J. Phys. Chem. C **115**, 8503–8512 (2011). https://doi.org/10.1021/jp112262u
20. H. Liu, R. Nakamura, Y. Nakato, Bismuth-copper vanadate $BiCu_2VO_6$ as a novel photocatalyst for efficient visible-light-driven oxygen evolution. ChemPhysChem **6**, 2499–2502 (2005). https://doi.org/10.1002/cphc.200500278
21. H. Song, C. Li, Z. Lou, Z. Ye, L. Zhu, Effective formation of oxygen vacancies in black $TiO_2$ nanostructures with efficient solar-driven water splitting. ACS Sustainable Chem. Eng. **5**, 8982–8987 (2017). https://doi.org/10.1021/acssuschemeng.7b01774
22. X. Chen, D. Zhao, K. Liu, C. Wang, L. Liu, B. Li, Z. Zhang, D. Shen, Laser-modified black titanium oxide nanospheres and their photocatalytic activities under visible light. ACS Appl. Mater. Interfaces **7**, 16070–16077 (2015). https://doi.org/10.1021/acsami.5b04568
23. V.A. Zuniga-Ibarra, S. Shaji, B. Krishnan, J. Johny, S.S. Kanakkillam, D.A. Avellaneda, J.A.A. Martinez, T.K.D. Roy, N.A. Ramos-Delgado, Synthesis and characterization of black $TiO_2$ nanoparticles by pulsed laser irradiation in liquid. Appl. Surf. Sci. **483**, 156–164 (2019). https://doi.org/10.1016/j.apsusc.2019.03.302
24. A. Yamakata, J.M. Vequizo, Curious behaviors of photogenerated electrons and holes at thedefects on anatase, rutile, and brookite $TiO_2$ powders: A review. J. Photochem. Photobiol. C **40**, 234–243 (2019). https://doi.org/10.1016/j.jphotochemrev.2018.12.00
25. D.A.H. Hanaor, C.C. Sorrell, Review of the anatase to rutile transformation. J. Mater. Sci. **46**, 855–874 (2011). https://doi.org/10.1007/s10853-010-5113-0
26. G.L. Newton, R. Milligan, Fluorescence detection of hydroxyl radicals. Radiat. Phys. Chem. **75**, 473–478 (2006). https://doi.org/10.1016/j.radphyschem.2005.10.011
27. J. Zhang, Y. Nosaka, Mechanism of the OH radical generation in photocatalysis with $TiO_2$ of different crystalline types. J. Phys. Chem. C **118**, 10824–10832 (2014). https://doi.org/10.1021/jp501214m
28. D. Chen, Z. Wan, T. Ren, H. Ding, W. Yao, R. Zong, Y. Zhu, Influence of defects on the photocatalytic activity of ZnO. J. Phys. Chem. C **118**, 15300−15307 (2014). https://doi.org/10.1021/jp5033349
29. T.S. Rajiaraman, S.P. Parikh, V.G. Gandhi, Black $TiO_2$: a review of its properties and conflicting trends. Chem. Eng. J. **389**, 123918 (2020). https://doi.org/10.1016/j.cej.2019.123918
30. S. Kim, Y. Cho, R. Rhee, Black $TiO_2$: what are exact functions of disorder layer. Carbon Energy **2**, 44–52 (2020). https://doi.org/10.1002/cey2.32

# Chapter 15
# Crystallization and Polymorphism of Amino Acids Controlled by High-Repetition-Rate Femtosecond Laser Pulses


**Teruki Sugiyama**

**Abstract** This chapter first reviews the history of laser-induced crystallization and polymorphism control and then presents the experimental results on crystallization and polymorphism obtained by high-repetition-rate femtosecond laser irradiation, which is based on various physical phenomena (optical trapping and laser ablation). Femtosecond laser pulses are focused on clusters of amino acid solutions (L-phenylalanine (L-Phe) and L-serine (L-Ser)) in solution. These clusters are gathered at a high local concentration in the focal volume, eventually leading to crystal nucleation. This phenomenon is called *optical trapping-induced crystallization* (OTIC). OTIC yields crystals with different molecular arrangements (polymorphs) depending on the laser irradiation conditions. Among the reported polymorphs are monohydrate and anhydrous crystals of both L-Phe and L-Ser, which exhibit similar thermal behaviors. However, unlike L-Ser, L-Phe has a benzene moiety in its chemical structure, so its crystallization and polymorphism phenomena are governed by multiphoton absorption under femtosecond laser irradiation and essentially differ from those of L-Ser. Herein, the mechanism of polymorph control is uniformly discussed in terms of classical nucleation theory. Polymorphs are controlled by the degree of local concentration achieved by laser irradiation. All phenomena and experimental results presented in this chapter are characteristic of high-energy lasers and provide many insights into the emerging field of high-energy chemistry.

**Keywords** High-repetition-rate femtosecond laser · Optical trapping · Crystallization · Polymorphism · Amino acids

## 15.1 Laser-Induced Crystallization and Polymorphism

Crystallization methods using high-intensity lasers have recently attracted much attention owing to their clean process, spatiotemporal controllability, and unique

T. Sugiyama (✉)
Department of Applied Chemistry, National Yang Ming Chiao Tung University, 1001 University Road, Hsinchu 30010, Taiwan
e-mail: sugiyama@nycu.edu.tw



Y. Ishikawa et al. (eds.), *High-Energy Chemistry and Processing in Liquids*,
https://doi.org/10.1007/978-981-16-7798-4_15

crystallization mechanism. Various laser-induced nucleation methods based on different photophysical and photochemical phenomena have been proposed thus far [1–6]. For example, Garetz and Myerson triggered crystallization by irradiating nanosecond laser pulses into a supersaturated aqueous solution of target compounds [1]. This technique, called non-photochemical laser-induced nucleation (NPLIN) because the crystallization proceeds without chemical reactions, is a pioneering laser-based crystallization technique. The nanosecond laser pulses cause nonlinear optical effects (optical Kerr effects) that align the target molecules. Under the strong electric field of the laser pulses, the target molecules form a highly ordered spatial arrangement that triggers nucleation in supersaturated solution without concentration change.

The optical trapping-induced crystallization (OTIC) method [7], first demonstrated by the authors in 2007, is another laser-induced nucleation method. This method triggers crystallization in solution using an optical technique called *optical trapping* or *optical tweezers* [8] implemented by a focused laser beam. Figure 15.1 is a schematic of the OTIC method. The usual light source is a continuous-wave (cw) near-infrared laser beam, which is focused on the solution containing the target molecules. Light–cluster interactions in the solution generate a gradient force (Lorentz force) that collects the target clusters into the focal volume, and the realized local concentration increase triggers crystallization. Uniquely among the laser-induced crystallization methods, OTIC achieves crystallization even in unsaturated solutions because concentration increases [9, 10]. In other words, this method can systematically investigate polymorphism in unsaturated solutions, which has been impossible in principle. The OTIC method also enables real-time monitoring of the crystallization dynamics. As the time and location of crystallization cannot be predicted, this feature is intriguing and valuable for spectroscopic elucidations of the crystallization mechanism.

On the other hand, polymorphism means that a molecule crystallizes into multiple molecular arrangements without changing its chemical structure. Polymorphism control has attracted much attention in crystal engineering, and pharmaceutical research since polymorphs differ in their density, solubility, melting point, shape,

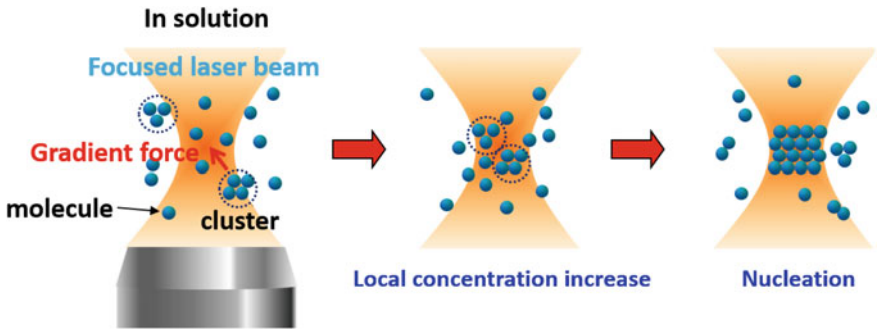


**Fig. 15.1** Schematic of the OTIC method

bioavailability, and other physical and chemical properties [11–15]. In 2001, Garetz and Myerson experimentally demonstrated the polymorphism control of glycine, the simplest amino acid, by manipulating laser polarization in the NPLIN method [16]. In this experiment, linear polarization (LP) yielded the most thermodynamically stable $\gamma$-glycine crystals, whereas circular polarization (CP) obtained metastable $\alpha$-glycine crystals. In 2010, the authors also reported the polymorphic control of glycine using the OTIC method. The results in unsaturated glycine solution were similar to those of NPLIN: LP achieved a 90% probability of producing $\gamma$-glycine crystals (Fig. 15.2a), whereas CP yielded only $\alpha$-glycine crystals (Fig. 15.2b) [10]. However, the results of various OTIC experiments imply different mechanisms of polymorph control in the OTIC and NPLIN methods [17].

This chapter presents crystallization and polymorphism control of two amino acids by the OTIC method using a focused high-repetition-rate femtosecond (fs) laser beam. The plausible control mechanisms are also discussed. As the amino acids, we selected L-phenylalanine (L-Phe) and L-serine (L-Ser). L-Phe (Fig. 15.3a) is an essential compound in the food industry and an active pharmaceutical ingredient used in the pharmaceutical industry [18, 19]. L-Ser (Fig. 15.3b) is found in the membrane of brain cells (neurons) and is an essential amino acid for phosphatidylserine synthesis

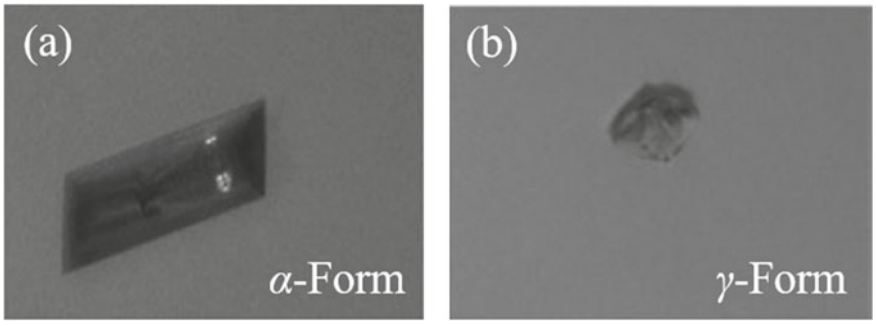


**Fig. 15.2** Bright-field images of $\alpha$- (**a**) and $\gamma$-glycine (**b**) crystals formed by the OTIC method with a continuous-wave near-infrared laser

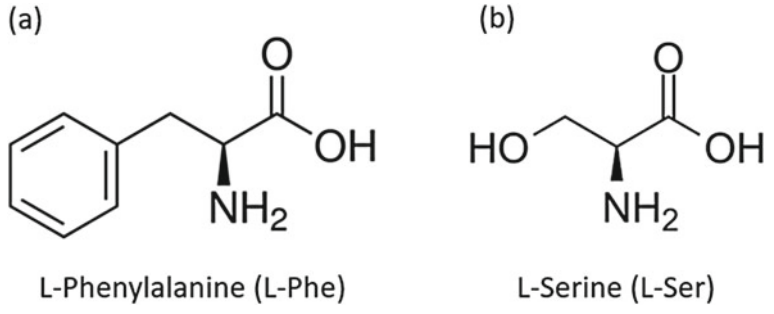


**Fig. 15.3** Chemical structures of L-phenylalanine (**a**, L-Phe) and L-serine (**b**, L-Ser)

**Table 15.1** Comparison of physical phenomena induced by cw and fs lasers

| Light source | cw laser | fs laser |
|---|---|---|
| Gradient force | Small | Large |
| Laser ablation | Rare | Frequent |

[20]. The chemical structures of these two amino acids differ mainly by the presence or absence of a benzene ring. The benzene ring of L-Phe significantly alters the multiphoton absorption cross section, leading to large differences in the laser-induced physical phenomena.

## 15.2 Comparison of Physical Phenomena Under cw and fs Laser Irradiation

Since the first demonstration of OTIC in 2007, most OTIC experiments have applied cw lasers as the trapping light source. Why, then, was the light source changed from a cw laser to a high-repetition-rate fs laser? To answer this question, Table 15.1 compares the crystallization-related physical phenomena triggered by fs and cw lasers.

Experimentally and theoretically, researchers have demonstrated that the gradient force is higher under high-repetition-rate fs laser pulses than under cw lasers with the same average power [21, 22]. The repetition rate of the fs laser pulses is also essential for optical trapping. Although fs laser pulses produce a stronger gradient force than cw lasers, the force is periodic and acts on the target with the same period as the pulse width. Therefore, a high repetition rate is necessary to accumulate sufficient effect of the gradient force for stable trapping of the target. In other words, at the low repetition rate (10 Hz) used in NPLIN, the effect of optical trapping is ignorable. Second, the energy of the focused fs laser should exceed a certain threshold, generating cavitation bubbles. For example, Yoshikawa et al. showed that cavitation bubbles or shock waves generated by fs laser ablation of a solution could locally and temporarily increase the concentration of the target, leading to crystal nucleation [6, 23]. This phenomenon increases the degree of freedom of polymorphic control.

## 15.3 Theoretical Treatments

### *15.3.1 Optical Trapping with High-Repetition-Rate Femtosecond Laser Pulses*

Optical trapping is governed by the gradient (Lorentz) force of a focused laser beam. Under irradiation with a fs laser, the high peak intensity enhances nonlinear effects

that increase the gradient force. The gradient force ($\mathbf{F}_{grad}$) and trapping potential energy ($U_{trap}$) with nonlinear effects are, respectively, given by [22, 24, 25]

$$\boldsymbol{F}_{grad} = (\mu/\varepsilon)^{1/2}[\alpha_0 + \alpha_1 I(r,t)]\nabla I(r)/2, \tag{15.1}$$

$$U_{trap} = -(\mu/\varepsilon)^{1/2}[\alpha_0 + \alpha_1 I(r,t)]I(r)/2, \tag{15.2}$$

where $\mu$ and $\varepsilon$ are the permeability and permittivity of the surrounding medium, respectively, $\alpha_0$ and $\alpha_1$ are the linear and nonlinear polarizability, respectively, and $I(r,t)$ is the laser intensity, which is a function of time and distance from the laser focus. With the second term removed, Eqs. 15.1 and 15.2 represent the gradient force and trapping potential energy of cw lasers. Note that the nonlinear gradient force and trapping potential energy are functions of polarizability ($\alpha_0$ and $\alpha_1$), which defines the ability to acquire an electric dipole moment. The linear polarizability ($\alpha_0$) is a function of the target refractive index ($n_p$) and the refractive index of the surrounding medium ($n_m$):

$$\alpha_0 = 4\pi\varepsilon a_3 \frac{\left(n_p/n_m\right)^2 - 1}{\left(n_p/n_m\right)^2 + 2} \tag{15.3}$$

Here, $a$ is the radius of the target. From Eqs. 15.1, 15.2, and 15.3, the gradient force clearly increases with target volume. The polarizability ($\alpha$) with nonlinear effects can also be approximated as

$$\alpha \approx \alpha_0 + \alpha_1 I(r). \tag{15.4}$$

Equation 15.4 means that the polarizability of the target increases with incident laser intensity. In other words, ultra-short laser pulses with high peak intensities (such as fs lasers) enhance the nonlinear effects and hence the gradient force.

### 15.3.2 Nucleation Rate Based on Classical Nucleation Theory

When polymorphs precipitate in solution, their nucleation rate ($J$) is given by

$$J = Aexp\frac{-16\pi\sigma^3\nu^2}{3(kT)^3(lnSS)^2} \tag{15.5}$$

based on classical nucleation theory. In Eq. (15.5), $A$ is the frequency factor, $\sigma$ and $\nu$ are the surface energy and density of the polymorph, respectively, $SS$ is the

supersaturation degree of the sample solution, $T$ is the absolute temperature, and $k$ is the Boltzmann constant. Clearly, $J$ is determined by the relative effects of the supersaturation degree and the surface energy of each polymorph. In a solution with a certain supersaturation degree, the thermodynamically most stable phase is always more supersaturated than the less stable phases. Meanwhile, the surface energy of each polymorph is related to the enthalpy of the polymorph, and the metastable phases usually have smaller surface energy than the most stable phase. Therefore, in solutions with sufficiently large supersaturation, the precipitation of the metastable phases with low surface energy is kinetically accessible. Such a phenomenon is known as the Ostwald step rule [26]. On the contrary, in a solution with a low *SS* value, the effect of *SS* dominates the surface energy, and the thermodynamically stable phase precipitates preferentially. In this chapter, which polymorphs precipitate is discussed in terms of nucleation rate theory.

## 15.4 Crystallization and Polymorphism of L-phenylalanine via High-Repetition-Rate Femtosecond Laser Pulses

### *15.4.1 Bidirectional Polymorphic Conversion [27]*

This section presents the crystallization and polymorphism dynamics of L-Phe by the OTIC method with focused high-repetition-rate fs laser pulses. The experimental sample was an unsaturated aqueous solution of L-Phe. The supersaturation value of L-Phe ($SS \sim 0.8$) was determined as $C/C_0$, where $C$ and $C_0$ are the sample and saturated solution concentrations, respectively [28, 29]. Figure 15.4 shows the time evolution of the crystallization behavior under high-repetition-rate fs laser pulses (800 nm, 80 MHz, 100 fs, and 300 mW). The beam was focused on the air/solution interface of

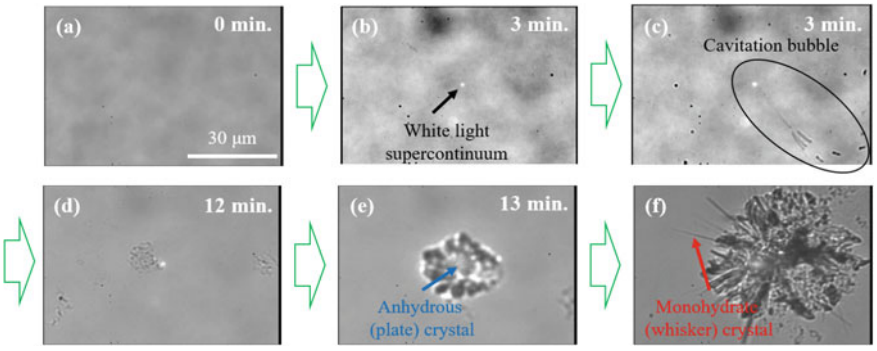


**Fig. 15.4** Transmission images of the time evolution of L-Phe crystallization by the OTIC method with high-repetition-rate fs laser pulses. Modified with permission from The Japan Society of Applied Physics [27] Copyright 2020

an unsaturated thin-film solution of L-Phe (Fig. 15.4a). After three minutes' irradiation, bright white emission was observed at the laser focus (Fig. 15.4b). This emission broadly covered the visible light region and was attributed to white supercontinuum (SC) light caused by self-phase modulation of the focused fs laser [30–32]. During the SC light emission, cavitation bubbles were continuously generated from the focal point and instantly and rapidly diffused outward (Fig. 15.4c). This result strongly supports that optical trapping for three minutes increases the local solute concentration (refractive index) because the efficiency of SC generation increases with a refractive index of the medium. Meanwhile, cavitation bubbles formed because the multiphoton absorption was enhanced by the high local concentration. After around 12 min, micrometer-sized crystals formed at the laser focus (Fig. 15.4d), which gradually grew over the next few minutes (Fig. 15.4e). Intriguingly, under the long-time irradiation to the formed anhydrous crystal, the whisker-like monohydrate crystals continuously formed on the surface of the anhydrous crystal (Fig. 15.4f).

Figure 15.5 shows the probability that crystallization is realized by 1 h of the fs laser irradiation after ten experiments at each laser power of 100–400 mW (0.14–0.54 J $cm^{-2}$). From Fig. 15.5, there appears to be a clear laser threshold between 100 and 150 mW to trigger crystallization. This indicates that not only the local concentration increase due to the optical trapping of the clusters but also the subsequent formation of the cavitation bubble plays a critical role in inducing crystallization. As the cavitation bubble formation also requires a concentration increase, we can consider that the gradient force triggers crystallization. As the laser power is increased, the crystallization probability decreases tremendously between 300 and 400 mW. At higher laser powers, a strong gradient force increases local concentration but simultaneously makes the generation of cavitation bubbles occur very frequently. Such continuously generated cavitation bubbles accelerate the diffusion of localized

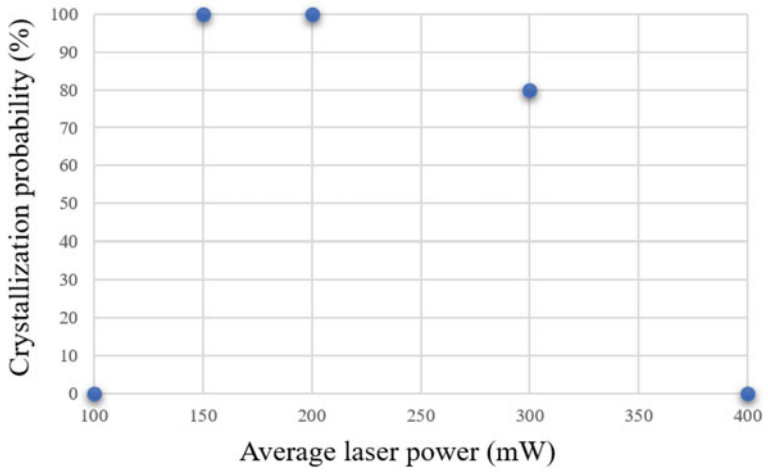


**Fig. 15.5** Probability of the anhydrous crystal formation over average laser power. Modified with permission from The Japan Society of Applied Physics [27] Copyright 2020

clusters at the focal point rather than increasing the local concentration at the bubble surface. In other words, stable optical trapping of the clusters is suppressed due to the frequent bubble generation, resulting in no crystallization.

*In-situ* Raman spectroscopy confirmed that the formed crystals were anhydrous crystals of L-Phe. Note that the threshold laser power for crystal nucleation is approximately 3–4 times lower in the OTIC method than the case upon the cw laser, and the crystallization time is about half that of the cw laser technique. Judging from these results, the focused fs laser irradiation indeed increases the gradient force. We further confirmed that anhydrous crystals form at laser energies above a certain threshold, indicating that the generation of a cavitation bubble is involved in the crystal nucleation mechanism. Therefore, the gradient force of the focused fs laser enhanced the local concentration of L-Phe molecules, and crystallization is generated at the surface of the cavitation bubble formed via multiphoton absorption. Two crystal polymorphs of L-Phe have been reported: monohydrate and anhydrate [29, 33], which are easily distinguishable by their apparent crystal shapes (whisker and plate), respectively. At room temperature, the monohydrate crystal is thermodynamically more stable than the anhydrate one, but this characteristic reverses above 310 K. Note that this OTIC experiment with high-repetition-rate fs laser always fields the thermodynamically metastable anhydrous crystals, regardless of laser power and polarization.

Very intriguingly, when the spontaneously precipitated monohydrate crystals were irradiated with a focused fs laser, they oppositely transitioned to the anhydrous form (Fig. 15.6). Immediately after irradiating the crowded monohydrate crystals (Fig. 15.6a) with focused fs laser pulses, a single stable cavitation bubble-sized several tens of micrometers formed at the laser focus (Fig. 15.6b). These cavitation bubbles obviously differed from those shown in Fig. 15.4c. As the laser irradiation continued, anhydrous crystals formed near the surface of the cavitation bubble, not at the laser focus (Fig. 15.6c). As anhydrous crystals are thermodynamically unstable at room temperature, their formation from the stable monohydrate form is an astonishing outcome, confirming that a high-intensity focused fs laser can arbitrarily control the polymorphic transition and achieve bidirectional polymorphic conversion. The mechanism of this bidirectional polymorphic conversion is discussed next.

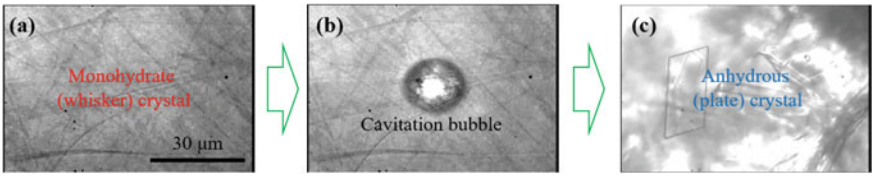


**Fig. 15.6** Polymorphic transition from monohydrate to anhydrous crystals of L-Phe under high-repetition-rate fs laser irradiation. Modified with permission from The Japan Society of Applied Physics Ref. [27] Copyright 2020

### 15.4.2 Polymorphic Transition Mechanisms

This section discusses the mechanism of the bidirectional polymorphic conversion under focused fs laser pulses. Figure 15.7a shows the mechanism by which anhydrous crystals convert to the monohydrate form. When an anhydrous crystal (panel i in Fig. 15.7a) is irradiated by focused fs laser pulses, it dissolves while many cavitation bubbles are continuously generated (panel ii in Fig. 15.7a). Similar behavior of cavitation bubble generation is observed in amplified fs laser-induced nucleation [34], suggesting that crystal nucleation is triggered when the solute concentration increases to sufficient levels at the cavitation bubble surface. However, in the original unsaturated solution, the concentration increase at the cavitation bubble surface cannot be significant. Based on classical nucleation theory (see Sect. 15.3.2), it is considered that a thermodynamically more stable monohydrate crystal formed on the anhydrous crystal surface (panel iii in Fig. 15.7a).

Figure 15.7b shows the mechanism by which monohydrate crystals transition to the anhydrous form. When exposed to fs laser pulses, the spontaneously precipitated monohydrate crystals (panel i in Fig. 15.7b) immediately convert to the anhydrous form. The monohydrate to anhydrous polymorphic transition always proceeds when the laser fluence exceeds a clearly defined threshold but never proceeds when the fs laser is replaced by a cw laser. In addition, the laser fluence in this experiment is ~30 times lower than the threshold energy of laser ablation of the mother crystal, implying that laser ablation of the crystals is unlikely to trigger the polymorphic transition. The critical aspect of this mechanism is the formation of one stable cavitation bubble under laser irradiation (panel ii in Fig. 15.7b). This cavitation bubble remains on the cover glass (inside the monohydrate crystals) and never floats to the outside, possibly because a large number of monohydrate crystals dramatically increases the viscosity

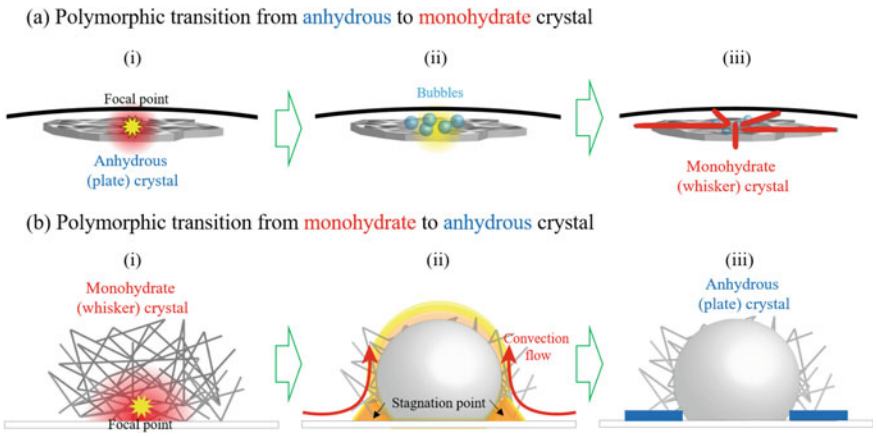


**Fig. 15.7** Schematics of bidirectional polymorphic conversion mediated by high-repetition-rate fs laser irradiation. Modified with permission from IOP Publishing Ref. [27] Copyright 2020

of the solution. A single stable cavitation bubble is also formed by focusing a cw laser on a gold substrate in aqueous solution [35]. Referring to the discussion in [35], it is inferred that both thermal convection caused by laser irradiation and the surface tension of the cavitation bubble promote the efficient mass transfer of clusters in solution to the stagnation point (panel ii in Fig. 15.7b) between the surface of the cavitation bubble and the glass. Under the thermocapillary effect, the concentration becomes exceptionally high at the stagnation point, promoting the formation of anhydrous crystals (panel iii in Fig. 15.7b). This mechanism is consistent with classical nucleation theory (Sect. 15.3.2). Thus, the mechanism of bidirectional polymorphic conversion can be explained by the difference in the degree of concentration increase at the surface of the generated cavitation bubble.

## 15.5 Crystallization and Polymorphism of L-serine Under a High-Repetition-Rate Femtosecond Laser

### *15.5.1 Crystallization and Polymorphism Dynamics of L-serine [36]*

This section outlines the crystallization and polymorphism dynamics of L-Ser under high-repetition-rate fs laser pulses in the OTIC method. The L-Ser solution was exposed to the same laser conditions as the L-Phe solution discussed above, but note that L-Ser lacks a benzene ring, so its multiphoton absorption cross-section is significantly lower than that of L-Phe. Accordingly, L-Ser and L-Phe should exhibit different physical phenomena under laser irradiation. Unlike the L-Phe experiment, the fs laser pulses in the L-Ser experiment were shifted from air–solution interface to near the contact line of the saturated L-Ser solution ($SS = 1.0$ [37]) because the crystallization probability of L-Ser is extremely low when the laser is focused at the air/solution interface. This result may indicate that L-Ser is more difficult to crystallize by the OTIC method than L-Phe.

Figure 15.8 shows the time evolution of L-Ser crystallization and polymorphism by the OTIC method with high-repetition-rate fs laser pulses. White SC light was observed immediately after the laser irradiation started (Fig. 15.8a). Given that the appearance time of the SC light lengthens with decreasing laser intensity, the concentration increase is much faster in L-Ser than in L-Phe, partly because the convection flow is tremendously suppressed along the thin contact line [38, 39]. Therefore, stable optical trapping is achieved in the L-Ser solution. After several seconds of laser irradiation, a spherical material was confirmed at the laser focus (Fig. 15.8b). Whether this spherical material is a highly concentrated droplet with a higher refractive index than the surroundings or a cavitation bubble (as observed in L-Phe) is not yet clarified. However, the generated cavitation bubble appeared to be highly viscous and did not diffuse into the surroundings; rather, it was trapped at the focal point. After a few more minutes of laser irradiation, plural crystals formed around the focal point

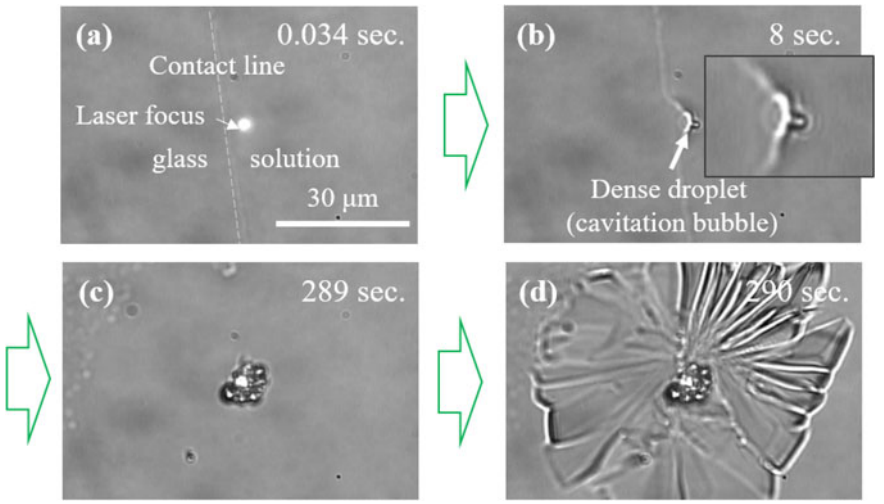


**Fig. 15.8** Bright-field images of the time evolution of L-Ser crystallization and polymorphism by the OTIC method with high-repetition-rate fs laser pulses. Modified with permission from Wiley Ref. [36] Copyright 2021

(Fig. 15.8c). However, unlike the L-Phe crystals, L-Ser crystals sometimes precipitated outside the laser focus. The details of this experimental result are not described here, but the local concentration increase spreads outward from the laser focus, as frequently observed in other OTIC experiments [9, 10, 17, 27]. The crystals grew under further laser irradiation (Fig. 15.8c and d) without the dissolution observed in the L-Phe solution. These results suggest a much smaller temperature increase in L-Ser than in L-Phe, likely owing to the small multiphoton absorption cross-section of L-Ser. Incidentally, when the pulsed fs lasers in the OTIC crystallization experiments were replaced with cw lasers at the same average power and wavelength, no crystal precipitated even after 30 min of irradiation. This result strongly supports that the enhanced gradient force under the high-repetition-rate fs laser pulses significantly improves the crystallization probability.

As confirmed by *in-situ* Raman spectroscopy (Fig. 15.9), the obtained L-Ser crystals can be monohydrate [39] or anhydrous [40]. The most thermodynamically stable form is monohydrate at temperatures below 311 K and anhydrous above 311 K [41]. Recall that the L-Phe polymorphs exhibit very similar thermal behaviors. In fact, the monohydrate form always precipitates by spontaneous evaporation at room temperature. However, unlike the L-Phe polymorphs, the two L-Ser polymorphs cannot be distinguished by their apparent shapes. Next, it was confirmed that the pulsed fs lasers in the OTIC crystallization experiments almost yield the metastable anhydrous form in the laser fluence range from 100 to 400 mW (0.14–0.54 J $cm^{-2}$). What increases the formation probability of the metastable anhydrous phase over the thermodynamically stable monohydrate phase is an open question. Considering the above-mentioned thermal behavior of L-Ser polymorphs, one guess that temperature

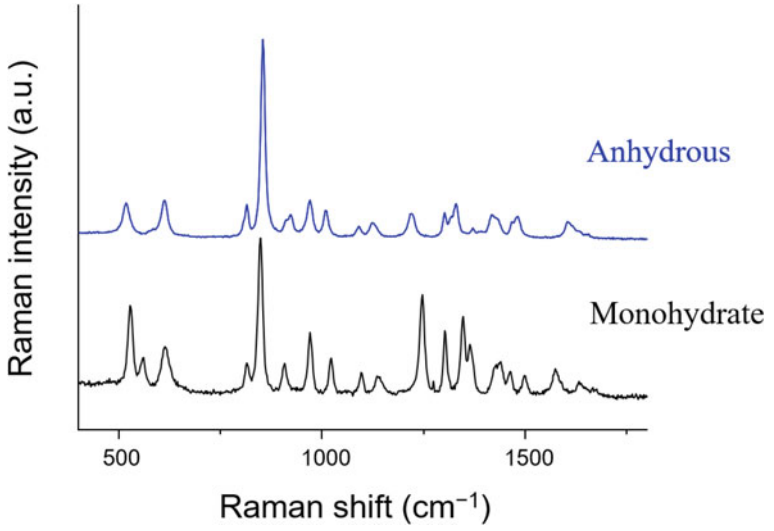


**Fig. 15.9** Raman spectra of the two types of L-Ser polymorphs produced by fs laser irradiation at 300 mW. Modified with permission from Wiley Ref. [36] Copyright 2021

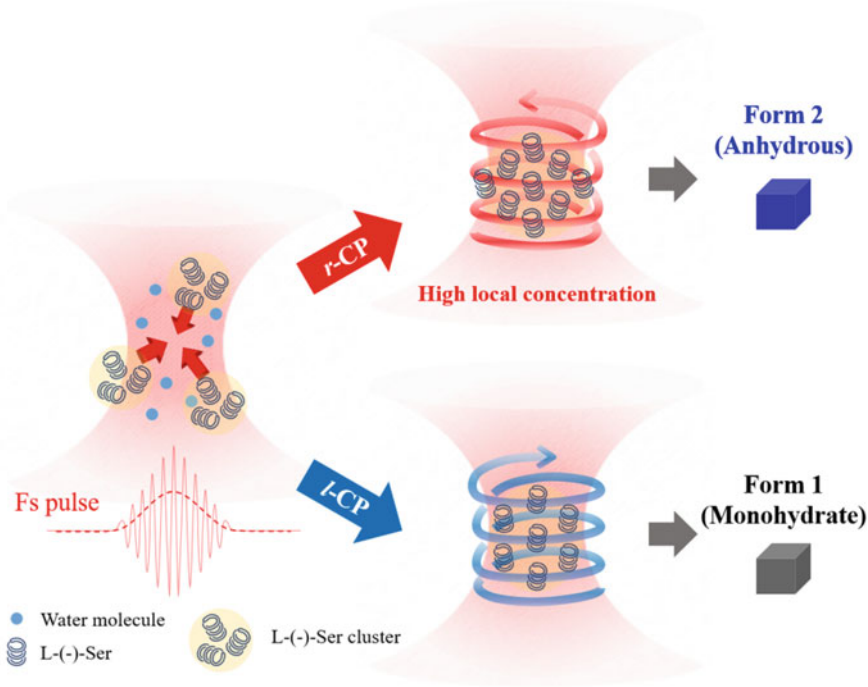


**Fig. 15.10** Schematic of L-Ser polymorphism under high-repetition-rate fs laser irradiation. Modified with permission from Wiley Ref. [36] Copyright 2021

elevation by laser heating may be a reasonable explanation. However, the temperature elevation in this experiment was minimal because the laser wavelength is 800 nm, which is minimally absorbed by water molecules [42]. Moreover, unlike L-Phe, L-Ser undergoes a negligible quantity of multiphoton absorption. Instead, as discussed in Sect. 15.3.2, the supersaturation is realized by the large gradient force, which optically collects the clusters in solution; consequently, the metastable anhydrous phase is predominantly formed.

### *15.5.2 Laser Polarization-Controlled Polymorphism*

This section introduces the remarkable experimental results of laser polarization-controlled L-Ser polymorphism. In these experiments, the handedness of CP is especially important. Fixing the laser power, the polarization of the laser pulses was adjusted to LP, right CP (*r*-CP), or left CP (*l*-CP), and the experiments were carried out as described in Sect. 15.5.1 (10 experiments per polarization). The formation probabilities of the monohydrate and anhydrous forms were determined from *in-situ* Raman spectra of the generated crystals. The LP and *r*-CP applications generated only the anhydrous form, whereas *l*-CP generated the monohydrate form with a probability of 60%. This result further supports that temperature elevation does not dominantly control polymorphism because all polarizations were applied at the same laser intensity.

Finally, we discuss the mechanism by which the handedness of CP light affects the L-Ser polymorphism using schematic as shown in Fig. 15.10. L-Ser is a chiral compound and is known to be L-(-)-Ser, meaning that the optical rotation of L-Ser molecules and clusters is levorotatory. Moreover, as L-Ser does not absorb photons in the visible and near-infrared regions, the levorotatory nature of L-Ser clusters should be maintained even at 800 nm (the wavelength of the fs laser pulses used in this study). A levorotatory optical rotation also means that *r*-CP light travels slower than *l*-CP light through the cluster, so the refractive index of the L-Ser cluster is higher for *r*-CP than for *l*-CP light. The increased refractive index of *r*-CP through the L-Ser cluster increases the $n_p$ in Eq. 15.3, in turn increasing the gradient force and hence the local concentration of L-Ser. Consequently, *r*-CP light increases the formation probability of anhydrous L-Ser, as theoretically described in Sect. 15.3.2. On the contrary, because the refractive index of the L-Ser cluster is relatively low under *l*-CP light, *l*-CP irradiation preferentially induces the thermodynamically stable monohydrate phase. Incidentally, L-Phe is also chiral, but no polymorphic control by the handedness of CP has been realized in this molecule. It is suggested that temperature elevation caused by the high multiphoton absorption cross section of L-Phe inhibits this polymorphic phenomenon.

## 15.6 Conclusion

This chapter introduced the crystallization and polymorphism of two kinds of amino acids, L-Phe and L-Ser, by the OTIC method with high-repetition fs laser pulses. When fs laser pulses are focused on aqueous solutions of the molecules, they generate a large gradient force that efficiently collects the clusters and remarkably increases the crystallization probability. In addition, when the multiphoton absorption cross section is sufficiently large (as in L-Phe), the formation of a cavitation bubble dominates. The local concentration is then raised by the synergy of the gradient force and cavitation bubble formation, enhancing the formation of the thermodynamically less stable anhydrous crystals. Moreover, fs laser pulses control the bidirectional polymorphic transition between the monohydrate and anhydrous forms, which is interpreted through the concentration increase at the cavitation bubble surface. While the local concentration accumulated by the enhanced gradient force determines the polymorphism of L-Ser, this finding can be explained by classical nucleation rate theory. An extremely rare experimental result is also realized, namely that polymorphism can be controlled by the handedness of CP light. The precise control of polymorphism has been sought for many years and is an essential technology for industrial applications. The presented experimental results and findings will facilitate our academic understanding of light–matter interactions and inspire novel innovations in light-based molecular structural control.

## References

1. B.A. Garetz, J.E. Aber, N.L. Goddard, R.G. Young, A.S. Myerson, Nonphotochemical, polarization-dependent, laser-induced nucleation in supersaturated aqueous urea solutions. Phys. Rev. Lett. **77**, 3475 (1996). https://doi.org/10.1103/PhysRevLett.77.3475
2. S. Veesler, K. Furuta, H. Horiuchi, H. Hiratsuka, N. Ferté, T. Okutsu, Crystals from light: photochemically induced nucleation of hen egg-white lysozyme. Cryst. Growth Des. **6**, 1631–1635 (2006). https://doi.org/10.1021/cg0506424
3. T. Okutsu, Photochemically-induced crystallization of protein. J. Photochem. Photobiol. C: Photochem. Rev. **8**, 143–155 (2007). https://doi.org/10.1016/j.jphotochemrev.2007.06.002
4. A.J. Alexander, P.J. Camp, Single pulse, single crystal laser-induced nucleation of potassium chloride. Cryst. Growth Des. **9**, 958–963 (2009). https://doi.org/10.1021/cg8007415
5. A. Ikni, B. Clair, P. Scouflaire, S. Veesler, J.M. Gillet, N. El Hassan, F. Dumas, A. Spasojević-de Biré, Experimental demonstration of the carbamazepine crystallization from non-photochemical laser-induced nucleation in acetonitrile and methanol. Cryst. Growth Des. **14** 3286–3299 (2014). https://doi.org/10.1021/cg500163c
6. H.Y. Yoshikawa, R. Murai, H. Adachi, S. Sugiyama, M. Maruyama, Y. Takahashi, K. Takano, H. Matsumura, T. Inoue, S. Murakami, H. Masuhara, Y. Mori, Laser ablation for protein crystal nucleation and seeding. Chem. Soc. Rev. **43**, 2147–2158 (2014). https://doi.org/10.1039/C3CS60226E
7. T. Sugiyama, T. Adachi, H. Masuhara, Crystallization of glycine by photon pressure of a focused cw laser beam. Chem. Lett. **36**, 1480–1481 (2007). https://doi.org/10.1246/cl.2007.1480

8. A. Ashkin, J.M. Dziedzic, J.E. Bjorkholm, S. Chu, Observation of a single-beam gradient force optical trap for dielectric particles. Opt. Lett. **11**, 288–290 (1986). https://doi.org/10.1364/OL.11.000288
9. T. Rungsimanon, K. Yuyama, T. Sugiyama, H. Masuhara, Crystallization in unsaturated glycine/$D_2O$ solution achieved by irradiating a focused continuous wave near infrared laser. Cryst. Growth Des. **10**, 4686–4688 (2010). https://doi.org/10.1021/cg100830x
10. C.S. Wu, P.Y. Hsieh, K. Yuyama, H. Masuhara, T. Sugiyama, Pseudopolymorph control of l-phenylalanine achieved by laser trapping. Cryst. Growth Des. **18**, 5417–5425 (2018). https://doi.org/10.1021/acs.cgd.8b00796
11. G.R. Desiraju, Polymorphism: the same and not quite the same. Cryst. Growth Des. **8**, 3–5 (2008). https://doi.org/10.1021/cg701000q
12. I. Weissbuch, R. Popovitz-Biro, M. Lahav, L. Leiserowitz, Understanding and control of nucleation, growth, habit, dissolution and structure of two- and three-dimensional crystals using "Tailor-made" auxiliaries. Acta Crystallogr. Sect. B **51**, 115–148 (1995). https://doi.org/10.1107/S0108768194012061
13. A. Llinàs, J.M. Goodman, Polymorph control: past, present, and future. Drug Discov. Today **13**, 198–210 (2008). https://doi.org/10.1016/j.drudis.2007.11.006
14. J. Bernstein, Polymorphism - a perspective. Cryst. Growth Des. **11**, 632–650 (2011). https://doi.org/10.1021/cg1013335
15. A.J. Cruz-Cabeza, N. Feeder, R.J. Davey, Open questions in organic crystal polymorphism. Commun. Chem. **3**, 142 (2020). https://doi.org/10.1038/s42004-020-00388-9
16. J. Zaccaro, J. Matic, A.S. Myerson, B.A. Garetz, Nonphotochemical, laser-induced nucleation of supersaturated aqueous glycine produces unexpected $\gamma$-polymorph. Cryst. Growth Des. **1**, 5–8 (2001). https://doi.org/10.1021/cg0055171
17. K. Yuyama, T. Rungsimanon, T. Sugiyama, H. Masuhara, Selective fabrication of $\alpha$- and $\gamma$-polymorphs of glycine by intense polarized continuous wave laser beams. Cryst. Growth Des. **12**, 2427–2434 (2012). https://doi.org/10.1021/cg300065x
18. M.O. Portmann, D. Kilcast, Psychophysical characterization of new sweeteners of commercial importance for the EC food industry. Food Chem. **56**, 291–302 (1996). https://doi.org/10.1016/0308-8146(96)00026-X
19. J. Bongaerts, M. Krämer, U. Müller, L. Raeven, M. Wubbolts, Metabolic engineering for microbial production of aromatic amino acids and derived compounds. Metab. Eng. **3**, 289–300 (2001). https://doi.org/10.1006/mben.2001.0196
20. Y. Hirabayashi, S. Furuya, Roles of L-serine and sphingolipid synthesis in brain development and neuronal survival. Prog. Lipid Res. **47**, 188–203 (2008). https://doi.org/10.1016/j.plipres.2008.01.003
21. L. Gong, B. Gu, G. Rui, Y. Cui, Z. Zhu, Q. Zhan, Optical forces of focused femtosecond laser pulses on nonlinear optical Rayleigh particles. Photonics Res. **6**, 138–143 (2017). https://doi.org/10.1364/PRJ.6.000138
22. W.Y. Chiang, T. Okuhata, A. Usman, N. Tamai, H. Masuhara, Efficient optical trapping of CdTe quantum dots by femtosecond laser pulses. J. Phys. Chem. B **118**, 14010–14016 (2014). https://doi.org/10.1021/jp502524f
23. H.Y. Yoshikawa, Y. Hosokawa, H. Masuhara, Explosive crystallization of urea triggered by focused femtosecond laser irradiation. Jpn. J. Appl. Phys. **45**, L23–L26 (2006). https://doi.org/10.1143/JJAP.45.L23
24. L. Pan, A. Ishikawa, N. Tamai, Detection of optical trapping of CdTe quantum dots by two-photon-induced luminescence. Phys. Rev. B **75**, 161305 (2007). https://doi.org/10.1103/PhysRevB.75.161305
25. Y. Harada, T. Asakura, Radiation forces on a dielectric sphere in the Rayleigh scattering regime. Opt. Commun. **124**, 529–541 (1996). https://doi.org/10.1016/0030-4018(95)00753-9
26. P.R. ten Wolde, D. Frenkel, Homogeneous nucleation and the Ostwald step rule. Z. Phys. Chem. Chem. Phys. **1**, 2191–2196 (1999). https://doi.org/10.1039/A809346F
27. C.S. Wu, H. Y. Yoshikawa, T. Sugiyama, Bidirectional polymorphic conversion by focused femtosecond laser irradiation. Jpn. J. Appl. Phys. **59**, SIIH02 (2020). https://doi.org/10.35848/1347-4065/ab7ae2

28. R. Mohan, K.K. Koo, C. Strege, A.S. Myerson, Effect of additives on the transformation behavior of L-phenylalanine in aqueous solution. Ind. Eng. Chem. Res. **40**, 6111–6117 (2001). https://doi.org/10.1021/ie0105223
29. J. Lu, Q. Lin, Z. Li, S. Rohani, Solubility of L-phenylalanine anhydrous and monohydrate forms: experimental measurements and predictions. J. Chem. Eng. Data. **57**, 1492–1498 (2012). https://doi.org/10.1021/je201354k
30. A. Brodeur, S.L. Chin, Ultrafast white-light continuum generation and self-focusing in transparent condensed media. J. Opt. Soc. Am. B **16**, 637–650 (1999). https://doi.org/10.1364/JOSAB.16.000637
31. S.L. Chin, A. Brodeur, S. Petit, O.G. Kosareva, V.P. Kandidov, Filamentation and supercontinuum generation during the propagation of powerful ultrashort laser pulses in optical media (white light laser). J. Nonlinear Opt. Phys. Mater. **8**, 121–146 (1999). https://doi.org/10.1142/S0218863599000096
32. A. Saliminia, S.L. Chin, R. Vallée, Ultra-broad and coherent white light generation in silica glass by focused femtosecond pulses at 1.5 μm. Opt. Exp. 13, 5731–5738 (2005). https://doi.org/10.1364/OPEX.13.005731
33. J. Lu, J. Wang, Z. Li, S. Rohani, Characterization and pseudopolymorphism of l-phenylalanine anhydrous and monohydrate forms. Afr. J. Pharm. Pharmacol. **6**, 269–277 (2012). https://doi.org/10.5897/AJPP11.842
34. Y. Hosokawa, H. Adachi, M. Yoshimura, Y. Mori, T. Sasaki, H. Masuhara, Femtosecond laser-induced crystallization of 4-(dimethylamino)-N-methyl-4-stilbazolium tosylate. Cryst. Growth Des. **5**, 861–863 (2005). https://doi.org/10.1021/cg049709y
35. T. Uwada, S. Fujii, T. Sugiyama, A. Usman, A. Miura, H. Masuhara, K. Kanaizuka, M. Haga, Glycine crystallization in solution by cw laser-induced microbubble on gold thin film surface. ACS Appl. Mater. Interfaces **4**, 1158–1163 (2012). https://doi.org/10.1021/am201799b
36. W.C. Wang, S.F. Wang, T. Sugiyama, L-serine polymorphism controlled by optical trapping with high-repetition-rate femtosecond laser pulses. J. China Chem. Soc. (2021) in print
37. R.M. Dannenfelser, S.H. Yalkowsky, Sci. Total Environ. **109–110**, 625–628 (1991). https://doi.org/10.1016/0048-9697(91)90214-Y
38. T. Tsuji, R. Nakatsuka, K. Nakajima, K. Doi, S. Kawano, Effect of hydrodynamic interparticle interaction on the orbital motion of dielectric nanoparticles driven by an optical vortex. Nanoscale **12**, 6673–6690 (2020). https://doi.org/10.1039/C9NR10591C
39. F. Nito, T. Shiozaki, R. Nagura, T. Tsuji, K. Doi, C. Hosokawa, S. Kawano, Quantitative evaluation of optical forces by single particle tracking in slit-like microfluidic channels. J. Phys. Chem. C **122**, 17963–17975 (2018). https://doi.org/10.1021/acs.jpcc.8b02701
40. P.T.C. Freire, F.M. Barboza, J.A. Lima, F.E.A. Melo, J.M. Filho, Raman spectroscopy of amino acid crystals, in *Raman Spectroscopy and Applications.* ed. by K. Maaz (IntechOpen Limited, London, 2017), pp. 210–215
41. C.J. Luk, Solubility and pseudo-polymorphic transitions of L-serine in water-methanol system, Thesis in Georgia Institute of Technology, 1, 1–103 (2005). http://hdl.handle.net/1853/6832
42. K. Linhong, L. Daniel, C. Petr, Refractive indices of water and ice in the 0.65- to 2.5-μm spectral range. Appl. Opt. **32**, 3531–3540 (1993). https://doi.org/10.1364/AO.32.003531

# Chapter 16
# Electrocatalysts Developed from Ion-Implanted Carbon Materials


**Tetsuya Kimata, Kazutaka Nakamura, and Tetsuya Yamaki**

**Abstract** Ion implantation is known as a powerful tool to modify a host material by energetic effects such as sputtering, impurity doping, and defect creation. In addition to semiconductor-device manufacturing, the development of catalytic materials has been an emerging application for realizing electrochemical energy conversion and storage devices including water-splitting and fuel cells. This chapter deals with ion implantation in different carbon materials implementing two strategic concepts based on morphology and electronic structures; i.e., nanoparticle (NP) formation and surface/interface modification. Initially, the metal-ion-implanted NPs were exposed on the top surface of the carbon support to work as an electrocatalyst, while they are embedded in the carbon support to indirectly affect the surface morphology and active sites of the surrounding carbon-based electrocatalysts. Next, the N-doping in carbon was very effective in controlling the surface of the carbon-based catalyst or the interface states between a metal-NP catalyst and a carbon support. Finally, implantation-induced defects in the graphitic lattice controlled the NP-support interface so that the electrocatalytic activity of the overlying NPs could be improved. Ion beam technology can offer a new approach for catalyst design toward the improvement of the activity and durability.

**Keywords** Ion implantation · Electrocatalyst · Nanoparticle · Carbon material · Electrochemical devices · Water electrolysis · Fuel cell

T. Kimata · T. Yamaki (✉)
Takasaki Advanced Radiation Research Institute, National Institutes for Quantum Science and Technology, 1233 Watanuki, Takasaki 370-1292, Gunma, Japan
e-mail: yamaki.tetsuya@qst.go.jp

K. Nakamura
Laboratory for Materials and Structures, Institute for Innovative Research, Tokyo Institute of Technology, 4259 Nagatsuta, Yokohama, Kanagawa 226-8503, Japan



Y. Ishikawa et al. (eds.), *High-Energy Chemistry and Processing in Liquids*,
https://doi.org/10.1007/978-981-16-7798-4_16

## 16.1 Introduction

High-energy chemistry usually deals with the interactions of high-energy radiation with matter and the chemical properties or reactivity of the thereby-induced short-lived species. This scientific discipline has attracted much attention due to its potential application in various fields including physics, biology, and materials science, reflecting the expectation that high-energy triggered reactions might be different from those caused by annealing or photo-irradiation. Ionizing radiation, such as electrons and γ-rays, are commonly used in high-energy chemistry research; if ion beams are used instead, an unprecedented impact can be given to the electronic and lattice systems in solids because of their extremely high linear energy transfer (LET) (defined as the mean energy deposited per unit path length in the absorbing material). For example, a 380 keV Ar ion in graphite has an LET value of 1300 keV/μm, whereas the value is 0.2 keV/μm for a $^{60}$Co γ photon.

Ion beam technology is an efficient tool for realizing material modification. In the process of collisions between the incoming ions and the target atoms, energetic ions transfer energy to the nuclei and electrons in the target material, resulting in a series of effects such as sputtering, impurity doping, and defect creation (target atomic displacement). This will cause some changes in the electronic and atomic structures of the material. Ion implantation cannot only achieve reliable and precise doping of almost all elements, but also enable deliberate defect engineering and morphology control, which are all important aspects of catalysis and catalyst preparation.

Figure 16.1 shows a schematic image of how the ion implantation technique can be used to create catalysts for electrochemical devices. There have been two main strategic concepts based on morphology and electronic structures for electrocatalyst design: nanoparticle (NP) formation and surface/interface modification. In these approaches, a critical implantation parameter is the ion dose, i.e., the fluence, which determines the total number of implanted ions. Low-fluence implantation, in which the implants are dispersed (isolated from one another), causes radiation-induced defects owing to the very large amount of energy transferred and may be used to engineer the defect structure and even the nano-morphology of the material. If the fluence of the implanted ions exceeds the solid solubility of the material, the implanted ions will start to diffuse and form precipitate nuclei, which may then grow into NPs; post-irradiation annealing treatment sometimes promotes NP formation. Furthermore, depending on their energy, the implanted ions will eventually stop, through cascade collisions, at a certain position; this results in the concentration of implanted ions being maximum near the average range. Thus, the depth distributions of implants, defects, and the resulting heterostructures or nanostructures in the target material can be controlled by varying the acceleration energy.

An electrocatalyst is a type of catalyst that participates in electrochemical reactions and functions at electrode surfaces or, most commonly, as the electrode surface itself. Major challenges of electrocatalysts focus on a variety of electrochemical energy conversion and storage devices including water-splitting and fuel cells. In the water-electrolysis system, hydrogen gas and oxygen gas are produced by a hydrogen

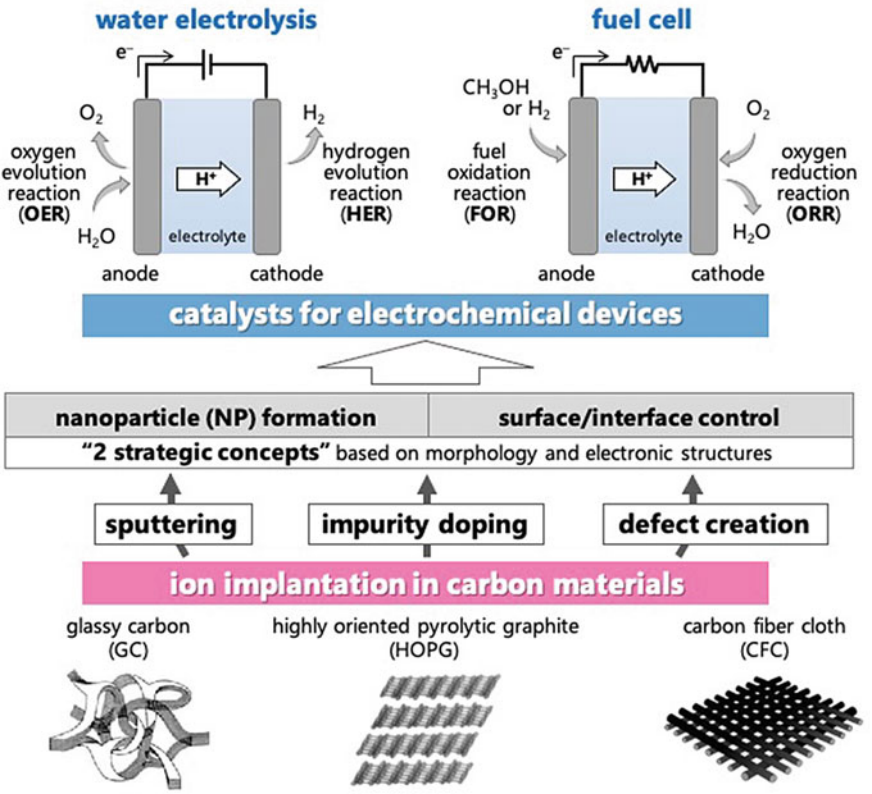


**Fig. 16.1** Schematic image of how ion implantation in carbon materials can be used to develop catalysts for electrochemical devices including water-splitting and fuel cells

evolution reaction (HER) and an oxygen evolution reaction (OER) at the cathode and anode, respectively. On the other hand, proton exchange membrane fuel cells (PEMFCs) involve the cathodic oxygen reduction reaction (ORR) and anodic fuel oxidation reaction (FOR) processes. While most PEMFCs are powered by the direct hydrogen supply as a fuel, some of them can be fueled by liquid methanol and referred to as direct methanol fuel cells (DMFCs). Noble or non-noble metal-based electrocatalysts are normally supported on carbon materials for high conductivity, high mechanical stability, high electrochemical or chemical stability, and high surface area. Besides, many studies have shown that the carbon materials themselves have electrocatalytic activities for the HER, ORR, etc.

This chapter describes the application of ion implantation in carbon materials to develop electrocatalysts for renewable energy storage and conversion devices. The target samples include glassy carbon (GC), highly oriented pyrolytic graphite

(HOPG), and carbon fiber cloth (CFC) for different research purposes. After introducing a trend toward this research field in Sect. 16.2, we report the NP preparation by ion implantation in carbon materials for the HER and ORR catalysts in Sect. 16.3. The resulting NPs have important roles in electrocatalysis; the embedded transition-metal-NPs indirectly affected the surface morphology and active site of the surrounding carbon-based electrocatalysts, while metal-carbide NPs exposed on the top surface could work directly as a catalyst. Section 16.4 describes the control of the surface or interface states by impurity doping. The N-doping in carbon was found very effective for the selective formation of the ORR active site on the carbon-based catalyst and improvement of the interfacial structure between a metal-NP catalyst and carbon support. Finally, in Sect. 16.5, we deal with the NP-carbon support interface controlled by atomic defects as a new approach of catalyst design using an ion implantation technique. Due to its high accuracy and controllability, ion beam technology can help researchers to quantitatively clarify the in-depth mechanism of the interfacial interaction and the structure-activity relationship as a significant challenge in electrocatalyst research, i.e., improvement of their activity and durability.

## 16.2 Research Trend in NP Synthesis Using Ion Implantation

Figure 16.2 shows ion implantation for NP formation in different substrates toward wide-ranging application fields. This technique was applied in glass matrices because it is unaffected by solubility restrictions or vaporization; thus, a large amount of NPs

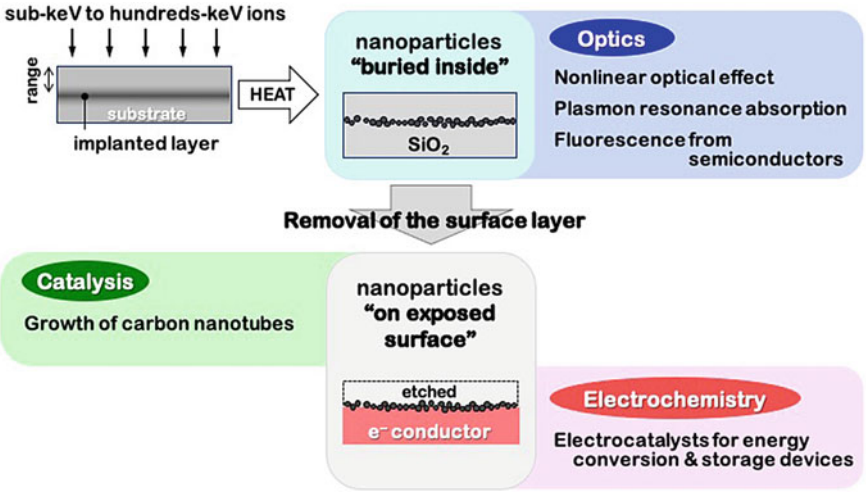


**Fig. 16.2** Ion implantation for NP formation in different substrates toward wide-ranging application fields

can be dispersed in a transparent dielectric material. The nonlinear optical properties of such NPs, in particular, the enhancement of the optical Kerr susceptibility by both dielectric and quantum-confinement effects, suggested a promising method for the production of all-optical switching devices. Indeed, it was reported that implantation of silica glass with 1.5 MeV $Au^+$ at $10^{17}$ ions/cm$^2$ and subsequent heating at 700–900 °C led to the formation of Au NPs with a large third-order nonlinear optical susceptibility, $\chi^{(3)}$, of $1.2 \times 10^{-7}$ esu [1]. Researchers have also been interested in producing NPs at certain depths to investigate plasmon resonance absorption and fluorescence from semiconductors.

In contrast to the above optical applications, for catalysts the surface layer must be removed to expose the buried NPs. For example, after a surface etching process, NPs in silicon dioxide ($SiO_2$) could be used as a catalyst for the growth of carbon nanotubes (CNTs) [2]. A 500-nm-thick thermally-oxidized $SiO_2$ layer on a Si wafer was implanted at room temperature with 100 keV Ni ions at fluences between $10^{15}$ and $10^{17}$ ions/cm$^2$ and was then heated at 900 °C in $N_2$ gas. The projected range of the implanted ions (defined as the depth with their maximum concentration) was estimated to be 75 nm by a Monte Carlo calculation using the "SRIM" code and Rutherford backscattering (RBS) measurements. Thus, the annealed samples were further dipped in an aqueous solution of 1% hydrogen fluoride for chemical etching of the surface $SiO_2$ layer and exposure of Ni NPs on the top surface. The resulting Ni NPs precipitated on a $SiO_2$ surface became a catalyst for the growth of CNTs through decomposition of hydrocarbon using a chemical vapor deposition process; interestingly, their controlled size determined the diameters of the grown CNTs. This work may provide an effective way for seeding catalyst NPs in high-aspect-ratio via/trench structures for microelectronic devices.

Applications in electrochemical devices need the electrode catalysts to have electric contact; in other words, catalyst NPs must be deposited on a conductive substrate. A versatile method was developed to prepare Pt NPs on the surface of an indium tin oxide (ITO) electrode for applications in DMFCs [3]. In the experiments, a sheet of ITO glass was implanted at room temperature with 21 keV Pt ions at a fluence of $1.0 \times 10^{17}$ ions/cm$^2$. In this example, small Pt NPs (average diameter of 8 nm) were uniformly deposited on the ITO surface without any post-annealing processes. This may be because (i) the projected range was very short and (ii) surface sputtering occurred concurrently with implantation. High methanol oxidation activity was confirmed by cyclic voltammetry (CV) in an aqueous solution containing 1.0 M $CH_3OH$ and 0.1 M $H_2SO_4$. The material showed excellent long-term stability, making it a good alternative FOR catalyst at the anode.

## 16.3 Ion-Implanted NP Electrocatalysts on Carbon Materials for HER and ORR Catalysts

In the past few decades, various efforts have been made to understand the key interfacial reaction process of electrochemical water-splitting. The purpose of catalyst design is to increase the number of active electrocatalytic sites or to improve the intrinsic activity of such active sites. To achieve these goals, it is usually necessary to change the electronic structure and microstructure–nanostructure of catalyst materials, both of which can be modulated by varying the interaction between the implanted ion and the material. Highly controllable and precise ion-beam technology can help reveal the relationships between the defect structure, electronic structure, and catalytic performance, possibly enabling further improvements in activity and durability.

The results of metal-ion implantation in carbon materials vary greatly depending on the miscibility of the two elements. If the implanted element has very low miscibility, its agglomeration by heat treatment is usually required to produce NPs. As an example, the formation of Ni NPs from Ni-ion-implanted CFC is described in Sect. 16.3.1. On the other hand, when the miscibility is high, such as for W, it reacts easily even at room temperature to produce carbide NPs. In Sect. 16.3.2, this is exemplified by the formation of various types of tungsten carbide NPs in W-ion-implanted GC substrates.

### *16.3.1 Nickel-Ion Implantation in CFC*

Transition-metal (Ni, Fe, and Co) NPs were embedded in large-scale CFC by ion implantation to prepare carbon-based catalysts with improved HER performance in acidic (0.5 M $H_2SO_4$), basic (1 M KOH), and neutral (0.5 M phosphate buffer) solutions [4]. As shown in Fig. 16.3, the Ni-ion-implantation was performed at 60 keV at fluences of $2 \times 10^{15}$, $2 \times 10^{16}$, $1 \times 10^{17}$, and $2 \times 10^{17}$ ions/cm$^2$, followed by annealing in an $N_2$ atmosphere at 500 °C. The projected range of implanted $Ni^+$ was estimated to be 47 nm.

The diameter of the embedded Ni NPs ranged from 10 to 30 nm, and their formation was attributed to the following mechanism. $Ni^+$ implantation can produce numerous vacancies in materials; implanted Ni atoms can be absorbed by the produced vacancies and their aggregation probably leads to the formation of NPs. With increasing $Ni^+$ fluence, the NPs will grow by absorbing more Ni atoms and merge with nearby NPs. At the same time, the surface C atoms would be stripped due to the surface sputtering effect; as a result, the NPs near the surface would be exposed. Finally, the exposed Ni NPs would be dissolved by the acid treatment to produce a nanoporous structure with pore sizes between 70 and 150 nm.

Density functional theory (DFT) calculations demonstrated that when graphene is embedded with Ni NPs, electrons in Ni NPs can flow to carbon atoms, which would

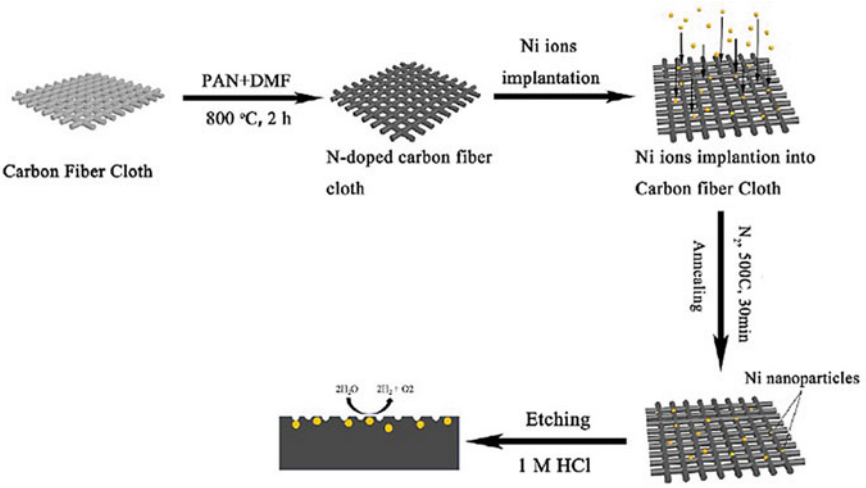


**Fig. 16.3** Schematic of the fabrication of Ni-NP-embedded CFC by $Ni^+$ implantation. Reprinted from Wu et al., Electrochim. Acta 353, 136475 (2020), with permission from Elsevier

effectively reduce the Gibbs free energy for $H^*$ adsorption (the asterisk denotes an adsorbed species). A similar effect would occur in Ni-NP-embedded CFCs and thus result in the enhanced HER activity. It was confirmed by using $Fe^+$ and $Co^+$ implantation that the metal-NP-embedded CFC was fabricated at large scale, for low cost, and with high efficiency; the present method is general for the fabrication of non-noble metal NP catalysts.

### *16.3.2 Tungsten-Ion Implantation in GC*

Implantation with W ions has so far been studied in terms of their reactivity with a matrix. The W-ion implantation in silica led to the formation of metallic-W precipitates with a small amount of W oxides [6]; however, the W-ion implantation in GC is expected to generate carbides [7]. In fact, tungsten carbide (WC) has been expected to be an alternative to noble metal catalysts because of its Pt-like electronic state [5]. Thus, Kato et al. prepared NPs of W carbides by W-ion implantation in a GC substrate and investigated their electrochemical and morphological properties [8]. GC, in which a lot of graphite-structure-shaped thin strips intertwine with each other, is the most commonly used electrode material in electrochemistry. The $W^+$ implantation was performed using an energy of 100 keV at nominal fluences up to $1.8 \times 10^{17}$ ions/cm$^2$. The implanted samples were analyzed by RBS, X-ray photoelectron spectroscopy (XPS), hydrodynamic voltammetry using a rotating disk electrode, and cross-sectional transmission electron microscopy (TEM).

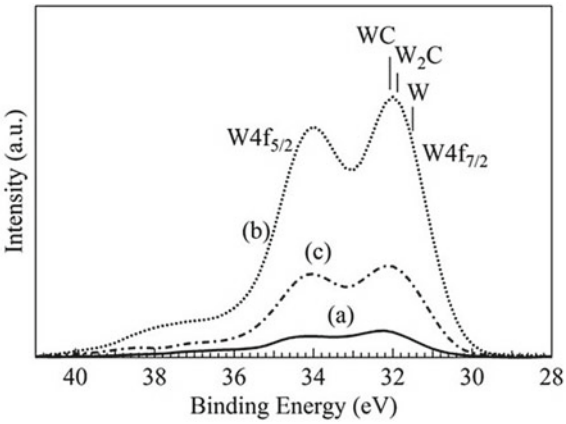


**Fig. 16.4** XPS W 4f spectra of the $W^+$-implanted GC sample after the $Ar^+$ sputtering for **a** 30, **b** 180, and **c** 300 s. The sputtering rate was 0.2 nm/s. The figure was taken from Kato et al., Trans. Mat. Res. Soc. Japan 38, 81 (2013)

According to the RBS results, a significant sputtering effect limited the maximum retained fluence to approximately $6 \times 10^{16}$ ions/cm$^2$. Figure 16.4 shows XPS W 4f spectra of the implanted GC substrate after $Ar^+$-beam sputtering for different times. The concentration of W increased during the course of sputtering and peaked at 180 s. A peak for the W $4f_{7/2}$ state at ca. 32.1 eV (~0.6 eV higher than that of metallic-W) can be ascribed to carbides, WC. The surface GC layer would be eroded away until the sputtering front reached the implanted layer, which had originally been distributed around the projected range (calculated at 55 nm using the "SRIM" code). The current density in the voltammogram, representing the electrochemical activity of the surface, was lower for the W-implanted sample than for the non-implanted one. This is probably caused by a decrease in the surface area resulting from the observed sputtering effect, because WC is known to have low activity in the measured potential range [9].

Subsequent electrochemical etching in a 0.1 M NaOH aqueous solution achieved the maximum area density of the NPs on the surface [10]. Figure 16.5 shows a cross-sectional TEM micrograph of the resulting sample, in which the implanted layer is situated between the GC substrate and a carbon layer deposited during specimen

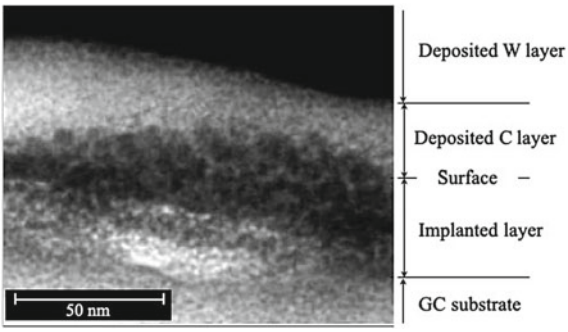


**Fig. 16.5** TEM micrograph of the GC substrate $W^+$-implanted at $2.4 \times 10^{16}$ ions/cm$^2$ and then etched electrochemically in an alkaline aqueous solution. During specimen preparation in a cross-sectional geometry, C and W layers were deposited on the surface

preparation. Particulate aggregates near the surface were found to contain spherical NPs with a diameter of <10 nm.

## 16.4 Surface/Interface States Controlled by Impurity Doping in HOPG

### *16.4.1 Surface Modification by Nitrogen-Ion Implantation for Carbon-Alloy ORR Electrocatalysts*

Many groups have reported that carbon materials themselves can exhibit significant ORR performance upon their optimized N-doping, without any precious or non-precious transition metal components [11, 12]. In other words, an increase in the current density and a decrease in the overpotential for the ORR in acidic and alkaline PEMFCs were observed for such metal-free N-doped systems when compared with undoped references. Most of these studies focused on N-doped CNTs and graphene, and a few also reported on carbon blacks, porous carbons, carbon nanoshells, and other materials [13]. In this regard, N-ion implantation offers the following two advantages over other energetic post-treatment methods: (i) a more balanced mix of nitrogen functionalities is produced, whereas pyrrolic-N (N directly bonded to two $sp^2$-hybridized C and one H neighbors) (see Fig. 16.6) was the dominant species created by plasma modification; (ii) controlled impurity densities of uniform distribution are created, especially in graphene and related nanostructures.

In addition, N implantation in HOPG was performed to obtain a detailed picture of the local electronic modifications in N-doped graphite induced by each different type of N atom, thereby leading to the identification of the active sites for the ORR. A HOPG substrate was irradiated at 300 K and normal incidence with a 200 or 500 eV N-ion beam at a fluence of $0.2 \times 10^{13}$ ions/cm$^2$, followed by annealing at $900 \pm 50$ K for 300 s to clean and thoroughly graphitize the surface. Two types of N species were identified at the atomic level: pyridinic-N (N bonded to two $sp^2$-hybridized C nearest neighbors) and graphitic-N (N bonded to three $sp^3$-hybridized C nearest neighbors) (see Fig. 16.6). Distinct localized $\pi$-electronic states appeared

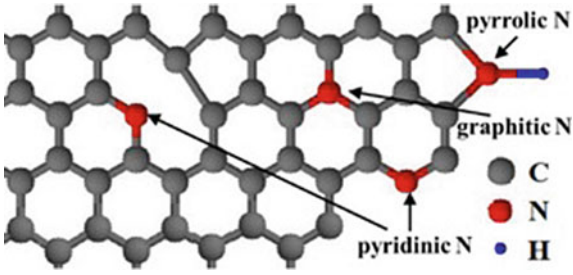


**Fig. 16.6** Nitrogen species doped in $sp^2$-bonded carbon atoms. The figure is obtained from the paper, Takahashi et al., IEEJ Trans. Ind. Appl. (Denki Gakkai Ronbunshi A) 139, 140 (2019)

in the occupied and unoccupied regions near the Fermi level at the carbon atoms around pyridinic-N and graphitic-N species, respectively [14].

The ORR active site was characterized by using newly designed HOPG model catalysts with well-defined π conjugation and well-controlled doping with N species: (i) pyridinic-N-dominated HOPG, and (ii) graphitic-N-dominated HOPG; and, for comparison, (iii) undoped HOPG with the edges patterned on the surface, and (iv) undoped HOPG annealed in ultra-high vacuum [12]. A key was extremely-sophisticated sample preparation using the additional $Ar^+$-beam irradiation and post-irradiation annealing in $NH_3$ at 973 K. As a result, pyridinic-N in N-doped graphitic carbons was found to create the active sites for ORR under acidic conditions. Carbon dioxide adsorption experiments indicated that pyridinic-N also created Lewis basic sites. The specific activities per pyridinic-N in the HOPG model catalysts were comparable with those of N-doped graphene powder catalysts. Thus, the ORR active sites in N-doped carbon materials would be carbon atoms with Lewis basicity next to pyridinic-N. The other paper evaluated the effect of surface structure imperfections, i.e., a roughness change, induced by sputtering due to the low-energy ion beam [15].

### *16.4.2 Interface Structures Between Platinum-NPs and a Nitrogen-Ion-Implanted Support*

An important trend in electrocatalysis began with the studies on the effects of doping in catalyst supports by Shukla et al. [16] and Roy et al. [17]. Their observations suggested that carbon-based catalyst supports could be intentionally modified to create strong, beneficial catalyst–support interactions, thereby substantially enhancing electrocatalytic activity and stability. Particularly, N-doping was found to provide as much as threefold to tenfold enhancement for both the FOR and the ORR in Pt/C-based catalyst systems for DMFCs and PEMFCs, respectively. Although this basic idea was expected to open the door to a game-changing new method for catalyst design with applications in various electrochemical devices, uncertainties associated with complex preparation of Pt/C powder samples made it difficult to determine the precise effect of N-doping. Therefore, researchers have developed geometrically well-defined model catalytic systems consisting of Pt NPs on clean, planar model substrates of N-ion-implanted HOPG.

Studies on the structural and chemical modifications in N-implanted HOPG identified the potential fundamental mechanisms and ascertained the nature of catalyst–support interactions for the enhanced activity and stability of Pt/C-based electrocatalysts [18, 19]. The N-implantation was done at room temperature using a non-mass-separated N-ion beam ($N_2$ and N ions) at different fluences between $10^{15}$ and $10^{17}$ ions/cm$^2$. Typical ion beam energy, ion current, and irradiation time were 100 eV, 10–12 mA, and 45 s, respectively. The incident angle of the beam was 35° to the surface to enhance surface doping and eliminate ion channeling. During the course of irradiation, the incremental increase in structural damage was marginal, while the

percentage of N on the HOPG surface continued to increase significantly. In the end, both the level of the damage and the amount of N reached saturation; a near-surface N saturation level of approximately 6–8 atomic % was achieved. The N implantation led to the transformation of the initial pure $sp^2$-hybridized graphitic carbon into $sp^3$-hybridized carbon together with N incorporation into the graphitic network in the graphitic, pyridinic, and pyrrolic forms.

Pt NPs were electrodeposited on the irradiated HOPG substrate from aqueous solutions containing $H_2PtCl_6$ and $HClO_4$. Doping a graphite support with N was found to affect both the morphology and the behavior of the overlying Pt NPs. Particularly, N-doping seemed to cause a significant decrease in the average Pt NP size and an increase in the Pt NP dispersion. Negatively charged, electron-rich donor states introduced on the graphite surface could act as local heterogeneous nucleation sites for Pt deposition, which facilitated the deposition of finer, better dispersed Pt NPs. Such a morphology was a highly desirable feature for Pt catalyst application; however, the catalytic enhancement in the N-doped sample could not be attributed to simple geometric effect alone, implying that there was also a contribution from other intrinsic effects.

Therefore, direct electronic structure determinations were conducted experimentally and theoretically to explore the nature of the electronic interactions between Pt NPs and N-doped carbon supports. According to capacitance and XPS measurements and quantum simulations using DFT [19], the N-doping would increase the electron transfer from the Pt NPs to the graphite support. The resulting decreased electron density of the Pt is likely to then facilitate the reactions on the electrode. The modified electronic structure of the Pt catalyst might alter the Pt-adsorbate bond strength and significantly enhance the durability.

## 16.5 Defect-Controlled Interface Between Platinum-NPs and Carbon Support

In this section, we discuss experiments in which the structure of the interface between the carbon support and Pt NPs was manipulated by ion-beam-induced defects in the carbon support. Such interfacial effects are newly proposed as a promising approach to obtain highly active and durable Pt NP electrocatalysts. As a model catalyst for examining the interface, HOPG substrates were implanted with chemically-inert Ar ions and then overlaid physically with Pt NPs. One major focus is the electronic and lattice structures of the $Ar^+$-implanted and Pt-deposited HOPG surface; Raman spectroscopy and X-ray absorption structure (XAS) measurements were used to explorer how the implantation affected the carbon support for the Pt NPs. The next hypothesis of special interest was that the vacancies introduced in the graphitic lattice could modify the electronic structure of the Pt NPs, which could then lead to the improvement of the ORR performance [20, 21]. The state of the Pt 5d valence band could be affected by the microscopic interaction with atomic vacancies, and

its quantitative information from DFT calculations was correlated with the ORR activity. The XPS analysis of the Pt 4f core levels provided the chemical state of the Pt atoms interacting with the implanted carbon support. We introduce the concept that altering the interfacial structure through ion-beam-induced defects can improve the ORR activity of Pt NP catalysts.

### *16.5.1 Structures of Ion-Implanted and Platinum-Deposited HOPG Surfaces*

Raman spectroscopy was performed to investigate the defect structure at the $Ar^+$-irradiated and Pt NP-deposited HOPG surface. The HOPG was irradiated with 380 keV $Ar^+$ at different fluences between $1.0 \times 10^{12}$ and $1.0 \times 10^{14}$ ions/cm$^2$, and then Pt NPs were deposited using radio-frequency (RF) magnetron sputtering for 60 s at room temperature. The mean particle sizes of the Pt NPs obtained on the non-irradiated HOPG and the HOPG irradiated at fluences of $1.0 \times 10^{12}$ and $5.0 \times 10^{13}$ ions/cm$^2$ were determined to be 2.85, 3.11, and 6.02 nm, respectively, based on TEM observations [22].

Figure 16.7 shows the Raman spectra of the pristine and pre-irradiated HOPG surfaces before and after the Pt deposition. The Raman spectrum of HOPG has three peaks between 500 and 2000 cm$^{-1}$; the D and D′ bands were observed at approximately 1350 and 1620 cm$^{-1}$, respectively, and the G band was seen at 1583.5 cm$^{-1}$. The surface structure of irradiated HOPG was examined by taking the D/D′ and D/G intensity ratios and G-peak shifts, thereby making further discussion on the configuration of the Pt-carbon support interface as well. Analysis of the D/D′ intensity ratio led to the following two key findings: (i) vacancy-like defects were formed on the HOPG surface by $Ar^+$-irradiation at fluences between $1.0 \times 10^{12}$ and $1.0 \times 10^{13}$ ions/cm$^2$; (ii) sp$^3$ defects were induced by irradiation at $5.0 \times 10^{13}$ ions/cm$^2$ or more [22].

Pt NPs were deposited on these irradiated HOPG surfaces, and then the G-peak positions were compared before and after the Pt deposition [23]. At a fluence of $5.0 \times 10^{13}$ ions/cm$^2$ or greater, the red Raman shifts were more obvious after the Pt deposition, as shown in Fig. 16.8a. This result indicates that the Pt deposition caused tensile stress in the graphitic structure of the HOPG irradiated at higher fluences. The phonon correlation length $L_a$ was evaluated from the peak intensity ratio (R = D/G), where $L_a = 4.4/R$ (nm). Figure 16.8b shows a plot of the $L_a$ value as a function of the fluence for the irradiated HOPG with and without the Pt NPs. Interestingly, the $L_a$ value decreased greatly by the Pt deposition at a fluence of $1.0 \times 10^{12}$ ions/cm$^2$, but this effect became minimized at the higher fluences. At a fluence of $1.0 \times 10^{13}$ ions/cm$^2$ (with Pt), the $L_a$ was calculated to be 3.59 nm, which implies that the approximately three point defects on the HOPG surface would be present underneath the Pt NP with a diameter of 5 nm.

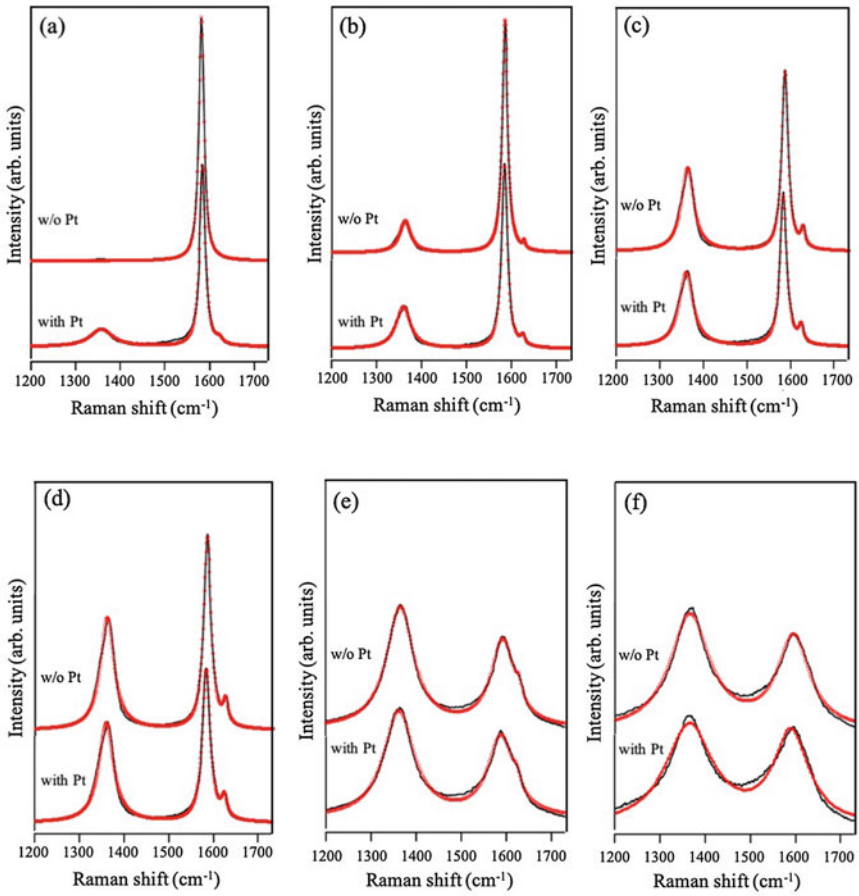


**Fig. 16.7** **a** Raman spectra of the non-irradiated HOPG without (w/o) and with Pt deposition. Raman spectra of the HOPG irradiated with $Ar^+$ at fluences of **b** $1.0 \times 10^{12}$, **c** $5.0 \times 10^{12}$, **d** $1.0 \times 10^{13}$, **e** $5.0 \times 10^{13}$, and **f** $1.0 \times 10^{14}$ ions/cm$^2$. Red circles and black curves represent experimental data and Lorentz curve fits, respectively. These figures were obtained by modifying Figs. 16.2 and 16.3 of the paper, Kimata et al., Nucl. Instrum. Meth. Phys. Res. B 444, 6 (2019)

Next, the electronic states of the interface between the Pt NPs and the irradiated carbon support were investigated by surface-sensitive XAS measurements at the C K-edge [24]. The HOPG substrates were irradiated with 380 keV $Ar^+$ at a fluence of $1.0 \times 10^{14}$ ions/cm$^2$. HOPG substrates were employed so that the electronic structure could be resolved into orbital components ($\sigma$ and $\pi$ bonds). Pt NPs were then deposited by RF magnetron sputtering for 20 s at room temperature. The Pt deposition was also done on non-irradiated HOPG substrates for comparison.

As shown in Fig. 16.9, the C K-edge XAS spectra for the HOPG, the irradiated HOPG, Pt/HOPG, and Pt/irradiated HOPG were measured and then fitted with Gaussian functions. The HOPG exhibited five main peaks from a C–C $\pi^*$ orbital (Peak A

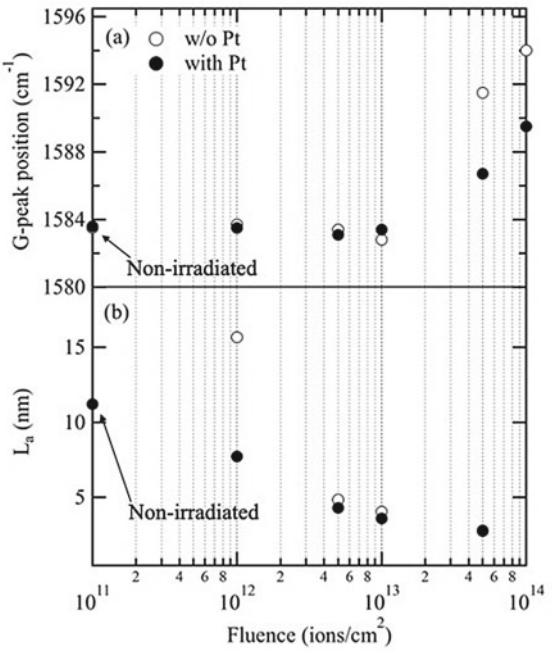


**Fig. 16.8** **a** Position of the G-peak and **b** value of $L_a$ plotted against the $Ar^+$ fluence (open circles: without Pt, filled circles: with Pt). This figure is obtained by modifying Figs. 16.4 and 16.5 of the paper, Kimata et al., Nucl. Instrum. Meth. Phys. Res. B 444, 6 (2019)

at ~285 eV), surface carbon with adsorbates (Peak B located at ~288 eV), $\pi_2$ orbital (Peak C at 289.0 eV), $\sigma^*$ orbital (Peak D at ~291.5 eV), and $\sigma_1$ orbital (Peak E at 292.5 eV). The shoulder structure around 284 eV (Peak F) was observed for Pt/non-irradiated HOPG, indicating the occurrence of Pt–C interaction at the interface. The intensity of this shoulder increased for Pt/irradiated HOPG. Therefore, the vacancies in the irradiated carbon support would induce changes in the Pt–C interaction, leading to different electronic structures at the interface. The previous paper reported that the Pt NPs on an irradiated carbon support were distorted [25]. According to the result of Fig. 16.9, the Pt–C interaction could be an origin of the observed distortion of the Pt NPs. This distortion is likely to lower the d-band center and improve the ORR activity of the Pt NPs.

### *16.5.2 Electronic Structure of Platinum-NPs on Defective Graphite Structure for Electrocatalytic Applications*

To investigate the influence of the defects in the carbon support on the electronic state of Pt atoms, DFT calculations were performed for Pt clusters on various defective graphite structures [26]. The model for the calculations comprised three layers of graphene and an icosahedral $Pt_{13}$ cluster. Each graphitic layer had a $5 \times 5$ structure, that is, 50 carbon atoms. To simulate the irradiation-induced defects, vacancies with

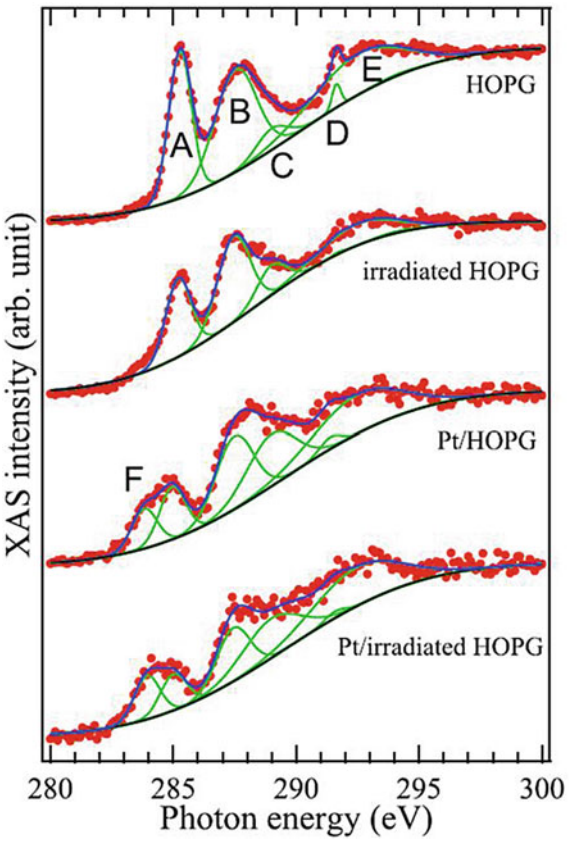


**Fig. 16.9** Peak fitting results for all XAS spectra. The red dots, blue line, and green lines indicate the experimental data, the fitting results, and the fitted peak components, respectively. Reprinted from Okazaki et al., J. Chem. Phys. 152, 124708 (2020), with the permission of AIP Publishing

different configurations [a single vacancy only in the upper layer (SV), a double vacancy only in the upper layer (DV), single vacancies in the upper two layers (2SV), and double vacancies in the upper two layers (2DV)] were introduced to the upper two layers.

Figure 16.10 shows the isosurfaces of the charge difference when the substrate structure was the 2DV. Charge accumulation and depletion mainly occurred in the vicinity of the support–cluster interface; the same tendency was clearly observed for all the support structures including the pristine graphite (PG). This suggests that the Pt atoms at the interface were mainly involved in the charge transfer between the $Pt_{13}$ cluster and the carbon support.

The position of the d-band center, $\epsilon_d$, (average energy of the d-states) relative to the Fermi level was calculated to gain insight into how this charge transfer affects the electronic structure of the interfacial Pt atoms [26]. As shown in Table 16.1, when a $Pt_{13}$ cluster was supported on a defective structure, $\epsilon_d$ was at least 0.14 eV more negative than the value for a $Pt_{13}$ cluster supported on the PG. This reduction

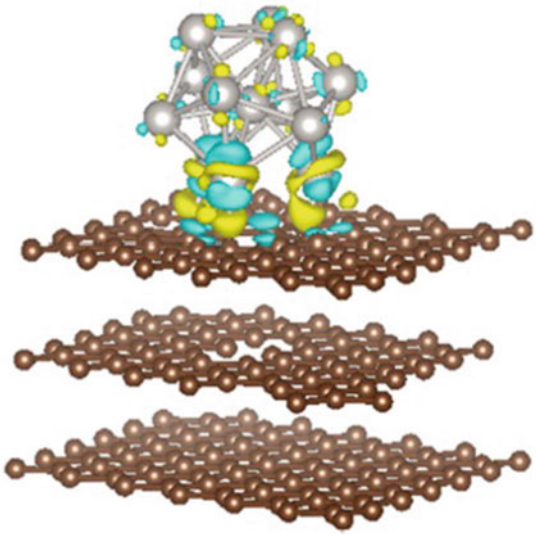

**Fig. 16.10** Isosurfaces of the charge density difference of a $Pt_{13}$ cluster on the graphite with 2DV. The density increases in the yellow regions and decreases in the blue regions. The isosurface value is 50 e/nm$^3$. Reprinted from Kakitani et al., Surf. Coat. Technol. 355, 259 (2018), with permission from Elsevier

**Table 16.1** Average d-band center values of the three Pt atoms in contact with pure graphite and with graphite layers containing various types of defective structures. This table is adapted from Table 1 of the paper, Kakitani et al., Surf. Coat. Technol. 355, 259 (2018)

| Substrate or defective structure | PG | SV | DC | 2SV | 2DV |
|---|---|---|---|---|---|
| d-band center (eV) | −2.79 | −2.95 | −2.94 | −3.09 | −2.93 |

weakens the binding of O and OH species on the Pt structure and promotes the rate-limiting step of the ORR (removal of adsorbed species from the Pt surface). Thus, ion-beam irradiation-induced lattice defects would lead to the enhancement of the ORR activity of Pt NPs.

Finally, a GC substrate was irradiated with Ar ions, and then Pt NPs were deposited on its surface. The C K-edge XAS measurements and DFT calculations in the above demonstrated the modification of the Pt–C interaction occurring at the Pt-carbon support interface and possibility of exhibiting high ORR activity. Thus, the XPS analysis was performed to confirm the $Ar^+$-implantation-induced interface structure which was correlated with the enhanced activity. The experiments using the GC substrate involved the irradiation with 380 keV $Ar^+$, heating at 400 °C in an $N_2$ atmosphere for 1 h to remove surface contaminations, and sputter deposition of Pt NPs on its surface. The diameter of the resulting NPs ranged from 5 to 10 nm [27].

Figure 16.11a shows the Pt 4f XPS spectrum of the Pt NPs on the GC substrate pre-irradiated with Ar ions at a fluence of $1.0 \times 10^{16}$ ions/cm$^2$, compared with the spectra of the Pt NPs on a non-irradiated substrate and a Pt foil standard sample. The Pt $4f_{7/2}$ peak in the prepared samples was broader on the high-energy side than the peak for the Pt foil, suggesting the presence of Pt–C bonding between the GC substrate and the deposited Pt NPs. Figure 16.11b compares C 1 s XPS spectra

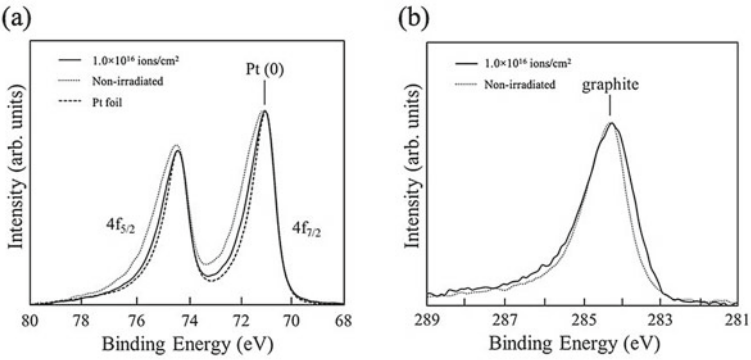


**Fig. 16.11** **a** Pt 4f XPS spectra of Pt NPs on a GC substrate pre-irradiated with 380 keV $Ar^+$ at a fluence of $1.0 \times 10^{16}$ ions/cm$^2$, Pt NPs on a non-irradiated GC substrate, and the standard Pt foil. **b** C 1 s XPS spectra of the same samples. Reprinted from Kimata et al., Surf. Coat. Technol. 306, 123 (2016), with permission from Elsevier

between the pre-irradiated and non-irradiated GC substrates with the Pt NPs. The spectrum of the irradiated GC substrate with the Pt NPs exhibited a wider peak than that for the non-irradiated one; a small bump on the low binding energy side was seen only in the spectrum of the irradiated GC substrate with the Pt NPs. This result can be attributed to carbide formation, confirming Pt–C bonding at the interface [27]. Electrochemical measurements indicated that the ORR activity of Pt NPs on GC substrates irradiated with Ar ions was increased compared with that of Pt NPs on non-irradiated GC substrates [28], suggesting that Pt–C bonding at the interface would be an origin of this improved catalytic activity of the Pt NPs.

## 16.6 Summary and Perspective

The 2030 Agenda for Sustainable Development, adopted by all United Nations Member States in 2015, includes 17 Sustainable Development Goals (SDGs), among which Goal 7 is targeted at ensuring universal access to affordable, reliable, and modern energy services for all. In this type of global framework, the Japanese government, like in other industrialized countries, declared its plan to go carbon neutral in real terms by 2050. Some of zero-emission, renewable energy technologies that provide an innovative solution to such a future clean society relate to water electrolysis and fuel cells for hydrogen production and utilization, respectively. Catalysts in the electrochemical energy conversion and storage devices, called electrocatalysts, are mostly noble or non-noble metal NPs on a carbon support or modified graphitic carbon materials themselves. We demonstrated that ion implantation could implement two strategic concepts based on morphology and electronic structures for electrocatalyst design and synthesis: the NP formation and surface/interface control

due to ion-irradiation effects on carbon materials such as impurity doping and defect creation.

In this chapter, we summarized recent work on ion implantation in carbon materials to develop the state-of-the-art catalysts for the HER in electrochemical water-splitting and for the ORR and FOR in fuel cells. A new approach involves controlling the interface between GC and the overlying Pt NPs by ion-beam induced atomic defects in the graphite lattice of the support, which modulated the electronic state of the Pt NPs for their high electrocatalytic activity. Experiments using more precise ion beam parameters will enable one to make full use of the advantages of accuracy and controllability to realize the optimal modification and the multi-level design of catalytic materials. Furthermore, researchers need to clarify the in-depth mechanism of the interfacial interaction and the structure–activity relationship as a significant challenge. Some in situ/*operando* characterization techniques of TEM, Raman spectroscopy, and XAS measurements can help achieve such fundamental purposes. Finally, since ion beam technology is known to be different from other chemical methods in introducing defect species as well as impurities, targeted theoretical calculations are imperative to guide and predict various defect engineering methods. Advanced electrocatalyst synthesis is likely to focus on the multi-element doping and defect introduction with more controllable contents and distributions. Exploration of these diverse complex systems will require the power of materials informatics (MI) including first-principles calculations and data sciences such as big data analysis, machine learning, and Bayesian inference. We believe that ion beam technology can be developed as a powerful tool in a wider range of catalytic applications and ultimately extended to many other fields.

**Acknowledgements** The authors would like to thank Mr. Sho Kato, Mr. Kenta Kakitani, Prof. Wei Mao, and Prof. Takayuki Terai of The University of Tokyo, Dr. Hiroyuki Okazaki, Dr. Shunya Yamamoto, Dr. Akira Idesaki, Dr. Hiroshi Koshikawa, and Dr. Tomitsugu Taguchi of QST, Dr. Daiju Matsumura of Japan Atomic Energy Agency, and Dr. Tomohiro Kobayashi of RIKEN. This work was supported in part by JSPS KAKENHI Grants No. 18H01923 and No. 21H04669, and Collaborative Research Project of Laboratory for Materials and Structures, Institute of Innovative Research, Tokyo Institute of Technology.

## References

1. K. Fukumi, A. Chayahara, K. Kadono, T. Sakaguchi, Y. Horino, M. Miya, J. Hayakawa, M. Satou, $Au^+$-ion-implanted silica glass with non-linear optical property. Jpn. J. Appl. Phys. **30**, L742–L744 (1991). https://doi.org/10.1143/JJAP.30.L742
2. A.R. Adhikari, M.B. Huang, D. Wu, K. Dovidenko, B.Q. Wei, R. Vajtai, P.M. Ajayan, Ion-implantation-prepared catalyst nanoparticles for growth of carbon nanotubes. Appl. Phys. Lett. **86**, 053104 (2005). https://doi.org/10.1063/1.1856699
3. F. Liang, H. Tian, M. Jia, J. Hu, Pt nanoparticles ion-implanted onto indium tin oxide electrodes and their electrocatalytic activity towards methanol. J. Power Sources **225**, 9–12 (2013). https://doi.org/10.1016/j.jpowsour.2012.09.093

4. L. Wu, H. Wu, X. Wang, H. Zhong, Z. Wang, G. Cai, C. Jiang, F. Ren, A general method for large-scale fabrication of metal nanoparticles embedded N-doped carbon fiber cloth with highly efficient hydrogen production in all pH range. Electrochim. Acta **353**, 136475 (2020). https://doi.org/10.1016/j.electacta.2020.136475
5. R.B. Levy, M. Boudart, Platinum-like behavior of tungsten carbide in surface catalysis. Science **181**, 547–549 (1973). https://doi.org/10.1126/science.181.4099.547
6. R. Bertoncello, A. Glisenti, G. Granozzi, G. Battaglin, F. Caccavale, E. Cattaruzza, P. Mazzoldi, Chemical interactions in titanium- and tungsten-implanted fused silica. J. Non-Cryst. Solids **162**, 205–216 (1993). https://doi.org/10.1016/0022-3093(93)91239-Y
7. A. Hoffman, P.J. Evans, D.D. Cohen, P.J.K. Paterson, Compaction, distribution, and chemical bonding of tungsten-implanted glassy carbon. J. Appl. Phys. **72**, 5687–5694 (1992). https://doi.org/10.1063/1.351919
8. S. Kato, T. Yamaki, S. Yamamoto, T. Hakoda, K. Kawaguchi, T. Kobayashi, A. Suzuki, T. Terai, Nanoparticle formation by tungsten ion implantation in glassy carbon, Trans. Mat. Res. Soc. Japan 38 (2013) 81–84. https://doi.org/10.14723/tmrsj.38.81
9. I.J. Hsu, D.A. Hansgen, B.E. McCandless, B.G. Willis, J.G. Chen, Atomic layer deposition of Pt on tungsten monocarbide (WC) for the oxygen reduction reaction. J. Phys. Chem. C **115**, 3709–3715 (2011). https://doi.org/10.1021/jp111180e
10. S. Kato, T. Yamaki, S. Yamamoto, T. Hakoda, K. Kawaguchi, T. Kobayashi, A. Suzuki, T. Terai, Preparation of tungsten carbide nanoparticles by ion implantation and electrochemical etching. Nucl. Instrum. Meth. Phys. Res. B **314**, 149–152 (2013). https://doi.org/10.1016/j.nimb.2013.05.052
11. H. Jiang, J. Gu, X. Zheng, M. Liu, X. Qiu, L. Wang, W. Li, Z. Chen, X. Ji, J. Li, Defect-rich and ultrathin N doped carbon nanosheets as advanced trifunctional metal-free electrocatalysts for the ORR, OER and HER. Energy Environ. Sci. **12**, 322–333 (2019). https://doi.org/10.1039/C8EE03276A
12. D. Guo, R. Shibuya, C. Akiba, S. Saji, T. Kondo, J. Nakamura, Active sites of nitrogen-doped carbon materials for oxygen reduction reaction clarified using model catalysts. Science **351**, 361–365 (2016). https://doi.org/10.1126/science.aad0832
13. K.N. Wood, R. O'Hayre, S. Pylypenko, Recent progress on nitrogen/carbon structures designed for use in energy and sustainability applications. Energy Environ. Sci. **7**, 1212–1249 (2014). https://doi.org/10.1039/C3EE44078H
14. T. Kondo, S. Casolo, T. Suzuki, T. Shikano, M. Sakurai, Y. Harada, M. Saito, M. Oshima, M.I. Trioni, G.F. Tantardini, J. Nakamura, Atomic-scale characterization of nitrogen-doped graphite: effects of dopant nitrogen on the local electronic structure of the surrounding carbon atoms. Phys. Rev. B **86**, 035436 (2012). https://doi.org/10.1103/PhysRevB.86.035436
15. Y. Hashimoto, S. Katafuchi, M. Yoshimura, T. Hara, Y. Hara, M. Hamagaki, Effect of low-energy nitrogen ion treatment of highly ordered pyrolytic graphite on oxygen reduction reaction activity. Nanomater. Nanotechnol. **7**, 1–8 (2017). https://doi.org/10.1177/1847980417690331
16. A.K. Shukla, M.K. Ravikumar, A. Roy, S.R. Barman, D.D. Sarma, A.S. Aricò, V. Antonucci, L. Pino, N. Giordano, Electro-oxidation of methanol in sulfuric acid electrolyte on platinized carbon electrodes with several functional-group characteristics. J. Electrochem. Soc. **141**, 1517–1522 (1994). https://doi.org/10.1149/1.2054955
17. S.C. Roy, P.A. Christensen, A. Hamnett, K.M. Thomas, V. Trapp, Direct methanol fuel cell cathodes with sulfur and nitrogen-based carbon functionality. J. Electrochem. Soc. **143**, 3073–3078 (1996). https://doi.org/10.1149/1.1837166
18. Y. Zhou, R. Pasquarelli, T. Holme, J. Berry, D. Ginley, R. O'Hayre, Improving PEM fuel cell catalyst activity and durability using nitrogen-doped carbon supports: observations from model Pt/HOPG systems. J. Mater. Chem. **19**, 7830–7838 (2009). https://doi.org/10.1039/B910924B
19. Y. Zhou, T. Holme, J. Berry, T.R. Ohno, D. Ginley, R. O'Hayre, Dopant-induced electronic structure modification of HOPG surfaces: implications for high activity fuel cell catalysts. J. Phys. Chem. C **114**, 506–515 (2010). https://doi.org/10.1021/jp9088386
20. I. Fampiou, A. Ramasubramaniam, Binding of Pt nanoclusters to point defects in graphene: adsorption, morphology, and electronic structure. J. Phys. Chem. C **116**, 6543–6555 (2012). https://doi.org/10.1021/jp2110117

21. D.-H. Lim, J. Wilcox, DFT-based study on oxygen adsorption on defective graphene-supported Pt nanoparticles. J. Phys. Chem. C **115**, 22742–22747 (2011). https://doi.org/10.1021/jp205244m
22. T. Kimata, K. Kakitani, S. Yamamoto, T. Yamaki, T. Terai, K.G. Nakamura, Platinum nanoparticles on HOPG surface modified by 380 keV $Ar^+$ irradiation: TEM and Raman studies. Radiat. Eff. Defects Solids **175**, 433–439 (2020). https://doi.org/10.1080/10420150.2020.1737866
23. T. Kimata, K. Kakitani, S. Yamamoto, T. Yamaki, T. Terai, K.G. Nakamura, Raman spectroscopy of $Ar^+$-irradiated graphite surface supporting platinum nanoparticles. Nucl. Instrum. Meth. Phys. Res. B **444**, 6–9 (2019). https://doi.org/10.1016/j.nimb.2019.02.005
24. H. Okazaki, K. Kakitani, T. Kimata, A. Idesaki, H. Koshikawa, D. Matsumura, S. Yamamoto, T. Yamaki, Changes in electronic structure of carbon supports for Pt catalysts induced by vacancy formation due to $Ar^+$ irradiation. J. Chem. Phys. **152**, 124708 (2020). https://doi.org/10.1063/1.5144568
25. K. Kakitani, T. Kimata, T. Yamaki, S. Yamamoto, D. Matsumura, T. Taguchi, T. Terai, X-ray absorption study of platinum nanoparticles on an ion-irradiated carbon support. Radiat. Phys. Chem. **153**, 152–155 (2018). https://doi.org/10.1016/j.radphyschem.2018.09.017
26. K. Kakitani, T. Kimata, T. Yamaki, S. Yamamoto, T. Taguchi, T. Kobayashi, W. Mao, T. Terai, The interface between platinum nanoparticle catalysts and an $Ar^+$-irradiated carbon support. Surf. Coat. Technol. **355**, 259–263 (2018). https://doi.org/10.1016/j.surfcoat.2018.01.044
27. T. Kimata, S. Kato, T. Yamaki, S. Yamamoto, T. Kobayashi, T. Terai, Platinum nanoparticles on the glassy carbon surface irradiated with argon ions. Surf. Coat. Technol. **306**, 123–126 (2016). https://doi.org/10.1016/j.surfcoat.2016.05.042
28. K. Kakitani, T. Kimata, T. Yamaki, S. Yamamoto, D. Matsumura, I. Shimoyama, A. Iwase, T. Kobayashi, T. Terai, Catalytic activity of Pt nanoparticles on a glassy carbon substrate pre-irradiated with Ar ions. QST Takasaki Ann. Rep. **2015**, 42 (2017)

# Chapter 17
# Bottom-up Synthetic Approaches to Carbon Nanomaterial Production in Liquid Phase by Femtosecond Laser Pulses


**Tomoyuki Yatsuhashi and Takuya Okamoto**

**Abstract** Carbon nanomaterials, which are widely used in a variety of scientific and industrial applications, have been synthesized by various methods such as mechanical milling of bulk carbons. Another top-down synthetic approach, the laser ablation of a carbon source such as graphite immersed in liquid, has been extensively studied because of its simplicity and validity. In contrast to those top-down approaches, we introduce bottom-up synthetic approaches to producing carbon nanomaterials by laser irradiation of organic molecules in this chapter. Focused intense femtosecond laser pulses trigger the ionization and subsequent reactions of reactants and/or solvents, followed by carbonization. The use of water as a liquid medium allows for the generation of reactive species such as hydrated electrons and hydroxyl radicals in very confined volumes. Depending on the reactive species participating in the primary reaction, the subsequent reactions and the characteristics of resultant carbon nanomaterials are determined. This molecular-based method can utilize a variety of molecules and could produce desired products, such as carbon nanoparticles with high-density fluorine atoms as well as hydrophilic carbon nanomaterials. Nanoparticle synthesis in the liquid phase can utilize not only neat liquid but also mixtures of molecules, aqueous solutions, water/organic bilayer solutions, and emulsions that serve optimal reaction environments for a novel avenue of nanomaterial production.

**Keywords** Filamentation · Heteroatom-doping · Hydrophilicity · Ionization · Oxidation · Reduction

T. Yatsuhashi (✉)
Department of Chemistry, Graduate School of Science, Osaka City University, 3-3-138 Sugimoto, Sumiyoshi 558-8585, Osaka, Japan
e-mail: tomo@osaka-cu.ac.jp

T. Okamoto
Research Institute for Electronic Science, Hokkaido University, Sapporo 001-0020, Hokkaido, Japan



Y. Ishikawa et al. (eds.), *High-Energy Chemistry and Processing in Liquids*,
https://doi.org/10.1007/978-981-16-7798-4_17

## 17.1 Introduction

Nanosized carbons are fundamental materials and have been used in a wide variety of applications such as catalysts, bioimaging, sensors, solar energy conversion, and so on [1–9]. A large number of methods for the synthesis of carbon nanomaterials of appropriate size, morphology, elemental composition, and surface characteristics have been proposed. These methods are categorized into the top-down and bottom-up approaches summarized in Fig. 17.1. In the case of top-down process, nanomaterials are obtained by the breakdown of bulk materials. In bottom-up process, on the other hand, nanomaterials are obtained by the growth of atoms or molecules (molecular fragments). These synthetic methods are also classified by the manufacturing process such as arc-discharge, pulsed laser deposition, milling, laser ablation in liquid, chemical vapor deposition, chemical reduction, co-precipitation, solvothermal method, sol–gel method, thermal decomposition, organic synthesis, and so on (Fig. 17.1). This section focuses on the use of pulsed lasers, which is a typical high-energy source, to produce carbon nanomaterials by physical or chemical processes.

Extensive and intensive studies on the synthesis of carbon nanomaterials in different phases (gas, liquid, solid) and on their interfaces (gas/solid, liquid/solid) by pulsed laser irradiation have been reported (Fig. 17.2) [10]. It should be noted that the mass production of nanomaterials by a laser-induced reaction is difficult in the gas phase since the density of a reactant is determined by its vapor pressure (Fig. 17.2a). Although the quantity of products is limited, interesting experiments that can be

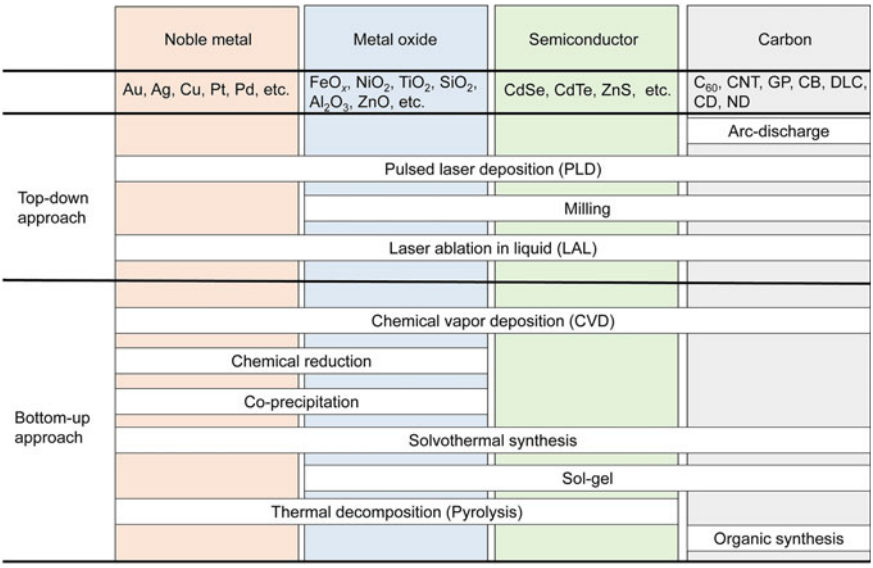


**Fig. 17.1** Brief summary of nanomaterial synthetic methods. CNT—carbon nanotube; GP—graphene; CB—carbon black; DLC—diamond-like carbon; CD—carbon dot; ND—nanodiamond

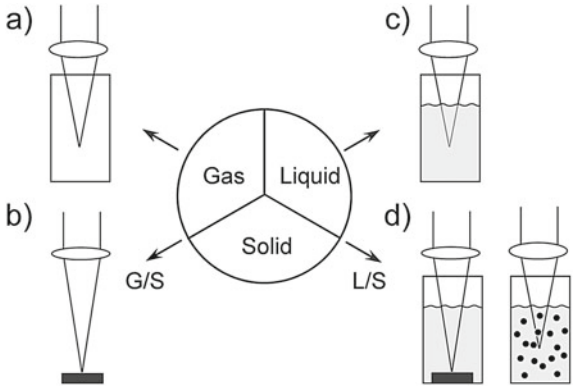


**Fig. 17.2** Nanomaterial production in various phases or interfaces by laser pulses. Reprinted with permission from [10]. Copyright 2017 The Laser Society of Japan

performed only by femtosecond laser pulses have been reported. Due to the large spectral bandwidth of femtosecond laser pulses, spatially confined microplasma can be formed by shaping laser pulses (790 nm, 35 fs) [11]. The production of spherical and non-spherical nanocarbons in the microplasma of methane was carried out. In contrast to the tightly focused reaction environments, amorphous carbon films and nanoparticles were formed in filaments (total length about 30−150 mm) generated in gaseous ethylene by focusing femtosecond laser pulses (800 nm, 45 fs) with a long focal lens [12].

It is advantageous to choose solid reactants because the density is much higher than that in the gas phase. Pulsed laser ablation/deposition (Fig. 17.2b) is known as a useful means of forming thin-layered films consisting of carbons such as amorphous diamond-like carbons (DLCs) [13, 14]. It should be noted that not only elemental carbons but also frozen molecules such as acetone [15], a series of normal aliphatic alcohols (790 nm, 130 fs) [16], and hexane (800 nm, 100 fs) [17] have been used as carbon sources. Liquid is also a good choice as a reactant since its density is comparable to that of solid. When we used organic liquid as a reactant (Fig. 17.2c), fragmentation followed by associations resulted in various carbon species. Production of aggregated carbons in organic liquid exposed to ultraviolet nanosecond laser pulses has been a well-known phenomenon [18]. However, the complicated reactions originating in the subsequent photoreactions as well as from photoheating are hard to control well enough to form desired products. In contrast, femtosecond laser irradiation of organic liquid is regarded as a moderate route for synthesizing a variety of polyynes. Polyyne formation was reported in aliphatic hydrocarbons [19, 20] (800 nm, 100 fs) and acetone (800 nm, 90 fs) [21], whereas polyynes and carbon nanoparticles (CNPs) (800 nm, 120 fs) [22] or DLCs (780 nm, 100 fs) [23] were formed in benzene.

Although a solid is served as in the cases of pulsed laser ablation/deposition, laser ablation in liquid (LAL) [24], in which a solid reactant immersed in liquid medium is exposed to laser pulses followed by ablation and subsequent production of nanomaterials (Fig. 17.2d), has been actively studied. LAL has been utilized to produce various nanomaterials consisting of metals, semiconductors, insulators, and carbons.

In comparison with experiments in the gas phase or at the gas/solid interface, LAL is advantageous because it enables rapid heating of reactants by laser pulses and cooling by the surroundings to confine the products. Extensive reviews about LAL from scientific and technological viewpoints have been published [25–36]. For the production of carbon nanomaterials by LAL, nanosecond laser pulses have mainly been used [37]. Here we refer to a variety of carbon products by LAL using femtosecond laser pulses: graphene and polyynes from a highly oriented pyrolytic graphite plate in water (800 nm, 35 fs) [38]; carbon dots (CDs) from graphite powder in various solvents (ethanol, ethylenediamine, *N*-methyl pyrrolidone) (800 nm, 150 fs) [39–43]; and nanodiamonds (NDs) from glassy carbon or graphite powder in organic solvent (acetone, ethanol) (800 nm, 100 fs) [44].

The discussion in this chapter focuses on carbon nanomaterial production in the liquid phase by femtosecond laser pulses as shown in Fig. 17.2c. Section 17.2 describes the characteristic phenomena caused by femtosecond laser pulses in condensed medium such as filamentation. In Sect. 17.3, the details of nanoparticle production in neat organic liquid are introduced not only from aromatics but also from other molecules, while in Sect. 17.4 we describe the synthesis of carbon nanomaterials in aqueous solution and a bilayer of water and organic liquid. Finally, in Sect. 17.5 we summarize the studies in this field.

## 17.2 Femtosecond Laser Pulses in Condensed Medium

This chapter describes the production of nanomaterials in organic liquid (Fig. 17.2c) particularly using femtosecond laser pulses. Unlike the case with nanosecond laser pulses, the penetration of femtosecond laser pulses into condensed medium as in the cases of Fig. 17.2c, d, causes the distortion of the pulses due to group velocity dispersion (GVD). In this chapter, we show only two parameters of laser pulses (wavelength, pulse durations) for each nanomaterial production. However, these values are listed only for reference and are not realistic to reproduce the actual experimental conditions. We would need whole parameters such as repetition rate, diameters and divergence of the incident beam (beam profile); emission spectrum and chirp information; the diameter and focal length of the lens; the material and thickness of the optical cell wall if one is used; the distance between the ideal focal plane and the wall of the optical cell (or the liquid surface), and so on. The most serious concern is the elongation or shortening of laser pulse duration depending on the chirp characteristics. If a transform-limited pulse is used for irradiation, the pulse duration in liquid should be elongated. We need to compensate the GVD to use the shortest pulse in desired location in liquid, but this is difficult to accomplish [45]. In addition, the high intensity of femtosecond laser pulses causes significant nonlinear effects, namely self-focusing. Thus, the ordinal index of the incident laser pulse, fluence (J $cm^{-2}$), might be an index. Furthermore, the peak laser intensity (W $cm^{-2}$) in condensed medium is not easily obtained due to the change in both pulse duration and focal area (volume).

If femtosecond laser pulses are tightly focused on liquid by a short focal-length lens with a high numerical aperture, optical breakdown is triggered by multiphoton ionization followed by avalanche ionization, and finally results in the generation of high-density plasma. Even under weakly focused condition, femtosecond laser pulses can ionize condensed medium at very low laser energy (below 1 μJ) [46]. Since the refractive index of plasma (electrons) is lower than that of the surroundings, the balance between self-focusing by a nonlinear refractive index of the medium and defocusing by plasma creates filaments which are accompanied by supercontinuum generation, namely by a white light laser, due to self-phase modulation as shown in Fig. 17.3 [47–49]. Figure 17.4 shows numerical simulation of the plasma density and laser intensity when negatively chirped femtosecond pulse (800 nm, 75 fs) penetrated in water through a microlens with low numerical aperture [50]. Filament is often called as low-density (cold) plasma but the density of electrons in laser-induced plasma in water reaches $10^{18}$ $cm^{-3}$ as shown in Fig. 17.4a, which is high enough to reduce not only noble metal ions but also lanthanoid ions with negative reduction potentials ($Sm^{3+}$, −1.55 V vs. SHE) [51]. The concern of filamentation for nanomaterial production is that the amount of product is expected to be small because

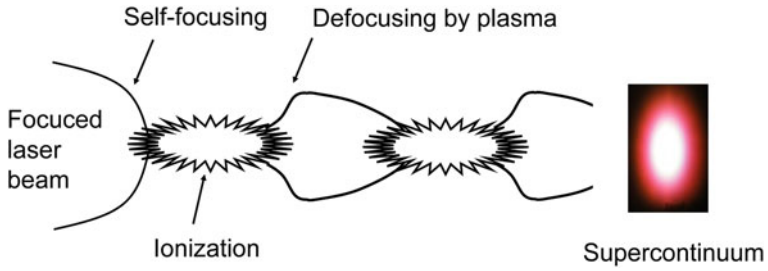


**Fig. 17.3** Schematic illustration of filament formation by focused femtosecond laser pulse accompanied by supercontinuum

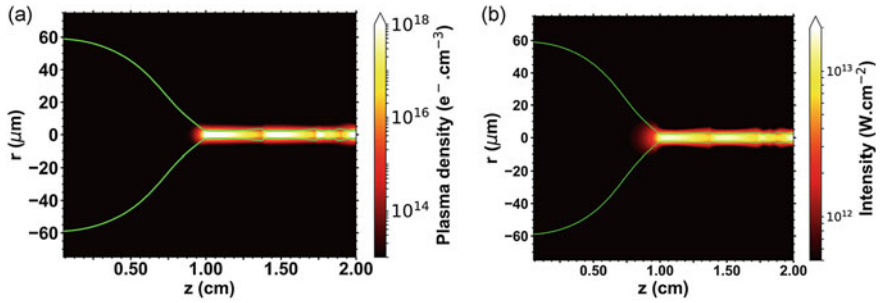


**Fig. 17.4** Numerical simulation of the **a** plasma density and **b** laser intensity when negatively chirped femtosecond pulse was focused on water using a microlens (numerical aperture = $3.3 \times 10^{-3}$). Horizontal and vertical axes correspond to laser propagation ($z$) and radial ($r$) direction. Adapted with permission from [50]. Copyright 2019 American Chemical Society

only a small part of the reactant solution is exposed to a filament, whose diameter is 10−100 μm. Nevertheless, filamentation-induced phenomena have attracted much attention in physics, chemistry, biology, and medicine from both fundamental and applied scientific perspectives [52–54].

Furthermore, the difference in laser intensity between gas and condensed medium should be mentioned. In a vacuum, it is easy to achieve laser intensity up to $10^{16}$ W cm$^{-2}$ by a conventional femtosecond laser system. In the gas phase, such a high-intensity laser electric field strips many electrons from a molecule, followed by Coulomb explosion [55, 56]. However, filamentation in condensed medium keeps the laser intensity constant, in a phenomenon called intensity clamping (ca. $10^{13}$ W cm$^{-2}$ as shown in Fig. 17.4b) [57]. As a result, the physical and chemical phenomena in the liquid phase triggered by femtosecond laser pulses are quite different from those in the gas phase, even though the incident laser energy (fluence) is the same. It is not possible to discuss simply what happens in the liquid phase based on experimental and theoretical results obtained in the gas phase.

## 17.3 Synthesis of Characteristic Carbon Nanomaterials in Neat Organic Liquids

As described in the introduction, CNPs and/or DLCs are formed from an aromatic hydrocarbon (benzene) by femtosecond laser irradiation. However, the production of carbon nanomaterials from other organic liquids has rarely been reported. The production of polyynes was known in aliphatic hydrocarbons (hexane and decane) [19] and in acetone [21], but the production of carbon nanomaterials (carbon precipitates) has not been reported in those organic liquids. In general, we cannot say what kind of molecule should be used to produce carbon nanomaterials because their production depends strongly on the properties of laser irradiation conditions. For example, the production of CNPs (800 nm, 120 fs) and/or DLCs (780 nm, 100 fs) from benzene by femtosecond laser irradiation was reported [22, 23]. Although no precipitates were formed, the coloration of benzene to pale yellow was observed after femtosecond laser irradiation under other experimental conditions (0.8 μm, 40 fs) [58]. There are no general answers at the moment, and any organic liquid may or may not be a source of carbon nanomaterials. As far as we know, the production of carbon nanomaterials by femtosecond laser irradiation of neat organic liquid has been reported for acetonitrile [59], benzene [22, 23], ethanol [60, 61], hexafluorobenzene [62], and toluene [63, 64].

Two of the difficulties arising from this bottom-up approach are the applicability and complexity of chemical reactions toward the formation of nanomaterials. Thus, it is challenging to control the chemical composition, structure, size, morphology, surface characteristics, and so on. The primary reaction of neat organic liquid exposed to femtosecond laser pulses is ionization (excitation). The primary

products are (solvated) electrons and the cation radicals of reactants. Secondary reactions are dependent on the reactants: recombination, fragmentation, ring cleavage, isomerization, and association. One focus of this method is on whether heteroatoms and/or hydrophilicity can be introduced. First, we introduce here the incorporation of heteroatoms into carbon nanomaterials by choosing liquid organic reactants. Doping nitrogen and/or fluorine atoms into carbon nanomaterials dramatically changes chemical, electronic, and mechanical properties such as solubility, catalytic activity, redox, and surface friction. Especially, the improvement of the luminescence and of the redox activity of carbon nanomaterials is important for bio-application and for the oxygen reduction reaction catalysts for fuel cells, respectively. We show the fluorine incorporation to CNPs by choosing hexafluorobenzene (HFB, $C_6F_6$) as a reactant [62]. The color of HFB in a quartz cuvette turned dense black after laser irradiation (0.8 μm, 40 fs). We then checked the characteristics of products by adding water to the resultant solutions. Figure 17.5a shows the appearance of the cuvette (left) just after laser irradiation and (right) after the addition of water followed by shaking. The lower and upper layers are HFB and water, respectively. Some carbon particles were observed in the upper part of the cuvette, but they were just floating on the water. The water phase stays transparent, and the resultant carbon particles are not dispersed in water. TEM observation shows that almost all particles were agglomerated (Fig. 17.5b). The agglomerated form did not change after the dilution by 100-fold HFB. As-prepared CNPs from neat HFB were hydrophobic, but in the next section we show that the particles can be dispersed in water by sonication.

The processes toward forming CNPs include ionization and presumably violent fragmentations of HFB. Thus, the resultant carbon particles should involve carbon and fluorine atoms. Since the reactions were carried out under an air atmosphere and HFB was not degassed and dehydrated prior to laser irradiation, the contamination of oxygen atoms was expected. The atomic compositions on the surface were

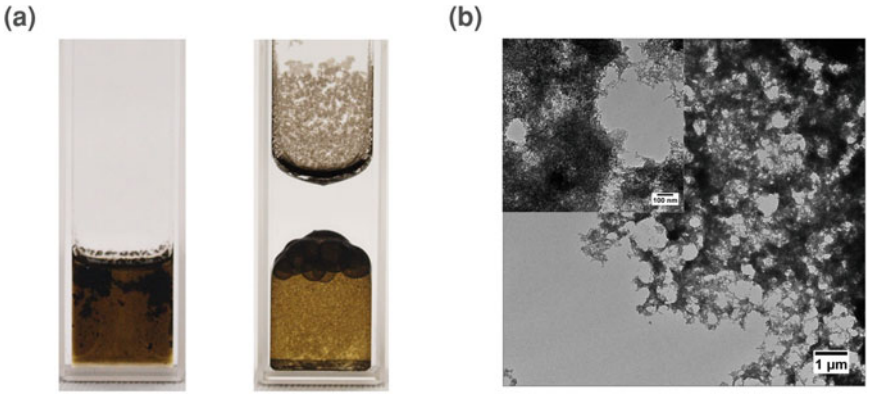


**Fig. 17.5** **a** The cuvette (left) just after laser irradiation of HFB and (right) after the addition of water followed by shaking. **b** TEM image of resultant carbon particles formed in HFB without centrifugation (scale bar: 1 μm; inset, 100 nm)

measured by an X-ray photoemission spectrometer (XPS), and those of the bulk carbon particles were measured by a scanning electron microscope equipped with an energy-dispersive X-ray spectrometer (SEM-EDS). Figure 17.6 shows the spectra of carbon particles produced in HFB measured by XPS and SEM-EDS. The F/C ratio of the CNPs was about 0.3–0.4, which in Fig. 17.7 is compared with those of other fluorine-containing carbon materials synthesized by different methods. The reactants were $C_6F_{13}CH_2CH_2OH$ (a, solvothermal method) [65], glucose and $(C_2H_5)_3N{\bullet}3HF$ (b, solvothermal method) [66], $C_6H_5CF_3$ (c, solution plasma) [67], and $C_6F_6$ (d, laser-induced filamentation) [62]. The F/C ratios of the reactants used in those methods were 1.63, 0.43, 0.5, and 1, respectively. Therefore, the F/C ratios of the products (surface measured by XPS) relative to that of the reactant were 0.14, 0.24, 0.10, and 0.37, respectively. Those compared for the bulk particles (measured by SEM-EDS) were 0.017, 0.26, 0.14, and 0.28, respectively. Based on these values, we suggest that femtosecond laser-induced filamentation is an efficient means of incorporating fluorine atoms to carbon particles.

Since the incorporation of fluorine atoms into CNPs was successful by choosing $C_6F_6$, we could expect the incorporation of heteroatoms by selecting suitable substituents on aromatics. In contrast, the association of fragments forming carbon

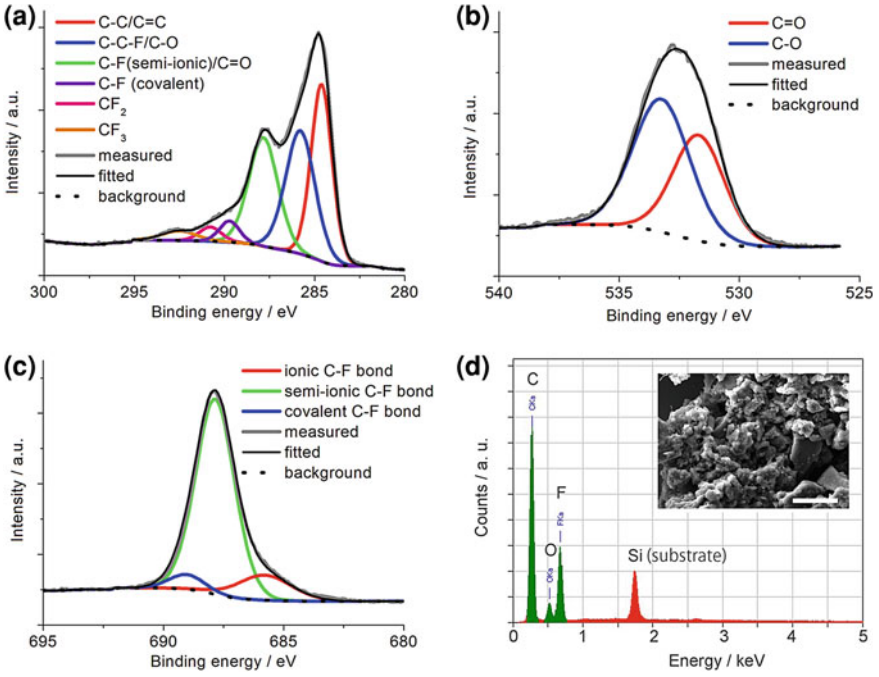


**Fig. 17.6** XPS (**a**, C1s; **b**, O1s; **c**, F1s) and (**d**) SEM–EDS spectra of CNPs produced in HFB. The inset of (d) shows the SEM image of agglomerated CNPs (scale bar: 30 μm). From [62] Copyright 2015 by John Wiley Sons, Inc. Adapted by permission of John Wiley & Sons, Inc

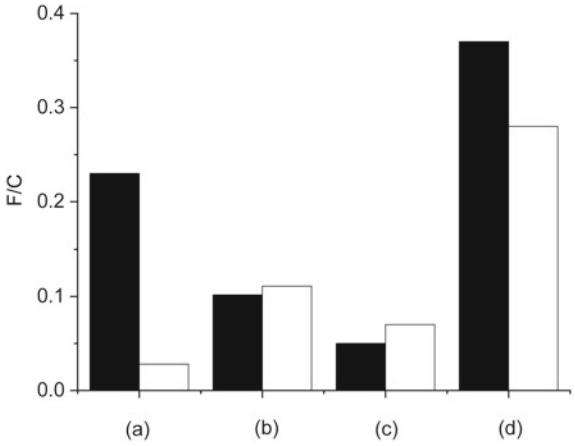


**Fig. 17.7** F/C atomic ratio of the surface (filled) and bulk (open) fluorine-containing carbon particles produced by different methods: **a** solvothermal method ($C_6F_{13}CH_2CH_2OH$), **b** solvothermal method ($(C_2H_5)_3$ N•3HF), **c** solution plasma ($C_6H_5CF_3$), **d** laser-induced filamentation ($C_6F_6$). Data were taken from [62, 65–67]

nanomaterials might not be expected for liquid non-aromatics. Actually, carbon networks larger than polyynes were not reported in the cases of acetone and aliphatic hydrocarbons. Therefore, the fact that CDs were formed from acetonitrile and ethanol is noteworthy because various organic liquids will be available as reactants in the future. To further understand the applicability of the filamentation chemistry of organic molecules, we first introduce the synthesis of nitrogen-doped luminescent CDs from acetonitrile (800 nm, 50 fs) [59]. Figure 17.8 shows wide and narrow scans of XPS spectra of CDs produced from acetonitrile. The N/C ratio of the product measured by XPS was reported to be 0.297 (surfaces of CDs), whereas that measured by elemental analysis was 0.571 (whole CDs). Since the N/C ratio of the reactant was 0.5 ($CH_3CN$), the resultant CDs gained more nitrogen atoms inside than the reactant acetonitrile. This result is very promising for the production of heteroatom-rich carbon nanomaterials because conventional solvent can be used as a source of valuable carbon nanomaterials. Supposing that not the whole molecule (N/C = 0.5) but only the CN fragments (N/C = 1) mainly contribute to the production of CDs, the large N/C ratio is not surprising. To understand the reaction mechanism, isotope-labeled reactant might be used to investigate the origins of carbons.

Production of NDs from ethanol (1025 nm, 500 fs) also indicates the further potential of filamentation chemistry for nanomaterial synthesis because carbon nanomaterials were formed from a molecule consisting of single bonds [60, 61], whereas aromatics and acetonitrile have double and triple bonds, respectively. If the quench of reactive carbon intermediates is not significant and/or important in the liquid phase, production of nanodiamonds in neat ethanol is expected because the deposition of DLC film was carried out by the laser ablation of frozen alcohol. In cases of laser ablation of frozen alcohol, the active and quenched forms of intermediates such as hydrogen, $CH_3$, $CH_4$, and CO were detected by mass spectroscopy in the ablation atmosphere [16]. Figure 17.9 is a picture of the supercontinuum and the absorbed energy with respect to the incident laser energy in ethanol. Under this experimental condition, filamentation starts at around 100 μJ, at which the absorption of laser

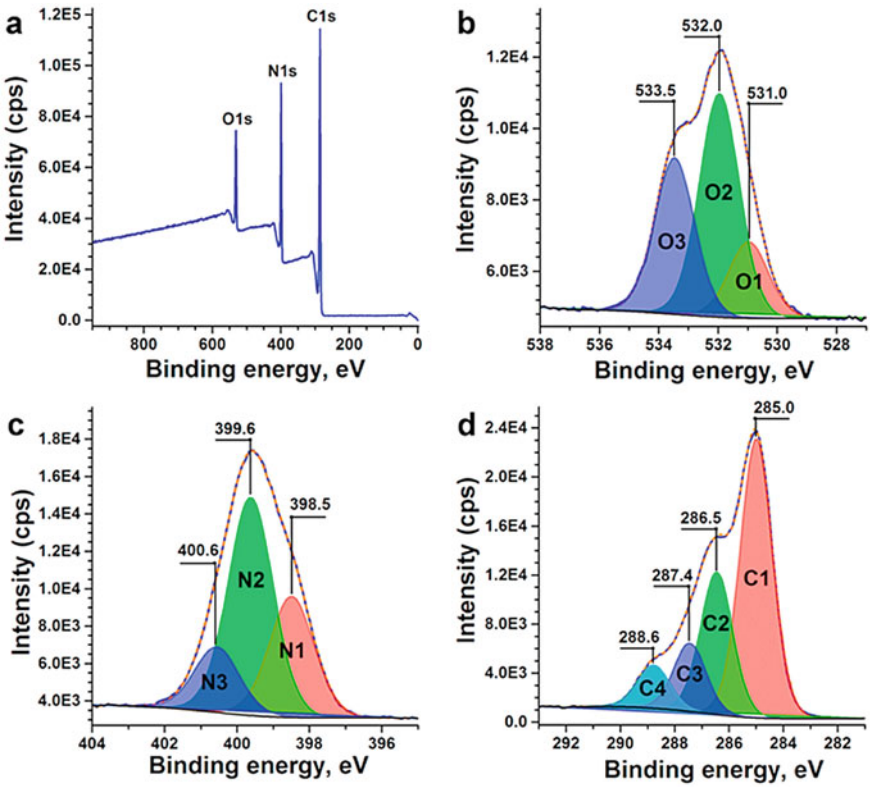


**Fig. 17.8** XPS wide **a** and narrow (**b**, O1s; **c**, N1s; **d**, C1s) scans of CDs produced from acetonitrile. Reprinted from [59], Copyright 2021, with permission from Elsevier

energy increased sharply. Figure 17.10 shows the emission spectra of $C_2$, neutral hydrogen (HI), and neutral (CI) and doubly ionized atomic carbons (CIII) as a function of incident laser energy. $C_2$ emission was noticeable when the incident laser energy was more than twice the energy of filament generation (Fig. 17.10c). The threshold laser energy of atomic carbon emission, which was higher than that of the carbon cluster, coincided with the appearance laser energy of NDs (>300 μJ). Consequently, the observation of the atomic line emissions of carbons, in addition to the observation of supercontinuum radiation, shows the importance of the atomic and molecular fragments generated in filaments as sources of NDs in liquid ethanol. Nee and coworkers suggested that intensity clamping inside filaments plays an important role in regulating ND size [60]. Although multiple filaments are formed at high incident laser energy, the interaction inside each filament is identical because the laser intensity is clamped inside any filament. Thus, the dissociation and nucleation processes occur in a "naturally controlled environment" for the formation of NDs with homogeneous size distribution. It was clarified that the observation of atomic emission lines as well as of the supercontinuum gives us fruitful information about

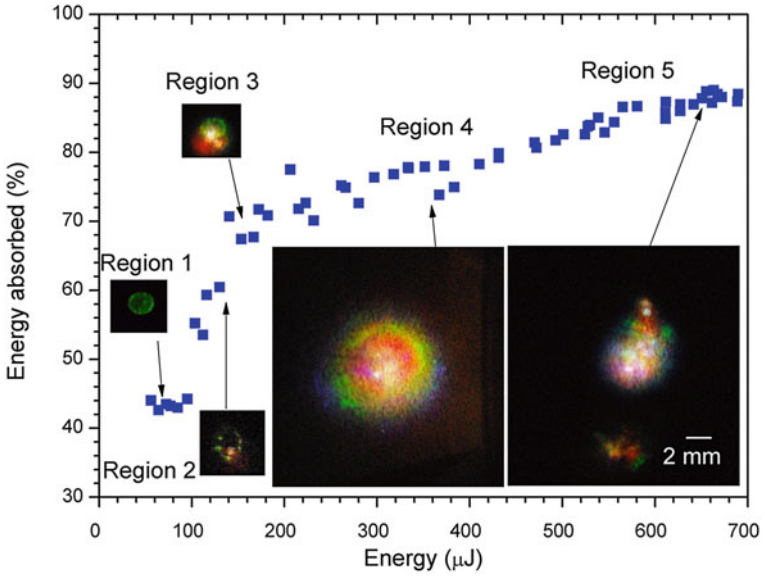


**Fig. 17.9** Ratio of absorbed energy by ethanol as a function of incident energy of femtosecond laser pulse. Filamentation began in region 2. Reprinted from [60] by The Authors licensed under CC BY 4.0

the fragmentation process and intermediates under filamentation in the liquid phase. Emission spectroscopy of the other components of plasma, such as F, CN, CF, OH, and molecular fragments, would be helpful for investigating the reaction mechanism underlying functionalized carbon nanomaterial production.

## 17.4 Production of Carbon Nanomaterials in Aqueous Solution, Bilayer of Organic Liquid and Water, and Living Cells

Bare CNPs usually form agglomerates due to their hydrophobic character. A lot of studies have been concerned with the control of size, morphology, and surface characteristics of CNPs. In order to use CNPs as chemical, biological, and medical materials, it is important to control the dispersion stability of CNPs in water. However, the modification of a CNP surface usually requires multistep processes by long-term heating with acid after the preparation of bare nanoparticles [68–70]. Therefore, the synthesis of hydrophilic CNPs in a one-pot, single-step process has been expected. Aggregation and/or agglomeration of CNPs cannot be avoided when we use neat organic liquid as described in Sect. 17.3 Thus, one can simply imagine that a hydrophilic character can be attached to CNPs by treating organic molecules

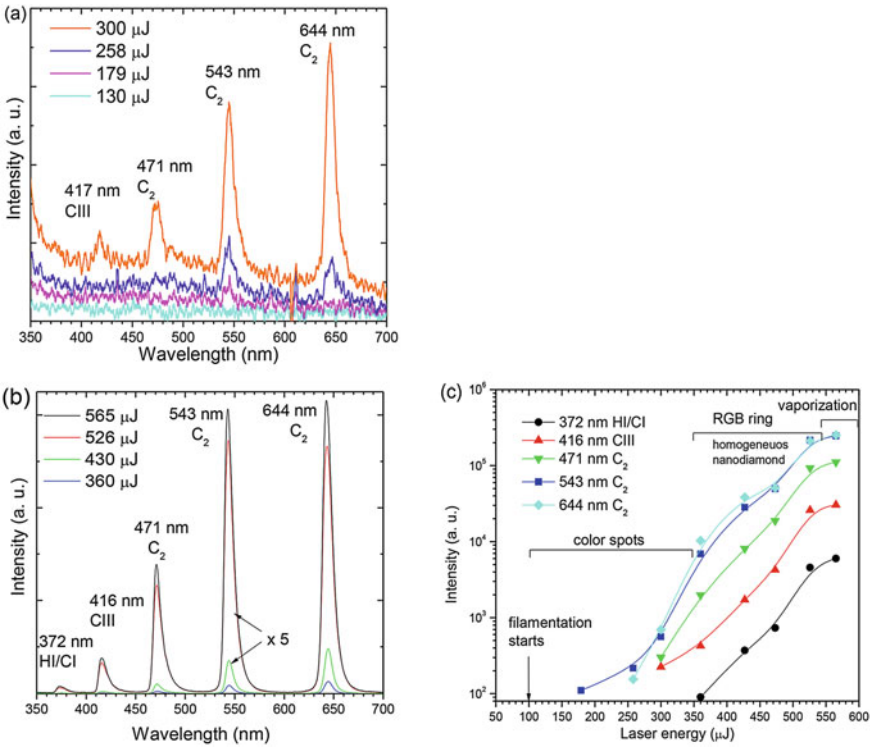


**Fig. 17.10** Emission spectra during femtosecond laser irradiation to ethanol under **a** low and **b** high incident energy conditions. **c** Intensity of emission as a function of incident laser energy. Reprinted from [61], Copyright 2019, with permission from Elsevier

in water by femtosecond laser pulses. It should be mentioned that the reactions of water dominate those of dissolved organic molecules in aqueous solution because the concentration of water is much higher than that of solute. The primary reactions occurring in water are ionization (17.1) and excitation (17.2) as in the cases of neat organic liquid. However, complicated chemical reactions follow in water as shown in (17.3−17.15). We show only representative reactions here. Strong oxidant (hydroxyl radical, $HO^{\bullet}$) and reductants (hydrated electron, $e^{-}_{aq}$; hydrogen radical, $H^{\bullet}$) are formed in the primary processes (17.1−17.5, < 1 ps). In the succeeding processes, those intermediates are consumed (17.6−17.15). The final products of water exposed to femtosecond laser pulses are $H_2$, $H_2O_2$, and $O_2$ [71]. Supposing that the subsequent exposures of organic molecules to those strong oxidants and/or reductants occur within their lifetimes, carbon nanomaterials or at least their intermediates are finally formed. The initial reactions of organic molecules with reactive species ($HO^{\bullet}$, $e^{-}_{aq}$, $H^{\bullet}$) generated by photolysis, radiolysis, and discharges have been well-studied. However, the details of the successive reactions as well as of the photoexcitation of the intermediates of carbon nanomaterials during laser irradiation

(filamentation) might not be clarified in situ.

$$H_2O \rightarrow H_2O^{+\bullet} + e^- \tag{17.1}$$

$$H_2O \rightarrow H_2O^* \tag{17.2}$$

$$e^- + H_2O \rightarrow e^-_{aq} \tag{17.3}$$

$$H_2O^{+\bullet} + H_2O \rightarrow H_3O^+ + HO^\bullet \tag{17.4}$$

$$H_2O^* \rightarrow HO^\bullet + H^\bullet \tag{17.5}$$

$$e^-_{aq} + O_2 \rightarrow O_2^{-\bullet} \tag{17.6}$$

$$e^-_{aq} + e^-_{aq} + 2H_2O \rightarrow H_2 + 2HO^- \tag{17.7}$$

$$e^-_{aq} + H^\bullet + H_2O \rightarrow H_2 + HO^- \tag{17.8}$$

$$e^-_{aq} + H_3O^+ \rightarrow H^\bullet + H_2O \tag{17.9}$$

$$e^-_{aq} + HO^\bullet \rightarrow HO^- \tag{17.10}$$

$$HO^\bullet + HO^\bullet \rightarrow H_2O_2 \tag{17.11}$$

$$HO^\bullet + H^\bullet \rightarrow H_2O \tag{17.12}$$

$$HO^\bullet + H_2 \rightarrow H^\bullet + H_2O \tag{17.13}$$

$$H^\bullet + H^\bullet \rightarrow H_2 \tag{17.14}$$

$$H^\bullet + O_2 \rightarrow HO_2^\bullet \tag{17.15}$$

We introduce an interesting example in which the production of hydrophilic or hydrophobic CNPs is dependent on the concentration of reactant (benzene) in water. A laser beam (0.8 μm, 40 fs) was focused on aqueous benzene solution in a quartz cuvette. The aqueous benzene solution ($2.2 \times 10^{-3}$ mol dm$^{-3}$) before and after irradiation was colorless and transparent, and Tyndall scattering was not observed. In contrast, the solution became colloidal after some induction period as we increased

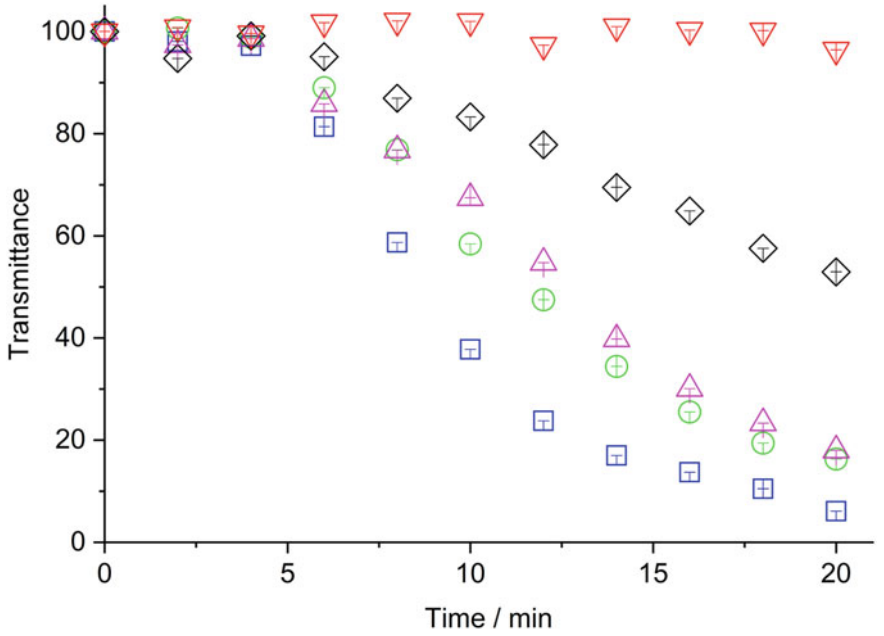


**Fig. 17.11** Time evolution of the transmittance of aqueous benzene solution. The concentration of benzene was $2.2 \times 10^{-3}$ (inverted triangles), $5.6 \times 10^{-3}$ (diamonds), $8.6 \times 10^{-3}$ (triangles), $1.2 \times 10^{-2}$ (circles), and $1.7 \times 10^{-2}$ mol dm$^{-3}$ (squares). The vertical bars show the standard deviation obtained in the five measurements

the benzene concentration. Thus, we observed the time evolution of the transmittance of the aqueous benzene solution by using a diode laser (635 nm) as shown in Fig. 17.11. The transmittance was not changed when the dilute ($2.2 \times 10^{-3}$ mol dm$^{-3}$) aqueous benzene solution was irradiated, as we observed by the naked eye. The transmittance was decreased after an induction period (<5 min) when the concentration of benzene was higher than $5.6 \times 10^{-3}$ mol dm$^{-3}$. As we increased the benzene concentration, the production of particles accelerated and the transmittance of the resultant solution decreased. Figure 17.12 shows the cuvette after laser irradiation of 1 cm$^3$ aqueous benzene (a, $9.0 \times 10^{-3}$ mol dm$^{-3}$; b, $1.5 \times 10^{-2}$ mol dm$^{-3}$). At first glance, both solutions seem to be colloidal, and particles are dispersed in water. However, the particle characteristics are not identified only by their appearance. We then shook the solution after adding 1 cm$^3$ benzene to confirm the particle characteristics. The particles did not move to the benzene layer from the diluted aqueous benzene (Fig. 17.12a, right), whereas most of the particles moved to the benzene layer from the concentrated aqueous benzene (Fig. 17.12b, right). Therefore, it is concluded that the affinity of the particles to water is determined by the initial concentration of benzene in water.

Hydrophilic CNPs were formed when we kept a low concentration of benzene in water. However, the production mass of CNPs should be low because it is limited

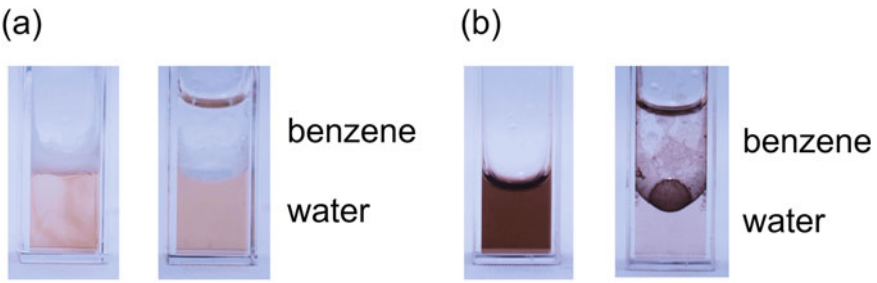


**Fig. 17.12** The cuvette after laser irradiation. The concentrations of aqueous benzene were **a** $9.0 \times 10^{-3}$ and **b** $1.5 \times 10^{-2}$ mol $dm^{-3}$. The solution just after laser irradiation (left) was shaken by hand with 1 $cm^3$ of benzene to confirm the distribution of CNPs between the benzene layer and the water layer (right)

by the total amount of benzene in water. Therefore, we needed a different strategy to produce more hydrophilic CNPs. Here we utilized the interface between benzene and water. Figure 17.13 shows the benzene/water bilayer solution after irradiation with femtosecond laser pulses (0.8 μm, 40 fs) [58]. The upper and lower layers are benzene and water, respectively. From left to right, the laser beam was focused on (a) the bottom of the water layer, (b) the benzene layer through the benzene/water interface (meniscus), and (c) the benzene layer. The use of the benzene/water bilayer dramatically enhanced the production of CNPs compared with that in neat benzene.

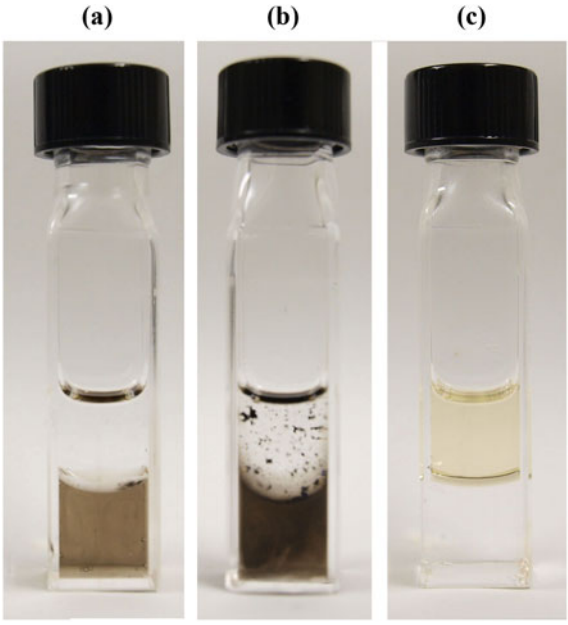


**Fig. 17.13** The cuvette after laser irradiation (0.8 μm, 40 fs). The laser beam was focused on **a** the bottom of the water layer, **b** the benzene layer through the benzene/water interface (meniscus), and **c** the benzene layer. Adapted with permission from [58]. Copyright 2015 The Chemical Society of Japan

As the nanoparticle generation in benzene was quite inefficient under our experimental conditions [58], CNP generation mechanism should have been different from that in neat benzene [22, 23]. In the case of (a), the black colloidal particles appeared not from the laser focal spot but from the benzene/water interface even though the laser was irradiated to the bottom of the water layer. The water layer finally became a homogeneous black colloidal solution, whereas the benzene layer was transparent. In the case of (b), dense particles were formed in the water layer and large particles also existed in the benzene layer. The particles were identified as (a) hydrophilic and (b) hydrophobic by shaking the solution, the same as in Fig. 17.12. The merits of using the benzene/water interface are (1) only hydrophilic CNPs were formed because the concentration of benzene in the water layer was limited by the interface, and (2) dense hydrophilic CNPs were formed because benzene was continuously supplied into the water through the interface. For these reasons, the bilayer solution should not be mixed if we need only hydrophilic CNPs.

It was finally found that the focal-position-dependent chemistry shown in Fig. 17.13 originated in the concentration of benzene in water, which is important for determining the secondary reactions [72]. As we mentioned earlier, one can simply imagine that CNPs can be made hydrophilic by treating organic molecules in water. This expectation is based on the fact that hydroxyl radical is generated in water by femtosecond laser irradiation (17.4 and 17.5). Figure 17.14a shows the IR spectra of hydrophilic and hydrophobic CNPs produced from benzene. As expected, hydroxyl groups were found in hydrophilic CNPs but not in hydrophobic CNPs. These results straightforwardly explain the affinity of CNPs to water. Thus, a simple question arises: What did determine the presence or absence of hydroxyl groups in CNPs. The bottom-up CNP production approach is initiated by the chemical reaction between reactive species generated in water and dissolved organic molecules. The reaction rate constants of benzene with $HO^{\bullet}$, $H^{\bullet}$, and $e^{-}_{aq}$ are $7.6 \times 10^9$, $5.3 \times 10^8$, and $1.2 \times 10^7$ $dm^3$ $mol^{-1}$ $s^{-1}$, respectively. Therefore, the addition of $HO^{\bullet}$ to benzene dominantly occurs. Figure 17.15 shows simplified reaction schemes of

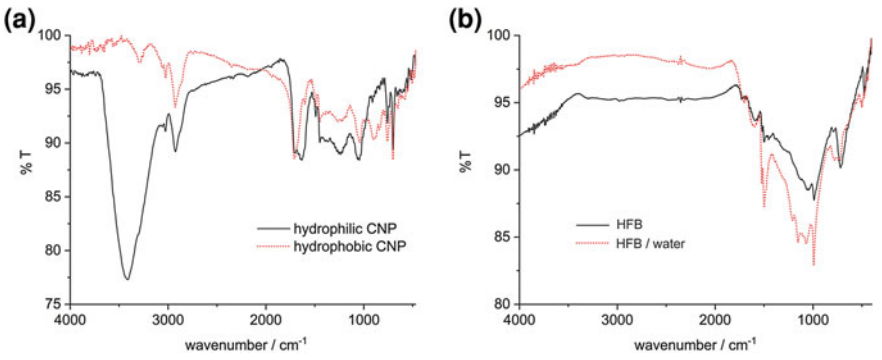


**Fig. 17.14** IR spectra of CNPs produced **a** in benzene/water bilayer and **b** in HFB or HFB/water bilayer.

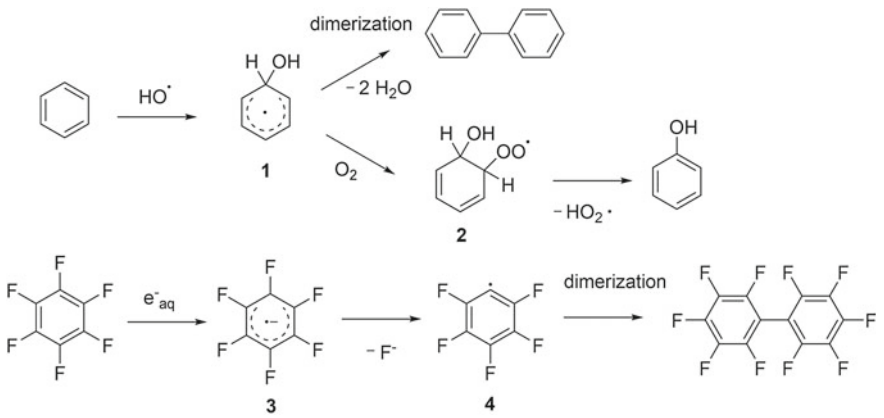


**Fig. 17.15** Simplified reaction schemes of benzene (upper) and HFB (lower) with reactive species generated in water by femtosecond laser pulses.

benzene with hydroxyl radical [73]. The chemical reaction of hydroxy cyclohexadienyl radical (**1**) branches to dimerization to form biphenyl or the addition of oxygen to hydroxy cyclohexadienyl peroxyl radical (**2**). The oxygen adduct **2** transforms to phenol. Since the reaction solution is saturated with oxygen due to the decomposition of water, phenol is formed when the concentration of benzene is low. If the concentration of benzene is sufficient, biphenyl forms. Phenol and biphenyl would further react with reactive species to lead large aromatics and would finally become CNPs with different surface characteristics. Figure 17.16 shows a gas chromatogram of the water layers in which hydrophilic or hydrophobic CNPs are formed. Although most of the peaks were not assigned, a lot of aromatic molecules were formed in the former case, indicating the complicated successive reactions, whereas biphenyl was the dominant species in the latter case.

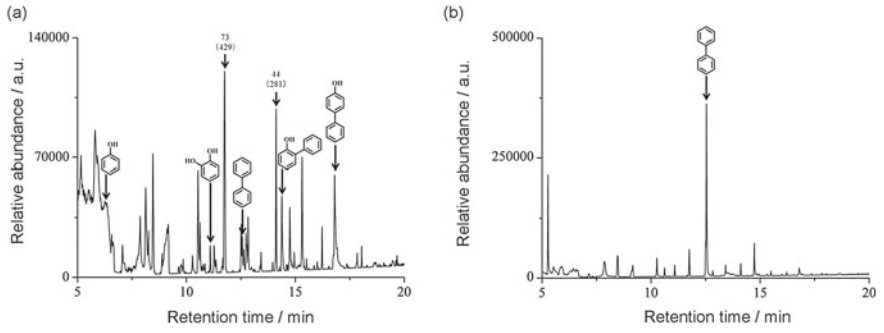


**Fig. 17.16** Gas chromatogram of water layer in which **a** hydrophilic or **b** hydrophobic CNPs are formed in benzene/water bilayer solution by femtosecond laser pulses. Adapted with permission from [72]. Copyright 2015 The Chemical Society of Japan

Although benzene and HFB are categorized as aromatics, the resultant CNPs show different characteristics. Figure 17.14b shows the IR spectra of CNPs produced from HFB or an HFB/water bilayer solution. The hydroxyl group and other hydrophilic functional groups were not found in either case. CNPs produced in neat HFB were introduced as hydrophobic carbon particles in Sect. 17.3 However, CNPs produced from the HFB/water bilayer solution showed a hydrophilic characteristic as in the case of benzene. Although their IR spectra were similar to each other, CNPs produced from HFB showed different affinities to water depending on the synthetic environment. These discrepancies are due to the fact that hydrophobic CNPs are highly agglomerated, whereas hydrophilic CNPs are isolated in water. Therefore, it was found that the former CNPs can be dispersed in water after sonication. Consequently, CNPs produced from HFB have a hydrophilic nature regardless of the synthetic environment. Actually, the origin of hydrophilicity is the dominance of semi-ionic and ionic C-F bonds, which would be very effective for the formation of hydrogen bonds with water. Analysis of the F1s peak of CNPs produced from the HFB/water bilayer solution measured by XPS showed that the ratios of ionic, semi-ionic, and covalent C-F bonds were 10.6, 85.3, and 4.1%, respectively [62]. Unlike hydrophilic CNPs produced from benzene, that produced from HFB did not have hydroxyl groups because the initial reaction of HFB with reactive species differs from that of benzene. The reaction rate constants of HFB with $e^-_{aq}$, $HO^\bullet$, and $H^\bullet$ were $2.0 \times 10^{10}$, $2.0 \times 10^9$, and $1.0 \times 10^7$ $dm^3\ mol^{-1}\ s^{-1}$, respectively. Unlike the case with benzene, the reduction of HFB by hydrated electrons to form anion radical (**3**) dominantly occurs (Fig. 17.15). Actually, we do not need water (hydroxyl radical) to form hydrophilic CNPs from HFB. Pentafluorobenzene radicals (**4**) formed by the release of fluorine anion from **3** dimerize to form octafluorobiphenyl as a secondary product. The further reactions of octafluoro biphenyl lead to large aromatics and would finally become CNPs without a hydroxyl substituent. Production of fluorine-rich CNPs is an important characteristic of the bottom-up method, but the heteroatom contents of carbon nanomaterials are not always high. For example, hydrated electrons initiate the reactions of dichloromethane ($CH_2Cl_2$) as in the cases of HFB, but almost chlorine-free and hydrophobic CNPs were formed from aqueous solution and/or a bilayer solution with water [74].

The bottom-up approach to forming hydrophilic CNPs from organic molecules by femtosecond laser irradiation depends on the initial reaction of reactants with reactive species and the following reactions. Although the chemical reactions toward CNPs are hardly traceable, the merit of the bottom-up approach is that a variety of organic molecules can be used as a carbon source. From this point of view, we introduce the synthesis of heteroatom (nitrogen, boron)-doped CDs using 2-aminopyrimidine-5-boronic acid (**5**) as a precursor [75]. Figure 17.17 shows the proposed production mechanism of CDs from aqueous **5** by femtosecond laser pulses (800 nm, 30 fs). The detachment of boronic acid radical initiates the cleavages of C-N bonds in the intermediates **6** and **7** followed by the production of corresponding linear-shaped intermediates **8** and **9**, which are expected to carbonize to form CDs under high-temperature and high-pressure conditions in filaments. Finally, glucose-sensitive and emissive carbon nanomaterials were formed by the attachment of boronic acids

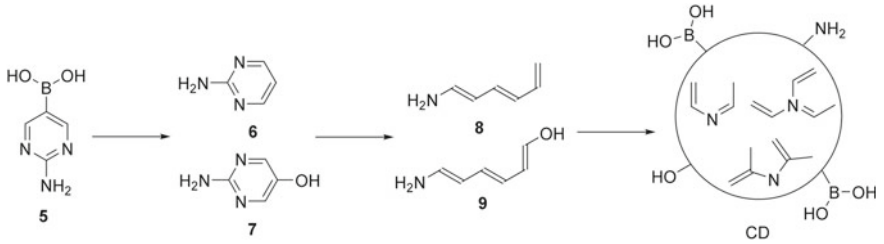


**Fig. 17.17** Proposed production mechanism of CDs from aqueous 2-aminopyrimidine-5-boronic acid (**5**) by femtosecond laser irradiation

to the surface of CDs, which include pyridinic, pyrrolic, and graphitic nitrogens. The IR spectra measurements revealed that **5** and the intermediates of CDs (**6**, **7**) disappeared after about 10 h of irradiation of femtosecond laser pulses. Furthermore, in situ measurements of emissions were carried out to monitor the reaction processes: second harmonic generation (SHG) by **6** and two-photon emission of CDs. SHG caused by **6** appeared after about 8 h of laser irradiation, gradually increased to a maximum value at 13 h, and then gradually diminished. In contrast, two-photon emission of CDs appeared after about 8 h laser irradiation and gradually increased to a constant value after around 12 h. In the case of ethanol, plasma emission gave fruitful information about the atomic fragments. In situ monitoring of the transformation of precursor molecules to intermediates and CDs by emission spectroscopy is especially advantageous for strong luminescent and photostable carbon nanomaterials. In addition to ex situ measurements such as mass spectroscopy, in situ measurements of transmittance, absorption spectra, and emission spectra could be used to investigate the details of chemical reactions from small intermediate to final products. Further, the reaction would be clarified by making full use of various methods. For example, in situ measurements of NMR spectra are now possible by flow systems.

Finally, we would like to introduce a very impressive approach to producing fluorescent CDs to probe intracellular dynamics [76]. Focusing femtosecond laser pulse trains (690 to 990 nm, 25 fs) from an oscillator by an objective lens onto mouse germinal vesicle oocytes creates fluorescence CDs in a very confined volume. Figure 17.18 shows that a bright green spot appeared after the laser irradiation without the injection of any exogenous fluorescent particles. From the observation of fluorescence images, luminescent spots were estimated to be less than 200 nm in size, which is the theoretical resolution limit of the objective lens used. Contrary to the processes carried out in a vessel, the locations of CDs can be precisely controlled under microscope. Moreover, this procedure can avoid the problem of the cell membrane preventing the delivery of exogenous probes to label the cell. The precise origin of fluorescent CDs is not known, but focusing femtosecond laser pulses produces bright spots regardless of the cell or its contents (cytoplasm, nucleus, and nucleolus). The Raman spectrum of the fluorescent spot clearly showed carbon-related bands (Fig. 17.19a), whereas such peaks were not detected anywhere else. Therefore, intracellular organic molecules should be carbonized to form CDs by femtosecond laser

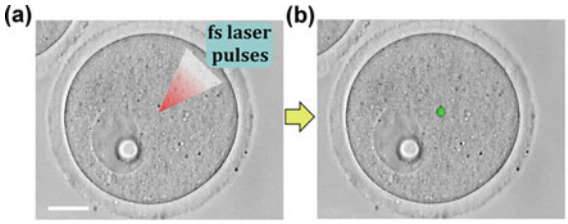


**Fig. 17.18** Combination of brightfield and fluorescent images of the oocyte **a** before and **b** after exposure to a laser pulse train. A spot produced in the intracellular material upon femtosecond laser irradiation shows green fluorescence. Scale bar is 20 μm. Adapted with permission from [76]. Copyright 2020 American Chemical Society

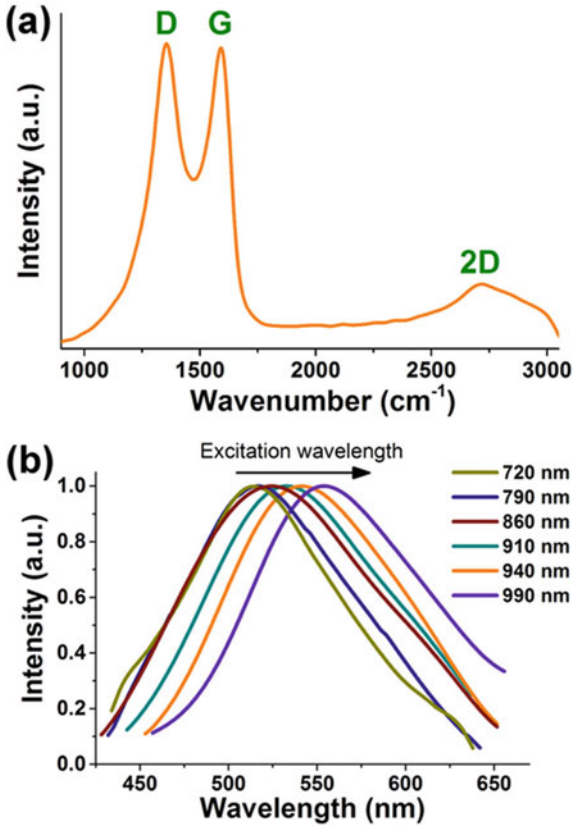


**Fig. 17.19** **a** Differential Raman and **b** normalized two-photon fluorescence spectra of CDs produced in the oocyte's cytoplasm by femtosecond laser irradiation. Reprinted with permission from [76]. Copyright 2020 American Chemical Society

pulses. Figure 17.19b shows the characteristic (two-photon) fluorescent behavior of CDs, namely excitation-wavelength-dependent fluorescence. The authors' preliminary results showed that the solution of amino acids or lipids also produced luminescent CDs. Therefore, the production of CDs in biomolecules would be a universal and promising technique that can label in any desired location within the cell while preserving the viability of a cell.

## 17.5 Summary

In this chapter, we introduced the production of carbon nanomaterials such as carbon nanoparticles, carbon dots, and nanodiamonds. The bottom-up syntheses of those carbon nanomaterials succeeded by the use of organic molecules as liquid reactants, aqueous solution, and bilayer solution with water. The advantages of the bottom-up approach are the addition of affinity to water and the control of atomic composition not only on the surface but also in whole materials. The concern with this unique process, however, is the complexity of the chemical reactions required to form the final products. Therefore, this method is not straightforward enough to determine what kind of materials will be produced by what kind of molecule. The photochemistry and/or chemical reactions of reactant and reaction intermediates are important to determine the physical and chemical properties of resultant carbon nanomaterials. To solve this issue, more examples must be accumulated. Thus far, the literature contains only limited numbers of examples that use femtosecond laser pulses. Although there are some restrictions, we can explore suitable reactants for our purpose from more than 100 million molecules. In contrast to LAL, in which the reactant solid has a usually uniform chemical composition, the bottom-up approach can mix molecules in desired ratios, and immiscible conditions, such as bilayer solution and emulsion [77, 78], can be utilized. Moreover, the experimental conditions can be controlled by optimizing various experimental parameters as in the cases of LAL. The bottom-up approach will be very useful and versatile if we can take advantages of those features.

**Acknowledgements** The authors would like to thank Ms. Kayo Nishikawa, Ms. Naoko Uchida, Mr. Tomoyuki Hamaguchi, Ms. Erina Miyasaka, Dr. Koji Mitamura, Prof. Kimihiro Matsukawa, Mr. Yuhei O. Tahara, Prof. Makoto Miyata for their contribution to carbon nanoparticle studies.

## References

1. M.F.L. De Volder, S.H. Tawfick, R.H. Baughman, A.J. Hart, Carbon nanotubes: present and future commercial applications. Science **339**, 535–539 (2013). https://doi.org/10.1126/science.1222453
2. S.Y. Lim, W. Shen, Z.Q. Gao, Carbon quantum dots and their applications. Chem. Soc. Rev. **44**, 362–381 (2015). https://doi.org/10.1039/c4cs00269e

3. F. Arduini, S. Cinti, V. Mazzaracchio, V. Scognamiglio, A. Amine, D. Moscone, Carbon black as an outstanding and affordable nanomaterial for electrochemical (bio)sensor design. Biosens. Bioelectron. 156 (2020) 112033. https://doi.org/10.1016/j.bios.2020.112033
4. S. Tajik, Z. Dourandish, K. Zhang, H. Beitollahi, Q.V. Le, H.W. Jang, M. Shokouhimehr, Carbon and graphene quantum dots: a review on syntheses, characterization, biological and sensing applications for neurotransmitter determination. RSC Adv. **10**, 15406–15429 (2020). https://doi.org/10.1039/d0ra00799d
5. Z.G. Khan, P.O. Patil, A comprehensive review on carbon dots and graphene quantum dots based fluorescent sensor for biothiols, Microchem. J. 157 (2020) 105011. https://doi.org/10.1016/j.microc.2020.105011
6. S. Kumar, M. Nehra, D. Kedia, N. Dilbaghi, K. Tankeshwar, K.H. Kim, Nanodiamonds: Emerging face of future nanotechnology. Carbon **143**, 678–699 (2019). https://doi.org/10.1016/j.carbon.2018.11.060
7. A. Sharma, J. Das, Small molecules derived carbon dots: synthesis and applications in sensing, catalysis, imaging, and biomedicine. J. Nanobiotechnol. **17**, 92 (2019). https://doi.org/10.1186/s12951-019-0525-8
8. J.L. Wang, Y.Z. Yang, X.G. Liu, Solid-state fluorescent carbon dots: quenching resistance strategies, high quantum efficiency control, multicolor tuning, and applications. Mater. Adv. **1**, 3122–3142 (2020). https://doi.org/10.1039/d0ma00632g
9. M.J. Molaei, The optical properties and solar energy conversion applications of carbon quantum dots: A review. Sol. Energy **196**, 549–566 (2020). https://doi.org/10.1016/j.solener.2019.12.036
10. T. Okamoto, N. Nakashima, T. Yatsuhashi, Chemical reactions and nanomaterial productions in liquid phase by femtosecond laser pulses (in Japanese). Rev. Laser Eng. **45**, 278–282 (2017). https://doi.org/10.2184/lsj.45.5_278
11. S.L. Shumlas, K.M. Tibbetts, J.H. Odhner, D.A. Romanov, R.J. Levis, D.R. Strongin, Formation of carbon nanospheres via ultrashort pulse laser irradiation of methane. Mater. Chem. Phys. **156**, 47–53 (2015). https://doi.org/10.1016/j.matchemphys.2015.02.017
12. A. Matsuda, T. Hayashi, R. Kitaura, A. Hishikawa, Femtosecond laser filamentation in gaseous ethylene: formation of hydrogenated amorphous carbon. Chem. Lett. **46**, 1426–1429 (2017). https://doi.org/10.1246/cl.170613
13. A. Hu, Q.B. Lu, W.W. Duley, M. Rybachuk, Spectroscopic characterization of carbon chains in nanostructured tetrahedral carbon films synthesized by femtosecond pulsed laser deposition, J. Chem. Phys. 126 (2007) 154705. https://doi.org/10.1063/1.2727450
14. F. Garrelie, A.S. Loir, L.C. Donnet, F. Rogemond, R. Le Harzic, M. Belin, E. Audouard, P. Laporte, Femtosecond pulsed laser deposition of diamond-like carbon thin films for tribological applications. Surf. Coat. Technol. **163**, 306–312 (2003). https://doi.org/10.1016/S0257-8972(02)00481-4
15. W. Inoue, M. Okoshi, N. Inoue, Fabrication of diamond-like carbon thin films by femtosecond laser ablation of frozen acetone. Appl. Phys. A **79**, 1457–1460 (2004). https://doi.org/10.1007/s00339-004-2810-z
16. M. Okoshi, W. Inoue, N. Inoue, Femtosecond laser ablation of frozen alcohols for deposition of diamond-like carbon thin films. Jpn. J. Appl. Phys. **47**, 4572–4577 (2008). https://doi.org/10.1143/Jjap.47.4572
17. M.J. Wesolowski, B. Moores, Z. Leonenko, R. Karimi, J.H. Sanderson, W.W. Duley, Synthesis of polymer-like hydrogenated amorphous carbon by fs-pulsed laser induced plasma processing of solid hexane. Plasma Process Polym. **9**, 701–708 (2012). https://doi.org/10.1002/ppap.201100206
18. R. Srinivasan, A.P. Ghosh, Ablation of liquid benzene by pulsed ultraviolet (248 or 308 nm) laser-radiation. Chem. Phys. Lett. **143**, 546–550 (1988). https://doi.org/10.1016/0009-2614(88)87064-7
19. Y. Sato, T. Kodama, H. Shiromaru, J.H. Sanderson, T. Fujino, Y. Wada, T. Wakabayashi, Y. Achiba, Synthesis of polyyne molecules from hexane by irradiation of intense femtosecond laser pulses. Carbon **48**, 1673–1676 (2010). https://doi.org/10.1016/j.carbon.2009.12.036

20. A.A. Zaidi, A. Hu, M.J. Wesolowski, X. Fu, J.H. Sanderson, Y. Zhou, W.W. Duley, Time of flight mass spectrometry of polyyne formation in the irradiation of liquid alkanes with femtosecond laser pulses. Carbon **48**, 2517–2520 (2010). https://doi.org/10.1016/j.carbon.2010.03.026
21. A. Hu, J. Sanderson, A.A. Zaidi, C. Wang, T. Zhang, Y. Zhou, W.W. Duley, Direct synthesis of polyyne molecules in acetone by dissociation using femtosecond laser irradiation. Carbon **46**, 1823–1825 (2008). https://doi.org/10.1016/j.carbon.2008.07.036
22. M.J. Wesolowski, S. Kuzmin, B. Moores, B. Wales, R. Karimi, A.A. Zaidi, Z. Leonenko, J.H. Sanderson, W.W. Duley, Polyyne synthesis and amorphous carbon nano-particle formation by femtosecond irradiation of benzene. Carbon **49**, 625–630 (2011). https://doi.org/10.1016/j.carbon.2010.10.008
23. T. Nakamura, Y. Mochidzuki, S. Sato, Synthesis of monodispersed DLC nanoparticles in intense optical field by femtosecond laser ablation of liquid benzene, in: 2007 Conference on Lasers and Electro-Optics (CLEO) (2007), JThD89
24. A. Fojtik, A. Henglein, Laser ablation of films and suspended particles in a solvent - formation of cluster and colloid solutions. Ber. Bunsen Phys. Chem. **97**, 252–254 (1993)
25. D.S. Zhang, B. Goekce, S. Barcikowski, Laser synthesis and processing of colloids: fundamentals and applications. Chem. Rev. **117**, 3990–4103 (2017). https://doi.org/10.1021/acs.chemrev.6b00468
26. G.W. Yang, Laser ablation in liquids: applications in the synthesis of nanocrystals. Prog. Mater. Sci. **52**, 648–698 (2007). https://doi.org/10.1016/j.pmatsci.2006.10.016
27. J. Xiao, P. Liu, C.X. Wang, G.W. Yang, External field-assisted laser ablation in liquid: an efficient strategy for nanocrystal synthesis and nanostructure assembly. Prog. Mater. Sci. **87**, 140–220 (2017). https://doi.org/10.1016/j.pmatsci.2017.02.004
28. D. Amans, W.P. Cai, S. Barcikowski, Status and demand of research to bring laser generation of nanoparticles in liquids to maturity. Appl. Surf. Sci. **488**, 445–454 (2019). https://doi.org/10.1016/j.apsusc.2019.05.117
29. R. Kumar, R.K. Singh, D.P. Singh, E. Joanni, R.M. Yadav, S.A. Moshkalev, Laser-assisted synthesis, reduction and micro-patterning of graphene: recent progress and applications. Coord. Chem. Rev. **342**, 34–79 (2017). https://doi.org/10.1016/j.ccr.2017.03.021
30. V. Amendola, D. Amans, Y. Ishikawa, N. Koshizaki, S. Scire, G. Compagnini, S. Reichenberger, S. Barcikowski, Room-temperature laser synthesis in liquid of oxide, metal-oxide core-shells, and doped oxide nanoparticles. Chem. Eur. J. **26**, 9206–9242 (2020). https://doi.org/10.1002/chem.202000686
31. H.L. Du, V. Castaing, D.C. Guo, B. Viana, Rare-earths doped-nanoparticles prepared by pulsed laser ablation in liquids. Ceram. Int. **46**, 26299–26308 (2020). https://doi.org/10.1016/j.ceramint.2020.04.291
32. B. Jaleh, M. Nasrollahzadeh, B.F. Mohazzab, M. Eslamipanah, M. Sajjadi, H. Ghafuri, State-of-the-art technology: recent investigations on laser-mediated synthesis of nanocomposites for environmental remediation. Ceram. Int. **47**, 10389–10425 (2021). https://doi.org/10.1016/j.ceramint.2020.12.197
33. D.S. Zhang, J. Liu, P.F. Li, Z.F. Tian, C.H. Liang, Recent advances in surfactant-free surface-charged, and defect-rich catalysts developed by laser ablation and processing in liquids. Chem. Nano Mat. **3**, 512–533 (2017). https://doi.org/10.1002/cnma.201700079
34. H.B. Zeng, X.W. Du, S.C. Singh, S.A. Kulinich, S.K. Yang, J.P. He, W.P. Cai, Nanomaterials via laser ablation/irradiation in liquid: a review. Adv. Funct. Mater. **22**, 1333–1353 (2012). https://doi.org/10.1002/adfm.201102295
35. Z.J. Yan, D.B. Chrisey, Pulsed laser ablation in liquid for micro-/nanostructure generation. J. Photochem. Photobiol. C **13**, 204–223 (2012). https://doi.org/10.1016/j.jphotochemrev.2012.04.004
36. D.Z. Tan, S.F. Zhou, J.R. Qiu, N. Khusro, Preparation of functional nanomaterials with femtosecond laser ablation in solution. J. Photochem. Photobiol. C **17**, 50–68 (2013). https://doi.org/10.1016/j.jphotochemrev.2013.08.002
37. D. Amans, M. Diouf, J. Lam, G. Ledoux, C. Dujardin, Origin of the nano-carbon allotropes in pulsed laser ablation in liquids synthesis. J. Colloid Interface Sci. **489**, 114–125 (2017). https://doi.org/10.1016/j.jcis.2016.08.017

38. P. Russo, A.M. Hu, G. Compagnini, W.W. Duley, N.Y. Zhou, Femtosecond laser ablation of highly oriented pyrolytic graphite: a green route for large-scale production of porous graphene and graphene quantum dots. Nanoscale **6**, 2381–2389 (2014). https://doi.org/10.1039/c3nr05572h
39. V. Nguyen, L.H. Yan, H.H. Xu, M.M. Yue, One-step synthesis of multi-emission carbon nanodots for ratiometric temperature sensing. Appl. Surf. Sci. **427**, 1118–1123 (2018). https://doi.org/10.1016/j.apsusc.2017.08.133
40. V. Nguyen, L.H. Yan, J.H. Si, X. Hou, Femtosecond laser-assisted synthesis of highly photoluminescent carbon nanodots for $Fe^{3+}$ detection with high sensitivity and selectivity. Opt. Mater. Express **6**, 312–320 (2016). https://doi.org/10.1364/Ome.6.000312
41. V. Nguyen, L.H. Yan, J.H. Si, X. Hou, Femtosecond laser-induced size reduction of carbon nanodots in solution: Effect of laser fluence, spot size, and irradiation time, J. Appl. Phys. 117 (2015) 084304. https://doi.org/10.1063/1.4909506
42. X.Y. Li, L.H. Yan, J.H. Si, Y.M. Xu, X. Hou, Control of the size and luminescence of carbon nanodots by adjusting ambient pressure in laser ablation process, J. Appl. Phys. 127 (2020) 083102. https://doi.org/10.1063/1.5128042
43. V. Nguyen, N. Zhao, L.H. Yan, P. Zhong, V.C. Nguyen, P.H. Le, Double-pulse femtosecond laser ablation for synthesis of ultrasmall carbon nanodots, Mater. Res. Express 7 (2020) 015606. https://doi.org/10.1088/2053-1591/ab6124
44. D.Z. Tan, S.F. Zhou, B.B. Xu, P. Chen, Y. Shimotsuma, K. Miura, J.R. Qiu, Simple synthesis of ultra-small nanodiamonds with tunable size and photoluminescence. Carbon **62**, 374–381 (2013). https://doi.org/10.1016/j.carbon.2013.06.019
45. G. Heck, J. Sloss, R.J. Levis, Adaptive control of the spatial position of white light filaments in an aqueous solution. Optics Commun. **259**, 216–222 (2006). https://doi.org/10.1016/j.optcom.2005.08.073
46. N. Nakashima, K. Yamanaka, M. Saeki, H. Ohba, S. Taniguchi, T. Yatsuhashi, Metal ion reductions by femtosecond laser pulses with micro-Joule energy and their efficiencies. J. Photochem. Photobiol. A **319**, 70–77 (2016). https://doi.org/10.1016/j.jphotochem.2015.12.021
47. S.L. Chin, S.A. Hosseini, W. Liu, Q. Luo, F. Theberge, N. Akozbek, A. Becker, V.P. Kandidov, O.G. Kosareva, H. Schroeder, The propagation of powerful femtosecond laser pulses in optical media: physics, applications, and new challenges. Can. J. Phys. **83**, 863–905 (2005). https://doi.org/10.1139/P05-048
48. A. Couairon, A. Mysyrowicz, Femtosecond filamentation in transparent media. Phys. Rep. **441**, 47–189 (2007). https://doi.org/10.1016/j.physrep.2006.12.005
49. L. Berge, S. Skupin, R. Nuter, J. Kasparian, J.P. Wolf, Ultrashort filaments of light in weakly ionized, optically transparent media. Rep. Prog. Phys. **70**, 1633–1713 (2007). https://doi.org/10.1088/0034-4885/70/10/R03
50. H. Belmouaddine, G.S. Madugundu, J.R. Wagner, A. Couairon, D. Houde, L. Sanche, DNA base modifications mediated by femtosecond laser-induced cold low-density plasma in aqueous solutions. J. Phys. Chem. Lett. **10**, 2753–2760 (2019). https://doi.org/10.1021/acs.jpclett.9b00652
51. D. Nishida, E. Yamade, M. Kusaba, T. Yatsuhashi, N. Nakashima, Reduction of $Sm^{3+}$ to $Sm^{2+}$ by an intense femtosecond laser pulse in solution. J. Phys. Chem. A **114**, 5648–5654 (2010). https://doi.org/10.1021/jp9109089
52. S.L. Chin, Femtosecond Laser Filamentation Induced Phenomena and Applications, in: K. Yamanouchi, D. Charalambidis (Eds.), Progress in Ultrafast Intense Laser Science XV, Springer International Publishing, 2020, pp. 1–19. https://doi.org/10.1007/978-3-030-47098-2_1
53. S.L. Chin, T.J. Wang, C. Marceau, J. Wu, J.S. Liu, O. Kosareva, N. Panov, Y.P. Chen, J.F. Daigle, S. Yuan, A. Azarm, W.W. Liu, T. Seideman, H.P. Zeng, M. Richardson, R. Li, Z.Z. Xu, Advances in intense femtosecond laser filamentation in air. Laser Phys. **22**, 1–53 (2012). https://doi.org/10.1134/S1054660x11190054
54. S.L. Chin, Femtosecond Laser Filamentation, Springer-Verlag, New York, 2010. https://doi.org/10.1007/978-1-4419-0688-5

55. T. Yatsuhashi, N. Nakashima, Multiple ionization and Coulomb explosion of molecules, molecular complexes, clusters and solid surfaces. J. Photochem. Photobiol. C **34**, 52–84 (2018). https://doi.org/10.1016/j.jphotochemrev.2017.12.001
56. N. Nakashima, S. Shimizu, T. Yatsuhashi, S. Sakabe, Y. Izawa, Large molecules in high-intensity laser fields. J. Photochem. Photobiol. C **1**, 131–143 (2000). https://doi.org/10.1016/S1389-5567(00)00009-5
57. C. Milian, A. Jarnac, Y. Brelet, V. Jukna, A. Houard, A. Mysyrowicz, A. Couairon, Effect of input pulse chirp on nonlinear energy deposition and plasma excitation in water. J. Opt. Soc. Am. B **31**, 2829–2837 (2014). https://doi.org/10.1364/Josab.31.002829
58. T. Yatsuhashi, N. Uchida, K. Nishikawa, Novel method of producing carbon nanoparticles on benzene/water interface with femtosecond laser plasma filament. Chem. Lett. **41**, 722–724 (2012). https://doi.org/10.1246/cl.2012.722
59. A.A. Astafiev, A.M. Shakhov, A.S. Kritchenkov, V.N. Khrustalev, D.V. Shepel, V.A. Nadtochenko, A.G. Tskhovrebov, Femtosecond laser synthesis of nitrogen-doped luminescent carbon dots from acetonitrile, Dyes Pigments 188 (2021) 109176. https://doi.org/10.1016/j.dyepig.2021.109176
60. C.H. Nee, S.L. Yap, T.Y. Tou, H.C. Chang, S.S. Yap, Direct synthesis of nanodiamonds by femtosecond laser irradiation of ethanol. Sci. Rep. **6**, 33966 (2016). https://doi.org/10.1038/srep33966
61. C.H. Nee, M.C. Lee, H.S. Poh, S.L. Yap, T.Y. Tou, S.S. Yap, Plasma synthesis of nanodiamonds in ethanol. Compos. B Eng. **162**, 162–166 (2019). https://doi.org/10.1016/j.compositesb.2018.10.071
62. T. Okamoto, K. Mitamura, T. Hamaguchi, K. Matsukawa, T. Yatsuhashi, Synthesis of fluorine-doped hydrophilic carbon nanoparticles from hexafluorobenzene by femtosecond laser pulses. ChemPhysChem **18**, 1007–1011 (2017). https://doi.org/10.1002/cphc.201600602
63. A.A. Astafiev, A.M. Shakhov, A.A. Vasin, Y.V. Kostina, V.A. Nadtochenko, Femtosecond laser synthesis of luminescent carbon dots from toluene. JETP Lett. **110**, 464–471 (2019). https://doi.org/10.1134/S0021364019190056
64. A. Ramadhan, M. Wesolowski, T. Wakabayashi, H. Shiromaru, T. Fujino, T. Kodama, W. Duley, J. Sanderson, Synthesis of hydrogen- and methyl-capped long-chain polyynes by intense ultrashort laser pulse irradiation of toluene. Carbon **118**, 680–685 (2017). https://doi.org/10.1016/j.carbon.2017.03.096
65. S.M. Lyth, W. Ma, J. Liu, T. Daio, K. Sasaki, A. Takahara, B. Ameduri, Solvothermal synthesis of superhydrophobic hollow carbon nanoparticles from a fluorinated alcohol. Nanoscale **7**, 16087–16093 (2015). https://doi.org/10.1039/c5nr03484a
66. P. Long, Y.Y. Feng, C. Cao, Y. Li, J.K. Han, S.W. Li, C. Peng, Z.Y. Li, W. Feng, Self-protective room-temperature phosphorescence of fluorine and nitrogen codoped carbon dots. Adv. Funct. Mater. 28 (2018) 1800791. https://doi.org/10.1002/adfm.201800791
67. G. Panomsuwan, N. Saito, T. Ishizaki, Simple one-step synthesis of fluorine-doped carbon nanoparticles as potential alternative metal-free electrocatalysts for oxygen reduction reaction. J. Mater. Chem. A **3**, 9972–9981 (2015). https://doi.org/10.1039/c5ta00244c
68. H.P. Liu, T. Ye, C.D. Mao, Fluorescent carbon nanoparticles derived from candle soot. Angew. Chem. Int. Ed. **46**, 6473–6475 (2007). https://doi.org/10.1002/anie.200701271
69. Y.P. Sun, B. Zhou, Y. Lin, W. Wang, K.A.S. Fernando, P. Pathak, M.J. Meziani, B.A. Harruff, X. Wang, H.F. Wang, P.J.G. Luo, H. Yang, M.E. Kose, B.L. Chen, L.M. Veca, S.Y. Xie, Quantum-sized carbon dots for bright and colorful photoluminescence. J. Am. Chem. Soc. **128**, 7756–7757 (2006). https://doi.org/10.1021/ja062677d
70. S.C. Ray, A. Saha, N.R. Jana, R. Sarkar, Fluorescent carbon nanoparticles: synthesis, characterization, and bioimaging application. J. Phys. Chem. C **113**, 18546–18551 (2009). https://doi.org/10.1021/jp905912n
71. S.L. Chin, S. Lagace, Generation of $H_2$, $O_2$, and $H_2O_2$ from water by the use of intense femtosecond laser pulses and the possibility of laser sterilization. Appl. Opt. **35**, 907–911 (1996). https://doi.org/10.1364/Ao.35.000907

72. T. Hamaguchi, T. Okamoto, K. Mitamura, K. Matsukawa, T. Yatsuhashi, Synthesis of hydrophilic and hydrophobic carbon nanoparticles from benzene/water bilayer solution with femtosecond laser generated plasma filaments in water. Bull. Chem. Soc. Jpn. **88**, 251–261 (2015). https://doi.org/10.1246/bcsj.20140247
73. X.M. Pan, M.N. Schuchmann, C. Vonsonntag, Oxidation of benzene by the OH radical - a product and pulse-radiolysis study in oxygenated aqueous-solution. J. Chem. Soc. Perkin Trans. **2**, 289–297 (1993). https://doi.org/10.1039/p29930000289
74. T. Okamoto, E. Miyasaka, K. Mitamura, K. Matsukawa, T. Yatsuhashi, Precipitation of dichloromethane as low-chlorine carbon nanoparticles from water by femtosecond laser pulses. J. Photochem. Photobiol. A **344**, 178–183 (2017). https://doi.org/10.1016/j.jphotochem.2017.05.011
75. W.K. Kipnusu, C. Donate-Buendia, M. Fernandez-Alonso, J. Lancis, G. Minguez-Vega, Nonlinear optics to glucose sensing: multifunctional nitrogen and boron doped carbon dots with solid-state fluorescence in nanoporous silica films, Part. Part. Syst. Char. 37 (2020) 2000093. https://doi.org/10.1002/ppsc.202000093
76. A.A. Astafiev, A.M. Shakhov, A.A. Osychenko, M.S. Syrchina, A.V. Karmenyan, U.A. Tochilo, V.A. Nadtochenko, Probing intracellular dynamics using fluorescent carbon dots produced by femtosecond laser In Situ. ACS Omega **5**, 12527–12538 (2020). https://doi.org/10.1021/acsomega.0c01535
77. Y. Horikawa, T. Okamoto, T. Nakamura, Y.O. Tahara, M. Miyata, S. Ikeda, K. Sakota, T. Yatsuhashi, Synthesis of iron-based nanoparticles from ferrocene by femtosecond laser irradiation: Suppression of the particle growth in a mixture of water and hexane, Chem. Phys. Lett. 750 (2020) 137504. https://doi.org/10.1016/j.cplett.2020.137504
78. T. Okamoto, T. Nakamura, K. Sakota, T. Yatsuhashi, Synthesis of single-nanometer-sized gold nanoparticles in liquid-liquid dispersion system by femtosecond laser irradiation. Langmuir **35**, 12123–12129 (2019). https://doi.org/10.1021/acs.langmuir.9b01854